Molecular-Scale Electronics

Molecular-Scale Electronics

Concept, Fabrication and Applications

Xuefeng Guo
Dong Xiang
Yu Li

WILEY-VCH

Authors

Xuefeng Guo
Peking University
College of Chemistry and Molecular Engineering
292 Chengfu Road
Haidian District
100871 Beijing
China

Dong Xiang
Nankai University
College of Electronic Information and Optical Engineering
No. 94 Weijin Road
300071 Tianjin
China

Yu Li
Peking University
College of Chemistry and Molecular Engineering
292 Chengfu Road
Haidian District
100871 Beijing
China

Library of Congress Card No.:
applied for

British Library Cataloguing-in-Publication Data
A catalogue record for this book is available from the British Library.

Bibliographic information published by the Deutsche Nationalbibliothek
The Deutsche Nationalbibliothek lists this publication in the Deutsche Nationalbibliografie; detailed bibliographic data are available on the Internet at <http://dnb.d-nb.de>.

Print ISBN: 978-3-527-34548-9
ePDF ISBN: 978-3-527-81888-4
ePub ISBN: 978-3-527-81890-7
oBook ISBN: 978-3-527-81891-4

Typesetting SPi Global, Chennai, India

Printing and Binding

Printed on acid-free paper

10 9 8 7 6 5 4 3 2 1

Contents

1

Introduction

What does the future hold for electronic devices? To what extent can their dimensions be reduced in the future? Forty years ago, the gate length of a transistor was approximately 10 μm; however, over the past few decades, traditional transistors have shrunk dramatically and now reach dimensions of about 3 nm in research devices [1, 2]. The further miniaturization of electronic devices remains extremely challenging, which is primarily due to either technique limitations or lack of fundamental understanding of transport mechanisms [3]. In this sense, it is remarkable that chemically identical molecules, with sizes on the order of 1 nm, can be synthesized in bulk while accomplishing a variety of electronic tasks, including conducting wire, rectification, memory, and switching; thus, they might have the potential to partly replace traditional solid-state device counterparts in the future. Comprehensive experimental findings in electron transport through individual molecules introduce the idea that beyond traditional complementary metal oxide semiconductor (CMOS) technologies, the ultimate goal for shrinking electrical circuits is the realization of molecular-scale/single-molecule electronics because single molecules constitute the smallest stable structures imaginable [4–7]. Molecular-scale electronics, which is the concept of creating functional electrical circuits based on properties inherent in individual or ensemble molecules, have several unparalleled advantages in comparison with silicon-based electronic devices. Firstly, the extremely reduced size of the molecules in order of 1 nm may enable heightened capacities and faster performances. Moreover, such small size of the molecule provides the ability to surpass the limit of conventional silicon circuit integration. Secondly, the abundant diversity in the molecular structures, which can be changed via flexible chemical designs, may lead to a direct observation of novel effects as well as the fundamental discovery of physical phenomena that are not accessible by using traditional materials or approaches. Thirdly, another attractive feature of this approach is the universal availability of molecules due to the ease of bulk synthesis, thus potentially leading to low-cost manufacturing.

In fact, molecular-scale electronics is currently a research area of focus because it not only meets the increasing technical demands of the miniaturization of traditional silicon-based electronic devices but also provides an ideal window of exploring the intrinsic properties of materials at the molecular level. Generally, molecular-scale electronics refers to the use of single molecules or nanoscale

Molecular-Scale Electronics: Concept, Fabrication and Applications,
First Edition. Xuefeng Guo, Dong Xiang, and Yu Li.

collections of single molecules as electronic components [2, 8–10]. The primary theme in this field is the construction, measurement, and understanding of the current–voltage responses of electrical circuits, in which molecular systems play an important role as pivotal elements [11]. Indeed, over the past decade, we observed significant developments achieved in both experiments and theory to reveal the electronic and photonic responses of these conceptually simple molecular junctions [5–12].

The history of molecular-scale electronics is surging forward with great momentum, and outstanding scientists have provided significant contributions to the development of molecular-sale electronics. Briefly, several pioneering studies were performed in the 1970s at the laboratory of Hans Kuhn along with Mann and coworkers [10, 13–15]. They developed the first effective self-assembly techniques (via molecular bond formation) to prepare molecular structures in which organic molecules adhered to solid substrate surfaces without using simple dispersion forces. Additionally, these groups reported a few of the earliest reproducible electrical transport measurements through molecules. After Mann and Kuhn's study, there were a number of important follow-up experiments and measurements [10]. During the same period, a visionary concept of exploiting the intrinsic functionalities of molecules for electronics (i.e. a single molecule could function as a rectifier) was sketched out by Aviram and Ratner [16]. Then, the desire of using molecules as functional units in electronic circuits motivated many researchers over the next few decades. A significant development occurred in 1982 with the development of a scanning probe microscopy (SPM) [17]. The SPM is a powerful technique regarded as a milestone in the history of molecular electronics, by which both the surface topography and its transport information can be addressed [18]. By using the SPM, Weiss and his colleagues performed the first experiment resembling transport through single molecules, thus launching a promising approach to realizing the goal [19]. Nonetheless, the SPM technique is limited to lab experiments and cannot be directly applied to realistic device fabrication. In addition to the development of the SPM, various techniques based on either metal or carbon nanoelectrodes have been introduced for single-molecule studies in the following years, including mechanically controllable break junctions, electromigration breakdowns, electrical chemical depositions, and surface diffusion mediated depositions [20–23].

The success of these techniques led to an explosion interest in using individual molecules in molecular-scale electronics and significantly promoted the development of the field. With improved measurement capability, a number of new effects beyond electronic transport, including electron-mechanics, thermoelectricity, optoelectronics, quantum interferences, and spin transports, were discovered at the single-molecule level [6, 24–27]. In contrast to metal electrodes, non-metal materials, such as conducting polymers and carbon-based materials, can be regarded as molecules themselves, and they possess a natural compatibility with the traditional silicon-based technique and excellent mechanical flexibility [28, 29]. Hence, the past decade was an exciting developmental period for non-metal-based molecular electronics. For example, nanotubes and graphene have been used as point contacts for creating robust single-molecule junctions with desired functions, thus paving the way for practical applications [30, 31].

The theory developed for interpreting the current–voltage characteristics in molecular junctions began to appear in the 1990s. The early approach was to use the Landauer formulation to explain the electron transport behavior [32, 33]. In this simple picture, the charge transport through the molecular junctions was interpreted in terms of elastic scattering with a key parameter, known as the "transmission coefficient," which describes how effective a molecule was in scattering the incoming electron from the right lead into the left lead. Additionally, more powerful formulations, including the non-equilibrium Green's function (NEGF) approach, Breit–Wigner formula and Simmons model, have been used to interpret the electron transport behaviors through a molecule [34–37]. In particular, the NEGF approach demonstrated the capability of combining both the elastic and inelastic effects with the metal–electrode coupling and gating effects [38]. However, practical molecular junctions are really complex, and the development of advanced theories that consider all of the factors, including real molecules, electrodes, molecule–electrode interfaces, electron–phonon interactions, spin–orbit interactions, and electron–solvent couplings, is of significant importance to the comprehensive advancement in the field [34]. The motivation for the theory development is far from saturated, and significant efforts are needed to reduce the gap between the theoretical calculations and the experimental data.

Nonetheless, numerous challenges need to be addressed before single-molecule devices can be used as commercial products. The basic challenge involves determining the structure–function relationships for the electronic transport (intra- or intermolecular) through a junction containing one or a few molecules. It is a complicated engineer since the behaviors of the molecular devices are strongly dependent on the electrode fabrication process, selection of electrode materials, contact chemistry, and number of molecules to be tested. Unlike traditional semiconductors that use a standard product line, there are no standard processes for molecular device fabrication thus far. A small variation in each process may result in a large change in molecular devices. The resulting challenge is the reproducibility. Generally, the passing current detected is small (~nA) when the target unit scales down to the single-molecule scale, and thus the current is sensitive to the environmental changes, e.g. contamination, radiation, humidity, temperature variation, and other external vibrations. Furthermore, molecular aging is another factor that leads to reproducibility problems. Another primary challenge involves developing a technology for the mass production of single-molecule devices at low cost. Although the molecules can be synthesized in large quantities, most widely used techniques, such as electron beam lithography (EBL) for nanoelectrode fabrication, are expensive for mass production. Decreasing the unit size and increasing the integration level without sacrificing cost remains a difficult task in the future.

Although it is a long way to achieve commercially available molecular electronics, basic researches in this area have advanced significantly. Specifically, the drive to create functional molecular devices has pushed the frontiers of both measurement capabilities and fundamental understanding of varied physical phenomena at the single-molecule level. The field of molecular electronics has become a fascinating playground for scientists to explore new fundamental

concepts and new applications. Several recent articles focused on specific experimental aspects of molecular electronics [11, 39–51]. In this comprehensive book, we offer a broad overview of this field, with a particular focus on several vital issues, such as fabricating techniques for molecular junction, discovering novel physical phenomena, using characterization techniques, and developing strategies for integrating molecular functionalities into electronic device configurations. We address the primary advances with the most general applicability and emphasize new insights into the development of efficient platform methodologies for building reliable molecular electronic devices with desired functionalities by using a combination of programmed bottom-up self-assembly and sophisticated top-down device fabrication. To do so, we first summarize a number of different efficient approaches for forming molecular-scale junctions and discuss various experimental techniques for examining these nanoscale circuits in detail. Then, we highlight the major contributions and new concepts of integrating molecular functionalities into the electrical circuits, which have been neglected in most previous books. Furthermore, the perspectives and key issues that are critical to the success of the next-generation single-molecule devices toward practical applications are discussed, such as device reproducibility, system integration, and theoretical simulation. These analyses are valuable for thoroughly understanding how device fabrication processes, such as the testbed architectures used, molecule number and defect density tested, as well as the nature of the electrode–molecule interface, influence the intrinsic properties of the molecules, which are of crucial importance to the development of future practical molecular electronic devices.

References

1 Lörtscher, E. (2013). Wiring molecules into circuits. *Nat. Nanotechnol.* 8: 381–384.
2 Wilson, L. (2015). *International Technology Roadmap for Semiconductors (ITRS)*. Semiconductor Industry Association.
3 Xiang, D., Wang, X.L., Jia, C.C. et al. (2016). Molecular-scale electronics: from concept to function. *Chem. Rev.* 116: 4318–4440.
4 Ratner, M.A. (2013). A brief history of molecular electronics. *Nat. Nanotechnol.* 8: 378–381.
5 Bryce, M.R. and Petty, M.C. (1995). Electrically conductive Langmuir–Blodgett-films of charge-transfer materials. *Nature* 374: 771–776.
6 Tour, J.M., Reinerth, W.A., Jones, L. et al. (1998). Recent advances in molecular scale electronics. *Ann. N.Y. Acad. Sci.* 852: 197–204.
7 Petty, M.C., Bryce, M.R., and Bloor, D. (1995). *An Introduction to Molecular Electronics*. New York: Oxford University Press.
8 Cuevas, J.C. and Scheer, E. (2010). *Molecular Electronics: An Introduction to Theory and Experiment*. River Edge, NJ: World Scientific.
9 Heath, J.R. (2009). Molecular electronics. *Ann. Rev. Mater. Res.* 39: 1–23.
10 Xin, N., Guan, J., Zhou, C. et al. (2019). Concepts in the design and engineering of single-molecule electronic devices. *Nat. Rev. Phys.* 1: 211–230.
11 Nitzan, A. and Ratner, M.A. (2003). Electron transport in molecular wire junctions. *Science* 300: 1384–1389.

12 Metzger, R.M. (2015). Unimolecular electronics. *Chem. Rev.* 115: 5056–5115.
13 Mann, B. and Kuhn, H. (1971). Tunneling through fatty acid salt monolayers. *J. Appl. Phys.* 42: 4398–4405.
14 Polymeropoulos, E.E. and Sagiv, J. (1978). Electrical conduction through adsorbed monolayers. *J. Chem. Phys.* 69: 1836–1847.
15 Netzer, L. and Sagiv, J. (1983). A new approach to construction of artificial monolayer assemblies. *J. Am. Chem. Soc.* 105: 674–676.
16 Aviram, A. and Ratner, M.A. (1974). Molecular rectifiers. *Chem. Phys. Lett.* 29: 277–283.
17 Binning, G., Rohrer, H., Gerber, C. et al. (1982). Surface studies by scanning tunneling microscopy. *Phys. Rev. Lett.* 49: 57–61.
18 Zandvliet, H.J.W. and van Houselt, A. (2009). Scanning tunneling spectroscopy. *Annu. Rev. Anal. Chem.* 2: 37–55.
19 Bumm, L.A., Arnold, J.J., Cygan, M.T. et al. (1996). Are single molecular wires conducting? *Science* 271: 1705–1707.
20 Reed, M.A., Zhou, C., Muller, C.J. et al. (1997). Conductance of a molecular junction. *Science* 278: 252–254.
21 Park, J., Pasupathy, A.N., Goldsmith, J.I. et al. (2002). Coulomb blockade and the Kondo effect in single-atom transistors. *Nature* 417: 722–725.
22 Xiang, J., Liu, B., Wu, S.T. et al. (2005). A controllable electrochemical fabrication of metallic electrodes with a nanometer/Angstrom-sized gap using an electric double layer as feedback. *Angew. Chem. Int. Ed.* 117: 1291–1294.
23 Bonifas, A.P. and McCreery, R.L. (2010). 'Soft' Au, Pt and Cu contacts for molecular junctions through surface-diffusion-mediated deposition. *Nat. Nanotechnol.* 5: 612–617.
24 Pasupathy, A.N., Bialczak, R.C., Martinek, J. et al. (2004). The Kondo effect in the presence of ferromagnetism. *Science* 306: 86–89.
25 Vazquez, H., Skouta, R., Schneebeli, S. et al. (2012). Probing the conductance superposition law in single-molecule circuits with parallel paths. *Nat. Nanotechnol.* 7: 663–667.
26 Diez-Perez, I., Hihath, J., Hines, T. et al. (2011). Controlling single-molecule conductance through lateral coupling of π orbitals. *Nat. Nanotechnol.* 6: 226–231.
27 Reddy, P., Jang, S.Y., Segalman, R.A. et al. (2007). Thermoelectricity in molecular junctions. *Science* 315: 1568–1571.
28 Akkerman, H.B., Blom, P.W.M., de Leeuw, D.M. et al. (2006). Towards molecular electronics with large-area molecular junctions. *Nature* 441: 69–72.
29 Sayed, S.Y., Fereiro, J.A., Yan, H.J. et al. (2012). Charge transport in molecular electronic junctions: Compression of the molecular tunnel barrier in the strong coupling regime. *Proc. Natl. Acad. Sci. U. S. A.* 109: 11498–11503.
30 Cao, Y., Dong, S., Liu, S. et al. (2012). Building high-throughput molecular junctions using indented graphene point contacts. *Angew. Chem. Int. Ed.* 124: 12228–12232.
31 Guo, X., Small, J.P., Klare, J.E. et al. (2006). Covalently bridging gaps in single-walled carbon nanotubes with conducting molecules. *Science* 311: 356–359.
32 Ratner, M.A., Davis, B., Kemp, M. et al. (1998). Molecular wires: Charge transport, mechanisms and control. *Ann. N. Y. Acad. Sci.* 852: 22–37.

33 Mujica, V., Kemp, M., and Ratner, M.A. (1994). Electron conduction in molecular wires. I. A scattering formalism. *J. Chem. Phys.* 101: 6849–6855.

34 Lindsay, S.M. and Ratner, M.A. (2007). Molecular transport junctions: Clearing mists. *Adv. Mater.* 19: 23–31.

35 Zimbovskaya, N.A. and Pederson, M.R. (2011). Electron transport through molecular junctions. *Phys. Rep.* 509: 1–87.

36 Wang, W.Y., Lee, T., and Reed, M.A. (2005). Electron tunnelling in self-assembled monolayers. *Rep. Prog. Phys.* 68: 523–544.

37 Lambert, C.J. (2015). Basic concepts of quantum interference and electron transport in single-molecule electronics. *Chem. Soc. Rev.* 44: 875–888.

38 Lin, L.L., Jiang, J., and Luo, Y. (2013). Elastic and inelastic electron transport in metal-molecule(s)-metal junctions. *Phys. E* 47: 167–187.

39 Aradhya, S.V. and Venkataraman, L. (2013). Single-molecule junctions beyond electronic transport. *Nat. Nanotechnol.* 8: 399–410.

40 Sun, L., Diaz-Fernandez, Y.A., Gschneidtner, T.A. et al. (2014). Single-molecule electronics: from chemical design to functional devices. *Chem. Soc. Rev.* 43: 7378–7411.

41 Tao, N.J. (2009). Electron transport in molecular junctions. *Nanoscience and Technology* : 185–193.

42 Shen, Q., Guo, X.F., Steigerwald, M.L. et al. (2010). Integrating reaction chemistry into molecular electronic devices. *Chem. Asian J.* 5: 1040–1057.

43 Galperin, M., Ratner, M.A., Nitzan, A. et al. (2008). Nuclear coupling and polarization in molecular transport junctions: beyond tunneling to function. *Science* 319: 1056–1060.

44 van der Molen, S.J. and Liljeroth, P. (2010). Charge transport through molecular switches. *J. Phys.: Condens. Matter* 22: 133001.

45 Natelson, D., Li, Y.J., and Herzog, J.B. (2013). Nanogap structures: Combining enhanced Raman spectroscopy and electronic transport. *Phys. Chem. Chem. Phys.* 15: 5262–5275.

46 Moth-Poulsen, K. and Bjornholm, T. (2009). Molecular electronics with single molecules in solid-state devices. *Nat. Nanotechnol.* 4: 551–556.

47 Carlson, A., Bowen, A.M., Huang, Y. et al. (2012). Transfer printing techniques for materials assembly and micro/nanodevice fabrication. *Adv. Mater.* 24: 5284–5318.

48 Tyagi, P. (2011). Multilayer edge molecular electronics devices: A review. *J. Mater. Chem.* 21: 4733–4742.

49 Flood, A.H., Stoddart, J.F., Steuerman, D.W. et al. (2004). Whence molecular electronics? *Science* 306: 2055–2056.

50 Li, T., Hu, W.P., and Zhu, D.B. (2010). Nanogap electrodes. *Adv. Mater.* 22: 286–300.

51 McCreery, R.L. and Bergren, A.J. (2009). Progress with molecular electronic junctions: meeting experimental challenges in design and fabrication. *Adv. Mater.* 21: 4303–4322.

2

Metal Electrodes for Molecular Electronics

In molecular electronic junctions, where molecules are used as electronic device components, the electrical signal comes in and out of the molecules via contact-coupled electrodes. The electrodes can be classified as metal or non-metal electrodes. The development of molecular electronics initially started from the use of metal electrodes. Hence, we first summarize the development of molecular devices based on metal electrodes and then move to those based on non-metal electrodes, particularly carbon-based electrodes. The typical methods for the different electrodes are listed in Table 2.1. It can be observed that each method has its own unique advantages as well as the disadvantages.

2.1 Single-Molecule Junctions

The initial idea of using individual molecules as active electronic elements provided the impetus to develop a variety of experimental platforms to probe their electronic transport properties. Among these platforms, single-molecule junctions based on a metal–molecule–metal architecture have received considerable attention and contributed significantly to the fundamental understanding of the physical phenomena required to develop molecular-scale electronic devices [1]. As mentioned earlier, the scanning probe microscopy (SPM) technique is regarded as a milestone in the history of molecule electronics because it has made a great contribution to the development of molecular electronics and continues to promote the advancement of molecular electronics in the future.

2.1.1 Scanning Probe Microscopy Break Junctions

Scanning probe microscopy typically includes both scanning tunneling microscopy (STM) and atomic force microscopy (AFM). STM plays a unique role in the field of molecular electronics via STM break junctions. The most commonly used method is the *in situ* molecular break junction technique, as skillfully demonstrated by Tao and coworkers [2, 3]. This *in situ* method can rapidly create thousands of molecular junctions by repeatedly moving a tip in and out of contact with the substrate electrode adsorbed with the sample molecules. The tip movement can be precisely controlled by a piezoelectric

Molecular-Scale Electronics: Concept, Fabrication and Applications,
First Edition. Xuefeng Guo, Dong Xiang, and Yu Li.

Table 2.1 Comparison of molecular junctions fabricated by different approaches.

Methods for molecular junctions	Number of molecules	Gating control	Addressability	Fabrication	Yield
Scanning probe microscopy	Single	Electrochemical	Difficult	Sophisticated	H
Mechanically controllable break junction	Single	Electrostatic	No	Sophisticated	H
Electromigration nanogap	Single	Electrostatic	Yes	Sophisticated	L
Electrochemical deposition	Single	Electrostatic	Yes	Sophisticated	H
Surface-diffusion-mediated deposition	Single	No	No	Sophisticated	H
Lift-and-float approach	Ensemble	No	Difficult	Straightforward	H
Liquid metal	Ensemble	Electrochemical	Difficult	Straightforward	H
Nanopore or nanowell	Ensemble	No	Yes	Straightforward	M
Nanoimprint lithography	Ensemble	No	Yes	Sophisticated	H
Self-aligned lithography	Ensemble	Electrostatic	Difficult	Straightforward	M
On-wire lithography	Ensemble	No	Difficult	Sophisticated	M
Buffer interlayer-based junction	Ensemble	No	Possible	Straightforward	H
Crosswire or crossbar	Ensemble	No	Possible	Sophisticated	M
On-edge molecular junction	Ensemble	No	Difficult	Straightforward	H
CNT-based junction	Single	Electrostatic	Yes	Sophisticated	M
Graphene-based junction	Single	Electrostatic	Yes	Sophisticated	H
Silicon-based junction	Ensemble	No	Difficult	Sophisticated	M
Polymer-based junction	Ensemble	No	Difficult	Sophisticated	M

In the yield column, H, M, and L indicate the high, middle, and low yield, respectively.

transducer (PZT), which is constructed with lead zirconate titanate. Typically, the molecules in the study have two end groups that bind to the tip and the substrate electrodes. The molecules have an opportunity to bridge both the tip and the substrate electrode when the tip is brought close enough to the substrate, as indicated in Figure 2.1. The tip is then pulled away from the substrate to break the metal–molecule–metal junction. By accurately controlling the movement of the tip, i.e. changing the distance between the tip and the substrate, the number of bridged molecules can be changed [3].

The conductance can be measured as a function of the relative tip displacement to yield conductance traces. Xu and Tao reported a simple and unambiguous measurement of a single-molecule conductance, achieved by repeatedly forming thousands of gold–molecule–gold junctions [2]. The conductance histograms were constructed from thousands of conductance traces revealed well-defined

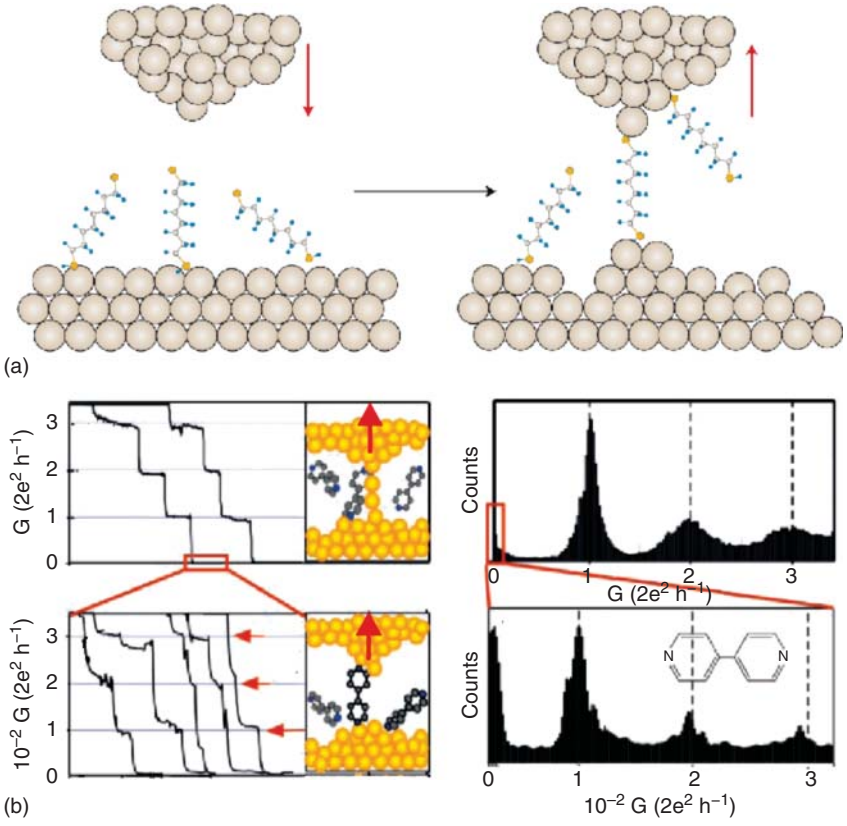

Figure 2.1 (a) STM-based technique used to form single Au–molecule–Au junctions. When the Au tip moves near the Au substrates, which are covered with target molecules, Au–molecule–Au junctions are formed. When the Au tip is pulled away, the molecular bridges then lose contact with either the tip or the Au substrate. Source: Reproduced with permission from Tao [4]. Copyright 2006, Springer Nature. (b) Single-molecule conductance measurements. The conductance of a gold–gold contact decreases in quantum steps as the tip is gradually pulled away from the substrate. The corresponding conductance histogram illustrates well-defined peaks near $1G_0$, $2G_0$, and $3G_0$ due to the conductance quantization. After the gold–gold contact is completely broken, a new series of conductance steps appear due to the formation of the molecular junctions. A conductance histogram shows peaks near $0.01G_0$, $0.02G_0$, and $0.03G_0$, which can be ascribed to one, two, and three molecules, respectively. Source: Reproduced with permission from Xu and Tao [2]. Copyright 2003, AAAS.

peaks at integer multiples of a fundamental conductance value. This observation provides a method to identify the conductance of a single molecule. By using the conductance histograms, Cheng et al. demonstrated that the formation of a direct Au—C bond was likely and determined that the conductance of these molecular junctions is ~100 times larger than that of the other binding groups [5]. By comparing the Au–N, Au–S, Au–P, and donor–acceptor bonds, Venkataraman et al. discovered that the binding strength and the conductivity gradually increased from Au–NH_2R and Au–SMeR to Au–PMe_2R [6, 7]. A detailed discussion related to the electrode–molecule contact interface can be found in a review article by

the Guo and coworkers [8]. These findings offer a new method for creating reproducible and highly conducting metal–organic contacts.

A technique closely related to STM is AFM, in which a force is used to control the tip-positioning [9]. The difference between AFM and STM should be noted. In STM, current instead of force is used to control the tip-positioning. Because the conductance properties of the molecules are generally unknown, the position of the probe with respect to the molecules is ambiguous, which may result in the penetration of the tip into the monolayer in the STM experiments. Conversely, with independent feedback signals, AFM allows the probe to be controllable in either the contact or the non-contact mode, thus effectively avoiding the tip penetration. However, one disadvantage of AFM is that the electrical properties of the target molecules are unavailable. To solve this problem, a significant improvement was demonstrated by Wold and Frisbie who described a new approach for the formation of metal–molecule–metal junctions by placing a conducting AFM tip in contact with a metal-supported molecular film, which is known as the conducting probe atomic force microscopy (CP-AFM) technique [10]. Although the conducting probe tip of the CP-AFM coated with a metallic layer is larger than an atomically sharp STM tip, the CP-AFM method measures both the mechanical and the electrical properties of the molecules simultaneously [3, 11]. By using the CP-AFM method, Aradhya et al. measured the conductance of pyridine derivatives and simultaneously acquired consistent force traces during the junction elongation, thus providing a quantitative characterization of the van der Waals' interactions at the metal/organic interfaces, as indicated in Figure 2.2 [12, 13].

In the STM or CP-AFM experiments, once the molecular junctions are formed, the tip (top electrode) can be fixed, and the characterization of the electron

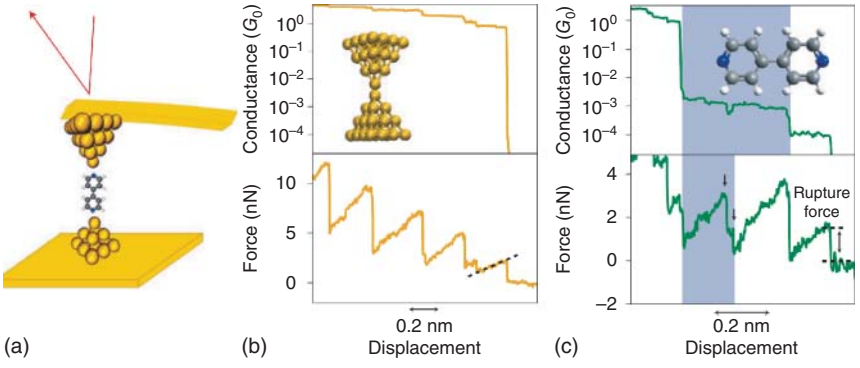

Figure 2.2 Working principle of AFM: (a) Schematic of a 4,4′-bipyridine junction formed between a gold-coated AFM tip and a gold substrate. By using a laser beam, the deflection of the cantilever can be monitored, and the corresponding mechanical force between the tip and the sample can be obtained. (b, c) Experimentally measured conductance (upper panel) and corresponding simultaneously acquired force (lower panel) traces during the junction elongation of bare gold junctions (b) and molecular junctions (c). The shaded areas in the upper panel represent high-conductance molecular regimes. The shaded areas in the low panel represent structural rearrangements within the high conductance regime. The dashed lines indicate a complete rupture of the molecular junctions. Source: Reproduced with permission from Aradhya et al. [12]. Copyright 2012, American Chemical Society.

transport through the molecule junction can be performed [14, 15]. To date, STM and AFM have revealed many interesting phenomena in single-molecule junctions, such as large magnetoresistance [16, 17], spin-split molecular orbitals [18], Kondo resonance [19], Coulomb blockade effect [20], negative differential resistance behavior [21, 22], strain-induced binding configuration [23], and redox switch [24, 25], significantly accelerating the development of molecular electronics. Additionally, over the past few decades, the electron transport pathway through the molecular junctions [26, 27] and the charge transport mechanisms [5, 28, 29] have been further understood. Correspondingly, these single-molecule junctions represent the possibility of achieving the ultimate goal of miniaturizing the electrical circuits and providing ideal platforms for probing the quantum transport phenomena.

In particular, experiments on individual molecules by using scanning probe microscopies have led to further insights into the quantum electronics of the molecular systems [30–32]. The conductance properties of solid-state mesoscopic structures are primarily dominated by quantum effects at low temperatures. For example, if partial electron waves propagating through the two branches of a ring-shaped mesoscopic structure interfere destructively with each other, the conductance will be suppressed. Conversely, if they interfere constructively, the conductance will be enhanced. For certain classes of molecular junctions, a similar quantum interference is expected to occur as the electron waves propagate through the molecular orbitals (or quasi-degenerate electronic states) that are separated in both space and energy [33, 34]. Guédon et al. reported the observation of a destructive quantum interference in the charge transport through the molecular junctions [31]. They synthesized a few rigid-conjugated molecular wires. Two exemplary molecular structures (AQ-DT and AC-DT) are illustrated in Figure 2.3. The two-dimensional conductance histograms indicated that the conductance of the AQ-DT was nearly 2 orders of magnitude lower than that of the AC-DT, as seen in Figure 2.3. This result is remarkable because the energy difference between the highest occupied molecular orbital (HOMO) and the lowest unoccupied molecular orbital (LUMO) levels is extremely similar for these molecules, and the two types of molecules possess the same end groups and a similar molecular length. Combined with the density functional theory (DFT) calculations, they demonstrated that there were three unaligned localized molecular orbitals (LMOs) for the AQ-DT. Thus, the electron can be transported through two different pathways via the LMOs, thereby yielding the phase difference within the HOMO–LUMO gap, i.e. the partial waves interfere destructively, which results in a poor conductance of the AQ-DT. Their investigation revealed that it is possible to control the degree of interference and change the value of the molecule conductance through chemical modifications of the molecular structure. Most of the studies have focused on quantum interference (QI) of the π-channel. Very recently, a series of saturated silicon-based molecules consisting of a σ-system bicyclo[2.2.2]octasilane moiety with the destructive quantum interference have been proposed [35].

The occurrence of the destructive quantum interference strongly depends on the molecular structure as well as the temperature. In an experiment, the vibrations are inherent to any molecular junction, particularly at room temperature.

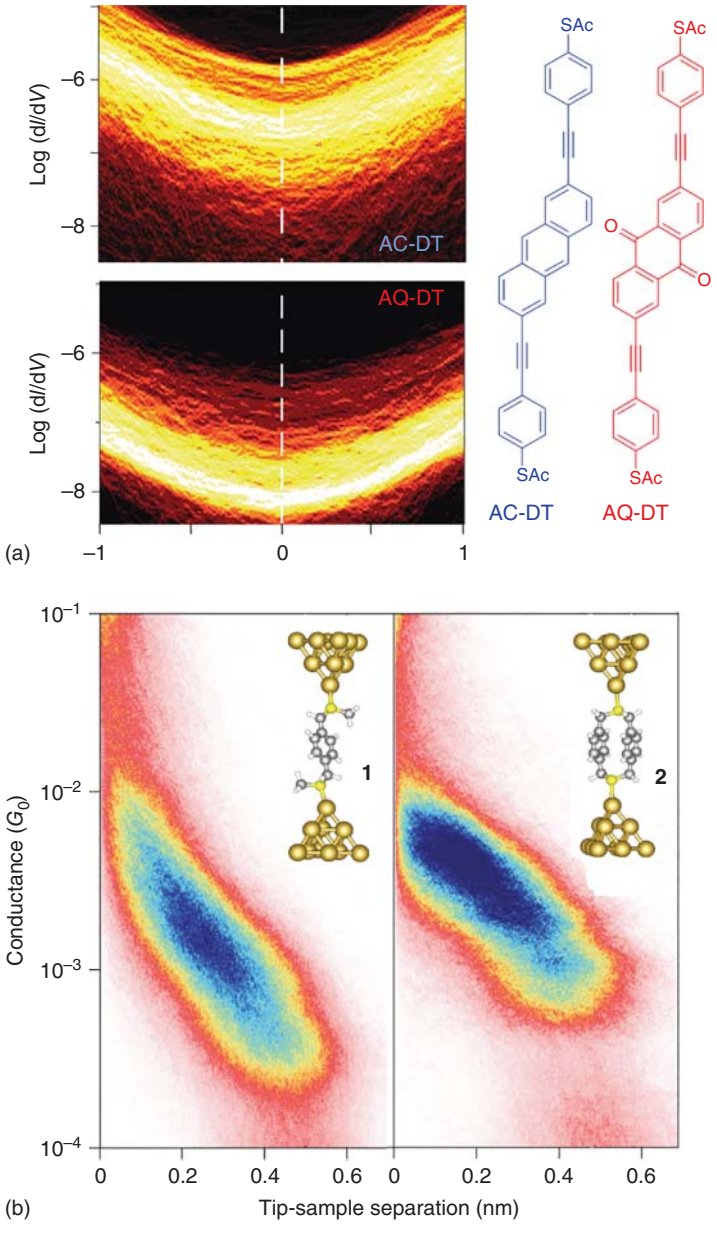

Figure 2.3 Quantum interference (a) Logarithmically binned two-dimensional histograms for d*I*/d*V* values versus a bias voltage *V*. The color scale indicates the number of counts. Right panel: Similar chemical structures of the investigated molecules AQ-DT and AQ-DT. Due to the destructive interference, the conductance of the AQ-DT is 2 orders of magnitude lower than that of the AC-DT. Source: Reproduced with permission from Guedon et al. [31]. Copyright 2012, Springer Nature. (b) Two-dimensional conductance–displacement histograms for junctions with molecules **1** and **2**; Inset: Chemical structures of the investigated molecules with single-(**1**) and double-(**2**) backbone molecules. Due to the constructive interference, the conductance of a double-backbone molecular junction is two times higher than that of a single-backbone junction. Source: Reproduced with permission from Vazquez et al. [30]. Copyright 2012, Springer Nature.

At a high temperature, the vibrations coupled to the electronic states may provide a strong decoherence mechanism in the molecular junctions, where the electron transport is governed by destructive interference effects. Consequently, the destructive interference between the involved pathways can be quenched [34]. With an appropriate molecular structure design, it is possible to observe the constructive quantum interference phenomenon. Vazquez et al. provided direct evidence for constructive quantum interference in molecular junctions at room temperature [30]. As indicated in Figure 2.3b (inset), they synthesized a series of molecular systems that contained either one backbone or two backbones in parallel that were bonded together co-facially by a common linker on each end. The conductance measurements indicated that the conductance of a double-backbone molecular junction could be two times higher than that of a single-backbone junction, thus providing clear evidence for constructive interference as electrons were transported through the parallel molecular wire components under ambient conditions at room temperature.

2.1.1.1 Beyond Traditional SPM Break Junctions

In the STM or AFM methods, one challenge is that even though molecules are adsorbed onto the substrate and form a well-defined molecule–substrate bottom contact, the tip–molecule contact is typically less well defined [3]. Moreover, due to the relatively large size of the tip, it will be difficult to directly address individual molecules if the tip attempts to contact the molecular layer, and the number of sandwiched molecules will be uncertain, which prevents the absolute conductance and electrical properties of the target molecule to be determined. Fortunately, different research groups have presented novel strategies to reduce the number of addressed molecules and create well-defined (strong) top contacts over the past few years, as indicated in Figure 2.4. These strategies can be classified as tip modification and substrate modification.

(1) *Electrochemical jump-to-contact scanning tunneling microscopy break junction* (*EC-STM*). Zhou et al. developed an electrochemical strategy for STM break junctions by establishing a chemically well-defined metallic contact through a jump-to-contact mechanism between the tip and the substrate, as indicated in Figure 2.4a [36, 42]. The gold tip is fixed above the substrate, and the tip is electrochemically deposited *in situ* with a foreign metal of interest until a bridge between the tip and the substrate is formed. Different foreign metals, such as Cu, Pd, and Fe, were successfully used to form a thin nanowire to bridge the tip and the substrate [36, 43]. When the tip was pulled away from the substrate, the elongation of the bridged nanowires generated two atomic-scale sharp electrodes, which made it feasible to form single-molecule junctions. The strategy presented in their study not only extends the capability of STM break junctions to create a variety of metal nanowires for further investigations, but also provides opportunities to generate well-defined metal–molecule–metal junctions with a variety of choices of metals in the junctions.

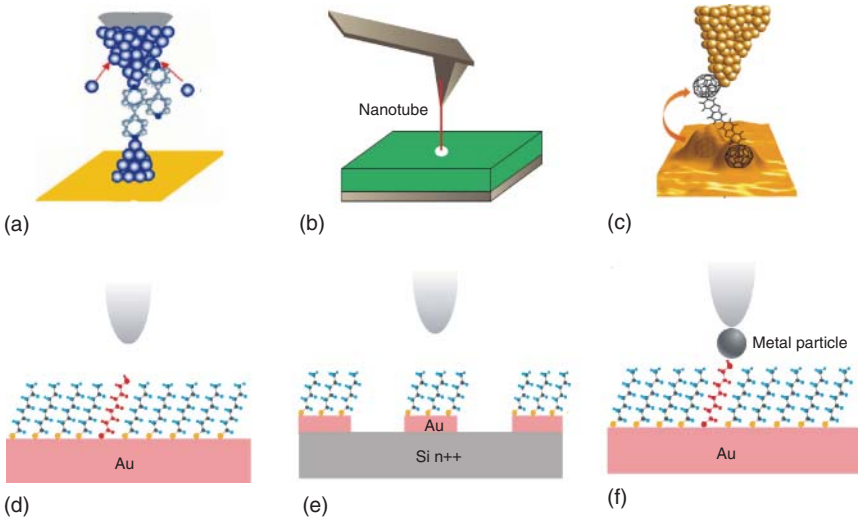

Figure 2.4 SPM-based molecular junctions. (a) Electrochemical jump-to-contact scanning tunneling microscopy break junction (EC-STM). Source: Reprinted with permission from Zhou et al. [36]. Copyright 2013, American Institute of Physics. (b) Attaching nanotubes to a metal-coated AFM tip. Source: Reprinted with permission from Wilson and Macpherson [37]. Copyright 2009, Springer Nature. (c) C_{60}-terminated SPM break junction. Source: Reprinted with permission from Leary et al. [38]. Copyright 2011, American Chemical Society. (d) Inserted target molecules into an ordered array of reference molecules. Source: Reprinted with permission from Bumm et al. [39]. Copyright 1996, AAAS. (e) Substrate-modified SPM junction. Source: Reprinted with permission from Smaali et al. [40]. Copyright 2012, American Chemical Society. (f) Nanoparticle-based SPM junction. Source: Reprinted with permission from Cui et al. [41]. Copyright 2001, AAAS.

(2) *Nanotube-tip-based SPM break junction.* In addition to producing smaller tips, the AFM researchers make great efforts to develop tips that were long enough, provided faithful representations of the surface topographies with high resolution, and mechanically non-invasive. Carbon nanotubes have demonstrated considerable potential to be used as AFM tips [37]. The main features of the carbon nanotubes are their nanometer-scale diameters, high aspect ratio, and remarkable mechanical and electrical properties. The carbon nanotubes were first used as AFM tips five years after their discovery [44]. It should be noted that to electrically probe molecules using this method, it should be ensured that the nanotubes are metallic; otherwise the electrical interpretation would be complicated. There are two key aspects to the fabrication of the nanotube AFM tips: attachment [45, 46] (the nanotube must be fixed to the AFM probe) and modification [47]. The fabrication, modification, and application of the nanotube-based SPM can be found in the article [37]. It is expected that with a proper modification to the end of the nanotube, it is feasible to form nanotube–molecule–metal junctions and characterize the properties of these molecular junctions, as shown in Figure 2.4b. To improve AFM to even higher resolutions, Gross et al. replaced the metal tip of conventional AFMs with a single molecule

of carbon monoxide (CO) [48, 49], which is extremely stable as well as subject to significantly smaller van der Waals forces when in close proximity to a sample. To demonstrate their new tool, the researchers applied their AFM tips to several types of molecules, and the observed spacing between individual atoms was as small as 0.14 nm, thus dramatically improving the resolution of AFM.

(3) *C_{60}-terminated SPM break junction*. One of the challenging goals of molecular electronics is to wire exactly one molecule between two electrodes due to the different coordination modes of the anchor group, especially under ambient conditions. To solve this problem, Leary et al. described a new and straightforward method for unambiguously addressing a single C_{60}–Fl_2–C_{60} molecule on a metal surface [38], as indicated in Figure 2.4c. Their strategy used C_{60}-terminal groups as molecular beacons to make molecules to be visualized, which allowed the single molecule to be accurately targeted using STM. The C_{60} groups not only provide a clear visual signature for the molecule but also serve as the effective anchoring groups. Once the tip and the surface are wired, the manner in which the conductance of a purely one-molecule junction evolves with time can be monitored by stretching the molecule in the junction, observing the characteristic current plateaus upon elongation, and performing a direct I–V spectroscopy. Thanks to C_{60} spherical geometry and the multi-interaction configurations of its carbon atoms with metal electrodes, it has been widely used as molecular bridges between two electrodes in break junctions, and different experiments had been performed to reveal this new class of molecules, which allows incorporation of many linkers between the two C_{60} termini. For example, Moreno-García et al. investigate charge transport in C_{60}-based dumbbell-type molecules recently [50]. Two distinct single molecule conductance states were observed, depending on the pressure exerted by the probe on the junction, thus allowing the molecule to function as a mechanically driven molecular switch.

(4) *Molecule layer-modified SPM junction*. One advantage of the SPM technology is that the gap size between the tip and the substrate can be continuously and accurately changed. By using a tip-withdraw strategy, the number of wired molecules can change, and the single-molecule junctions can be addressed. However, it will be a significant challenge to address the individual molecules when the molecule only possesses one bonding group, for which the tip-withdraw strategy did not work efficiently. One way to solve this problem is to embed target molecules into the matrix of another, which is often the less conducting molecule, as shown in Figure 2.4d. Bumm et al. presented an approach to study the current through high-conductance molecular wire candidates inserted into a non-conducting alkanethiol monolayer [39]. In this approach, the target molecules were taller (higher) than the surrounding poor conducting molecules, thus ensuring that only the target molecules were contacted. This strategy provides a method to study single-molecule electrical properties when the *in situ* break junction technology is unavailable.

(5) *Substrate-modified SPM junction*. Clement et al. reported a new approach that allows the conductance of up to a million of junctions to be measured

within a single CP-AFM image [51], as indicated in Figure 2.4e. They first fabricated a large array of single crystal Au nanodots on a highly doped silicon substrate. Then, a molecular layer was formed at the nanodot surface. Finally, a conducting AFM tip was driven to contact the molecules, and a metal–molecule–metal–silicon junction was subsequently formed. Because the diameter of the nanodots is less than 10 nm, the number of adsorbed molecules can be less than one hundred [40]. Because the Au nanodots are fabricated by using electron beam lithography (EBL) and an annealing process, which have high geometrical, positional, and crystal uniformity, this approach is useful for studying electron transport through molecular junctions.

(6) *Nanoparticle-based SPM junction*. The nanoparticles have a smaller size compared with the traditional SPM tip and can be easily visualized by using the SPM technology, thus suggesting a potential application for molecular break junctions. Cui et al. [41] presented an approach using a conducting AFM to contact gold nanoparticles capped by alkanedithiol molecules, which were embedded in a matrix of alkanethiols molecules. The octanethiol monolayer acts as a molecular insulator, which isolates the dithiol molecules from one another. The thiol groups at the top of the film are attached to the nanoparticles by incubating the monolayer with a gold nanoparticle solution. A gold-coated conducting AFM probe was used to locate and contact individual particles bonded to the monolayer, as indicated in Figure 2.4f. The measured I–V characteristics can be categorized into several distinct sets of curves that are integer multiples of a fundamental curve, and the fundamental curve presents the single-molecule I–V response. In addition to measuring the molecular conductivity, this approach can avoid the effects of variations in the contact force and other problems encountered with the non-bonded contacts. One drawback of this strategy is that, because the Au nanoparticles are typically coated with an organic surfactant layer, the tip and the nanoparticle may form an additional tunneling junction (Coulomb island). Consequently, the electron transport between the tip and the substrate via the nanoparticle may exhibit Coulomb blockade effects [20].

2.1.1.2 Applications of SPM Beyond Electron Transport

The application of SPM in molecular electronics is not only limited to measuring the properties of the electron transport through the molecular junctions, i.e. SPM has been extended to vast regimes. We tentatively classify these additional SPM applications into five groups, which are presented in the following paragraphs.

(1) *Imaging*. SPM allows the single-molecule structure, bond structure [52, 53], and charge distribution with sub-molecular resolution to be imaged [54]. In this attractive field, several pioneer groups provided significant contributions [48, 49, 52, 55, 56]. Here, we just provide one of the pioneering studies. de Oteyza et al. used a non-contact AFM to investigate the reaction-induced changes in the detailed internal bond structure of individual molecules on the silver surface [55]. Both the reactant and the final products were probed at the single-molecule level. Their bond-resolved images revealed how the

thermally induced complex bond rearrangement resulted in unexpected products. Combined with the DFT calculation, they proposed a detailed reaction pathway.

(2) *Optoelectronics and stereoelectronics*. Addressing the optical properties and understanding their influence on electronic transport in individual molecular-scale devices, known as "molecular optoelectronics," is an area with potentially important applications. However, the mismatch between the optical (approximately at the micrometer scale) and the molecular-length scales (approximately at the nanometer scale) became an obstacle to the experimental investigations. The SPM technique reduces this obstacle and plays an important role in the single-molecule optoelectronic studies in two aspects: optical spectroscopies and optical control [1]. Raman is a typical optical spectroscopy method. Recently, Liu et al. used the STM-based break junction technique combined with the Raman spectroscopy to perform simultaneous conductance and Raman measurements on single-molecule junctions, thus providing detailed structural information [57]. Experiments that probe electroluminescence, which is photon emission induced by a tunneling current, also offer insight into the structure–conductance correlations. For example, Qiu et al. demonstrated the simultaneous measurement of differential conductance and photon emissions from individual molecules by using STM [58]. Instead of depositing molecules directly on a metal surface, they used an ultrathin alumina insulating film to decouple the molecule from the metal. This critical improvement prevents the metal electrodes from quenching the radiated photons, and the emitted photons carry additional molecular fingerprint information. For an advanced technical overview from a different perspective, readers can refer to two recent comprehensive reviews on molecular optoelectronics [59, 60].

Over the past few decades, chemists have made considerable efforts to develop a fundamental understanding of stereoelectronics to establish how the electronic properties of molecules relate to their conformation; the recent developments of the single-molecule STM technique provide the tools to change the conformation with a level of control previously unimagined. For example, by using the STM technology, Venkataraman et al. performed a systematical conductance measurement of biphenyl junctions as a function of the molecular twist angles, thus building a comprehensive mapping of how the junction conductance changes with the molecular conformation [61]. In another example, Su et al. demonstrated the dependence of single-molecule conductance on a stereoelectronic effect in permethyloligosilanes with methylthiomethyl electrode linkers [62]. This result occurs because the strong σ conjugation in the oligosilane backbone couples the stereoelectronic properties of the sulfur–methylene σ bonds that terminate the molecule. Additional discussion regarding the conformation-induced switching is provided in Section 9.7.

(3) *Heating*. Local heating is known to be an important factor in the design of conventional silicon-based microelectronics. It is natural to question how important this effect is in the electrode–molecule–electrode structures. Huang et al. investigated the current-induced local heating effects in single

molecules covalently bound to two electrodes by measuring the force required to break the molecule–electrode bonds [63]. Because the breakdown process is thermally activated, the breaking force can be used to extract the effective temperature of the molecular junction. They demonstrated that the local temperature of a 1,4-benzenedithiol-based (BDT) molecular junction could be raised to 463 K by applying a bias voltage of up to 1 V. The heat dissipation and transport in the molecular devices remain poorly characterized due to experimental challenges. Lee et al. used custom-fabricated scanning probes with integrated nanoscale thermocouples to investigate the heat dissipation in the electrodes of single-molecule junctions [64]. Their results clearly related the electronic transmission characteristics of the atomic-scale junctions to their heat dissipation properties, thus enabling the study of heat transport in atomic and molecular junctions, which is an important and challenging scientific and technological goal. From an opposing perspective, another interesting and challenging issue is how to use the environmental heat, such as converting heat energy to electricity at the molecular level. We highlight the recent significant advances in thermoelectricity by using different molecular junction platforms in Sections 5.3 and 9.7.

(4) *Mechanics*. Mechanical forces can be used to manipulate the molecular junction geometries [65, 66] and the molecular orbital alignments by pulling and compressing a single molecule junction [67]. Tao and coworkers performed a pioneering study to determine the change in the electromechanical properties of a molecular junction as the junction was stretched and compressed [67]. It was found that the conductance increased by more than an order of magnitude during stretching and then decreased as the junction was compressed. This finding was attributed to a strain-induced shift in the molecular orbital toward the Fermi level of the electrodes, thus leading to a resonant enhancement of the conductance. By using the CP-AFM technology, Xu et al. performed simultaneous force and conductance measurements on Au metal–molecule–metal junctions. In their experiment, the spring constant of the molecular junction and the dependence of the conductance on the stretching force were determined [68]. By controlling the stretching force and the stretching rates, the breakdown mechanism of the molecule junctions [66] and the breaking mechanism of the nanotubes were revealed [69], which possessed extremely high tensile strengths.

(5) *Nanolithography*. In addition to its well-known capabilities discussed earlier, SPM recently demonstrated significant potential for patterning material structures at the nanometer scale. It has received attention from not only the scientific community, but also the industry. By using STM, the single atoms can be directly manipulated to form a nanostructure [70]. The AFM equipped with a gold-coated tip can be used to provide a localized electron source for exposing ultrathin poly(methyl methacrylate) (PMMA) resists to make a pattern [71]. Furthermore, SPM can be used to make nanostructures by material deposition in which the STM tip acts as an emission source [72, 73]. Recently, Pires et al. presented a new method to pattern molecular resists with a half pitch down to 15 nm by using the local desorption of a

glassy organic resist with a heatable SPM probe [74]. He et al. presented the well-patterned nanogap electrodes fabricated by mechanically scratching the graphene-based substrate with an AFM tip [75]. A detailed discussion on the SPM-based nanolithography can be found in the review paper [76–78].

As a molecule is sandwiched between electrodes to form an electrode–molecular–electrode junction, the properties of electron transport are not only determined by the molecule itself, but also influenced by molecule–electrode contacts, and the latter may sometimes dominate electron transport. Unfortunately, the nature of the electrode–molecule contacts, i.e. the specific geometry of the contact, is hard to be controlled. It is a great challenge to reveal the role of contact/bonding geometry in determining the measured current and deserves a further investigation.

To address this issue, Xu and coworkers reported a systematical study that focuses on molecule–electrode contact effects on the conductance of a single molecule by combining an STM break-junction method with STM PZT modulation [79–81]. In order to address the dynamic geometry of the molecule/electrode contact, an AC voltage was applied to the PZT to regularly change the distance between the substrate and tip, thus the contact configurations were correspondingly modulated. The transient conductance of the molecular junctions during the separation process was monitored simultaneously, as shown in Figure 2.5 [81]. In the experiments, a widely studied molecule (octanedithiol, C8) with bonding groups at both ends was chosen as the test molecule.

They first measured the conductance of the single C8 molecule without PZT modulations. The transient conductance is presented in Figure 2.5a,b. It is found that approximate 40% of the conductance curves show clear conductance plateaus during the separation process, and the conductance plateaus are mostly around the integer multiples of $2.5 \times 10^{-4}\ G_0$ (major peaks) with very small fluctuations. In contrast, the conductance curves show many fluctuations when the PZT modulations were applied. Especially, additional minor conductance plateau (about one quarter of $2.5 \times 10^{-4}\ G_0$) was observed as shown by Figure 2.5c,d. This major peaks and minor peaks were attributed to the two S–Au contact configurations, namely, top contact and hollow contact, which means that PZT modulations can reflect detailed contact geometry during the junction stretching process.

2.1.2 Mechanically Controllable Break Junctions

2.1.2.1 Work Principle and Advantages

The idea of mechanically controllable break junctions (MCBJs) was initially introduced by Moreland and Ekin to investigate the tunneling characteristics of superconductors in 1985 [82, 83]. Muller and van Ruitenbeek further developed this idea to investigate the atomic point contacts during 1989–1998 [84–86]. This MCBJ method was first used by Reed and coworkers to measure the properties of single molecules in 1997 [87, 88]. The work principle of the MCBJ is relatively simple with unique advantages, and it has been widely used in the

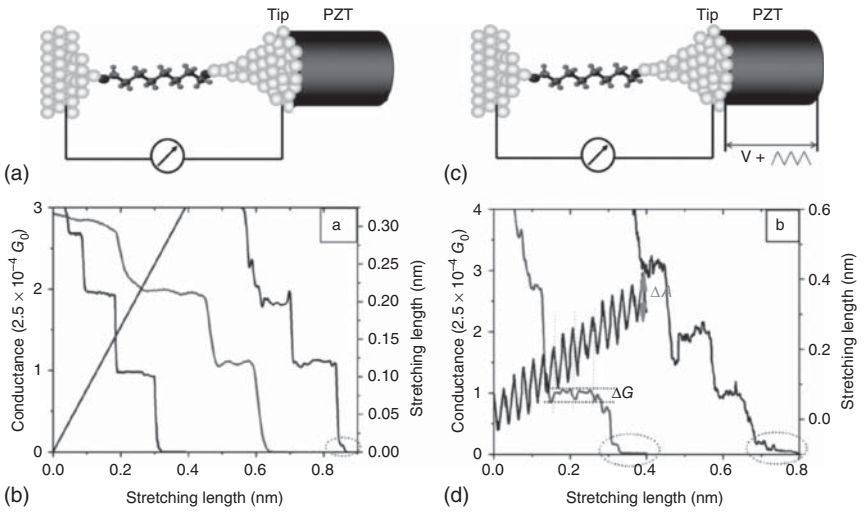

Figure 2.5 Single-molecule conductance measurement with and without contact configuration modulations. (a) Schematic illustration of a single-molecule conductance measurement without contact configuration modulations. (b) Transient conductance curves of a 1,8-octanedithiol molecule covalently bonded to two gold electrodes. The measurements were performed in toluene containing 1 mm octanedithiol without PZT modulation. The major conductance plateaus are mostly around the integer multiples of 2.5×10^{-4} G_0 with very small fluctuations. (c) Schematic illustration of a single-molecule conductance measurement with contact configuration modulations. The experiment was carried out by superimposing a small AC voltage to the PZT while repeatedly stretching the molecular junction by using the STM break-junction method. (d) Typical curves obtained with PZT modulations. The conductance fluctuates around the major conductance value of 2.5×10^{-4} G_0 with a phase shift of about 180° and new plateau below the major conductance value was observed. Source: Reproduced with permission from Xu [81]. Copyright 2007, John Wiley and Sons.

field of molecule electronics. A detailed study with respect to the fabrication progress, application, and outlook of the MCBJ techniques can be found in a recently published report [89].

As shown in Figure 2.6a, an MCBJ setup typically consists of three parts: a flexible substrate containing a macro-fabricated metal wire or patterned nanostructure, a push rod to break the nanostructure, and a counter support to bend the substrate. In the early stages of the MCBJ setup, a small piece of a metallic wire with a notch in the middle is fixed onto a flexible substrate [82]. The substrate can be bent due to the three-point counter support configuration. A vertical (Z direction) movement of the push rod, which can be accurately controlled by an operator, can exert a force on the flexible substrate. When the substrate is bent, the metal wire starts to elongate, resulting in a decrease in the cross section at the notch. A further elongation will eventually lead to a complete fracture of the metal wire at the notch point. After breaking the metal wire, two clean facing electrodes are automatically generated. The distance between the electrodes can be accurately controlled by bending or relaxing the substrate. After integrating the molecules with anchoring groups at both ends into the tunable gap, the opposite electrodes can be bridged, and the electronic properties of the molecules can be addressed.

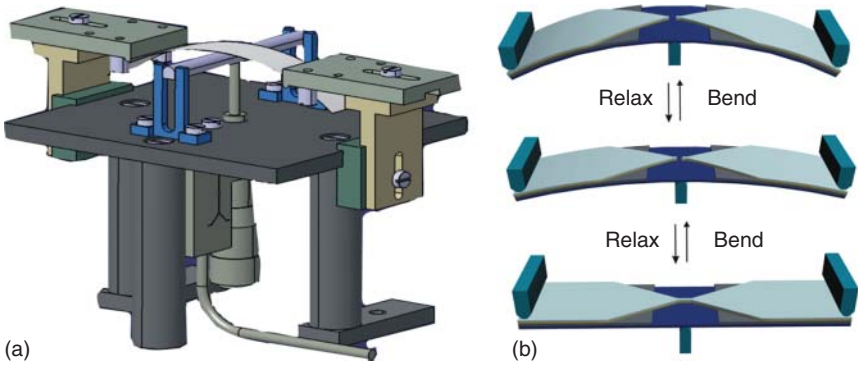

Figure 2.6 MCBJ setup and work principle. (a) Side-view schematic of the MCBJ setup. A MCBJ setup mainly consists of three parts: a flexible substrate containing a patterned nanostructure, a push rod for breaking the nanostructure, and a counter support. (b) Working principle of the MCBJ setup. A suspended metal bridge with a constriction is micro-fabricated onto the substrate. When the push rod exerts a bending force on the substrate, the movement (ΔZ) in the Z direction causes an elongation of the constriction until a break occurs in the metal bridge, resulting in the formation of two separated nanoscale electrodes. The gap size (ΔX) between the two electrodes can be precisely controlled by bending or relaxing the substrate. Source: Reproduced with permission from Xiang et al. [89]. Copyright 2013, American Chemical Society.

Due to the mechanical configuration of the three-point bend apparatus, as indicated in Figure 2.6b, a long vertical movement (ΔZ) of the push rod will result in only a short horizontal gap size change (ΔX) between two electrodes. The attenuation factor, r, is defined as $r = \Delta X/\Delta Z$. Here, ΔX is the gap size change between the two nanoelectrodes, and ΔZ is the displacement of the push rod. The attenuation factor can be estimated by a geometrical configuration of the setup [90]. In a typical nanofabricated chip, the attenuation factor can be estimated as $r = \Delta X/\Delta Z = 6ut/L^2$, where u is the length of the suspended metal bridge, t is the thickness of the substrate, and L is the distance between the outer supports above the spring steel substrate [90, 91]. For instance, u is approximately 1×10^{-3} mm in an EBL-defined sample, t is approximately 0.3 mm with a spring steel substrate, and L is approximately 30 mm in our homemade MCBJ setup. By using these parameters, we can determine that $r = \Delta X/\Delta Z = 6ut/L^2 = 6 \times 10^{-3} \times 0.3/30 \times 30 = 2 \times 10^{-6}$, which indicates that the gap size can be controlled with sub-ångström precision and that the mechanical stress can be accurately changed. Also, the attenuation factor can be accurately calculated from the data obtained in the experiment (tunneling current versus displacement of the push rod) [92]. Briefly, the gap size change (ΔX) can be deduced from the measured tunneling current, and the corresponding displacement of the push rod (ΔZ) can be recorded by the driven software of the push rod. Then, the value of r can be calculated based on the formula $r = \Delta X/\Delta Z$.

Typically, there are three types of driving approaches for the push rod: piezoelectric actuator [93], motor via gear-coupling [94, 95], and motor via differential screw [96]. For the first type, a piezoelectric actuator generally comprises a longitudinal effect-type laminated piezoelectric element. When a voltage is applied to the piezoelectric element, it will expand in the horizontal direction, and a push

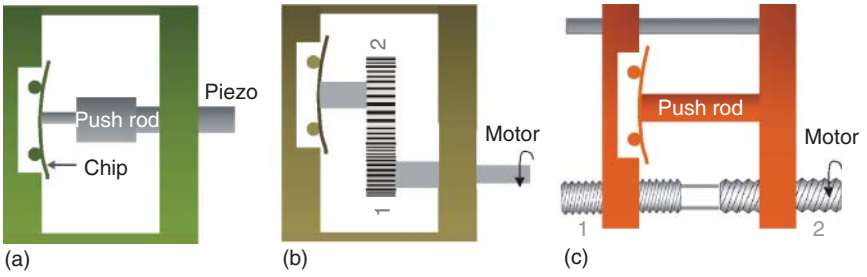

Figure 2.7 Schematic of three typical types of MCBJ setups. (a) Piezoelectric actuator, in which the displacement of the push rod is driven by the piezo actuator. (b) Motor drive via gear-coupling. The small gear (1) couple the large gear (2), reducing the movement speed of the push rod. (c) Motor drive via differential screw. The tiny pitch difference between screw (1) and screw (2) guarantees a precise control of the push rod.

force will be generated to bend the substrate, as illustrated in Figure 2.7a. The advantage of this strategy is that the movement of the push rod can be precisely controlled with nanometer accuracy in a sensitive feedback system. The disadvantages of this strategy are that (i) it is relatively expensive for a piezo actuator push rod, especially when a long-distance movement of the push rod is required; (ii) typically, only a weak force can be generated in the cryogenic environment, e.g. 4K, and the weak force makes it hard to bend the substrate. For the second type, a motor via gear coupling is used to drive the push rod, in which the movement speed of the push rod can be rapidly reduced, as shown in Figure 2.7b. Using gear-coupling combined with a smart motor, the movement of the push rod can be accurately controlled. The flaw in this strategy is that a tiny discrete movement of the push rod always exists due to the mechanical gear-coupling, resulting in a discontinuous change in the gap size. For the third type, a differential-screw push uses two screws with different pitches, as indicated in Figure 2.7c. The slight pitch difference between screw 1 and screw 2 enables operators to accurately control the movement of the push rod with high resolution while simultaneously guaranteeing a continuous gap change.

The MCBJ technique has several advantages. (i) The MCBJ setup can be easily integrated with other systems, such as a Raman spectrometer or high vacuum transmission electron microscopy (TEM) system, due to its small size and flexible configuration [97, 98]. (ii) The influence of contaminants is decreased because a fresh break cross section of the gold bridge is mechanically created in the MCBJ experiment without additional chemical treatments [99]. (iii) With advanced lithographic techniques, the electrodes can be scaled down to molecular dimensions, which make it well suitable for single-molecule measurements [100]. Moreover, the number of bridged molecules can be changed by accurately controlling the gap size, e.g. a few molecules will break from one of the electrodes due to a further increase in the gap size. (iv) The most impressive feature of the MCBJ technique is its high mechanical stability of the system in comparison with other techniques, such as the STM technique [89]. Because the electrodes are rigidly fixed to the same substrate at a short distance (less than 1 μm by the advanced lithographic fabrication), the length of the freestanding parts

is significantly shorter than the tip in a typical STM setup, which results in an extremely stable electrode with a high resonant frequency. Furthermore, as discussed earlier, the amazing attenuation factor spontaneously leads to the fact that the motion of the push rod (ΔZ) causes a reduced horizontal displacement (ΔX) in the electrodes by several magnitudes. This attenuation indicates that any disturbing effect from the push rod, e.g. mechanical vibration, thermal expansion, or voltage instability with piezoelectric component, can be strongly suspended.

In addition to the important advantages of the MCBJ technique, the main disadvantages can be described. (i) The MCBJs cannot be operated in a manner similar to the crossbars to address a specific cross-section, which limits the potential applications in information processing. (ii) Unlike the STM technique, the MCBJs cannot obtain the surface topography of the sample. Nevertheless, as a fundamental research technique with considerable mechanical stability, MCBJs are powerful and practical for investigating single-molecule properties.

2.1.2.2 MCBJ Chip Fabrication

The fabrication of the MCBJ chip is summarized in Figure 2.8. According to the fabrication methods, there are three main types of MCBJ chips: mechanically cut-based, electrochemically-deposition-based [106], and nanofabricated [90, 107]. Based on the structure of the chip, it can be classified as a two-terminal chip [102] or a three-terminal chip [108]. In the three-terminal chip, one of the electrodes generally operates as the gate electrode by which the electron transport can be modulated, and the other two electrodes are used as the source and the drain electrodes.

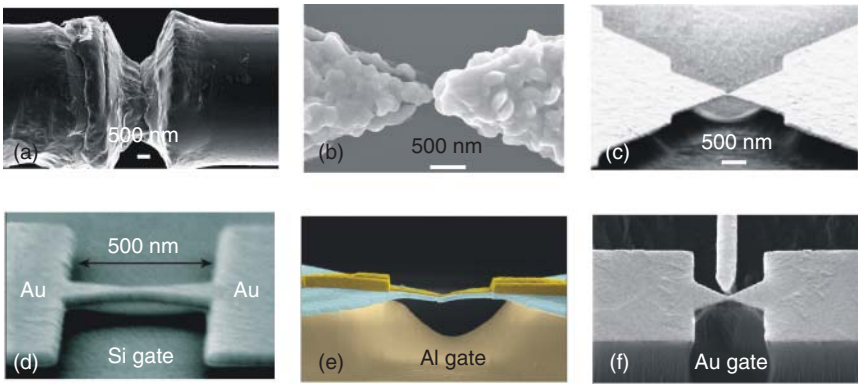

Figure 2.8 Typical MCBJ chips. (a) Mechanical cut to create a notch on the gold wire. (b) Electrochemically-deposition-based electrodes. Source: Reproduced with permission from Yi et al. [101]. Copyright 2006, John Wiley and Sons. (c) EBL-defined electrodes on flexible metal substrates. Source: Reproduced with permission from Lortscher et al. [102]. Copyright 2006, John Wiley and Sons; (d) Suspended gating (indirectly contacted) above a doped silicon substrate. Source: Reproduced with permission from Parks et al. [103]. Copyright 2010, AAAS. (e) Back gate in direct contact with the source and drain electrodes. Source: Reproduced with permission from Perrin et al. [104]. Copyright 2013, Springer Nature. (f) Side gating with a nanometal electrode. Source: Reproduced with permission from Xiang et al. [105]. Copyright 2013, American Chemical Society.

An early low-cost macrofabricated chip for an MCBJ experiment is presented in Figure 2.8a. A thin metal wire, normally less than a few millimeters in diameter, was fixed onto an insulated flexible substrate by using two drops of glue. A notch was created by using a knife through a mechanical cut in the middle of the metal wire to allow it to easily break when subjected to a bend force. These types of chips are cheap and simple to fabricate. The disadvantages of this macrofabricated chip can be described as follows. (i) The large size and the rough surface of the electrode are not quite suitable for a single-molecule investigation. (ii) Contamination may occur because the mechanical cut is typically performed in an ambient environment. (iii) There is a limited attenuation factor, which indicates that the mechanical stability of the macrofabricated chips is not as good as that of the microfabricated chip.

The chips for the MCBJ experiments can also be fabricated by using electrodeposition on template electrodes that were predefined on the substrate (Figure 2.8b) [101, 109, 110]. The initial electrodes, which have a relatively large gap, are generally fabricated using optical lithographic techniques on the substrates. The gap is then narrowed and fused by depositing specific atoms onto the electrodes. The fused nanobridge can be reopened by controlling the substrate bend configuration. This strategy, which combines the electrochemical deposition advantages with the MCBJ advantages, e.g. the use of optical lithography instead of EBL, is facile for the fabrication, and the gap size can be changed *in situ* [111]. The disadvantage of this strategy is that the fabrication process is time-consuming, and contamination is likely due to the electrochemical process.

Recently, advanced EBL and reactive ion etching (RIE) techniques were used to fabricate the MCBJ chip based on a flexible substrate [102, 105]. Figure 2.8c illustrates a typical EBL fabricated MCBJ chip [102]. The chip fabrication process consists of several key steps: (i) an isolating layer (polyimide or silicon dioxide several micrometers thick) is spun onto the substrate, such as thin silicon wafer, spring steel sheet, or bronze sheet; (ii) a standard EBL process is performed to define the metal wire with a constriction in the middle; and (iii) the isolating layer is partly removed by an RIE to obtain a suspended metal bridge.

A significant development of the MCBJ is the introduction of gating control. Ralph and coworkers initially reported the implementation of both electrostatic gating and mechanical adjustability within the same single-molecule device by adding a bottom gate electrode to a mechanically controlled break junction [112]. To fabricate the bottom-gated chip, a thick silicon dioxide film was first grown on top of a doped silicon wafer. Then, an EBL process was performed to pattern the gold electrode structure. Finally, hydrofluoric acid was used to remove the SiO_2 under the gold electrode, thus suspending it above the silicon substrate. In this chip, the doped conductive silicon was used as the gate electrode, as shown in Figure 2.8d. This newly designed chip combines both the ability to mechanically adjust the spacing between the electrodes and the ability to shift the energy levels of the molecules.

Zant and coworkers further developed the bottom gate architecture for the independent mechanical and electrostatic tuning of charge transport [104, 113], as shown in Figure 2.8e. In contrast to previous gated mechanical break junctions, the source–drain electrodes are suspended above the gate electrode, and

the fabricated source–drain electrodes are in contact with the gate electrode via a thin Al_2O_3 insulator. It was demonstrated that the electrical continuity of the gate electrode was maintained upon the bending of the substrate and successfully achieved mechanical and electrical control of charge transport through the nanoscale island by using such bottom gating. The technique was further applied to the molecular electronics investigation, which clarified the dominant role of the image-charge effects in the single-molecule junctions. A minor fault in this design is that the available gap size range was limited to avoid the partial breakage of the gate dielectric.

Inspired by the bottom gating, Xiang et al. proposed a new design for the MCBJ chips by adding a side-gate electrode near the source–drain electrode [105], as shown in Figure 2.8f. By using the advanced EBL and RIE methods, a suspended metal bridge and a gate electrode in plane were fabricated simultaneously. The Au gate electrode was located a few nanometers away from the suspended metal bridge. By using this non-contact side-gate electrode, the position of the molecular energy level was shifted, and the electron transport characteristics were modulated. The advantage of this design is that the gate electrode can remain unchanged during the operation, i.e. the fracture of the gate electrode can be avoided when one tries to break the metal wire or to obtain a large gap by deeply bending the substrate. The shortcoming in this design is that the gate efficiency is average and strongly depends on the distance between the gate electrode and the molecular junctions.

2.1.2.3 MCBJ Applications

Due to their advantages, e.g. excellent mechanical stability, continuously precise tunable gap size, atomic scale electrodes, and minimum contamination, MCBJs have been extensively used for investigating molecular electronics [32, 114, 115]. Here, we highlight several significant reports detailing the applications of the MCBJs. Additional information on the MCBJ-based functional devices is presented in Chapter 9. A review of the overall applications of the MCBJ can be found elsewhere [89].

(1) *Surface-enhanced Raman scattering*. Surface-enhanced Raman scattering (SERS) , which provides fingerprint information of the molecules, has been a subject of renewed interest since the late 1990s, primarily motivated by the observation of SERS from single molecules. Detailed information on the SERS technique is addressed later in Section 7.4. Here, we just show the novel idea to combine the MCBJs with the SERS technique. Tian et al. reported a combined SERS and MCBJ method to measure the SERS signals of molecules located inside the nanogap between two electrodes [97]. The enhancement of the SERS intensity with decreasing gap sizes was observed, indicating that the signals were obtained from the molecules inside the gap. These experiments provide us with a better understanding of the mechanism of the SERS and lead to detecting and studying single molecules. Later, simultaneous measurements of the conductance and the SERS were performed in a solution by using nanofabricated MCBJ electrodes, and the geometrical and electronic structural dynamics of a single-molecule

junction was revealed [116]. The dynamics of the 4,4′-bipyridine motion were observed between the vertical and the tilting configurations in the Au nanogap, i.e. a slight increase in the tilting angle of the molecule could lead to an increase in the energies of the Raman modes and a decrease in the conductance of the molecular junctions.

(2) *Electron transport*. Due to the feature of continuous precise control of the gap size, the size between electrodes can be reduced to be as small as that of a single atom, assisting the formation of metal–molecule–metal junctions and the investigation of electron transport. For example, the conductance of single organic molecules wired by chains of metal atoms was recently addressed, revealing that hybrid junctions can exhibit a metallic-like conductance, and the conductance is insensitive to further elongation of the junction [117]. Liu et al. determined that single naphthalene and anthracene molecular junctions could exhibit well-defined high conductance values ($\sim 0.3G_0$), which are close to the values of the metal atomic contacts [118]. The high conductance was attributed to a direct π-binding of the molecules to the Au electrodes. This study demonstrated that the direct π-binding method is one of the promising approaches to fabricate highly conductive and structurally well-defined molecular junctions. Van der Zant and coworkers studied the effects of electrode separation on the molecular orbital levels in porphyrin metal complex-bridged molecular junctions based on the MCBJs [104]. They found that both the occupied and unoccupied energy levels moved significantly toward the Fermi level upon reduction of the electrode spacing, e.g. increasing the electrode separation by a few ångströms could lead to a substantial increase in the transport gap and level shifts as high as hundreds of millielectronvolt. Supported by the DFT calculations, the dominant role of the image-charge effects was clarified in the single-molecule junctions. The conductance and electron transport characterization of different metal complexes were also extensively studied using the MCBJ method [111, 119, 120].

(3) *Control of the spin state*. Single-molecule spintronics investigate the electron transport through magnetic molecules (such as transition-metal complexes) that have an internal spin degree of freedom. A detailed introduction of molecular spintronics can be found elsewhere [121]. To understand and control individual molecules, it is important to read and further control their spin state. Ralph and coworkers performed experiments in which they controllably stretched individual cobalt complexes while simultaneously measuring the current flow through the molecules. It was demonstrated that the molecule's spin states and the magnetic anisotropy can be manipulated in the absence of a magnetic field by modifying the molecular symmetry through stretching the molecular junction, revealing a new mechanism of spin control in single-molecule devices [103]. Weber et al. measured the electronic transport through a single-molecule junction containing two coupled spin centers that were confined on two Co^{2+} ions by using the MCBJ method [122]. It was demonstrated that the electronic states of the coupled spin system could be repeatedly switched between the pseudo-singlet state and the pseudo-triplet state by applying a finite bias. More details are presented in Section 9.5.

(4) *Vibrational states*. The changes in the molecular conformation, contact geometry, and molecular vibration in the electron transport can be revealed by inelastic electron tunneling spectroscopic (IETS) and noise spectroscopic measurements [123, 124]. By combining the IETS with mechanical control and electrode material variation, Kim et al. successfully separated the effects of the contact geometry and the molecular conformation [123]. This experiment demonstrated that the mechanical strain of different electrode materials could be imposed onto the molecules, thus opening a new route for controlling the charge transport through individual molecules. Tsutsui et al. reported the observation of inelastic contributions to the electrical conductance and current fluctuations in single-organic molecule junctions [125]. They analyzed the conductance fluctuations in molecular junctions under a high field and found stepwise increases in the current oscillation amplitudes at distinct voltages, indicating that the field-induced current noises originated from inelastic excitations of vibration modes inherent to the target molecules. Recently, a combination of the real-time conductance fluctuations and the noise spectroscopy measurements on a series of single-molecule junctions employing the MCBJ technique demonstrated that the telegraph-like current fluctuations at room temperature should not originate from either the electron trapping or detrapping processes or the molecule re-conformation, thus putting light on the fundamental understanding of the current fluctuation mechanism [99, 126].

One limitation of the MCBJ applications, especially the application in the production of highly integrated molecular commercial devices, is the out-plane push rod components. In other words, the movement of the push rod is out of the source–drain plane, which blocks the on-chip mass fabrication and hinders the further reduction in the device dimension. Also, it is difficult to use this MCBJ method to control the number of junctions simultaneously, which limits its commercial application. To overcome the problem mentioned previously, the following strategies can be potentially used: (i) a novel push rod is required. It has been reported that a micrometer-scale motor has been put into use, which may be utilized as a potential push rod to reduce the device size in the future; (ii) Discovering a new architecture that is not limited to a three-point apparatus may lead from fundamental research to application-related research. For example, Chao et al. introduced an idea to fabricate a completely on-chip structure by using a thermal actuator that generated rectilinear displacements and forces by leveraging deformations [127]. Although this idea remains in the theory simulation stage, the experimental realization of this idea will be helpful in mass production; and (iii) as an additional option, one can use a terahertz wave (optical wave) to replace the traditional push rod. For example, a structure can be designed that is similar to a bi-material micro-cantilever [128]. This biomaterial cantilever will be deformed and deflected when it is exposed to the terahertz radiation. With a suitable on-chip design, this cantilever deflection can be used to form a junction within one plane. Thus, multi-junction controllability and highly integrated molecular electronic devices may be available.

Recently, Hong and coworkers has conducted a series of research and obtained good achievements by the MCBJ technique. For example, they explored photo-thermal reaction processes of a photochromic dihydroazulene (dha)/vinylheptafulvene (vhf) system [129]. To probe the photoreaction process of dha-6, the *in situ* UV irradiation system was introduced to the MCBJ setup. In the initial state (dha-6 solution without UV irradiation), all the molecular junctions are formed by trapping the dha-6 into the nanogaps (dha-6 junction). With UV irradiation (365 nm), the dha-6 undergoes a ring-opening process of the five-membered ring to form vhf, as shown in Figure 2.9a. Simultaneously, they obtained corresponding conductance–distance traces. They finally found the reversibility and multiple switching possibilities during the reaction using the well-distinguished conductance states of single-molecule dha/vhf junctions [129]. Statistical analysis of the break junction experiments provides a quantitative approach for probing the reaction kinetics and reversibility, including the occurrence of isomerization during the reaction. Another research is about the switching of charge transport pathways via delocalization changes in single-molecule metallacycle junctions, as shown in Figure 2.9b. They found that the conductance of the metallacycles junction with phosphonium group is more than 1 order of magnitude higher than that without phosphonium group. Based on X-ray diffraction and UV−Vis absorption spectroscopy, they revealed that the attached phosphonium group makes metallacycles more delocalized, which shortened the preferred charge transport pathway and significantly enhanced the single molecule conductance. At the same time, they reported the feasibility of the conductance distinction of two small molecule isomers (DPP derivatives, 2,5-dihexyl-3,6-bis(4-(methylthio)phenyl)-2,5-dihydropyrrolo[3,4-c]pyrrole-1,4-dione [SDPP] and DPP derivatives, 2-hexyl-4-(hexyloxy)-3,6-bis(4-(methylthio) phenyl)pyrrolo[3,4-c]pyrrol-1(2H)-one(SPPO [SPPO]) in single-molecule junctions by using the MCBJ technique, as shown in Figure 2.9c. They demonstrated that combination of stimuli-response and quantum interference can be an efficient strategy to enhance isomer recognition and conductance switching in single-molecule junctions.

Low-dimensional structures, such as atomic and molecular junctions, are promising thermoelectric materials with quantum confinement effects. Tsutsui et al. introduced a novel device to simultaneously evaluate the conductance and thermopower of atomic and molecular junctions [132]. As shown in Figure 2.10a, a microheater consisting of Pt coils with a 300 nm line-space was fabricated by using the original structure of microchips. Thus, the device can generate a temperature gradient where an electrode close to the Pt coil is hot due to Joule heating from a variable voltage and the other electrode away from the Pt coil is cold, and simultaneously, the local junction configurations can be adjusted by the MCBJ setup, as shown in Figure 2.10b [132]. The negative thermopower in the Au atomic chain is observed at a low voltage, which mirrors the quantum nature. However, there is positive thermopower at an increased voltage, which is ascribed to the disordered Au nanocontacts that result from excessive local heating. Meanwhile, a sensitivity of the thermoelectricity on the atomic contact configurations or the BDT molecular junction was observed. The microheater-embedded MCBJ, as an improvement on the MCBJ, is a direct and

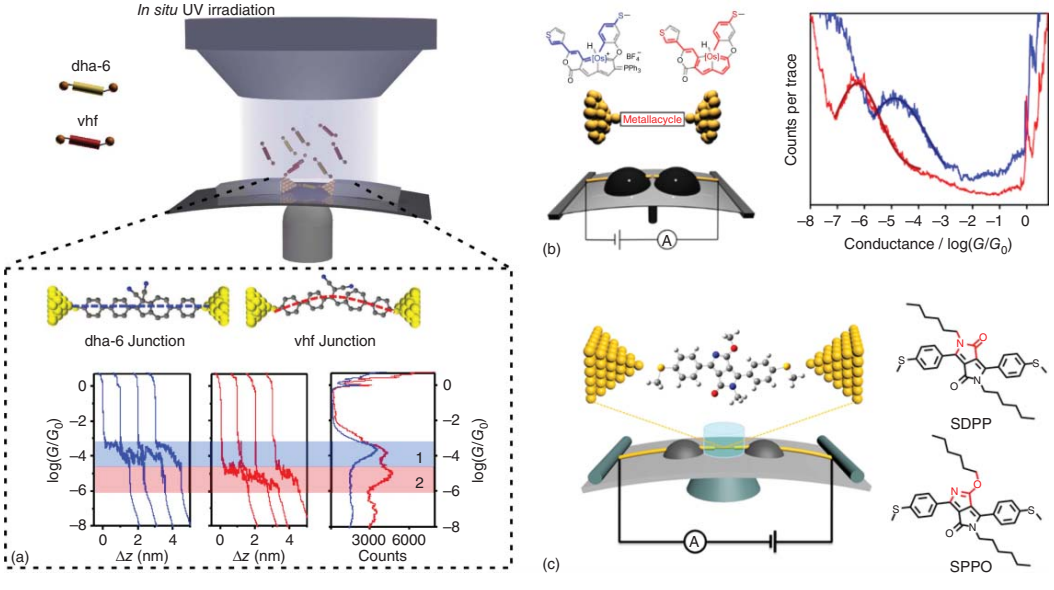

Figure 2.9 Latest developments of original mechanically controllable break junction (MCBJ) techniques. (a) Schematic of the MCBJ measurements during the photo-conversion of dihydroazulene under the *in situ* ultraviolet (UV) irradiation (top). Typical individual conductance–distance traces recorded in break junction measurements; blue for the dha-6 junction and red for the vhf junction (bottom). Source: Reproduced with permission from Huang et al. [129]. Copyright 2017, Springer Nature; (b) Single-molecule osmacycle junctions made by an MCBJ setup and conductance histograms for two kinds of molecules. Source: Reproduced with permission from Li et al. [130]. Copyright 2017, American Chemical Society. (c) Schematic of an MCBJ setup and the two diketopyrrolopyrrole (DPP) isomers. Source: Reproduced with permission from Zhang et al. [131]. Copyright 2018, American Chemical Society.

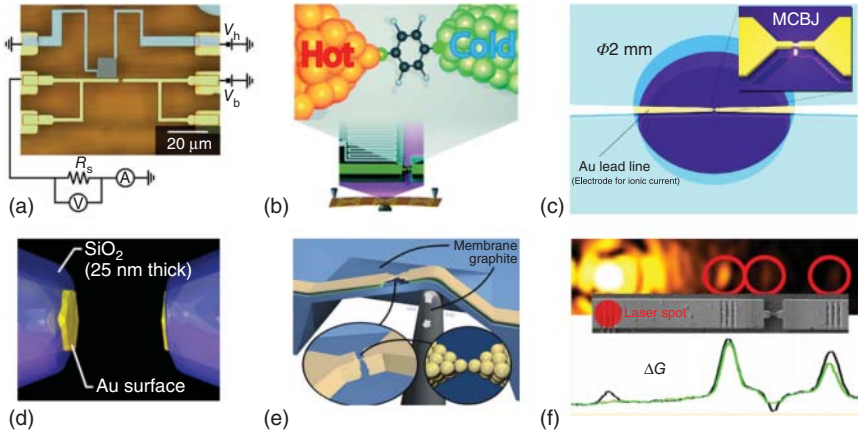

Figure 2.10 Modifications of a basic MCBJ configuration. (a) Optical microscopic image of a microheater-embedded MCBJ consisting of a Pt coil (gray) and a free-standing Au junction (yellow) on a polyimide-coated phosphor bronze substrate. (b) Schematic of a microheater-embedded mechanically controllable break junction with hot and cold electrodes at room temperatures. Source: Reproduced with permission from Morikawa et al. [132]. Copyright 2014, The Royal Society of Chemistry. (c) Schematic illustration of MCBJ electrodes symmetrically placed in a liquid container with a diameter of 2 mm. Source: Reproduced with permission from Doi et al. [133]. Copyright 2014, American Chemical Society. (d) The formed Au electrodes are covered with SiO_2 except the fresh breakage surface with an area of approximately 80 nm × 80 nm. Source: Reproduced with permission from Arima et al. [107]. Copyright 2014, AIP Publishing LLC. (e) The chips with the membranes are then clamped onto a stretching mechanism consisting of a sample holder which carries the chip and a fine tip controlled by a uniaxial piezostage. Source: Reproduced with permission from Waitz et al. [134]. Copyright 2008, American Institute of Physics. (f) A sample showing three gratings on the left and the right side of the constriction (top) and light-induced conductance change (bottom). Source: Reproduced with permission from Benner et al. [135]. Copyright 2014, American Chemical Society.

powerful approach to probe low-dimensional thermoelectric structures by using thermopower measurements [136].

In previous sections, the basic MCBJ was introduced in detail. However, it is difficult to investigate some additional phenomena, such as thermoelectricity; therefore, the basic MCBJ needs to be modified. To tackle the current noise-jamming problem in electrolyte solutions, as this noise probably affects electrical signals through the junctions, Doi et al. modified the basic MCBJ to determine the mechanisms responsible for the background current [133]. Figure 2.10c shows a scanning electron microscopy (SEM) image of an MCBJ with a nanogap formed by the self-breaking method, and the nanogap is symmetrically immersed in a cylindrical structure with a diameter of 2 mm. Subsequently, NaCl aqueous solutions with various concentrations fill the cylindrical structure, with an external electrical field applied to control ionic transport. The results revealed that the current noise increases as the ionic concentration increased. By solving the time-dependent Nernst–Planck and Poisson equations, it was observed that the applied field and length of the nanogap produced a significant effect on the ionic response. The experimental

and theoretical results are conducive to the exploration of the background current and lay a good foundation for follow-up studies. To suppress the effects of electronic noise and ionic current in an electrolyte solution, Taniguchi and coworkers proposed a SiO_2-coated MCBJ method where the electrodes in MCBJ are entirely enclosed with a thin SiO_2 layer [107]. As shown in Figure 2.10d, two SiO_2 layers that are under and on top of the electrodes, respectively, were deposited by a chemical vapor deposition based on the E-beam lithography technique.

In addition, the contact between pushrod and chips generally is straight shape. Sheer et al. achieved a single-atom contact by fabricating silicon membrane substrate and fine tip as shown in Figure 2.10e. With this method, it allowed to control more than one junction on the same chip. Detailed explanation can be seen in Ref. [134]. Recently, Sheer et al. further integrated line gratings into the metallic leads that increased the surface plasmon polarizations (SPP) excitation efficiency; see Figure 2.10f [135]. They found a clear distance and polarization dependence of the conductance enhancement, demonstrating the direct impact of surface plasmon polariton (SPPs) to the conductance change by both thermal expansion and photo-assisted transport (PAT). These innovative structures and results have a huge impact on the design of opto-nanoelectronic devices whose conductance is controllable by the excitation of SPPs [135]. Due to the increased attention on single molecular junctions, there will be more modifications of MCBJ devices in the near future.

In general, the mechanical force is generated by a motor or piezo actuator in MCBJs. There exists another form of the mechanical force to prepare nanoscale junctions, such as a thermally mechanical stress [137–140]. Wang et al. proposed a double-V shaped symmetrical structure based on a thermal actuator [137]. The working principle is shown in Figure 2.11. In brief, a suspended double-V shaped beam was prefabricated on the silicon substrate. The four pads at the end of the V shaped beams were fixed on the substrate, and the two beams were connected in the middle part via a nanobridge as shown in Figure 2.11a. Deformation of the beams will appear due to the thermal expansion when an external electric

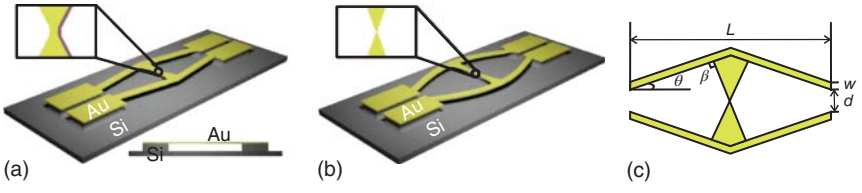

Figure 2.11 Structure of the double-V symmetrical model. (a) Diagram of the initial double-V shaped structure. Au beams with a nanobridge were suspended on the Si substrate. Inset: diagram of nanobridge before deformation. Bottom: the front view of the structure. (b) Schematic of the structure after deformation upon the thermal heating. All these four ends are fixed, when they are applied an electric current, the V beam would expand outwards due to the Joule heating, and finally made the fracture of the nanobridge between two beams. (c) Major structural parameters for the double-V symmetrical model. (*L*: beam length, *w*: beam width, θ: beam angle, *d*: distance between two V-shaped beams, β: corner angle). Source: Reproduced with permission from Wang et al. [137]. Copyright 2017, World Scientific Publishing.

voltage is applied to the beams, resulting in the displacement of two beams in opposite directions. Subsequently, the nanoconstriction in the middle part will be stretched as shown in Figure 2.11b. Ultimately, the stretch force will lead to the break of the constriction and thus the formation of nanoelectrodes.

In addition, they put forward a strategy to precisely adjust the period of metal nanograting *in situ* based on the double-V shaped symmetrical structure by designing horizontal nanograting and vertical nanograting on the nanobridge part, in which the period of nanograting can be modulated with sub-nanometer accuracy in two opposite directions [137]. The stronger force and larger displacement of the V-shaped structure can be achieved by increasing the current. It is expected that the V-shaped structure proposed will find various applications in high bandwidths and highly integrated single-molecule devices and nanoscale sensors.

2.1.3 Electromigration Breakdown Junctions

The phenomenon of electromigration has been well-known for over one hundred years. In an applied electric field, the momentum of the moving electrons can be transferred to the metal atom, which results in the gradual movement of the atoms. Electromigration has been considered as the primary failure mode in microelectronic circuitry for a long time. Recently, it has been well suited to fabricate nanogapped electrodes and molecular-based devices [141]. Generally, a constriction is fabricated in the metal (e.g. gold) wire for nanogap formation. The current density is largest at the constriction part, which favors electromigration. A local reduction in the constriction width increases the local current density, thus leading to the eventual breakage of the nanowire into two distinct (source and drain) electrodes. To incorporate the molecules into the electromigration breakdown junctions (EBJs), two different approaches were developed. One approach is to deposit the molecules onto the electrode surface, after which the breaking process is performed [142]. The other approach first breaks the nanowire and then assembles the molecules into the separated electrodes [143].

In contrast to the MCBJs, the nanogapped junctions formed by electromigration cannot make substantial repeatable measurements with the same junction. Thus, a large number of devices need to be fabricated to examine the statistical behaviors of the molecular junctions [144]. Additionally, two primary issues need to be carefully handled when processing the electromigration procedures. The first is to heat in the breakage of a nanowire. The second is the gap size control. When the gap distance is comparable with the molecular length, only then it is possible to bridge the two electrodes by molecules. To control the gap size, several strategies have been introduced, which are addressed later in detail.

Although electromigration is a thermally assisted process that requires Joule heating to start gap formation, excessive heating should be avoided because it can result in undesired melting of the metal, destruction of the molecules, and formation of gold debris (islands) inside the gap [145]. Unintentional metal debris in the gap interferes with the insertion of the molecules of interest and may mask the intrinsic molecular signals [145, 146]. This metal debris can exhibit the same behavior as the molecules, e.g. similar current–voltage

characterization, Coulomb blockade, and Kondo effect [146–148]. To distinguish the molecular transport from the transport through small gold grains or other imperfections, three strategies are typically used: (i) The lead–molecule coupling in three-terminal devices can be used to realize this distinction because metal grains and molecules exhibit completely different behaviors on the gating voltage [145, 146]; (ii) Using specific characterization techniques, e.g. inelastic-tunneling spectroscopy, addresses the molecular vibration modes to realize the distinction [142, 149]; and (iii) Using functional molecules, i.e. the molecules with magnetic properties or light-sensitive molecules, will behave differently from that expected for gold grains [150]. To reduce the metal debris in the nanogap, one relatively simple method is to reduce the resistance in series with the junction. By minimizing the total series resistance of the system, the temperature should be kept low during the electromigration process [151].

2.1.3.1 Device Fabrication

The wire with a constriction was typically defined by using optical lithography or the EBL. By employing the lithographic technique, different types of metal wires were prepared. Following the electromigration process, different types of nanogaps, such as gold nanogaps [151], zinc nanogaps [152], nickel nanogaps [153], silver nanogaps [154], platinum nanogaps [155], and palladium nanogaps [156], were fabricated. In addition to the standard lithographic method used to fabricate the metal wire, several novel methods were recently reported. (i) Optical lithography combined with focused ion beam (FIB) lithography. Asghar et al. reported the use of an FIB to "scratch" and remove a thin layer of gold wires predefined by optical lithography. The scratch results in thinning of the metal wire at the designated point, which is unavailable by using the standard optical lithography. Combining FIB scratching with electromigration provides an elegant approach to create nanoscale break junctions at an exact location with an extremely narrow distribution of the nanogap sizes [157]. (ii) Electrochemical deposition combined with electromigration. Valladares et al. reported a method to repeatedly generate a nanogap [153]. In brief, an electrochemical deposition technique was used to bridge two electrodes. During the deposition process, a metal atom was deposited at the predefined electrodes, and the gap width decreased exponentially with time until the electrode gaps were eventually bridged. Once the bridge was formed, the *ex situ* electromigration technique was used to reopen the nanogap. (iii) Evaporation synchronized with electromigration. Naitoh et al. developed a procedure for the fabrication of Au electrodes by using evaporation synchronized with electromigration [158]. The key point is that the electromigration process was performed simultaneously with the metal evaporation process. It was demonstrated that the application of this method can form nanogaps with a gap size as small as 1 nm, and the gap size can be simply controlled by changing the magnitude of the applied voltage.

In addition to metal materials, non-metal materials, such as graphene [159, 160] and single-walled carbon nanotubes (SWCNTs) [161], can use the electromigration technique to fabricate the nanogap. For example, Zhang et al. reported visualizing the electrical breakdown of suspended graphene sheets [160]. By using a pulsed electrical breakdown technique, narrow gaps

were formed in suspended single to few-layer graphene devices. It was observed that the broken region started from the center of the graphene sheet and expanded. Upon a further increase in the amplitude of the pulse voltage, the graphene sheet was completely broken but remained freestanding. This observation underscores the potential of all-carbon devices to be integrated with graphene electronics. An additional discussion on molecular devices based on carbon-based electrodes is provided in Section 3.2.

Because a gate electrode can be easily fabricated on the substrate by using the standard lithographic technique before the electromigration process, the EBJ is especially advantageous in creating three-terminal device configurations, in which the molecule energy level can be changed based on the applied gate voltage [147, 150]. The gate coupling efficiency factor (α), which describes the effectiveness of the molecular orbital gating, is of key importance to a three-terminal device. For example, if $\alpha = 0.1$ eV V^{-1}, then the molecular orbital energy changes by 0.1 eV when 1 V is applied to the gate electrode. To obtain a large gate coupling efficiency, two conditions need to be satisfied: (i) a large local electrostatic field is generated upon the gate voltage [146]; and (ii) the molecule resides near the gate metal–dielectric interface to reduce screening by the electrodes [142].

Typically, two types of gate geometries were used. The first type, noted as bottom gating, is commonly used [146, 147]. In this geometry, a gate electrode is fabricated beneath source–drain electrodes that are separated by an insulation layer. Currently, two materials are frequently used for bottom gating: highly doped Si substrates with a thermally grown SiO_2 layer on the surface and Al strips with a native oxide Al_2O_3 layer on the surface. An example of the Al gate electrodes is provided in Figure 2.12. Two factors, which are (i) a higher relative dielectric constant of the Al gating and (ii) a thinner insulation layer (Al_2O_3), result in the gating efficiency of aluminum-based devices to be higher than that of silicon-based devices [146].

The second geometry is an in-plane side-gate electrode, in which the gate electrode and the source–drain electrodes are located in the same plane [145]. In this geometry, the electrical field is enhanced by the thickness of the gate electrodes, especially on the gate side compared with a typical back-gate configuration. Generally, to directly visualize the electromigration process and discriminate the trapped molecules/metal clusters from dusts inside the gap, a TEM requires the use of electron transparent substrates, which are non-compatible with the most common three-terminal devices that have a back-gate electrode. This side-gate geometry is relatively compatible with the transmission electron microscopy inspection and can overcome this problem. Besides these advantages, the side-gate geometry also faces the challenge, that is, the gating potential could be screened by the source–drain electrodes, which means that only the molecules facing the gate electrodes can be influenced by the gate electrodes.

2.1.3.2 Gap Size Control

As mentioned earlier, controlling the gap size is of key importance to the electromigration method. The earlier electromigration approaches that used a single voltage ramp normally yielded a thermal runaway and a random distribution of the gap sizes. Most of the gap sizes are larger than hundreds of nanometers,

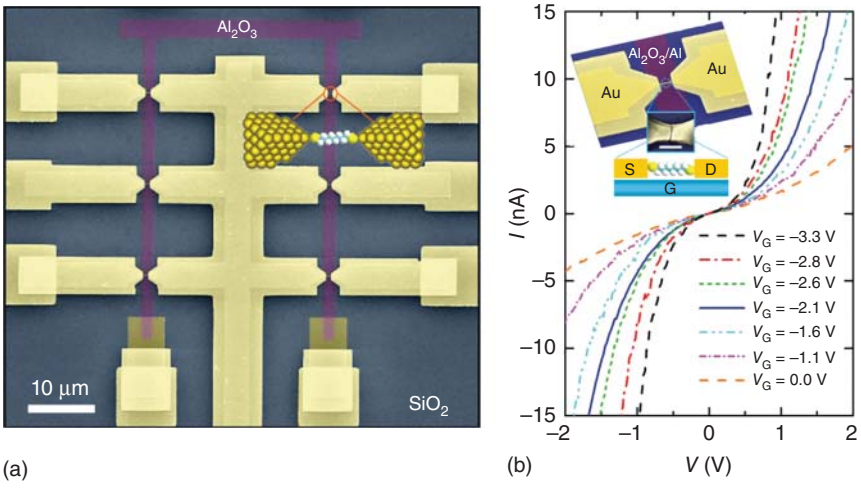

Figure 2.12 Electromigration breakdown molecular junctions. A nanogap was obtained by breaking Au wires by using the electromigration technique. (a) SEM image of the device pattern. The entire structure was fabricated on an oxidized silicon wafer. The yellow regions represent the Au electrodes, and the purple region represents the oxidized Allium gate electrode. (b) Gate-controlled *I*–*V* curves measured at 4.2 K of an Au–octanedithiol–Au junction. Inset: Device structure and schematic. Source: Reproduced with permission from Song et al. [142]. Copyright 2009, Springer Nature.

resulting in the unsuitability for the single molecule investigation. There are two typical strategies, i.e. self-breaking and feedback-control, used to control the gap size between the eventually formed electrodes.

Self-breaking The self-breaking method has recently proven to be an efficient technique for reducing the gap size and avoiding the nano-debris formation [162]. In this method, a nanosized metal junction is gradually shrunk by using a typical electromigration procedure where bias ramps are applied repetitively. When the metal junction was narrowed to the atomic size, the active breaking process was stopped, and the junction was held under a very low field condition. The atom-sized contact then ruptures spontaneously due to the thermal fluctuations, efficiently avoiding excessive heating. By employing this self-break method, O'Neill et al. demonstrated that no signs of metal clusters or metal islands inside the gap, a problem that is often observed in the traditional electromigration techniques [162]. Tsutsui et al. demonstrated that 0.5 nm electrode gaps could be achieved by using the MCBJ technique assisted with the self-breaking method [163].

The self-breaking process is relatively easy for gold (Au) electrodes at room temperature due to the high mobility of the Au atoms and the residual stress on the wire after electromigration. However, for other metals, such as Pt, self-breaking is not possible at room temperature due to the higher activation barrier. Fortunately, Prins et al. found that self-breaking did occur at a temperature approximately 100 °C or higher. Based on these results, they developed a method by which they performed electromigration and self-breaking of Pt nanowires at

lifted temperatures. Then, the sample was cooled to room temperature to freeze the atomic mobility. This process results in nanogaps that are free of metallic clusters and relatively stable at room temperature for months [155].

Feedback-control A feedback-controlled electromigration (FCE) technique was recently developed, which actively adjusted the applied voltage in response to the changing conductance of the weak link to controllably create the nanoscale junctions [148, 164]. The distinctive advantage of the FCE is that the feedback is used to ensure that the nanogap formation occurs through electromigration at a regulated onset temperature in the constriction region, and a small gap size can thus be obtained. Unlike earlier electromigration approaches that used a single voltage ramp, the FCE typically uses a programmed algorithm to govern the electromigration process [165, 166]. For example, Xiang et al. used a LabVIEW-programmed voltage algorithm to control the electromigration process [165]. The process for their method involved four steps. (i) An initial voltage bias was applied to the metal wire, and the initial wire resistance was measured. (ii) A bias voltage was then increased gently in a ramp, and the wire resistance was measured simultaneously. (iii) When the resistance change ratio exceeded a predefined threshold, the applied voltage was reduced by 5%. (iv) A new reference resistance value was measured again, and the cycle was repeated.

In addition to the resistance as well as the effective conductance, the noise can also be used as a feedback signal. Dong and Parviz observed that the measured relative current noise immediately before the nanogap formation increased 2 orders of magnitude higher than the resistance in the first stage of the electromigration process [167]. The considerable change in the current noise during the electromigration process makes it an attractive candidate to be used as a parameter in the control feedback loop to break the wires. They also presented initial results for using the noise to control the disassembly process. In a typical two-terminal system, a fixed bias voltage U_0 is applied to the junction resistance as well as the series lead resistance. Consequently, as electromigration begins to shrink the junction, the junction resistance increases, and the voltage that falls to the junction increase. The power dissipated in the junction increases proportionally to the junction resistance, which may cause a thermal runaway and destroy the junctions. To overcome this problem, Schönenberger and coworkers developed a highly reproducible method to fabricate metallic electrodes with a nanometer separation by using four terminal devices [168]. The four terminals comprise two symmetric pairs of contacts. In one pair, the bias voltage U_0 is supplied, and in the other pair, the voltage drop U_J over the junction is simultaneously measured. Regardless of the actual value of the junction resistance, the source maintains a constant U_J value. This novel design effectively avoids the thermal instability because the power over the junction will decrease with a fixed U_J and an increased junction resistance.

The limitation of the FCE is that it is time-consuming to fabricate a complex circuitry because the formation of multiple nanogaps requires each junction to undergo the FCE process individually. To overcome this problem, Johnston et al. developed a technique by using the FCE that permits the simultaneous fabrication of dozen of nanogaps at room temperature in a single processing step [169].

In their experiments, the formation of parallel nanogaps is achieved by a balanced simultaneous process that uses a novel arrangement of nanoscale shorts between the parallel constrictions where the nanogaps are formed. This technique can be potentially used for constructing complex circuits of molecular-scale electronic devices.

2.1.3.3 Electromigration Applications

Imaging the Electromigration Process Several research groups found that the gaps formed during electromigration may contain metal nanoparticles that might produce artifacts for the molecular signals [148, 170, 171]. Taychatanapat et al. addressed this issue by observing the electromigration process in real time within an SEM [172]. It was found that the amount of series resistance in the electromigration circuit is a critical parameter in controlling the overall morphology of the junction after electromigration. This study provides a direct confirmation that the simple voltage ramp with no added series resistance in the circuit gradually changes the wire morphology without the formation of any visible nanoparticles.

Unfortunately, SEM images of the nanogaps do not have the sub-nanometer resolution required to view the detailed structure of the nanogap; thus, it is a big challenge to view the electromigration process at the atom-scale resolution. To address this critical issue, Strachan et al. prepared electromigrated nanogaps on free-standing SiN_x membranes that are transparent to the high-energy electrons and are thus compatible with the TEM at a sub-nanometer resolution [173]. It was determined that the junction pinched away from the edges of the original leads for the samples prepared by using the FCE technique. They pointed out that the electrodes were clear of residual debris left from the evaporation procedures, and it was possible to avoid potential parasitic conductance channels through spurious metallic particles by using the electromigration samples.

Moreover, Strachan et al. used real-time TEM imaging to monitor the dynamics of the FCE process at the sub-nanometer scale, which was not accessible to the earlier electromigration investigations [166]. It was determined that well-defined crystal facets appeared during the nanogap formation, indicating a layer-by-layer electromigration process. Furthermore, it was observed that the electromigration process is reversible, e.g. the void can be refilled with gold atoms when the applied voltage is reversed. This finding is clear evidence that the nanogap does not melt during the FCE process, which is contrary to what occurs during the single voltage ramp procedure.

Although several attempts have been made to develop electron transparent substrates and perform two-terminal transport measurements in addition to the TEM inspection [166, 174, 175], it is a considerable challenge to perform these measurements with bottom-gated devices. Gao et al. first demonstrated a technique to perform three-terminal transport measurements that were compatible with the *ex situ* TEM inspection [176]. An electron-transparent Si_3N_4 membrane was used as the substrate, and A Cr/Au layer was deposited on the backside of the membrane, which served as the back gate. The nanogaps were formed on the membrane by using electromigration. The three-terminal electron transport

measurements were performed without molecules at cryogenic temperatures, and the Coulomb blockade features were observed. After the transport measurements, the Cr/Au back gate was removed to make the substrate transparent, and the TEM inspection was conducted *ex situ* again on these samples. The TEM inspection revealed the presence of a few nanoparticles in agreement with the transport measurements. In other words, the sample topology deduced from the differential conductance (dI/dV) plots agreed with the one used for the TEM. This technique can be used to reduce the ambiguous interpretation by providing more information on the sample topology and the structure.

Inelastic Electron Tunneling Spectroscopy (IETS) With the $I-V$ characterization, it is difficult to distinguish the molecular transport from the transport through small gold debris or other imperfections [146]. Molecule-specific features (such as vibrational modes or gate coupling) can distinguish the presence of single molecules in the gap from spurious gold dots [143]. An IETS provides not only a characterization technique to identify the molecules in the junctions, but also important insights into how the interaction of tunneling charge carriers with molecular vibrational modes influences the overall charge transport characteristics. Most of the IETS studies have been performed based on the enormous number of molecules in the monolayer junctions. At the single-molecule level, Song et al. measured the vibrational signatures of the molecular junctions by using the IETS, which was confirmed by the estimated conductance [177]. The Au–S stretch mode was clearly observed in the measurement, and the IETS were extremely sensitive to the chemical structures of the target molecules, suggesting that a reliable metal–molecule contact was formed. The IETS provided unambiguous experimental evidence of the existence of molecules in the nanogap electrodes fabricated using the electromigration technology.

Surface-Enhanced Raman Spectroscopy Surface-Enhanced Raman spectroscopy (SERS) is a useful tool for accessing vibrational and chemical information down to the single-molecule level. The SERS typically relies on plasmon excitations in metal nanostructures to concentrate the incident radiation. Generally, the SERS platforms involve metal nanoparticles to generate the required electromagnetic enhancements. The electromigration technique provides a true nanoscale gap between the extended electrodes instead of discrete sub-wavelength nanoparticles. The ability to fabricate precise gaps on demand combined with the simultaneous electronic transport measurements of the nanogap provides the fingerprint information of the molecules [178]. Ward et al. used the nanoscale gap structures prepared by using the electromigration technology to perform simultaneous measurements of the electronic transport and the SERS [179]. It was observed that the conductance changes often correlated with sudden changes in the intensity of different sets of Raman modes. These correlated fluctuations in the tunneling conductance and the SERS intensity could not be explained by the changes in the gap configuration due to the fact that the tunneling conductance depended exponentially on the gap geometry (e.g. conductance could change by a factor of 10 for a 0.1 nm change in the gap separation); however, the electromagnetic enhancement was not as strongly

affected by the gap size. The experiments suggested that both the SERS and the conductance changes were most likely due to changes in the conformation and the binding of the individual molecules, indicating a single- or few-molecule SERS sensitivity.

Typically, incident light with an electric field polarized across the gap (along the nanowire) is well known to induce the strongest SERS enhancements [97]. Surprisingly, Herzog et al. observed that for a nanogap located within a nanowire, the greatest enhancement and resulting SERS signal occurred when the electric field of the incident light was polarized along the gap (transverse to the nanowire) [180]. This polarization dependence was interpreted by the striking asymmetries in the nanogap fabricated by using the electromigration technique. Due to the intrinsic asymmetries of the nanogap, the dipolar plasmon mode that resonated transversely across the nanowire coupled with dark multi-polar modes, thus causing the intense hybrid plasmon modes to be significantly stronger than that of the longitudinal modes in the structures. These results put light on the understanding of the nature of plasmons in the asymmetric structures and open the possibility of further geometric optimization of the near field-far field. In a further study, the same group developed the Raman technology to address vibrational and electronic heating *in situ* in nanoscale junctions fabricated by using the electromigration technology [181]. When the current flowed through the molecules, the inelastic processes transferred energy from the electrons to the local molecular vibrational modes. In the presence of optical radiation, direct optical absorption and the decay of plasmon excitations produced hot electrons and holes in the metal. These hot electrons and a hot substrate can excite the molecular vibrational modes during the Raman scattering processes. It was demonstrated that the SERS could be used to determine the effective temperature in the molecular junction regime. By measuring the Stokes spectrum, anti-Stokes spectrum, and electrical transport characterization, it was revealed that the mode-specific vibrations could be pumped by both optical excitation and direct current with effective temperatures exceeding several hundred degrees Kelvin. These experiments open a new window to investigate local heating in the molecular junctions [181].

Kondo Effect When a quantum dot (e.g. nanocrystal and nanotube) is attached to the metallic electrodes via the tunneling barriers, the electron transport is dominated by single-electron charging and energy-level quantization [182]. As the coupling to the electrodes increases, higher-order tunneling and correlated electron motion will lead to new phenomena, including the Kondo effect, which results from the exchange interaction between an unpaired localized spin and the conduction electrons in the metallic electrodes. Most of the studies on the Kondo phenomena in quantum dots were typically performed on systems where precise control over the spin degrees of freedom was difficult. By using a chemical design, the spin and the orbital degrees of freedom can be controlled for those molecules (e.g. metal ion complex), thus providing a new system for the Kondo phenomena investigations. Liang et al. first reported the observation of the Kondo effect in single-molecule junctions, where an individual divanadium molecule was trapped in the nanogap by the electromigration method and served

as a spin impurity [182]. In the differential conductance maps (dI/dV as a function of the gate voltage V_G and the source–drain voltage V_{SD}), a diamond-shape pattern was observed, indicating the achievement of a single electron transistor. More significantly, the Kondo resonance (i.e. a sharp zero-bias conductance peak) was clearly observed, and it was demonstrated that this Kondo resonance could be tuned reversibly by using the gate voltage to alter the charge and the spin state of the molecules.

In another example, the Kondo effect in C_{60} single-molecule junctions was investigated [183]. Yu et al. used the electromigration technique to fabricate C_{60}-based single-molecule transistors, and demonstrated that each of them could act as a single-electron device in the Coulomb blockade regime at low temperatures. Interestingly, sidebands parallel to the zero-bias peak were observed, thus indicating the conduction processes that involved both multi-body correlations and inelastic coupling to the vibrational modes. In the same year, Pasupathy et al. measured Kondo-assisted tunneling by using C_{60} molecules in contact with ferromagnetic nickel electrodes fabricated by the electromigration method [184]. It was demonstrated that the C_{60} molecules could be strongly coupled to nickel (Ni) electrodes to exhibit the Kondo effect. More importantly, it was revealed that ferromagnetism could suppress Kondo-assisted tunneling; however, Kondo correlations were still present within the ferromagnetic electrodes. They found that a Kondo peak split was strongly affected by the magnetic moment alignment in the two electrodes under an applied magnetic field, hence proving a new window to modulate the Kondo resonance.

2.1.4 Electrochemical Deposition Junctions

As mentioned earlier, it is difficult to use the MCBJ method to fabricate an integrated microchip due to the drive apparatus [89]. The electromigration method is unlikely to reproducibly fabricate nanogaps with a precise tunable width [177]. Unlike the electromigration and the MCBJ methods, electrochemical method, e.g. electrodeposition or electrodissolution, is reversible and device-compatible [185–187]. By electrodepositing metal atoms onto a specific face of the electrodes, the gap between two facing electrodes can be sequentially narrowed. The electrochemical process can be reversed in an electrodissolution mode for controlled etching/dissolution of the metal atoms from a wire/electrode; thus, the gap can be widened.

The working principle of the electrochemical deposition method is sophisticated [186]. Briefly, an array of original metal electrode pairs was fabricated by using the EBL [187, 188] or optical lithography [189] techniques on a chip (such as thermally oxidized Si wafer). The separation between two facing electrodes in each pair was normally larger than dozens of nanometers. It should be noted that the electrodes were typically covered with Si_3N_4 [188], SiO_2 [189], or photoresists [101], except for a window exposing the gap region of the electrodes to the electrolyte for electrochemical deposition and etching. This insulating layer reduced the leakage current due to ionic conduction. When a voltage was applied between the counter electrode (CE) and the working electrode (WE) in the electrolytes, the metal ions were reduced to metal atoms at the surface of the WE.

The gap was then reduced due to the electrodeposition of the Au atoms onto the electrodes layer by layer. By using the electrochemical deposition, different metals can be deposited to form junctions of heterogeneous compositions, e.g. the deposition of Cu on Au leads [190].

A key issue of the electrochemical method is the use of a feedback system to precisely control the gap width. There are several strategies using different experimental parameters as feedback signals to control the gap size. (i) Using the electrochemical current and the electrolyte conductance as a feedback indicator to critically monitor the gap width, especially when the gap is narrowed below the sub-micrometer scale [185, 191]. The electrodeposition process was stopped by switching off the potentiostat when the conductance reached a preset value. This provides an accurate and reproducible way to control the gap width below a couple of nanometers. (ii) Using the tunneling current as a feedback indicator to accurately monitor the electrochemical deposition or etching [186, 192]. During the electrodeposition process, the current flow between the two work electrodes was monitored throughout the experiment. Initially, the current was small due to the ionic leakage current; however, it increased rapidly when the gap was small enough to detect a tunneling current across the gap. The tunneling current served as a feedback signal to control the deposition process. This method provides the possibility of achieving a suitable gap fitting different molecules. However, this promising method has a limitation: the gap width range is small; typically, the gap is less than 1 nm because it is based on the detection and the feedback of the tunneling current. (iii) Using the electrode potential (V_{gap}) as the feedback indicator [189, 193]. In the previous report, both of the facing electrodes served as the WE, and the metal layer was deposited on both of them simultaneously. Tian and coworkers introduced a new design in which the pair of facing electrodes served as the WE and the reference electrode (RE) [189, 193]. Experiments were performed on this new electrode arrangement by applying a controlled current between the WE and the CE, as shown in Figure 2.13a. Metal atoms were deposited layer by layer only on the WE, and the gap width between the WE and the RE was reduced. The value of V_{gap} (between the WE and the RE) decreased and eventually reached zero, thus indicating that the WE and RE electrodes were fully connected. In this way, the monitored V_{gap} can be used as a feedback signal to control the gap width. The disadvantage of this strategy is that the asymmetric deposition will result in asymmetric electrodes, as illustrated in Figure 2.13b–e. (iv) Utilizing high-frequency impedance in the feedbacks system [194, 195]. Liu and coworkers reported a new system that demonstrated an interesting frequency dependency on the final gap size. In their design, both electrodes of the gap were used as cathodes to symmetrically deposit the metal. The symmetric design guaranteed that the current signal traveled only in the symmetric circuit loop, and the faradic current was recorded independently on the electrochemical workstation. The amplitude of the AC voltage (V_m) recorded at one electrode decreased as the gap distance was close enough. The time evolution of V_m in a complete deposition process is strongly dependent on the frequencies, thus making it a promising tool to control the gap size [194]. (v) Using a self-termination reaction to control the gap size. Majima and coworkers demonstrated a self-termination reaction during electroless gold plating (EGP), which

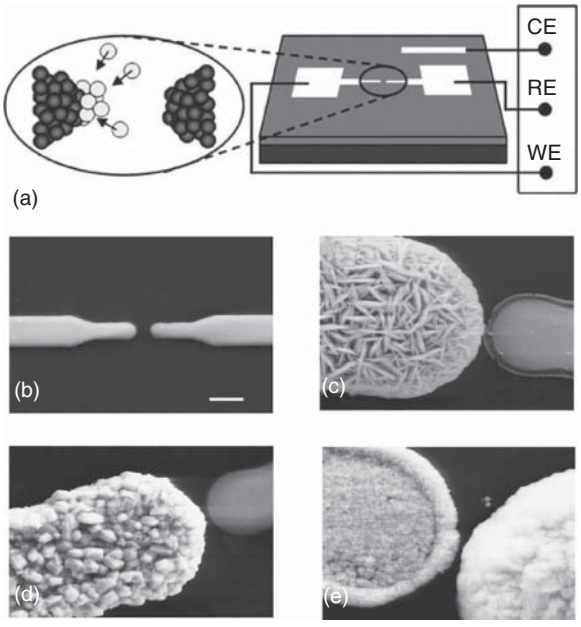

Figure 2.13 Electrochemical deposition. (a) Schematic drawing of the experimental setup. A pair of original facing gold electrodes was fabricated on silicon wafers. Three electrodes were used: counter electrode (CE), work electrode (WE), and reference electrode (RE). The gap was reduced by electrochemically depositing metal atoms on the WE. (b) The original electrodes were separated by two micrometers; (c–e) Layer-by-layer metal atom deposition using different constant current densities: 1.0 mA cm^{-2} (c), 0.4 mA cm^{-2} (d), and 0.1 mA cm^{-2} (e). Source: Reproduced with permission from Liu et al. [189]. Copyright 2005, Elsevier.

provided a uniform gap separation with different initial separations [196, 197]. They designed and implemented a chemical reaction in which the growth of the plating layer in the space between the electrodes was self-terminated. Briefly, the probability of the ions and the reducing agent accessing the nanogap decreased as the gap narrowed opposition to other areas. Therefore, the electroless plating rate between the electrodes decreased as the gap separation decreased, even becoming zero when no plating ions were transported into the nanogap. By using this method, nanogap electrodes for nanodevices with a separation of 3.0 nm were simultaneously mass-produced at a yield of 90% [197].

The structure of the electrochemically deposited material can be tuned by the deposition current [189], electrode potential [101], electrolyte concentration [189], and plating mode (pulse or DC) [198]. After systematic studies, Liu et al. pointed out that it was essential to select a suitable constant current (I_{dep}) to ensure that the deposited layers were smooth and compact rather than rough or loose [189]. They found that a relatively small deposition current led to a more uniform and compact electrode, as shown in Figure 2.13b. Yi et al. reported that the morphology of the electrode surface could be modified by the applied electrochemical potential [101], which created nanoelectrodes with rounded surfaces at high over potentials and needle-like surfaces at low over potentials.

Although the electrode shape and the gap size can be accurately controlled by the electrochemical deposition method, this deposition method cannot offer a gap size change *in situ*, e.g. the gap size cannot be changed to match the length of the target molecules after the molecule is integrated into the gap. To overcome this problem, two strategies were introduced, i.e. deposition combined with the MCBJ [106, 109, 110] and deposition combined with the STM [43, 110, 199]. Three groups did the main contributions to the combined deposition method with the MCBJ method, i.e. Tian's group, Tao's group, and Mayer's group. It was demonstrated by Tian and coworkers that the chip fabricated by the deposition method can be further etched to obtain a suspended metal bridge [106]. By using an MCBJ setup, the substrate of the chip can be bent to break the metal bridge mechanically, offering a tunable gap size *in situ*. In this way, a series of molecule junctions can be fabricated with a high yield, and the properties of the single molecules can be correspondingly investigated [97, 109]. Tian and coworkers also presented an electrochemical strategy to extend the capability of the STM break junctions to create nanowires as well as nanogaps by using various metals [43, 200]. The principle of the approach was based on the electrochemical atom on an STM tip. The tip was driven toward the surface to a sufficiently close distance within an extremely short period of time to allow a jump-to-contact occurrence, which led to the transfer of the deposited atoms from the tip to the substrate surface to create a nanoconstriction. Subsequently, the nanoconstriction was gradually stretched and eventually broken to create two sharp nanoelectrodes. This strategy has been successfully proven to measure the conductance of Cu, Pd, Fe, and various single molecules.

2.1.5 Surface-Diffusion-Mediated Deposition Junctions

The introduction of molecular devices into integrated circuits will most likely use the metal evaporation and deposition technique to form top contacts; however, this approach often results in the metal atoms penetrating or damaging the molecular layer. McCreery and coworkers reported a method of forming "soft" metallic contacts on the molecular layers by using surface-diffusion-mediated deposition (SDMD), in which the metal atoms were deposited remotely and then diffused onto the molecular layer [201, 202]. By employing the SDMD method, one can eliminate the problems of penetration and damage.

The SDMD fabrication process is illustrated schematically in Figure 2.14. In brief, pyrolyzed photoresist films (PPF) or carbon films were fabricated on thermally oxidized silicon wafers. PPF/carbon provides the necessary surface chemistry to allow the formation of a C—C bond between the conducting PPF and the molecular layer. A patterned SiO_2 mask was fabricated on top of the PPF surface by optical lithography. An RIE process was used to etch the unprotected PPF and optimized to create a nearly vertical sidewall beneath the etching mask. The undercutting caused the etching mask to overhang the underlying PPF sidewall, as shown in Figure 2.14b. Then, the molecular layers were electrochemically grafted to the PPF/carbon sidewall, resulting in a covalently bonded molecular layer. Lastly, metallic contacts (Au) were deposited by using electron beam evaporation in a vacuum chamber followed by a diffusion process

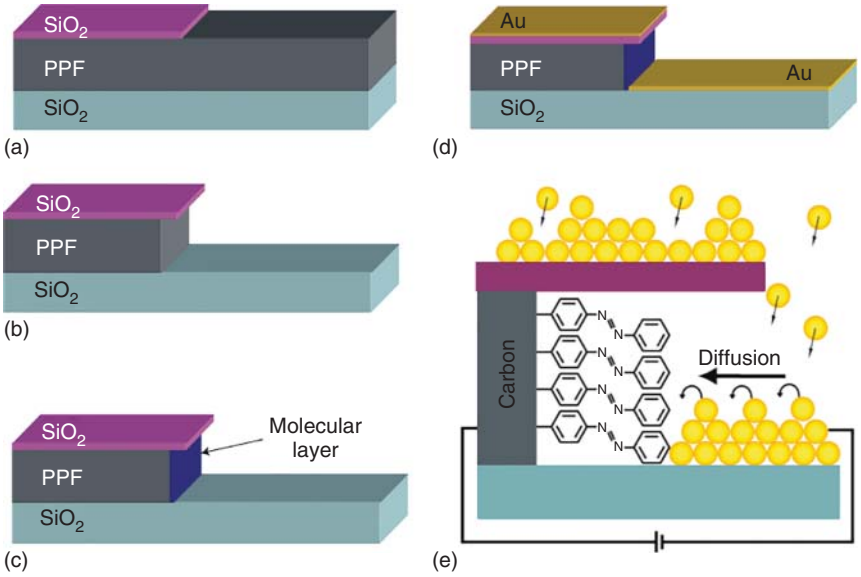

Figure 2.14 *In situ* surface-diffusion-mediated deposition technique. (a–d) Schematic of the SDMD process (a) SiO_2 etching mask was patterned on a PPF layer by optical lithography. (b) Sidewall was formed via reactive ion etching. (c) Molecular layer was adsorbed on the surface of the PPF layer. (d) Au surface diffusion during metal deposition mediates second contact formation. Source: Reprinted with permission from Bonifas and McCreery [201]. Copyright 2010, Nature Publishing Group. (e) Schematic of the atom-diffusion process to complete the molecular junctions. One terminal of molecules was attached to the conductive carbon sidewall, and another terminal of molecules was attached to the diffusion gold atom. The overhanging SiO_2 mask prevented the depositing Au atoms from directly landing on the molecular layer. Source: Reprinted with permission from Bonifas and McCreery [202]. Copyright 2011, American Chemical Society.

to complete the formation of the molecular junctions. It should be noted that for direct electron-beam evaporation on the molecular layers, metal deposition occurred in a direction normal to the molecular surface, without shielding the molecular layer from radiation from the evaporation source. However, for the SDMD process, the deposition angle can be varied with respect to the surface, and the overhang of the etching mask shadowed the molecular layer from direct impingement of both incident metal atoms and radiation from the evaporation source. The key step in the SDMD process is that electronic contact with the molecular layer was achieved via surface diffusion of the deposited metal atoms toward the molecular layer, as indicated in Figure 2.14e.

The remote deposition and diffusion method reduces the metal atom momentum and allows the kinetic energy and the heat of the depositing metals to be dissipated away from the molecular layer. Thus, the SDMD method can eliminate the molecular damage caused by heating and metal penetration. In the experiment, the conductance steps were clearly observed during the process when the metal atoms contacted individual molecules one at a time within a monolayer. The conductance histogram extracted from the real-time

conductance curves indicated clear multiple peaks, which were dependent on the types of target molecules. Hence, the ability to fabricate molecular junctions containing single to tens of molecules "one molecule at a time" was really demonstrated. The molecular junctions fabricated by using this method exhibited excellent yield (typically >90%) and reproducibility and allowed the effects of the molecular-layer structure, thickness, and work function of the contact materials on the conductance to be examined.

2.2 Ensemble Molecular Junctions

In addition to the single-molecule junctions, ensemble molecular junctions, which are formed from more than a few or self-assembled monolayers (SAMs) of molecules, are another important branch of molecular-scale electronics. Currently, there are mainly three universal strategies for forming ensemble molecular junctions for large-area electrical measurements: (i) direct formation of metal electrodes by using either electron beam/thermal evaporation or electrochemical deposition, (ii) incorporation of electrically conducting polymers/nanomaterials as an electrode, and (iii) utilization of liquid metals as electrodes. The following section details the fabrication of ensemble molecular junctions by using different state-of-art methods, including lift-and-float, liquid metal contact, nanopore and nanowell, on-wire lithography (OWL), nanoimprint lithography, crossbar or crosswire, self-aligned lithography, buffer interlayer-based junctions, and on-edge molecular junctions (OEMJs).

2.2.1 Lift-and-Float Approach

The flotation of metals on target substrates provides an efficient way to overcome the physical damage that is involved in most vacuum deposition procedures for top contacting. This method relies on capillary interactions, induced by the liquid–solid interfaces between two solids, and a common liquid for transferring thin solid metal films onto solid substrates modified by molecules. The idea, termed as a lift-off float-on (LOFO) approach, was inspired by the sample preparation in transmission electron microscopy experiments to deposit GaAs on foreign substrates [203] and primarily developed by Cahen et al. [204–206].

Briefly, the general procedure for the LOFO approach includes four steps, as shown in Figure 2.15: (i) evaporating the metal film, denoted as a leaf, onto a solid support, such as a glass slide; (ii) detaching the metal leaf from the solid substrate and floating it at the liquid surface; (iii) adsorbing a molecular layer onto the substrate or the metal film or both to add molecular functionality; and (iv) attaching the metal film to the target substrate by using a liquid mediated process to complete the metal–molecule–substrate junction.

By using the LOFO method, several different types of molecular junctions, such as Au–molecule–GaAs, Au–molecule–Si, and Au–molecule–ZnO, were created and deeply investigated by Cahen and coworkers [204, 208, 209]. Vilan et al. first reported the fabrication of the Au–molecule–GaAs junction by using the LOFO

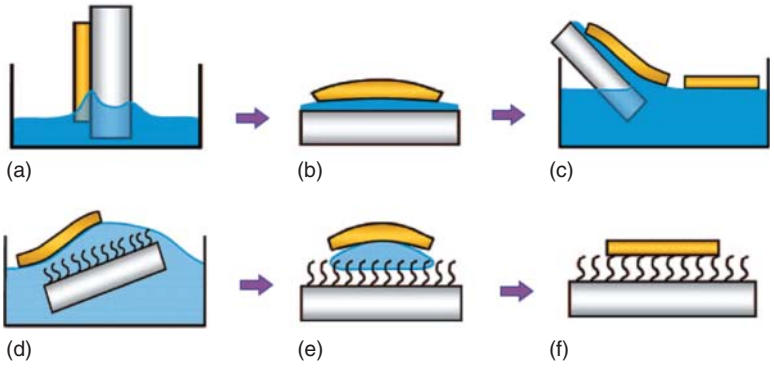

Figure 2.15 Schematic description of the lift-off, float-on (LOFO) procedure: (a–c) Lift-off of the evaporated leaf (metal layer) from a glass slide. (a) The glass slide is partly inserted into a detaching agent to induce the peeling process. (b) The disjoining pressure detaches the leaf from the glass substrate. (c) The metal leaf floats on solvent due to the capillary interaction. (d, e) Float-on of the leaf on the solid substrate. (d) The metal pad floats on the substrate adsorbed with molecules. (e) The solvent is rapidly removed to prevent the wrinkling of the leaf. (f) The metal/monolayer/substrate is completed. Source: Reprinted with permission from Haick and Cahen [207], Copy right 2008, American Chemical Society.

approach [204]. By adsorbing a series of functional molecules, whose dipoles varied systematically, onto single crystals of n-type GaAs semiconductors, diodes were produced with an effective barrier height that could be tuned by using the molecule's dipole moment. These barrier heights correlated with the change in the work function of the GaAs surface after molecular modification. Remarkably, it was demonstrated that the molecules could control the electrical characteristics of the metal–semiconductor junctions without the need for electrons to be transferred onto and through the molecules. These results suggest that the properties of electronic devices can be tuned by using molecular dipoles instead of actual electrons being transported through the molecules [204].

Later, Salomon et al. replaced GaAs with ZnO to form Au–molecule–ZnO junctions and demonstrated that the molecular control over the effective barrier height was more effective with ZnO (ionic semiconductor) than that with GaAs (covalent semiconductor) [209]. Their results further proved that the molecular dipoles could control the electrical characteristics of semiconductor–metal junctions, without needing electrons to pass through the molecules due to the electrostatic interactions between the substituent groups of the adsorbed molecules and the top metal contact. These systematical experiments performed by Cahen and coworkers demonstrated that the free semiconductor surface, e.g. surface state density, could dominate the junction behavior instead of direct metal–semiconductor interactions [210].

Normally, Au is used to fabricate the top electrode (metal leaf). To lift off contacts between the gold and the substrate, the LOFO method requires a detaching agent, such as HF or acetic acid solutions. For gold, this may be an easy treatment, but it is too harsh for other metals, such as Ag, Al, and Cu (used for low cost fabrication of molecular junctions). Because these metals react vigorously with alkalis and acids to form metal-hydroxides and halides, such contamination hinders the

stable electronic contact to the molecules. Recently, Ikram et al. put forward a relatively simple method for forming Ag and Al electrical contacts on the soft surfaces of monolayer molecules without using chemical etching treatments. In their experiments, the glass substrates were first spin-coated with a thin layer of the starch solution as a sacrificial layer. Then, Ag contacts were formed by screen printing conductive silver pastes onto the glass substrate, and similar contacts of aluminum were also deposited onto the glass substrates using thermal evaporation. With this method, metal contacts can be easily lifted off by dissoluting the sacrificial layer in water.

The primary advantage of the LOFO method is that the pinholes involved in the atom deposition, physical damages due to the overload force, and chemical damages expected from the electrochemical deposition can be relatively avoided. Another advantage of the LOFO method is that it is relatively suitable for studying biological molecules. This LOFO method does not rely on the actual chemical binding of the molecules to the top metal layer, and the surfaces that are to be bound are kept wet until the establishment of the electrical contact at (or very close to) room temperature, which makes it suitable for electronic devices incorporating biological molecules. Beside these advantages, challenges in the LOFO method remain, even though several improvements had been introduced to overcome these challenges [205, 211]. For example, it is a considerable challenge to accurately control the force between the floating electrodes and the substrates, e.g. it is hard to behave like an AFM to make a defined contact between the top electrodes and the molecules. In fact, the repulsion between the floating film and the substrate is often observed, which may generate an additional air gap between the top electrode and the molecular layer. Additionally, it is difficult to completely prevent wrinkling of the thin metal film (float film) during contacting process.

Melosh and coworkers further developed a polymer-assisted lift-off (PALO) process to overcome the wrinkling problem and made a big step toward actual integrated molecular devices [206]. This method allowed for the transfer of the top parallel electrodes onto molecular films without experiencing macroscopic distortion or damage. The key component is a hydrophobic polymer, i.e. a backing layer on the top electrodes, thus guaranteeing the mechanical stability and a thermodynamic driving force to eliminate wrinkling. By using this technique, high-quality metal–electrode devices can be fabricated in parallel over a wide range with lithographically defined geometry. Furthermore, the floating parallel electrodes were transferred to the substrates to create a cross bar structure. No shorted molecular junctions were observed for over 90% of the examined devices. The PALO method combined several advantages of the nano-transfer-print (denoted as nTP, which will be introduced later) and the LOFO methods, namely, parallel electrodes fabrication, small electrode sizes, high-quality metal films, and non-damaging deposition.

2.2.2 Liquid Metal Contact

The liquid metal contact is relatively stable and can effectively prevent problems that are encountered with the direct evaporation of metal top contacts, such as metal atom penetration into the junction and mechanical damage. Reynolds and

coworkers first introduced a method to use liquid metal electrodes to form the molecular junctions [212, 213]. By using a clean mercury (Hg) drop electrode as the top electrode, electrical measurements were performed on multilayer molecular films. In their experiments, a number of different bottom contacts based on barium, cadmium, calcium, copper, and lead were used [212]. They found that a mercury drop was the satisfactory material at the time to form a contact with low resistance and without physical damage.

The principle used to form the Hg–molecule–Ag is relatively simple, as illustrated in Figure 2.16 [214]. The junction can be formed by a mechanical contact between an SAM on a mercury drop and an SAM on the silver film supported by a silicon wafer. An SAM-coated silver film was placed in a beaker and covered with a hexadecanethiol-containing solution used to form the SAM on the Hg drop. The SAM on the Hg drop was formed *in situ* on the drop surface suspended from a syringe. A micromanipulator allowed mechanical contact between the SAM on the Hg drop and the SAM on the Ag film. The diameter of the Hg drop was ~1 mm, and the contact area was $\sim 5 \times 10^{-3}$ cm^2. A related junction in which the organic film was sandwiched between two mercury drops was also possible [215, 216]. Similarly, the Hg–molecules–Si junction can be generated by placing an Hg drop on the monolayer above the silicon wafer by using the hanging mercury drop electrode apparatus [217].

Using an Hg drop as an electrode has several advantages [216]. Firstly, the Hg surface, as a liquid, is free of structural features e.g. edges, terraces, and pits, which normally result in defects in the adsorbed monolayer. Secondly, the formed junctions are stable and reproducible, i.e. less than 20% of the junctions form short circuits. Thirdly, Hg forms well-ordered SAMs after coming into contact with the target molecules for a short time, and Hg can host a large variety of molecules [218]. Finally, the Hg drop can conform to the topography of the solid

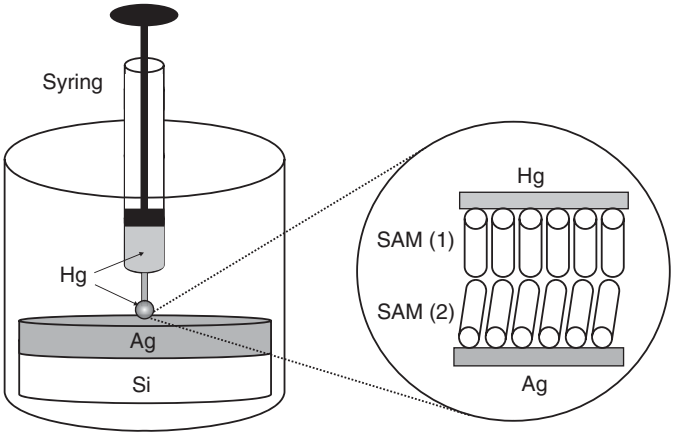

Figure 2.16 Schematic illustration of the fabrication of the Hg–molecule–Ag junction. The electrical junction was formed by the mechanical contact of the two SAMs. SAM (1) indicates the SAM on the solid Hg electrode, and SAM (2) indicates the SAM on the Ag electrode. The Hg drop was suspended from a syringe and assembled molecules *in situ*. Source: Reprinted with permission from Chabinyc et al. [214], Copyright 2002, American Chemical Society.

surfaces, thus forming a good conformal contact with the molecular layers on a solid surface. However, Hg may have harmful effects on the health of the user, which is a disadvantage of this method.

The method based on liquid metal alloy electrodes was developed by Whiteside and coworkers [219–224]. They initially introduced an idea where eutectic gallium–indium (EGaIn) could replace Hg and be used as one of the electrodes [220, 223, 224]. The work function of EGaIn (~4.2 eV) is close to that of Hg (~4.5 eV); however, EGaIn does not flow until it experiences a critical surface stress. In their experiments, an EGaIn drop suspended from the needle of a syringe was brought into contact with the bare Ag surface, and the syringe was then raised until the EGaIn separated into a conical tip. The top EGaIn tip protruding from the needle did not typically retract into a semispherical droplet. Thus, the contact area can be dramatically reduced [224]. The thin Ga_2O_3 layer (~1 nm) on the surface of the EGaIn electrode due to oxidation may play an important role in the system. This film of Ga_2O_3, which is similar to a protective layer, helps prevent the formation of metal filaments, leading to high yields of the molecular junctions. The effects of the Ga_2O_3 thin films were extensively investigated, and it was demonstrated that the molecular structure of the SAM, and not the characteristics of the Ga_2O_3 film, dominated the observed electron transport behavior [221]. This method also has disadvantages: it suffers from user-dependent variations in the details of the formation of tips and the SAM//GaO_x/EGaIn contacts, and the mechanical stability of the junctions is limited by the details of the micromanipulator on which the top electrode is mounted [225].

Combined with optical lithography, Whitesides and coworkers further presented a method for fabricating small arrays of tunneling junctions based on liquid metal alloy electrodes. These junctions had EGaIn top electrodes stabilized in microchannels and ultraflat silver bottom electrodes [223, 225]. These junctions by using the EGaIn did not require a clean room, ultrahigh vacuum, toxic substances, such as the previously used Hg, or a second SAM. By using this method, several significant results on the electron transport through molecules were achieved, such as the following: (i) The role of the binding group and the purity of the thiols in the performance of the molecular diodes were revealed [226]; (ii) The dependency of the tunneling decay coefficient on the topography of the bottom electrodes as well as the rate of charge transport on the molecule structure were studied [227–229]; and (iii) The effects of the molecule structure and the molecular interaction on the electron transport were extensively addressed [220, 230, 231].

Nevertheless, the optical lithography process is time-consuming and relatively high cost for production. Wan and coworkers put forward a low-cost strategy to form the molecular junctions sandwiched between the tin/indium electrodes, known as capillary tunnel junctions [232, 233]. The capillary tunnel junctions are formed within a commercially available capillary fiber with a ~0.1 mm diameter. As illustrated in Figure 2.17, there are three primary steps used to prepare this type of capillary tunnel junction. (i) The melted tin or indium is filled into the fiber to a target height due to the capillary effect, which happens when the temperature is slightly higher than the melting point of tin or indium. The fiber will be filled

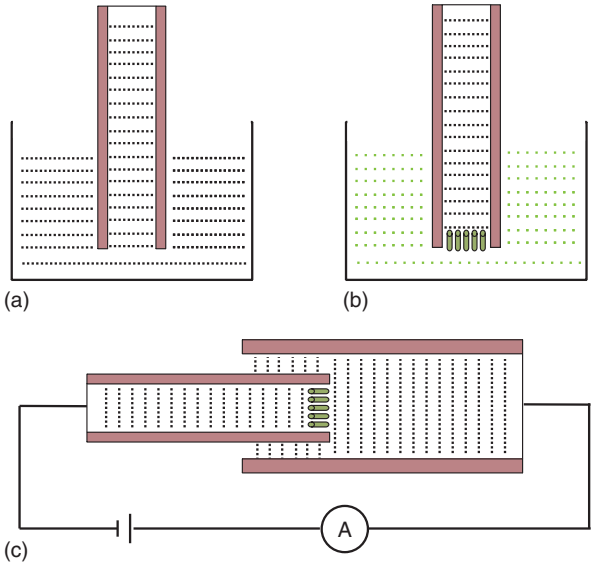

Figure 2.17 Schematic of the preparation procedure for a capillary junction. (a) The fiber is filled with liquid tin or indium via the capillary effect at high temperatures. (b) The end point of the fiber is immersed into the solution to form an SAM on the solid metal (tin or indium) surface at room temperature. (c) The SAM modified fiber is inserted into another fiber with a larger diameter filled with tin to complete the molecule junction. Source: Reprinted with permission from Liu et al. [233]. Copyright 2004, American Chemical Society.

with solid tin or indium when it is cooled to room temperature. (ii) The end point of the fiber is then immersed into the molecule-containing solution to obtain an SAM at the metal surface. (iii) The SAM modified fiber is subsequently inserted into another fiber with a larger diameter filled with tin or indium to seal the SAM inside the capillary fiber. Finally, the molecule junction will be completed as the temperature is again cooled to room temperature.

The molecular junctions based on the capillary fibers were stable and could be used permanently. Tin or indium was selected as the electrode materials because of their relatively low melting points and wide applications in optoelectronic devices. Both tin and indium are the main constituents of transparent conductive glasses. Moreover, the naturally existing hydroxyl groups at the tin oxide or indium oxide surfaces provide a potential for functionalization via molecular self-assembly approaches. The primary limitation of this method is that the contact area as well as the distance between the two electrodes is fixed as the junction is formed. Another disadvantage of this method is that physical damage to the molecular layer may appear when the small fiber is inserted into the large fiber to complete the molecular junction.

2.2.3 Nanopore and Nanowell

The molecular junctions fabricated via a hole, such as a nanopore or a nanowell, to our best knowledge, were first introduced by Reed and coworkers [88, 234, 235]. The starting substrate for the nanopore device fabrication was a double-sided polished silicon wafer, on which a thin Si_3N_4 layer was deposited. By using optical lithography, RIE, and wet etching techniques, a window of the silicon nitride membrane suspended over the silicon wafer was obtained. All of the following processes were performed based on this silicon nitride membrane [235]. (i) A hole with a bowl-shaped geometry (~50 nm in diameter) was created through

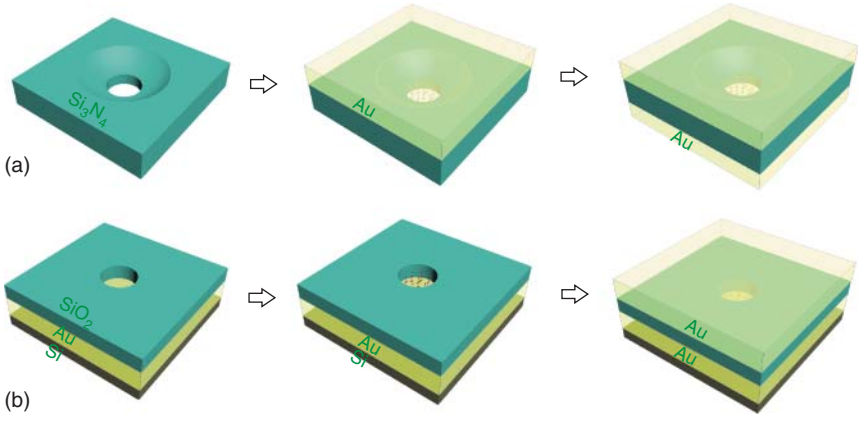

Figure 2.18 Schematic of the molecular device structure based on a hole: nanopore versus nanowell. (a) Nanopore based molecular junctions. A pore was made through the Si_3N_4 membrane via etching. The top Au electrode was obtained by evaporating Au onto the top side of the membrane, which filled the top end of the pore. After self-assembling the molecules on the top electrode, the pore was filled to complete the molecular junction by evaporating Au onto the bottom side of the membrane. (b) Nanowell-based molecule junctions. A hole was drilled through the SiO_2 layer to the bottom Au layer. After self-assembling the molecules on this bottom electrode, the hole was filled with Au to complete the Au–molecule–Au junction.

the membrane through the EBL and RIE methods, as shown in Figure 2.18a. (ii) An Au layer (~200 nm thickness) was evaporated onto the top side of the membrane, which filled the pore with Au and worked as the top electrodes. (iii) The sample was then immediately transferred into a solution to assemble a molecular layer on the top electrode surface. (iv) Then, the sample was loaded into a vacuum chamber to thermally deposit the bottom Au electrode to complete the Au–molecule–Au junction. Because several delicate processes were involved during the sample fabrication, the electrical behavior typically varied from sample to sample. Song et al. presented a statistical method to determine the intrinsic electronic transport properties of these SAM-based devices [236]. Another disadvantage of this nanopore strategy is that the fabrication yield of the molecular junctions is relatively low (~2%) due to the metal atom penetration into the molecular layer, which creates a short device during the period of evaporating the bottom Au electrode [236]. Several improved processes had been introduced to reduce the short phenomenon, such as using a packed assembled monolayer, low temperature evaporation metal atom, and precisely controlling the atom evaporation rate [235].

Nanowell-based molecular junctions were first presented by Tour and coworkers [234]. The nanowell is a planar device as opposed to the nanopore, in which a hole is created through the wafer. As illustrated in Figure 2.18b, the nanowell devices were fabricated on silicon wafers that had pre-patterned gold electrodes covered with silicon dioxide. By using the FIB technique instead of the EBL technique, a small hole (10–40 nm in diameter) was drilled in the silicon dioxide layer [234]. A hole with a diameter as small as 1 nm was also reported by employing

the FIB technique [237]. Due to the small size of the hole, the yield of the short devices was reduced. Furthermore, in comparison with the nanopore, the fabrication process was simplified in three aspects: evaporating at a faster deposition rate, performing the evaporation on an uncooled substrate, and eliminating the step of bottom electrode evaporation [237]. However, the formation of the metal filaments that short the junctions cannot be completely eliminated by directly evaporating the metal atoms above the molecular layer, especially for those holes with a large diameter. In order to overcome this shorting problem and increase the yield of the molecular junctions, a conducting buffer layer can be inserted between the metal layer and the molecular layer, thus preventing the damage to the molecular layer. The conducting interlayer can be a highly conductive hybrid polymer PEDOT:PSS [238], multilayer graphene [239], or SWCNT layer [240]. The strategy of inserting a conducting interlayer to create large-area molecular junctions will be addressed in detail in Section 2.2.7.

2.2.4 On-Wire Lithography

This procedure, which is known as on-wire lithography (OWL), combines advances in the template-directed synthesis of nanowires with the electrochemical deposition. OWL was initially introduced by Mallouk and coworkers [241]. The initial idea for OWL is similar to the method discussed in the Section 2.2.3, i.e. nanopore-based junctions. A primary difference between them is that the pore in the OWL is fabricated based on the polycarbonate membrane instead of silicon wafers, and the polycarbonate membrane is completely dissolved in dichloromethane. After removing the membrane, nanowire segments with a sandwiched molecular layer can be obtained, thus forming the metal–molecule–metal junction. Later, this idea was further developed and popularized by Mirkin and coworkers, in which a precisely controlled gap was initially obtained [242–244].

As shown in Figure 2.19, the OWL procedure can be briefly described as follows: [242] (i) The typical electrochemical growth of pillars consisting of multiple layers of at least two different metals in a porous alumina template, in which one of the metal layers is used as a sacrificial segment; (ii) removal of the template, thus producing nanowires with different segments; (iii) formation of a layer of silica (thickness is approximately half of the nanowire diameter) on the nanowire-coated substrate by using plasma-enhanced chemical vapor deposition. Then, the nanowire with a silica supporting layer was released from the substrate by the ultrasonic cleaner; and (iv) removal of the sacrificial segment from the wire by using wet etching to generate nanowire structures with gaps accurately controlled by the length of the original sacrificial segments. It is anticipated that OWL could dramatically boost the development of molecular electronics.

The last critical step is to bridge the nanogaps with the molecules, and two different strategies have been presented to bridge the gap with the molecules. (i) "Dip-pen nanolithography" so called the DPN strategy [246]. In this strategy, an atomic force microcopy is used, and the molecules are delivered from the AFM tip to the gap area of the nanowire via a capillary transport in a manner similar to

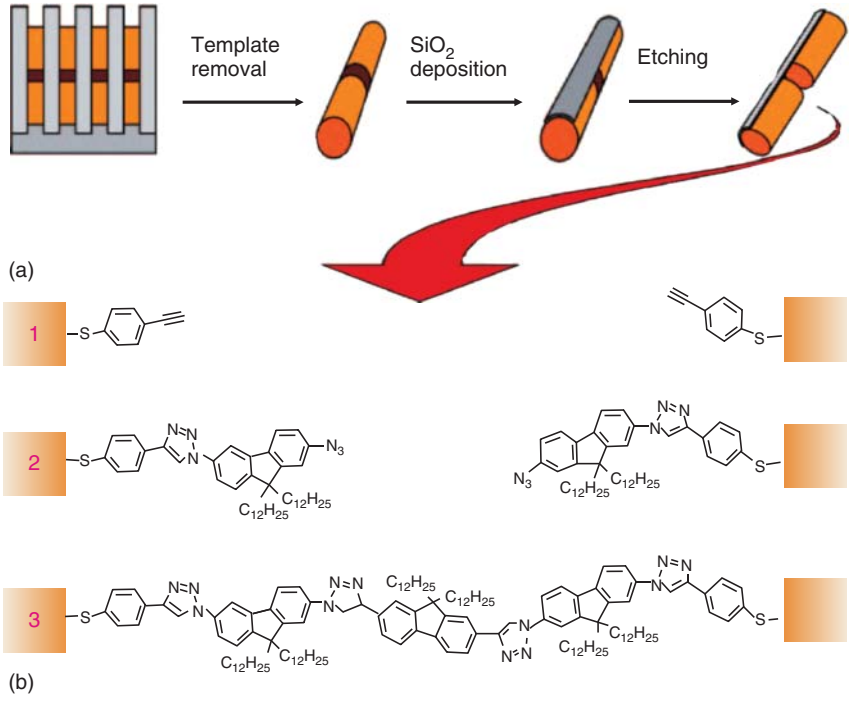

Figure 2.19 On-wire lithography. (a) Schematic of the OWL for fabricating metal electrodes. (b) Schematic illustration of the click chemistry within the nanogaps prepared by the OWL. The junction was closed by a stepwise in-gap oligomer assembly. Source: Reprinted with permission from Maryor. [245]. Copyright 2008, American Chemical Society.

that of a dip pen. Thus, the molecules are immobilized onto the microelectrodes and fill the gap. This strategy is suitable for a larger gap size. Qin et al. successfully deposited conducting polymers into a 13 nm gap by using the DPN method and studied the transport properties with and without the conducting polymer [242]. (ii) Self-assembly. In this strategy, the molecules are self-assembled onto the electrode surface. The molecule will bridge the two opposite electrodes when the molecular length is comparable with the gap size between the electrodes [245]. However, there is a mismatch in the length because the molecule length is typically a few nanometers, whereas the gap size is generally dozens of nanometers. Fortunately, the nanowire, which is dozens of nanometers in diameter, and sub-3-nm gaps were obtained by using fine control and optimization of the conditions in each fabrication step [243, 247, 248].

As discussed earlier, the previous study on the molecular junction fabrication primarily relies on the *ex situ* syntheses of molecular wires followed by the subsequent insertion of the molecules into the gap separated by the nanorods. In this *ex situ* approach, the molecular length should be similar to the gap size, which limits the yield of the molecular junction. To circumvent the problems, Mirkin and coworkers used click chemistry for the *in situ* modular synthesis of molecular wires to bridge OWL-fabricated nanogaps [249]. Click chemistry

is a synthetic approach popularized by Sharpless and coworkers that involves controlling reactions step by step [250]. The general scheme for bridging the nanogaps by using click chemistry for molecular junction fabrication is illustrated in Figure 2.19b. Firstly, 4-ethynyl-1-thioacetylbenzene was assembled into a monolayer on the surfaces of the electrodes, which are located at opposite ends of an OWL-fabricated nanogap (Step 1). Then, the device was immersed in a solution containing 2,7-diazidofluorene. One of the azide groups in 2,7-diazidofluorene reacted with the alkyne group from Step 1 to form a 1,2,3-triazole unit at one end, and the azide group at the other end was left unchanged (Step 2). This structure can be further extended through a reaction with 2,7-diethynyl-fluorene (Step 3), which, in turn, can react again with the azide groups. By following the appropriate number of reaction cycles, the molecular wires grow from the opposing electrodes and eventually bridge the nanogap. One advantage of forming molecular wires by using the click methodology within the OWL-fabricated nanogaps is that *in situ* fabrication is challenging for other existing testbeds due to the limited gap space or solution-processable problems. By monitoring the process through Raman spectroscopy or X-ray photoelectron spectroscopy, one can watch and confirm the gap closed process [251, 252].

The advantages of using the OWL method to form nanoelectrodes include (i) the ability to fabricate sub-5-nm gaps in high yield with precise dimensional control (the diameter of the wire is controlled by the template-pore diameter, and the length of the wire and the size of the gap are controlled electrochemically) [248]; (ii) the remarkable simplicity, stability, and reproducibility of the OWL method to offer a transport testbed; and (iii) the flexible selection of the source and drain electrode materials by thermally depositing different types of metals [247]. Recently, the applications of the OWL technology have dramatically increased beyond molecular junctions, such as the fabrication of nanotube-bridged nanorods [253, 254], graphene ribbons by using OWL-based nanomasks [255], free-standing nanorings [256], and resettable electronic logic gates [257], enhancement of the electric field/Raman spectroscopy [258–260], and biological applications [243].

2.2.5 Transfer Printing Techniques

In an attempt to reduce electrical shorts between the contacts, mercury droplets, lift-off float-ons, nanowells, and OWL were introduced and successfully demonstrated the ability to increase the yield of the molecular junctions. Although these approaches are able to produce laboratory test structures, they are not easily scaled up for the fabrication of circuits and systems containing molecular devices. In this sense, the nanotransfer imprinting lithographic (NIL) approach is rapid and simple and occurs readily under ambient conditions, offering a promising approach to fabricate integrated molecular devices.

Melosh and coworkers first introduced this novel approach to fabricate top-contact electrodes in Au/1,8-octanedithiol/GaAs junctions [261]. As illustrated in Figure 2.20, their nanotransfer printing procedure can be briefly stated as follows: (i) the GaAs substrate is first etched to remove the native oxide layer and then immediately exposed to 1,8-octanedithiol to form an SAM on

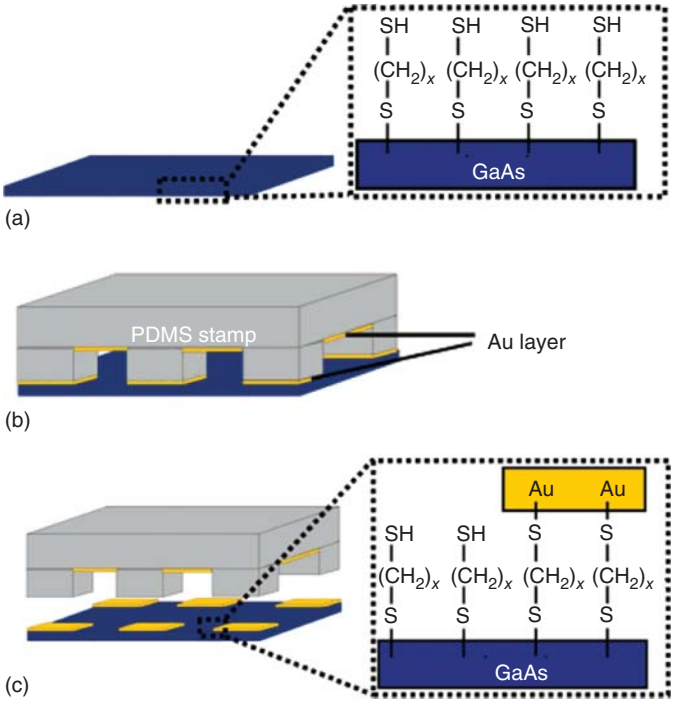

Figure 2.20 Schematic of the nanotransfer printing procedure. (a) The GaAs substrate is first etched in concentrated NH_4OH or HCl and then immediately exposed to a 1,8-octanedithiol vapor or solution for self-assembly. (b) The gold-coated elastomeric PDMS stamp is brought into contact with the treated substrate. (c) Removing the stamp from the substrate completes the nanoimprinting process. The Au on the PDMS stamp is bonded by the molecules and transferred to the molecule-coated GaAs substrate. Source: Reprinted with permission from Loo et al. [261]. Copyright 2003, American Chemical Society.

the GaAs surface; (ii) a gold-coated elastomeric polydimethylsiloxane (PDMS) stamp is brought into contact with the substrate, and the GaAs-molecule-Au junctions are formed; and (iii) removing the stamp from the substrate completes the printing process. The elasticity and the mechanical conformability of the PDMS stamp ensure a good contact at the stamp/substrate interface. Because the adhesion of Au to PDMS is poor compared with the Au–S bonding, the stamp can be easily removed from the substrate to complete the pattern-transfer process. Subsequently, current–voltage and photoresponse experiments were performed. It was determined that the current densities were independent of the contact area for the NIL-fabricated devices, thus confirming that the current distribution is uniform in the NIL-fabricated junctions.

In the NIL approach, direct Au/GaAs contact can be successfully avoided and move a big step forward to fabricate integrated molecular devices. However, challenges for reliable interface remain. One challenge is that the top electrode roughness may generate small gaps between the metal and the organic monolayer, leading to unreliable electrical responses. In other words, it is difficult to obtain an ultrasmooth surface when a metal layer is evaporated on the PDMS mold, which

may generate an additional air gap and obstruct the analysis of the actual molecular properties. Hacker and coworkers demonstrated a novel fabrication route for high-quality molecular junctions bonded to ultrasmooth silicon and ultrasmooth gold by using a flip-chip lamination approach [262]. Generally, it is easy to obtain large-area ultrasmooth silicon bottom electrodes; however, obtaining the ultrasmooth top gold electrodes is quite difficult. To generate an ultrasmooth gold layer, Hacker et al. directly evaporated a gold layer onto an ultrasmooth Si substrate previously treated with a fluorinated releasing layer. This ultrasmooth gold layer can be attached by using the stamp (similar to PDMS). After peeling it off from the silicon substrates, the ultrasmooth gold layer attached to the stamp can be obtained. Then, the functional molecules were self-assembled on this gold layer. Lastly, the gold electrodes and another silicon electrode were laminated together to form a high-quality molecular junction.

Another challenge for the NIL is the resolution limitation. Generally, the potential minimum dimension of the NIL has been limited to approximately 50 nm due to the deformation, collapse, and merging of the molds during transfer printing, resulting from the low modulus of the elastomeric molds. Although a relatively improved resolution of 20 nm was reported by adjusting the modulus and the surface energy of the elastomers [263], the partial deformation and degraded quality of the elastomeric molds still remain significant issues. The resolution of the NIL can be enhanced by using hard molds with a block copolymer (BCP) self-assembly [264]. Jeong et al. reported an NIL method to create a pattern with sub-10-nm resolution by using the BCP self-assembly [265]. The microphase separation of two mutually incompatible blocks in a BCP led to the formation of ordered arrays with sub-30-nm structures. After the transfer of the BCP films onto the substrate, they could be converted easily into sub-10-nm SiO_x nanostructures by employing plasma oxidation treatments. It was further demonstrated that the BCP patterns with a line width of 8–16 nm could be successfully transferred onto a wide range of materials. The resolution of the NIL can also be enhanced by employing soluble polymer. Sanetra et al. reported that junctions with half-pitches down to 50 nm could be fabricated in a parallel process. In their experiments, the transfer of the top electrode was facilitated by a water-soluble polymer film, which supported the lifting process of the nanometer-sized electrode and enhanced the yield of the transfer process [266]. The primary disadvantage of the NIL is that it requires a molecular layer that adheres to the top contact, usually with a thiol group, which restricts the materials that can be used [206]. Here, we only present a brief introduction and discussion to the NIL technique. The detailed technique development, wide application, and limitation of the NIL technique can be found elsewhere [267–269].

One promising device architecture to achieve next-generation memory and logic devices based on metal–molecule–metal junctions may be the crossbar/crosswire latch [266, 270, 271]. Because it can be fabricated in parallel, it has the potential for achieving high-throughput production with low cost [272]. In the crossbar and crosswire methods, electrodes are placed on top of each other with a sandwiched molecular layer. A crossbar is a set of rectangular block wires with microscopic dimensions that cross each other with a functional layer in the cross-points. The critical step in the fabrication of the molecular junctions

is to apply the metal top electrode array above the bottom electrode array. In principle, the top electrode can be fabricated by metal deposition through a shadow mask consisting of parallel lines [273]. However, vapor-deposited metals normally create shorts in the SAMs due to the filamentary growth, even though several novel techniques have been introduced to reduce this problem [274–276]. Alternatively, the nanotransfer printing (stamp printing) [261, 277, 278] and the direct metal-transfer [279, 280] techniques were used to fabricate the high-yield crossbar structures, in which shorting was eliminated.

In reality, the SAMs typically have defects due to several reasons: (i) step edges due to the roughness of the electrode surface; (ii) pin holes or filaments formed during the top electrode evaporation; and (iii) impurities or residuals on the electrode surface introduced in the lithography process. To reduce defects in the SAMs, Nijhuis and coworkers presented a method to create a crossbar array based on Ga_2O_3/EGaIn stabilized in the microchannels in a transparent polymer (PDMS) [281]. The primary fabrication process is schematically depicted in Figure 2.21a. In their experiments, an ultraflat template-stripped silver (Ag^{TS}) electrode embedded in a cured optical adhesive (OA) was used as the bottom substrate. The pattern of Ag electrodes was fabricated by using a standard lithography technique. Then, a glass substrate was affixed to the silver electrode pattern by using a cured UV-curable adhesive. An OA interacts strongly with the Ag and the glass support but not the wafer. After cleaving the Ag/adhesive/glass composite from the wafer, the bottom substrate was obtained. Subsequently, a microchannel in the PDMS was aligned perpendicularly to the bottom electrodes after the SAMs were formed. Lastly, the microchannels were filled with Ga_2O_3/EGaIn to complete the crossbar device. The crossbar devices fabricated by using this method have a few clear advantages. (i) They are mechanically stable, and it is possible to perform J–V measurements over a broad range of temperatures. (ii) They do not require metal deposition, either by electron-beam evaporation or by sputtering directly onto the SAMs, to form a top electrode. (iii) They do not suffer from alloying between the metal electrodes or require intermediate layers of the conducting polymer's processing steps.

Recently, Shimizu et al. presented a process known as polymer-assisted lift-off (PALO), which is a promising printing technique that rapidly forms crossbar junctions [206, 282]. The fabrication process is shown in Figure 2.21b. (i) The PMMA was spin-cast as a hydrophobic backing layer onto the metal electrodes, which was previously patterned on a sacrificial substrate. (ii) The Si substrate was then slowly dipped into a buffer solution of acetic acid, where the polymer–Au layer was detached from the substrate and floated on top of the aqueous solution without wrinkling due to the surface tension of the water. (iii) The crossbar device was assembled by floating the metal–polymer film onto a bottom substrate, which was patterned with the bottom electrodes and adsorbed with the molecules. Due to the hydrophobicity of the polymer and the molecular film, the polymer was drawn into contact with the substrate once an initial point of contact was made. (iv) Lastly, the crossbar device was completed after the polymer layer was removed via etching. This PALO method allows for the transfer of a top metal contact onto molecular films without macroscopic distortion or damage. The key component is a hydrophobic polymer backing

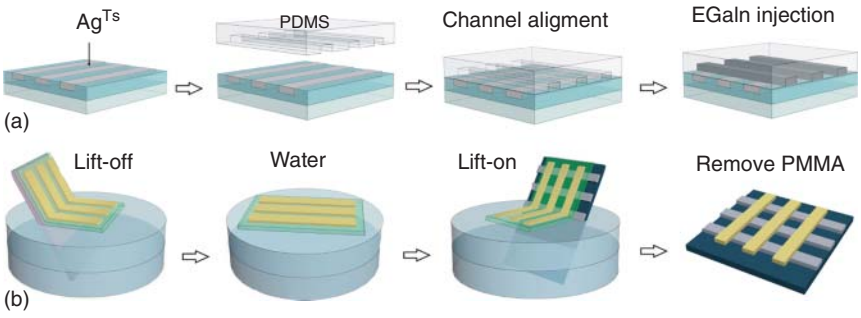

Figure 2.21 Schematic of the two types of crossbar fabrication. (a) Processes for microchannel-assisted crossbar formation. An ultraflat, template-stripped silver (Ag^{TS}) electrode embedded in a cured optical adhesive (OA) was used as the bottom electrode. Then, a microchannel in a transparent PDMS was brought perpendicular to the bottom electrode. Lastly, the microchannels were filled with Ga_2O_3/EGaIn to complete the crossbar devices. Source: Reprinted with permission from Nijhuis et al. [223]. Copyright 2010, American Chemical Society. (b) Processes for producing PALO crossbars. The PMMA was spin-cast as a hydrophobic backing layer onto the electrode-patterned substrates. Subsequently, the metal–polymer layer was lifted off onto the water surface upon immersion of the substrate. The crossbar device was assembled by floating the metal–polymer film onto a bottom substrate followed by the removal of the PMMA to complete the crossbar device. Source: Reprinted with permission from Shimizu et al. [206]. Copyright 2006, John Wiley and Sons.

layer on the preformed top electrodes that provide mechanical stability and a thermodynamic driving force to eliminate wrinkling. Originally, this technique was developed to generate and transfer electrodes in the large micrometer range. Sanetra et al. presented a modified PALO-based process that combined soft lithography and nanoimprint lithography [266]. It was demonstrated that not only was it a low-cost technique but also highly integrated crossbar junctions with half-pitches of 50 nm could be also fabricated in a parallel process.

In addition to the crossbar architecture, another similar and popular architecture used to form molecular junction is crosswire architecture [267]. As early as decades ago, Lieber and coworkers selected different types of nanowires to produce the crossed wire junctions [283]. They demonstrated that an electric-field-directed assembly could be used to create highly integrated nanowire arrays. The crossed nanowire junctions were obtained by using layer-by-layer alignments with the electric field applied in orthogonal directions in the two assembly steps [283]. Later, Yoon et al. reported a versatile and highly scalable crossed-nanowire molecular junction device that enabled the direct measurement of current–voltage–temperature characteristics simultaneously with inelastic electron tunneling and Raman vibrational spectra on the same junction [284]. In their experiments, the bottom electrode was fabricated via a lithographical process. A separately synthesized nanowire with a flat surface was used as a top contact. To accurately position the top wire perpendicular to the bottom wire preassembled with an SAM, a dielectrophoretic method was used. This highly flexible nanofabrication process allows wide variations in the wire diameters and the types of nanowires, with expansion to diverse materials, including semiconductors, superconductors, and nanotubes [284].

A primary challenge in fabricating the crossbar-/crosswire-based molecular junctions is to form an intimate contact between the molecular layer and the second electrode, i.e. it is not easy to form a tight molecule/electrode contact in each cross-point, especially when it is fabricated via the transfer printing method without an external compression force. Kushmerick et al. proposed a new type of crosswire-based tunnel junctions, in which a molecular monolayer was sandwiched between two macroscopic gold wires under a controllable force [285, 286]. As shown in Figure 2.22a, the wires were mounted in a custom-built

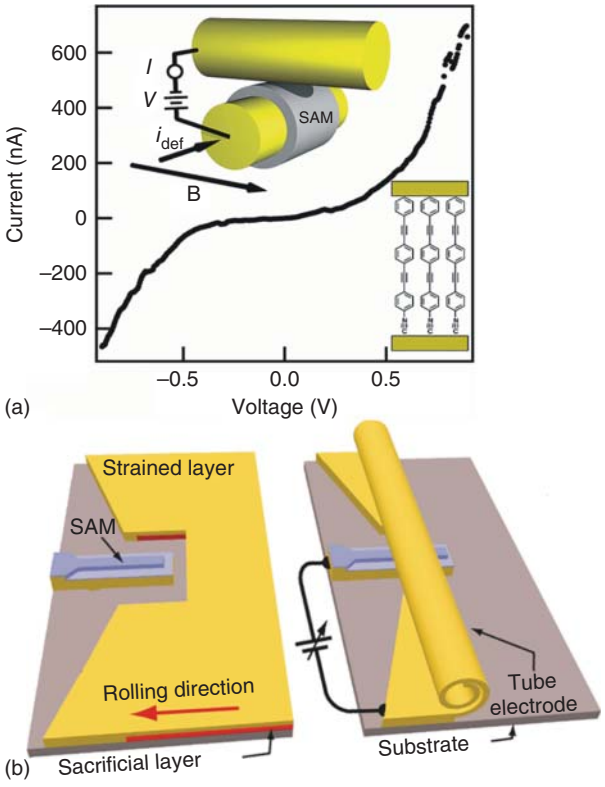

Figure 2.22 Schematic of the crosswire-based tunnel junctions. (a) Schematic of the crossed wire tunnel junction controlled by the Lorentz force. The crossed wires were mounted in a custom-built test, and the wire spacing was controlled by the Lorentz force; the DC current in one wire deflected it in a magnetic field to bring the wires gently together to form a junction at the contact point. Inset: *I*–*V* characteristics of the metal–molecule–metal junction. Source: Reprinted with permission from Kushmerick et al. [286]. Copyright 2003, American Chemical Society. (b) Molecular heterojunctions based on the strained nanomembranes. The left image depicts the device structure before the membrane rolling, and the right image depicts the device structure after rolling. The strained layer consists of a metallic nanomembrane patterned on top of a sacrificial layer. Once the sacrificial layer is selectively removed, the strained layer curls toward the Au finger structure, which was previously adsorbed with the molecular layer. After the rolling process, the tube-shaped electrode rests on top of the Au finger, thus establishing a molecular junction. Source: Reprinted with permission from Bufon et al. [287]. Copyright 2011, American Chemical Society.

test stage so that they were crossed and the wire spacing was controlled by the Lorentz force; the DC current in one wire deflected it in a magnetic field [286]. The deflection current was slowly increased to bring the wires gently together to form a junction at the point contact. The I–V characteristics of the junctions were obtained by ramping the bias voltage (V) while monitoring the current flow (I) across the junction (Figure 2.22a, inset). In this crosswire testbed, the features of these types of junctions were analyzed, and the characterization of the different types of molecules was studied [285, 286]. Additionally, the vibronic contributions to the charge transport as well as the selection rules in the IETS were revealed [149, 285]. Kushmerick and coworkers further applied this Lorentz force-assisted crosswire method to different materials, providing a primary contribution to this testbed [288]. However, the number of contacted molecules and their orientation on the wire were not well-defined because of the surface curvature of the wires in the device architecture [289].

Another strategy used to form a tight contact between the top wire and the bottom wire is illustrated in Figure 2.22b, in which metal–molecule–metal heterojunctions were fabricated based on rolled-up metallic nanomembranes [287]. The strained layer consists of a metallic nanomembrane patterned on top of a sacrificial layer. Once the sacrificial layer is selectively removed, the strained layer rolls toward the Au finger structure, where the alkanethiol SAM that has chain lengths considerably larger than the roughness of the finger surface was pre-assembled on the surface. After the rolling process, the tube-shaped electrode is placed on top of the Au finger, establishing an electrical connection through the SAM. The strained nanomembrane-based electrodes provide a soft yet robust contact on top of the SAM, where short circuits via pinholes are largely prevented. Due to the nature of this fabrication approach, the devices can be patterned in parallel on-chip and even be integrated with preexisting structures on a wafer. The primary challenge for fabricating this type of structures lies in the ability to accurately control/adjust the force between the tube electrode and the SAM, even though the metal electrode can intimately contact with the molecular layer.

2.2.6 Self-Aligned Lithography

When using the click chemistry strategy, extra attention should be given to the "bridge" molecules. These "bridge" molecules may be randomly attached to arbitrary points on the electrodes or even bind both of their surface-active groups to the same electrode, reducing the yield of the molecular junctions. In order to mitigate this problem, one potential approach is to select a bifunctional molecule such that only one end of the molecule reacts with the electrode; the second functional group has no affinity for the electrode. Then, a second molecule is used to bridge the gap between the termini of the first molecule. The second molecule is selected to have a double affinity for the second functional group of the first molecule but no affinity at all for the electrode surface, e.g. cobalt ions [290]. To test this strategy within molecular electronic devices, a new technique, known as self-aligned lithography, has been created to fabricate molecular-scale electrical testbeds [251]. With this self-aligned electrodes, they demonstrated that reaction chemistry offers molecular materials an overwhelming amount of diversity

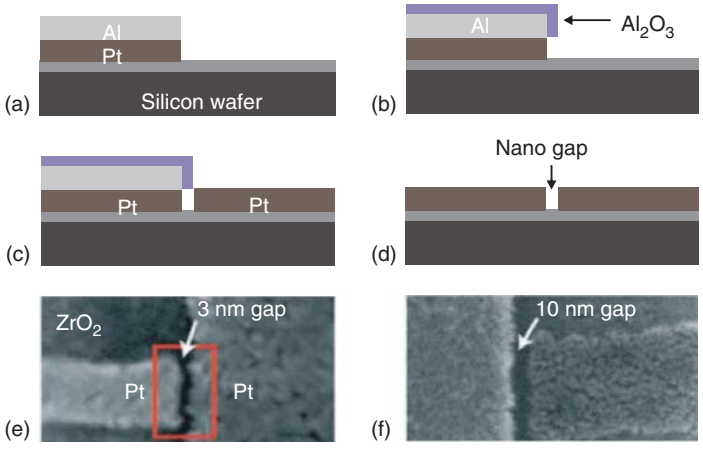

Figure 2.23 Fabrication process of nanoscale electrodes based on self-aligned lithography. (a) Al on Pt was patterned by the EBL on a silicon wafer coated with ZrO_2. (b) Al was oxidized in the ambient aluminum to produce an overhanging aluminum oxide layer. (c) The CE was produced via platinum evaporation separated by the amount of Al_2O_3 overhang. (d) Closely spaced platinum electrodes were obtained by dissolving the aluminum/aluminum oxide layer. Scanning electron micrograph (SEM) images illustrate a 3-nm gap (e), and a 10-nm gap (f). Source: Reprinted with permission from Tang et al. [251]. Copyright 2007, John Wiley and Sons.

and functionality and could provide a method for nanoscale electronics to be synthesized rather than fabricated.

The primary steps to produce nanoscale electrodes via the self-aligned lithographic approach are depicted in Figure 2.23. Firstly, a thin layer of ZrO_2 was deposited onto a clean silicon wafer by using atomic layer deposition. The first Al/Pt electrode (~200 nm wide, ~3 nm thick) was defined by the EBL. To obtain the narrowest gaps, a thin SiO_2 was added between the Pt and the Al films to aid the subsequent removal of the thin Al film. After being exposed to ambient oxygen, a native oxide layer was formed on the Al surface; the oxide on the edge of the Al film produced an overhanging structure over the Pt electrode, as shown in Figure 2.23b. Then, the second electrode (~30 nm wide), which consisted of 2.5 nm Pt defined by electron-beam evaporation/lithography, overlapped with the first electrode, as indicated in Figure 2.23c. The overlapping part and the oxidized aluminum were removed using a tetramethylammonium hydroxide solution to complete the nanosized gaps (Figure 2.23d). The key advantage of this technique is that it is a self-aligned lithographic process capable of producing large numbers of molecular-scale gaps with a remarkably high yield.

Kim and coworkers presented another simple semiconductor process to fabricate nanogap arrays for potential applications in molecular electronics, as shown in Figure 2.24 [291]. The basic idea behind the fabrication is using suspended silicon nanowires as a mask for the metal evaporation [292]. The gap size is controlled by the height of the suspended Si nanowire, width of the Si nanowires, and evaporation angle. It was demonstrated that sub-10-nm gap arrays could be achieved by using this method. To verify the practical viability of the nanogap array, the fabricated nanogap devices were applied to

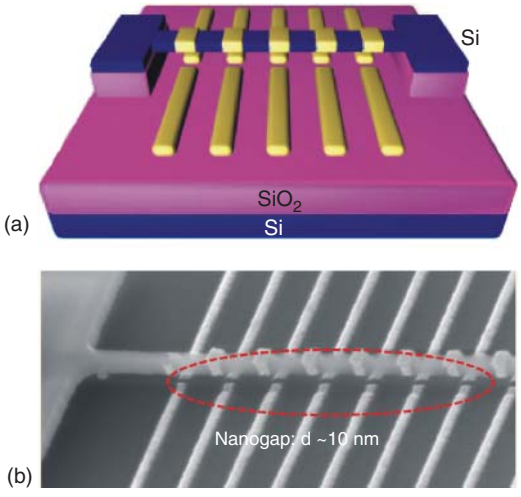

Figure 2.24 Nanogap array fabrication. (a) A schematic diagram of the nanogap arrays fabricated via a suspended silicon nanowire mask. A silicon-on-insulator (SOI) with a 100 nm top silicon layer and 200 nm buried oxide was used as the substrate. (b) Side-view SEM image of the metal nanogap arrays. The gap size between the opposing metal electrodes is 1–10 nm. Source: Reprinted with permission from Yu et al. [291]. Copyright 2009, John Wiley and Sons.

DNA-mediated single-charge tunneling devices, and revealed the electrical properties of the DNA-linked gold nanoparticles [291].

2.2.7 Buffer Interlayer-Based Junction

SAMs may offer a promising route that might lead to the fabrication of reliable devices by using the nanopore or nanowell techniques. Unfortunately, electrical shorts in SAMs are often formed during the vapor deposition of metal thin films for the top electrode, which causes electrical shorts in the molecular junctions and low device yield of the junctions. An efficient way to prevent the penetration of the metal atom into the SAM and avoid shorting is to insert a buffer interlayer between the top electrode and the SAM. The material for the buffer interlayer can be nanoparticles [241], aluminum oxide [293], conducting polymers [238, 294], and graphene [239, 295].

Akkerman et al. first reported a method for manufacturing high-yield molecular junctions with diameters up to 100 μm [238]. The reported method involves processing the molecular junctions in the holes of a lithographically patterned photoresist and then inserting a conducting polymer buffer layer between the metal top electrode and the SAM. The detailed fabrication process is illustrated in Figure 2.25. (i) A thin chromium adhesion layer and a 40 nm gold bottom electrode were vapor-deposited onto silicon wafers with a thermally grown oxide. (ii) A photoresist was spin-coated onto the wafer, and holes were produced using a standard photolithography technique. (iii) The substrate was submerged in a freshly prepared ethanol solution containing alkane dithiol. After the self-assembly of the alkane dithiolate on the bottom gold electrode, a water-based suspension of poly (3,4-ethylenedioxythiophene) stabilized with poly (4-styrenesulphonic acid) (PEDOT:PSS) was spin-coated on top of the SAM with a thickness of a hundred nanometers. (iv) The top gold electrode was vapor-deposited through a shadow mask. Lastly, the exposed PEDOT:PSS was removed by RIE, in which the top electrode acted as a self-aligned etching mask.

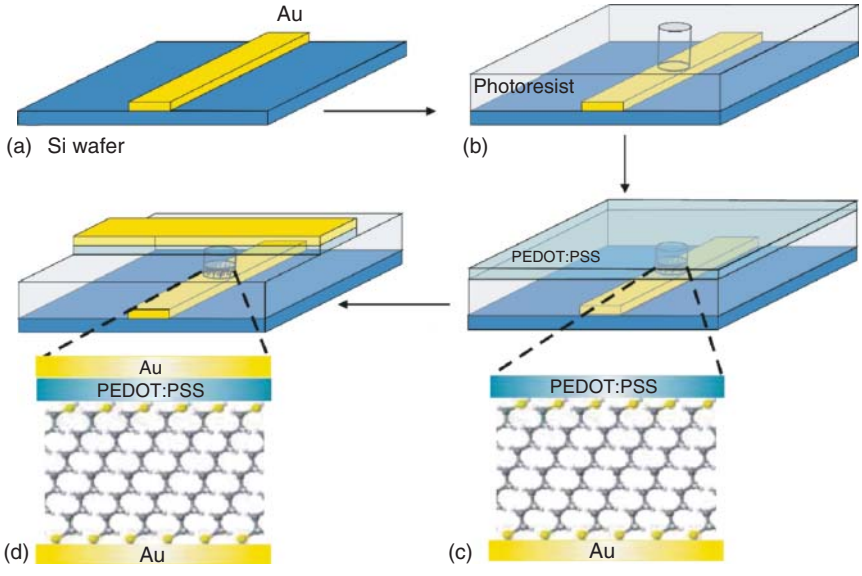

Figure 2.25 Processing steps of large-area molecular junctions. (a) The bottom gold electrodes were deposited on a silicon wafer. (b) The photoresist was spin-coated onto the wafer, and holes were photolithographically defined in the photoresist layer. (c) A highly conductive polymer PEDOT:PSS was spin-coated above the photoresist layer as a top electrode. A self-assembled molecule layer was sandwiched between a gold bottom electrode and the conducting polymer. (d) The junction was completed by the deposition of gold on top of the polymer through a shadow mask, and the redundant PEDOT:PSS was removed by reactive ion etching. Source: Reprinted with permission from Akkerman et al. [238]. Copyright 2006, Springer Nature.

The junctions fabricated by using this method demonstrated excellent stability and reproducibility, and the obtained conductance per unit area was similar to those achieved by using other methods. This simple fabrication process is potentially low cost and could lead to practical molecular device fabrication.

Later, Boer and coworkers did further contribution to systematically utilize this type of technology (e.g. the image potential, barrier height, and tunneling decay coefficient (β) in this large-area junction were determined [296, 297]; the effects of molecular concentration and the fabrication parameters to the electrical characterization were investigated [298, 299]; and the bias window as well as the application regime were expanded [300, 301]). Moreover, the stability of this type of large-area molecular junctions was analyzed by the same group [302]. It was demonstrated that this molecular junction was quite stable under ambient conditions for more than two years. Additionally, a transition temperature of 50 °C was observed, above which the resistance decreased exponentially with temperature. They also observed that the contact resistance and the transition voltage of the PEDOT:PSS–interlayer molecular junctions decreased as the temperature increased, which was attributed to the increased grain size of the PEDOT-rich cores and the removal of the residual water from the PEDOT:PSS–molecules interface [303]. By using the conducting polymer interlayer technique, the

functional molecular electronic devices on both the rigid and flexible substrates were further investigated by Lee and coworkers. The stability of the molecular junctions on the flexible substrates was tested under mechanical stress configurations [304], the electrical properties of the redox molecules [305], and photoswitching molecules were thoroughly investigated [306].

Although the fabrication of the PEDOT:PSS-based molecular electronic devices is very useful for producing high-yield molecular devices, the use of a conductive polymer has a few limitations and presents a few uncertainties to be used as a platform for molecular electronics. (i) The electrical properties of these molecular junctions may be influenced by the thermal treatment. The low transition temperature (50 °C) limits the process window during the fabrication and the temperature window during operation [302]. (ii) The contact between the PEDOT:PSS and the molecules is not fully understood. The resistance of the devices fabricated by using this technique is sensitive to the temperature and is different to those of the molecular junctions that do not have the polymer interlayer due to the poor contact between the PEDOT:PSS and molecules. (iii) The electrical characterization of the junctions depends on the type of the isolating layer (photoresist or SiO_2) and the molecular contact groups (hydrophilic or hydrophobic) [307], which may limit its further application. Thus, it is eager to develop alternative solid-state molecular device structures beyond the PEDOT:PSS-based molecular structure.

Graphene, with its outstanding electronic properties, chemical stability and mechanical properties, is considered to be a good electrode candidate for molecular junctions [308]. Wang et al. first reported a new approach for fabricating reliable solid-state molecular devices using multilayer graphene as the buffer interlayer [239]. Instead of spin-coating the conducting polymer above the SAM, they transferred a multilayer graphene film onto the SAM surface as the buffer interlayer by using chemical vapor deposition, as shown in Figure 2.26. The properties of the interface between the graphene and the molecules were statistically investigated. It was demonstrated that these graphene-based devices had a low resistance comparable with those of pure metal–molecule–metal devices, and the yield of these molecular devices was found to be approximately 90%, regardless of the properties of the contact groups (hydrophobic or hydrophilic). Particularly, this new method produced excellent durability, thermal stability, and long lifetimes for the devices.

An additional branch of graphene research, which is to chemically exfoliate graphite oxides into individual graphene oxide (GO) sheets and subsequently convert them into chemically derived graphene (CDG), provides a low-cost solution-processing route that can be incorporated into large-area molecular junctions. Recently, Nørgaard and coworkers reported the use of solution-processed ultrathin CDG films for non-destructive fabrication of the molecular electronic junctions [295]. Molecular features, such as non-linear charge transport properties and molecular length dependence of the junction resistance, have been confirmed in this CDG-based junction. Due to the tunable optoelectronic properties of the GO, it was predicted that the GO would be an attractive material for the optoelectrical applications [295]. One year later, they further employed ultrathin GO films as transparent top contacts for light

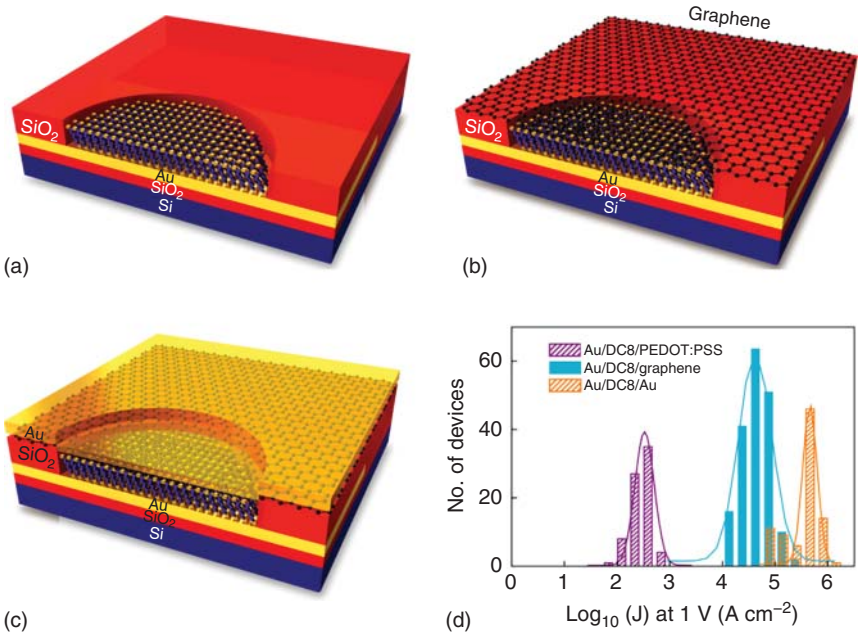

Figure 2.26 Graphene-based large-area molecular junctions. (a–c) Junction fabrication process: (a) SAM of alkanethiol on the exposed Au bottom electrode. (b) Alkanethiol molecular layer sandwiched between the Au bottom electrode and the graphene top electrode. (c) The junction was completed using Au vapor deposition above the graphene film. (d) Histogram of the logarithmic current densities at 1 V with different types of top electrodes (PEDOT:PSS, graphene and Au, respectively). Source: Reprinted with permission from Wang et al. [239]. Copyright 2011, John Wiley and Sons.

switchable solid-state molecular junctions [309]. The flexible, conductive, and transparent GO films permitted the molecular monolayers to be photoswitched *in situ* while simultaneously enabling the charge transport measurements across the molecules, thus resulting in a significant development for the application of large-area molecular junctions.

2.2.8 On-Edge Molecular Junction

OEMJs were independently and nearly contemporarily developed by several groups [310–313]. Unlike planar metal break junctions, the OEMJs are out-of-plane (perpendicular) to the junction plane. It is a prerequisite to fabricate an inorganic tunnel junction with exposed vertical side edges for the OEMJ approach. On the exposed side edges, the molecular channels are covalently bridged over the insulator gap. The primary strength of the OEMJs lies in its enabling larger numbers of control experiments, in which the actual effects arising from the bridged molecules can be addressed because molecules are able to be curtailed to retrieve the characteristics of the original bare junctions [310, 312].

A popular method for producing an OEMJ is chemical etching. Chemical SiO_2 etching was used in pioneer OEMJ experiments (Figure 2.27a,b). After the

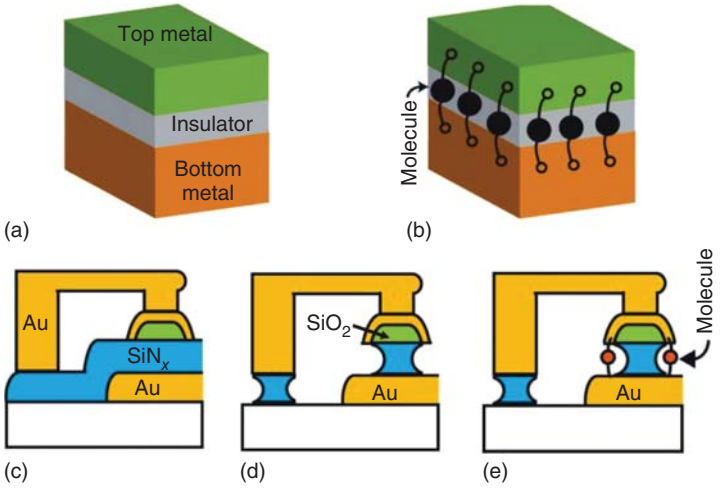

Figure 2.27 Schematic of OEMJ devices. (a, b) Molecular junction designs before (a) and after (b) attaching molecules. Source: Reprinted with permission from Tyagi [314]. Copyright 2005, Royal Society of Chemistry . (c–e) Fabrication process for molecular junctions. (c) Using SiN_x as an insulator layer. (d) Etching SiN_x to obtain the exposed electrodes. (e) Bridging the molecular channels across the gap between the top and the bottom electrodes. Source: Reprinted with permission from Ashwell et al. [310]. Copyright 2007, Royal Society of Chemistry.

etching process, the yielded gap size between two conducting silicon electrodes (~7 nm) was larger than the typical physical length of the molecules [313]. Correspondingly, a multistep chemistry approach was used to tether the molecules with nanoparticles to increase the effective length of the conducting channels [313]. The use of metallic electrodes enables a simple and more stable metal-molecular binding. To connect the molecules to the metal electrodes instead of the semiconducting surface, Tornow and coworkers produced molecular electrodes with an altered design in which the vertical gap on the exposed edges was produced by selective etching of a gallium arsenide (GaAs) spacer between two aluminum gallium arsenide (AlGaAs) electrodes [315]. Subsequently, the gold metallization of the exposed AlGaAs edges was performed to produce highly conducting electrodes for molecular bonding. The average gap (~8 nm) between the electrodes was suitable for the selective long molecular junctions. Ashwell et al. made an improvement to reduce the gap size by introducing a thin layer of silicon nitride (SiN_x) between the gold electrodes, as shown in Figure 2.27c–e [310]. Hence, a minimum vertical separation of ~3.5 nm between two gold electrodes on both sides was produced. After the molecular channels were bridged over the silicon nitride gap, a >3 order increase in the effective device current with respect to the background current was observed. The device current reverted to the background level after breaking down the molecular channels in their experiments, thus substantiating the fact that the increased current originated from the molecular channels.

In OEMJs, an important issue is that the background current, i.e. the leakage current passing through the insulator layer [316], should be engineered to be

considerably smaller than that through the molecular channels. To reduce the leakage current, one can increase the thickness of the insulator layer; however, this method is limited by the fact that one should keep the insulator thickness smaller than the physical length of the molecules to form a junction. The leakage current of a tunnel junction can be reduced by using additional three methods: (i) shrinking the junction area to reduce the leakage current. For example, Chen et al constructed a Pt–AlO_x–Pt junction by using a chemical etching protocol and achieved a typical junction area of $\sim 200 \times 200\ nm^2$ with a leakage current as small as ~0.04 pA [311]; (ii) growing high-quality ultrathin insulators. The leakage is strongly affected by the morphology, materials, and quality of the insulator layers; and (iii) creating atomically smooth bottom electrodes. An atomically smooth bottom electrode enables the use of thinner insulators and simultaneously yields a low leakage current.

Recently, Pang et al. developed a method to acquire both the electrical and chemical information by combining the on-edge strategy with the nanopore approach [317]. For these devices, the tunnel gap was defined as a dielectric layer (Al_2O_3) with a thickness of ~2 nm, deposited by atomic layer deposition. RIE was used to drill a nanopore through the layers so that the tunnel junction can be exposed to the molecules in the solution. After the metal electrodes were functionalized with recognition molecules, which can capture the DNA nucleotides, the identities of the individual nucleotides were revealed by the fluctuating tunnel current associated with the single-molecule binding events. Due to the small size of the nanopore (few micrometers in diameter), the experiment can be performed in an analyte solution with a relatively small leakage current. Therefore, the chemical information can be obtained. It was clearly demonstrated that the junctions produced signals that changed with the DNA nucleotide in solution. Furthermore, the devices provided clear signals of the nanomolar concentrations of the analyte and operated reliably for several hours [317].

The OEMJ design possesses the following merits. Firstly, the molecules are only attached onto a prefabricated tunnel junction via surface chemistry; hence, no damage is caused to the molecular channels. In other approaches, e.g. the direct deposition of the top metal electrode on to the molecular monolayer, the molecules' properties are likely to be changed due to the penetration of the metal atoms; the application of an intense electric field during the electromigration step for generating a nanometer gap may alter the molecule's property. Secondly, different types of metals, including a single molecular magnet and complex molecular clusters, can be used for the electrodes, even the bottom and top electrodes can be fabricated with different types of metals, respectively. Conversely, other approaches are limited to a few types of metals. Thirdly, the OEMJs can be produced in an extremely large-scale integrated circuit layout by using conventional microfabrication techniques, thus offering a low-cost approach.

The challenging issue of the OEMJs is the extreme difficulty of exploring the charge transport properties through individual molecules. The effective number of attached molecular channels is governed by the width of the bottom electrode. To host only single molecules, the width of the bottom electrode needs to be decreased to a few nanometers in width, and its mechanical stability needs

to be maintained, which is an intractable task. The additional limitation of the OEMJ method is that the introduction of a third electrode or a gate electrode to control the electron transport is not straightforward. Thus far, only chemical gating is available for the OEMJ method. Potential strategy for adding a solid gating electrode can be described as follows: (i) burying an inner conducting core inside the insulation layer, in which the conducting core can be used as the gating electrode; and (ii) using the FIB technique to cut the wire (contains three layers, metal–insulation–metal), which will result in a gap of few nanometers in width to appear around the cutting point. One side of the gap can be used as the source–drain electrode, while the other side can be used as the gate electrode. In this way, new functional devices with electrical gating may be available.

2.2.9 Suspended-Wire Molecular Junctions

Suspended-wire molecular junctions (SWMJs) was developed from the OWL, which we had introduced in the Section 2.2.4 [241, 318–320]. The main difference between them is that OWL self-assembled molecules between two segments of a nanowire and SWMJs self-assembled molecules on the surface of nanowires. This suspended wire molecular junctions method was originally proposed by Noy et al. [321]

SWMJs were fabricated by trapping Au or Ag nanowires, which were capped with an SAM of desired molecules onto lithographically defined Au leads by using a dielectrophoresis technique. Thus, NWs needs to be prepared firstly and the detailed fabrication technique can be found in the reference [321]. Once the Au and Ag NWs are covered by SAMs, the NWs are trapped between two Au leads by dielectrophoresis to form the "suspended wire" junctions. Briefly, a drop of NWs in solution is placed on the sample, while an AC voltage (~1 MHz frequency) is applied between a biased electrode and an RE (see Figure 2.28) for a few minutes. The drop is then washed away and blown dry with nitrogen. Noy et al. demonstrated that the yield of suspended nanowires in this process is about 40% [321]. They also proved that although the nanowires that were completely covered with a molecular layer could potentially form two molecular junctions in each SWMJ,

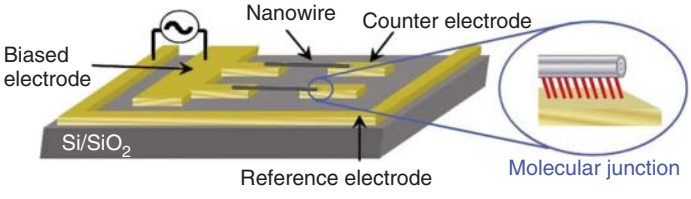

Figure 2.28 Schematic of the electrophoresis setup. AC bias is applied between a biased electrode and a reference electrode for a few minutes. After the formation of suspended nanowire, the drop is then washed away and dried with nitrogen. The molecular junction will be formed between the end of nanowire and CE. Source: Reprinted with permission from Noy et al. [321]. Copyright 2010, John Wiley and Sons.

only one junction per suspended nanowire (and a metal to metal contact on the other end) was formed.

Some major advantages of this technique are as follows: Firstly, the distance of the gaps in the junctions can be accurately controlled by the length of the molecules; Secondly, the molecular junctions are stable and easy to be integrated with other systems; Thirdly, a large number of molecular junctions can be integrated on-chip and have both high production and high success ratio. Because of these advantages, SWMJs have been used in the following aspects:

(1) *Demonstrating the effect of plasmons on the conductivity of molecular junctions*. The surface plasmon (SP) fields formed in the ~1 nm gap between the metal surfaces is particularly important due to the wide range of applications in single-molecule detection [322–335]. However, because of the small regions, it is also a great challenge to accurately determine the magnitude of plasmonic fields in ~1 nm scale gaps. SWMJs can solve this problem. The size of the gaps in the junctions can be varied and precisely determined by the embedded molecules, thus enabling unequivocal determination of plasmonic field enhancements in nanogaps that are 1–2 nm in scale [336]. Noy et al. initially used SWMJs to demonstrate the response of molecular junctions to SPPs [321]. Laser irradiation of selected junctions (laser light impinges on one side of the nanowire where the junction is located) was carried out by using a microscope and laser polarization parallel to the nanowires. Finite-difference time-domain (FDTD) simulations showed that plasmon was excited and propagated along the nanowire to the other side of the structure. They estimated the temperature increment under the lasers to be not more than 5 K, thus the current change due to temperature variation can be negligible. Based on the fact that the observed current enhancement seems to be related to the wavelength and laser power, the current enhancement is explained by a photon-assisted tunneling mechanism (we will address this point in Section 9.1.2.3 in more detail). One year later, Arielly et al. compared a set of junctions based on alkyl thiolated molecules with identical HOMO–LUMO gap and different lengths, and observed an exponential dependence of the plasmonic field enhancement on gap size, which confirmed the photon-assisted tunneling mechanism [336]. They further observed a current rectification phenomenon of the molecular junction upon laser irradiation. The current rectification was described quantum mechanically by the PAT theory. According to this model, under light irradiation a certain fraction of the tunneling charge across a gap undergoes inelastic scattering events as a result of the interaction with the oscillating (SP) field. They pointed out that the magnitude of rectification could be used to accurately determine the effective oscillating potentials in the junctions induced by the irradiating laser.

(2) *Detection of redox events in molecular junctions*. Redox molecular junctions have great promise for nanoelectronics because they exhibit large nonlinear effects in the current–voltage response, such as negative differential

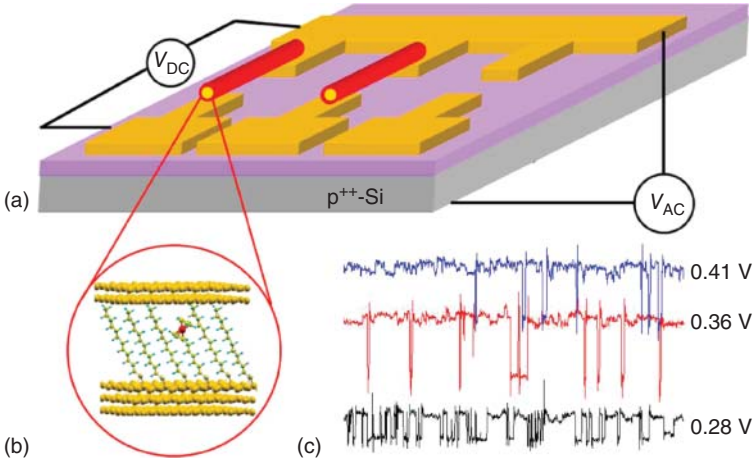

Figure 2.29 Description of the experimental system for real-time detection of redox events in molecular junctions. (a) Schematics of monolayer-covered Au nanowires suspended on lithography-defined Au contact pads on top of an oxide covered Si substrate. Alignment of nanowires is achieved by dielectrophoresis by using an AC voltage, V_{AC}, between a common contact pad and the underlying heavily doped Si substrate. Measurement of a certain junction is performed by applying a DC voltage, V_{DC}, between the common pad and the relevant floating pad. (b) Schematics of a part of a mixed monolayer with one 6-(ferrocenyl)hexanethiol molecule and diluting thiol-alkyl chains. The ferrocene group is coupled to one side of the junction via an alkyl chain, and to the other via space. (c) I–t traces showing two-level fluctuations signals at different bias voltages. Source: Reprinted with permission from Arielly et al. [338]. Copyright 2014, American Chemical Society.

resistance and hysteresis [337]. Arielly et al. report the experimental system by employing suspended molecular junctions, which enabled real-time detection of redox events in molecular junctions at low temperatures and revealed stochastic fluctuations in current–time (I–t) traces under constant voltage biases [338]. They found that this two-level fluctuating signal in current–time traces was potential-dependent amplitude and frequency, see Figure 2.29. Also, they have measured hundreds of SWMJs with monolayers of molecules such as alkanes with various lengths and various oligophenylene ethynylenes. In all these junctions, a two-level fluctuation signal had never been observed. They argued that the fluctuations were caused by slow redox reactions, which changed the redox state of the molecules. On this basis, they established the laser pulse-pair sequence (LPPS) scheme to monitor the oxidation state of the molecule within a junction with picosecond resolution and to determine the value of the relevant redox rate constants, which is found to be $(80\,\text{ps})^{-1}$ [339].

(3) *Measuring the heating accompanying plasmonic structures under illumination*. Precise determination of the temperature of illuminated junctions is crucial in molecular electronics. Previously optical methods to characterize the local temperature lack the spatial resolution to probe hot spots with few nanometers in size and therefore typically report average values over a diffraction limited length scale [340–344]. Nachman et al. demonstrated that

IETS of molecular junctions can be used to precisely measure the temperature of plasmonic hot spots with spatial accuracy under illumination, since the shape and width of the IETS peaks strongly depend on the local temperature [345]. We can envision that a combination of such a measurement with other optical methods such as Raman imaging, could be used to precisely determine the heat dissipation properties of structures and materials with nanoscale spatial resolution.

References

1 Aradhya, S.V. and Venkataraman, L. (2013). Single-molecule junctions beyond electronic transport. *Nat. Nanotechnol.* 8: 399–410.
2 Xu, B.Q. and Tao, N.J.J. (2003). Measurement of single-molecule resistance by repeated formation of molecular junctions. *Science* 301: 1221–1223.
3 Chen, F., Hihath, J., Huang, Z. et al. (2007). Measurement of single-molecule conductance. *Annu. Rev. Phys. Chem.* 58: 535–564.
4 Tao, N.J. (2009). Electron transport in molecular junctions. *Nanoscience and Technology*: 185–193.
5 Cheng, Z.L., Skouta, R., Vazquez, H. et al. (2011). In situ formation of highly conducting covalent Au-C contacts for single-molecule junctions. *Nat. Nanotechnol.* 6: 353–357.
6 Park, Y.S., Whalley, A.C., Kamenetska, M. et al. (2007). Contact chemistry and single-molecule conductance: A comparison of phosphines, methyl sulfides, and amines. *J. Am. Chem. Soc.* 129: 15768–15769.
7 Kamenetska, M., Quek, S.Y., Whalley, A.C. et al. (2010). Conductance and geometry of pyridine-linked single-molecule junctions. *J. Am. Chem. Soc.* 132: 6817–6821.
8 Jia, C. and Guo, X. (2013). Molecule-electrode interfaces in molecular electronic devices. *Chem. Soc. Rev.* 42: 5642–5660.
9 Wold, D.J. and Frisbie, C.D. (2001). Fabrication and characterization of metal-molecule-metal junctions by conducting probe atomic force microscopy. *J. Am. Chem. Soc.* 123: 5549–5556.
10 Wold, D.J. and Frisbie, C.D. (2000). Formation of metal-molecule-metal tunnel junctions: Microcontacts to alkanethiol monolayers with a conducting AFM tip. *J. Am. Chem. Soc.* 122: 2970–2971.
11 Li, W., Sepunaru, L., Amdursky, N. et al. (2012). Temperature and force dependence of nanoscale electron transport via the Cu protein azurin. *ACS Nano* 6: 10816–10824.
12 Aradhya, S.V., Frei, M., Hybertsen, M.S. et al. (2012). Van der Waals interactions at metal/organic interfaces at the single-molecule level. *Nat. Mater.* 11: 872–876.
13 Wagner, C., Fournier, N., Tautz, F.S. et al. (2012). Measurement of the binding energies of the organic-metal perylene-teracarboxylic-dianhydride/Au(111) bonds by molecular manipulation using an atomic force microscope. *Phys. Rev. Lett.* 109: 076102.

14 Pan, S., Fu, Q., Huang, T. et al. (2009). Design and control of electron transport properties of single molecules. *Proc. Natl. Acad. Sci. U. S. A.* 106: 15259–15263.

15 Xie, Z.T., Baldea, I., Smith, C.E. et al. (2015). Experimental and theoretical analysis of nanotransport in oligophenylene dithiol junctions as a function of molecular length and contact work function. *ACS Nano* 9: 8022–8036.

16 Schmaus, S., Bagrets, A., Nahas, Y. et al. (2011). Giant magnetoresistance through a single molecule. *Nat. Nanotechnol.* 6: 185–189.

17 Fei, X.M., Wu, G.F., Lopez, V. et al. (2015). Spin-dependent conductance in Co/C-60/Co/Ni single-molecule junctions in the contact regime. *J. Phys. Chem. C* 119: 11975–11981.

18 Schwoebel, J., Fu, Y., Brede, J. et al. (2012). Real-space observation of spin-split molecular orbitals of adsorbed single-molecule magnets. *Nat. Commun.* 3: 953.

19 Madhavan, V., Chen, W., Jamneala, T. et al. (1998). Tunneling into a single magnetic atom: Spectroscopic evidence of the Kondo resonance. *Science* 280: 567–569.

20 Andres, R.P., Bein, T., Dorogi, M. et al. (1996). "Coulomb staircase" at room temperature in a self-assembled molecular nanostructure. *Science* 272: 1323–1325.

21 Wang, W., Ji, Y., Zhang, H. et al. (2012). Negative differential resistance in a hybrid silicon-molecular system: resonance between the intrinsic surface-states and the molecular orbital. *ACS Nano* 6: 7066–7076.

22 Chen, L., Hu, Z., Zhao, A. et al. (2007). Mechanism for negative differential resistance in molecular electronic devices: local orbital symmetry matching. *Phys. Rev. Lett.* 99: 146803.

23 Rascon-Ramos, H., Artes, J.M., Li, Y.H. et al. (2015). Binding configurations and intramolecular strain in single-molecule devices. *Nat. Mater.* 14: 517–522.

24 Li, Z.H., Li, H., Chen, S.J. et al. (2014). Regulating a benzodifuran single molecule redox switch via electrochemical gating and optimization of molecule/electrode coupling. *J. Am. Chem. Soc.* 136: 8867–8870.

25 Baghernejad, M., Zhao, X.T., Ornso, K.B. et al. (2014). Electrochemical control of single-molecule conductance by Fermi-level tuning and conjugation switching. *J. Am. Chem. Soc.* 136: 17922–17925.

26 Li, Z. and Borguet, E. (2012). Determining charge transport pathways through single porphyrin molecules using scanning tunneling microscopy break junctions. *J. Am. Chem. Soc.* 134: 63–66.

27 Wang, G., Kim, T.-W., Jo, G. et al. (2009). Enhancement of field emission transport by molecular tilt configuration in metal-molecule-metal junctions. *J. Am. Chem. Soc.* 131: 5980–5985.

28 Loth, S., Etzkorn, M., Lutz, C.P. et al. (2010). Measurement of fast electron spin relaxation times with atomic resolution. *Science* 329: 1628–1630.

29 Kumagai, T., Hanke, F., Gawinkowski, S. et al. (2014). Controlling intramolecular hydrogen transfer in a porphycene molecule with single atoms or molecules located nearby. *Nat. Chem.* 6: 41–46.

30 Vazquez, H., Skouta, R., Schneebeli, S. et al. (2012). Probing the conductance superposition law in single-molecule circuits with parallel paths. *Nat. Nanotechnol.* 7: 663–667.

31 Guedon, C.M., Valkenier, H., Markussen, T. et al. (2012). Observation of quantum interference in molecular charge transport. *Nat. Nanotechnol.* 7: 304–308.

32 Manrique, D.Z., Huang, C., Baghernejad, M. et al. (2015). A quantum circuit rule for interference effects in single-molecule electrical junctions. *Nat. Commun.* 6: 6389.

33 Markussen, T., Stadler, R., and Thygesen, K.S. (2010). The relation between structure and quantum interference in single molecule junctions. *Nano Lett.* 10: 4260–4265.

34 Ballmann, S., Hartle, R., Coto, P.B. et al. (2012). Experimental evidence for quantum interference and vibrationally induced decoherence in single-molecule junctions. *Phys. Rev. Lett.* 109: 056801.

35 Garner, M.H., Li, H., Chen, Y. et al. (2018). Comprehensive suppression of single-molecule conductance using destructive σ-interference. *Nature* 558: 415–419.

36 Zhou, X.-Y., Peng, Z.-L., Sun, Y.-Y. et al. (2013). Conductance measurement of pyridyl-based single molecule junctions with Cu and Au contacts. *Nanotechnology* 24: 465204.

37 Wilson, N.R. and Macpherson, J.V. (2009). Carbon nanotube tips for atomic force microscopy. *Nat. Nanotechnol.* 4: 483–491.

38 Leary, E., Teresa Gonzalez, M., van der Pol, C. et al. (2011). Unambiguous one-molecule conductance measurements under ambient conditions. *Nano Lett.* 11: 2236–2241.

39 Bumm, L.A., Arnold, J.J., Cygan, M.T. et al. (1996). Are single molecular wires conducting? *Science* 271: 1705–1707.

40 Smaali, K., Clement, N., Patriarche, G. et al. (2012). Conductance statistics from a large array of sub-10 nm molecular junctions. *ACS Nano* 6: 4639–4647.

41 Cui, X.D., Primak, A., Zarate, X. et al. (2001). Reproducible measurement of single-molecule conductivity. *Science* 294: 571–574.

42 Li, J.J., Bai, M.L., Chen, Z.B. et al. (2015). Giant single-molecule anisotropic magnetoresistance at room temperature. *J. Am. Chem. Soc.* 137: 5923–5929.

43 Zhou, X.-S., Wei, Y.-M., Liu, L. et al. (2008). Extending the capability of STM break junction for conductance measurement of atomic-size nanowires: an electrochemical strategy. *J. Am. Chem. Soc.* 130: 13228–13230.

44 Dai, H.J., Hafner, J.H., Rinzler, A.G. et al. (1996). Nanotubes as nanoprobes in scanning probe microscopy. *Nature* 384: 147–150.

45 Nishijima, H., Kamo, S., Akita, S. et al. (1999). Carbon-nanotube tips for scanning probe microscopy: preparation by a controlled process and observation of deoxyribonucleic acid. *Appl. Phys. Lett.* 74: 4061.

46 Hafner, J.H., Cheung, C.L., Oosterkamp, T.H. et al. (2001). High-yield assembly of individual single-walled carbon nanotube tips for scanning probe microscopies. *J. Phys. Chem. B* 105: 743–746.

47 Wilson, N.R. and Macpherson, J.V. (2003). Single-walled carbon nanotubes as templates for nanowire conducting probes. *Nano Lett.* 3: 1365–1369.

48 Gross, L., Mohn, F., Moll, N. et al. (2009). The chemical structure of a molecule resolved by atomic force microscopy. *Science* 325: 1110–1114.

49 Lee, H.J. and Ho, W. (1999). Single-bond formation and characterization with a scanning tunneling microscope. *Science* 286: 1719–1722.

50 Moreno-Garcia, P., La Rosa, A., Kolivoska, V. et al. (2015). Charge transport in C_{60}-Based dumbbell-type molecules: Mechanically induced switching between two distinct conductance states. *J. Am. Chem. Soc.* 137: 2318–2327.

51 Clement, N., Patriarche, G., Smaali, K. et al. (2011). Large array of sub-10-nm single-grain Au nanodots for use in nanotechnology. *Small* 7: 2607–2613.

52 Zhang, J., Chen, P., Yuan, B. et al. (2013). Real-space identification of intermolecular bonding with atomic force microscopy. *Science* 342: 611–614.

53 Chiang, C.-l., Xu, C., Han, Z. et al. (2014). Real-space imaging of molecular structure and chemical bonding by single-molecule inelastic tunneling probe. *Science* 344: 885–888.

54 Mohn, F., Gross, L., Moll, N. et al. (2012). Imaging the charge distribution within a single molecule. *Nat. Nanotechnol.* 7: 227–231.

55 de Oteyza, D.G., Gorman, P., Chen, Y.-C. et al. (2013). Direct imaging of covalent bond structure in single-molecule chemical reactions. *Science* 340: 1434–1437.

56 Baro, A.M., Miranda, R., Alaman, J. et al. (1985). Determination of surface-topography of biological specimens at high-resolution by scanning tunnelling microscopy. *Nature* 315: 253–254.

57 Liu, Z., Ding, S.Y., Chen, Z.B. et al. (2011). Revealing the molecular structure of single-molecule junctions in different conductance states by fishing-mode tip-enhanced Raman spectroscopy. *Nat. Commun.* 2: 305.

58 Qiu, X.H., Nazin, G.V., and Ho, W. (2003). Vibrationally resolved fluorescence excited with submolecular precision. *Science* 299: 542–546.

59 van der Molen, S.J. and Liljeroth, P. (2010). Charge transport through molecular switches. *J. Phys.: Condens. Matter* 22: 133001.

60 Galperin, M. and Nitzan, A. (2012). Molecular optoelectronics: The interaction of molecular conduction junctions with light. *Phys. Chem. Chem. Phys.* 14: 9421–9438.

61 Venkataraman, L., Klare, J.E., Nuckolls, C. et al. (2006). Dependence of single-molecule junction conductance on molecular conformation. *Nature* 442: 904–907.

62 Su, T.A., Li, H., Steigerwald, M.L. et al. (2015). Stereoelectronic switching in single-molecule junctions. *Nat. Chem.* 7: 215–220.

63 Huang, Z., Xu, B., Chen, Y. et al. (2006). Measurement of current-induced local heating in a single molecule junction. *Nano Lett.* 6: 1240–1244.

64 Lee, W., Kim, K., Jeong, W. et al. (2013). Heat dissipation in atomic-scale junctions. *Nature* 498: 209–212.

65 Zhou, J., Chen, F., and Xu, B. (2009). Fabrication and electronic characterization of single molecular junction devices: A comprehensive approach. *J. Am. Chem. Soc.* 131: 10439–10446.

66 Huang, Z., Chen, F., Bennett, P.A. et al. (2007). Single molecule junctions formed via au-thiol contact: Stability and breakdown mechanism. *J. Am. Chem. Soc.* 129: 13225–13231.

67 Bruot, C., Hihath, J., and Tao, N. (2012). Mechanically controlled molecular orbital alignment in single molecule junctions. *Nat. Nanotechnol.* 7: 35–40.

68 Xu, B.Q., Xiao, X.Y., and Tao, N.J. (2003). Measurements of single-molecule electromechanical properties. *J. Am. Chem. Soc.* 125: 16164–16165.

69 Yu, M.F., Lourie, O., Dyer, M.J. et al. (2000). Strength and breaking mechanism of multiwalled carbon nanotubes under tensile load. *Science* 287: 637–640.

70 Eigler, D.M. and Schweizer, E.K. (1990). Positioning single atoms with a scanning tunneling microscope. *Nature* 344: 524–526.

71 Majumdar, A., Oden, P.I., Carrejo, J.P. et al. (1992). Nanometer-scale lithography using the atomic force microscope. *Appl. Phys. Lett.* 61: 2293–2295.

72 Mamin, H.J., Guethner, P.H., and Rugar, D. (1990). Atomic emission from a gold scanning-tunneling-microscope tip. *Phys. Rev. Lett.* 65: 2418–2421.

73 Min, S.Y., Kim, T.S., Kim, B.J. et al. (2013). Large-scale organic nanowire lithography and electronics. *Nat. Commun.* 4: 1773.

74 Pires, D., Hedrick, J.L., De Silva, A. et al. (2010). Nanoscale three-dimensional patterning of molecular resists by scanning probes. *Science* 328: 732–735.

75 He, Y., Dong, H., Li, T. et al. (2010). Graphene and graphene oxide nanogap electrodes fabricated by atomic force microscopy nanolithography. *Appl. Phys. Lett.* 97: 133301.

76 Tseng, A.A., Jou, S., Notargiacomo, A. et al. (2008). Recent developments in tip-based nanofabrication and its roadmap. *J. Nanosci. Nanotechnol.* 8: 2167–2186.

77 Rosa, L.G. and Liang, J. (2009). Atomic force microscope nanolithography: Dip-pen, nanoshaving, nanografting, tapping mode, electrochemical and thermal nanolithography. *J. Phys.: Condens. Matter* 21: 483001.

78 Tseng, A.A., Notargiacomo, A., and Chen, T.P. (2005). Nanofabrication by scanning probe microscope lithography: A review. *J. Vac. Sci. Technol. B Microelectron. Process. Phenom.* 23: 877–894.

79 Zhou, J. and Xu, B. (2011). Determining contact potential barrier effects on electronic transport in single molecular junctions. *Appl. Phys. Lett.* 99: 042104.

80 Zhou, J., Guo, C., and Xu, B. (2012). Electron transport properties of single molecular junctions under mechanical modulations. *J. Phys.: Condens. Matter* 24: 164209.

81 Xu, B. (2007). Modulating the conductance of a Au-octanedithiol-Au molecular junction. *Small* 3: 2061–2065.

82 Moreland, J. and Ekin, J.W. (1985). Electron-tunneling into superconducting filaments using mechanically adjustable barriers. *Appl. Phys. Lett.* 47: 175–177.

83 Moreland, J. and Ekin, J.W. (1985). Electron-tunneling experiments using Nb-Sn break junctions. *J. Appl. Phys.* 58: 3888–3895.

84 Muller, C.J., van Ruitenbeek, J.M., and Dejongh, L.J. (1992). Experiments on mechanically controllable break junctions of Niobium and Platinum. *Inst. Phys. Conf. Ser.* 127: 171–174.

85 Muller, C.J., van Ruitenbeek, J.M., and Dejongh, L.J. (1992). Conductance and supercurrent discontinuities in atomic-scale metallic constrictions of variable width. *Phys. Rev. Lett.* 69: 140–143.

86 Scheer, E., Agrait, N., Cuevas, J.C. et al. (1998). The signature of chemical valence in the electrical conduction through a single-atom contact. *Nature* 394: 154–157.

87 Reed, M.A., Zhou, C., Muller, C.J. et al. (1997). Conductance of a molecular junction. *Science* 278: 252–254.

88 Zhou, C., Deshpande, M.R., Reed, M.A. et al. (1997). Nanoscale metal self-assembled monolayer metal heterostructures. *Appl. Phys. Lett.* 71: 611–613.

89 Xiang, D., Jeong, H., Lee, T. et al. (2013). Mechanically controllable break junctions for molecular electronics. *Adv. Mater.* 25: 4845–4867.

90 Vrouwe, S.A.G., van der Giessen, E., van der Molen, S.J. et al. (2005). Mechanics of lithographically defined break junctions. *Phys. Rev. B* 71: 035313.

91 Bohler, T., Grebing, J., Mayer-Gindner, A. et al. (2004). Mechanically controllable break-junctions for use as electrodes for molecular electronics. *Nanotechnology* 15: S465–S471.

92 Gruter, L., Gonzalez, M.T., Huber, R. et al. (2005). Electrical conductance of atomic contacts in liquid environments. *Small* 1: 1067–1070.

93 Xiang, D., Zhang, Y., Pyatkov, F. et al. (2011). Gap size dependent transition from direct tunneling to field emission in single molecule junctions. *Chem. Commun.* 47: 4760–4762.

94 Moreno-Garcia, P., Gulcur, M., Manrique, D.Z. et al. (2013). Single-molecule conductance of functionalized oligoynes: length dependence and junction evolution. *J. Am. Chem. Soc.* 135: 12228–12240.

95 Gulcur, M., Moreno-Garcia, P., Zhao, X.T. et al. (2014). The synthesis of functionalised diaryltetraynes and their transport properties in single-molecule junctions. *Chem. Eur. J.* 20: 4653–4660.

96 Martin, C.A., Smit, R.H.M., van Egmond, R. et al. (2011). A versatile low-temperature setup for the electrical characterization of single-molecule junctions. *Rev. Sci. Instrum.* 82: 053907.

97 Tian, J.H., Liu, B., Li, X.L. et al. (2006). Study of molecular junctions with a combined surface-enhanced Raman and mechanically controllable break junction method. *J. Am. Chem. Soc.* 128: 14748–14749.

98 Rodrigues, V. and Ugarte, D. (2002). Metal nanowires: atomic arrangement and electrical transport properties. *Nanotechnology* 13: 404–408.

99 Xiang, D., Lee, T., Kim, Y. et al. (2014). Origin of discrete current fluctuations in a single molecule junction. *Nanoscale* 6: 13396–13401.

100 Smit, R.H.M., Noat, Y., Untiedt, C. et al. (2002). Measurement of the conductance of a hydrogen molecule. *Nature* 419: 906–909.

101 Yi, Z.W., Banzet, M., Offenhausser, A. et al. (2010). Fabrication of nanogaps with modified morphology by potential-controlled gold deposition. *Phys. Status Solidi-RRL* 4: 73–75.

102 Lortscher, E., Ciszek, J.W., Tour, J. et al. (2006). Reversible and controllable switching of a single-molecule junction. *Small* 2: 973–977.

103 Parks, J.J., Champagne, A.R., Costi, T.A. et al. (2010). Mechanical control of spin states in spin-1 molecules and the underscreened Kondo effect. *Science* 328: 1370–1373.

104 Perrin, M.L., Verzijl, C.J.O., Martin, C.A. et al. (2013). Large tunable image-charge effects in single-molecule junctions. *Nat. Nanotechnol.* 8: 282–287.

105 Xiang, D., Jeong, H., Kim, D. et al. (2013). Three-terminal single-molecule junctions formed by mechanically controllable break junctions with side gating. *Nano Lett.* 13: 2809–2813.

106 Tian, J.H., Yang, Y., Liu, B. et al. (2010). The fabrication and characterization of adjustable nanogaps between gold electrodes on chip for electrical measurement of single molecules. *Nanotechnology* 21: 274012.

107 Arima, A., Tsutsui, M., Morikawa, T. et al. (2014). Fabrications of insulator-protected nanometer-sized electrode gaps. *J. Appl. Phys.* 115: 114310.

108 Parks, J.J., Champagne, A.R., Hutchison, G.R. et al. (2007). Tuning the Kondo effect with a mechanically controllable break junction. *Phys. Rev. Lett.* 99: 026601.

109 Yi, Z.W., Trellenkamp, S., Offenhausser, A. et al. (2010). Molecular junctions based on intermolecular electrostatic coupling. *Chem. Commun.* 46: 8014–8016.

110 Tian, J.H., Yang, Y., Zhou, X.S. et al. (2010). Electrochemically assisted fabrication of metal atomic wires and molecular junctions by MCBJ and STM-BJ methods. *ChemPhysChem* 11: 2745–2755.

111 Wen, H.M., Yang, Y., Zhou, X.S. et al. (2013). Electrical conductance study on 1,3-butadiyne-linked dinuclear ruthenium(II) complexes within single molecule break junctions. *Chem. Sci.* 4: 2471–2477.

112 Champagne, A.R., Pasupathy, A.N., and Ralph, D.C. (2005). Mechanically adjustable and electrically gated single-molecule transistors. *Nano Lett.* 5: 305–308.

113 Martin, C.A., van Ruitenbeek, J.M., and van der Zant, H.S.J. (2010). Sandwich-type gated mechanical break junctions. *Nanotechnology* 21: 265201.

114 Li, Y., Kaneko, S., Fujii, S. et al. (2015). Symmetry of single hydrogen molecular junction with Au, Ag, and Cu electrodes. *J. Phys. Chem. C* 119: 19143–19148.

115 Frisenda, R., Gaudenzi, R., Franco, C. et al. (2015). Kondo effect in a neutral and stable all organic radical single molecule break junction. *Nano Lett.* 15: 3109–3114.

116 Konishi, T., Kiguchi, M., Takase, M. et al. (2013). Single molecule dynamics at a mechanically controllable break junction in solution at room temperature. *J. Am. Chem. Soc.* 135: 1009–1014.

117 Yelin, T., Vardimon, R., Kuritz, N. et al. (2013). Atomically wired molecular junctions: Connecting a single organic molecule by chains of metal atoms. *Nano Lett.* 13: 1956–1961.

118 Liu, C.Y., Kaneko, S., Komoto, Y. et al. (2015). Highly conductive single naphthalene and anthracene molecular junction with well-defined conductance. *Appl. Phys. Lett.* 106: 103103.

119 Ponce, J., Arroyo, C.R., Tatay, S. et al. (2014). Effect of metal complexation on the conductance of single-molecular wires measured at room temperature. *J. Am. Chem. Soc.* 136: 8314–8322.

120 Xiang, D., Pyatkov, F., Schroper, F. et al. (2011). Molecular junctions bridged by metal ion complexes. *Chem. Eur. J.* 17: 13166–13169.

121 Sanvito, S. (2011). Molecular spintronics. *Chem. Soc. Rev.* 40: 3336–3355.

122 Wagner, S., Kisslinger, F., Ballmann, S. et al. (2013). Switching of a coupled spin pair in a single-molecule junction. *Nat. Nanotechnol.* 8: 575–579.

123 Kim, Y., Song, H., Strigl, F. et al. (2011). Conductance and vibrational states of single-molecule junctions controlled by mechanical stretching and material variation. *Phys. Rev. Lett.* 106: 196804.

124 Secker, D., Wagner, S., Ballmann, S. et al. (2011). Resonant vibrations, peak broadening, and noise in single molecule contacts: the nature of the first conductance peak. *Phys. Rev. Lett.* 106: 136907.

125 Tsutsui, M., Taniguchi, M., and Kawai, T. (2010). Single-molecule identification via electric current noise. *Nat. Commun.* 1: 138.

126 Sydoruk, V.A., Xiang, D., Vitusevich, S.A. et al. (2012). Noise and transport characterization of single molecular break junctions with individual molecule. *J. Appl. Phys.* 112: 138.

127 Meng, C., Huang, P., Zhou, J.W. et al. (2015). Thermally controllable break junctions with high bandwidths and high integrabilities. *Chin. Phys. Lett.* 32: 076201.

128 Gong, C., Zhao, Y.J., Dong, L.Q. et al. (2013). The tolerable target temperature for bimaterial microcantilever array infrared imaging. *Opt. Laser Technol.* 45: 545–550.

129 Huang, C., Jevric, M., Borges, A. et al. (2017). Single-molecule detection of dihydroazulene photo-thermal reaction using break junction technique. *Nat. Commun.* 8: 15436.

130 Li, R., Lu, Z., Cai, Y. et al. (2017). Switching of charge transport pathways via delocalization changes in single-molecule metallacycles junctions. *J. Am. Chem. Soc.* 139: 14344–14347.

131 Zhang, Y.P., Chen, L.C., Zhang, Z.Q. et al. (2018). Distinguishing diketopyrrolopyrrole isomers in single-molecule junctions via reversible stimuli-responsive quantum interference. *J. Am. Chem. Soc.* 140: 6531–6535.

132 Morikawa, T., Arima, A., Tsutsui, M. et al. (2014). Thermoelectric voltage measurements of atomic and molecular wires using microheater-embedded mechanically-controllable break junctions. *Nanoscale* 6: 8235–8241.

133 Doi, K., Tsutsui, M., Ohshiro, T. et al. (2014). Nonequilibrium ionic response of biased mechanically controllable break junction (MCBJ) electrodes. *J. Phys. Chem. C* 118: 3758–3765.

134 Waitz, R., Schecker, O., and Scheer, E. (2008). Nanofabricated adjustable multicontact devices on membranes. *Rev. Sci. Instrum.* 79: 093901.

135 Benner, D., Boneberg, J., Nurnberger, P. et al. (2014). Lateral and temporal dependence of the transport through an atomic gold contact under light

irradiation: Signature of propagating surface plasmon polaritons. *Nano Lett.* 14: 5218–5223.

136 Tsutsui, M., Morikawa, T., He, Y. et al. (2015). High thermopower of mechanically stretched single-molecule junctions. *Sci. Rep.* 5: 11519.

137 Wang, L., Zhao, Z., and Xiang, D. (2017). On-chip break junctions and period-adjustable grating driven by thermal stress. *Nano* 12: 1750139.

138 Que, L., Park, J.-S., Gianchandani, Y. B. (1999). Bent-beam electro-thermal actuators for high force applications. *Twelfth IEEE International Conference on Micro Electro Mechanical Systems MEMS'99* (pp. 31–36). Orlando, FL, USA: IEEE.

139 Que, L., Park, J.S., and Gianchandani, Y.B. (2001). Bent-beam electrothermal actuators-Part I: Single beam and cascaded devices. *J. Microelectromech. Syst.* 10: 247–254.

140 Maloney, J.M., Schreiber, D.S., and DeVoe, D.L. (2004). Large-force electrothermal linear micromotors. *J. Micromech. Microeng.* 14 (2): 226.

141 Park, H., Lim, A.K.L., Alivisatos, A.P. et al. (1999). Fabrication of metallic electrodes with nanometer separation by electromigration. *Appl. Phys. Lett.* 75 (2): 301.

142 Song, H., Kim, Y., Jang, Y.H. et al. (2009). Observation of molecular orbital gating. *Nature* 462: 1039–1043.

143 Van der Zant, H.S.J., Osorio, E.A., Poot, M. et al. (2006). Electromigrated molecular junctions. *Phys. Stat. Sol. B* 243: 3408–3412.

144 Kim, T.-W., Wang, G., Lee, H. et al. (2007). Statistical analysis of electronic properties of alkanethiols in metal-molecule-metal junctions. *Nanotechnology* 18: 315204.

145 Mangin, A., Anthore, A., Della Rocca, M.L. et al. (2009). Transport through metallic nanogaps in an in-plane three-terminal geometry. *J. Appl. Phys.* 105: 014313.

146 van der Zant, H.S.J., Kervennic, Y.V., Poot, M. et al. (2006). Molecular three-terminal devices: fabrication and measurements. *Faraday Discuss.* 131: 347–356.

147 Ueno, S., Tomoda, Y., Kume, W. et al. (2012). Field-emission-induced electromigration method for the integration of single-electron transistors. *Appl. Surf. Sci.* 258: 2153–2156.

148 Houck, A.A., Labaziewicz, J., Chan, E.K. et al. (2005). Kondo effect in electromigrated gold break junctions. *Nano Lett.* 5: 1685–1688.

149 Kushmerick, J.G., Lazorcik, J., Patterson, C.H. et al. (2004). Vibronic contributions to charge transport across molecular junctions. *Nano Lett.* 4: 639–642.

150 Henderson, J.J., Ramsey, C.M., del Barco, E. et al. (2007). Fabrication of nanogapped single-electron transistors for transport studies of individual single-molecule magnets. *J. Appl. Phys.* 101: 09E102.

151 Trouwborst, M.L., van der Molen, S.J., and van Wees, B.J. (2006). The role of Joule heating in the formation of nanogaps by electromigration. *J. Appl. Phys.* 99: 114316.

152 Lee, C.H., Han, J.H., Schneider, S.C. et al. (2011). Suspended and localized single nanostructure growth across a nanogap by an electric field. *Nanotechnology* 22: 405301.

153 Valladares, L., Felix, L.L., Dominguez, A.B. et al. (2010). Controlled electroplating and electromigration in nickel electrodes for nanogap formation. *Nanotechnology* 21: 445304.

154 Baik, J.M., Lee, S.J., and Moskovits, M. (2009). Polarized surface-enhanced Raman spectroscopy from molecules adsorbed in nano-gaps produced by electromigration in silver nanowires. *Nano Lett.* 9: 672–676.

155 Prins, F., Hayashi, T., van Steenwijk, B.J.A.D. et al. (2009). Room-temperature stability of Pt nanogaps formed by self-breaking. *Appl. Phys. Lett.* 94: 123108.

156 Arzubiaga, L., Golmar, F., Llopis, R. et al. (2013). Tailoring palladium nanocontacts by electromigration. *Appl. Phys. Lett.* 102: 193103.

157 Asghar, W., Ramachandran, P.P., Adewumi, A. et al. (2010). Rapid nanomanufacturing of metallic break junctions using focused ion beam scratching and electromigration. *J. Manuf. Sci. Eng.* 030911: 132.

158 Naitoh, Y., Ohata, T., Matsushita, R. et al. (2013). Self-aligned formation of sub 1 nm gaps utilizing electromigration during metal deposition. *ACS Appl. Mater. Inter.* 5: 12869–12875.

159 Lu, Y., Goldsmith, B., Strachan, D.R. et al. (2010). High-on/off-ratio graphene nanoconstriction field-effect transistor. *Small* 6: 2748–2754.

160 Zhang, H., Bao, W.Z., Zhao, Z. et al. (2012). Visualizing electrical breakdown and ON/OFF states in electrically switchable suspended graphene break junctions. *Nano Lett.* 12: 1772–1775.

161 Qi, P., Javey, A., Rolandi, M. et al. (2004). Miniature organic transistors with carbon nanotubes as quasi-one-dimensional electrodes. *J. Am. Chem. Soc.* 126: 11774–11775.

162 O'Neill, K., Osorio, E.A., and van der Zant, H.S.J. (2007). Self-breaking in planar few-atom Au constrictions for nanometer-spaced electrodes. *Appl. Phys. Lett.* 90: 133109.

163 Tsutsui, M., Taniguchi, M., and Kawai, T. (2008). Fabrication of 0.5 nm electrode gaps using self-breaking technique. *Appl. Phys. Lett.* 93: 163115.

164 Strachan, D.R., Smith, D.E., Johnston, D.E. et al. (2005). Controlled fabrication of nanogaps in ambient environment for molecular electronics. *Appl. Phys. Lett.* 86: 043109.

165 Xiang, C.X., Kim, J.Y., and Penner, R.M. (2009). Reconnectable sub-5 nm nanogaps in ultralong gold nanowires. *Nano Lett.* 9: 2133–2138.

166 Strachan, D.R., Johnston, D.E., Guiton, B.S. et al. (2008). Real-time TEM imaging of the formation of crystalline nanoscale gaps. *Phys. Rev. Lett.* 100: 056805.

167 Dong, J. and Parviz, B.A. (2006). Using noise for controlled disassembly of nanoscale gold wires. *Nanotechnology* 17: 5124–5130.

168 Wu, Z.M., Steinacher, M., Huber, R. et al. (2007). Feedback controlled electromigration in four-terminal nanojunctions. *Appl. Phys. Lett.* 91: 053118.

169 Johnston, D.E., Strachan, D.R., and Johnson, A.T.C. (2007). Parallel fabrication of nanogap electrodes. *Nano Lett.* 7: 2774–2777.

170 Heersche, H.B., de Groot, Z., Folk, J.A. et al. (2006). Kondo effect in the presence of magnetic impurities. *Phys. Rev. Lett.* 96: 017205.

171 Sordan, R., Balasubramanian, K., Burghard, M. et al. (2005). Coulomb blockade phenomena in electromigration break junctions. *Appl. Phys. Lett.* 87: 013106.

172 Taychatanapat, T., Bolotin, K.I., Kuemmeth, F. et al. (2007). Imaging electromigration during the formation of break junctions. *Nano Lett.* 7: 652–656.

173 Strachan, D.R., Smith, D.E., Fischbein, M.D. et al. (2006). Clean electromigrated nanogaps imaged by transmission electron microscopy. *Nano Lett.* 6: 441–443.

174 Rudneva, M., Gao, B., Prins, F. et al. (2013). In situ transmission electron microscopy imaging of electromigration in platinum nanowires. *Microsc. Microanal.* 19: 43–48.

175 Fischbein, M.D. and Drndic, M. (2007). Sub-10 nm device fabrication in a transmission electron microscope. *Nano Lett.* 7: 1329–1337.

176 Gao, B., Osorio, E.A., Gaven, K.B. et al. (2009). Three-terminal electric transport measurements on gold nano-particles combined with ex situ TEM inspection. *Nanotechnology* 20: 415207.

177 Song, H., Kim, Y., Ku, J. et al. (2009). Vibrational spectra of metal-molecule-metal junctions in electromigrated nanogap electrodes by inelastic electron tunneling. *Appl. Phys. Lett.* 94: 103110.

178 Natelson, D., Li, Y.J., and Herzog, J.B. (2013). Nanogap structures: combining enhanced Raman spectroscopy and electronic transport. *Phys. Chem. Chem. Phys.* 15: 5262–5275.

179 Ward, D.R., Halas, N.J., Ciszek, J.W. et al. (2008). Simultaneous measurements of electronic conduction and Raman response in molecular junctions. *Nano Lett.* 8: 919–924.

180 Herzog, J.B., Knight, M.W., Li, Y.J. et al. (2013). Dark plasmons in hot spot generation and polarization in interelectrode nanoscale junctions. *Nano Lett.* 13: 1359–1364.

181 Ward, D.R., Corley, D.A., Tour, J.M. et al. (2011). Vibrational and electronic heating in nanoscale junctions. *Nat. Nanotechnol.* 6: 33–38.

182 Liang, W., Shores, M.P., Bockrath, M. et al. (2002). Kondo resonance in a single-molecule transistor. *Nature* 417: 725–729.

183 Yu, L.H. and Natelson, D. (2004). The Kondo effect in C_{60} single-molecule transistors. *Nano Lett.* 4: 79–83.

184 Pasupathy, A.N., Bialczak, R.C., Martinek, J. et al. (2004). The Kondo effect in the presence of ferromagnetism. *Science* 306: 86–89.

185 Morpurgo, A.F., Marcus, C.M., and Robinson, D.B. (1999). Controlled fabrication of metallic electrodes with atomic separation. *Appl. Phys. Lett.* 74: 2084–2086.

186 Li, C.Z., He, H.X., and Tao, N.J. (2000). Quantized tunneling current in the metallic nanogaps formed by electrodeposition and etching. *Appl. Phys. Lett.* 77: 3995–3997.

187 Wu, Y.X., Hong, W.J., Akiyama, T. et al. (2013). Batch fabrication of gold-gold nanogaps by E-beam lithography and electrochemical deposition. *Nanotechnology* 24: 235302.

188 Li, X.L., He, H.X., Xu, B.Q. et al. (2004). Measurement of electron transport properties of molecular junctions fabricated by electrochemical and mechanical methods. *Surf. Sci.* 573: 1–10.

189 Liu, B., Xiang, J., Tian, J.H. et al. (2005). Controllable nanogap fabrication on microchip by chronopotentiometry. *Electrochim. Acta* 50: 3041–3047.

190 Meszaros, G., Kronholz, S., Karthauser, S. et al. (2007). Electrochemical fabrication and characterization of nanocontacts and nm-sized gaps. *Appl. Phys. A* 87: 569–575.

191 Kervennic, Y.V., Van der Zant, H.S.J., Morpurgo, A.F. et al. (2002). Nanometer-spaced electrodes with calibrated separation. *Appl. Phys. Lett.* 80: 321–323.

192 He, H.X., Boussaad, S., Xu, B.Q. et al. (2002). Electrochemical fabrication of atomically thin metallic wires and electrodes separated with molecular-scale gaps. *J. Electroanal. Chem.* 522: 167–172.

193 Xiang, J., Liu, B., Wu, S.T. et al. (2005). A controllable electrochemical fabrication of metallic electrodes with a nanometer/angstrom-sized gap using an electric double layer as feedback. *Angew. Chem. Int. Ed.* 44: 1265–1268.

194 Qing, Q., Chen, F., Li, P.G. et al. (2005). Finely tuning metallic nanogap size with electrodeposition by utilizing high-frequency impedance in feedback. *Angew. Chem. Int. Ed.* 44: 7771–7775.

195 Chen, F., Qing, Q., Ren, L. et al. (2005). Electrochemical approach for fabricating nanogap electrodes with well controllable separation. *Appl. Phys. Lett.* 86: 123105.

196 Serdio, V.M., Azuma, Y., Takeshita, S. et al. (2012). Robust nanogap electrodes by self-terminating electroless gold plating. *Nanoscale* 4: 7161–7167.

197 Yasutake, Y., Kono, K., Kanehara, M. et al. (2007). Simultaneous fabrication of nanogap gold electrodes by electroless gold plating using a common medical liquid. *Appl. Phys. Lett.* 91: 203107.

198 Lee, Y., Ahn, S.K., and Roh, Y. (2005). Comparison of nanometer-scale gold structures electrodeposited on Au and Pt seed electrode. *Surf. Coat. Technol.* 193: 137–141.

199 Kiguchi, M. and Murakoshi, K. (2006). Fabrication of stable Pd nanowire assisted by hydrogen in solution. *Appl. Phys. Lett.* 88: 253112.

200 Zhou, X.S., Liang, J.H., Chen, Z.B. et al. (2011). An electrochemical jump-to-contact STM-break junction approach to construct single molecular junctions with different metallic electrodes. *Electrochem. Commun.* 13: 407–410.

201 Bonifas, A.P. and McCreery, R.L. (2010). 'Soft' Au, Pt and Cu contacts for molecular junctions through surface-diffusion-mediated deposition. *Nat. Nanotechnol.* 5: 612–617.

202 Bonifas, A.P. and McCreery, R.L. (2011). Assembling molecular electronic junctions one molecule at a time. *Nano Lett.* 11: 4725–4729.

203 Yablonovitch, E., Hwang, D.M., Gmitter, T.J. et al. (1990). Van der waals bonding of GaAs epitaxial liftoff films onto arbitrary substrates. *Appl. Phys. Lett.* 56: 2419–2421.

204 Vilan, A., Shanzer, A., and Cahen, D. (2000). Molecular control over Au/GaAs diodes. *Nature* 404: 166–168.

205 Vilan, A. and Cahen, D. (2002). Soft contact deposition onto molecularly modified GaAs. Thin metal film flotation: principles and electrical effects. *Adv. Funct. Mater.* 12: 795–807.

206 Shimizu, K.T., Fabbri, J.D., Jelincic, J.J. et al. (2006). Soft deposition of large-area metal contacts for molecular electronics. *Adv. Mater.* 18: 1499–1504.

207 Haick, H. and Cahen, D. (2008). Contacting organic molecules by soft methods: Towards molecule-based electronic devices. *Acc. Chem. Res.* 41: 359–366.

208 Selzer, Y. and Cahen, D. (2001). Fine tuning of $Au/SiO_2/Si$ diodes by varying interfacial dipoles using molecular monolayers. *Adv. Mater.* 13: 508–511.

209 Salomon, A., Berkovich, D., and Cahen, D. (2003). Molecular modification of an ionic semiconductor-metal interface: ZnO/molecule/Au diodes. *Appl. Phys. Lett.* 82: 1051–1053.

210 Haick, H., Ambrico, M., Ligonzo, T. et al. (2006). Controlling semiconductor/metal junction barriers by incomplete, nonideal molecular monolayers. *J. Am. Chem. Soc.* 128: 6854–6869.

211 Ikram, I.M., Rabinal, M.K., Kalasad, M.N. et al. (2009). Formation of electronic junctions on molecularly modified surfaces by lift-and-float electrical contacts. *Langmuir* 25: 3305–3309.

212 Race, H.H. and Reynolds, S.I. (1939). Electrical properties of multimolecular films. *J. Am. Chem. Soc.* 61: 1425–1432.

213 Li, J.-C., Wu, J.Z., Zhou, C. et al. (2013). Latest studies on metal-molecule-metal junctions. *Acta Phys. Chim. Sin.* 29: 1123–1144.

214 Chabinyc, M.L., Chen, X.X., Holmlin, R.E. et al. (2002). Molecular rectification in a metal-insulator-metal junction based on self-assembled monolayers. *J. Am. Chem. Soc.* 124: 11730–11736.

215 Slowinski, K., Fong, H.K.Y., and Majda, M. (1999). Mercury-mercury tunneling junctions. 1. Electron tunneling across symmetric and asymmetric alkanethiolate bilayers. *J. Am. Chem. Soc.* 121: 7257–7261.

216 Rampi, M.A. and Whitesides, G.M. (2002). A versatile experimental approach for understanding electron transport through organic materials. *Chem. Phys.* 281: 373–391.

217 Yaffe, O., Scheres, L., Puniredd, S.R. et al. (2009). Molecular electronics at metal/semiconductor junctions. Si inversion by sub-nanometer molecular films. *Nano Lett.* 9: 2390–2394.

218 von Wrochem, F., Gao, D., Scholz, F. et al. (2010). Efficient electronic coupling and improved stability with dithiocarbamate-based molecular junctions. *Nat. Nanotechnol.* 5: 618–624.

219 Holmlin, R.E., Ismagilov, R.F., Haag, R. et al. (2001). Correlating electron transport and molecular structure in organic thin films. *Angew. Chem. Int. Ed.* 40: 2316–2382.

220 Thuo, M.M., Reus, W.F., and Nijhuis, C.A. (2011). Odd-even effects in charge transport across self-assembled monolayers. *J. Am. Chem. Soc.* 133: 2962–2975.

221 Reus, W.F., Thuo, M.M., Shapiro, N.D. et al. (2012). The SAM, not the electrodes, dominates charge transport in metal-monolayer// Ga_2O_3/Gallium-Indium eutectic junctions. *ACS Nano* 6: 4806–4822.

222 Cademartiri, L., Thuo, M.M., Nijhuis, C.A. et al. (2012). Electrical resistance of Ag^{TS}–$S(CH_2)_{n-1}CH_3$//Ga_2O_3/EGaIn tunneling junctions. *J. Phys. Chem. C* 116: 10848–10860.

223 Nijhuis, C.A., Reus, W.F., Barber, J.R. et al. (2010). Charge transport and rectification in arrays of SAM-based tunneling junctions. *Nano Lett.* 10: 3611–3619.

224 Chiechi, R.C., Weiss, E.A., Dickey, M.D. et al. (2008). Eutectic gallium-indium (EGaIn): A moldable liquid metal for electrical characterization of self-assembled monolayers. *Angew. Chem. Int. Ed.* 47: 142–144.

225 Wan, A., Jiang, L., Sangeeth, C.S.S. et al. (2014). Reversible soft top-contacts to yield molecular junctions with precise and reproducible electrical characteristics. *Adv. Funct. Mater.* 24: 4442–4456.

226 Jiang, L., Yuan, L., Cao, L. et al. (2014). Controlling leakage currents: the role of the binding group and purity of the precursors for self-assembled monolayers in the performance of molecular diodes. *J. Am. Chem. Soc.* 136: 1982–1991.

227 Yuan, L., Jiang, L., Zhang, B. et al. (2014). Dependency of the tunneling decay coefficient in molecular tunneling junctions on the topography of the bottom electrodes. *Angew. Chem. Int. Ed.* 53: 3377–3381.

228 Yoon, H.J., Shapiro, N.D., Park, K.M. et al. (2012). The rate of charge tunneling through self-assembled monolayers is insensitive to many functional group substitutions. *Angew. Chem. Int. Ed.* 51: 4658–4661.

229 Thuo, M.M., Reus, W.F., Simeone, F.C. et al. (2012). Replacing -CH_2CH_2- with -CONH- does not significantly change rates of charge transport through Ag^{TS}-SAM//Ga_2O_3/EGaIn junctions. *J. Am. Chem. Soc.* 134: 10876–10884.

230 Nerngchamnong, N., Yuan, L., Qi, D.C.A. et al. (2013). The role of van der Waals forces in the performance of molecular diodes. *Nat. Nanotechnol.* 8: 113–118.

231 Fracasso, D., Muglali, M.I., Rohwerder, M. et al. (2013). Influence of an atom in EGaIn/Ga_2O_3 tunneling junctions comprising self-assembled monolayers. *J. Phys. Chem. C* 117: 11367–11376.

232 Fan, X.L., Wang, C., Yang, D.L. et al. (2002). Molecule rectifier fabricated by capillary tunnel junction. *Chem. Phys. Lett.* 361: 465–468.

233 Liu, Y.H., Fan, X.L., Yang, D.L. et al. (2004). Tunneling characteristics of octadecyl derivatives on tin and indium electrodes. *Langmuir* 20: 855–861.

234 Majumdar, N., Gergel, N., Routenberg, D. et al. (2005). Nanowell device for the electrical characterization of metal-molecule-metal junctions. *J. Vac. Sci. Technol. B* 23: 1417–1421.

235 Chen, J., Reed, M.A., Rawlett, A.M. et al. (1999). Large on-off ratios and negative differential resistance in a molecular electronic device. *Science* 286: 1550–1552.

236 Song, H., Lee, T., Choi, N.-J. et al. (2007). A statistical method for determining intrinsic electronic transport properties of self-assembled alkanethiol monolayer devices. *Appl. Phys. Lett.* 91: 253116.

237 Krapf, D., Wu, M.Y., Smeets, R.M.M. et al. (2006). Fabrication and characterization of nanopore-based electrodes with radii down to 2 nm. *Nano Lett.* 6: 105–109.

238 Akkerman, H.B., Blom, P.W.M., de Leeuw, D.M. et al. (2006). Towards molecular electronics with large-area molecular junctions. *Nature* 441: 69–72.

239 Wang, G., Kim, Y., Choe, M. et al. (2011). A new approach for molecular electronic junctions with a multilayer graphene electrode. *Adv. Mater.* 23: 755–760.

240 He, J.L., Chen, B., Flatt, A.K. et al. (2006). Metal-free silicon-molecule-nanotube testbed and memory device. *Nat. Mater.* 5: 63–68.

241 Mbindyo, J.K.N., Mallouk, T.E., Mattzela, J.B. et al. (2002). Template synthesis of metal nanowires containing monolayer molecular junctions. *J. Am. Chem. Soc.* 124: 4020–4026.

242 Qin, L.D., Park, S., Huang, L. et al. (2005). On-wire lithography. *Science* 309: 113–115.

243 Banholzer, M.J., Qin, L., Millstone, J.E. et al. (2009). On-wire lithography: Synthesis encoding and biological applications. *Nat. Protoc.* 4: 838–848.

244 Braunschweig, A.B., Schmucker, A.L., Wei, W.D. et al. (2010). Nanostructures enabled by on-wire lithography (OWL). *Chem. Phys. Lett.* 486: 89–98.

245 Mayor, M. (2009). Watching the gap close. *Angew. Chem. Int. Ed.* 48: 5583–5585.

246 Piner, R.D., Zhu, J., Xu, F. et al. (1999). "Dip-pen" nanolithography. *Science* 283: 661–663.

247 Chen, X., Yeganeh, S., Qin, L. et al. (2009). Chemical fabrication of heterometallic nanogaps for molecular transport junctions. *Nano Lett.* 9: 3974–3979.

248 Osberg, K.D., Schmucker, A.L., Senesi, A.J. et al. (2011). One-dimensional nanorod arrays: independent control of composition, length, and interparticle spacing with nanometer precision. *Nano Lett.* 11: 820–824.

249 Chen, X., Braunschweig, A.B., Wiester, M.J. et al. (2009). Spectroscopic tracking of molecular transport junctions generated by using click chemistry. *Angew. Chem. Int. Ed.* 48: 5178–5181.

250 Kolb, H.C., Finn, M.G., and Sharpless, K.B. (2001). Click chemistry: Diverse chemical function from a few good reactions. *Angew. Chem. Int. Ed.* 40: 2004–2021.

251 Tang, J.Y., Wang, Y.L., Klare, J.E. et al. (2007). Encoding molecular-wire formation within nanoscale sockets. *Angew. Chem. Int. Ed.* 46: 3892–3895.

252 Mayor, M. (2009). Watching the gap close. *Angew. Chem. Int. Ed.* 48: 5583–5585.

253 Lee, B.Y., Heo, K., Schmucker, A.L. et al. (2012). Nanotube-bridged wires with sub-10 nm gaps. *Nano Lett.* 12: 1879–1884.

254 Nam, G.-H., Lee, J.-H., Zahari, N.E.M. et al. (2014). Single-bundle carbon-nanotube-bridged nanorod devices with control of gap length. *J. Phys. Chem. C* 118: 10463–10471.

255 Zhou, X., Shade, C.M., Schmucker, A.L. et al. (2012). OWL-based nanomasks for preparing graphene ribbons with sub-10 nm gaps. *Nano Lett.* 12: 4734–4737.

256 Liusman, C., Li, S., Chen, X. et al. (2010). Free-standing bimetallic nanorings and nanoring arrays made by on-wire lithography. *ACS Nano* 4: 7676–7682.

257 Meng, F., Hervault, Y.-M., Shao, Q. et al. (2014). Orthogonally modulated molecular transport junctions for resettable electronic logic gates. *Nat. Commun.* 5: 3023.

258 Pedano, M.L., Li, S., Schatz, G.C. et al. (2010). Periodic electric field enhancement along gold rods with nanogaps. *Angew. Chem. Int. Ed.* 49: 78–82.

259 Osberg, K.D., Rycenga, M., Harris, N. et al. (2012). Dispersible gold nanorod dimers with sub-5 nm gaps as local amplifiers for surface-enhanced Raman scattering. *Nano Lett.* 12: 3828–3832.

260 Schmucker, A.L., Barin, G., Brown, K.A. et al. (2013). Electronic and optical vibrational spectroscopy of molecular transport junctions created by on-wire lithography. *Small* 9: 1900–1903.

261 Loo, Y.L., Lang, D.V., Rogers, J.A. et al. (2003). Electrical contacts to molecular layers by nanotransfer printing. *Nano Lett.* 3: 913–917.

262 Coll, M., Miller, L.H., Richter, L.J. et al. (2009). Formation of silicon-based molecular electronic structures using flip-chip lamination. *J. Am. Chem. Soc.* 131: 12451–12457.

263 Williams, S.S., Retterer, S., Lopez, R. et al. (2010). High-resolution PFPE-based Molding techniques for nanofabrication of high-pattern density, sub-20 nm features: a fundamental materials approach. *Nano Lett.* 10: 1421–1428.

264 Liang, X., Jung, Y.-S., Wu, S. et al. (2010). Formation of bandgap and subbands in graphene nanomeshes with sub-10 nm ribbon width fabricated via nanoimprint lithography. *Nano Lett.* 10: 2454–2460.

265 Jeong, J.W., Park, W.I., Do, L.-M. et al. (2012). Nanotransfer printing with sub-10 nm resolution realized using directed self-assembly. *Adv. Mater.* 24: 3526–3531.

266 Sanetra, N., Karipidou, Z., Wirtz, R. et al. (2012). Printing of highly integrated crossbar junctions. *Adv. Funct. Mater.* 22: 1129–1135.

267 Carlson, A., Bowen, A.M., Huang, Y. et al. (2012). Transfer printing techniques for materials assembly and micro/nanodevice fabrication. *Adv. Mater.* 24: 5284–5318.

268 Lan, H.B. and Liu, H.Z. (2013). UV-nanoimprint lithography: Structure, materials and fabrication of flexible molds. *J. Nanosci. Nanotechnol.* 13: 3145–3172.

269 Kooy, N., Mohamed, K., Pin, L.T. et al. (2014). A review of roll-to-roll nanoimprint lithography. *Nanoscale Res. Lett.* 9: 1–13.

270 He, Z.B., Zhang, W.J., Tang, Y.B. et al. (2009). Crossbar heterojunction field effect transistors of CdSe:In nanowires and Si nanoribbons. *Appl. Phys. Lett.* 95: 253107.

271 Linn, E., Rosezin, R., Tappertzhofen, S. et al. (2012). Beyond von Neumann-logic operations in passive crossbar arrays alongside memory operations. *Nanotechnology* 23: 305205.

272 Kim, K.H., Gaba, S., Wheeler, D. et al. (2012). Functional hybrid memristor crossbar-array/CMOS system for data storage and neuromorphic applications. *Nano Lett.* 12: 389–395.

273 Martin, P., Della Rocca, M.L., Anthore, A. et al. (2012). Organic electrodes based on grafted oligothiophene units in ultrathin, large-area molecular junctions. *J. Am. Chem. Soc.* 134: 154–157.

274 Anariba, F., Steach, J.K., and McCreery, R.L. (2005). Strong effects of molecular structure on electron transport in carbon/molecule/copper electronic junctions. *J. Phys. Chem. B* 109: 11163–11172.

275 Xia, Q., Yang, J.J., Wu, W. et al. (2010). Self-aligned memristor cross-point arrays fabricated with one nanoimprint lithography step. *Nano Lett.* 10: 2909–2914.

276 Bang, G.S., Chang, H., Koo, J.R. et al. (2008). High-fidelity formation of a molecular-junction device using a thickness-controlled bilayer architecture. *Small* 4: 1399–1405.

277 Li, J.C. (2009). Optoelectronic switching of addressable self-assembled monolayer molecular junctions. *Chem. Phys. Lett.* 473: 189–192.

278 Li, J.C., Wang, D., and Ba, D.C. (2012). Effects of temperature and light illumination on the current-voltage characteristics of molecular self-assembled monolayer junctions. *Phys. Chem. C* 116: 10986–10994.

279 Kim, J.J., Cho, B., Kim, K.S. et al. (2011). Electrical characterization of unipolar organic resistive memory devices scaled down by a direct metal-transfer method. *Adv. Mater.* 23: 2104–2107.

280 Jeong, H., Kim, D., Kim, P. et al. (2015). A new approach for high-yield metal-molecule-metal junctions by direct metal transfer method. *Nanotechnology* 26: 025601.

281 Nijhuis, C.A., Reus, W.F., Barber, J.R. et al. (2012). Comparison of SAM-based junctions with Ga_2O_3/EGaIn top electrodes to other large-area tunneling junctions. *J. Phys. Chem. C* 116: 14139–14150.

282 Jiao, L.Y., Fan, B., Xian, X.J. et al. (2008). Creation of nanostructures with poly(methyl methacrylate)-mediated nanotransfer printing. *J. Am. Chem. Soc.* 130: 12612–12613.

283 Duan, X.F., Huang, Y., Cui, Y. et al. (2001). Indium phosphide nanowires as building blocks for nanoscale electronic and optoelectronic devices. *Nature* 409: 66–69.

284 Yoon, H.P., Maitani, M.M., Cabarcos, O.M. et al. (2010). Crossed-nanowire molecular junctions: A new multispectroscopy platform for conduction-structure correlations. *Nano Lett.* 10: 2897–2902.

285 Kushmerick, J.G., Holt, D.B., Yang, J.C. et al. (2002). Metal-molecule contacts and charge transport across monomolecular layers: measurement and theory. *Phys. Rev. Lett.* 89: 086802.

286 Kushmerick, J.G., Naciri, J., Yang, J.C. et al. (2003). Conductance scaling of molecular wires in parallel. *Nano Lett.* 3: 897–900.

287 Bufon, C.C.B., Espinoza, J.D.A., Thurmer, D.J. et al. (2011). Hybrid organic/inorganic molecular heterojunctions based on strained nanomembranes. *Nano Lett.* 11: 3727–3733.

288 Yu, L.H., Gergel-Hackett, N., Zangmeister, C.D. et al. (2008). Molecule-induced interface states dominate charge transport in Si-alkyl-metal junctions. *J. Phys.: Condens. Matter* 20: 374114.

289 Song, H., Reed, M.A., and Lee, T. (2011). Single molecule electronic devices. *Adv. Mater.* 23: 1583–1608.

290 Shen, Q., Guo, X.F., Steigerwald, M.L. et al. (2010). Integrating reaction chemistry into molecular electronic devices. *Chem-Asian J.* 5: 1040–1057.

291 Yu, H.Y., Ah, C.S., Baek, I.B. et al. (2009). Nanogap array fabrication using doubly clamped freestanding silicon nanowires and angle evaporations. *Etri. J.* 31: 351–356.

292 Wang, J.D., Wang, Z.X., Li, Q.C. et al. (2013). Revealing interface-assisted charge-transfer mechanisms by using silicon nanowires as local probes. *Angew. Chem. Int. Ed.* 52: 3369–3373.

293 Preiner, M.J. and Melosh, N.A. (2008). Creating large area molecular electronic junctions using atomic layer deposition. *Appl. Phys. Lett.* 92: 213301.

294 Milani, F., Grave, C., Ferri, V. et al. (2007). Ultrathin π-conjugated polymer films for simple fabrication of large-area molecular junctions. *ChemPhysChem* 8: 515–518.

295 Li, T., Hauptmann, J.R., Wei, Z. et al. (2012). Solution-processed ultrathin chemically derived graphene films as soft top contacts for solid-state molecular electronic junctions. *Adv. Mater.* 24: 1333–1339.

296 Akkerman, H.B., Naber, R.C.G., Jongbloed, B. et al. (2007). Electron tunneling through alkanedithiol self-assembled monolayers in large-area molecular junctions. *Proc. Natl. Acad. Sci. U. S. A.* 104: 11161–11166.

297 Kronemeijer, A.J., Katsouras, I., Huisman, E.H. et al. (2011). Universal scaling of the charge transport in large-area molecular junctions. *Small* 7: 1593–1598.

298 Akkerman, H.B., Kronemeijer, A.J., van Hal, P.A. et al. (2008). Self-assembled-monolayer formation of long alkanedithiols in molecular junctions. *Small* 4: 100–104.

299 Van Hal, P.A., Smits, E.C.P., Geuns, T.C.T. et al. (2008). Upscaling, integration and electrical characterization of molecular junctions. *Nat. Nanotechnol.* 3: 749–754.

300 Katsouras, I., Kronemeijer, A.J., Smits, E.C.P. et al. (2011). Extending the voltage window in the characterization of electrical transport of large-area molecular junctions. *Appl. Phys. Lett.* 99: 013303.

301 Asadi, K., Katsouras, I., Harkema, J. et al. (2012). Organic field-effect transistors as a test-bed for molecular electronics: a combined study with large-area molecular junctions. *Org. Electron.* 13: 2502–2507.

302 Akkerman, H.B., Kronemeijer, A.J., Harkema, J. et al. (2010). Stability of large-area molecular junctions. *Org. Electron.* 11: 146–149.

303 Wang, G., Na, S.I., Kim, T.W. et al. (2012). Effect of PEDOT:PSS-molecule interface on the charge transport characteristics of the large-area molecular electronic junctions. *Org. Electron.* 13: 771–777.

304 Park, S., Wang, G., Cho, B. et al. (2012). Flexible molecular-scale electronic devices. *Nat. Nanotechnol.* 7: 438–442.

305 Jeong, H., Kim, D., Wang, G. et al. (2014). Redox-induced asymmetric electrical characteristics of ferrocene-alkanethiolate molecular devices on rigid and flexible substrates. *Adv. Funct. Mater.* 24: 2472–2480.

306 Kim, D., Jeong, H., Lee, H. et al. (2014). Flexible molecular-scale electronic devices composed of diarylethene photoswitching molecules. *Adv. Mater.* 26: 3968–3973.

307 Neuhausen, A.B., Hosseini, A., Sulpizio, J.A. et al. (2012). Molecular junctions of self-assembled monolayers with conducting polymer contacts. *ACS Nano* 6: 9920–9931.

308 Seo, S., Min, M., Lee, S.M. et al. (2013). Photo-switchable molecular monolayer anchored between highly transparent and flexible graphene electrodes. *Nat. Commun.* 4: 1920.

309 Li, T., Jevric, M., Hauptmann, J.R. et al. (2013). Ultrathin reduced graphene oxide films as transparent top-contacts for light switchable solid-state molecular junctions. *Adv. Mater.* 25: 4164–4170.

310 Ashwell, G.J., Wierzchowiec, P., Bartlett, C.J. et al. (2007). Molecular electronics: connection across nano-sized electrode gaps. *Chem. Commun.*: 1254–1256.

311 Chen, W., Liu, X.Q., Tan, Z.K. et al. (2006). Fabrication and characterization of novel cross point structures for molecular electronic integrated circuits. *J. Vac. Sci. Technol. B* 24: 3217–3220.

312 Tyagi, P., Li, D.F., Holmes, S.M. et al. (2007). Molecular electrodes at the exposed edge of metal/insulator/metal trilayer structures. *J. Am. Chem. Soc.* 129: 4929–4938.

313 Howell, S.W., Dirk, S.M., Childs, K. et al. (2005). Mass-fabricated one-dimensional silicon nanogaps for hybrid organic/nanoparticle arrays. *Nanotechnology* 16: 754–758.

314 Tyagi, P. (2011). Multilayer edge molecular electronics devices: A review. *J. Mater. Chem.* 21: 4733.

315 Luber, S.M., Strobel, S., Tranitz, H.P. et al. (2005). Nanometre spaced electrodes on a cleaved AlGaAs surface. *Nanotechnology* 16: 1182–1185.

316 Brinkman, W.F. (1970). Tunneling conductance of asymmetrical barriers. *J. Appl. Phys. A* 41: 1915.

317 Pang, P., Ashcroft, B.A., Song, W.S. et al. (2014). Fixed-gap tunnel junction for reading DNA nucleotides. *ACS Nano* 8: 11994–12003.

318 Cai, L.T., Skulason, H., Kushmerick, J.G. et al. (2004). Nanowire-based molecular monolayer junctions: Synthesis, assembly, and electrical characterization. *J. Phys. Chem. B* 108: 2827–2832.

319 Cai, L., Cabassi, M.A., Yoon, H. et al. (2005). Reversible bistable switching in nanoscale thiol-substituted oligoaniline molecular junctions. *Nano Lett.* 5: 2365–2372.

320 Selzer, Y., Cai, L.T., Cabassi, M.A. et al. (2005). Effect of local environment on molecular conduction: isolated molecule versus self-assembled monolayer. *Nano Lett.* 5: 61–65.

321 Noy, G., Ophir, A., and Selzer, Y. (2010). Response of molecular junctions to surface plasmon polaritons. *Angew. Chem. Int. Ed.* 49: 5734–5736.

322 Holmlin, R.E., Haag, R., Chabinyc, M.L. et al. (2001). Electron transport through thin organic films in metal-insulator-metal junctions based on self-assembled monolayers. *J. Am. Chem. Soc.* 123: 5075–5085.

323 Keller, A., Atabek, O., Ratner, M. et al. (2002). Laser-assisted conductance of molecular wires. *J. Phys. B At. Mol. Opt. Phys.* 35: 4981.

324 Lehmann, J., Kohler, S., Hanggi, P. et al. (2002). Molecular wires acting as coherent quantum ratchets. *Phys. Rev. Lett.* 88: 228305.

325 Jiang, J., Bosnick, K., Maillard, M. et al. (2003). Single molecule Raman spectroscopy at the junctions of large Ag nanocrystals. *J. Phys. Chem. B* 107: 9964–9972.

326 Lehmann, J., Kohler, S., Hanggi, P. et al. (2003). Laser controlled molecular switches and transistors. *Chem. Phys. Lett.* 368: 282–288.

327 Galperin, M. and Nitzan, A. (2005). Current-induced light emission and light-induced current in molecular-tunneling junctions. *Phys. Rev. Lett.* 95: 206802.

328 Beebe, J.M., Kim, B., Gadzuk, J.W. et al. (2006). Transition from direct tunneling to field emission in metal-molecule-metal junctions. *Phys. Rev. Lett.* 97: 026801.

329 Galperin, M., Nitzan, A., and Ratner, M.A. (2006). Molecular transport junctions: current from electronic excitations in the leads. *Phys. Rev. Lett.* 96: 166803.

330 Fang, Y., Seong, N.H., and Dlott, D.D. (2008). Measurement of the distribution of site enhancements in surface-enhanced Raman scattering. *Science* 321: 388–392.

331 Ioffe, Z., Shamai, T., Ophir, A. et al. (2008). Detection of heating in current-carrying molecular junctions by Raman scattering. *Nat. Nanotechnol.* 3: 727–732.

332 Haiss, W., Martin, S., and Scullion, L.E. (2009). Anomalous length and voltage dependence of single molecule conductance. *Phys. Chem. Chem. Phys.* 11: 10831–10838.

333 Kinkhabwala, A., Yu, Z.F., Fan, S.H. et al. (2009). Large single-molecule fluorescence enhancements produced by a bowtie nanoantenna. *Nat. Photonics* 3: 654–657.

334 Cao, L., Nome, R.A., Montgomery, J.M. et al. (2010). Controlling plasmonic wave packets in silver nanowires. *Nano Lett.* 10: 3389–3394.

335 Ittah, N. and Selzer, Y. (2011). Electrical detection of surface plasmon polaritons by 1 G_0 gold quantum point contacts. *Nano Lett.* 11: 529–534.

336 Arielly, R., Ofarim, A., Noy, G. et al. (2011). Accurate determination of plasmonic fields in molecular junctions by current rectification at optical frequencies. *Nano Lett.* 11: 2968–2972.

337 Lu, W., Ji, Z.Q., Pfeiffer, L. et al. (2003). Real-time detection of electron tunnelling in a quantum dot. *Nature* 423: 422–425.

338 Arielly, R., Vadai, M., Kardash, D. et al. (2014). Real-time detection of electron tunnelling in a quantum dot. *J. Am. Chem. Soc.* 136: 2674–2680.

339 Arielly, R., Nachman, N., Zelinskyy, Y. et al. (2017). Picosecond time resolved conductance measurements of redox molecular junctions. *J. Chem. Phys.* 146: 092306.

340 Hallback, A.S., Oncel, N., Huskens, J. et al. (2004). Inelastic electron tunneling spectroscopy on decanethiol at elevated temperatures. *Nano Lett.* 4: 2393–2395.

341 Kim, Y., Hellmuth, T.J., Buerkle, M. et al. (2011). Characteristics of amine-ended and thiol-ended alkane single-molecule junctions revealed by inelastic electron tunneling spectroscopy. *ACS Nano* 5: 4104–4111.

342 Kornbluth, M., Nitzan, A., and Seideman, T. (2013). Light-induced electronic non-equilibrium in plasmonic particles. *J. Chem. Phys.* 138: 174707.

343 Herzog, J.B., Knight, M.W., and Natelson, D. (2014). Thermoplasmonics: Quantifying plasmonic heating in single nanowires. *Nano Lett.* 14: 499–503.

344 Kumarasinghe, C.S., Premaratne, M., Bao, Q. et al. (2015). Theoretical analysis of hot electron dynamics in nanorods. *Sci. Rep.* 5: 12140.

345 Nachman, N. and Selzer, Y. (2017). Thermometry of plasmonic heating by Inelastic Electron Tunneling Spectroscopy (IETS). *Nano Lett.* 17: 5855–5861.

3

Carbon Electrodes for Molecular Electronics

While ordinary metal electrode-based molecular junctions remain operational, different experimental platforms based on non-metal materials have been constructed, thus leading to new possibilities for molecular-scale electronics. Among these new testing systems, carbon electrode–molecule junctions, where carbon nanomaterials, including single-walled carbon nanotubes (SWCNTs) and graphene, are used as point contacts, are particularly promising because of their unique advantages. Firstly, both SWCNTs and graphene are molecular chemicals made entirely of sp^2-hybridized carbon atoms arranged in a honeycomb lattice [1, 2], thus offering a natural compatibility with organic/biological molecules. Secondly, these crystalline carbon nanomaterials exhibit extraordinary electronic properties with high stability and chemical flexibility due to their π-conjugated skeletons. Unlike mobile metal electrodes, they are atomically stiff and naturally functional at their ends. When lithographically patterned as point contacts, they are end-functionalized by carboxylic acid groups. These functional groups could be used to form robust covalent bonds at the molecule/electrode interface through amide linkages that can endure chemical treatments and external stimuli, thus significantly improving the device stability. Thirdly, they are easily available in large areas through bottom-up chemical approaches and can be easily micro-/nanofabricated onto a large range of substrates with high accuracy. Finally, another unique feature of these nanocarbons results from the fact that the low-dimensional nature is molecular in size, ensuring the number of bridged molecules down to the single-molecule level. Because of all of these features, carbon nanomaterials, such as SWCNTs and graphene, are most likely better suited as nanoscale electrode materials for molecular electronics, as commented in the special issue of *Nature Nanotechnology* in June 2013 [3]. In this chapter, we detail the methodologies used to develop robust molecular electronics platforms based on SWCNTs and graphene.

3.1 Carbon Nanotube-Based Electrodes

Since their discovery in the 1990s [4], carbon nanotubes have led to a significant amount of research due to their tremendous potential applications in the chemical, physical, and electrical fields [5]. Although they have the simplest chemical

Molecular-Scale Electronics: Concept, Fabrication and Applications,
First Edition. Xuefeng Guo, Dong Xiang, and Yu Li.

composition and atomic bonding configuration, their electronic properties are highly dependent on chirality and diameter. This structural dependence leads to infinite electrical diversity and richness, thus offering unlimited opportunities to tune the energy alignments between the tubes and the molecules of interest. Another important distinction between SWCNTs and metal contacts is that SWCNTs are molecularly sized in their diameter, centimeter-scale long, and functional on their ends (not their sides). Therefore, in conjunction with the remarkable properties mentioned earlier, SWCNTs are good contacts for modular single-molecule devices. To form the SWCNT electrodes, there are several efficient ways to cut the SWCNTs and obtain nanogaps, such as focused ion beam (FIB) etching, electrical breakdown, and lithography-defined oxidative cutting. The FIB etching method uses high-energy ion beams to etch the SWCNTs as well as the substrates [6]. After FIB etching, the tube edges were treated with nitric acid to introduce the carboxylic acid end groups. Then, these functional groups were used to bridge the individual DNA molecules, allowing direct electrical measurements of DNAs by using the SWCNT electrodes. The key step is that the interelectrode spacing was controlled by adjusting the ion beam current and the exposure time, which is challenging due to the use of the high-energy ion beams. In the following discussions, two reliable methodologies with more universality to build molecular devices based on SWCNT point contacts, including electrical breakdown and lithography-defined oxidative cutting, will be primarily introduced.

3.1.1 Electrical Breakdown

Similar to the formation of metal electrodes by using electromigration previously discussed, the electrical breakdown of the SWCNTs will occur when a high-density current passes through them, eventually resulting in a gap by truncating a complete tube [7]. It was determined that the size of these gaps was extremely sensitive to the air exposure because this electrical breakdown was initiated by oxidation at a particular power in air [8]. This result implies that nanogaps with different sizes could be achieved in the middle region of a nanotube by varying the proportion of the oxidative gas in the cutting environment, potentially providing a way to fabricate the SWCNT electrodes.

In 2004, two independent studies on miniaturized organic transistors based on carbon nanotube electrodes were reported by Qi et al. [9] and Tsukagoshi et al. [10]. In the former study, molecular-thickness pentacene was deposited into the gap on a single SWCNT fabricated by the electrical breakdown (Figure 3.1a). The reported size of the nanogaps could be reproducibly controlled in the range of 1–3 nm by varying the lengths of the SWCNTs with a ~2 nm diameter. The scale of this channel is only able to accommodate several organic molecules of interests, which could circumvent the low carrier mobility problem to afford ballistic organic field-effect transistors (OFETs) with high performances. It was demonstrated that the smallest OFETs based on the SWCNT electrodes with a channel length of $L \approx 1$–3 nm and a width of ~2 nm indicated a strong capability of effective conductance modulation (Figure 3.1b). However, in ultrashort OFETs with bulky metal source/drain (S/D) electrodes that were lithographically

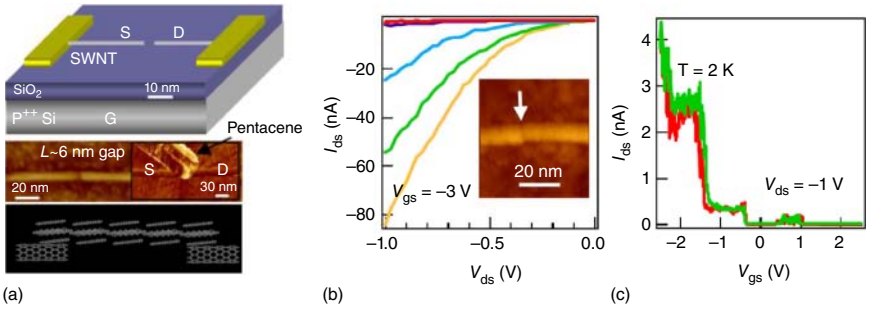

Figure 3.1 SWCNT electrodes for ultra-small OFETs. (a) Top: Schematic demonstration of a cut SWCNT with a nanoscale gap used as the source and drain electrodes of an OFET. The doped Si serves as a back gate. Middle-left: AFM image of a cut SWCNT (diameter ≈ 2 nm, and gap size measured to be ~6 nm after correction of the tip size effect). Middle-right: AFM image of a vapor-deposited pentacene crystallite bridging a cut SWCNT. Bottom: Drawing of a pentacene crystallite bridging two SWCNT electrodes. (b) I_{ds}–V_{ds} curves for a device recorded at $V_{gs} = -3$, -2, -1, 0, and 1 V at room temperature. Inset: An AFM image of the SWCNT after electrical cutting and before pentacene deposition. (c) $I_{ds} - V_{gs}$ curves (at $V_{ds} = 1$ V) for the same device at $T = 4$ and 2 K. Source: Reproduced with permission from Qi et al. [9]. Copyright 2004, American Chemical Society.

patterned as the control, the electrostatic gating was ineffective due to the screening of the gate electric fields by the S/D electrodes. In addition to the measurements at room temperature, this study also tested the properties of the devices with different-sized nanogaps at low temperatures (e.g. 2 and 4 K). When the size (1–3 nm) of the nanogaps approached that of the pentacene, step-like features were observed in the I–V spectra (Figure 3.1c), which could be related to the tunneling currents through the discrete molecular orbitals of the pentacene while the devices with larger gaps became insulated in the entire gate-voltage range. In the latter study conducted by Tsukagoshi and coworkers [11], the device structure was fabricated similarly. They revealed that the electrode leads are composed of six-membered carbon rings, common for the compositing unit of pentacene, which will facilitate local epitaxial adhesion due to the commensurate absorption of the van der Waals force connection, thus resulting in an effective electron injection. Additionally, the carbon nanomaterial electrodes have a smaller difference in the organic molecules regarding the thermal expansion coefficient compared with that of metal electrodes. This difference ensures the stiffness of the molecule–electrode interface, thus providing additional possibilities for temperature-dependent measurements. For example, the carbon nanotube-based device was still conductive when cooled to 4.2 K, whereas several organic transistors with metal electrodes exhibited no conduction below the liquid-nitrogen temperature because the connection interface was damaged due to different degrees of expansion. The advantages of using carbon nanotubes as electrodes promise new opportunities for forming new types of molecular FETs and exploring the intrinsic transport properties of few and even single molecules [12–15].

By following the impressive studies mentioned earlier, Marquardt et al. [16] conducted single-molecule electroluminescence measurements based on molecular devices by using free-standing SWCNTs as electrodes. Similarly, these SWCNT electrodes with a nanogap of <10 nm were fabricated controllably through the electrical breakdown in combination with the regulation of the oxygen partial pressure. The organic molecules of interest with special designs were incorporated into the nanogap using two types of interactions: electrostatic attraction between the polarizable π-systems (oligo(phenylene ethynylene) [OP]) on both sides of the molecules and the nanotube electrodes and $\pi-\pi$ stacking between the terminal phenanthrene units and the nanotubes, both of which could produce a strong connection, thus ensuring the execution of the systematical experiments (Figure 3.2a). Generally, for use as efficient electrodes, an SWCNT with an excellent metallic transport property is required; however, the amount of delocalized electrons should be limited to avoid the quenching of the excited state of the molecule because the low-level orbital in the excited state is necessary for luminescence (Figure 3.2b). Fortunately, the metallic carbon nanotubes have perfect ballistic transport properties with a simultaneous suppressed degree of electron delocalization, thus ensuring the successful observation of electroluminescence (Figure 3.2c). This finding is remarkable because it provides visible evidence for the current flow through rigidly mounted

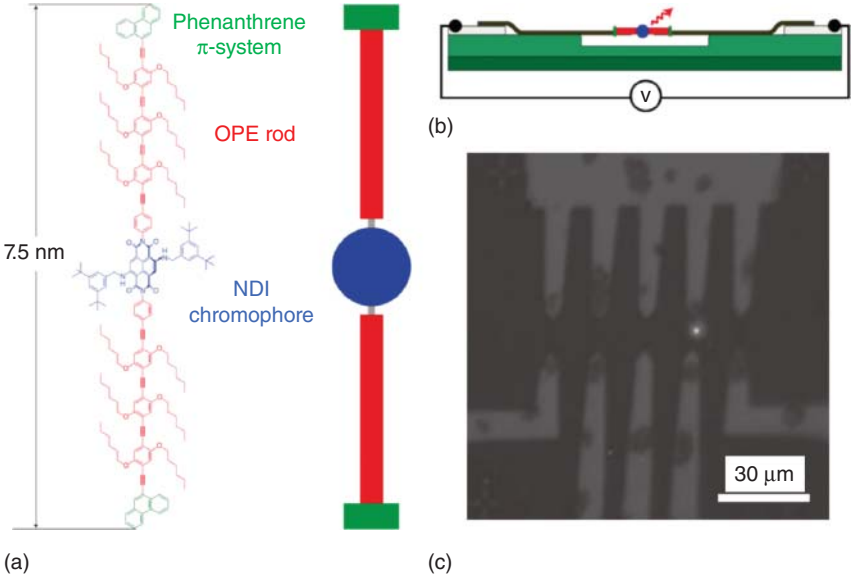

Figure 3.2 Single-molecule electroluminescence. (a) Chemical structure of the molecule, which consists of a central 2,6-dibenzylamino core-substituted naphthalenediimide (NDI) chromophore (blue), two oligophenyleneethynylenes (OPEs) rods (red), and phenanthrene anchor units (green). (b) Schematic drawing of the device geometry. (c) Optical micrograph of an image acquired for 20 minutes with one device under a bias of $V = 4$ V and without external illumination. A bright electroluminescent spot is visible at the location of the biased carbon nanotube–molecule junction. Source: Reproduced with permission from Marquardt et al. [16]. Copyright 2010, Springer Nature.

carbon nanotube–molecule junctions and the likelihood of obtaining molecular light-emitting devices with different emission chromophores.

In another study, Wei et al. [17] developed a new process through a combination of the electrical breakdown and the electron beam-induced decomposition (EBID) to fabricate nanotube nanogaps with a controllable size. In the process, wide nanogaps of approximately 10–60 nm were initially formed on the nanotubes by using a high-density current (Figure 3.3a,b) followed by exposure to organic vapors (such as ethanol or toluene) to absorb the organic molecules in the cavity or on the surfaces of the nanotubes (Figure 3.3c). Then, the scanning electron microscopy (SEM) provided an electron beam with an appropriate energy to induce the EBID to regulate the gap size of the nanotube electrode while avoiding the destruction of the carbon nanotubes (Figure 3.3d). Because this process allowed an *in situ* and real-time characterization during the nanotube diameter broadening and nanogap narrowing process, it is relatively feasible and facile to control the nanogap size in a relatively accurate manner. Importantly, after the EBID process, a π-conjugated surface stemming from the deposition of sp^2-rich amorphous carbon was formed, thus offering the option to develop molecular electronics by bridging the circuits with similar π-conjugated molecules, such as DNA, through π-stacking interaction (Figure 3.3e,f).

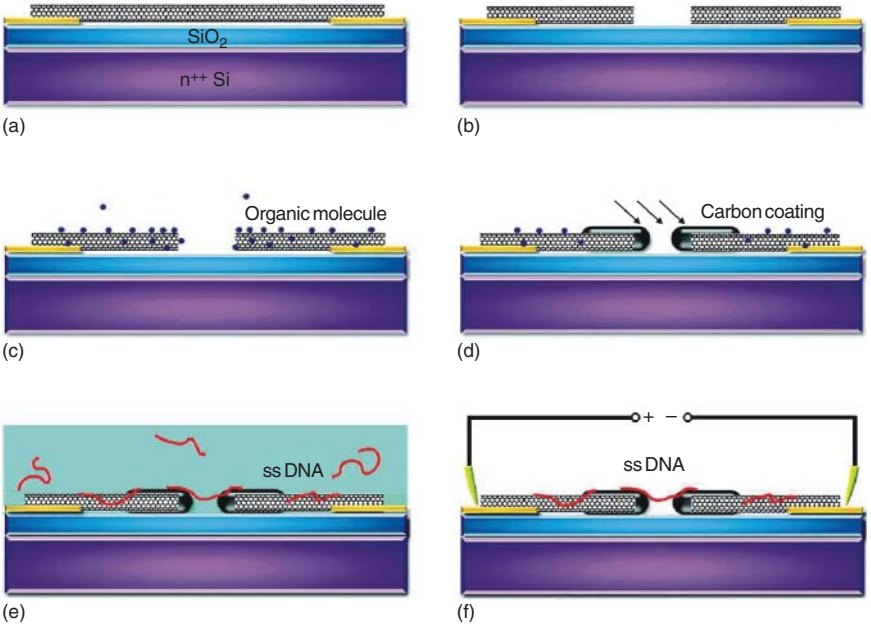

Figure 3.3 Schematic diagram of fabricating nanotube electrodes by the EBID. (a) Building a nanotube transistor. (b) Cutting the nanotubes by using the electrical breakdown. (c) Adsorbing organic molecules on or in the carbon nanotube (CNT). (d) Irradiating the gap of the CNT with an electron beam for *in situ* observation in the SEM. (e) Assembling DNA molecules between the CNT electrodes by being immerged in a DNA buffer solution. (f) Measuring the electronic properties of the bridged DNA molecules. Source: Reproduced with permission from Wei et al. [17]. Copyright 2008, American Chemical Society.

As described previously, the electrical breakdown methodology is useful for achieving nanoscale gaps within carbon nanotubes with relative controllability and efficiency. Although the electrical breakdown method has achieved remarkable progress, several considerable challenges remain, such as the lack of precise control of the gap size and electrode geometry, weak interfacial connection due to π-stacking or the van der Waals forces caused by physical absorption, and complex extra treatment to obtain different degrees of vacuum. Therefore, there is a significant need to develop new techniques to readily fabricate nanogaps in a fully controllable manner, which is of particular importance to advance molecular-scale electronics for either rigorous scientific research or large-scale potential industrial applications.

3.1.2 Lithography-Defined Oxidative Cutting

Chemically, carbon nanotubes are composited by sp^2-hybridized carbons, which can be easily activated by using programmable techniques, thus providing several opportunities to establish new connections with the outside world, such as the carboxylic group. Driven by this proposal, Guo et al. successfully developed a reliable method in 2006 to fabricate nanoscale gaps in SWCNTs based on a combination of high-resolution electron beam lithography (EBL) and precise oxidation by oxygen plasma [18]. At the cutting position, the SWCNT leads with the carboxylic groups will be terminated, making it possible to form a robust connection between the SWCNTs and the molecules by using chemically covalent bond, such as the amide linkage. This result is remarkable because the covalent linkages significantly improve the device stability. This fact is of crucial importance to develop functional SWCNT-molecule single-molecule junctions that function as sensors and switches, thus leading to practical molecular devices.

The lithography-defined oxidative cutting process for fabricating SWCNT point contacts is described in the following text. Briefly, arrays of SWCNT-based transistors fabricated by using photolithography are spin-coated by a blanket layer of poly(methyl methacrylate) (PMMA), where an ultra-small window is open to expose individual SWCNTs through high-resolution e-beam lithography. Then, oxygen plasma is injected through the lithography-defined window to produce two-faced electrodes capped with carboxylic groups by precise local oxidation, which offers access to linking with molecules containing amine terminations through amidation (Figure 3.4). It should be noted here that the size of these nanogaps could be controlled through different degrees of oxidation, i.e. varying the time of exposure to oxygen. Under optimal conditions, such carboxylic group-functionalized SWCNT electrodes, separated by a molecular-length gap, can be produced with 20–25% yields. This type of molecular electronic device can be used to explore the intrinsic properties of individual molecules or achieve special functions, which are determined by the designation of corresponding molecules i.e. the core component of the devices.

This lithographic method has three remarkable advantages as listed in the following text. Firstly, the end-points of the SWCNT electrodes are oxidized to produce carboxylic groups, which enable the system to form covalent bonds between the electrodes and the bridging molecules terminated by the diamines.

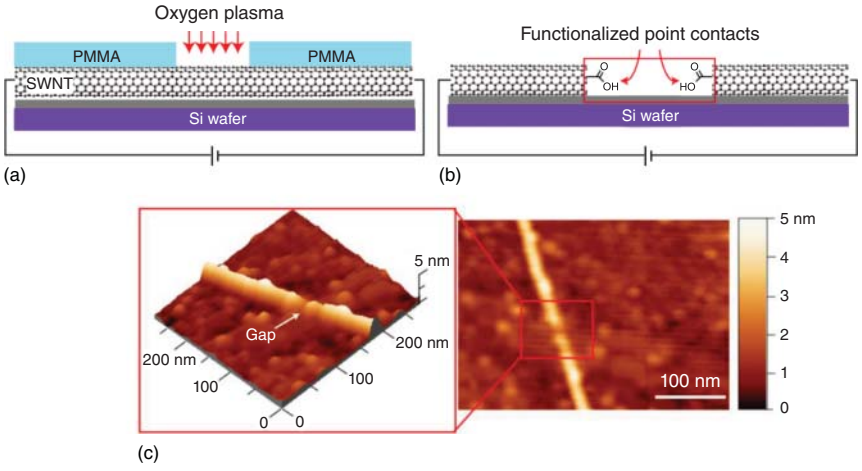

Figure 3.4 Lithography-defined oxidative cutting process for fabricating SWCNT point contacts. (a) Precise cutting of SWCNTs with oxygen plasma introduced through an opening in a window of PMMA defined with e-beam lithography. (b) Oxidative opening of a tube produces two-point contacts functionalized on their ends with carboxylic acids and separated by as little as 2 nm. (c) AFM image of the gap cut into the SWCNT. Inset is the height profile of the isolated tubes. The diameter of the SWCNT is ~1.6 nm, which is estimated from the height profile. Source: Reproduced with permission from Guo et al. [18]. Copyright 2006, AAAS.

Because of the robustness of the interfacial connection, this type of molecular devices can tolerate extra stimuli and chemical treatments, thus significantly improving the device stability. Secondly, due to their naturally quasi-1D geometric scale, these SWCNT electrodes provide only limited sites for molecular connection. When combined with a special designation for the molecules, such as introducing long side chains, the purity of the single-molecule measurements can be ensured, which has the potential for uncovering a wealth of intrinsic information at the single-molecule level. Thirdly, the entire fabrication process is implemented under ambient environment conditions, which can largely decrease the difficulty and complexity to achieve such sophisticated devices. Additionally, this fabrication process can be easily extended to industrial mass production in the future because all the operations in the process as well as the three-terminal device architecture are compatible with conventional micro- and nanofabrication techniques, which have been completely developed in modern industry.

In the initial study, four molecules with different lengths and structures were incorporated into the nanogaps between the SWCNT electrodes for two purposes: to demonstrate the capacity and universality of this platform for various molecular bridges and calibrate the etching process based on the molecular rulers (Figure 3.5a). For the former, electrical measurements were sequentially performed on devices before cutting, after cutting, and after connecting with the molecular bridges. As indicated in Figure 3.5b, by using molecule **1** as a representative, the black curve indicated the source–drain current (I_{ds}) plotted against the gate voltage (V_{gs}) at a constant source-drain bias voltage (V_{ds} = 50 mV)

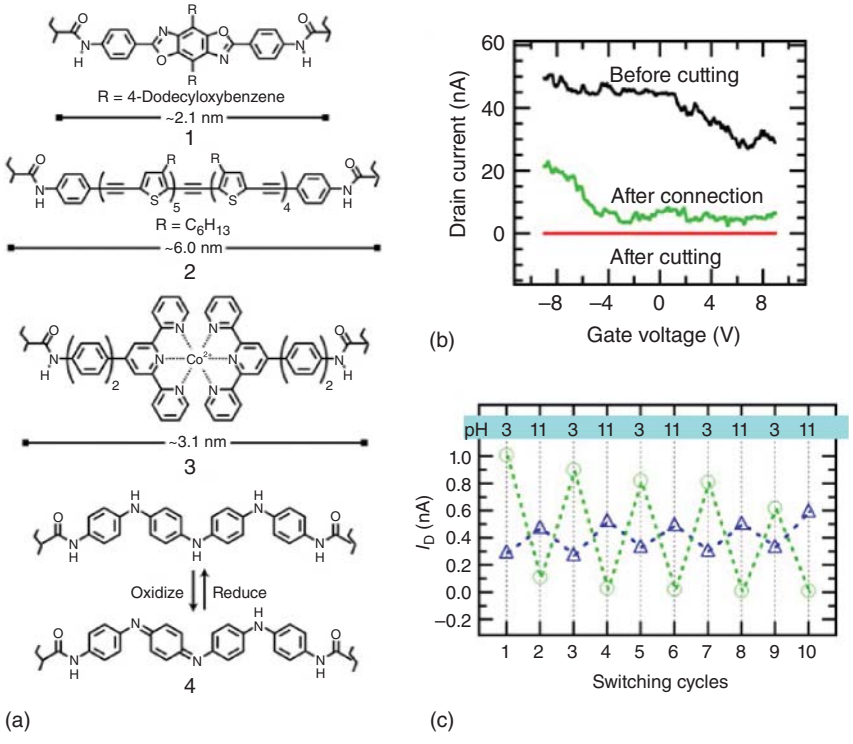

Figure 3.5 Reconnect SWCNT electrodes using molecules. (a) Molecular bridges (**1**–**4**) spanning the SWCNT leads. Oligoaniline **4** provides a redox- and pH-sensitive molecular bridge. (b) Drain current (*I*) as a function of the gate voltage (V_G) at a bias voltage of 50 mV for a metallic tube reconnected with **1**. Electrical measurements were made before cutting (black curve), after cutting with an oxygen plasma (red curve), and after connecting (green curve). (c) Green circles demonstrating the ON-state resistance for oligoaniline **4**, of which the conductance can be altered through protonation or deprotonation when alternately immersed in solutions of low and high pH. The blue triangles depict small changes in the ON-state resistance for **2** when alternately immersed in solutions of low and high pH. Source: Reproduced with permission from Guo et al. [18]. Copyright 2006, AAAS.

before cutting. The device before cutting demonstrated a metallic behavior. The red trace, taken after cutting, indicated no conductance down to the noise limit of the measurement (≤~2.0 pA). The green trace depicted the devices after molecular connection of the SWCNT leads. These measurements clearly proved that this platform of building single-molecule junctions could be generalized for different molecular wires. Regarding the latter, different reconnection yields for molecular bridges with different sizes could provide useful guidance for controlling specific etching degrees to achieve gaps with the appropriate scales for reconnection. Briefly, these experimental efforts offer a promising way to fabricate true single-molecule devices with high stability and reproducibility, thus setting the foundation for probing the intrinsic properties of the molecular materials. For example, after introducing target molecule **4** into the molecular

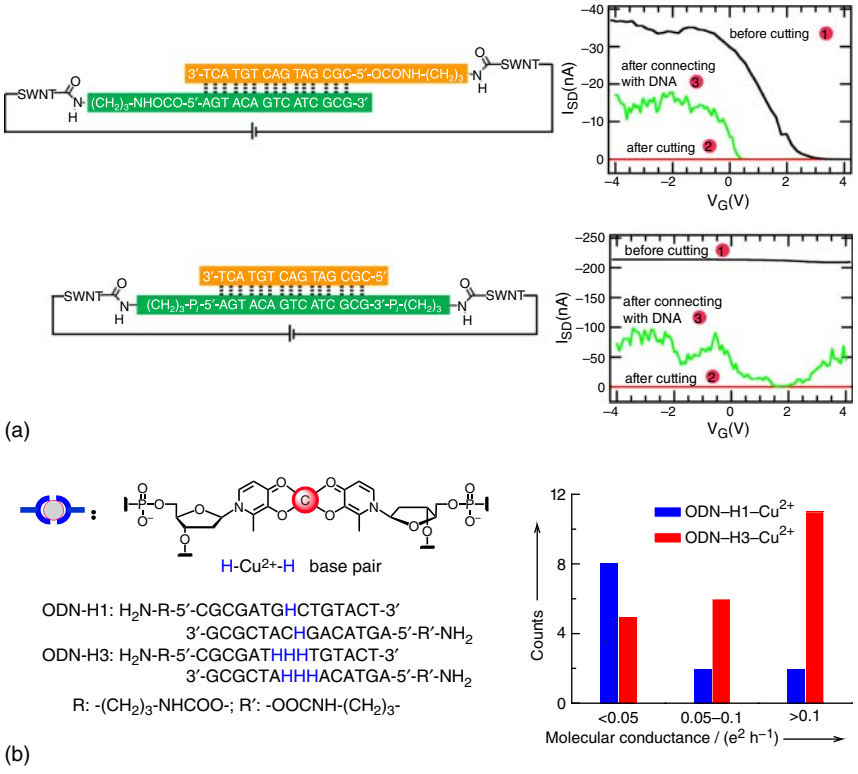

Figure 3.6 DNA conductivity. (a) I_{SD} versus V_G at a constant V_{SD} (50 mV) for a semiconducting SWCNT device (top) and a metallic SWCNT device (bottom) (black curve: 1), after cutting (red curve: 2), and after connecting with the DNA sequence shown (green curve: 3). Source: Guo et al. [19]. Reproduced with permission from Springer Nature. (b) Left: Molecular structure of the Cu^{2+}-mediated base pair based on hydroxypyridone nucleobases (H) and the DNA sequences; right: statistical conductance comparison between ODN–H_1–Cu^{2+} and ODN–H_3–Cu^{2+} duplexes. Source: Reproduced with permission from Liu et al. [20]. Copyright 2011, John Wiley and Sons.

circuits based on the SWCNT electrodes, functional devices that were sensitive to the pH at the single-molecule level were achieved (Figure 3.5c).

Another important example is to explore the electrical conductivity of individual DNA molecules [19, 20]. For a long time, the question of whether DNAs are conductive was controversial [21]. To prove DNA conductivity, Guo et al. developed a general method to integrate DNA strands between SWCNT electrodes and measure their electrical properties (Figure 3.6a) [19]. In this experiment, the DNA sequences were modified with amines on either the 5′ terminus or both the 3′ and 5′ termini and coupled to SWCNT electrodes through amide linkages, thus allowing the electrical properties of the double-stranded DNAs to be measured. It was determined that the well-matched duplex DNA in the gap exhibited an average resistance of approximately 1 MΩ, which resembled the electrical characteristics of the aromatic stacked planes of graphite. In combination with other reports based on metal electrodes [6, 22–24], which

described the charge transport in single DNA molecules as coherent tunneling, incoherent hopping or both, these results provided direct evidence that clarified the DNA conductivity. However, the conductivity of wild DNAs was found to be limited, thus hampering the development of DNA-based nanoelectronics. To improve the DNA conductivity, Guo and coworkers further demonstrated the direct charge transport measurement of individual metallo-DNA duplexes by using single-molecule break junctions (Figure 3.6b) [20]. By comparing the conductance between ODN–H_1–Cu^{2+} and ODN–H_3–Cu^{2+}, it was demonstrated that the ODN–H_3–Cu^{2+} devices tended to exhibit a higher conductance than the ODN–H_1–Cu^{2+} devices. This result may be attributed to the synergistic effect of increased rigidity of the π-stacking and the electronic coupling for hole transfer induced by the metal ions. This study is the first direct experimental support for the hypothesis that the precise arrangement of the metal-mediated base pairs into the DNA scaffolds may improve the insufficient electrical conductance of the DNA duplexes. These findings provide a foundation for DNA-based hybrid materials as conductive biocompatible bridges that may interface electronic circuits with biological systems.

As demonstrated earlier, the SWCNT electrode–molecule single-molecule junctions provide a promising device platform for building true single-molecule devices with high stability. Based on this approach, functional molecular devices have been created to detect molecular conformation transformation, protein/substrate binding, and DNA hybridization at the single-molecule level. More information about its further applications toward functional single-molecule biosensors and switches is provided in Sections 9.5 and 9.7, respectively. However, this approach has challenges stemming primarily from two aspects: the connection yield is relatively low (generally ~5%) and the device-to-device properties vary primarily due to the variability in the properties of the SWCNTs that depend on their chirality and diameter. To solve these issues, it is urgent to develop another efficient strategy to build high-throughput molecular junctions with high reproducibility.

3.2 Graphene-Based Electrodes

Graphene, another typical allotropy of carbon, is a two-dimensional (2D) zero-bandgap semimetal carbon material with extraordinary electronic properties that has received worldwide attention since its discovery by Geim and coworkers in 2004 [2]. Its high mobility and the ease with which it can be doped with either holes or electrons make it suitable as a platform for sensors, electrodes in field-effect transistors, and transparent contacts for photovoltaic devices [25–33]. Particularly, graphene does not have the inherent variability of the SWCNTs and can circumvent the problems that concern the SWCNTs as discussed earlier. Therefore, 2D graphene, compared with one-dimensional SWCNTs, has the capability of largely simplifying the device fabrication process and creating stable molecular devices in high yield, thus potentially providing complementary contacts to test the intrinsic properties of different molecular devices with molecular sizes in all dimensions. In Section 3.2, we focus

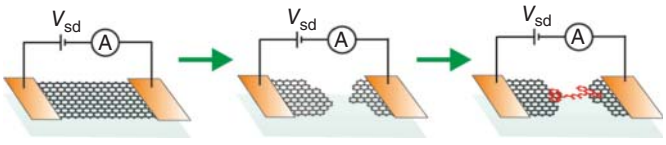

Figure 3.7 Schematic of the feedback-controlled electroburning process and the ideal device configuration. The device was created by assembling molecules terminated with anthracene groups through π–π stacking. Source: Reproduced with permission from Prins et al. [34]. Copyright 2011, American Chemical Society.

on the methodologies developed for fabricating the second class of carbon electrode–molecule single-molecule junction: graphene electrode–molecule single-molecule junctions.

3.2.1 Electroburning

One early example that used graphene electrodes in molecular-scale electronics was reported by Prins et al. [34]. In this study, they used feedback-controlled electroburning to slice a few-layer graphene sheet (Figure 3.7). The gaps have separations of approximately 1–2 nm, as estimated from a Simmons model for tunneling. Then, the devices were created by assembling molecules of interest inside the graphene nanogaps through π–π stacking (Figure 3.7). It was determined that the molecular junctions displayed gateable I–V characteristics at room temperature. However, it is difficult to control the electrode geometry and the resulting gap size due to the use of the electroburning process and the few-layer graphene sheets. Therefore, the development of a reliable approach to fabricate graphene point contacts for creating single-molecule junctions with high stability remains a considerable challenge. Recently, Ullmann et al. not only present a fabrication scheme based on epitaxial graphene nanoelectrodes by employing an electrical breakdown protocol but also identified a suitable molecule (a molecular wire with fullerene anchor groups) to make a reliable graphene point contacts [35]. With these two components, stable electrical characteristics were recorded. Interestingly, electrical measurements show that single-molecule junctions with graphene and with gold electrodes display a striking agreement, which motivated a hypothesis that the differential conductance spectra are rather insensitive to the electrode material.

3.2.2 Dash-Line Lithography

To solve these issues, Guo and coworkers recently developed a new method, known as dash-line lithography (DLL), to create a robust single-molecule electronic device based on indented graphene point electrodes [36]. The key feature of this technique is the ability to produce carboxylic acid-terminated graphene point contact arrays with gaps that are $\leq$10 nm. Briefly, a design AutoCAD®, a software of Autodesk Inc. (CAD) file with a 5 nm-width dash line (A: 150 nm) exposed to an electron beam (e-beam) and separated by B (40 nm) (Figure 3.8a) was designed to open an indented window in a spin-cast layer of PMMA by using

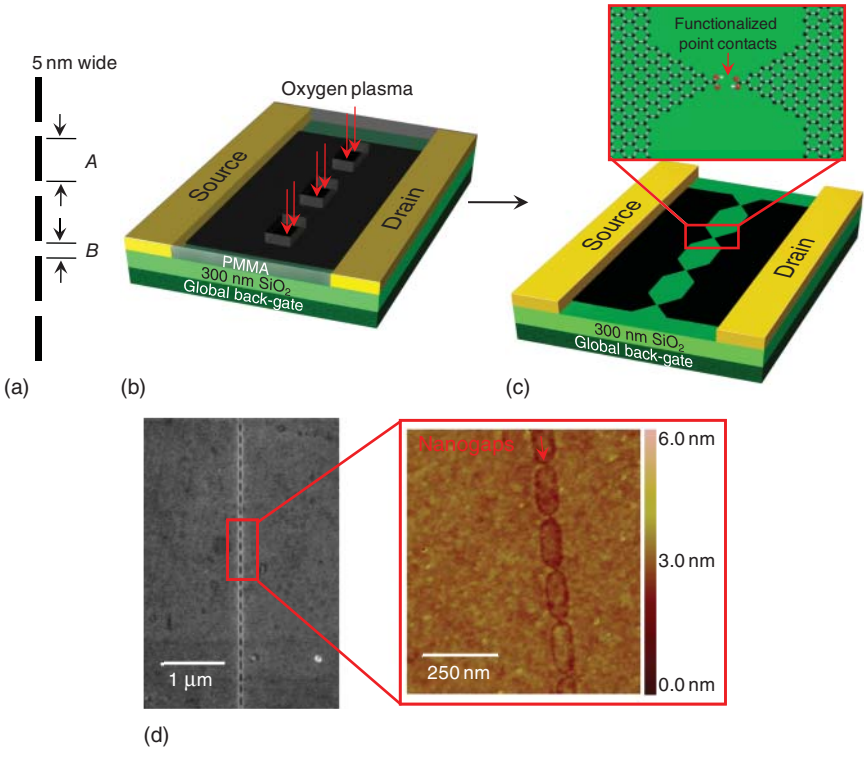

Figure 3.8 Fabrication of indented graphene point contact arrays. (a) A design CAD file with a 5 nm-width dash line (*A*: 150 nm and *B*: 40 nm) used for the cutting process. (b) Precise cutting of the graphene sheets using oxygen plasma through an indented PMMA window defined by the EBL. (c) Indented graphene point contacts formed by oxidative cutting were functionalized by carboxylic acid end groups and separated by as little as a few nanometers. (d) SEM and AFM images of a representative indented graphene point contact array. Source: Reproduced with permission from Cao et al. [36]. Copyright 2012, John Wiley and Sons.

ultrahigh-resolution EBL (Figure 3.8b). The single-layer graphene sheet with high quality was then locally cut through the open window via oxygen plasma ion etching (Figure 3.8c). By exploiting the gradual etching and undercutting of the PMMA, narrow gaps between the indented graphene point contacts arrays were achieved (Figure 3.8d). These point contacts reacted with the conductive molecules derivatized with amines to form stable molecular devices through amide linkages.

Similar to the SWCNT case, the size of these nanogaps can be controlled through the regulation of the etching process. Three different-length molecules (Figure 3.9a) were selected as molecular rulers to characterize the relationship between the cutting yield and the reconnection yield by electrical measurements, as indicated in Figure 3.9b. This characterization helped optimize the device fabrication conditions. Based on the statistical data presented in Figure 3.9b, under optimized conditions, the maximum connection yield for these molecules was determined to be ~50%, which corresponded to the cutting yield of ~28%.

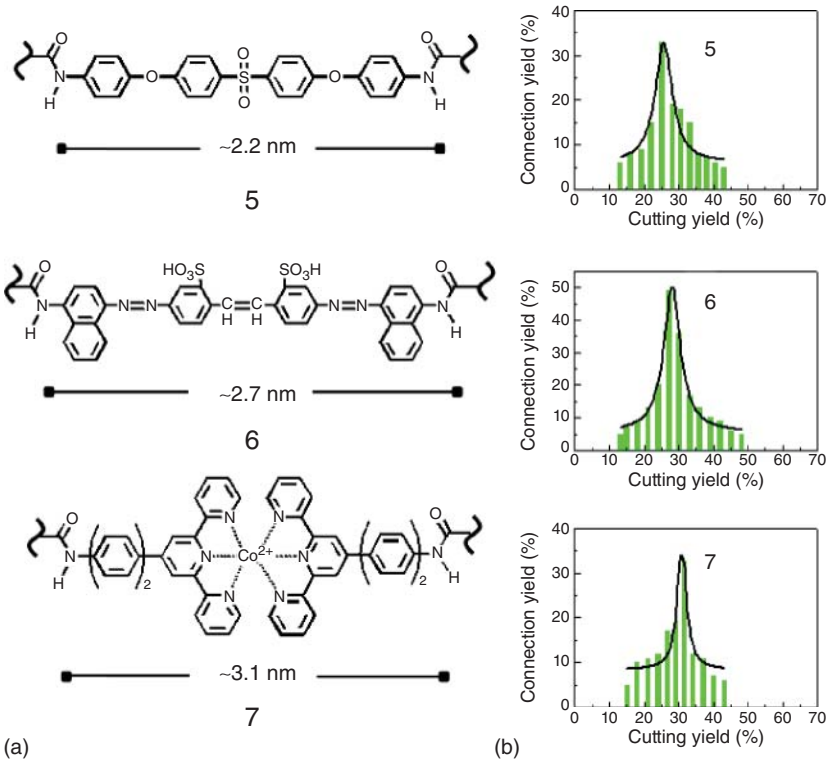

Figure 3.9 Improvement in the device fabrication. (a) Molecular bridges (**5**–**7**) spanning the graphene point electrodes. (b) Statistical data of the connection yields as a function of the cutting yields for each corresponding molecule. The simulated curves are depicted in black. Source: Reproduced with permission from Cao et al. [36]. Copyright 2012, John Wiley and Sons.

This connection value significantly exceeds those of previous studies [37], in which the connection yield was considerably lower when using metal or SWCNT leads. Based on this data, the analysis of the number of junctions that contribute to the charge transport by using the binomial distribution demonstrated that, in most cases, only one or two junctions contributed to the charge transport of the devices [12, 36].

One apparent advantage of this methodology is that the DLL technique largely simplifies the device fabrication process and creates stable molecular devices in high yield. The ease of device fabrication and device stability denotes the graphene-molecule single-molecule junctions as a new-generation testbed for molecular electronics. However, most of the previous studies rely primarily on the *ex situ* synthesis of the molecular wires (e.g. dithiolated molecules) followed by their subsequent insertion into the nanogapped electrodes, thus complicating the systems because of the strong tendency for oxidative oligomerization and aggregation of the molecules. To solve these problems, based on the previously developed method, Guo et al. demonstrated the capability of the *in situ* construction of complex molecular wires through the implementation of a multiple-step

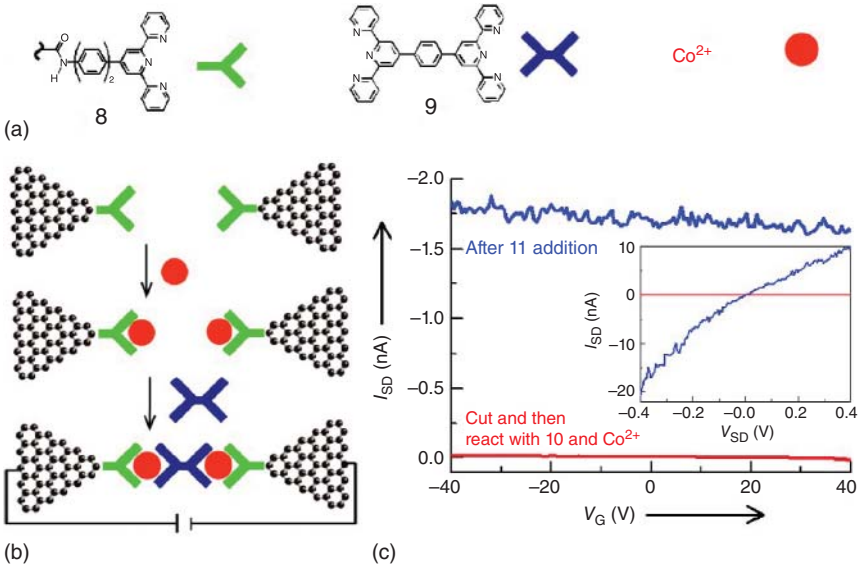

Figure 3.10 *In situ* construction of complex molecular wires. (a) Molecular structures used for device reconnection and specific recognition for Co^{2+}. (b) Schematic strategies for bridging graphene point contacts through a three-step strategy. (c) Device characteristics for the reconnected device through a three-step sequence, $V_{SD} = -50$ mV. Inset depicts I_{SD} versus V_{SD} data for the same device after the reactions with **6** and cobalt ions (red) as well as after the addition of **7** (blue) at the zero gate bias. Source: Reproduced with permission from Cao et al. [55]. Copyright 2013, John Wiley and Sons.

reaction sequence (amide formation and coordination reaction) between the molecular-scale graphene point contacts [38]. For example, a three-step strategy is presented in Figure 3.10. Firstly, the graphene point contacts were primed with a terpyridyl ligand **8** (Figure 3.10a), which only has a single amine group to react with the graphene electrodes; however, it has a tridentate aromatic pocket available for the subsequent coordination chemistry (Figure 3.10b). There was essentially no detectable current (≤100 fA) (red curve in Figure 3.10c). Then, the primed devices were immersed in a diluted methanol solution of cobalt acetate (~10^{-5} M). After the second step of cobalt ion treatment, each of the I–V characteristics of the devices were carefully screened and determined as either reconnected or open. The circuits that were open indicated zero conductance up to the noise limit of the measurement (≤100 fA) (red curve in Figure 3.10c). Each of these devices should contain two cobalt ions, one on each facing end of the nanogap, and each cobalt ion should be available for further coordination. In the third step of this sequence, hexapyridyl **9** (Figure 3.10a) was added (~10^{-5} M in chloroform), and the conductivity of the devices was measured (blue curve in Figure 3.10c). The inset in Figure 3.10c indicates the I_{SD} as a function of the V_{SD} for the same device after sequential reactions with **8** and cobalt ions during cutting (red) and after the further addition of **9** (blue). The connection yield for this three-step strategy was ~9%. In addition to the *in situ* construction of the molecular junctions, the researchers also achieved reversible switching

between distinct conductance states when an azobenzene molecule (molecule **6** in Figure 3.9) was either illuminated by lights with different wavelengths or exposed to different pH values, thus providing the possibility of integrating multiple functionalities into a single molecular device [38]. Collectively, these results demonstrated the capability of installing molecular functionalities into electronic devices in a new platform of DLL-generated graphene–molecule junctions. Additional details on this topic can be found in Section 9.7.

3.3 Other Carbon-Based Electrodes

As discussed in detail in Chapter 2, molecular junctions based on the metal–molecule–metal architectures provide useful insights into the charge transport at the molecular level, thus leading to a better understanding of the underlying fundamental principles of molecular-scale electronics. However, nanoscale metal electrodes are mechanically unstable due to the high atomic mobility of the metal atoms. Furthermore, most of the metal electrodes (except Au) can be oxidized easily under atmosphere conditions. Additionally, the typical electrode density of the states near the Fermi energy is nearly energy independent, which will hamper their further applications because metal-based molecular junctions generally have smooth and featureless transmission probabilities near the Fermi energy. Carbon-based electrodes, such as graphite, have a remarkable mechanical strength as well as a variable highly dispersive density of states near its Fermi energy [39] and strong non-covalent interactions through the van der Waals-based $\pi-\pi$ stacking [16, 34, 40]. This result implies that these materials can be used to create molecular junctions by combining metal with the carbon electrodes. Recently, Kim et al. [41] demonstrated the formation of molecular junctions by using the scanning tunneling microscopy (STM)

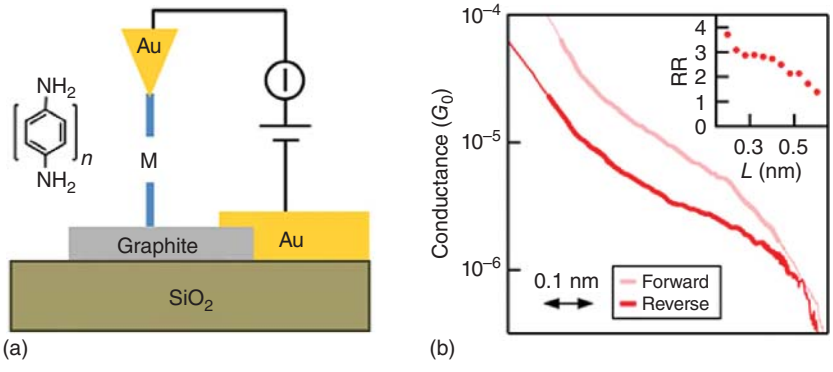

Figure 3.11 Schematic and rectification data for graphite/molecule/Au junctions. (a) Schematic of the junctions and the molecular structure. (b) Conductance profiles determined from 2D conductance-displacement histograms for the junctions measured under forward and reverse-bias conditions. The inset depicts the rectification ratio as a function of displacement for these junctions. Source: Reproduced with permission from Kim et al. [41]. Copyright 2014, PNAS.

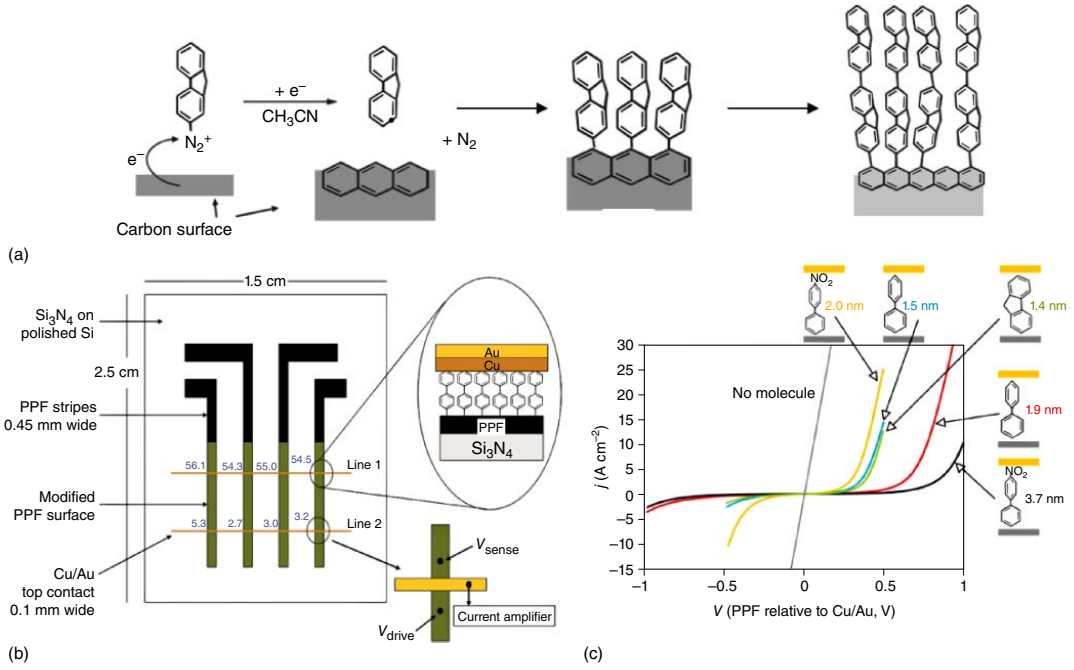

Figure 3.12 PPF/molecule/metal structures. (a) Surface modification by reducing a diazonium reagent. (b) Schematic of PPF/molecule/Cu/Au molecular junctions. (c) Overlay of *J*–*V* curves for molecular junctions fabricated from diazonium-derived adlayers at carbon (PPF). Source: Reproduced with permission from Anariba et al. [49]. Copyright 2005, ACS Publications.

technique, where an Au metal tip and a microfabricated graphite substrate were used as the two electrodes (Figure 3.11a). One remarkable feature of this junction is that the mechanical strength of the graphite and the single-crystal properties of their substrates allowed measurements to be taken over a few thousands of junctions without any change in the surface properties. The conductance of a series of graphite/amine-terminated oligophenyl/Au molecular junctions was measured, and it was determined that the conductance decayed exponentially with the molecular backbone length, which is consistent with a decay constant observed in the same measurements with two Au electrodes. Interestingly, despite the inherent symmetry of the oligophenylamines, rectification was observed in these junctions (Figure 3.11b). This observation occurred because the highly energy-dependent graphite density of the states contributes variations to the transmission that, when coupled with an asymmetric voltage drop across the junction, leads to the rectifying effect. These results indicate the possibility of creating hybrid molecular-scale devices with purposefully designed functionalities by using layered 2D materials.

The McCreery group developed a carbon fabrication technique for electronics applications with the pyrolysis of photoresist polymers to form "pyrolyzed photoresist films" (PPFs) [42–46]. The stability of the method used to anchor the molecular layer to the large substrate is essential for making the top contact in fabricating the molecular junction. For the case of C—C surface bonds, bonded layers have been shown to be stable on sp^2-hybridized graphitic carbon to >500 °C in ultrahigh vacuum (UHV) [47, 48]. The fabrication process for surface modification by reducing a diazonium reagent was utilized initially for making carbon interdigitated electrodes by pyrolysis of lithographic structures made from commercial photoresist used in the microelectronics industry (Figure 3.12a). This process results in a flat (<0.5 nm RMS by atomic force microscopy [AFM]), irreversible carbon surface with high coverage and sparse pinholes mainly composed of sp^2 bond. PPF has been used to make a variety of carbon nanostructures, of which many have been used for electrochemistry [50]. Furthermore, they integrated the PPF/molecule/metal structure into electrical circuits (Figure 3.12b) with different molecules sandwiched inside and systematically invested their J/V characteristics (Figure 3.12c). For wide applications, recently, they developed audio distortion circuit [51] and photovoltaic devices [52–54].

References

1 Dai, H. (2002). Carbon nanotubes: Synthesis, integration, and properties. *Acc. Chem. Res.* 35: 1035–1044.

2 Novoselov, K.S., Geim, A.K., Morozov, S.V. et al. (2004). Electric field effect in atomically thin carbon films. *Science* 306: 666–669.

3 (2013). The molecular electronics special issue. *Nat. Nanotechnol.* 8: 377–467.

4 Iijima, S. (1991). Helical microtubules of graphitic carbon. *Nature* 354: 56–58.

5 Ajayan, P.M. and Ebbesen, T.W. (1997). Nanometre-size tubes of carbon. *Rep. Prog. Phys.* 60: 1025–1044.

6 Roy, S., Vedala, H., Roy, A.D. et al. (2008). Direct electrical measurements on single-molecule genomic DNA using single-walled carbon nanotubes. *Nano Lett.* 8: 26–30.

7 Collins, P.G., Arnold, M.S., and Avouris, P. (2001). Engineering carbon nanotubes and nanotube circuits using electrical breakdown. *Science* 292: 706–709.

8 Collins, P.G., Hersam, M., Arnold, M. et al. (2001). Current saturation and electrical breakdown in multiwalled carbon nanotubes. *Phys. Rev. Lett.* 86: 3128.

9 Qi, P., Javey, A., Rolandi, M. et al. (2004). Miniature organic transistors with carbon nanotubes as quasi-one-dimensional electrodes. *J. Am. Chem. Soc.* 126: 11774–11775.

10 Tsukagoshi, K., Yagi, I., and Aoyagi, Y. (2004). Pentacene nanotransistor with carbon nanotube electrodes. *Appl. Phys. Lett.* 85: 1021–1023.

11 Yagi, I., Tsukagoshi, K., Watanabe, E. et al. (2004). Carbon nanotubes with a nanogap for nanoscale organic devices. *Microelectron. Eng.* 73: 675–678.

12 Feldman, A.K., Steigerwald, M.L., and Guo, X. (2008). Molecular electronic devices based on single-walled carbon nanotube electrodes. *Acc. Chem. Res.* 41: 1731–1741.

13 Cao, Y., Steigerwald, M.L., Nuckolls, C. et al. (2011). Current trends in shrinking the channel length of organic transistors down to the nanoscale. *Adv. Mater.* 22: 20–32.

14 Guo, X., Xiao, S., Myers, M. et al. (2009). Photoresponsive nanoscale columnar transistors. *Proc. Natl. Acad. Sci. U. S. A.* 106: 691–696.

15 Liu, S., Wei, Z., Cao, Y. et al. (2011). Ultrasensitive water-processed monolayer photodetectors. *Chem. Sci.* 2: 796–802.

16 Marquardt, C.W., Grunder, S., Baszczyk, A. et al. (2010). Electroluminescence from a single nanotube-molecule-nanotube junction. *Nat. Nanotechnol.* 5: 863–867.

17 Wei, D., Liu, Y., Cao, L. et al. (2008). Real time and *in situ* control of the gap size of nanoelectrodes for molecular devices. *Nano Lett.* 8: 1625–1630.

18 Guo, X., Small, J.P., Klare, J.E. et al. (2006). Covalently bridging gaps in single-walled carbon nanotubes with conducting molecules. *Science* 311: 356–359.

19 Guo, X., Gorodetsky, A.A., Hone, J. et al. (2008). Conductivity of a single DNA duplex bridging a carbon nanotube gap. *Nat. Nanotechnol.* 3: 163–167.

20 Liu, S., Clever, G.H., Takezawa, Y. et al. (2011). Direct conductance measurement of individual metallo-DNA duplexes within single-molecule break junctions. *Angew. Chem. Int. Ed.* 50: 8762–8762.

21 Genereux, J.C. and Barton, J.K. (2010). Mechanisms for DNA charge transport. *Chem. Rev.* 110: 1642–1662.

22 Xu, B.Q., Zhang, P.M., Li, X.L. et al. (2004). Direct conductance measurement of single DNA molecules in aqueous solution. *Nano Lett.* 4: 1105–1108.

23 Xiang, L., Palma, J.L., Bruot, C. et al. (2015). Intermediate tunnelling–hopping regime in DNA charge transport. *Nat. Chem.* 7: 221–226.

24 Liu, S.P., Weisbrod, S.H., Tang, Z. et al. (2010). Direct measurement of electrical transport through G-quadruplex DNA with mechanically controllable break junction electrodes. *Angew. Chem. Int. Ed.* 49: 3313–3316.

25 Wan, X., Huang, Y., and Chen, Y. (2012). Focusing on energy and optoelectronic applications: A journey for graphene and graphene oxide at large scale. *Acc. Chem. Res.* 45: 598–607.

26 Yang, W., Ratinac, K.R., Ringer, S.P. et al. (2010). Carbon nanomaterials in biosensors: Should you use nanotubes or graphene? *Angew. Chem. Int. Ed.* 49: 2114–2138.

27 Liu, S. and Guo, X. (2012). Carbon nanomaterials field-effect-transistor-based biosensors. *NPG Asia Mater.* 4: e23.

28 Cao, Y., Liu, S., Shen, Q. et al. (2009). High-performance photoresponsive organic nanotransistors with single-layer graphenes as two-dimensional electrodes. *Adv. Funct. Mater.* 19: 2743–2748.

29 Cao, Y., Wei, Z., Liu, S. et al. (2010). High-performance Langmuir–Blodgett monolayer transistors with high responsivity. *Angew. Chem. Int. Ed.* 49: 6319–6323.

30 Liu, W., Jackson, B.L., Zhu, J. et al. (2010). Large scale pattern graphene electrode for high performance in transparent organic single crystal field-effect transistors. *ACS Nano* 4: 3927–3932.

31 Di, C.-a., Wei, D., Yu, G. et al. (2008). Patterned graphene as source/drain electrodes for bottom-contact organic field-effect transistors. *Adv. Mater.* 20: 3289–3293.

32 Lee, W.H., Park, J., Sim, S.H. et al. (2011). Surface-directed molecular assembly of pentacene on monolayer graphene for high-performance organic transistors. *J. Am. Chem. Soc.* 133: 4447–4454.

33 Tsutsui, M. and Taniguchi, M. (2012). Single molecule electronics and devices. *Sensors* 12: 7259–7298.

34 Prins, F., Barreiro, A., Ruitenberg, J.W. et al. (2011). Room-temperature gating of molecular junctions using few-layer graphene nanogap electrodes. *Nano Lett.* 11: 4607–4611.

35 Ullmann, K., Coto, P.B., Leitherer, S. et al. (2015). Single-molecule junctions with epitaxial graphene nanoelectrodes. *Nano Lett.* 15: 3512–3518.

36 Cao, Y., Dong, S., Liu, S. et al. (2012). Building high-throughput molecular junctions using indented graphene point contacts. *Angew. Chem. Int. Ed.* 51: 12228–12232.

37 Li, T., Hu, W.P., and Zhu, D.B. (2012). Nanogap electrodes. *Adv. Mater.* 22: 286–300.

38 Jia, C., Li, H., Jiang, J. et al. (2013). Interface-engineered bistable [2]rotaxane-graphene hybrids with logic capabilities. *Adv. Mater.* 25: 6752–6259.

39 Ahmed, T., Kilina, S., Das, T. et al. (2012). Electronic fingerprints of DNA bases on graphene. *Nano Lett.* 12: 927–931.

40 Seo, S., Min, M., Lee, S.M. et al. (2013). Photo-switchable molecular monolayer anchored between highly transparent and flexible graphene electrodes. *Nat. Commun.* 4: 1920.

41 Kim, T., Liu, Z.-F., Lee, C. et al. (2014). Charge transport and rectification in molecular junctions formed with carbon-based electrodes. *Proc. Natl. Acad. Sci. U. S. A.* 111: 10928–10932.

42 Kostecki, R., Song, X., and Kinoshita, K. (1999). Electrochemical analysis of carbon interdigitated microelectrodes. *Electrochem. Solid-State Lett.* 2: 465–467.

43 Kostecki, R., Song, X.Y., and Kinoshita, K. (2000). Influence of geometry on the electrochemical response of carbon interdigitated microelectrodes. *J. Electrochem. Soc.* 147: 1878–1881.

44 Ranganathan, S., Mccreery, R., Majji, S.M. et al. (2000, 2000). Photoresist-derived carbon for microelectromechanical systems and electrochemical applications. *J. Electrochem. Soc.* 147: 277–282.

45 Ranganathan, S. and McCreery, R.L. (2001). Electroanalytical performance of carbon films with near-atomic flatness. *Anal. Chem.* 73: 893–900.

46 Bergren, A.J., Harris, K.D., Deng, F. et al. (2008). Molecular electronics using diazonium-derived adlayers on carbon with Cu top contacts: critical analysis of metal oxides and filaments. *J. Phys.: Condens. Matter* 20: 374117.

47 McCreery, R.L., Wu, J., and Kalakodimi, R.P. (2006). Electron transport and redox reactions in carbon-based molecular electronic junctions. *Phys. Chem. Chem. Phys.* 8: 2572–2590.

48 Allongue, P., Delamar, M., and Desbat, B. (1997). Covalent modification of carbon surfaces by aryl radicals generated from the electrochemical reduction of diazonium salts. *J. Am. Chem. Soc.* 119: 201–207.

49 Anariba, F., Steach, J.K., and McCreery, R.L. (2005). Strong effects of molecular structure on electron transport in carbon/molecule/copper electronic junctions. *J. Phys. Chem. B* 109: 11163–11172.

50 McCreery, R., Bergren, A., Morteza-Najarian, A. et al. (2014). Electron transport in all-carbon molecular electronic devices. *Faraday Discuss.* 172: 9–25.

51 Bergren, A.J., Zeer-Wanklyn, L., Semple, M. et al. (2016). Musical molecules: The molecular junction as an active component in audio distortion circuits. *J. Phys.: Condens. Matter* 28: 094011.

52 Ivashenko, O., Bergren, A.J., and McCreery, R.L. (2016). Light emission as a probe of energy losses in molecular junctions. *J. Am. Chem. Soc.* 138: 722–725.

53 Ivashenko, O., Bergren, A.J., and McCreery, R.L. (2016). Monitoring of energy conservation and losses in molecular junctions through characterization of light emission. *Adv. Electron. Mater.* 2: 1600351.

54 Greig, S., Morteza-Najarian, A., McCreery, R. et al. (2016). Surface plasmon driven lowering of the electron emission order in a carbon/gold bilayer film. *Appl. Phys. Lett.* 109: 221104.

55 Cao, Y., Dong, S., Liu, S., et al. (2013). Toward functional molecular devices based on graphene–molecule junctions. *Angew. Chem. Int. Ed*. 52: 3906–3910.

4

Other Electrodes for Molecular Electronics

Generally, materials used as electrodes in molecular junctions should have superior properties in four aspects. (i) The first premise is good electrical conductivity, which can maintain its high value with dimension scale down. (ii) The second is the stability of the material composition and configuration, which is of great importance for resisting external perturbation/oxidation and ensuring the success of forming molecular junctions. (iii) The third is the abundant availability by using either bottom-up or top-down approaches. (iv) Lastly, the fourth is the ease of material processing, which should be compatible with industrial micro/nanofabrication techniques. Based on these considerations, the past two decades have witnessed a large variety of materials being used in molecular electronics, ranging from conventional noble metals to novel carbon allotropies, which continuously and creatively update the paradigms for device architecture and operation. In addition to the materials mentioned earlier, there were also other attempts to expand the research regimes of molecular electronics, including silicon and polymer-based nanoelectrode systems, as discussed in the following section.

4.1 Silicon-Based Electrodes

It is well known that silicon materials led to the prosperity of the modern microelectronics industry because of their nearly perfect fitness for complementary metal oxide semiconductor (CMOS) technology, such as controllable conductivity and tunable Fermi level by doping [1]. Physically, the work function of silicon can be varied by changing the doping, type, and density without changing the interface structure and chemical binding, which will facilitate the interfacial energy level alignment [2]. Chemically, the incorporation of the organic molecule onto silicon is directional and stable, which is different from the case of thiols incorporated on Au. In the case of the Au—S bonds, the thiolates can move easily from one Au site to another at room temperature, even without applying a voltage, because the energy barrier between the two chemisorbed modes on Au (the corrugation energy) is approximately 2.5 kcal mol^{-1} (~0.11 eV mol^{-1}). Conversely, the corrugation energy is ~4 eV for Si—C and ~4.7 eV for Si—O—C in the downside of the stable binding to Si, whereas the upside is more robust

Molecular-Scale Electronics: Concept, Fabrication and Applications,
First Edition. Xuefeng Guo, Dong Xiang, and Yu Li.

against substrate oxidation to withstand heating and other harsh conditions. In fact, among the other binding chemistries, only the C—C bonding to graphite is comparable with the Si—C or Si—O—C binding modes [3]. Additionally, the currently developed micro-/nano-processing techniques are established for silicon materials. Collectively, silicon materials have clear advantages when used as efficient electrodes for molecular junctions.

Currently, molecular devices based on silicon electrodes use a fabrication process that first completes the construction of the contact structure and then the molecular connection. This approach is designed for avoiding two troublesome issues: (i) perturbations stemming from high temperatures and solvents used during conventional silicon processing after molecule deposition; and (ii) short-circuit effects resulting from the process of depositing metal electrodes on the self-assembled monolayers (SAMs) of molecules previously grafted on the silicon surface [4]. Based on these considerations, the combination of classical photolithographic techniques and selective etching methods, including wet and dry etching, is used to fabricate silicon-based electrodes [5]. For molecular bridging, the ever-developing silicon-related chemistry provides a large abundance of approaches to form the relatively robust electrode–molecule interface, which can be exemplified by the developed photo-assisted reactions to construct the Si—O—C [6] or direct Si—C [7] linkages. By using these methods, several prototypes of molecular devices based on silicon electrodes have been developed. Berg et al. [8] manufactured a series of silicon nanogaps with a gap size ranging from 3 to 7 nm by partly removing the silicon dioxide insulator from a silicon–oxide–silicon material stack with a selective oxide etchant. Dirk et al. [5] detailed a simple four-step procedure to create a one-dimensional nanogap on a buried oxide substrate that relied on conventional photolithography and metal evaporation. The feasibility of forming molecular circuits by using these nanogaps was further verified by electrical measurements of the 1,8-octanedithiol and 5 nm Au nanoparticles after attachment. This approach was further extended by Howell et al. [9] through a self-assembling approach based on the reaction of silicon with a diazonium salt.

A challenging issue in molecular electronics is the difficulty in identifying the number of molecules spanning the junction due to the naturally bulky dimension of the electrodes. To solve this problem, a study established in 2010 by Ashwell et al. appeared to introduce this particular consideration [10]. The construction of molecular silicon electrodes with a vertical architecture was reported (Figure 4.1a). Briefly, a highly doped n-type Si (111) bottom electrode and a polycrystalline Si top, which were separated with a V-shape gap of ~7 nm (Figure 4.1b), were fabricated by using programmable CMOS processing and chemical etching. Then, the molecular bridge was achieved by the *in situ* synthesis of conjugated wires within the nanogaps. In this study, 4-ethynylbenzaldehyde, which has been covalently grafted to the Si electrodes by a simple thermally activated addition reaction, was used as a molecular bridge to connect the targeted molecules terminated with amines, thus forming the sandwich structure (Figure 4.1a). Therefore, the molecule–electrode interface is robust due to the Si—C covalent bond connection, consequently ensuring the charge transport (Figure 4.1c). In the following study [11], the authors further

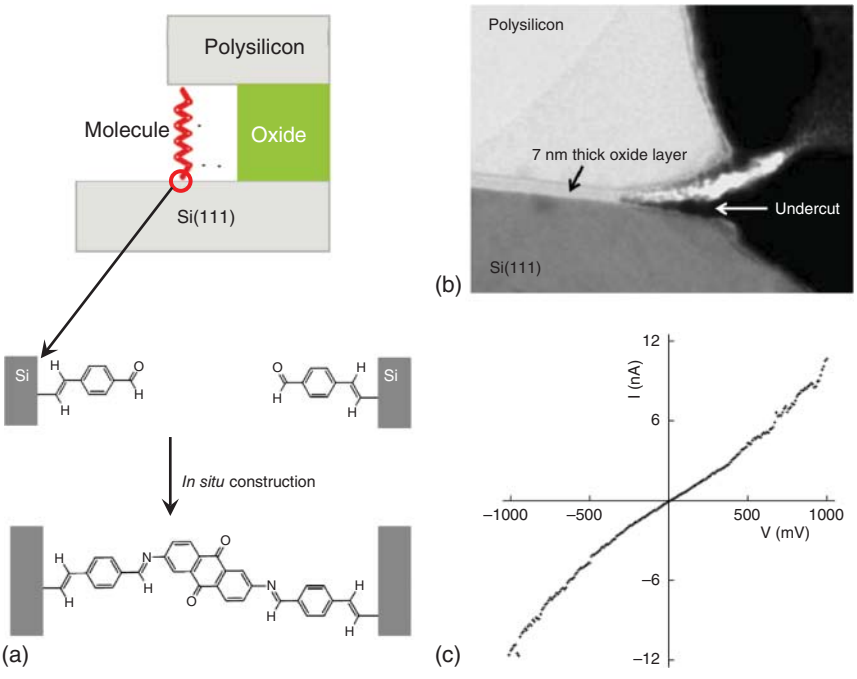

Figure 4.1 Molecular devices based on silicon electrodes. (a) Schematic representation of single-molecule junctions between the silicon electrodes. Inset: chemical method for *in situ* construction of the interfacial connection by grafting 4-ethynylbenzaldehyde, Si—CH=CH—C_6H_4—CHO to activate the surfaces and then coupling with molecules with amine end groups; (b) transmission electron microscope (TEM) cross section of the V-shaped electrode gap obtained by undercutting the gate oxide layer. (c) *I–V* characteristics of the silicon nanogap-bridged devices achieved by following the grafting reaction for five minutes in a solution of the amino-terminated linker, which may ensure the linkage of few or even single molecules. Source: Reproduced with permission from Ashwell et al. [10]. Copyright 2010, American Chemical Society.

reduced the scale of the molecular junctions to a span of ~2.8 nm with the featured device characteristics. It should be noted that the nanogaps between the silicon electrodes are likely to reconnect a large number of molecules. Importantly, a deliberate mismatch between the molecule length and the nanogap scale, in combination with different *in situ* assembling times, was introduced to limit the number of bridges, thus constructing few- or single-molecule devices. By using this testbed, the transport properties of two types of molecular wires (oligofluorenes and anthraquinone) were measured.

For the initial exploration of silicon materials used in molecular electronics, this approach is significant for scaling the mature silicon system to a molecular scale. However, to generalize this method, certain challenges remain. Firstly, although the CMOS processing techniques have a high degree of professional proficiency, the construction of these types of molecular electronics platforms is still complex, especially for commercial applications. Secondly, the chemical stability and the electrical conductance of the silicon electrodes are not suitable

to provide molecular devices with high performance and stiffness against harsh environments. Thirdly, it is difficult to determine the number of molecular bridges in the molecular junctions. Therefore, there are numerous issues in the system that need to be further studied.

4.2 Polymer-Based Electrodes

Despite the significant achievements mentioned earlier, it is still difficult to fabricate a practical single-molecule integrated circuit. One of the reasons is the lack of viable methods for wiring each functional molecule: how to create conductive nanowires at the designated positions, and how to ensure chemical bonding between the nanowires and the functional molecules. One possible solution is to integrate each molecule into the electrical circuits with atomic precision. Recently, a novel method known as "chemical soldering" was reported in 2011 by Yuji Okawa et al. [12], in which they connected a single functional molecule with a single conductive polymer nanowire via covalent bonds. Briefly, functional phthalocyanine (Pc) molecules were placed on an SAM of diacetylene compounds (Figure 4.2a). A scanning tunneling microscope (STM) probe tip was then positioned on the molecular row of the diacetylene compound and then stimulated its chain polymerization to form conductive polydiacetylene (PDA) nanowires (Figure 4.2b,c). Because the front edge of the chain polymerization had a reactive chemical species, the resulted polymer nanowire reacted with an encountered phthalocyanine molecule and formed a connection through chemical bonding. By using this approach, a resonant tunneling diode stemming from a single phthalocyanine molecule bridging two conductive polymer nanowires (Figure 4.2c, bottom) was demonstrated.

The integration of using new materials as efficient electrodes in molecular electrical circuits remains an active and challenging area of research because it

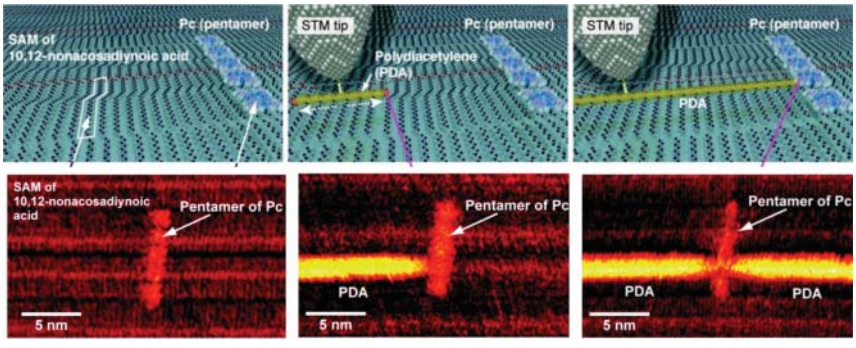

Figure 4.2 Schematic images of chemical soldering. (a) Top: illustration of a Pc pentamer adsorbed to an SAM of 10,12-nonacosadiynoic acid; bottom: corresponding STM image. (b) Top: chain polymerization initiated by an STM tip; bottom: STM image obtained after initiating chain polymerization. The fabricated PDA chain, which is seen as a bright line, is connected to a Pc molecule. (c) Top: polymer chain reached the adsorbed molecule and a spontaneous chemical bond formation occurred; bottom: STM image depicting two PDA chains connected to a single Pc molecule. Source: Reproduced with permission from Okawa et al. [12]. Copyright 2011, American Chemical Society.

can offer a wealth of opportunities to construct robust interfacial connections, tune energy level alignments, and establish novel device architectures. It is of crucial importance to solve the critical issue of the electrode–molecule contact interface and develop true single-molecule circuits for the next generation of electronics with higher efficiencies and lower power dissipations. Specifically, the introduction of using semiconductors, such as silicon and low-dimensional nanomaterials, as nanoscale electrodes presents significant physical, chemical, and technological advantages, and the development of conductive polymer-based electrodes holds great potential for all-synthesized molecular electronic circuits, thus leading to new branches in molecular electronics.

References

1 Buriak, J.M. (2002). Organometallic chemistry on silicon and germanium surfaces. *Chem. Rev.* 102: 1271–1308.
2 Salomon, A., Boecking, T., Seitz, O. et al. (2007). What is the barrier for tunneling through alkyl monolayers? Results from n- and p-Si–alkyl/Hg junctions. *Adv. Mater.* 19: 445–450.
3 Cahen, D. and Kahn, A. (2003). Electron energetics at surfaces and interfaces: Concepts and experiments. *Adv. Mater.* 15: 271–277.
4 Adam Johan, B., Kenneth, D.H., Fengjun, D. et al. (2008). Molecular electronics using diazonium-derived adlayers on carbon with Cu top contacts: Critical analysis of metal oxides and filaments. *J. Phys.: Condens. Matter* 20: 374117.
5 Dirk, S.M., Howell, S.W., Zmuda, S. et al. (2005). Novel one-dimensional nanogap created with standard optical lithography and evaporation procedures. *Nanotechnology* 16: 1983–1985.
6 Miramond, C. and Vuillaume, D. (2004). 1-Octadecene monolayers on Si(111) hydrogen-terminated surfaces: Effect of substrate doping. *J. Appl. Phys.* 96: 1529–1536.
7 Sieval, A.B., Demirel, A.L., Nissink, J.W.M. et al. (1998). Highly stable Si–C linked functionalized monolayers on the silicon (100) surface. *Langmuir* 14: 1759–1768.
8 Berg, J., Che, F., Lundgren, P. et al. (2005). Electrical properties of Si–SiO_2–Si nanogaps. *Nanotechnology* 16: 2197–2202.
9 Howell, S.W., Dirk, S.M., Childs, K. et al. (2005). Mass-fabricated one-dimensional silicon nanogaps for hybrid organic/nanoparticle arrays. *Nanotechnology* 16: 754–758.
10 Ashwell, G.J., Phillips, L.J., Robinson, B.J. et al. (2010). Molecular bridging of silicon nanogaps. *ACS Nano* 4: 7401–7406.
11 Ashwell, G.J., Phillips, L.J., Robinson, B.J. et al. (2011). Synthesis of covalently linked molecular bridges between silicon electrodes in CMOS-based arrays of vertical Si/SiO_2/Si nanogaps. *Angew. Chem. Int. Ed.* 50: 8722–8233.
12 Okawa, Y., Mandal, S.K., Hu, C. et al. (2011). Chemical wiring and soldering toward all-molecule electronic circuitry. *J. Am. Chem. Soc.* 133: 8227–8233.

5

Novel Phenomena in Single-Molecule Junctions

In the past few decades, various techniques for preparing nanogapped electrodes have emerged, which has promoted the rapid development of single-molecule electronics from both experimental and theoretical aspects. In order to study the intrinsic quantum phenomena and achieve the required functions, it is important to fully understand the charge transport characteristics of single-molecule devices. Because charge transport in a single-molecule junction is essentially a quantum domain, molecular electronics offers unique opportunities to discover fundamental physical phenomena and directly observe effects that are not available in traditional methodological studies. These effects include quantum interference (QI) [1–3], the Coulomb blockade [4], the Kondo effect [4, 5], and so on. Furthermore, devices with various remarkable functionalities, for example, molecular thermoelectric devices [6, 7] and molecular spintronic devices [8, 9], have been realized recently.

5.1 Quantum Interference

The goal of single-molecule electronics is to make transformative and viable electronic devices happen. In a pure electronic picture, QI is a built-in property of many molecules commonly used in molecular junctions. QI arises due to the wave nature of the electrons when the device length scale becomes comparable with the electronic phase coherence length. QI effect occurs if partial electron waves propagating through the two branches of a molecular junction interfere with each other. The conductance is suppressed or enhanced, while electron waves interfere with each other destructively or constructively. Essentially, QI effect provides new insights and methods toward controlling charge transport at the level of the wave function through chemical design, potential, and electrical control.

5.1.1 Prediction of QI Effects

There are several methods to judge if QI will occur in electron transport through molecular junctions. Latha and coworkers proposed an "atom-counting" approach to forecast destructive QI in cyclic and acyclic π-conjugated

Molecular-Scale Electronics: Concept, Fabrication and Applications,
First Edition. Xuefeng Guo, Dong Xiang, and Yu Li.

molecules [10]. By arrow pushing in π-conjugated resonance forms, QI can be simply predicted with a pen and a paper. Firstly, draw the chemical structure of the molecular bridge with Au atoms attached to each linker atom. Secondly, try to draw a reasonable resonance structure that delocalizes one Linker–Au bond onto the other Au atom by using arrow-pushing formalisms. If it is possible to draw a resonance structure where there is a positive charge on one Au atom and a negative charge on the other Au atom, QI should not occur. Finally, if there are no resonance structures that can be drawn, which meets the criteria in the second step, the molecule should demonstrate destructive QI.

Despite the ease and the speed of this pen-and-paper approach, it can only be used to predict QI in π-conducting systems. In addition, it also cannot be used to quantitatively predict the conductance value or the position of the anti-resonance peak. To overcome these issues, Lambert et al. summarized a magic ratio rule (MRR) that is determined by QI within the core of polycyclic aromatic hydrocarbons (PAHs). The conductance ratios of molecules with the same core are equal to the square of the ratio of their magic numbers [11]. The MRR provides a useful starting point for chemists to design appropriate molecules for molecular electronics with desired functions.

However, if scientists want to probe quantum effect qualitatively, both the Huckel and density functional theory calculations on model systems should be used. Scientists start with the calculation between transmission $T(E)$ and energy to make the resonances related to the position of the molecular orbitals of the isolated molecule [12]. The transmission coefficient $T(E)$ yields electrical conductance according to the Landauer formula [1], a new current–voltage relationship, and novel thermoelectrical properties can be explored. In these cases, destructive interference is evident for sharp dips in the transmission on a logarithmic scale. By calculating the transmission probability of non-equilibrium Green's function, they can visualize the relation between the key electronic parameters and the positions of normal resonant peaks and anti-resonant peaks induced by QI in the conductance spectrum [13].

5.1.2 Signature of Quantum Interference

The single-molecule electronics community has focused its attention mostly on destructive QI, which is characterized by a sharp dip or an "anti-resonance" in the transmission probability calculations or in differential conductance experiments. Among the community, Sence Jan van der Molen and coworkers found the direct evidence of QI by critically analyzing the $T(E)$ transmission dip theoretically and $\mathrm{d}I/\mathrm{d}V$ versus potential plots experimentally [14]. By comparing the $T(E_F)$ values between 2,6-Bis[(4-acetylthiophenyl)ethynyl]anthracene (AC-DT) and 2,6-Bis[(4-acetylthiophenyl)ethynyl]-9,10-anthraquinone (AQ-DT) and with the transformation of the frontier molecular orbitals into an equivalent set of maximally localized molecular orbitals (LMOs), it is theoretically clear that an electron with energy E lying inside the highest occupied molecular orbital–lowest unoccupied molecular orbital (HOMO–LUMO) gap can traverse the molecule by means of two distinct paths: directly from the left to the right LMO (Figure 5.1a), or via the energetically higher LMO (Figure 5.1c). For

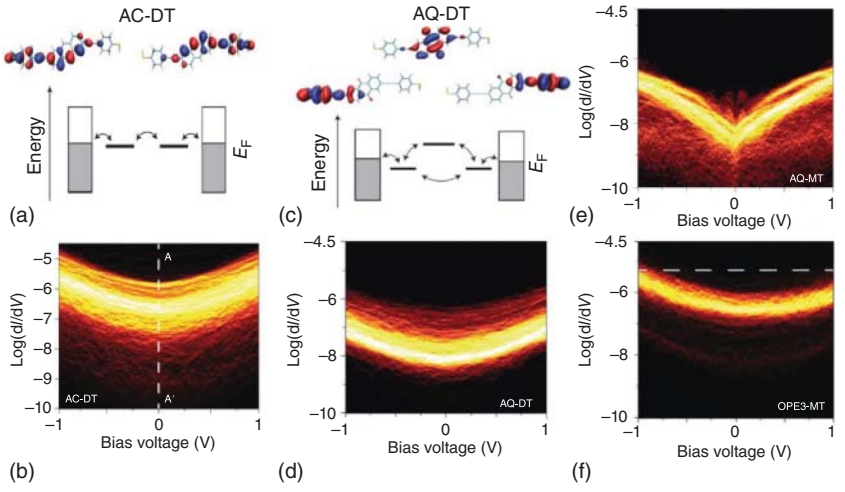

Figure 5.1 Signature of quantum interference. (a, c) Schematic transport models derived from the localized molecular orbitals presented in the upper parts (a: AC-DT; c: AQ-DT). (b, d) Logarithmically binned two-dimensional histogram for d*I*/d*V* values versus bias voltage *V* for AC-DT and AQ-DT (in Ω^{-1}). (e, f) Logarithmically binned two-dimensional histograms of d*I*/d*V* (in Ω^{-1}) versus bias voltage *V* for AQ-MT (e), and OPE3-MT (f). Source: Reprinted with permission from Guedon et al. [14]. Copyright 2012, American Chemical Society.

AC-DT, because there is only a single path available, no interference effects occur for AC-DT (Figure 5.1b). In contrast, it is confirmed in theory that destructive QI occurs for AQ-DT (Figure 5.1d).

However, the logarithmically binned dI/dV line versus bias of AQ-DT is still U-shaped as AC-DT is. So it is not directly evident to confirm QI in AQ-DT experimentally. Then, they analyzed 2-[(4-acetylthiophenyl)ethynyl]-6-(phenylethynyl)-9,10-anthraquinone (AQ-MT) and found that the dI/dV curves are nearly symmetric in both calculation and experiment, although AQ-MT is contacted asymmetrically. It seems quite interesting that another asymmetrical OPE3-MT does not show the symmetric dI/dV dip in both calculation and experiment. So the symmetry in Figure 5.1e must therefore be a consequence of $T(E)$ being symmetric around E_F or, equivalently, of E_F lying near the interference minimum. Figure 5.1e, f constitute direct evidence for QI in AQ-MT molecular junctions.

QI effects arising from cross-conjugation in such conjugated molecules have been demonstrated experimentally as described above, but they have also been predicted for π systems that are close enough in space to interact [15]. Unlike for conjugation patterns, which is an intrinsic property, this type of QI is extremely sensitive to the conformation; the two π systems must be precisely aligned to form a through-space conjugation interaction. So, Ryan C. Chiechi and coworkers applied [16] self-assembled monolayers to study conformation-driven QI effects mediated by through-space conjugation. They investigated the tunneling transport through space in face-on or edge-on arrangement by using pseudo-*p*-bis((4-(acetylthio)phenyl)ethynyl)-*p*-[2,2]cyclophane (PCP) or 2,6-bis(((4-acetylthio)

phenyl)ethynyl)-9,10-dihydroantracene (AH). 1,4-bis(((4-acetylthio)phenyl) ethynyl) benzene (OPE3) and 2,6-bis(((4-acetylthio)phenyl)ethynyl) antracene (AC) were also used because they have same end-to-end lengths as PCP and AH and they are conjugated through bonds. They confirmed that destructive QI might be "switched on" by small changes in conformation. All of the conductance heatmaps except for AH are U-shaped, which is a sign of non-resonant tunneling. The heatmap for AH has a sharp dip in the center and negative curvature near ±1 V, which is a sign that a destructive interference feature exists in the bias window.

Slightly different from SAMs to change the conformation, van der Zant and coworkers [17] showed that the destructive interference can be turned on or off by mechanically controlling its conformation within the same molecular system. By using a combination of *ab initio* calculations and single-molecule conductance measurements, they demonstrated the existence of a quasiperiodic destructive quantum-interference pattern along the breaking traces of π-stacked molecular dimers (Figure 5.2). As shown in Figure 5.2a, b, the resulting zero-bias conductance strongly depends on the stacking geometry of the molecules, with sharp conductance drops over several orders of magnitude. These conductance drops can be traced back to destructive quantum-interference effects that occur exactly at the Fermi energy of the electrodes for a specific dimer conformation. In particular, the drops in conductance observed for S-OPE3 resulted from the QI effects and occurred when the intermolecular couplings had the opposite signs. The

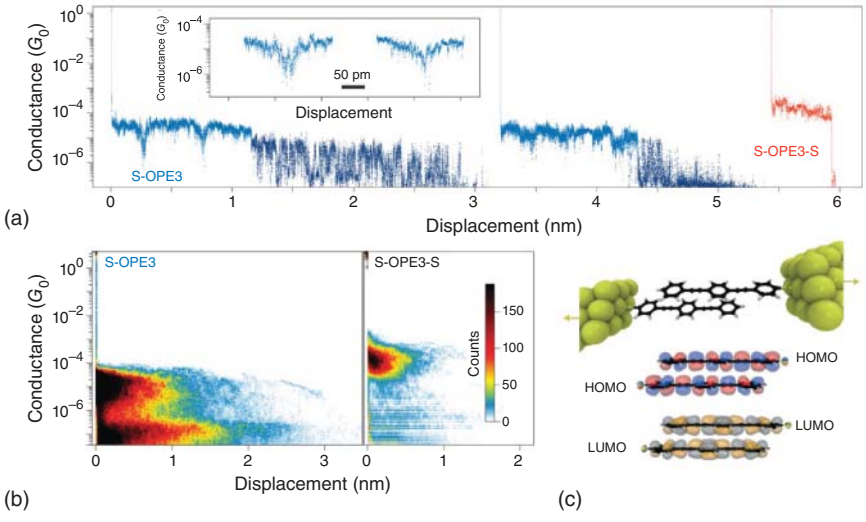

Figure 5.2 Quantum interference in a π-stacked dimer. (a) Examples of breaking traces measured in the presence of S-OPE3 (blue) and S-OPE3-S (red). The inset in (a) shows a zoom-in on the drops observed in the monothiol molecule, which is attributed to the quantum-interference effects. (b) 2D conductance–displacement histogram of S-OPE3 and S-OPE3-S built from 1878 and 1000 consecutive traces, respectively. (c) Representation of the two electrodes in the break junction connected by a π-stacked dimer. Source: Reprinted with permission from Frisenda et al. [17]. Copyright 2016, Springer Nature.

results demonstrate that it is possible to control the molecular conductance over more than 1 order of magnitude and with a sub-ångström resolution by exploiting the subtle structure–property relationship of π-stacked dimers (Figure 5.2c).

5.1.3 Different Transport Pathways

According to Kirchhoff's circuit laws, the net conductance of two parallel paths in an electronic circuit is the sum of the individual conductance. Latha and coworkers synthesized a series of molecular systems that contain either one backbone or two backbones in parallel, bonded together cofacially by a common linker on each end [18]. Single-molecule conductance measurements and transport calculations based on the density functional theory showed that the conductance of a double-backbone molecular junction can be more than twice that of a single-backbone junction, providing clear evidence for constructive interference.

Besides a multi-branched molecular structure, different configurations can induce the interference of transport components along different pathways. For example, scientists studied the molecules in either a *para-* or a *meta-*configuration and found that the conductance through a single meta-coupled benzene ring is more than an order of magnitude lower than through a para-coupled benzene [19]. Especially, molecules consisting of phenyl rings have been explored due to the configuration in which the anchoring units are connected. Under this background, scientist investigated the conductive properties of oligo(phenyleneethynylene) (OPE)-type molecules possessing three aromatic rings (Figure 5.3a). The single-molecule conductances were found to satisfy the quantum circuit rule $\frac{G_{\mathrm{ppp}}}{G_{\mathrm{pmp}}} = \frac{G_{\mathrm{mpm}}}{G_{\mathrm{mmm}}}$ [20]. Molecules were of the type $X{-}Y{-}X$, where X represents pyridyl anchors with para (p), meta (m), or ortho (o) connectivities and Y represents a phenyl ring with p and m connectivities. This demonstrates that the contribution to the conductance from the central ring is independent of the para versus meta nature of the anchor groups.

Based on the study in configuration of anchoring units, Colin J. Lambert and coworkers inserted one nitrogen atom into the *m*-OPE core [21]. They observed if the substituted nitrogen is in a meta position relative to both acetylene linkers, the daughter conductance remains as low as the parent. While the substituted nitrogen is in an ortho position relative to one acetylene linker and a para position relative to the other, destructive QI is alleviated and the daughter conductance is high. In fact, their goal is to capture the role of connectivity in determining the electrical conductance of such parents and daughters. By applying molecules consisting of bipartite parental cores in which odd-numbered sites are connected to even-numbered sites only (Figure 5.3b), the effect of heteroatom substitution onto an odd-numbered site is summarized by the following qualitative rules: *i*, *j* are different "atom sites" in a graphene-like polyaromatic hydrocarbon (PAH) molecule (i) when *i* and *j* are odd, both parent and daughter have low conductances, (ii) when *i* is odd and *j* is even, or vice versa both parent and daughter have high conductances, and (iii) when *i*, *j* are both even, the parent has a low conductance and the daughter a high conductance.

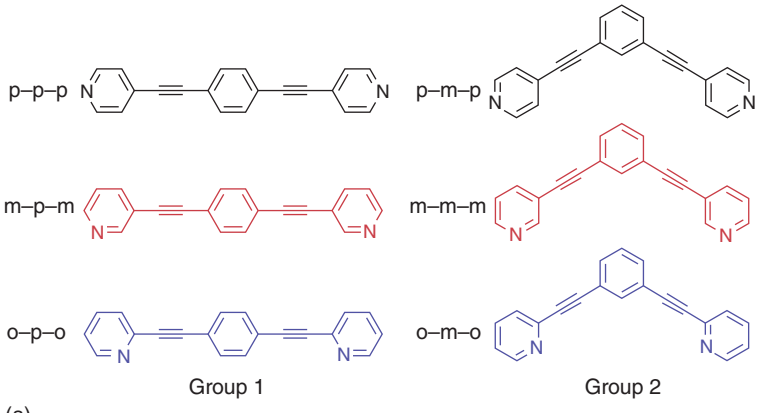

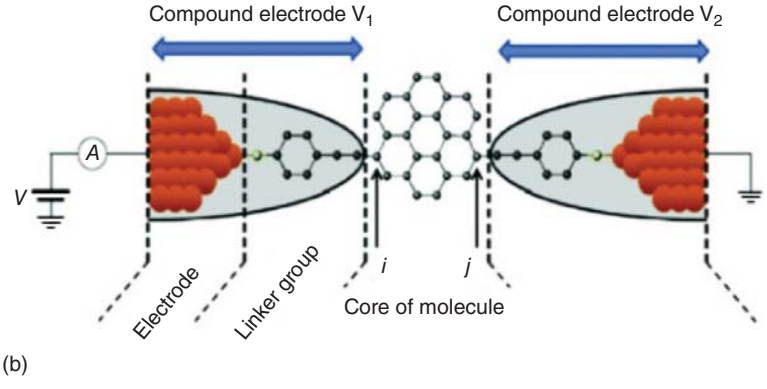

Figure 5.3 Different configurations for quantum interference. (a) Chemical structures. These are divided into two groups, based on the presence of a para (group 1) or meta (group 2) central phenyl ring. Source: Reprinted with permission from Manrique et al. [20]. Copyright 2015, Springer Nature. (b) A PAH core, weakly coupled to compound electrodes. Source: Reprinted with permission from Sangtarash et al. [21]. Copyright 2016, American Chemical Society.

5.1.4 Chemical Design to Tune Quantum Interference

Tuning the QI effect in charge transport at the single-molecule level by chemical design is an underlying topic that scientists pay attention to. Hong and coworkers found that protonation alleviated the destructive interference, thus resulting in the occurrence of the largest conductance change in the protonated azulene molecular junctions [22]. Three azulene derivatives with different connectivities were synthesized and reacted with trifluoroacetic acid to form the protonated states. The conductances the protonated states produced were more than 1 order of magnitude higher than the neutral states, which suggested the shortening of the preferred charge transport pathway and that protonation significantly enhanced the single-molecule conductance.

In addition, they found that the conductance of the metallacycle junction with phosphonium group is more than 1 order of magnitude higher than that without

phosphonium group [23]. By analyzing X-ray diffraction and UV–Vis absorption spectroscopy, it is suggested that the attached phosphonium group makes metallacycles more delocalized. The attached phosphonium group in the metallacycles provides the access to tune the metallacycles by delocalization effect, which leads to the conductance difference higher than 1 order of magnitude. The delocalization effect could offer a new avenue to tune charge transport in molecular materials and devices.

Recent observations of QI in single-molecule junctions confirm the essential role of quantum effects in molecular systems. These effects are central to a broad range of chemical processes and may be beneficial for the design of single-molecule electronic functionalities. Here we have shown the direct evidence of QI in experiments. QI effects can be turned on or off within the same molecular system by controlling its conformation or controllable chemical design. Thus, QI effects give us opportunities to "switch off" electronic communication between different parts of a molecule. With the right substituents, we are able to tune the position of this interference feature that lies very close to the Fermi energy. These essential studies provide us new insights into the functionality and application we can use in QI. Much more work needs to be done to understand the true nature of QI effects in single-molecule electronics.

5.2 Coulomb Blockade and Kondo Resonance

The research scale for single-molecule junctions is the nanoscale or an even smaller scale, which gives rise to remarkable quantum transport phenomena, such as the Coulomb blockade, the Kondo effect, etc. A brief description of the two quantum phenomena will be introduced in this section. The Coulomb blockade effect is drastically determined by the coupling strength between molecules and two electrodes. Coulomb blockade emerges in the relatively weak coupling mechanism because the energy of an electron in the molecules is too small to tunnel into the molecular island, and there is mutual repulsion between electrons in and outside the molecules, which results in the single-electron transport regime. However, the Coulomb blockade is absent in a comparatively strong coupling mechanism due to the broadening of the frontier molecular orbital levels.

The Coulomb blockade effect can be eliminated by adding a gate electrode to a two-terminal junction to resonantly modulate the molecular energy levels with the Fermi levels of the source and drain [24]. Based on the Coulomb blockade, there are some potential real devices that can be developed, such as single-electron transistors (SETs), single-electron memory, and so on. As a result, the study of the Coulomb blockade effect is capable of promoting basic understanding of the electron transport mechanism in molecular junctions.

The Kondo effect, also called the Kondo resonance in the conductance, plays a significant part in electron transport. Found in metals including magnetic impurities, the Kondo effect manifests as a type of abnormal minimum in the resistance as a consequence of an exchange coupling between the spins of localized magnetic impurity systems and delocalized conduction electrons [25].

In single-molecule junction configurations, the localized spin of the molecule can be screened by the conducting electron spin in the electrodes in the exchange coupling process [26], resulting in a conductance peak at a low bias voltage (the Kondo resonance in the conductance). With the mechanically controllable break junction (MCBJ) technique, Wagner et al. reported a switch between the pseudo-singlet state and the pseudo-triplet state, which was respectively assigned to the absence and occurrence of a Kondo-like anomaly [27]. Recently, Frisenda et al. investigated the Kondo effect in a neutral and stable all-organic radical single-molecule break junction in two-terminal and three-terminal solid-state electronic devices [28]. They found that the Kondo anomaly is robust regardless of mechanical and electrostatic changes.

It was also worth mentioning that different nuclear spin states should lead to different conductance states and thus could be used to encode information or induce switching. The most universally used molecular spin switches can be divided into two categories: spin-crossover compounds and valence-conversional molecules. In the first type, bias-dependent switching was reported in molecular junctions with a spin-crossover coordination compound as the functional center. van der Zant and coworkers [29] reported that a new single-molecule-switching concept based on the coordination-sphere-dependent spin state of Fe^{II} species by using $[Fe^{II}(tpy)_2]$ complexes was fabricated using the MCBJ technique. Because the Fe^{II} ion changes from a low-spin state to a high-spin state at a threshold voltage owing to the distortion of the coordination sphere under a high electric field, single molecule spin switch has been successfully realized.

For the second type, the valence state change of the valence state transition molecules is related to the conductance state or the applied magnetic field. Voltage-induced conductivity switch is implemented in a single molecule. It was demonstrated that a high/low current ratio of more than 1000 was generated at a bias voltage of <1.0 V based on a device containing both Mo compounds [30]. This behavior was attributed to the oxidation and/or reduction of Mo ions mediated by weakly coupled local molecular orbitals with spin-polarized ground states.

In addition, a three-terminal nuclear spin quantum bit transistor composed of a $TbPc_2$ single-molecule magnet fabricated by electromigration has been used for electromigration measurement [31]. By scanning the magnetic field at a constant source–drain and gate bias, the electron spin state changes between the $|\uparrow\rangle$ and $|\downarrow\rangle$ states, resulting in a conductance transition [31]. Lutz and coworkers [32] realized the Ho atom based on MgO loading, and there was a Fe atom next to Ho to increase the reversible switch of the magnetic field felt by Ho. These studies not only provided valuable information for the further development of the Kondo effect, but also laid the foundation for further exploration of charge transport in single-molecule electronics.

Based on above-two quantum transport phenomena, a number of research groups moved on and conducted the bulk of related studies. Combined the characteristics of both the Kondo effect (due to the entanglement from strong electronic interactions) and QI (due to competing electron transport pathways), transport through a spin-degenerate molecule can be either enhanced or blocked by the Kondo correlations, depending on molecular structure,

contacting geometry, and applied gate voltages [33]. Figure 5.4a illustrates how a renormalized Kondo resonant conductance is evolved into a novel Kondo blockade regime of the suppressed conductance due to QI. As shown in Figure 5.4b, the Kondo blockaded conductance occurs near a QI node in the exchange co-tunneling. It can be concluded that the quantum chemistry techniques could be used to accomplish the Kondo model mapping for larger molecules. Besides, quantum effects dominating transport characteristics can be used to create functional devices, especially archetypal SETs [34]. Figure 5.4c shows the schematic of a single-cluster junction accomplished by the scanning tunneling microscope (STM) technique; the Au tip is coated with an insulating wax before immersion in a solution of the target clusters in propylene carbonate (PC). According to the current measurement, beyond these voltage thresholds, the current through the junction increases sharply, shown in Figure 5.4d. The

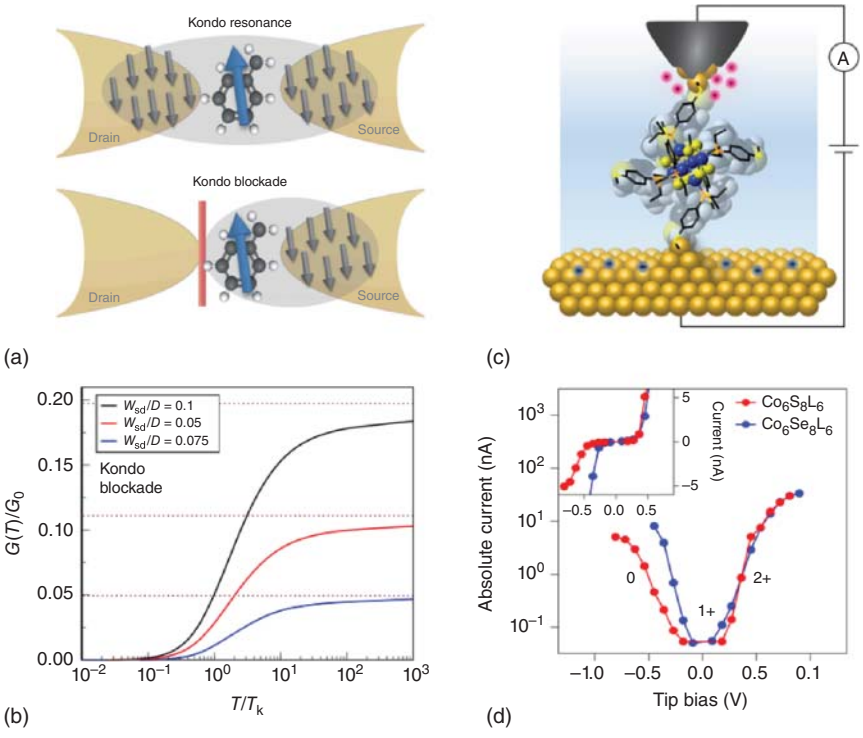

Figure 5.4 Coulomb blockade and Kondo resonance. (a) Interplay between quantum interference and electronic interactions in single molecule junctions. (b) Kondo blockaded conductance near a quantum interference node in the exchange co-tunneling. Source: Reproduced with permission from Mitchell et al. [33]. Copyright 2017, Nature Publishing Group. (c) Schematic of the scanning tunneling microscopy break junction (STM-BJ) measurement in an ionic environment. The Au tip is coated with an insulating wax before immersion in a solution of the target clusters in PC. (d) Semi-logarithmic plot of the current versus tip bias for Co6S8L6 (red trace) and Co6Se8L6 (blue trace) measured in PC. Inset: Current blockade region at low tip bias on a linear scale. Source: Reproduced with permission from Lovat et al. [34]. Copyright 2017, Springer Nature.

device is turned on when the temporary occupation of the core states by a transiting carrier is energetically enabled, resulting in a sequential tunneling process and an increase in current by a factor of ~600. This is a new way to design room-temperature molecular-scale transistors with multiple states and functionalities. In summary, both the Coulomb blockade and the Kondo effect arise from the electron–electron interactions in single-molecule quantum dots. Therefore, the integrated studies for both effects offer an effective method to further explore the quantum transport properties in single molecular devices.

5.3 Thermoelectricity

The thermoelectricity of molecular junctions, which measures the induced voltage drop or the induced current across the junctions between two electrodes with a temperature difference, is important to understand the basic scientific mechanism of the thermoelectronic effect at the single-molecule level and improve the technologies for converting wasted heat into the useful electrical energy [35]. Furthermore, thermoelectronic characterizations, especially the Seebeck coefficient ($S_{\text{junction}} = \Delta V/\Delta T$), of the molecular junctions can determine the type of charge carriers (either p- or n-type) and the relative energy position of the Fermi level of the electrodes with respect to the HOMO or LUMO levels of the connected molecules [6]. In the off-resonance limit, the S_{junction} of the molecular junctions at zero applied voltage can be related to the transmission function ($T(E)$) at the Fermi level by using the Landauer formula as follows:

$$S(E_{\text{F}}) = -\frac{\pi^2 K_{\text{B}}^2 T}{3e} \frac{\partial \ln(T(E))}{\partial E}\bigg|_{E=E_{\text{F}}} \tag{5.1}$$

where k_{B} is the Boltzmann constant; e is the charge of the electron; T is the average temperature of the junctions; and E_{F} is the Fermi level. In other words, the S_{junction} is related to the slope of $T(E)$ at the Fermi level of the systems. With the Fermi level in the middle of the HOMO and LUMO levels in most molecular junctions (Figure 5.5), when the HOMO level is closer to E_{F} for a p-type transport, a negative slope of the $T(E)$ and a positive value of S_{junction} are obtained. However, for an n-type transport with an LUMO level closer to E_{F}, a positive slope of the $T(E)$ and a negative value of S_{junction} are achieved. Therefore, by using the S_{junction} value, the type of charge carriers and the relative position between E_{F} and the HOMO or LUMO levels can be determined based on the thermoelectronic investigations of the molecular junctions.

Based on the Landauer formula of the S_{junction}, it is reasonable to conclude that the slope of the transmission function ($T(E)$) determines the thermoelectronic characteristics of the molecular junctions. When the transmission function is simplified to a single Lorentzian shape peak form, $T(E)$ can be written as follows:

$$T(E) = \sum_{i=1}^{N} \frac{4\Gamma_{i,\text{L}}\Gamma_{i,\text{R}}}{(\Gamma_{i,\text{L}} + \Gamma_{i,\text{R}})^2 + 4(E - E_i)^2} \tag{5.2}$$

where i indicates the molecular orbital (HOMO or LUMO); E_i is the molecular energy level from E_{F}; and $\Gamma_{i,\text{L}}$ and $\Gamma_{i,\text{R}}$ are the broadening of the ith orbitals due

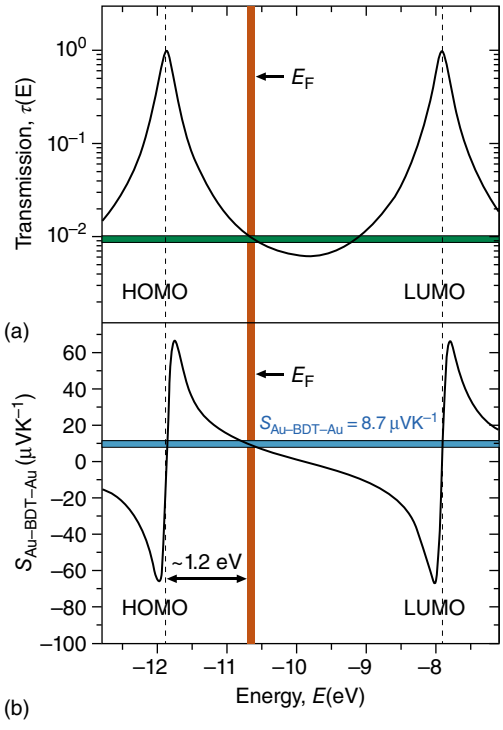

Figure 5.5 Theory of thermoelectricity in representative Au–1,4-benzenedithiol (BDT)–Au molecular junctions. (a) Theoretical prediction of the transmission function of an Au–BDT–Au junction plotted as a function of the position of the Fermi level of the Au electrodes with respect to the HOMO and LUMO levels. (b) Predicted Seebeck coefficient of the Au–BDT–Au junction plotted as a function of the position of the Fermi level with respect to the HOMO and LUMO levels. Source: Reproduced with permission from Reddy et al. [6]. Copyright 2007, AAAS.

to the coupling with the left and right electrodes, respectively. In other words, in addition to the relative energy position between E_F and the ith orbitals, the broadening of the molecular orbitals can also be investigated using the thermoelectronic measurements of the molecular junctions. Thus far, the experimental characterization of thermoelectricity for molecular junctions is limited. However, a few key results have emerged, such as the Seebeck coefficient determination and its modulation, thus offering a promising research branch of molecular electronics. Detailed information and discussions are provided in Section 9.7.

Reddy et al. experimentally studied the thermoelectricity properties of 1,4-benzenedithiol (BDT), 4,4′-dibenzenedithiol, and 4,4″-tribenzenedithiol at room temperature by trapping molecules between two gold electrodes with a temperature difference across them. They revealed that the Seebeck coefficients of these molecular junctions to be +8.7, +12.9, and +14.2 microvolts per kelvin ($\mu V\,K^{-1}$), respectively [6]. The ability to study thermoelectricity in molecular junctions provides the opportunity to exploring molecular thermoelectric energy conversion. The same group further demonstrated that electrostatic control of thermoelectric properties via a gate electrode is possible [36]. The main challenge for the investigation of thermal electricity in three terminal molecular junctions is that creating big temperature differentials in three-terminal devices is almost impossible. Nevertheless, Kim et al. showed that extremely large temperature gradients can be established in nanoscale gaps bridged by molecules, while simultaneously controlling their electronic structure via a gate electrode. By employing this platform, they studied different types of molecular

junctions, and demonstrated that the Seebeck coefficient as well as the electrical conductance of molecular junctions can be simultaneously increased by electrostatic control. Additionally, they showed that thermoelectric properties can be significantly enhanced when the dominant transport orbital was located close to the Fermi level of the electrodes. These results illustrate the intimate relationship between the thermoelectric properties and charge transmission characteristics of molecular junctions.

Recently, probing the thermopower (Seebeck effect) of molecular junctions has enabled studies of the relationship between thermoelectricity and the molecular structure [37]. Furthermore, Cui et al. reported the observation of Peltier cooling in molecular junctions – a critical step for establishing molecular-based refrigeration [38]. By integrating conducting-probe atomic force microscopy with custom-fabricated picowatt-resolution calorimetric microdevices, they created an experimental platform that enables the unified characterization of electrical, thermoelectric, and energy dissipation characteristics of molecular junctions. By using this platform, we studied gold junctions with different types of molecules and revealed the relationship between heating/cooling and charge transmission characteristics. Their experimental conclusions are supported by self-energy-corrected density functional theory calculations and will promote the extraordinarily efficient energy conversion as theoretically predicted [39–41].

5.4 Electronic–Plasmonic Conversion

Photonic elements can carry information with a capacity of 1000 times more than that of electronic components. However, due to the optical diffraction limit, these elements are difficult to be integrated into modern-day nanoelectronics, such as three-dimensional integrated circuits [42, 43]. Especially, surface plasmon polaritons can be confined to subwavelength dimensions and can carry information at high speeds (>100 THz). To combine the nanoelectronics (small dimensions) with the optics (fast operating speed), on-chip electronic–plasmonic transducers that directly convert electrical signals into plasmonic signals (and vice versa) is really required. Du et al., for the first time, reported electronic–plasmonic transducers based on metal–insulator–metal tunnel junctions (MIM-TJs) coupled to plasmonic waveguides [44]. They studied the plasmon excitation efficiency of an MIM-TJ (the plasmon source) via a second MIM-TJ (the plasmon detector), both connected to a plasmonic waveguide without the need for plasmon-to-photon conversions any more.

Figure 5.6a shows how two MIM-TJs are plasmonically coupled via their Au leads, which serve as the plasmonic waveguide. In the system, one tunneling junction functions as the plasmon source via an inelastic tunneling process and the other one works as the plasmon detector via optical rectification (modulation of the tunneling current by plasmons). Surface plasmon polariton (SPPs) are excited by the source junction, propagate along the Au plasmonic waveguide, and are detected by the detector tunneling junction. Figure 5.6b schematically shows an MIM-TJ that consists of an Al electrode (40 nm in thick) with its native layer of

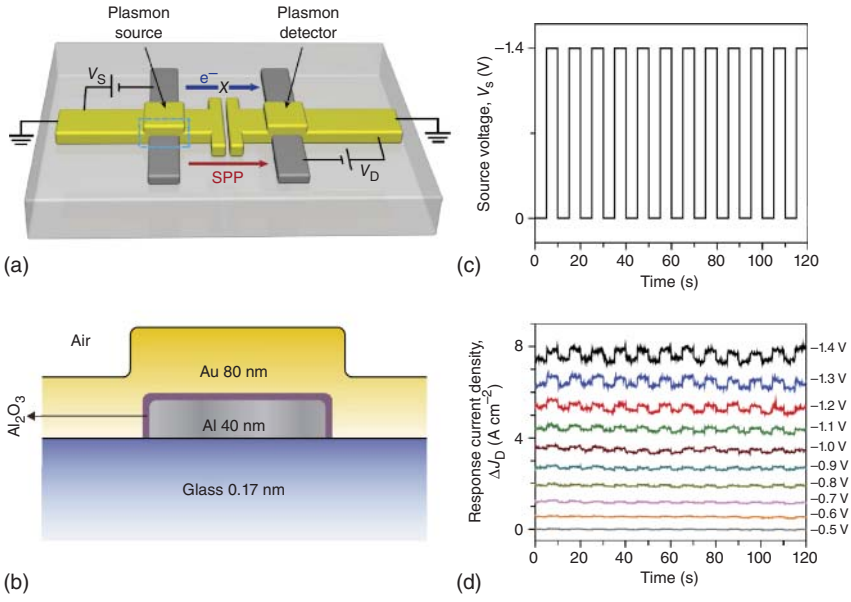

Figure 5.6 The realization of an on-chip electronic–plasmonic transducer. (a) Schematic illustration of the device consisting of two metal–insulator–metal tunnel junctions connected to a plasmonic waveguide. The left junction generates the plasmon source and the right junction detects the plasmon. SPPs are excited when a source bias voltage V_S is applied, and they propagate via the plasmonic waveguide to the detector. The plasmon modulates the tunneling current that flows across the detector with a detector bias V_D. (b) Schematic of an M–I–M (Au/AlO_x/Al) tunnel junction. (c) Time trace of V_S in square waveform. (d) Time trace of response current intensity (ΔJ_D) for V_S in (c). Source: Reproduced with permission from Ref. Du et al. [44]. Copyright 2017, Springer Nature.

~2 nm as the tunneling barrier and an Au electrode. By applying a bias across the MIM-TJ, electrons flow as a result of quantum-mechanical tunneling. The plasmons was excite inside the tunnel junction, the so-called MIM–SPP mode and propagating along the Au electrodes.

Figure 5.6c shows that a square voltage waveform was applied to the source V_S with maxima at 0 and −1.4 V. The detector voltage V_D was fixed at a constant ranging from −0.5 to −1.4 V. They found that the response current intensity (ΔJ_D) faithfully followed the input signal V_S and increased with V_D, as shown by Figure 5.6d. On the basis of their electrical measurement together with photon emission image, they demonstrated that these junctions can be readily integrated into existing technologies, thus promising potential applications in on-chip integrated plasmonic circuits.

Recently, Dong et al. [45], reported such electrically driven single-photon emission. They used effective quenching inhibition and nanocavity plasma enhancement to achieve stable single-molecule electroluminescence. Single-photon emission driven by a well-defined isolated single-molecule emitter was achieved by combining electronic decoupling with a resonant plasma nanocavity enhanced emission formed by an ultra-thin dielectric spacer and an STM

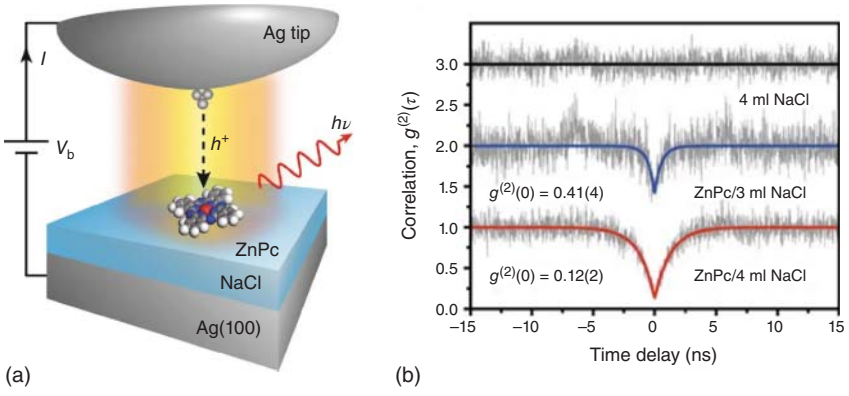

Figure 5.7 The realization of electrically driven single-photon emission. (a) STM induced schematic diagram of a single molecule fluorescence decoupled from an NaCl layer to an Ag (100) substrate. The molecular fluorescence is produced by exciting highly localized tunneling electrons on a single ZnPc molecule. (b) Second-order correlation measurements of single-molecule electroluminescence at the molecular lobe of ZnPc (−2.5 V, 100 pA) and NaCl (−2.5 V, 500 pA). The black, red, and blue lines are single exponential fits to the data. For the convenience of observation, the curves have been shifted up by a multiple. Source: Reproduced with permission from Dong et al. [45]. Copyright 2017, Springer Nature.

junction. Figure 5.7a shows a schematic of an isolated ZnPc molecular emitter that was electronically decoupled from a silver (100) metal substrate by a thin layer of sodium chloride (NaCl). Silver (Ag) tips with plasmonic properties were used to provide strong resonance plasmon enhancement for molecular fluorescence excited by highly localized tunneling electrons. Figure 5.7b shows the results of photon correlation measurements for the tip located above the lobe of an isolated ZnPc molecule on 3 ml (blue) or 4 ml NaCl (red) and on the exposed 4 ml NaCl surface (black). The apparent anti-collision dip in the second-order correlation function $[g^{(2)}(\tau)]$ was observed at zero time for molecular electroluminescence from a single ZnPc molecule absorbed on either the 3 or 4 ml NaCl surface. Therefore, in the same year, they further demonstrated about Fano resonance and Lamb shift at the single molecular level by using a single molecular emitter as a unique optical probe to coherently couple with a highly restricted plasmon nanocavity. This provided new insights into the physical mechanisms of coherent coupling beyond the dipole-coupled model [46].

References

1 Lambert, C.J. (2015). Basic concepts of quantum interference and electron transport in single-molecule electronics. *Chem. Soc. Rev.* 44: 875–888.
2 Guédon, C.M., Valkenier, H., Markussen, T. et al. (2012). Observation of quantum interference in molecularcharge transport. *Nat. Nanotechnol.* 7: 305.

3 Ballmann, S., Härtle, R., Coto, P.B. et al. (2012). Experimental evidence for quantum interference and vibrationally induced decoherence in single-molecule junctions. *Phys. Rev. Lett.* 109: 056801.

4 Park, J., Pasupathy, A.N., Goldsmith, J.I. et al. (2002). Coulomb blockade and the Kondo effect in single-atom transistors. *Nature* 417: 722–725.

5 Liang, W., Shores, M.P., Bockrath, M. et al. (2002). Kondo resonance in a single-molecule transistor. *Nature* 417: 725.

6 Reddy, P., Jang, S.-Y., Segalman, R.A. et al. (2007). Thermoelectricity in molecular junctions. *Science* 315: 1568–1571.

7 Nozaki, D., Avdoshenko, S.M., Sevincli, H. et al. (2014). Quantum interference in thermoelectric molecular junctions: A toy model perspective. *J. App. Phys.* 116: 074308.

8 Kim, W.Y. and Kim, K.S. (2009). Tuning molecular orbitals in molecular electronics and spintronics. *Acc. Chem. Res.* 43: 111–120.

9 Sanvito, S. (2011). Molecular spintronics. *Chem. Soc. Rev.* 40: 3336–3355.

10 Su, T.A., Neupane, M., Steigerwald, M.L. et al. (2016). Chemical principles of single-molecule electronics. *Nat. Rev. Mater.* 1: 16002.

11 Lambert, C.J. and Liu, S.-X. (2018). A magic ratio rule for beginners: a chemist's guide to quantum interference in molecules. *Chem. Eur. J.* 24: 4193–4201.

12 Solomon, G.C., Andrews, D.Q., Hansen, T. et al. (2008). Understanding quantum interference in coherent molecular conduction. *J. Chem. Phys.* 129: 054701.

13 Nozaki, D., Avdoshenko, S. M., Sevincli, H. et al. (2013). Prediction of quantum interference in molecular junctions using a parabolic diagram: understanding the origin of Fano and anti- resonances. *Progress in Nonequilibrium Green's Functions* V; 427.

14 Guedon, C.M., Valkenier, H., Markussen, T. et al. (2012). Observation of quantum interference in molecular charge transport. *Nat. Nanotechnol.* 7: 305–309.

15 Solomon, G.C., Herrmann, C., Vura-Weis, J. et al. (2010). The chameleonic nature of electron transport through π-stacked systems. *J. Am. Chem. Soc.* 132: 7887–7889.

16 Carlotti, M., Kovalchuk, A., Wachter, T. et al. (2016). Conformation-driven quantum interference effects mediated by through-space conjugation in self-assembled monolayers. *Nat. Commun.* 7: 13904.

17 Frisenda, R., Janssen, V.A.E.C., Grozema, F.C. et al. (2016). Mechanically controlled quantum interference in individual π-stacked dimers. *Nat. Chem.* 8: 1099–1104.

18 Vazquez, H., Skouta, R., Schneebeli, S. et al. (2012). Probing the conductance superposition law in single-molecule circuits with parallel paths. *Nat. Nanotechnol.* 7: 663–667.

19 Arroyo, C.R., Tarkuc, S., Frisenda, R. et al. (2013). Signatures of quantum interference effects on charge transport through a single benzene ring. *Angew. Chem. Int. Ed.* 52: 3152–3155.

20 Manrique, D.Z., Huang, C., Baghernejad, M. et al. (2015). A quantum circuit rule for interference effects in single-molecule electrical junctions. *Nat. Commun.* 6: 6389.

21 Sangtarash, S., Sadeghi, H., and Lambert, C.J. (2016). Exploring quantum interference in heteroatom-substituted graphene-like molecules. *Nanoscale* 8: 13199–13205.

22 Yang, G., Sangtarash, S., Liu, Z. et al. (2017). Protonation tuning of quantum interference in azulene-type single-molecule junctions. *Chem. Sci.* 8: 7505–7509.

23 Li, R., Lu, Z., Cai, Y. et al. (2017). Switching of charge transport pathways via delocalization changes in single-molecule metallacycles junctions. *J. Am. Chem. Soc.* 139: 14344–14347.

24 Moth-Poulsen, K. and Bjørnholm, T. (2009). Molecular electronics with single molecules in solid-state devices. *Nat. Nanotechnol.* 4: 551–556.

25 Zimbovskaya, N.A. and Pederson, M.R. (2011). Electron transport through molecular junctions. *Phys. Rep.* 509: 1–87.

26 Rakhmilevitch, D., Korytár, R., Bagrets, A. et al. (2014). Electron-vibration interaction in the presence of a switchable Kondo resonance realized in a molecular junction. *Phys. Rev. Lett.* 113: 236603.

27 Wagner, S., Kisslinger, F., Ballmann, S. et al. (2013). Switching of a coupled spin pair in a single-molecule junction. *Nat. Nanotechnol.* 8: 575–579.

28 Frisenda, R., Gaudenzi, R., Franco, C. et al. (2015). Kondo effect in a neutral and stable all organic radical single molecule break junction. *Nano Lett.* 15: 3109–3114.

29 Harzmann, G.D., Frisenda, R., van der Zant, H.S.J. et al. (2015). Single-molecule spin switch based on voltage-triggered distortion of the coordination sphere. *Angew. Chem. Int. Ed.* 54: 13425–13430.

30 Schwarz, F., Kastlunger, G., Lissel, F. et al. (2016). Field-induced conductance switching by charge-state alternation in organometallic single-molecule junctions. *Nat. Nanotechnol.* 11: 170–176.

31 Thiele, S., Balestro, F., Ballou, R. et al. (2014). Electrically driven nuclear spin resonance in single-molecule magnets. *Science* 344: 1135–1138.

32 Natterer, F.D., Yang, K., Paul, W. et al. (2017). Reading and writing single-atom magnets. *Nature* 543: 226–228.

33 Mitchell, A.K., Pedersen, K.G.L., Hedegard, P. et al. (2017). Kondo blockade due to quantum interference in single-molecule junctions. *Nat. Commun.* 8: 15210.

34 Lovat, G., Choi, B., Paley, D.W. et al. (2017). Room-temperature current blockade in atomically defined single-cluster junctions. *Nat. Nanotechnol.* 12: 1050–1054.

35 Aradhya, S.V. and Venkataraman, L. (2013). Single-molecule junctions beyond electronic transport. *Nat. Nanotechnol.* 8: 399–410.

36 Kim, Y., Jeong, W., Kim, K. et al. (2014). Electrostatic control of thermoelectricity in molecular junctions. *Nat. Nanotechnol.* 9: 881–885.

37 Cui, L.J., Miao, R.J., Jiang, C. et al. (2017). Perspective: thermal and thermoelectric transport in molecular junctions. *J. Chem. Phys.* 146: 092201.

38 Cui, L.J., Miao, R.J., Wang, K. et al. (2018). Peltier cooling in molecular junctions. *Nat. Nanotechnol.* 13: 122–127.

39 Finch, C.M., Garcia-Suarez, V.M., and Lambert, C.J. (2009). Giant thermopower and figure of merit in single-molecule devices. *Phys. Rev. B* 79: 033405.

40 Bergfield, J.P., Solis, M.A., and Stafford, C.A. (2010). Giant thermoelectric effect from transmission supernodes. *ACS Nano* 4: 5314–5320.

41 Dubi, Y. and Di Ventra, M. (2011). Colloquium: heat flow and thermoelectricity in atomic and molecular junctions. *Rev. Mod. Phys.* 83: 131–155.

42 Brongersma, M.L. and Shalaev, V.M. (2010). The case for plasmonics. *Science* 328: 440–441.

43 Ozbay, E. (2006). Plasmonics: merging photonics and electronics at nanoscale dimensions. *Science* 311: 189–193.

44 Du, W., Wang, T., Chu, H.S. et al. (2017). Highly efficient on-chip direct electronic–plasmonic transducers. *Nat. Photonics* 11: 623–627.

45 Zhang, L., Yu, Y.J., Chen, L.G. et al. (2017). Electrically driven single-photon emission from an isolated single molecule. *Nat. Commun.* 8: 580.

46 Zhang, Y., Meng, Q.S., Zhang, L. et al. (2017). Sub-nanometre control of the coherent interaction between a single molecule and a plasmonic nanocavity. *Nat. Commun.* 8: 15225.

6

Supramolecular Interactions in Single-Molecule Junctions

Supramolecular chemistry, which originated from Emil Fischer's lock-and-key image, Paul Ehrlich's receptor idea, and Alfred Werner's coordination chemistry, has long been and continues to be actively investigated by the scientific community. These concepts exactly overlap with the electronic devices at the molecular level, namely, a molecular device can be defined as an assembly of a discrete number of molecular components designed to achieve a specific function [1]. In a historical perspective, the Nobel prize laureate, J. M. Lehn, gave the most authoritative and widely accepted definition of supramolecular chemistry, namely, "the chemistry beyond the molecule, bearing on organized entities of higher complexity that result from the association of two or more chemical species held together by intermolecular forces [2]." Since 1990, the fundamental supramolecular chemistry began to grow up exponentially with the development of the more unambiguous fundamental concept such as molecular recognition, self-assembly, and so forth. With the benefit of the increasing nanodevice techniques today, the molecular-level probe of the more complicated systems (supramolecular systems) offered the opportunity to explore the interaction in the supramolecular system.

6.1 Hydrogen Bonds

Hydrogen bonds can occur between different parts of a single molecule or between molecules that play an important role in the orientation of this world. The researchers have paid great attention to the hydrogen bond in the ensemble level for decades. With the booming of nanotechnology, Lindsay's group gave the first attempt to investigate the natural hydrogen bond during DNA base pairing representing a fundamental interaction in biochemical processes, with a scanning tunneling microscope (STM) technique in 2009 [3, 4]. Even with their genius design of the experiment and the establishment of a creative mechanical model, they read out the hydrogen only in base resolution instead of in the single-bond resolution. The main reason for their failure of single-bond recognition is probably the nature of the DNA base pair, which conventionally form as pairs, namely, G≡C and A=T. Even so, the exploration enthusiasm of the essential genetic information carrier DNA never ends for the scientific world.

Molecular-Scale Electronics: Concept, Fabrication and Applications,
First Edition. Xuefeng Guo, Dong Xiang, and Yu Li.

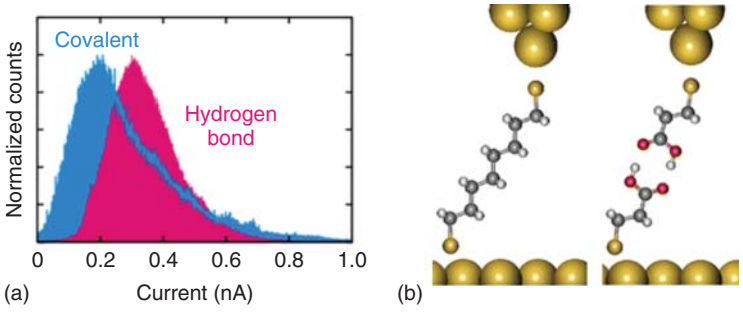

Figure 6.1 Hydrogen bond measurements based on STM. (a) Current histograms constructed from *I*–*t* plots. Pink: measurements made by using C_2COOH tips over C_2COOH-covered surfaces. $f_{whm} = 0.23$. Blue: measurements made by using Au tips and C_8DT-covered surfaces. $f_{whm} = 0.26$. (b) Schematic of tunneling current measurement. Source: Reprinted with permission from Nishino et al. [6]. Copyright 2013, American Chemical Society.

Chang et al. investigated the hydrogen bond interaction in nucleoside-base pairs by combining STM and conductive probe atomic force microscopy (CP-AFM) techniques [3]. They proposed an electromechanical model to combine the atomic force detection and tunneling current performance simultaneously, thus allowing counting hydrogen bonds in DNA base pairs. He et al. reported the single-molecule DNA hybridization dynamics with single-base resolution by using SiNW-based single-molecule electrical biosensors [5]. The authors used an electronic circuit based on point decorated silicon nanowires as electrical probes, and directly exploited the folding/unfolding process of individual hairpin DNAs with sufficiently high signal-to-noise ratio and bandwidth.

Few years later, Nishino et al. investigated the artificial hydrogen bond formed by a carboxylic dimmers, which is chemically decorated onto the functionalized tip and substrate with the STM technique (Figure 6.1) [6]. They determined the H-bond via spontaneous formation of a chemical interaction between the STM tip and sample molecules. Compared with the covalent σ bonded alkanes, they demonstrated that the conductivity of the H-bond between the carboxylic dimmers depends on the length of the H-bond linkers. Their projected density of states (PDOSs) calculation attributed the conductivity to the H-bonded moieties' density of states with a positive relationship. The more complicated double-stranded DNA (dsDNA) has been challenged with a similar functional tip [7].

Another strategy by utilizing graphene-molecule-graphene single molecule junctions (GMG-SMJs) has been employed in hydrogen bond investigations. Guo and coworkers designed and constructed a quadrupolar hydrogen-bond dimer with two identical ureido pyrimidinedione (UPy) molecules incorporated into the graphene point contact through amide linkages (Figure 6.2a) [8]. The quadrupolar hydrogen-bond dimer increased the strength of hydrogen bonds and device conductivity, which led to better performance and afforded more profound dynamic information in real-time electrical detection. Typically, in a weakly polar solvent such as diphenyl ether, four conductive microstates could be

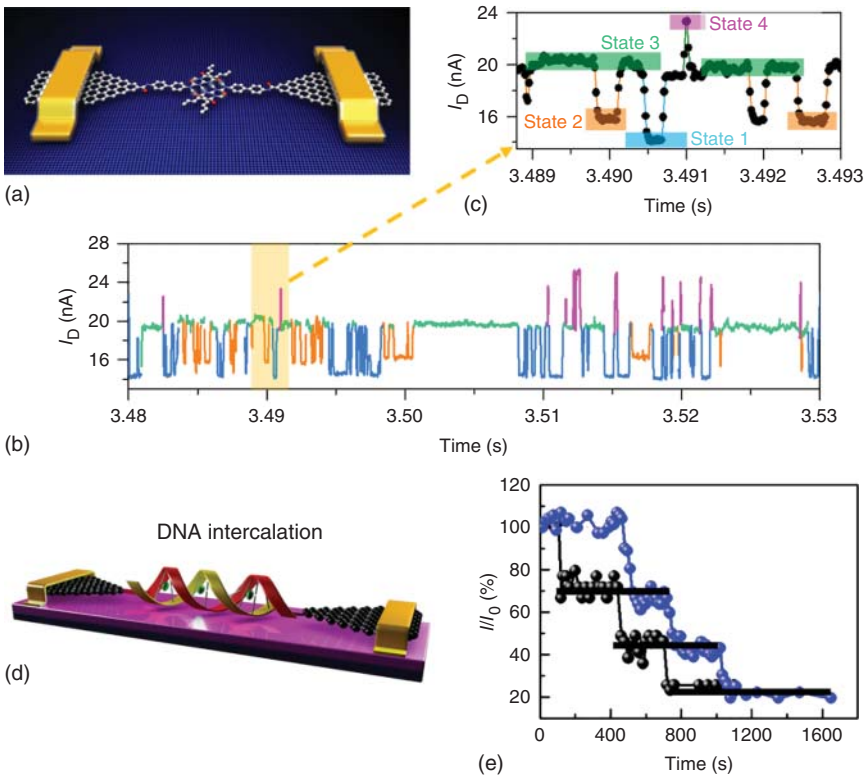

Figure 6.2 Hydrogen bond measurements based on GMG-SMJs. (a) Schematics of a quadrupolar hydrogen-bond-assembled single-molecule junction. Source: (a) Reprinted with permission from Zhou et al. [8]. Copyright 2018, Springer Nature. (b, c) *I–t* curves recorded in diphenyl ether at different time scales and $V_{bias} = 300$ mV. (d) Schematics of double-stranded DNA single-molecule junctions and (e) corresponding *I–t* curves showing stepwise intercalation events at different EB concentrations (black: 5.0×10^{-7} mol l^{-1}; blue: 5.0×10^{-13} mol l^{-1}). Source: (b–e) Reprinted with permission from Wang et al. [9]. Copyright 2015, The Royal Society of Chemistry.

distinguished by real-time monitoring of junction conductance (Figure 6.2b, c). According to the results of theoretical calculations, the three main conductance states were assigned to the intrinsic state, the isomerized state, and the proton transfer state, respectively. Additionally, a transient weak interaction between the solvent and hydrogen bonds was suggested to afford the fourth state. Both experimental and theoretical results consistently revealed that hydrogen bonds were stochastically rearranged mainly through intermolecular proton transfer and tautomerism, confirming the possibility of intrinsically transducing an exquisite hydrogen-bond dynamic process into real-time electrical signals with single-bond resolution. In another experiment, the local distortions and unwinding of the DNA structure induced by the stepwise intercalation of ethidium bromide (EB) were monitored in real time (Figure 6.2d,e) [9].

6.2 π–π Stacking Interactions

Aromatic–aromatic or π–π stacking interactions are essential non-covalent intermolecular forces, similar to hydrogen bonding. Aromatic stacks, which are formed via self-assembly, are promising for the construction of molecular electronic devices with tunable electronic functions, in which non-covalently bound π-stacks were regarded as replaceable modular components. They can contribute to molecular recognition processes when extended conformation is formed from building blocks with aromatic moieties. In 2008, Wu et al. reported a pioneer π–π stack with the mechanically controllable break junction (MCBJ) technique [10]. They rationally designed five oligophenyleneethynylenes (OPEs)–dithiol/monothiol molecules in total for investigation. What is interesting is that the conductance of OPE-monothiol molecules was observed to have an even equal magnitude to the molecule with anchors on both sides, since molecules with only one anchor group are not expected to form a stable molecular bridge. They believed that the connection between the electrodes is made possible by a π–π stacking interaction between a pair of molecules. According to the length derived from the conductance traces, they figured out the tunneling picture as shown in Figure 6.3. The author showed for the first time that π–π stacking can be used as the dominant guiding force for the formation of molecular bridges in few-molecule electronic junctions.

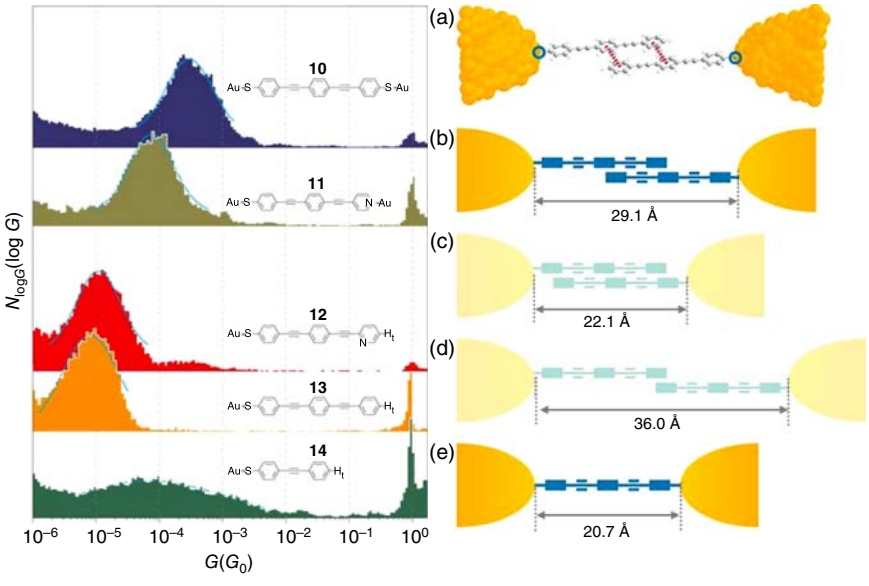

Figure 6.3 π–π stacking interactions. Conductance histograms for the different molecules and illustration of possible stacking configurations. Staggered π–π stacking configuration of a pair of OPE-monothiol molecules within which the aromatic rings are shifted by half of the ring length. (Left) (a–e) Simplified representation of different configurations of OPE molecules between the electrodes, where a rectangle indicates a phenyl ring. The acetyl protected OPE-type rods molecule **10**–**14**. Source: Reprinted with permission from Wu et al. [10]. Copyright 2008, Springer Nature.

For further interest, more OPEs and their derivatives have been studied as prototypes [11]. Zheng and coworkers reported a conductance of 5.1×10^{-6} G_0 for OPE-dithiol by I–V curve measurements with an electrochemically assisted mechanically controllable break junction (EC-MCBJ) technique [12, 13]. The conductance was much lower than the previous work [10, 14]. They ascribed the lower conductance to the π–π stacking interaction between two OPE-dithiol molecules [15]. Martín et al. developed a series of molecules featured with different steric hindrance and anchoring groups [16]. They expected the bulky *tert*-butyl substituents on the phenyl rings to prevent the π–π stack interaction. Their results gave evidence that for metal–molecule–metal junctions involving OPE-monothiols, the second contact must be formed by the interaction of the π-electrons of the terminal phenyl ring with the metal surface. For a more specific study, Frisenda et al. investigated individual π-stacked S-OPE3 dimers for the quantum interference effect with the MCBJ technique [17]. Their *ab initio* calculation indicated a quasiperiodic destructive quantum interference along the breaking traces of π-stacked molecular dimers. Consequently, they ran experiments with a π-stacked dimer of S-OPE3 bridges between lithographically defined metallic Au electrodes, which are then progressively moved away from each other with sub-ångström control as shown in Figure 6.4. The 2D conductance histogram showed significant differences between S-OPE3 and S-OPE3-S (Figure 6.5a, b). Pronounced peaks and drops were probed for S-OPE3 while for S-OPE3-S only one region of high counts was observed. These practical

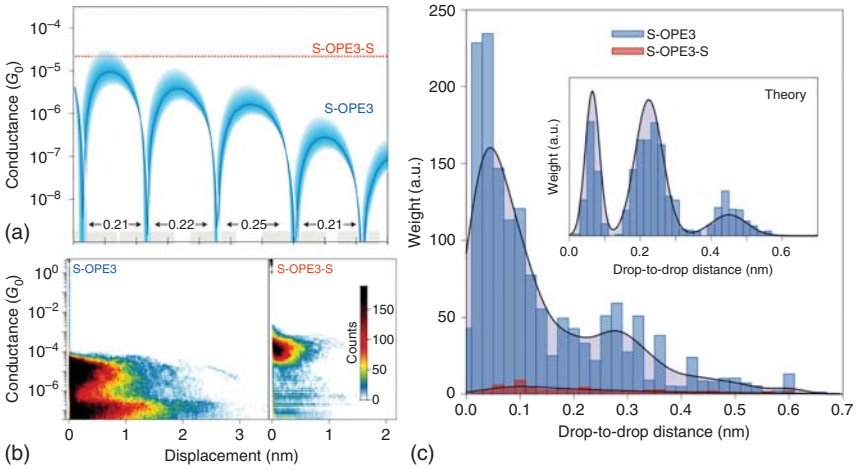

Figure 6.4 Simulations of the electronic transport properties of S-OPE3 and S-OPE3-S. (a) The panel shows the conductance of S-OPE3 in the wide-band-limit approximation calculated at the Fermi energy (plain blue line). The shaded area around it corresponds to a variation of the Fermi energy of ±0.5 eV. The horizontal dashed line marks the conductance of S-OPE3-S. (b) 2D conductance–displacement histogram of S-OPE3 and S-OPE3-S built from 1878 and 1000 consecutive traces, respectively. (c) Histograms of the weighted drop-to-drop distance obtained from the statistical analysis, performed with 131 traces of S-OPE3 and 259 traces of S-OPE3-S. Source: Reprinted with permission from Frisenda et al. [17]. Copyright 2000, Springer Nature.

results are consistent with the theoretical prediction. In addition, a higher-order statistical analysis of the single-trace drop-to-drop distance showed two peaks located at 0.05 and 0.27 nm, respectively (Figure 6.4c). Despite that the first peak that falls below the limitation of the detection algorithm, the second peak is close to the theoretical prediction (0.21–0.25 nm). Their results indicated the possibility to exploit the subtle structure–property relationship of π-stacked systems to control the molecular conductance over a few orders of magnitude and with sub-ångström resolution. In addition, more π-stack benzene systems have drawn attentions in the past decades, for instances, fully conjugated oligo(phenylene vinylene)s (OPVs) [19], less conjugated oligophenylenes [20, 21], and the other is represented by paracyclophanes featuring through-space conjugation between π-stacked benzene rings [22–25].

In comparison with the spontaneously formed π–π stacking in molecular junctions, Chen et al. designed and synthesized an archetypal folded luminogen molecule (*Z*)-*o*-BPTPE, which is a tetraphenylethene (TPE) derivative, containing a pair of well π-stacked biphenyls tethered by a vinyl group, as shown in Figure 6.5 [18]. The π–π stacking in (*Z*)-*o*-BPTPE was rigidified and greatly stabilized, thus showing advantage in producing more reliable and reproducible single-molecule junctions. The π-stacked region of (*Z*)-*o*-BPTPE constructed by the benzene ring offered a through-space conjugation. Additionally, the author also developed a through-bond conjugation stem from the vinyl group that holds two biphenyls together as a second channel, which is more favorable than the alkyl chain in paracyclophane in terms of electronic conductivity. Their absorption property study and theoretical calculation predicted the weak through-bond conjugation and efficient through-space conjugation. The conductance behavior confirmed that the pronounced conductance peaks of *f*-TPE–PPy and *l*-TPE–PPy appear at ~1.40 and ~1.50 nS. Analogously, *f*-TPE–PEPy showed a nearly equal conductance (~0.50 nS) to that of *l*-TPE–PEPy (~0.55 nS) (Figure 6.5c). Considering poor π-conjugation and lower highest occupied molecular orbital (HOMO) energy levels and larger HOMO–LUMO gaps of folded molecules *f*-TPE–PPy and *f*-TPE–PEPy, their practical conductance is comparable with the better-conjugated linear molecules. The author believed that the through-bond tunneling channel and the through-space tunneling channel between π-stacked biphenyls existed simultaneously in the folded molecules presented, which improved the charge-transfer probability and partially compensated the loss of through-bond conjugation.

With increasing interest in the π-stacked system, more complicated systems have been studied. Inspired by the previous work – non-anchoring junction and columnar coordination cages techniques, Kiguchi et al. comprised aromatic stacks enclosed in self-assembled cages [26–30]. At the beginning, they designed homo discrete π-stacked systems and systematically investigated the electron transport properties [28, 30]. To control charge transport properties, they developed a hetero π-stacked complexes (Figure 6.6) [29]. They sealed two parallel π-donor triphenylene (**17**) in cages, yielding a **15**•(**17**•**17**) as a resistor. On the other hand, the π-acceptor naphthalenediimide (**15** and **16**) inclusion made **15**•(**16**•**17**) complex a rectifier. Only a single peak at $5 \times 10^{-3}\ G_0$ was observed in the homo complex **15**•(**17**•**17**), while the hetero complex **15**•(**16**•**17**) has two

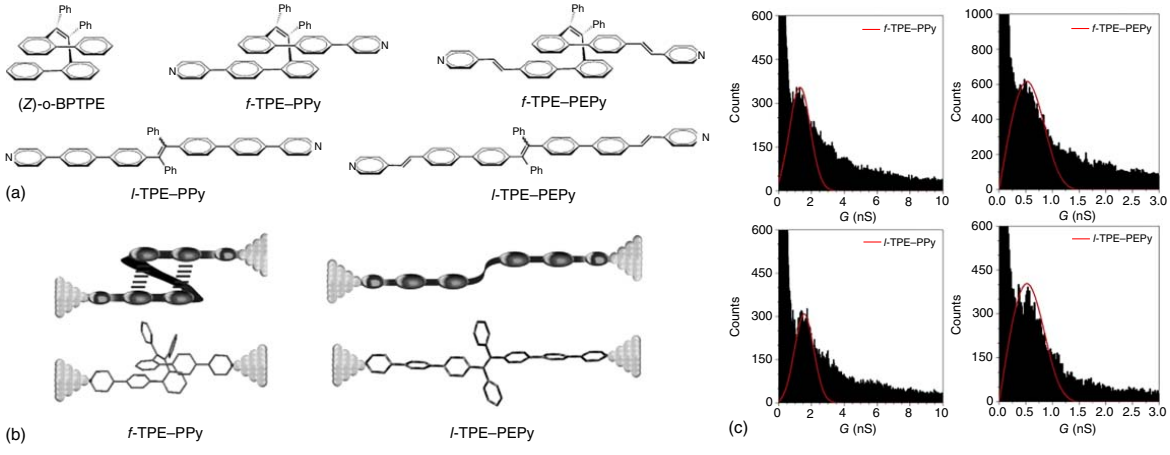

Figure 6.5 TPE-based single-molecule junctions. (a) Chemical structures of (*Z*)-*o*-BPTPE (CCDC 955718), *f*-TPE–PPy (CCDC 1030245), and *f*-TPE–PEPy (CCDC 1030246). Hydrogens are omitted for clarity. (b) Representation of circuits of *f*-TPE–PPy and *l*-TPE–PPy anchored onto gold electrodes. (c) Conductance histogram of *f*-, *l*-TPE–PPy and *f*-, *l*-TPE–PEPy. Source: Reprinted with permission from Chen et al. [18]. Copyright 2000, John Wiley and Sons.

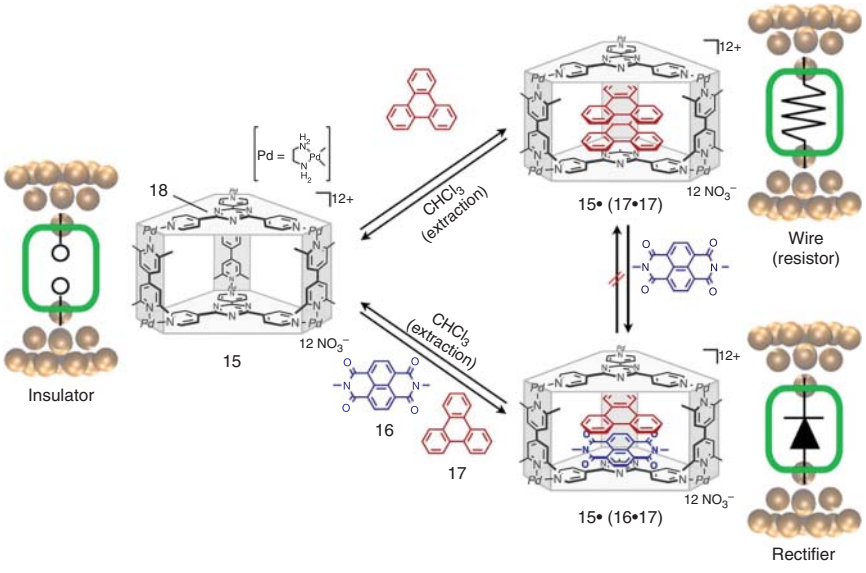

Figure 6.6 Schematic representation of single-molecule junctions sandwiched by two Au electrodes and the corresponding electronic components of the junctions. Columnar cage **15** can accommodate a pair of naphthalenediimide (**16**) and triphenylene (**17**) or a dimer of **17**, in which the enclosed aromatic pair is bookended by the electron-poor triazine panels **18** of the cage. Empty cage **15**, homo π-stacked complex **15**•(**17**•**17**), and hetero π-stacked complex **15**•(**16**•**17**) behave as close as an insulator, a wire (resistor), and a rectifier, respectively. Heterocomplex **15**•(**16**•**17**) is more stable than homocomplexes **15**•(**16**•**16**) and **15**•(**17**•**17**). Although homocomplex **15**•(**17**•**17**) is quantitatively formed, homocomplex **15**•(**16**•**16**) is obtained at very low yield and is therefore not discussed in this study. Source: Reprinted with permission from Fujii et al. [29]. Copyright 2015, American Chemical Society.

distinct peaks at $3 \times 10^{-3}\, G_0$ and $1 \times 10^{-4}\, G_0$. The two separated conductance peaks of hetero complex **15**•(**16**•**17**) originated from the donor–acceptor and acceptor–donor direction inside the cages. Knowing that different conformation existed in hetero complex **15**•(**16**•**17**), they further studied the current-bias voltages characteristics carefully to confirm the rectification properties directly.

6.3 Host–Guest Interactions

Host–guest complexes are the assembly of the supramolecular lock-and-key image. Since the molecular device has been proposed, numerous host–guests complexes have been focused on [31–33]. The pronounced conception for these complexes is that the host molecule provides a large hydrophobic cavity to the guest molecule with a microenvironment for chemical reactions and also offers an opportunity for the novel electron transport properties [34, 35].

In 2004, Tao and coworkers [36] demonstrated that the binding of a guest species onto a single host molecule could be studied electrically by wiring the host molecule to two electrodes. In this study, peptides were selected as the host molecules because of the unlimited number of different sequences that could

be tuned to obtain an optimal binding strength and specificity for the selected guest, i.e. transition-metal ions, such as Cu^{2+} and Ni^{2+}. The specific binding of peptides with the metal ions was expected using deprotonated peptide bonds, which could change the molecular configuration and alter the charge transport pathway. Therefore, the difference in the molecular conductance before and after binding can be used to reflect the chemical reaction, which also laid the foundation for metal-ion sensors with molecular sensitivity.

Despite the demonstration of detecting metal ion binding in this study, the application for actual single-molecule sensors is inhibited because the research was established based on an STM setup, whose two-terminal architecture is so sophisticated that it is more commonly used for fundamental science rather than actual applications. Furthermore, this limitation originates from the instability of the Au–S contact interface. To solve these problems, an improved approach was introduced by Guo et al., who successfully developed novel molecular devices by using carbon electrodes based on single walled carbon nanotubes (SWCNTs) [37] in 2006 and graphene [38] in 2012 (as discussed in Chapter 3). Based on this reliable approach, another system was constructed to demonstrate host–guest binding at the single-molecule level. Firstly, a molecule containing two terpyridyl ligands linked by a Co^{2+} was integrated to a pair of carbon electrodes by covalent amide bonds. Interestingly, the conductance of the host–guest junctions could disappear and appear repeatedly to form cycles through alternate treatments of ethylenediaminetetraacetic acid (EDTA) and Co^{2+}. This strategy is reliable because it was proven by another study from the same group, where the capability of construction of a single-molecule device by covalently bridging a host molecule containing a crown ether (BPP34C10DAM) as a functional center between nanogapped graphene electrodes with amide bonds (Figure 6.7a–c) [39]. Bias voltage-dependent current measurements confirmed the formation of GMG-SMJs (Figure 6.7e, black and red). In the presence of the guest molecule (MV^{2+}), a new higher current level appeared (Figure 6.7e, blue), and binary states were observed (Figure 6.7f), which was attributed to the dynamic interplay between host and guest molecules at the solid–liquid interface (Figure 6.7d). Specifically, the association of guest and host molecules ($MV^{2+} \subset$ BPP34C10DAM) provided a more conductive channel originating from the delocalization of the molecular lowest unoccupied molecular orbital (LUMO), which led to higher conductance. The Gaussian fits of bimodal current histograms allowed binding constants (K_a) to be derived from the Langmuir isotherm as $K_a = \alpha/(1-\alpha)C$ (α is the fraction of the BPP34C10 host complexed with MV^{2+}, and C is the concentration of MV^{2+}), while other thermodynamic parameters including the Gibbs free energy ($\Delta G°$), enthalpy ($\Delta H°$), and entropy ($\Delta S°$) of complexation were deduced from the van't Hoff equation: $-RT\ln(K_a) = \Delta H° - T\Delta S°$ (R is ideal gas constant, and T is temperature). In addition to the above, I–t data for binary states were statistically fitted using QuB software (Figure 6.7f), and idealized two-level fluctuations were analyzed to provide a set of kinetic parameters for $MV^{2+} \subset$ BPP34C10, including the high- and low-current-state lifetimes τ_{high} and τ_{low} (Figure 6.7g) and the corresponding (de)complexation rate constants $k_a = 1/\tau_{low}$ and $k_d = 1/\tau_{high}$ (Figure 6.7h). Finally, the Arrhenius plots of temperature-dependent $\ln(k)$

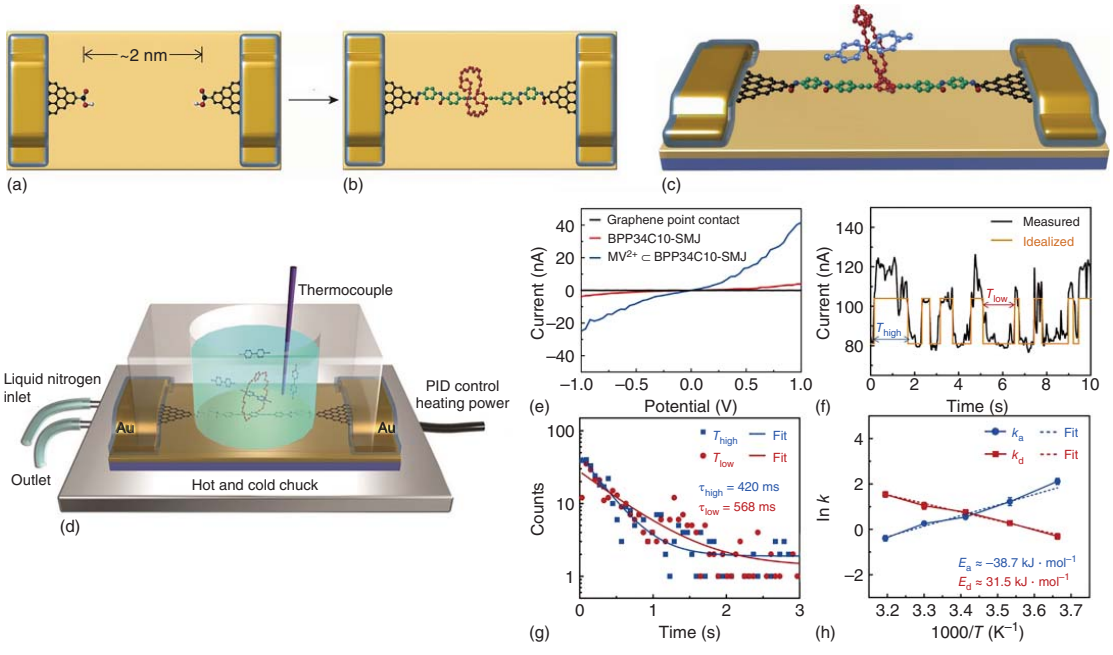

Figure 6.7 Host–guest interactions. (a–c) Schematics of $MV^{2+} \subset$ BPP34C10DAM GMG-SMJ device construction. (d) Schematics of the SMJ device–liquid interface characterization platform. (e) *I–V* curves of the device recorded at different stages. (f) *I–t* curve of the above device and the corresponding idealized fit obtained using QuB software. (g) Plots of time intervals of two current states for the idealized fit in (f), and the corresponding Arrhenius plots (h) of association/dissociation rate constants and activation energies in Me_2SO at 293 K. V_{bias} = 100 mV. Source: Reprinted with permission from Wen et al. [39]. Copyright 2016, AAAS.

in Me_2SO demonstrated a linear dependence of $\ln(k)$ on $1/T$ (Figure 6.7h), and the activation energies of (de)complexation processes were obtained as $E_a = \sim -38.7\,kJ\,mol^{-1}$ and $E_d = \sim 31.5\,kJ\,mol^{-1}$. These results demonstrate that the single-molecule electrical approach is sufficiently powerful to analyze and extract all thermodynamic and kinetic parameters, thus offering unlimited opportunities for probing more complex chemical/biological processes.

The rotation of single C—C bond in the conventional π-conjugated molecular wire makes the coupling difference between two neighboring parts that have various angles, which makes the conductance of an actual single π-conjugated molecular wire hard to be determined. To address this issue, Kiguchi and his coworkers designed a cyclic molecule permethylated α-cyclodextrin (PM α-CD) covered molecule **19** (Figure 6.8a) and uncovered molecule **20** as control [35]. PM α-CD molecule restricts the access of the surrounding π-conjugated molecules to the central π-conjugated molecule in the single-molecule junction. They believed that this method offers the possibility to measure a stipulated conductance of π-conjugated molecular wires. They determined the electrical conductance with the scanning tunneling microscope break junction (STM-BJ) technique. The typical conductance traces are shown in Figure 6.8b, with the appearance of the plateaus at integer multiples of $3 \times 10^{-4}\,G_0$ (covered molecules) or $6 \times 10^{-4}\,G_0$ (uncovered molecules). They considered these integer plateaus as one, two, and three covered (uncovered) molecules bridging between Au electrodes. The conductance histogram gave the statistical evidence that the conductance of covered molecules is smaller than the uncovered ones. With consideration of the theoretical calculation, the rotational barrier of covered molecule **19** was higher. Finally, according to the X-ray diffraction measurement, they proved that the PM α-CD can restrict effectively the rotation of the π-conjugated molecule C—C bond and the larger size of the cavity provided a proper distance to ignore the intermolecular interactions between neighboring π-conjugated molecules. Therefore, hosting

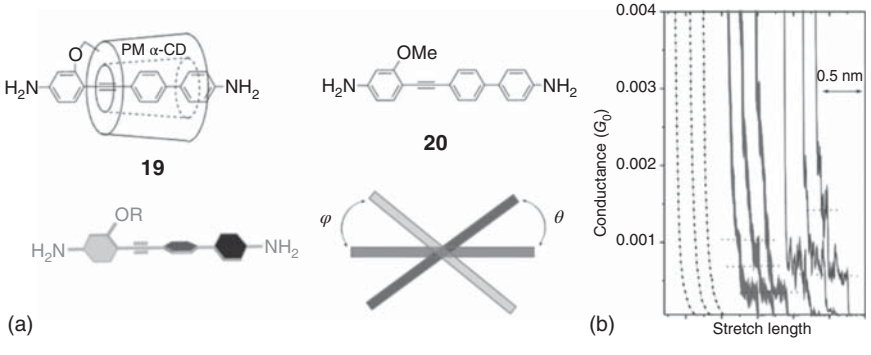

Figure 6.8 Strategy used for preventing the rotation of single C—C bond. (a) Structures of covered (**19**) and uncovered (**20**) molecules. (b) Typical conductance traces of Au point contacts broken in the tetraglyme solution containing covered (thick line) and uncovered (thin line) molecules. Source: Reprinted with permission from Kiguchi et al. [35]. Copyright 2012, John Wiley and Sons.

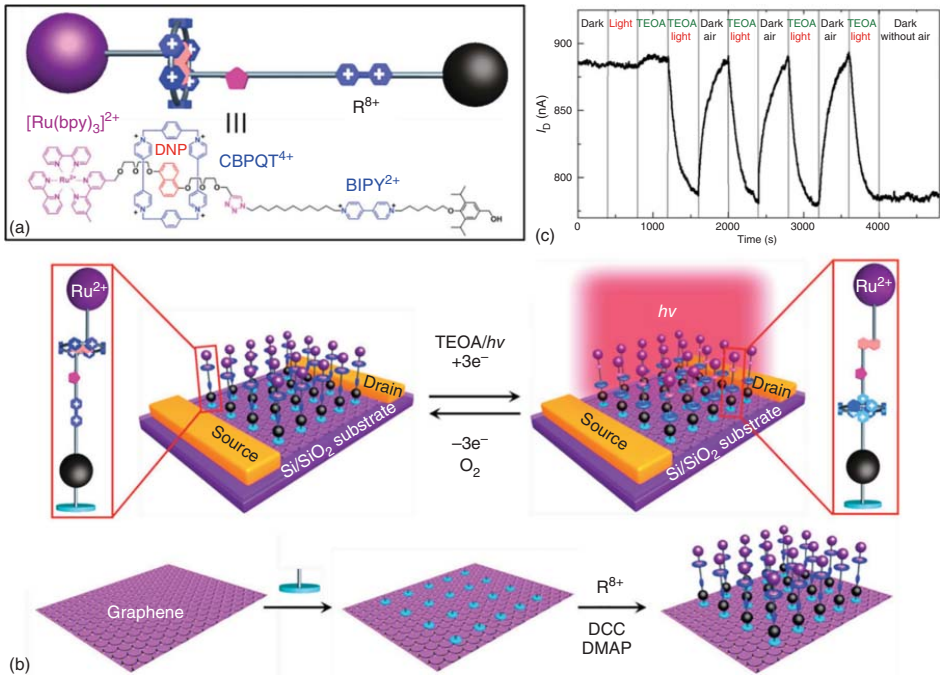

Figure 6.9 The [2]rotaxane–graphene hybrid optoelectronic device. (a) The structural formulas and graphical representations of the 1-pyrenebutanoic acid (PBA) used to link the bistable [2]rotaxane molecules non-covalently to the surface of the graphene. (b) Schematic representation of graphene transistors decorated with light-activated switchable [2]rotaxanes in the presence of triethanolamine (TEOA) as a sacrificial electron donor. A two-step strategy was employed in the assembly of the bistable [2]rotaxane molecules onto a graphene surface without altering the structure and properties of graphene covalently. (c) The *I*–*t* plot for a [2]rotaxane-decorated CVD-grown graphene under different conditions. DCC, N,N′-dicyclohexylcarbodiimide; DMAP, 4-dimethylamiopryidine. Source: Reprinted with permission from Jia et al. [40]. Copyright 2013, John Wiley and Sons.

π-conjugated molecules into a host molecule like CDs is promising to control single-molecule devices precisely.

Analogously, Zhang et al. investigated a cucurbit[8]uril (CB[8]) complexes [34]. As the Kiguchi's work stated earlier, such an encapsulation leads to reduced conductance and a reduced spread of conductance value. Inspired by the previous work, Zheng et al. presented cucurbit[8]uril (CB[8]) and viologen molecular bridges. Their results showed that the conductance of viologen derivatives increased upon encapsulation within the hydrophobic CB[8] cavity. They attributed the reduction to the reduced outer sphere reorganization energy within the framework of a Marcus-type model for electron transfer.

For wide applications, Jia et al. integrated a bistable [2]rotaxane R^{8+}-totaxanes with graphene as the sensing element to create hybrid optoelectronic devices (Figure 6.9a) [40]. They connected [2]rotaxane molecules non-covalently with the graphene surface by means of π–π stacking interactions (Figure 6.9b). In the presented [2]rotaxane molecule, the cyclobis(paraquat-*p*-phenylene) ($CBPQT^{4+}$) ring encircles a dumbbell, which consists of (i) a photocatalytic ruthenium(II)-tris(2,2′-bipyridine) ($[Ru(bpy)_3]^{2+}$) stopper, (ii) a π-electron rich 1,5-dioxynaphthalene (DNP) recognition site, (iii) a 4,4′-bipyridinium ($BIPY^{2+}$) unit, and (iv) a hydroxyl function for attaching to the graphene surface. When exposing the bistable [2]rotaxane-graphene hybrid device to triethanolamine (TEOA) and light, the ring component $CBPQT^{4+}$ underwent a discrete translational motion along the dumbbell component and reversed this process when exposed to air again. The *I*–*t* plot for a [2]rotaxane-decorated chemical vapor deposition (CVD)-grown graphene shown in Figure 6.9c presented the analogous bistable story. They utilized the two light-activated states of bistable rotaxane R^{8+} to electronically gate the graphene, as well as changing the electronic structure synergic effects to construct the logic-controllable hybrid device. The authors believed that this photoresponsive behavior of the bistable [2]rotaxane-decorated graphene devices can be endowed with binary logic.

6.4 Charge-Transfer Interactions

Supramolecular donor–acceptor dyads constitute a versatile kind of molecular assemblies with a variety of active electronic properties of molecular devices via donor–acceptor interactions. Although the charge-transfer interactions include intramolecular and intermolecular ones, for the supramolecules, we only present the latter one. Since 1973, the pioneering design, tetrathiafulvalene–tetracyanoquinodimethane (TTF–TCNQ) systems, appeared [41]. The charge transfer between the TTF–TCNQ can indeed take place at the interface. Alves et al. integrated the TTF–TCNQ into flexible field-effect transistors (FETs) (Figure 6.10a, b) [42]. Their results showed the potential of new physical phenomena in TTF–TCNQ supramolecules. With the development of the nanotechnique, recently García et al. investigated π-extended tetrathiafulvalene (exTTF) and its charge-transfer complex with (2,3,5,6-tetrafluoro-7,7,8,8-tetracyanoquinodimethane) F_4TCN (Figure 6.10c) [43]. The conductance has been measured and there was not obvious plateaus observed for

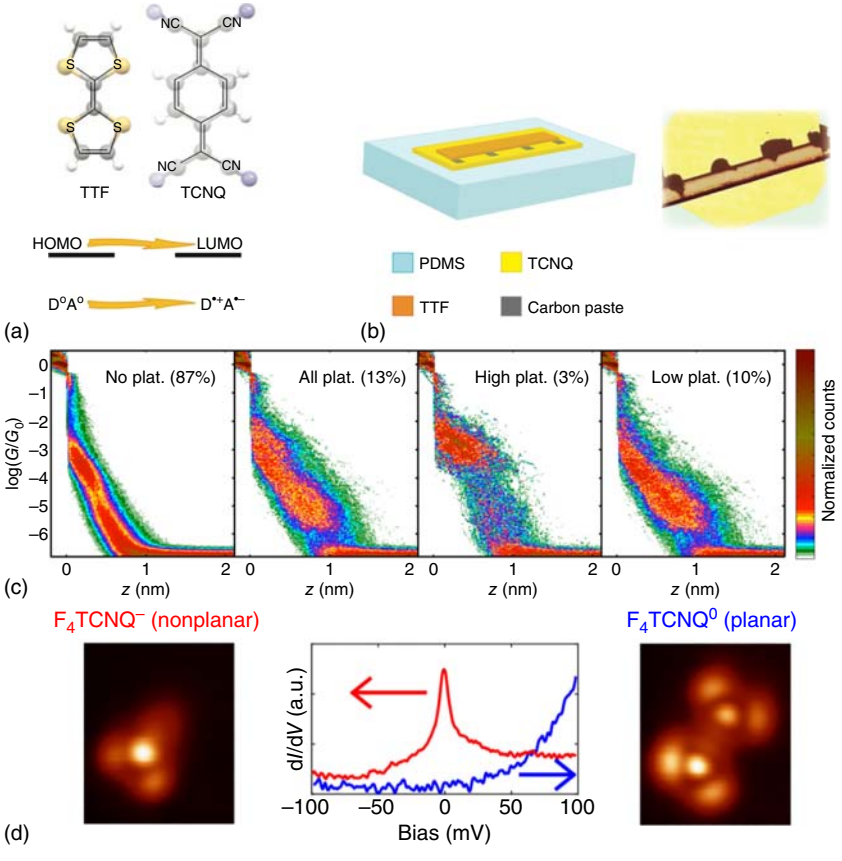

Figure 6.10 Charge transfer in the TTF–TCNQ system. (a) The first metallic charge-transfer compound TTF and TCNQ molecules. Source: (a) Reproduced with permission from Alves et al. [42]. Copyright 2008, Springer Nature. (b) Schematic of a TTF–TCNQ device, (c) 2D histograms corresponding to the charge-transfer complex between exTTF and F_4TCNQ after exposing a gold substrate to the solution of the complex in dichloromethane (DCM). PDMS, polydimethylsiloxane. Source: (c) García et al. [43]. https://creativecommons.org/licenses/by/2.0. Licensed Under CC BY 2.0. (d) F_4TCNQ adsorption on graphene on Ir (111). Source: (d) Reprinted with permission from Kumar et al. [44]. Copyright 2017, American Chemical Society.

individual exTTFs. However, the situation changed when the system turned to be exTTF–F_4TCNQ. Two pronounced plateaus had been obtained. According to the theoretical calculation, the conductance of exTTF was below the measurement sensitivity. In contrast, the lower conductance plateau corresponded to the exTTF–F_4TCNQ complex. In another experiment, the significant charge-transfer interaction between F_4TCNQ cyano groups and the underlying graphene consisting of carbon atoms drives dramatic changes in the electronic structure and adsorption geometry of the F_4TCNQ molecule over distinguishing sites of epitaxial graphene unit cells (Figure 6.10d) [44].

A fullerene–porphyrin complex is another widely investigated donor–accepter dyads. Nishino et al. studied the electron transport properties of the fullerene–

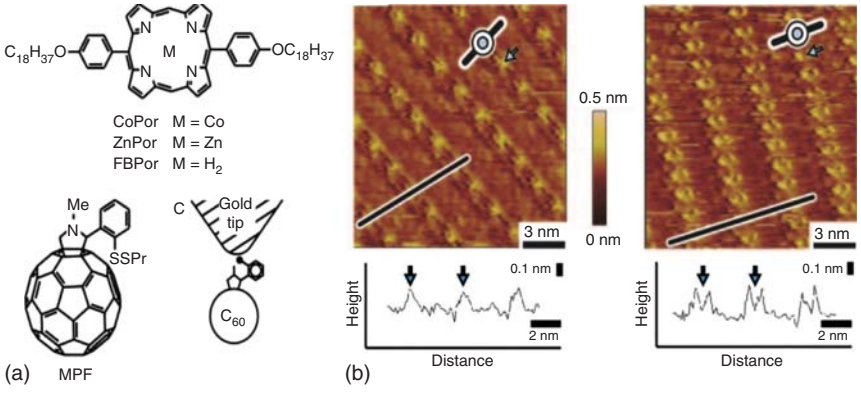

Figure 6.11 Structures of sample and tip molecules. (a) Chemical structures of the sample porphyrins and a fullerene derivative used as a precursor to the molecular tip. (b) STM images of CoPor monolayers physisorbed onto HOPG. The insets schematically show the molecular arrangement in the images. White rings, blue circles, and bars represent pyrrole moieties, Co(II) ions, and alkyl chains, respectively. The cross-sectional profiles measured along with the lines in the STM images are presented under the images. Blue arrows in the images and cross-sectional profiles indicate the position of Co(II) ions. Source: Reprinted with permission from Nishino et al. [45]. Copyright 2005, PNAS.

porphyrin complex with an STM tip (Figure 6.11a) [45]. Cobalt(II) 5,15-bis-(4-octadecyloxyphenyl)porphyrin (CoPor) was used to form the monolayers that were physisorbed onto highly oriented pyrolytic graphite (HOPG). They chemically decorated the STM tip by a fullerene derivative (Figure 6.11a), in which ordered arrays of porphyrin rings were observed as shown in Figure 6.11b, left. Central protrusions were observed for the porphyrin rings, which corresponded to the large tunneling probability of central cobalt(II) ions associated with the half-filled d_{z^2} orbital of the cobalt(II) ion. In contrast, when the STM tip was molecularly decorated with *N*-methyl 2-(2-propyldithiophenyl)-fulleropyrrolidine (MPF), different STM images were observed (Figure 6.11b, right). The cobalt(II) ions were observed as depressions and the pyrrole moieties surrounding them appeared as protrusions, which reveal that the tunneling electrons are localized at the pyrrole moieties. The authors demonstrated that the electron tunneling enhanced by the charge-transfer interaction was localized at the pyrrole moieties.

Consequently, the analogous strategy of the physical adsorption of the porphyrin derivatives onto HOPG through π-stacked interaction continued [46]. In terms of gold substrates, however, the electronic coupling between gold substrates and porphyrin derivatives falls below the lower limitation of detection (Figure 6.12a,b), which shows no obvious plateaus observed. The authors developed a ligation-mediated coupling, instead of introducing anchoring group into porphyrin derivatives. 4-aminothiophenol (4-ATP) has been bonded to the gold substrate through thiol groups, then they were stacked along axial coordination with tetraphenylporphyrinatometal (MTPP) to form more conductive molecular junctions with the fullerene-modified tip. A surprisingly strong interaction of 4-ATP to MTPP–fullerene complexes led to a higher conductance plateaus

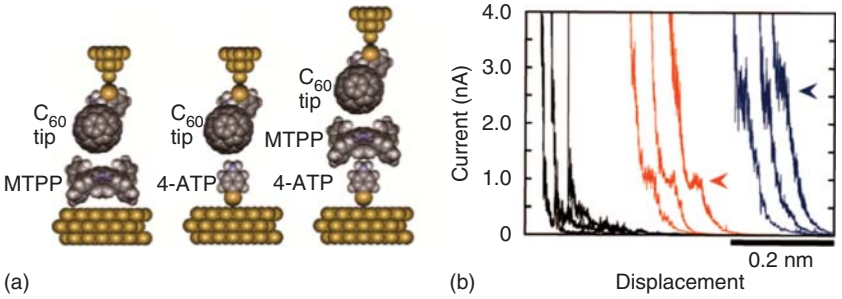

Figure 6.12 Porphyrin–fullerene dyad. (a) Schematic illustration of molecular junctions created using a C_{60} tip. (b) Representative *I–z* traces for the molecular junctions presented in (a). Source: Reprinted with permission from Bui et al. [46]. Copyright 2000, Springer Nature.

shown in Figure 6.12. In addition, a rectification was obtained under the opposite bias voltage.

Another widely investigated complex is related to the thiophene-based materials. Vezzoli et al. studied the electron transport properties of the dialkylterthiophene/dialkylbenzene–tetracyanoethylene (TCNE) complexes via an STM-BJ technique [47]. The conductance increased significantly with formation of the dialkylterthiophene/dialkylbenzene–TCNE charge-transfer complexes. They attributed the enhanced conductance properties to the Fano resonance generated near the metal electrodes' Fermi level.

References

1 Balzani, V., Credi, A., and Venturi, M. (2006). *Molecular Devices and Machines: A Journey into the Nanoworld*. Wiley.
2 Lehn, J.-M. (1995). *Supramolecular Chemistry*. Weinheim, Germany: Wiley-VCH.
3 Chang, S., He, J., Kibel, A. et al. (2009). Tunnelling readout of hydrogen-bonding-based recognition. *Nat. Nanotechnol.* 4: 297–301.
4 Zhang, J., Chen, P., Yuan, B. et al. (2013). Real-space identification of intermolecular bonding with atomic force microscopy. *Science* 342: 611–614.
5 He, G., Li, J., Ci, H. et al. (2016). Direct measurement of single-molecule DNA hybridization dynamics with single-base resolution. *Angew. Chem. Int. Ed.* 128: 9036–9040.
6 Nishino, T., Hayashi, N., and Bui, P.T. (2013). Direct measurement of electron transfer through a hydrogen bond between single molecules. *J. Am. Chem. Soc.* 135: 4592–4595.
7 Nishino, T. and Bui, P.T. (2013). Direct electrical single-molecule detection of DNA through electron transfer induced by hybridization. *Chem. Commun.* 49 (33): 3437.
8 Zhou, C., Li, X., Gong, Z. et al. (2018). Direct observation of single-molecule hydrogen-bond dynamics with single-bond resolution. *Nat. Commun.* 9: 807.

9 Wang, X., Gao, L., Liang, B. et al. (2015). Revealing the direct effect of individual intercalations on DNA conductance toward single-molecule electrical biodetection. *J. Mater. Chem. B* 3: 5150–5154.

10 Wu, S., González, M.T., Huber, R. et al. (2008). Molecular junctions based on aromatic coupling. *Nat. Nanotechnol.* 3: 569.

11 Li, C., Stepanenko, V., Lin, M.J. et al. (2013). Charge transport through perylene bisimide molecular junctions: An electrochemical approach. *Phys. Stat. Sol. B* 250: 2458–2467.

12 Yang, Y., Liu, J., Feng, S. et al. (2016). Unexpected current–voltage characteristics of mechanically modulated atomic contacts with the presence of molecular junctions in an electrochemically assisted–MCBJ. *Nano Res.* 9: 560–570.

13 Yang, Y., Chen, Z., Liu, J. et al. (2011). An electrochemically assisted mechanically controllable break junction approach for single molecule junction conductance measurements. *Nano Res.* 4: 1199–1207.

14 Kaliginedi, V., Moreno-García, P., Valkenier, H. et al. (2012). Correlations between molecular structure and single-junction conductance: a case study with oligo(phenylene-ethynylene)-type wires. *J. Am. Chem. Soc.* 134: 5262–5275.

15 Zheng, J.-T., Yan, R.-W., Tian, J.-H. et al. (2016). Electrochemically assisted mechanically controllable break junction studies on the stacking configurations of oligo(phenylene-ethynylene)s molecular junctions. *Electrochim. Acta* 200: 268–275.

16 Martín, S., Grace, I., Bryce, M.R. et al. (2010). Identifying diversity in nanoscale electrical break junctions. *J. Am. Chem. Soc.* 132: 9157–9164.

17 Frisenda, R., Janssen, V.A.E.C., Grozema, F.C. et al. (2016). Mechanically controlled quantum interference in individual π-stacked dimers. *Nat. Chem.* 8: 1099–1104.

18 Chen, L., Wang, Y.-H., He, B. et al. (2015). Multichannel conductance of folded single-molecule wires aided by through-space conjugation. *Angew. Chem. Int. Ed.* 54: 4231–4235.

19 Sikes, H.D., Smalley, J.F., Dudek, S.P. et al. (2001). Rapid electron tunneling through oligophenylenevinylene bridges. *Science* 291: 1519–1523.

20 Xing, Y., Park, T.-H., Venkatramani, R. et al. (2010). Optimizing single-molecule conductivity of conjugated organic oligomers with carbodithioate linkers. *J. Am. Chem. Soc.* 132: 7946–7956.

21 Arroyo, C.R., Tarkuc, S., Frisenda, R. et al. (2013). Signatures of quantum interference effects on charge transport through a single benzene ring. *Angew. Chem. Int. Ed.* 125: 3234–3237.

22 Batra, A., Kladnik, G., Vázquez, H. et al. (2012). Quantifying through-space charge transfer dynamics in π-coupled molecular systems. *Nat. Commun.* 3: 1086.

23 Seferos, D.S., Blum, A.S., Kushmerick, J.G., and Bazan, G.C. (2006). Single-molecule charge-transport measurements that reveal technique-dependent perturbations. *J. Am. Chem. Soc.* 128 (34): 11260.

24 Schneebeli, S.T., Kamenetska, M., Cheng, Z. et al. (2011). Single-molecule conductance through multiple π–π-stacked benzene rings determined

with direct electrode-to-benzene ring connections. *J. Am. Chem. Soc.* 133: 2136–2139.

25 Molina-Ontoria, A., Wielopolski, M., Gebhardt, J. et al. (2011). [2,2′]Paracyclophane-based π-conjugated molecular wires reveal molecular-junction behavior. *J. Am. Chem. Soc.* 133: 2370–2373.

26 Kiguchi, M., Tal, O., Wohlthat, S. et al. (2008). Highly conductive molecular junctions based on direct binding of benzene to platinum electrodes. *Phys. Rev. Lett.* 101: 046801.

27 Yamauchi, Y., Yoshizawa, M., Akita, M. et al. (2009). Engineering double to quintuple stacks of a polarized aromatic in confined cavities. *J. Am. Chem. Soc.* 132: 960–966.

28 Kiguchi, M., Takahashi, T., Takahashi, Y. et al. (2011). Electron transport through single molecules comprising aromatic stacks enclosed in self-assembled cages. *Angew. Chem. Int. Ed.* 50: 5708–5711.

29 Fujii, S., Tada, T., Komoto, Y. et al. (2015). Rectifying electron-transport properties through stacks of aromatic molecules inserted into a self-assembled cage. *J. Am. Chem. Soc.* 137: 5939–5947.

30 Kiguchi, M., Inatomi, J., Takahashi, Y. et al. (2013). Highly conductive $[3 \times n]$ gold-ion clusters enclosed within self-assembled cages. *Angew. Chem. Int. Ed.* 52: 6202–6205.

31 Coulston, R.J., Onagi, H., Lincoln, S.F. et al. (2006). Harnessing the energy of molecular recognition in a nanomachine having a photochemical on/off switch. *J. Am. Chem. Soc.* 128: 14750–14751.

32 Natali, M. and Giordani, S. (2012). Molecular switches as photocontrollable "smart" receptors. *Chem. Soc. Rev.* 41: 4010–4029.

33 Stucky, G.D. and Mac Dougall, J.E. (1990). Quantum confinement and host/guest chemistry: Probing a new dimension. *Science* 247: 669–678.

34 Zhang, W., Gan, S., Vezzoli, A. et al. (2016). Single-molecule conductance of viologen–cucurbit[8]uril host–guest complexes. *ACS Nano* 10: 5212–5220.

35 Kiguchi, M., Nakashima, S., Tada, T. et al. (2012). Single-molecule conductance of π-conjugated rotaxane: new method for measuring stipulated electric conductance of π-conjugated molecular wire using STM break junction. *Small* 8: 726–730.

36 Xiao, X.Y., Xu, B.Q., and Tao, N.J. (2004). Changes in the conductance of single peptide molecules upon metal-ion binding. *Angew. Chem. Int. Ed.* 43: 6148–6152.

37 Guo, X., Small, J.P., Klare, J.E. et al. (2006). Covalently bridging gaps in single-walled carbon nanotubes with conducting molecules. *Science* 311: 356–359.

38 Cao, Y., Dong, S., Liu, S. et al. (2012). Building high-throughput molecular junctions using indented graphene point contacts. *Angew. Chem. Int. Ed.* 51: 12228–12232.

39 Wen, H.M., Li, W.G., Chen, J.W. et al. (2016). Complex formation dynamics in a single-molecule electronic device. *Sci. Adv.* 2: e1601113.

40 Jia, C., Li, H., Jiang, J. et al. (2013). Interface-engineered bistable [2]rotaxane-graphene hybrids with logic capabilities. *Adv. Mater.* 25: 6752–6759.

41 Anderson, P., Lee, P., and Saitoh, M. (1973). Remarks on giant conductivity in TTF–TCNQ. *Solid State Commun.* 13: 595–598.
42 Alves, H., Molinari, A.S., Xie, H. et al. (2008). Metallic conduction at organic charge-transfer interfaces. *Nat. Mater.* 7: 574–580.
43 García, R., Herranz, M.Á., Leary, E. et al. (2015). Single-molecule conductance of a chemically modified, π-extended tetrathiafulvalene and its charge-transfer complex with F_4TCNQ. *Beilstein J. Org. Chem.* 11: 1068–1078.
44 Kumar, A., Banerjee, K., Dvorak, M. et al. (2017). Charge-transfer-driven nonplanar adsorption of F_4TCNQ molecules on epitaxial graphene. *ACS Nano* 11: 4960–4968.
45 Nishino, T., Ito, T., and Umezawa, Y. (2005). A fullerene molecular tip can detect localized and rectified electron tunneling within a single fullerene–porphyrin pair. *Proc. Natl. Acad. Sci. U. S. A.* 102: 5659–5662.
46 Bui, P.T., Nishino, T., Yamamoto, Y. et al. (2013). Quantitative exploration of electron transfer in a single noncovalent supramolecular assembly. *J. Am. Chem. Soc.* 135: 5238–5241.
47 Vezzoli, A., Grace, I., Brooke, C. et al. (2015). Gating of single molecule junction conductance by charge transfer complex formation. *Nanoscale* 7: 18949–18955.

7

Characterization Techniques for Molecular Electronics

The typical methods for characterizing molecular electronic devices are presented in Table 7.1. Each method has its own unique advantages and falls into five primary categories: microscopic, electrochemical, electrical, optical, and optoelectronic. The microscopic methods for molecular electronics have been discussed in Chapters 1–6, and the electrochemical technique is regarded as a classic method, thus falling beyond our primary interest. Here, we mainly address the electrical techniques characterizing the intrinsic optoelectronic properties of individual molecules, including inelastic electron tunneling spectroscopy (IETS), temperature–length–variable transport measurement, noise spectroscopy, transition voltage spectroscopy (TVS), thermoelectricity, and optoelectronic spectroscopy.

7.1 Inelastic Electron Tunneling Spectroscopy

In molecular junctions, the optical spectroscopy has not yet been used as a standard tool for two main reasons: (i) in a conventional vertical metal–molecule–metal device structure, it is difficult for light to penetrate through a metal electrode to probe the molecular layer, and (ii) the sample is as small as a single molecule, implying a small signal-to-noise ratio [18]. IETS, which is associated with the interaction between the transporting electrons and the molecular vibrations, is relatively suitable for a small gap, making it a primary characterization technique to identify the chemical species and supply the fingerprint information of molecular junctions [19–21]. The IETS can make an unambiguous determination of the molecular species in the junction because the impurities (such as nanoparticles) present completely different IETS features in comparison with the target molecules. Furthermore, it has an ultrahigh sensitivity to the molecular conformation and the contact geometry of the molecular junctions. By using sophisticated comparisons between the experiments and the theoretical computations, the IETS can be more useful for characterizing numerous aspects of the molecular junctions, such as the conformation of molecules, orientation of molecules, and electronic pathways [19]. Additionally, the IETS is not subject to the selection rules as infrared (IR) or Raman spectroscopy. Both IR- and Raman-active vibrational modes can appear in the IETS. These advantages prove

Molecular-Scale Electronics: Concept, Fabrication and Applications,
First Edition. Xuefeng Guo, Dong Xiang, and Yu Li.

Table 7.1 Typical methods for characterizing molecular electronic devices.

Techniques	Methods	Primary functions	References
Microscopy	Scanning tunneling microscopy	Image, carrier transport properties	[1]
	Atomic force microscopy	Conductance, nanolithography	[2]
	Scanning electron microscopy	Surface topography, component properties	[3]
Electrochemistry	Cyclic voltammetry	Redox potential, electrochemical reaction	[4]
	AC impedance spectroscopy	Density and resistance of molecule layer	[5]
	Chronocoulometry	Electrode surface area, concentration	[6]
Electrical	Inelastic electron tunneling spectroscopy (IETS)	Fingerprint information of molecules	[7]
	Length–temperature variation	Electron transport mechanism	[8]
	Noise spectroscopy	Localized states, transmitting channels	[9]
	Transition voltage spectroscopy	Energy level alignments	[10]
	Thermoelectricity	Type of charge carriers	[11]
Optical	Enhanced Raman spectroscopy	Structural, vibrational, and polarization	[12]
	Infrared spectroscopy	Vibrational modes, chemical structure	[13]
	Ultraviolet–visible spectroscopy	Energy gap, rate constant of reaction	[14]
Optoelectronics	X-ray photoelectron spectroscopy	Elemental composition, chemical state	[15]
	Ultraviolet photoelectron spectroscopy	Molecular orbital energies	[16]
	Photoemission spectroscopy	Interface electronic structure, orientation	[17]

that the IETS is a powerful and informative spectroscopic tool that can be used for probing molecular junctions and devices [22, 23].

7.1.1 History and Background

The IETS was initially measured by Jaklevic and Lambe in 1966 [24]. This pioneering study demonstrated that it was possible to obtain the vibrational spectra sandwiched in the Al–Al_2O_3–Pb tunnel junctions and clearly showed the anomalous

peaks in the d^2I/dV^2 versus V curves. In the past two decades, metal–insulator–adsorbate–metal (MIAM) junctions were typically used to study the surface effects on the vibrational modes as well as the electron–phonon interactions in the molecular systems. Another important advance was made in 1998 by Stipe et al. when IETS at a single-molecule level was demonstrated by employing scanning tunneling microscopy (STM) [25]. This technology, known as STM–IETS, is capable of mapping the phonon activation within a molecule adsorbed on a solid surface to perform a type of phonon imaging. It was demonstrated that the vibrational microscopy from the spatial imaging of the inelastic tunneling channels could be further used to distinguish the two isotopes [25, 26]. Recently, it was reported that the IETS could be directly modulated by an external gate voltage. It was found that the IETS was resonantly enhanced in the Au–molecule–Au junctions due to the fact that the transport orbital strongly coupled with the internal vibrational modes upon a gating voltage [7].

Figure 7.1 presents the expected IETS behavior as the applied voltage V_{SD} is increased. When a small negative bias is applied to the left metal electrode, the Fermi level of the left electrode is lifted. When an electron with an occupied state on the left side tunnels into an empty state on the right side with a conserved energy, it is known as an elastic tunneling process [19]. However, if there is a vibrational mode with a frequency of ω localized inside this barrier, and the applied bias is large enough such that $eV \geq \hbar\omega$, then the electron can lose a quantum of energy $\hbar\omega$ to excite the vibrational mode, where $\hbar$ is Planck's constant divided by 2π [20]. In the case of molecular junctions, the transporting electron can deposit $\hbar\omega$ onto the molecule to excite the molecular vibrational mode. This inelastic tunneling process opens an additional transmission channel for the electron, resulting in an increased current. Thus, the total tunneling current shows a nonlinearity characteristic and has a kink at the point ($V_{\hbar\omega} = \hbar\omega/e$). Typically, only a small fraction of electrons inelastically tunnel through the junction due to the small cross section for such an excitation, and thus the nonlinearity in the current only manifests as a small change in the slope of the I–V characteristics.

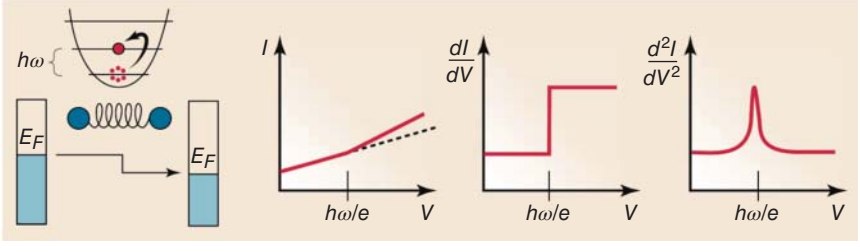

Figure 7.1 The expected inelastic electron tunneling spectroscopy behavior as the applied voltage increases via a vibrational resonance. For a bias energy (eV) larger than the vibrational energy ($\hbar\omega$), the transporting electron can deposit $\hbar\omega$ onto the molecule to excite the molecular vibration mode. Then, an additional transmission channel is open, resulting in a current increase. The change caused by opening the vibrational resonance channel at $eV_{sd} = \hbar\omega$ becomes a step in the differential conductance (dI/dV) plot and a peak in the d^2I/dV^2 plot. A plot of d^2I/dV^2 versus V is typically referred to as the IETS spectrum. Source: Reprinted with permission from Galperin et al. [18]. Copyright 2008, AAAS.

It is more common to plot the differential conductance ($\mathrm{d}I/\mathrm{d}V$ versus V) curve, allowing the steps at $V_{\hbar\omega}$ to be observed, where each phonon mode is activated. A popular way to display the data is to plot the trace as $\mathrm{d}^2I/\mathrm{d}V^2$ versus V, in which the peaks at $V_{\hbar\omega}$ can be clearly observed.

7.1.2 IETS Measurement

The IETS signal can be obtained by a mathematical differential approach that computes the numerical derivatives of the directly measured I–V curves [27, 28]. However, this method is generally not easily achieved in practice due to insufficient signal-to-noise ratios or limited resolutions of the instrumentation used to acquire the data. In practice, the IETS signal, which is proportional to the second derivative of the I–V curve, can be directly measured by an AC modulation method by employing a lock-in amplifier [29, 30]. In this strategy, a small AC voltage with a certain frequency ω is superimposed on the main DC bias so that the current can be written as follows:

$$IV = I(V_{\mathrm{DC}} + V_{\mathrm{AC}}\cos(\omega t)) \tag{7.1}$$

By using the Taylor series expansion about V_{DC}, the expression can be obtained as follows:

$$I(V) = I\left(V_{\mathrm{DC}} + \left.\frac{\mathrm{d}I}{\mathrm{d}V}\right|_{V_{\mathrm{DC}}} V_{\mathrm{AC}}\cos(\omega t) + \frac{1}{2}\left.\frac{\mathrm{d}^2I}{\mathrm{d}V^2}\right|_{V_{\mathrm{DC}}} [V_{\mathrm{AC}}\cos(\omega t)]^2 + \ldots \right. \tag{7.2}$$

This equation can be rewritten by using a trigonometric double angle formula as follows:

$$I(V) = I\left(V_{\mathrm{DC}} + \left.\frac{\mathrm{d}I}{\mathrm{d}V}\right|_{V_{\mathrm{DC}}} V_{\mathrm{AC}}\cos(\omega t) + \frac{1}{4}\left.\frac{\mathrm{d}^2I}{\mathrm{d}V^2}\right|_{V_{\mathrm{DC}}} [V_{\mathrm{AC}}^2\cos(2\omega t)] + \ldots \right. \tag{7.3}$$

Thus, by measuring the output of the system at the frequency ω as the DC bias is slowly swept, a signal that is directly proportional to $\mathrm{d}I/\mathrm{d}V$ can be obtained, i.e. the differential conductance. Moreover, by measuring the output at 2ω, it is possible to directly obtain the IETS spectrum [20, 30]. So far, the AC modulation technique by using a lock-in amplifier is very popular for the IETS measurement [7, 25].

To verify that the observed spectra are indeed valid IETS data, the line width broadening can be examined as a function of modulation voltage and temperature [25, 31]. The full width at the half maximum (FWHM) of the $\mathrm{d}^2I/\mathrm{d}V^2$ vibrational peak can be written as follows:

$$V = [(1.7V_{\mathrm{m}})^2 + (5.4kT/e)^2 + W^2]^2 \tag{7.4}$$

where V_{m} is the AC modulation voltage; k is the Boltzmann constant; T is the temperature; and W is the intrinsic line width, which can be determined from a fit to the modulation broadening data [25]. Based on this formula, it can be determined that the line width will increase as the temperature and the modulation voltage increase.

The IETS has been measured on different test platforms, and each platform demonstrates its own unique features and limitations. The first focused IETS experimental study on adsorbed molecules was performed based on Al–Al_2O_3–Pb tunnel junctions [24, 30]. The fabrication of this MIAM tunnel junction is summarized elsewhere [30]. Based on this type of molecular junctions, the relationships between the IETS, IR, and Raman spectroscopies were revealed, noting that the IETS is a new vibrational spectroscopy complementary to the IR and Raman spectroscopies, but governed by different selection rules that allow optically forbidden transitions to be easily observed [30, 32, 33]. However, the tunnel current was relatively small in this type of molecular junctions due to the effects of the insulation layer, which decrease the sensitivity of the IETS. To overcome this problem, the IETS measurements were directly performed in the metal–molecule–metal junctions [31, 34, 35]. For example, Wang et al. reported the IETS measurements for metal–molecule–metal junctions fabricated by using the nanopore strategy, in which the effects arising from the insulation layer were avoided [31]. However, the yield of forming the nanopore junctions was relatively low due to the penetration of metal atoms into the molecular layer, which may short the junctions. One of the most fruitful techniques for the IETS measurement arose from the pioneering work of Gregory, in which a metal junction between two crossed wires was delicately made, and the distance between the two wires could be adjusted via a deflecting Lorentz force [36]. One main feature of this crosswire platform is that the distance between the two wires is adjustable, and the filament can be completely avoided. Kushmerick et al. demonstrated that the reproducible molecular junctions could be formed by using this method with a sufficient stability for clear IETS measurements and selection rule investigations [34, 37, 38]. Yoon et al. further demonstrated that the crossed nanowire molecular junction was a versatile and highly scalable device platform, which allowed a direct correlation between the junction conduction properties and the molecular structure by using both the IETS and surface-enhanced Raman scattering (SERS) on the same junction [39]. However, in practice, it is not easy to obtain the IETS signal of exact single molecules due to the large surface area of the crossed wires. The first definite observation of the IETS for a single molecule was obtained in the STM platform [40, 41]. In the STM implementation of the IETS, the junction was formed by using a sharp metallic tip, a vacuum gap, and a surface with the adsorbed molecules. By using this STM–IETS approach, elegant imaging and vibrational spectroscopic studies on a single molecule can be performed simultaneously [42, 43]. Another advantage of the STM–IETS method is that the changes in the conductance and the vibrational modes of a single molecule can be simultaneously recorded when the junction is stretched [44]. Despite this great achievement, the vibrational spectroscopy by using STM has met the challenge because the extreme mechanical stability is needed to suspend the small changes in the tunneling currents. For example, the tunneling physics requires a tunneling gap stability of 0.01 Å to maintain a stable conductance within 2%, which is a difficult target for STM due to the piezo drift [25]. To obtain a reproducible IETS signal at the single-molecule level, the IETS of single molecules was performed in the molecular junctions fabricated by

the electromigration method [45–47], in which the mechanical stability was guaranteed by sacrificing the adjustable gap size. Recently, the IETS signals were obtained based on the mechanically controllable break junctions (MCBJs) by several groups [48–50], in which both the mechanical stability and the adjustable gap size were available. However, it is impossible to obtain a photographic image via the MCBJ platform in comparison with that achieved by STM. Therefore, each platform for the IETS has its own unique advantages and disadvantages, and several intrinsic and interesting molecular properties were revealed, as discussed in Section 7.1.3.

It is relatively easy to obtain the IETS with certain molecular junctions. However, it is difficult to directly determine which vibrations occur in the IETS, i.e. which part of the molecules primarily contributes to the IETS signal. One point of view is that the IETS signal originates mainly from the molecular parts closest to the electrodes [38]. To accurately investigate which vibrational modes are active in the IETS, Okabayashi et al. introduced the isotope labeling of alkanethiols with specifically synthesized isotopically substituted molecule [21, 51–54]. They systematically deuterated different parts of the alkanethiol ($CD_3(CH_2)_7S$, $CH_3(CH_2)_6CD_2S$, and $CD_3(CD_2)_7S$). Subsequently, the IETS was systematically measured with these partially and fully deuterated self-assembled monolayers (SAMs). It was revealed that the IETS weights of the peaks [F (ν[C–C]), K (CH_2 wagging), and L (CH_2 scissoring)] did not change appreciably with the deuteration of the CH_2 closest to the sulfur atom ($CH_3(CH_2)_6CD_2S$). Supported by the first principle calculations, they provided unambiguous assignments of the IETS peaks and demonstrated the minimal site-selectivity for the IETS measurement, i.e. the terminal groups provided almost the same contribution to the IETS signals as the middle part of the molecules, thus providing new insights into the electron transport through molecules [54].

It should be noted that the IETS features may be reversed, i.e. the peaks could be transited to the dips within the same type of molecular junctions. The IETS measurement is extremely sensitive to the electrode–molecule coupling, and the IETS contribution to the current is strongly dependent on the transmission of the junction [55]. It is known that the transmission of the junction is influenced by the strength of the electrode–molecule coupling, which is dependent on both the tilted angle of the molecule and the binding site of the end group. In the low transmission regime, the possibility of inelastic charge transport can result in an enhanced probability of forward scattering, which leads to a positive contribution to the current. However, in the range of higher transmissions, the electron back scattering increases due to a momentum transfer to the excited mode, leading to a negative contribution to the current [56, 57]. Hence, in the low-conductance tunneling regime, the inelastic excitations appear as the peaks in the IETS feature. Conversely, the excitation of the vibrational modes results in the dips in the IETS when the transmission exceeds the threshold transmission value. This varied IETS contribution to the current in the different conductance regimes (high or low conductance) was revealed by Kim et al. [58]. In their experiments, the electrode–molecule coupling was changed by mechanically stretching or pushing the molecular junctions by using a low-temperature MCBJ technique. By tuning the transmission probability via stretching the

benzenedithiol (BDT) molecular junctions, they observed reversed contributions of vibronic excitations on the charge transport, i.e. an anti-symmetry IETS feature in the low- and high-conductance regimes [58]. This transition from a peak to a dip was also carefully observed in single octanedithiol molecular junctions by Hihath et al. based on the STM technique [59]. Their experiments and analysis provided a considerable contribution to the development of the IETS measurement as well as the theory interpretation.

7.1.3 IETS Applications

An ongoing challenge for single-molecule electronics is to understand the molecular conformation and the local geometry at the molecule–surface interface. Typically, it is an extreme challenge to acquire such information inside the junction by most of the characterization techniques [19]. The IETS probes the electron–phonon interactions in the molecular junctions, which are in turn extremely sensitive to the changes in the molecular geometry and the molecular conformation. Therefore, the IETS can be a powerful tool for studying the molecular and metal contact geometries in molecular electronic devices [60, 61], such as the orientation of the adsorbed molecules [62, 63] and the tilted angle at the interface [31]. By comparing the calculated spectra with the experimental results, the most likely conformations of the molecule under different experimental conditions can be successfully determined [64]. With the help of the theoretical calculations, it becomes possible to fully understand and assign the complicated experimental IETS and, more importantly, provide the structural information of molecular electronic devices [23, 65].

Single-molecule inelastic tunneling investigations not only provide the molecular structure as well as the interfacial information but can also be used to generate real-space imaging of the molecular structure and the chemical bonding. Ho's group, who first performed the single-molecule IETS measurement [25], recently demonstrated an approach based on the STM technique to image the skeletal structure and bonding in an adsorbed molecule by using a single-molecule inelastic tunneling probe [66]. They constructed a novel inelastic tunneling probe based on STM to sense the local potential energy landscape of an adsorbed molecule with a carbon monoxide CO-terminated tip. As the CO-terminated tip scanned over the molecule during imaging, the changes in the energy and intensity of the hindered translational vibration of CO were measured by the IETS. This low-energy CO vibration sensed the spatially-varying potential energy landscape of the molecule and its surroundings. The capability of STM to image the molecular structure and chemical bonds broadens its previous applications to determine the electronic and vibrational properties of single molecules.

The switching mechanism in molecular junctions can be identified by the IETS. To date, various possible mechanisms for conductance switching behavior have been proposed, including oxidation/reduction of molecules [67], rotation of functional groups [68], interactions with neighbor molecules [69], fluctuation of bonds [70], and effects of molecule–metal hybridization [71]. However, the lack of a proper characterization tool to determine the exact structure of the

molecular junctions makes it difficult to distinguish the different switching mechanisms. Fortunately, the IETS has proven to be extremely useful in distinguishing the mechanisms by comparing the theoretical and experimental IETS [72–75]. For example, Cao et al. conducted hybrid density functional theory calculations for the IETS of an oligoaniline dimer dithiolate junction. Both the conjugation changes and the oxidation effects on the IETS have been demonstrated. The comparison between the calculated IETS and the experimental spectra confirmed that the observed conductance switching was most likely induced by the conjugation change rather than the oxidation [74]. Hihath et al. observed that the conductance switching occurring in a single octanedithiol molecular junction was approximately a factor of 2 [59]. More interestingly, it was determined that although the general features of the inelastic electron tunneling (IET) spectrum in this junction were the same before and after switching, the energies of certain peaks for this single molecule junction could be either blue or red-shifted after the conductance change, thus implying a small reorganization of the entire junction structure [59]. This finding revealed that conductance switching could result from a change in geometry. The IETS was further used to reveal the detailed switching information under light irradiation. Azobenzene-derivative molecules can change their conformation due to a cis–trans transition when exposed to ultraviolet or visible light irradiation. Kim et al. demonstrated that the cis–trans isomers possessed unambiguously different IETS fingerprints, which enabled an alternative technique for identifying the state of the azobenzene-based molecular switches [76]. Additionally, the IETS was used to reveal the switching mechanism due to the effects of hydration on the molecular junctions. In a pioneering study, Long et al. used magnetically assembled microsphere junctions incorporating thiol monolayers to reveal the current change mechanism when the junction was exposed to air [75]. A prominent S–H stretching vibration mode was observed, and the Au–S mode was missing in the IETS after the device was exposed to air. These results indicate that upon exposure to air, the water molecules are rapidly associated with the electronegative thiolate moiety, thus disrupting the Au—S bond to the electrode and decreasing the current. These detrimental effects on molecular conduction revealed by the IETS are important for understanding the electron transport through gold–thiol molecular junctions once exposed to atmospheric conditions.

The IETS was further used to elucidate the transport mechanisms in the molecular junctions. Hihath et al. performed I–V measurements as well as IETS measurements on the diode molecule [77]. They found that the current rectification occurred at relatively low biases, indicating a significant change in the elastic transport pathway. Interestingly, the peaks in the IETS were symmetric around the zero bias and depicted no significant changes in shape or intensity in the forward or reverse bias directions. This result indicated that despite the change in the elastic transmission probability, there is little impact on the inelastic pathway in a diode molecule. In another example, Tao and coworkers observed simultaneous changes in the conductance and vibrational modes of a single molecule as the junctions were stretched [44, 78]. By using the STM technique, the vibrational modes in a single molecule junction were measured, and the differential

conductance was recorded as the strain in the junction was changed by separating the two electrodes. This unique approach allowed the changes in the conductance to be correlated with the changes in the configuration of a single molecule junction. This approach opened up a new door of better understanding of the relationship between the molecular conductance, electron–phonon interactions, and the configuration. This approach was latterly employed in the MCBJ experiments for revealing the molecule–electrode contact as well as the information of the molecular conformation change [76, 79–81]. A case in point is that the different behavior of the thiol-ended and amine-ended molecular junctions was systemically examined by Kim et al. [80] The vibrational modes ν (Au–S) and ν (Au–N) in the IETS while increasing the electrode separation were compared. The comparison indicated that the ν (Au–S) mode was extremely stable, and no significant changes in the vibrational energy were observed during the stretching of the Au–ODT–Au, junction. Conversely the energy of the ν (Au–N) mode in the Au–ODA–Au junction was red-shifted while increasing the electrode separation. This behavior was consistent with an increase in the Au—N bond length due to its weak bond strength going along with the reduction of the force constant. The IETS measurements provided unambiguous evidence that the Au—N bond was weaker than the Au—S bond. Combined with the conductance trace measurement during stretching (the conductance plateau of the thiol-ended octane junctions was significantly longer than that of the amine-ended octane junctions), it was demonstrated that for amine-ended molecular junctions, no atomic chains were pulled under stretching, whereas the Au electrodes were strongly deformed for the thiol-ended molecular junctions. By characterizing the molecular vibrational modes and the metal-phonon modes in alkanedithiol molecular junctions with mechanically controlled nanogaps and an electrode material variation strategy, Kim et al. further demonstrated that the effects of the contact geometry and the molecular conformation on the IETS could be distinguished [82].

By using the IETS technique, the quantum interference as the electron transports through molecular junctions can be investigated [83]. In most theoretical studies, only the elastic contributions to the current are considered. For molecules with a destructive quantum interference, the elastic current is effectively blocked, leading to a suppressed level of the elastic current. This allows the inelastic contributions to the current carried by vibrations to become important. Lykkebo et al. calculated the IETS of cross-conjugated molecules, which exhibited a destructive quantum interference. They found that the inelastic contribution to the current was larger than that for molecules without interference, and the overall behavior of the molecule was dominated by the quantum interference feature [83]. Furthermore, they predicted that the overtone modes (several small peaks besides the typical vibration modes) should be present in the IETS of the cross-conjugated molecules, although the overtone modes were generally thought to not exist. They studied the origin of the overtones and revealed that the interference features in these molecules were the key ingredient.

Although the IETS technique possesses many merits and becomes a powerful method for characterizing molecular junctions, there are still several obstacles that limit its further applications. Firstly, the IETS requires cryogenic

temperatures (typically liquid He) for an experimental investigation to suppress the thermal effect, which is unavailable in most laboratories. Secondly, only certain specific vibrational modes can be detected in a given molecule, partly due to the low signal-to-noise ratio in the IETS measurements [38, 84]. Additionally, certain modes arising from the backbone may be masked by modes arising from the large anchoring groups [85]. Thirdly, the analysis of the IETS is not always unambiguous, especially for systems with a large number of nuclei and numerous bonds, i.e. there are a large number of possible modes that can result in the peaks for molecules containing many atoms [86]. Finally, discrepancies and device-to-device variations may occur in the IETS data, which can originate from defects in the molecular junctions and other elements, such as insulating walls introduced during the device fabrication process and from the particular junction structure [87].

7.2 Temperature–Length–Variable Transport Measurement

The temperature–length–variable transport measurement in molecular junctions, i.e. performing the electrical measurement with a variable molecular length or under different temperatures, is a useful technique for revealing the transport mechanism as electrons transport through the molecular junctions [8, 88]. The conduction mechanisms listed in Table 7.2 indicate their characteristic relationships between the current density (J), temperature, and voltage. Based on whether thermal activation is involved, the conduction mechanisms can generally be classified in two distinct categories: (i) direct tunneling or Fowler–Nordheim tunneling, which does not have temperature-dependent electrical behavior; and (ii) thermionic or hopping conduction, in which the electrical responses are strongly dependent on the temperature [89].

Table 7.2 Types and mechanisms of conduction.

Conduction mechanism [89, 90]	Current density (J)	Temperature dependence	Voltage dependence
Direct tunneling (low bias)	$J \sim V \exp(-)\frac{2d}{\hbar}\sqrt{2m\Phi}$	None	$J \sim V$
Fowler–Nordheim tunneling	$J \sim V^2 \exp\left(-\frac{4d\sqrt{2m}\Phi^{3/2}}{3q\hbar V}\right)$	None	$\ln\left(\frac{J}{V^2}\right) \sim \frac{1}{V}$
Thermionic emission	$J \sim T^2 \exp\left(-\frac{\Phi - q\sqrt{qV/4\pi\epsilon d}}{kT}\right)$	$\ln\left(\frac{J}{T^2}\right) \sim \frac{1}{T}$	$\ln(J) \sim V^{1/2}$
Hopping conduction	$J \sim Vd \exp\left(-\frac{\Phi}{kT}\right)$	$\ln\left(\frac{J}{V}\right) \sim \frac{1}{T}$	$J \sim$ V
Space–charge-limited conduction	$J \sim V^2/d^3$	None	$J \sim V^n$

The tunneling mechanism is often refer as "non-resonant," in which the tunneling electron energies do not exactly match with the molecular orbital energies [90]. For the sufficiently short conjugated molecules, the electrons can pass through the molecular junctions via a tunneling process, i.e. an electron crosses the molecular junctions in a single step without an appreciable residence time on the molecules. In this case, the junction resistance can increase exponentially with the molecular length as follows [8]:

$$R = R_0 \exp(\beta d) \tag{7.5}$$

where R_0 is the effective contact resistance; d is the molecular length; and β is a structure-dependent tunneling attenuation factor depending on the effective tunneling barrier height. The tunneling barrier height is often approximated as the energy difference between the Fermi level of the electrodes (E_F) and the closest molecular frontier orbital (e.g. E_{HOMO} or E_{LUMO}).

Conversely, the hopping construction mechanism is a "resonant" process, in which charges can be injected into the frontier orbitals of the wired molecules and transported by an incoherent hopping mechanism. In other words, the electron first enters into the molecular orbitals from the source electrode and then drifts through a series of discrete steps to reach the drain electrode [91]. For longer conjugated molecular wires at moderate temperatures, the tunneling process is strongly suppressed, and the thermally activated hopping transport is often dominated [92]. The activation energy (E_a) corresponds to the energy required to reach the transition state for the electron transfer within the molecule. The resistance can be predicted to be linearly dependent on the molecular length as follows [90]:

$$R = R_0 + \alpha d = \alpha_\infty \, d \, \exp\left(-\frac{E_a}{kT}\right) \tag{7.6}$$

where R_0 is the contact resistance; d is the molecule length; k is the Boltzmann constant; and T is the temperature. In this equation, $\exp(-E_a/kT)$ can be regarded as a molecular specific parameter presenting a unit resistance per unit length. Based on Eqs. (7.5) and (7.6), the R versus d data can be used to determine the transport mechanism, i.e. if the dependence on d is exponential, then the mechanism is likely tunneling, and if it is linear, then it is likely hopping. Additionally, the temperature dependence of R can be used to confirm the transport mechanism.

Frisbie and coworkers first provided direct evidence for a change in the transport mechanism from tunneling to hopping in oligophenyleneimine (OPI) molecular junctions [8]. They used a conducting atomic force microscopy (AFM) to contact the OPI molecular wires, which grew from a substrate-controlled aryl imine addition chemistry. It was demonstrated that near 4 nm in length, the mechanism of transport in the wires changed from tunneling to hopping, as evidenced by the striking changes in the length, temperature, and electric field dependence of the current–voltage (I–V) characteristics. As shown in Figure 7.2, the resistance was exponentially dependent on the molecular length ($\beta \sim 3.0\,\text{nm}^{-1}$) for short molecular wires (OPI 1–OPI 4). However, there was a much flatter resistance versus molecular length relation ($\beta \sim 0.9\,\text{nm}^{-1}$) for long molecule wires (OPI 5–OPI 10). Furthermore, from a plot of R versus d,

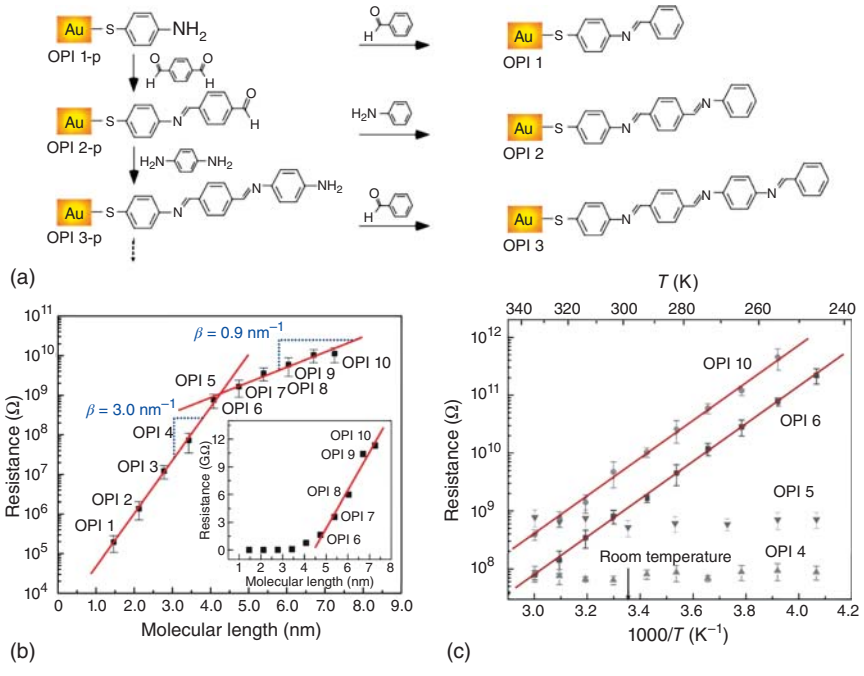

Figure 7.2 Measurements of the molecular wire resistance with CP-AFM. (a) Molecular structure and synthetic route to OPI-p and OPI monolayers on gold substrates. (b) Semi-log plots of *R* versus *L* for the gold/wire/gold junctions. Straight lines are linear fits based on Eq. (7.5). Inset: A linear plot of *R* versus *L*, demonstrating that the resistance is linearly dependent on the molecular length for long OPI wires. (c) Arrhenius plots for OPI 4, OPI 5, OPI 6, and OPI 10. Straight lines are linear fits to the data, demonstrating that the resistance is strongly dependent on temperature for long OPI wires. Source: Reprinted with permission from Choi et al. [8]. Copyright 2008, AAAS.

as depicted in the inset of Figure 7.2b, it was determined that the resistance was linearly dependent on length for long wires, indicating a hopping transport mechanism. This change in the transport mechanism was confirmed by measuring the resistance versus temperature, i.e. the resistance is independent of temperature for short wires and strongly affected by temperature for long wires.

Frisbie and coworkers further performed length-dependent conduction measurements and temperature-dependent conduction measurements for oligonaphthalenefluoreneimine (ONI) wires [93], oligophenylenetriazole (OPT) wires [94], and oligotetrathiafulvalene-pyromelliticdiimide-imine (OTPI) wires [95] to better understand the change in the transport mechanisms. They observed the transition from tunneling to hopping at approximately 4–5 nm for ONI, OPT, and OTPI, which was a similar distance to that of the OPI molecules [93, 94]. Inspired by Frisbie and coworkers' research, the length–temperature–variable transport measurement has become a popular technique for distinguishing the transition of the transport mechanisms [92, 96–98]. It should be noted that the critical point for the transport mechanism transition strongly depends on the molecular structure; for example, Tada and colleagues observed a transition in

the direct current transport from tunneling to hopping at approximately 4.5 nm in single oligothiophene molecular wires [91]. Wang and coworkers revealed that a transition occurred at approximately 2.75 nm for the oligo(*p*-phenylene ethynylene) (OPE) molecular wires [99]. Wandlowski and coworkers determined that a transition from coherent transport via tunneling to a hopping mechanism occurs when the oligo(aryleneethynylene) (OAE) wires are longer than 3 nm. Ferreira et al. examined the conductance of well-defined porphyrin self-assembled molecular wires up to 14 nm in length, thus determining a transition in the conduction regime at 6.5 nm [100].

It should be mentioned that, although a pronounced temperature dependence and a small decay factor are commonly characteristics of hopping, it is reported that coherent tunneling can also lead to the apparent temperature dependence of the conductance in the case of resonance tunneling [101]. In far off-resonance, where the energy dependence of the transmission coefficient is not pronounced, the molecular conductance is nearly temperature-independent. However, in the case of resonant tunneling, the temperature dependence of the Fermi distribution function of the leads can lead to the conductance dependence on temperature [101]. Based on the electrical measurements of single-molecule junctions by using STM, Nichols and coworkers presented that the conductance of oligoporphyrin wires as long as 5–10 nm had a strong dependence on the temperature and a weak dependence on the length of the wires. Although it is widely accepted that such behavior indicates a thermally assisted hopping mechanism, they successfully proved that the observed temperature and length dependences were consistent with coherent tunneling via the density functional theory calculations and an accompanying analytical model [102].

The mechanism of rectification can also be clarified via temperature–length–variable transport measurements. For example, Nijhuis et al. examined the SAMs of alkanethiolates with ferrocene termini by using liquid-metal top electrodes and found that these junctions rectified currents with large rectification ratios [103]. One might assume that this observation was due to the space asymmetry of the junction. However, the temperature-variable transport measurements indicated that the values of the current density (J) were dependent on T at the negative biases but independent of T at the positive biases. This observation indicated that tunneling was the dominant mechanism of the charge transport at the positive biases, whereas hopping was the dominant mechanism of the charge transport at the negative biases. A model was successfully developed to clarify the rectification mechanisms, i.e. the rectification of the Fc-terminated SAMs was due to the charge transport processes that changed with the polarity of the bias: from tunneling (at positive biases) to hopping (at negative biases) [103]. The rectification properties of the ferrocene-alkanethiolate SAMs was also investigated by Jeong et al. [43] using a conductive polymer interlayer between the top electrode and the SAM [104]. Interestingly, it was found that the current density (J) was dependent on the temperature at both the positive and negative biases. Particularly, a decrease in J as the temperature increased was observed at a high positive bias ($V_g > 0.6$ V), which was never observed at the negative bias. This unique feature could not be explained by the change in the transport mechanism (i.e. the change between tunneling and hopping). This observation was attributed

to the redox-induced conformational changes in the ferrocene-alkanethiolates [43].

In addition to tunneling and hopping, several classical mechanisms in the molecular junctions, including thermionic emission, field ionization (i.e. Fowler–Nordheim tunneling), and space-charge-limited conduction, were distinguished via temperature–length–variable transport measurements combined with the I–V measurements. Among these mechanism, the Fowler–Nordheim tunneling is independent of temperature and is predicted to yield a linear plot of $\ln(J/V^2)$ versus $1/V$, where V is the bias voltage. Yan et al. investigated the charge transport in molecular electronic junctions from 4.5 to 22 nm, one of the longest distances reported thus far [105]. They found that hopping is important for thicker films at low electric fields (low bias), whereas field ionization becomes dominant at high electric fields (high bias). This mechanism was consistent with the field-induced ionization of the molecular orbital or the interface states to generate charge carriers. Following the ionization, the empty state could be rapidly refilled from the biased electrode or reorganized to form a new conducting channel.

Generally, it is necessary to perform length-dependence, temperature-dependence, and I–V characteristics measurements to fully determine the transport mechanism [88]. If only length-dependence measurements can be performed, it is still useful for revealing the junction properties because the effective contact resistance R_0, and the tunneling attenuation factor β can be extrapolated from the plots of resistance versus molecular length. Based on the equation, $R = R_0 \exp(\beta d)$, the plots of $\log R$ versus d yield estimates of β from the slope and R_0 from the zero length intercept. A comparison of the R_0 values for different junctions will clearly indicate the relative roles of the contact resistance. Searching for a robust molecular wire that could transport a charge over a long distance (i.e. small β) became one of the major important goals of molecular electronics. Several innovative groups revealed numerous types of molecular wires among the smallest β values, which were able to transport the charge efficiently over long distances [100, 106–108]. Frisbie and coworkers systemically investigated the effects of the linking groups and the metal work function to the factor β [109]. They determined that β was not simply characteristic of the molecular backbone but strongly affected by the number of chemical contacts, i.e. thiol contact or dithiol contact; however, β was independent of the metal work function Φ because of the weak Fermi level pinning ($[E_F - E_{HOMO}]$ varied only weakly with Φ).

7.3 Noise Spectroscopy

The noise measurements in mesoscopic tunneling junctions have been studied for a long time, e.g. in semiconductor double barriers, quantum point contacts, and Coulomb blockaded Josephson junctions [110]. Recently, significant results obtained from the measurements in molecular tunneling junctions were reported [9, 111–114]. Noise spectroscopy allows the special features of a single-molecule charge transport to be studied, which are not accessible

by standard current–voltage measurements. In addition to the I–V behavior, noise characteristics can provide useful fundamental information on molecular junctions, such as the local environment and metal–molecule interfaces of the molecule junctions [9, 115, 116], electron–phonon interactions [110, 111, 117], transmission probability of the conduction channel [9, 112, 113], and stability of the junctions [115, 118]. Understanding the conductance fluctuations and the corresponding noise characteristics is of great significance for developing molecular-scale devices because it influences the performance and the reliability of the devices, especially for molecular switches and memories. The mechanisms of noise generation can be distinguished by two different phenomena: whether the spectral density $S_{\mathrm{II}}(f)$ depends on the frequency or not. There are two types of noises in which the spectral density is independent of the frequency. One is the thermal noise, also known as the Johnson–Nyquist noise, and the other is the shot noise. In contrast to these frequency-independent noises, the flick noise and the generation–recombination noise are frequency-dependent.

7.3.1 Thermal Noise and Shot Noise

Thermal noise is generated by the thermal agitation of the charge carriers (generally the electrons) inside an electrical conductor at equilibrium, which occurs regardless of any applied voltage. This noise results from fluctuations in the quantum occupation of the electronic states and, consequently, the temperature-dependent statistical distribution of the kinetic energy of the electrons. It leads to a variation in the current despite the mean value of the current being zero, i.e. no current flow [119]. The thermal noise is also known as the Johnson–Nyquist noise and can be expressed as follows [119]: $S_{\mathrm{II}}(f) = 4k_{\mathrm{B}}T/R$, or $S_{\mathrm{II}}(f) = 4k_{\mathrm{B}}TG$, where k_{B} is the Boltzmann constant; T is the ambient temperature; R is the equivalent resistance; and G is the conductance.

In contrast to the thermal noise, the shot noise is the result of the current fluctuations induced by the discrete charges and is highly dependent on the correlations between the tunneling charges. The shot noise is due to the non-equilibrium electron distribution and occurs only when a net current flows a defined barrier (the current pass through the system fluctuates around the average value) [119]. For $k_{\mathrm{B}}T \ll eV$, the shot noise power can be expressed as $S_{\mathrm{II}}(f) = 2eIF$, where I is the average current; and F is the Fano factor, which characterizes the correlations of the tunneling charge [9]. The Fano factor can be extracted from the dependence of noise on the applied bias current based on this equation. For a system that has N conductance channels, each of which has a transmission probability (τ), F can be given by the equation as follows [112]:

$$F = \frac{\sum_{n=1}^{N} \tau_n(1-\tau_n)}{\sum_{n=1}^{N} \tau_n} \tag{7.7}$$

Thus, the shot noise and the conductance measurements can be used to analytically determine the transmission probabilities for at least the two-channel case. In the case where one may have a single perfect transmitting channel ($\tau \approx 1$) for which the electrons are in a coherent state across the entire structure, the

shot noise vanishes ($F = 0$). This result is possible when a mesoscopic system is comparable with a few typical lengths that determine the level of correlation between the electrons. Therefore, by measuring the level of the shot noise, one can gain insights into the mesoscopic electronic properties that are not accessible by using standard conductance measurements [112]. In the absence of a correlation between the tunneling charges, the Fano factor would indicate a full shot noise (Poissonian shot noise), i.e. $F = 1$. For a transmission probability between 0 (high-barrier tunneling junction) and 1 (perfect transmitting channel) ($0 < F < 1$), the noise level is determined by the partition noise: the degree of freedom for the electron to choose between being transmitted or reflected [112]. In the case of $F > 1$, the shot noise, also known as the super-Poissonian shot noise, is associated with a correlation between the tunneling charges resulting from the Coulomb repulsion and scattering [9, 120].

7.3.2 Generation–Recombination and Flicker Noise

The generation–recombination noise and the flicker noise are two typical noises that are frequency-dependent. To explain the frequency-dependent noise behavior, the Lorentz oscillator model can be used. Let us imagine that the fluctuations arise from the elementary processes, and each process has its own time constant τ_0. A single process leads to an auto-correlation function proportional to e^{-t/τ_0}. Hence, the Fourier transform of its noise density spectroscopy represents a Lorentz curve and can be expressed as follows:

$$S_{II}(f) \propto \frac{1/\pi\tau_0}{4\pi f^2 + (1/\tau_0)^2} \tag{7.8}$$

$$\tau_0 = 1/2\pi f_0 \tag{7.9}$$

where f_0 is the characteristic frequency, which can be obtained from the inflection position of the noise spectra. Equations (7.8) and (7.9) depict the noise spectroscopy of a single fluctuator, $S_{II}(f) \propto f^{-2}$ in the case $f \gg f_0$. For a finite number of fluctuators, the time constant τ_0 will have a broadened distribution. For an adequate number of fluctuators, the summation will approximately lead to $S_{II}(f) \propto f^{-1}$ [119].

One example of a single Lorentz fluctuation is the generation–recombination noise, which typically appears in semiconducting materials. In the solid-state physics of semiconductors, the carrier generation and the recombination process, e.g. the charge carrier transition between the impurity levels and the conduction band, lead to a random fluctuation of the mobile charge carrier (electrons and holes) number. Furthermore, the generation–recombination noise has been found in the metal–insulator–metal tunneling junction. For example, Rogers et al. studied the conductance fluctuation of metal–insulator–metal tunneling junctions with a small amplitude [121]. They found that the measured voltage noise spectrum could be resolved into a limited number of distinct Lorentzian conductance noise spectra. The generation–recombination noise

was attributed to the filling and emptying processes of the localized electron states in the tunneling barrier. Changes in the occupation of such states resulted in the changes of the local tunneling barrier and thus the fluctuations in the conductance. In addition to the generation–recombination process, the trapping/detrapping processes in the molecular junctions as well as the molecular structural changes can also lead to a Lorentz fluctuation [9, 118].

Another frequency-dependent noise is the flicker noise, also known as the $1/f$ noise. In contrast to the frequency-independent noise, there is no global theory to describe the flicker noise, even though it occurs in all electronic devices, resistances, semiconductor devices, and molecular devices. There are several processes that may be responsible for this noise: generation–recombination processes, varying mobility of charge carriers, fluctuating impurities, movement of defects, and so on [114, 119]. Although the source of the $1/f$ noise is a complicated issue, the $1/f$ noise has been widely used to characterize the electron transport properties [9, 111, 114], which will be discussed latter in detail.

7.3.3 Noise Spectroscopy Measurements

The noise signal characterization can be analyzed based on the real-time current curves. However, this current temporal measurement only depicts limited time fragments. To understand the mechanism of the conductance fluctuation thoroughly, a statistical measurement is needed. Noise spectroscopy is a powerful tool that is used to investigate the statistical features of the current fluctuation. By using this method, each noise spectrum is automatically obtained by averaging hundreds of individual spectra with a spectrum analyzer. In any measurement of the electrical conductance, the current is not constant in time but exhibits fluctuations around a mean value. If we use the $K_I(t)$ to denote the auto-correlation function of the current, then $K_I(t) = \langle \Delta I(t')\Delta I(t'+t)\rangle$. Its Fourier transform is the spectral density $S_I(f)$: $S_I(f) = 2\int K_I(t)\exp(-i2\pi ft)\mathrm{d}t$.

Generally, the shunt resistance R_S is inserted into the circuit for the current measurement, converting the current into a voltage signal. Then, the voltage signal is detected by a spectrum analyzer. The measured voltage fluctuations are accumulated and fast Fourier transformed by the spectrum analyzer, resulting in a voltage noise power spectrum $S_V(f)$ over the bandwidth of interest. This is also known as the spectral power distribution. The expected noise level is very small, especially at 4 K. In order to measure such small signals, a battery is used as the voltage source, and the signal is first amplified several times by two wide band preamplifiers. To suppress the noise of the preamplifiers, two sets of preamplifiers in parallel feed the signals into a spectrum analyzer. The spectrum analyzer can be operated in the cross spectrum mode and determines the Fourier transform of the cross-correlation signal from the two amplifiers [114, 122]. The correlation techniques can eliminate the additional voltage noises originating from the two amplifiers. The detailed information concerning the measurement system of both the monolayer and single-molecule junctions can be found elsewhere, which were reported by several research groups [9, 111–114].

7.3.4 Application of Noise Spectroscopy

Each type of noise spectroscopy, e.g. flick noise, shot noise, and random noise, has been used to study the properties of bare metallic nanocontacts as well as molecular junctions [113, 114, 123]. Schönenberger and coworkers were the first to focus on the flick noise investigation of bare metallic nanocontacts at the single atom level. By using electromigration and MCBJs, they measured the magnitude of the $1/f$ noise in tunable metallic nanoconstrictions. It was demonstrated that as a function of R, the normalized noise S_V/V^2 showed a pronounced crossover from $\propto R^3$ in low-Ohmic junctions to $\propto R^{1.5}$ in high-Ohmic junctions, as illustrated in Figure 7.3a [114], where S_V is the voltage noise power spectral density, V is the applied voltage, and R is the resistance of the nanocontacts. The measured power changed from 3 to 1.5, indicating that the $1/f$ noise was generated in the bulk, and reflected the transition from diffusive to ballistic transport. According to Hooge's law, $S_V/V^2 \propto 1/N$, where N denotes the number of statistically independent fluctuators in the volume [114]. If a characteristic length of the junction is denoted by l, then the junction volume is $\sim l^3$. In a diffusive transport through a wire of length L and cross section A, the resistance R can be given by $R = \rho L/A$. Hence, $R \sim l^{-1}$. Due to $S_V/V^2 \propto 1/N \sim l^{-3}$, it is reasonable to obtain $S_V/V^2 \propto R^3$. However, in the ballistic transport regime, where the characteristic length of the junction becomes shorter than that of the scattering mean-free path, the conductance is determined by the number of transport channels that are proportional to the junction area. Then, $R \sim A^{-1} \sim l^{-2}$. Consequently, $S_V/V^2 \propto R^{1.5}$. Therefore, their research opened a window for the electron transport mechanism investigation using the $1/f$ noise characterization.

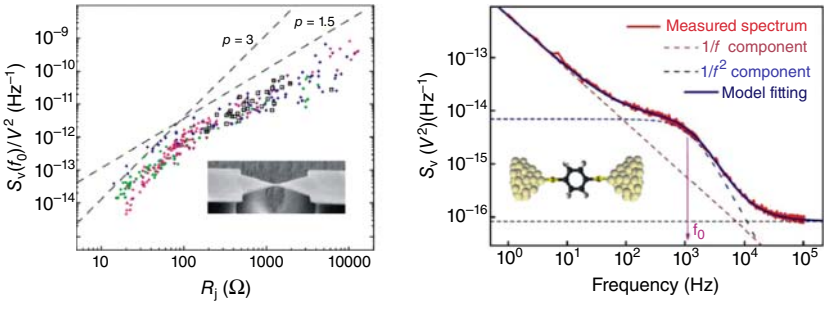

Figure 7.3 Noise features for a bare gold and molecule junction. (a) Magnitude of the $1/f$ noise as a function of the junction resistance R_J, shown as a log–log scattering plot of $S_V(f_0)/V^2$ for four MCBJ samples obtained in the process of stretching the samples. Here, $f_0 = 100$ kHz. An scanning electron microscope (SEM) image of the MCBJ sample was shown in the inserted figure. The dashed lines are guides lines for the expected power-law dependencies of $S_V(f_0)/V^2$ in the diffusive ($p = 3$) and ballistic transport regimes ($p = 1.5$). Source: (a) Reprinted with permission from Wu et al. 2008 [114]. Copyright 2008, American Physical Society. (b) The voltage noise power spectral density of single BDT molecules, which bridge two gold electrodes, as depicted in the inserted figure. The solid red curve is the measured total noise density, and the solid blue curve is a fit to the experimental data, which takes $1/f$, $1/f^2$, and the thermal noise components into consideration. The noise components are depicted by the different colored dashed lines. Source: (b) Reprinted with permission from Xiang et al. [123]. Copyright 2015, American Institute of Physics.

Shot noise measurements have proven to be a powerful method for evaluating the Fano factor as well as the number and transparency of channels for the charge transmission [18]. van Ruitenbeek and coworkers first studied the shot noise in bare atom-size metallic contacts [122]. In their study, the MCBJ technique was used to obtain a stable point metallic contact at cryogenic temperatures. They were interested in the amount of noises above the thermal noise, which they called the excess noise. To measure the excess noise, white noise was sent from a calibration source through a 1 V series resistance to measure the frequency responses of the setup. After a concise data analysis, the excess noise was obtained. They demonstrated that they indeed achieved the shot noise by plotting the excess noise values as a function of the bias current [122]. By applying a fitting to this plot, a nearly linear dependence of the excess noise on the bias current was clearly observed, which agreed well with the shot noise feature, i.e. $S_{\mathrm{II}}(f) = 2eIF$. The Fano factor can be derived from the slope of the linear fitting curve. Interestingly, the smallest value of $(0.02 \pm 0.005)\ 2eI$ was observed for a contact with a conductance $\sim G_0$. This finding, $F \sim 0$, indicated that the conductance was due to the mostly fully transmitted modes ($T_n \approx 1$) based on Eq. (7.7). Furthermore, a small value of the Fano factor F was obtained for G near integer conductance values, which indicated the quantum suppression of the shot noise as $G = nG_0$. Similar experiments were also performed on aluminum, which indicated a much weaker suppression of the shot noise, revealing that the conductance at $G = G_0$ was not carried by a fully transmitted mode for the aluminum nanowire [122].

Recently, van Ruitenbeek and coworker further used the shot noise to infer the transmission coefficients in the dominant channels of the carrier transport through single deuterium molecules [112]. The shot noise measurement process was optimized to remove the effects from other types of noises. Once a stable contact was identified, they first took a $\mathrm{d}I/\mathrm{d}V$ curve by using the lock-in technique. Then, the zero-bias noise spectrum was recorded, which showed the thermal (Johnson–Nyquist) noise. Subsequently, the total noise at was measured at the finite biases, which consisted of a white shot noise, thermal noise, and $1/f$ noise (dominant at low frequencies). After dropping the $1/f$ noise, compensating for the roll-off and subtracting the thermal noise for a series of bias currents on a given contact, the dependence of the excess noise was obtained as a function of the bias current. It was determined that the shot noise was strongly suppressed when the currents passed through the Pt–D2–Pt junctions; a similar phenomenon was presented in the bare gold junctions at $G = G_0$. Therefore, this study indicated that the transport in the Pt–D2–Pt bridges was carried dominantly by one nearly fully transparent channel [112]. Hence, these results, in return, verified that the junction was indeed formed by only a single molecule.

In contrast to the previous noise measurements at low temperatures, Natelson and coworkers presented the measurements of the shot noise in the Au break junctions acquired under room temperature and ambient conditions [113, 124]. Using the MCBJ technique and a high-frequency technique, the noise data and the conductance histograms for the Au junctions were acquired simultaneously at room temperature. The measured shot noise showed a strong suppression at precisely the same conductance values as the peaks in the conductance histograms. This result demonstrated that the quantum suppression of the noise

due to fully transmitting contacts survived even at room temperature. It should be noted that the inelastic processes were much stronger compared to those at low-temperature experiments. One interpretation for this observation was provided: the inelastic processes can operate on length scales longer than the single nanometer junction size, and inelastic processes, such as electron–phonon scattering, can remove energy from the "hot" electron system and redistribute electrons between the different quantum channels, leading to the suppression of the shot noise at room temperature. Although their experiments were performed without molecules, these results indicated that the noise characterizations could be used as a tool to study the inelastic transport process in the molecular junctions.

Although the effects of the electron–vibration interactions in the atomic-scale junctions with a single conduction channel received considerable attention [58, 113, 125, 126], the more general case of junctions with several conduction channels has received very little attention. Recently, Ben-Zvi et al. studied the electron–vibration interaction in multichannel molecular junctions, i.e. the benzene junctions and carbon dioxide junctions sandwiched by the Pt electrodes [127]. It is well known that the activation of the electron–vibration interactions can either enhance or suppress the conductance. However, the relationship between the electron–vibration interaction contribution to the conductance and the transmission distribution in the conduction channel is unclear (e.g. the exact number of channels is unclear). Ben-Zvi et al. overcame the difficulties and extracted the transmission probabilities of the main conductor channels by the shot noise measurements [127]. They found: (i) for all of the junctions that yielded the conductance suppression due to the vibration activation, one dominant channel (high transmission properties) was clearly observed; and (ii) for those junctions that yielded conductance suppression, the conduction channels were more equally distributed, i.e. all of the channels had transmission probabilities less than 0.5. The analysis of the vibration activation effects on the conductance in view of the distribution of conduction channels confirmed the theory that a high-conductance junction (with a dominant conduction channel) typically demonstrated conductance suppression due to the inelastic tunnel process [127, 128].

The theoretical shot noise studies in the molecular junctions also received extensive attention [110, 129, 130]. By combining the Monte Carlo methods with the Langevin approach, Koch et al. successfully calculated the shot noise of tunneling currents with a model: transport through the molecule was to be dominated by a single, spin degenerate electronic level in the presence of one vibrational mode with a frequency ω_0 [129]. They reported Franck–Condon physics, which is a characteristic of molecules, could lead to a low-bias current suppression (Franck–Condon blockade) and large Fano factors (10^2–10^3) in single-molecule devices, which originated from the coupling of the electronic and vibrational degrees of freedom. The Fano factor enhancement has been explained by the avalanche-like transport of electrons interrupted by long times without a charge transfer. One year later, Galperin et al. thoroughly investigated the inelastic tunneling effects on the noise properties of the molecular junctions [110]. The inelastic tunneling and its influence on the zero frequency noise

based on a simple one-level molecular junction model was investigated, which arbitrarily selected one molecular orbital to support the resonance transmission beyond a certain voltage bias threshold. This molecular orbital was coupled to a local oscillator representing the molecular nuclear subsystem. By employing this one-level model within the non-equilibrium Green function (NEGF) methodology, they investigated inelastic effects on the noise spectrum in molecular junctions in both the weak and strong electron–phonon coupling regimes. In the weak coupling regime, it was found that the noise amplitude could increase or decrease due to an inelastic channel opening and based on the distance of the resonance as well as the junction asymmetry. Particularly, it was determined that the relative Fano factor decreased when the molecule was far from the resonance. Their calculation and analysis suggested the usefulness of the "noise spectroscopy" for measuring the values of the electron–vibration coupling on the bridging molecules [110]. Haupt et al. employed the extended NEGF technique to determine the cumulant generating function, from which the current I and the noise S can be easily calculated [131]. The key idea for this approach is to modify the Hamiltonian by adding a time-dependent phase to the tunneling matrix elements. An analytical expression was successfully derived for the inelastic noise at an arbitrary temperature and distinguished the terms that corresponded to the simple renormalization of the transmission coefficients. By applying the theory to the experimentally relevant case of a deuterium molecular junction [112], they predicted a significant positive contribution to the total noise due to the inelastic processes [131]. Kumar et al. further pointed out that the inelastic signal, i.e. the signal due to the vibration excitations, could become negative as the transmission probability decreased below a certain transmission value [117]. They argued that the negative contribution to the noise arose from the coherent two-electron processes mediated by the electron–phonon scattering and the Pauli exclusion principle [117]. Let us assume that two electrons are injected from the left lead with a high energy E and a low-energy E-$\hbar\omega_0$, respectively. If the higher energy electron emits a phonon, it would lose an energy $\hbar\omega_0$ and tend to occupy the same outgoing state as the low-energy electron. This inelastic process tends to reduce the noise and make a negative contribution by narrowing the energy distribution of the outgoing electrons. However, this process would be blocked at the perfect transmission, i.e. with a high transmission probability. Thus, the inelastic process can make either a positive or a negative contribution to the total noise. Therefore, the theoretical calculations performed by different groups indicate that the shot noise can be used as a powerful tool to address the particular characterization as the charges transport through the molecular junctions, which is unavailable using the I–V characteristics.

Recently, several groups used random telegram noises to study the electron transport properties and the stability of the molecular junctions [115, 118, 119, 132]. Kim et al. studied the noise characteristics of the charge transport through alkyl-based monolayer Au–molecule–Au junctions [9]. Specifically, the random telegraph noise (RTN) was examined. Firstly, it was determined that all the spectra followed a $1/f$ (at a low frequency regime) and a $1/f^2$ (at a high frequency regime) power law depending on the frequency. This result indicated a superposition of the $1/f$ and the generation–recombination

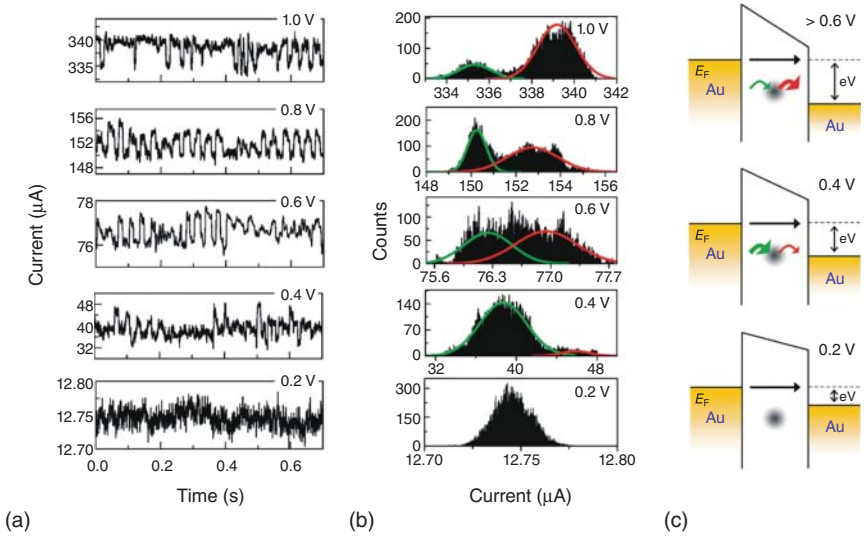

Figure 7.4 Random telegraph noises. (a) Time-dependent two-level random telegram noises of Au–HDT–Au junctions under different biases. The random telegram noise was recorded at room temperature for 0.7 seconds. (b) Corresponding current histograms for the random telegram noise. Two peaks in the histograms were observed when the applied bias was above 0.4 V. The histograms are fitted with the Gaussian peaks, where the green and red lines indicate the trapping and detrapping events, respectively. (c) Schematic trapping and detrapping processes in the molecular junction with a single localized trap. Source: Reprinted with permission from Kim et al. 2010 [9]. Copyright 2010, American Chemical Society.

noise (the Lorentzian distribution) in the measured spectroscopy. The Lorentzian distribution noise spectra may result from the trapping/detrapping processes of the charge carriers to/from the localized states in the molecular junctions. They pointed out that the localized states could be formed by defects that may unintentionally be introduced into the molecular layer in the junction fabrication process. To verify this trapping/detrapping interpretation, they further measured the time-dependent current fluctuations, referred as the RTN as shown in Figure 7.4. In this figure, a discrete temporal fluctuation was observed under the different bias voltages. Interestingly, it was observed that the low current events prevailed at a low bias (below 0.6 V), which indicated that the trapping process resulting from the charging effect on a localized state occurred in the molecular barrier. Conversely, the high current events became predominant with an increasing bias (above 0.6 V), which agreed with the fact that a large potential difference could lead to the reemission of the trapped charge carriers (detrapping process). Their study demonstrates that noise characterization is useful for evaluating the influences of the localized states on the charge transport in molecular or other electronic junctions [9].

In contrast to the experiment mentioned above, several groups studied the telegram noise in single-molecule junctions under small bias voltages (below 0.2 V) [115, 118, 119, 132]. The total measured noise spectroscopy showed a transition from $S_V \propto f^{-1}$ at a low frequency to $S_V \propto f^{-2}$ at a high frequency by independent

groups [118, 119, 123, 132]. One noise spectroscopy for benzene-dithiol junctions is illustrated in Figure 7.4b. The total noise spectroscopy in this figure can be described as follows:

$$S_V(f) = \frac{A}{f} + \frac{B}{1 + (f/f_0)^2} + 4kTR \tag{7.10}$$

where A and B represent the amplitudes of the $1/f$ and $1/f^2$ noise components, respectively; f_0 is the characteristic frequency, which can be derived from the inflection position of the total noise spectra; R is the junction resistance; and T is the ambient temperature. Equation (7.10) provides a good fit of the experimental data. The measured noise spectroscopy indicated that the telegram-like noise still existed in this single-molecule junction, which was later confirmed by the real-time dependent conductance measurements [123, 132]. It should be noted that such a small bias voltage (below 0.2 V) is not enough to cause both the trapping and detrapping events. Additionally, single-molecule junctions contain much less defects (e.g. particles and impurities) in comparison with monolayer junctions. So, where does the telegram-like noise come from? In the case of single-molecule junctions, the stability of the junction becomes a dominant factor, which strongly affects the current characterization. Thereby, the stability should be considered for the interpretation of the telegram-like noise. To explain the telegram-like fluctuations in view of the junction stability, several mechanisms have been proposed and can be primarily classified into three groups: (i) dynamic reconfigurations of the molecular backbone structure [118, 119, 133]; (ii) movement of the surface metal atoms tethered to the molecules [115, 134]; and (iii) bond breakage and reconnection for the metal–molecule contacts [70]. The reconfiguration changes can occur without the complete bond breakage and involve the near-configuration states with similar electric properties, leading to a small amplitude telegram-like current fluctuation. A direct evidence supporting this mechanism is that the telegram-like current fluctuation was enhanced as the pass current increased [115]. If the telegram noise originates from the current induced by the dynamic reconfigurations of the molecules, then an enhanced telegram fluctuation was expected as the current increased. Please note, the local junction temperature also increased as the pass current increased, promoting the movement of the metal atoms tethered to the molecule. Hence, the telegram-like noise may originate from the atom moving at the electrode surface, especially for those junctions with a fresh electrode surface after physical breakage. One clear evidence of this type of interpretation is that the telegram-like fluctuation was suppressed in a densely molecular packed environment [115]. Thus, the telegraph-like current fluctuation in fresh molecular junctions is more likely associated with the rearrangement of the metal atoms tethered with a molecule. In contrast to the small amplitude current fluctuation discussed above, Brunner et al. observed a larger fluctuation in the solution environment, which was reasonably attributed to the formation and the thermally driven breakage of bonds between a molecule and a metal electrode [132].

The noise analyses can provide valuable insights into single-molecule science but are not limited to electron transport properties and junction stability. Tsutsui and coworkers extended the application of the current noise to identify

single-molecule junctions [27]. They found stepwise increases in the current oscillation amplitudes at distinct voltages, synchronous to the voltages in which the vibration modes were activated due to the inelastic tunneling. The specific change in the noise amplitudes was attributed to the electron–vibration interaction. The vibration interactions in the molecular junctions are known to cause local heating and increase the junction temperature above the bath temperature, which may lead to an increase in the noise amplitude, as noted by the authors. These results suggest that the field-induced current noise can be used as a complementary tool for the IETS in single-molecule identification [27]. Noise spectroscopy can also be extended to study biomolecules, for instance, several groups used RTNs for sequencing biomolecules such as DNA and amino acids [135, 136]. They demonstrated that single amino acids could be identified using electron tunneling currents measured as individual molecules passing through a nanoscale gap between the electrodes.

7.4 Optical and Optoelectronic Spectroscopy

Electronic characterization methods, such as the $I–V$ curve and the TVS, are critical for analyzing the device behavior but do not provide direct information on the molecular energy and structure. To obtain more detailed information on the molecular structure, location of the relevant molecular orbitals, density of the adsorbed molecules, and thickness of the monolayer, numerous optical spectroscopic tools have been applied. When these approaches are combined with the photoelectron spectroscopic methods, correlations between the chemical features and the electronic performance can be assessed. Photoelectron spectroscopies have a high surface sensitivity, which makes them attractive for characterizing thin molecular layers as well as single-molecule junctions [137]. Furthermore, there are various operation modes that can provide useful information on different aspects of a molecular device [138].

7.4.1 Raman Spectroscopy

Raman spectroscopy (named after one of its discoverers, the Indian scientist Sir C.V. Raman, who received the Nobel Prize in 1930) is a spectroscopic technique used to observe vibrational, rotational, and other low-frequency modes in a system [139]. Raman spectroscopy is now commonly used in chemistry to provide fingerprint information by which molecules can be identified and quantitatively analyzed [139]. The technique involves shining a monochromatic light source (such as laser light) on a sample and detecting the scattered light. The majority of the scattered light is of the same frequency as the excitation source, which is known as Rayleigh or elastic scattering. A very small amount of the scattered light is shifted up or down in energy from the incident laser due to interactions between the incident electromagnetic waves and the vibrational energy levels of the molecules in the sample. For a spontaneous Raman effect, a photon excites the molecule from an original vibrational energy state to a

virtual energy state for a short period of time, then the molecule returns to a new vibrational energy state accompanied with a photon emission process. The difference in the energy between the original rovibronic state and this resulting rovibronic state leads to a shift in the emitted photon's frequency away from the incident laser wavelength. Plotting the intensity of this shifted light versus frequency results in a Raman spectrum of the sample. The energy shift and the corresponding wave-number shift provide information on the vibrational modes in the system.

Raman scattering is an example of inelastic scattering because of the energy and momentum transfer between the photons and the molecules during the interaction, and it should not be confused with emission (such as fluorescence), where a molecule in an excited electronic state instead of a virtual energy state emits a photon of energy and returns to a ground electronic state [140]. The intensity of the Raman scattering is proportional to the electric dipole–electric dipole polarizability derivative, which differs from IR spectroscopy, where the interaction between the molecule and the light is determined by the electric dipole moment derivative; thus, this contrasting feature allows one to analyze vibrational modes that might not be IR active via Raman spectroscopy [141].

Currently, the Raman spectroscopy is extensively used to identify unknown molecules, especially biomolecules [142, 143], because the Raman scattering directly exhibits the fingerprint vibrational modes of the target Raman-active molecule. In accordance with the need for identifying an unknown molecule at the single-molecule level, researchers have sought methods capable of achieving this goal, i.e. SERS and tip-enhanced Raman scattering (TERS), in which an enormously enhanced Raman signal was detected when molecules were adsorbed onto the surface of a roughened metal surface. Briefly, the enhancements of the SERS are classified into two categories: electromagnetic and chemical. The former is believed to be the predominant enhancement because it largely amplifies both the incident and the scattered electromagnetic fields. The latter is related to an increase in the polarizability of the adsorbed molecule. Detailed information on the enhanced mechanism, platform for the Raman spectroscopy investigation, and new strategy for implementing the SERS can be found in several impressive reports [144–147].

Recently, the Raman spectroscopy was used to probe the structural change in single molecules during time-dependent dynamic processes, and several significant important results were reported [144]. As had mentioned in Section 2.1.3, Ward et al. reported simultaneous measurements of electronic conduction and real-time Raman responses in molecular junctions formed by using the electromigration technique [148]. These conductance/Raman observations demonstrated that the electromigrated nanogaps between the extended electrodes could achieve enhancements sufficient for single-molecule SERS sensitivity, thus leading to an investigation of single-molecule structural changes. Following this study, Konishi et al. further reported the SERS of a single molecule under conditions of an *in situ* current flow in MCBJ-based molecular junctions [149]. Significant changes in the SERS intensity and the selectivity of the Raman vibrational bands that are coincident with current fluctuations provide information related to the electronic structural dynamics of a single molecule

in their experiments. Another recent advance is that Jiang et al. reported a method that combined molecule-resolution STM and tip-enhanced Raman spectroscopy [150]. This method provides a powerful tool for the real-time study of vibrational, rotational, and other low-frequency modes of molecules, which not only chemically identifies the molecules adsorbed on a surface but also yields information on the adsorption configuration and the chemical bonding between molecules. Generally, direct probing of the dynamic structure and chemical changes in the nanoscale molecular junctions upon application of an electric field remains a major challenge. By using *in situ* gap-mode Raman spectra, Cui et al. established a relationship between the applied electrochemical gate field and the conformational changes in sandwiched molecular junctions, such as the torsion angle of the molecules [151].

Furthermore, the Raman spectroscopy was employed to investigate vibrational and electronic heating in the nanoscale junctions. Until now, understanding and controlling the flow of heat is a major challenge in nanoelectronics. When a junction is driven out of equilibrium by light or the electric charge flow, the vibrational and electronic degrees of freedom cannot be described by a single temperature. In a pioneering study, Ward et al. demonstrated that a surface-enhanced Raman spectroscopy can be used to determine the effective temperatures in a biased metallic nanoscale junction covered with molecules (the junction was fabricated by using the electromigration method) [152]. Using an anti-Stokes electronic Raman emission followed by a delicate calibration, they demonstrated that the effective electronic temperature at small bias voltages can reach values up to several times that of the values measured when there is no current, i.e. molecular vibrations show mode-specific pumping by both optical excitation and current with effective temperatures exceeding several hundred kelvins.

During the past four decades, considerable efforts and ingenuity have been made, thus leading to the continuous development of theoretical and experimental progress regarding the Raman spectroscopy. However, a few challenges in performing Raman spectroscopy still remain, which include the reproducible generation of hot spots providing sufficient signal amplification to sensitively detect single molecules, compatibility under various conditions, and establishment of robust statistical strategies [144]. The strength of the SERS is its high content of molecular information combined with sensitivity, quantification, and multiplexing. Other vibrational spectroscopy techniques (such as fluorescence microscopy, ultraviolet–visible [UV–Vis] spectroscopy, and IETS) also have their own unique advantages [138]. Comparing and combining the performance of the SERS with other existing techniques will supply and confirm comprehensive information on the studied molecular junctions.

7.4.2 Ultraviolet–Visible Spectroscopy

UV–Vis spectroscopy refers to the absorption spectroscopy or reflectance spectroscopy in the UV–Vis spectral region. UV–Vis uses light in the visible and adjacent regions, i.e. the regime between the near-ultraviolet and the near-IR ranges, measures the molecule transitions from the ground state to the excited state. This technique is a complementary technique to the fluorescence spectroscopy, which

addresses the molecular transitions from the excited state to the ground state [153]. The instrument used in UV–Vis spectroscopy is called a UV–Vis spectrophotometer. It measures the intensity of light (I) passing through the sample and compares it with the intensity of incident light (I_0) before passing through the sample. The ratio $T = I/I_0$ is known as the transmittance. The UV–Vis spectrophotometer can also be configured to measure the reflectance. In this case, the spectrophotometer measures the intensity of the reflected light from the sample and compares it with the intensity of light reflected from a reference material. This ratio is known as the reflectance.

The UV–Vis spectroscopy can be used to address the molecular energy structure [154]. For example, those molecules containing π-electrons or non-bonding electrons can absorb the energy of the ultraviolet or visible lights to excite these electrons to higher antibonding molecular orbitals. When the energy gap between the highest occupied molecular orbital (HOMO) and the lowest occupied molecular orbital (LUMO) is low, electrons will be easily excited, leading to an absorption of longer wavelength. Therefore, the peak's position in spectroscopy indicates the energy structure of the interested molecules. The wavelengths of the absorption peaks and the amplitude of the peaks also correlated with the types of bonds in a given molecule; thus, the UV–Vis spectroscopy is valuable in determining the functional groups within a molecule [155]. According to the Beer–Lambert law, the absorbance of a solution is directly proportional to the concentration of the absorbing species in the solution. Thus, for a fixed path length, the UV–Vis spectroscopy can be used to determine the concentration of the absorber in a solution [156]. Furthermore, the UV–Vis can be applied to determine the rate constant of a chemical reaction based on the concentration measurement [157]. The rate constant of a particular reaction can be determined by measuring the UV–Vis absorbance spectrum at specific time intervals to observe the changes in the levels of absorbed wavelength over time in accordance with the solution color changes (energy state change). From these measurements, the concentration as well as the reaction rate can be calculated.

7.4.3 X-ray Photoelectron Spectroscopy

X-ray photoelectron spectroscopy (XPS) is a widely used technique for analyzing the surface chemistry of a material. In the 1950s, Kai Siegbahn and coworkers developed the XPS for surface chemical analysis and received the Nobel Prize for this pioneering and outstanding work [158]. The XPS can measure the elemental composition, empirical formula, chemical state, and electronic state of the elements within a material. In principle, the XPS spectra are typically obtained by irradiating a solid surface with a beam of X-rays in high vacuum and simultaneously measuring the kinetic energy as well as the number of electrons that are emitted from the top of the material being analyzed. When an atom or molecule absorbs an X-ray photon, an electron can be ejected. The kinetic energy of the ejected electron depends on the photon energy ($h\nu$) and the binding energy of the electron based on the equation $E_{\text{binding}} = E_{\text{photon}} - (E_{\text{kinetic}} + \emptyset)$, where E_{binding} is the binding energy of the electron and can be regarded as the energy required to remove the electron from the material surface, E_{photon} is the energy of the X-ray

photons, E_{kinetic} is the kinetic energy of the electron that can be measured by the instrument, and Ø is the work function of the material detected. For an electron ejection, the excitation energy must be large enough for the electrons to overcome the work function of the solid. Since the energy of an X-ray with a particular wavelength is known, and the emitted electrons' kinetic energies can be measured, the electron binding energy of each of the emitted electrons can be determined using this equation.

A typical XPS spectrum is a plot of the number of electrons detected (y-axis) versus the binding energy of the electrons detected (x-axis). Because the inner shell electrons for each element have a different binding energy, the XPS peaks at the characteristic binding energy values can be used to identify each element that exists in the surface of the material being analyzed. The number of detected electrons in each of the characteristic peaks directly related to the number of elements within the XPS sampling volume. Thus, the XPS can be used to identify the elements as well as the amount in the targeted material. Please note that the binding energy depends not only on the element from which the electron is emitted but also on the orbitals from which the electron is ejected as well as the chemical environment of the atom from which the electron was emitted. Thus, by measuring the kinetic energy of the emitted electrons, it is possible to determine which elements are near a material's surface and their "chemical states," which refers to the local bonding environment of the studied species. The local bonding environment of a species in a study is affected by its formal oxidation state, identity of its nearest-neighbor atom, and bonding hybridization to the nearest-neighbor atom. Thus, the so-called chemical shift (peak shift), which is dependent on the chemical environment, can be observed. In return, the chemical shift provides the chemical state information, such as the molecular structural information.

The XPS has been widely applied in the field of molecular electronics [159]. For example, the XPS can be used as a tool to check the thin film thickness of the molecular layer due to the finite mean free path length, which is a function of the kinetic energy of the photoelectron. Using the XPS, the thickness of the molecular layer on the substrate (such as Au) can be calculated by the relative intensities of the specific peaks and a standard length SAM on Au as Refs. [95, 160]. By analyzing the XPS, one can obtain insight into the molecule-adsorbed state and the configuration at the interface [161]; furthermore, the XPS was used to reveal the interaction information between the molecular layer and the top contacts and verify that the intended functional groups remained intact after the fabrication of the junction [162, 163]. With the development of third-generation synchrotron light sources and promoted resolution, the XPS was developed to become an outstanding tool to study surface properties, even surface reactions, at an unprecedented level [164].

7.4.4 Ultraviolet Photoelectron Spectroscopy

The ultraviolet photoelectron spectroscopy, denoted as UPS, refers to the measurement of the kinetic energy spectra of the photoelectrons emitted by molecules that have absorbed ultraviolet photons. The UPS method was developed by David W. Turner et al. during the 1960s [165]. Similar to the XPS,

it is also based on the photoelectric effect discovered by Albert Einstein in 1905. In comparison with the XPS, which is based on high energy X-ray sources to study the energy levels of the atomic core electrons, the UPS uses a helium discharge lamp (with wavelengths in the ultraviolet region) to study the valence electrons with more accuracy. As Einstein's photoelectric law is applied to a free molecule, the kinetic energy of an emitted photoelectron is based on the equation $E_K = h\nu - I$, where h is Planck's constant, ν is the frequency of the ionizing light, and I is the ionization energy for the formation of a singly charged ion [166]. Based on Koopmans' theory, each ionization energy may be identified by the energy of a molecular orbital [167]. The ultraviolet photoelectron spectrum of a molecule contains a series of peaks, and each corresponds to one valence-region molecular orbital energy level [137].

In the UPS technique, the valence-level instead of the core-level orbitals was probed, which yields insights into the alignment of the contact energy levels and the molecular orbitals [168]. By combining the UPS measurement with the I–V measurement (showing negative differential resistance [NDR]), Yaffe et al. demonstrated that the energy difference between the Fermi level and the LUMO was considerably smaller than that between the Fermi level and the HOMO, indicating that the lowest unoccupied molecular orbital primarily controlled the charge transport [169]. Hill et al. used the photoemission spectroscopy (PES) to investigate the interfacial energy formed by the deposition of different molecular thin films on various metals [170]. They found that the interface electron and the hole barriers were not simply defined by the difference between the work functions of the metals and the organic solids, demonstrating the breakdown of the vacuum level alignment rule at interfaces between the organic molecular solids and metals [170]. Additionally, the high resolution of the UPS allows the observation of the fine structures due to the vibrational levels of the molecules, which facilitate the assignment of the peaks to bonding, non-bonding, or antibonding molecular orbitals [164, 171]. The UPS method was later extended to the study of the solid surfaces, where it was generally known as PES [172].

7.5 Data Characterization Approaches

7.5.1 Transition Voltage Spectroscopy

7.5.1.1 TVS Models

Measuring the energy level alignment in the molecular junctions, especially the position of frontier molecular levels with respect to the Fermi levels (E_F) of the electrodes, is of crucial importance to study the mechanisms of the charge transport and realize the functions of the molecular junctions. One approach to obtain the molecular energy level alignments of the molecular junctions is to measure the peak position in the dI/dV curve, which requires the use of a bias voltage that forces the E_F of the electrodes to reach the position of the molecular levels where the electrons can resonantly transport. However, in most cases, such as alkane-based molecular junctions, a high applied voltage leads to a high electronic field, which could break the junctions before the dI/dV peak is reached.

Based on the mechanism of the field emission, Beebe et al. found that the position of the nearest molecular energy level with respect to the E_F of the electrodes in the molecular junctions can be determined from the I–V measurements, also known as "transition voltage spectroscopy" (TVS) [10]. With this TVS technique, an inflection point (V_{trans}) can be obtained, which is equal to the effective barrier height (Φ) and corresponds to the energy offset between the E_F of the electrode and the closest frontier molecular orbital, either HOMO or LUMO.

To demonstrate the effectiveness of the TVS, Beebe et al. simplified the molecular charge transport as electron tunneling through a rectangular barrier using the Simmons model (Figure 7.5a) [10]. In the zero-bias limit, for electron tunneling through the rectangular barrier, the relationship between the current and the voltage can be described as follows:

$$I \propto V \exp\left[-\frac{2d\sqrt{m_e \emptyset}}{\hbar}\right] \tag{7.11}$$

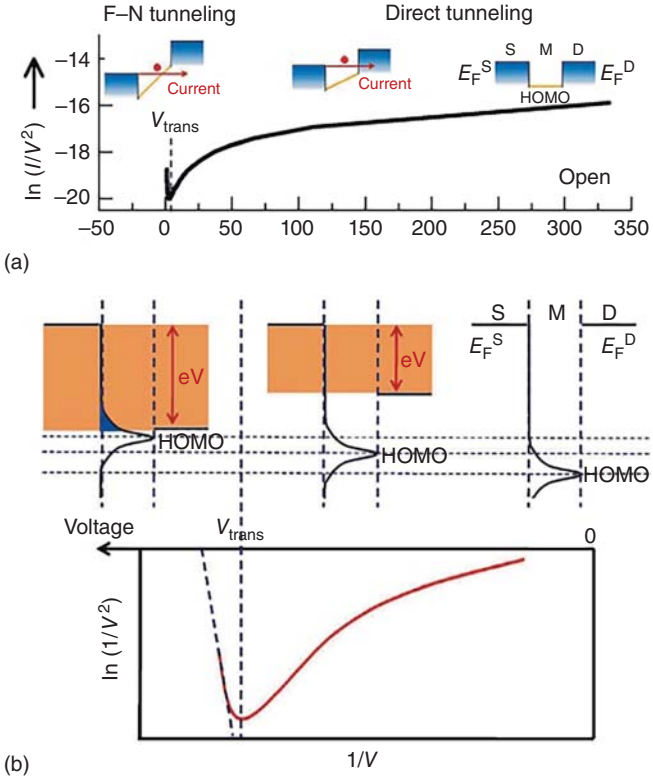

Figure 7.5 Schematic models for qualitatively explaining the transition of the F–N plots. (a) An F–N plot for a typical molecular junction. The insets depict the Simmons tunneling barrier model to explain the inflection of the F–N curve. (b) The corresponding resonant model for explaining the inflection of the F–N curve. Source: Reproduced with permission from Jia et al. [173]. Copyright 2013, John Wiley and Sons.

where m_e is the electron effective mass and d is the width of the barrier, which is typically equal to the length of the connected molecules. Therefore, $\ln(I/V^2)$ is proportional to $\ln(1/V)$. At the opposite limit, for the applied bias voltage exceeding the barrier height, the tunneling barrier changes from trapezoidal to triangular, and the I–V dependence can be described as follows:

$$I \propto V^2 \exp\left[-\frac{4d\sqrt{2m_e\emptyset^3}}{3\hbar qV}\right] \tag{7.12}$$

where q is the electronic charge. From the Eq. (7.12), it can be deduced that $\ln(I/V^2)$ against $1/V$ has a linear relationship in the high-voltage regime with the triangular barrier. Therefore, electron tunneling through the triangular barrier has the characteristics of Fowler–Nordheim (F–N) tunneling or field emission. From the plot of $\ln(I/V^2)$ versus $1/V$ (the F–N curve), a well-defined minimum voltage point, i.e. an inflection point (V_{trans}), can be obtained, which results from the fact that the mechanism of the charge transport transits from direct tunneling with a trapezoidal barrier to F–N tunneling with a triangular barrier. This fact demonstrates that the value of V_{trans} is equal to the barrier height (Φ) and the energy offset between E_F and the closest molecular energy level. For a hole-dominated molecular transport, the nearest molecular energy level is the HOMO of the molecules, i.e. $\Phi = E_F - E_{HOMO}$, whereas for LUMO-dominated electron transport, $\Phi = E_{LUMO} - E_F$.

Remarkably, by measuring the Au–molecule–Au junctions formed from the π-conjugated thiols, Beebe et al. discovered that V_{trans} changed linearly with the energy offset between the E_F of the Au electrodes and the HOMO, which was determined using UPS [10]. Additionally, for a series of alkanethiol-based junctions with various molecular lengths, it was determined that V_{trans} was constant across the alkane series, which was consistent with the fact that the HOMO–LUMO energy alignment of these molecules is independent of the molecular length [174]. All of these important observations demonstrate that the TVS can be used as a promising technique to determine the energy level of the dominant charge transport orbital in a given molecular junction.

However, due to the simplicity of the Simmons model, the presented experimental data were far from being fully understood. To improve the understanding, Huisman et al. [175] introduced a coherent resonant molecular transport model. In this model, the molecular levels are Lorentz-broadened by coupling with the electrodes at both electrode–molecule interfaces, thus leading to a better consistency with the experiments. Furthermore, based on the resonant tunneling model, Araidai et al. [176] theoretically calculated the transition behavior of the F–N curve by using the transmission function of the resonant peaks, where either the Lorentzian or Gaussian functions were used to describe the shape of the resonant peaks. By analyzing the relationship between the behavior of the F–N plot and the transmission function, the inflection (V_{trans}) in the F–N curve occurs when the resonant peak responsible for the charge carrier transport has a certain amount of its tail entering the bias window (Figure 7.5b). Because the resonant peak typically corresponds to the nearest molecular energy level of the molecular

junctions, the V_{trans} in the F–N curve is proportional to the energy offset between E_F and the closest molecular orbital.

Because the I–V curves for the charge transport in the molecular junctions can be approximated to a generic parabolic shape for either the resonant or off-resonant tunneling, Vilan et al. [177] studied the TVS using a Taylor expansion (TyEx) view. Other than the original view of the TVS, where the TVS indicates the tunneling transition between the different charge transport regimes, the interpretation of the TVS in the TyEx view is established as a genuine characteristic over the full bias range of the charge tunneling. In this TyEx view, V_{trans} is closely related to a bias-dependent perturbation of V_0, a bias scaling factor, which can be deduced from the third coefficient of the TyEx expression of the conductance. In other words, the TVS reflects the conductance nonlinearity of the junctions, which partially originates from the energy level alignment. During resonant tunneling, V_0 is proportional to the height of the tunneling barrier in most metal–molecule–metal junctions, whereas for off-resonant or deep tunneling, V_0 is proportion to the ratio between the barrier height and the barrier width. For a specific case, a highly nonlinear charge transport and non-physical TVS values could be observed in the semiconducting electrode-based molecular junctions due to the small bias-dependent density of the states for the semiconducting electrode. Therefore, the TVS measurements when the current becomes "superquadratic" with the bias voltage are a promising tool for studying the respective energy level alignment in most molecular junctions.

7.5.1.2 Applications of TVS

Because the asymmetry of the molecular junctions has a significant effect on the inflection behavior of the F–N plot, the TVS has been used to investigate the asymmetry and the energy level alignment of several asymmetric molecular junctions. Intuitively, the asymmetric voltage drops on both sides of the metal–molecule interfaces will lead to different barrier heights for carrier tunneling. Correspondingly, the polarity-dependent different values of V_{trans} can be observed to confirm the asymmetric interfacial contacts in the molecular junctions [10]. This polarity-dependent V_{trans} was also confirmed by Bâldea et al. who calculated the ambipolar TVS using asymmetric molecule–electrode couplings [178]. Furthermore, based on extensive *ab initio* calculations by using an analytical model of a Lorentzian-shaped transmission function, Chen et al. [179] found that asymmetry coupling at the two molecule–electrode interfaces had a significant effect on the ratio between V_{trans} and the energy offset of the nearest molecular orbital (ε_0) to E_F. The ratio $|\varepsilon_0 - E_F|/V_{trans}$ increased from 0.86 for a symmetric junction to 2.0 for a completely asymmetric junction. Based on experimental investigations of the asymmetric coupling effect of the molecule junctions using the TVS, Wang et al. [180] observed a similar tendency: by increasing the asymmetric coupling degree, the energy offset ($|\varepsilon_0 - E_F|$) was decreased, and V_{trans} became smaller.

The length of the molecules has a clear effect on the energy level alignment and the charge transport process in the molecular junctions. Using the TVS, the length-dependent properties of the molecular junctions with conjugated and non-conjugated molecules have been widely studied. For most molecular

junctions formed from conjugated molecules, where the voltage drop is expected to span the entire molecule, the ratio between V_{trans} and the frontier conducting orbital with respect to E_F is approximately constant [174]. For example, in HOMO-dominated molecular junctions with aromatic series, V_{trans} decreased with an increase in the molecular lengths because the conjugating effect and the coupling effect lifted the HOMO level of the molecules with an increased length [181]. However, for molecular junctions with non-conjugated alkyl molecules, V_{trans} is relatively length-independent. This result is partially due to the unchanged molecular energy level for the alkyl molecules with different molecular lengths [182]. Furthermore, for non-conjugated systems, the frontier orbitals are expected to be strongly localized at the end groups of the molecules, which leads to a voltage drop at the interfaces and thus the length-independent V_{trans} [183]. Additionally, it was determined that the voltage drop in the molecular junctions was affected by the temperature [184]. By using the TVS investigations of 2-[4-(2-mercaptoethyl)-phenyl] ethanethiol (Me-PET)-based molecular junctions with either Au or Al electrodes, the voltage drop at low temperatures occurred at the contact interfaces in the injection barrier dominated transport, whereas at high temperatures, the voltage drop occurred along the entire molecule in the molecular barrier dominated transport. Because V_{trans} in the TVS is deduced from the tunneling model, when the connected molecules are long enough for transferring the charge transport from tunneling to hopping, the inflection behavior of the F–N plot changes [93]. For the conjugated junctions with a hopping transport, it was determined that the F–N plot had three distinct transport regimes, corresponding to Ohmic conduction, field emission and a space charge-limited conduction regime between them.

The electrode properties, especially the contact interfaces, generally affect the charge transport in the molecular junctions. The TVS is widely used to study the interface-related properties of the molecular junctions. For molecular junctions with various electrodes having different work functions, such as Ag, Au, and Pt, it was determined that for HOMO-dominated molecular junctions with thiol linkages, V_{trans} decreased with an increase in the work functions of the electrodes. However, for LUMO-dominated molecular junctions with isocyanide linkages, V_{trans} changed in the opposite direction, which corresponded to the energy offset between the dominated molecular orbital and the electrode E_F [109, 174]. Furthermore, it was determined that the degree of V_{trans} variation is considerably slower than that of the changes of the work functions. This result can be ascribed to the specific bonding site for the S atom end group in different electrodes, where S atoms are most likely bound to the hollow-bridge site of the Ag/Au surface and the adatom site of the Pt electrode [185]. For non-metal electrodes, such as carbon nanotubes, theoretical calculations demonstrated that V_{trans} corresponds to the voltages that exhibit an NDR, which only occur during the coherent transport in molecular junctions when the tail of the resonant peak comes into the bias window [186]. For a fixed molecular junction, the fluctuations of the Coulomb interaction at the contacts have minimal effect on V_{trans} [187]. However, from the statistical TVS studies of the alkanedithiol- and biphenyldithiol-based single-molecule junctions, Guo et al. [188] determined that the molecule–electrode contact geometry had a

slight effect on V_{trans} because different V_{trans} values were obtained for molecular junctions with different conductance values. Furthermore, from individual thiol-tethered porphyrin molecular junctions with Au electrodes, Bennett et al. [189] determined a multi-peaked distribution of the V_{trans} values, which is due to the existence of a small number of distinct configurations at the interfacial contacts. For molecular junctions made from the tip-substrate technique, the distance between the molecule and the electrodes at the interfacial contacts was determined to have an effect on V_{trans}, which is because different molecular orbitals participate in the charge transport with varying distances [190]. Additionally, the chemical states of the electrodes in the molecular junction can be monitored using the TVS. For example, for molecular junctions made from Hg, GaIn or Si electrodes, the oxidization of the electrode surface was observed at a lower value of V_{trans} for the junctions [191]. Although the contact geometry, molecular conformation, and the electrode local density of states (LDOS) have apparent effects on V_{trans}, the fluctuations of V_{trans} are extremely small in most cases, which distinguishes the TVS as an effective tool for studying the charge transport in molecular junctions [192].

Because the TVS is able to qualitatively measure the energy offset between the nearest molecular energy level and E_F, it was used to monitor the gating effect for the molecular junctions. One good example is that by using single-molecule transistors with ~3 nm thick Al_2O_3 films as a back gate dielectric layer, Song et al. [7] used the TVS to quantitatively monitor the energy level shift process of the molecular orbital gating. For both the Au–1,8-octanedithiol (ODT)–Au and Au–1,4-BDT–Au junctions, the value of V_{trans} was observed to shift toward the lower bias with an increasingly negative applied gate voltage (V_G). This effectiveness of the molecular orbital gating can be estimated using $\alpha = \Delta V_{trans}/\Delta V_G$ as the gate efficiency factor. The positive large values of $\alpha = +0.25$ for the ODT junctions and $\alpha = +0.22$ for the BDT junctions indicated a strong gate coupling efficiency for the HOMO-mediated charge transport. For the Au–benzodifuran (BDF)–Au junctions with similar gate structure, Xiang et al. [193] determined that the gate efficiency factor is as small as ~0.035, again proving the effectiveness of the TVS. In addition to electrostatic gating, the chemical gating effect in the molecular junctions can be analyzed by using the TVS. With different substituents attached to the pyridinoparacyclophane (PC) moiety as the edge-on chemical gate, the energy offsets obtained from the statistical V_{trans} indicated that the orbital energy level could be tuned by changing the attached gating substituents from strong electron acceptors to strong electron donors [194]. In graphene–molecule junctions with photochromic diarylethene derivatives as the key elements, Guo and coworkers [173] demonstrated a photogated transition (V_{trans}) using TVS measurements, which originated from the optically controlled open/closed isomerization as well as the distinct electronic structures of the functional diarylethene center.

Lastly, the TVS is a potential tool for distinguishing molecular junctions from vacuum tunneling junctions. For example, Trouwborst et al. [195] measured the TVS of Au–vacuum–Au junctions, where voltages up to 3 V were applied over small vacuum gaps of clean electrodes at cryogenic temperatures. They determined that V_{trans} was sensitive to the local configuration of the Au electrodes,

which can be ascribed to the LDOS of Au. Furthermore, V_{trans} decreased with an increase in the tunneling distance. A similar relation between V_{trans} and the vacuum gap width was also found in the W–vacuum–Au junctions and the W–vacuum–Pt junctions at room temperature, where V_{trans} decreased linearly with an increase of the gap width [196]. However, this relation between V_{trans} and the gap width is considerably weaker than the prediction from standard vacuum tunneling models, which is partially due to the image charge effect. Because this variation of V_{trans} with the gap width is comparable with that in molecular junctions, it is difficult to use only this distance-dependent relation to differentiate the molecular junctions from the vacuum junctions. In certain cases, the absolute values of V_{trans} for vacuum junctions could reach >1.4 V, which is significantly larger than that of the molecular junctions, particularly those formed from conjugated molecules. For the origin of V_{trans} in the vacuum junctions, by using the theoretical calculation, Bâldea et al. proposed that it may be due to the electron states (or resonances) at the surface of the electrodes [197]. This result has been proven by Wu et al. [185, 198] who used metal–vacuum–metal junctions with atomically sharp electrodes to determine that V_{trans} was determined by the LDOS resulting from the 6p atomic orbitals of the apex metal atoms. A higher energy position of the metal 6p atomic orbitals led to a larger V_{trans} value of the metal–vacuum–metal junctions.

7.5.2 One Dimensional (1D), Two Dimensional (2D) Histogram and QuB

The single-molecule conductance can be determined by using a conventional one-dimensional (1D) conductance histogram constructed from hundreds of individual conductance traces recorded in the electrodes separation process [199]. Typical conductance traces and the corresponding 1D conductance histogram are shown in Figure 7.6a,b, respectively [200]. It can be found that each conductance traces as presented in Figure 7.6a is different due to the fluctuations. In order to determine the probable conductance, statistical data analysis such as 1D histograms is needed. Histograms are generated by counting how often the data fall into a specific conductance regime, and it can be generated by commercial software such as Origin. These 1D histograms exhibit peaks, the center value of which is the most probable conductance of a single molecule. However, the 1D conductance histogram only involves one significant parameter: conductance, which could not reveal other detailed features hidden in the current–distance traces (i.e. the junction length and correlation between two traces).

To have a straightforward glance at junction evolution feature, two-dimensional (2D) conductance histogram is widely used recently [200–203]. The 2D conductance–displacement histograms provide access to the dynamic structure of the junctions during elongation processes. The histograms are constructed by setting a specific conductance value (for example, $1G_0$) as a first data point, assigning it as a relative distance from $z = 0$ for each trace, and then overlapping all of the individual traces in 2D space [204]. In other words, this 2D histogram is achieved by superimposing hundreds of conductance traces that are shifted to the identical starting point and then illustrating the data points with an

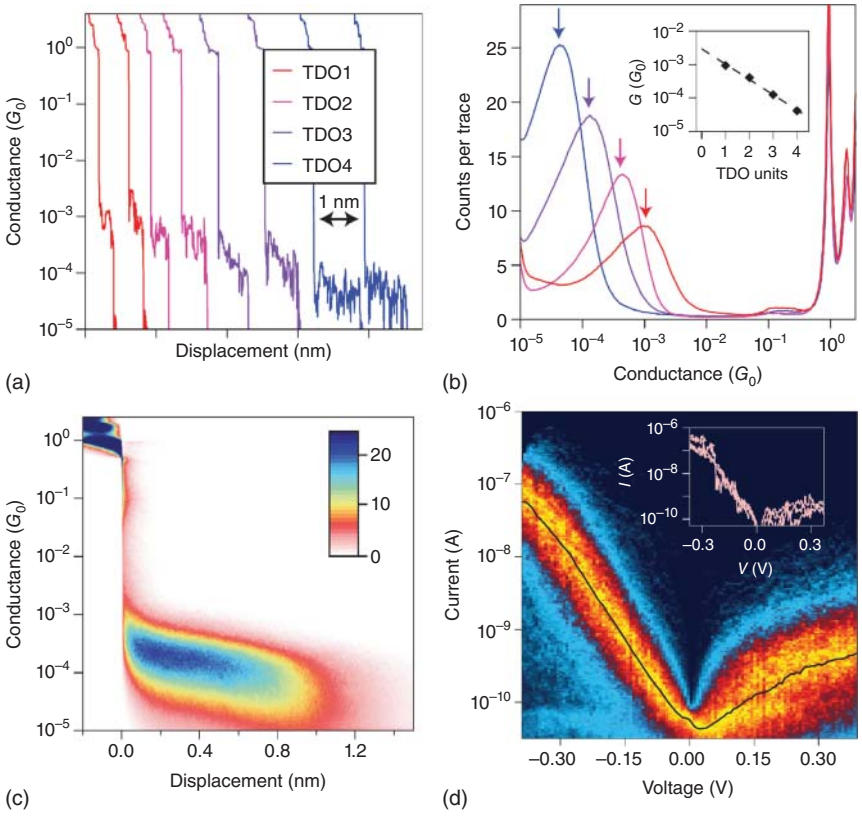

Figure 7.6 1D and 2D histograms. (a) Sample conductance versus displacement traces. These traces display molecule-specific conductance features, which persist for longer displacements as the molecular length increases from TDO1 to TDO4. (b) 1D log-binned conductance histograms, each composed of 20 000 traces as shown in (a). The arrows in the histogram indicate the peak-conductance positions. Inset: plot of the conductance as a function of the number of oxidized thiophene monomer units (*n*) in TDO1–TDO4. (c) 2D conductance–displacement histogram for TDO3 molecules created by aligning all the traces at the point where the conductance crosses 0.5 G_0, and then overlaying them. The color bar indicates the number of counts per 1000 traces. Source: (c) Reproduced with permission from Dell et al. [200]. Copyright 2015, Springer Nature. (d) Two-dimensional absolute current versus voltage histogram for TDO5. Inset: Examples of exceptionally rectifying junctions. Source: (d) Reproduced with permission from Capozzi et al. [201]. Copyright 2015, Springer Nature.

additional coordinate binned in color code. The color in 2D histogram indicates the counts of specific conductance value. By using this method, the average junction length prior to junction rupture can be clearly reflected, as shown in Figure 7.6c. Other than junction length information, many other interesting features have been observed in 2D histograms of molecular junctions. For example, conductance switching between two conductance states has been clearly monitored by using 2D histogram method [203]. In order to unravel the relationship between specific signals in individual conductance traces, such as the relation between two conductance values, Makk et al. developed a

conductance 2D auto-correlation histogram (C-2DACH) by introducing a time series analysis [205]. The 2D histogram had been employed to show statistically the feature of absolute current versus voltage, as shown by Figure 7.6d [201]. In this way, the rectification behavior as well as the rectification ratios of the molecular junctions can be addressed.

Neither the conductance histogram nor the 2D histogram is related to the time domain. However, the dynamics at the single molecular level is crucial in chemical and biological processes. The real-time monitoring of the molecular states at the single molecular level offers the way to understand the dynamic process. Conventionally, an elementary single-molecule reaction follows a single-step Poisson process that is stochastic, memory-free, and independent. The dwell time can be extracted and analyzed from the I–t profile with QuB technique [206]. The QuB software is an integrated, model-based, and optimized suite of programs that is capable to fit multistate models of single/multi channels of data with time varying external electric, mechanical, or chemical stimuli. Generally, the QuB software is capable to deal with the raw data, and extract a model from the trajectory. First of all, to fit the baseline by least-squares curve fitting and a combined Viterbi–Kalman idealization. After the baseline correction, the data was idealized as a sequence of open and close times. This transfer from data points to events improves the efficiency of the following analysis. With the identification of the burst events, channel count, number of conductance classes, and its mean amplitudes determine the model kinetics. Subsequently, the software will calculate and optimize the real-time data based on the hidden Markov inverse model [207, 208]. The information of single events hidden in ensemble average can be obtained. Recently, Guo and coworkers reported an experimental evidence of the formation dynamics of individual carbocation intermediates with a strong solvent dependence in a nucleophilic-substitution reaction with carefully investigation of the I–t trajectories by the QuB software (Figure 7.7) [209]. As Figure 7.7a shows, the real-time conductance measurements (black dots) was idealized (red line); it suggested that the lifetimes (τ_{low}/τ_{high}) of the acetate and carbocation forms are derived from the probability distributions of the dwell times (T_{low}/T_{high}) of the low- and high-conductance states. According to the hidden Markov chain model, $\tau_{low} = 5320 \pm 790\,\mu s$ and $\tau_{high} = 2540 \pm 200\,\mu s$, respectively, they demonstrated that the reactions behaved like a Poisson process (Figure 7.7b). Furthermore, they discussed the feasibility of the competitive reactions between different nucleophiles (Figure 7.7c,d). In Figure 7.7e, a third conductance state occurred occasionally. They suggested that the novel conductance state is probably corresponded to the bromide formation, which is competitive with the acetate formation due to the similar electronic structures. With QuB analysis, they demonstrated a single-molecule way to overcome the difficulty of realizing label-free, real-time electrical measurements of fast reaction dynamics with single-event sensitivity and high temporal resolution and revealed the molecular mechanisms of classical chemical reactions. Similar works of dynamic detection for a variety of reactions have been published with the statistical analysis by utilizing the QuB software [210–212].

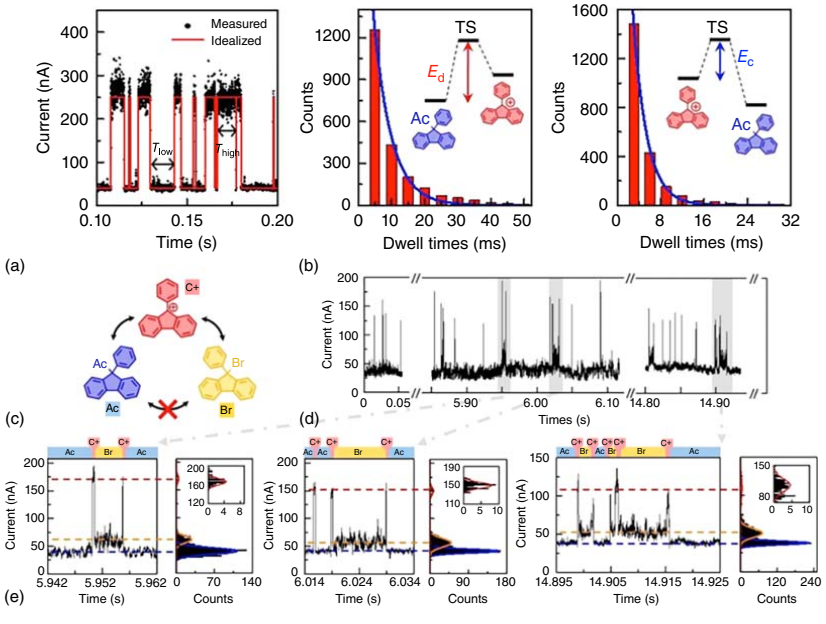

Figure 7.7 Analysis by using the QuB software. (a) Measured *I*–*t* trajectories (black dots) of a graphene-molecule-graphene single-molecule junction (GMG-SMJ) in the solution of acetic acid (HAc)–trifluoroacetic (TFA) (25%/75%, vol/vol). The red line shows the idealized two-level interconversion by using a QuB software. (b) Plots of time intervals of the (left) low- and (right) high-conductance states derived from *I*–*t* trajectories of a GMG-SMJ in the solution of HAc–TFA (25%/75%, vol/vol). The distributions were fit well by a single-exponential decay function (blue lines). Insets show the corresponding reaction pathways. (c) Schematic representation of competitive reactions of carbocation with Ac^- and Br^-. (d, e) Representative *I*–*t* trajectories and corresponding enlarged views of a GMG-SMJ, which was submerged into a HAc/Br^-/TFA ternary solution (25% HAc/75% TFA [v/v]; Br^-, 10 μmol/l). Ac, Br, and C^+ represent the acetate form, the bromide form, and the carbocation form, respectively. Source: Reproduced with permission from Gu et al. [209]. Copyright 2018, American Chemical Society.

References

1 Aradhya, S.V. and Venkataraman, L. (2013). Single-molecule junctions beyond electronic transport. *Nat. Nanotechnol.* 8: 399–410.
2 Garcia, R., Knoll, A.W., and Riedo, E. (2014). Advanced scanning probe lithography. *Nat. Nanotechnol.* 9: 577–587.
3 Leary, R., Midgley, P.A., and Thomas, J.M. (2012). Recent advances in the application of electron tomography to materials chemistry. *Acc. Chem. Res.* 45: 1782–1791.
4 Tian, H.H., Li, Y.C., Shao, H.B. et al. (2015). Thin-film voltammetry and its analytical applications: A review. *Anal. Chim. Acta* 855: 1–12.
5 Kashyap, D., Dwivedi, P.K., Pandey, J.K. et al. (2014). Application of electrochemical impedance spectroscopy in bio-fuel cell characterization: a review. *Int. J. Hydrogen Energy* 39: 20159–20170.
6 Vivek, J.P., Monsur, A., and Burgess, I.J. (2013). Differential capacity and chronocoulometry studies of a quaternary ammonium surfactant adsorbed on Au(111). *Surf. Interface Anal.* 45: 1402–1409.
7 Song, H., Kim, Y., Jang, Y.H. et al. (2009). Observation of molecular orbital gating. *Nature* 462: 1039–1043.
8 Choi, S.H., Kim, B., and Frisbie, C.D. (2008). Electrical resistance of long conjugated molecular wires. *Science* 320: 1482–1486.
9 Kim, Y., Song, H., Kim, D. et al. (2010). Noise characteristics of charge tunneling via localized states in metal–molecule–metal junctions. *ACS Nano* 4: 4426–4430.
10 Beebe, J.M., Kim, B., Gadzuk, J.W. et al. (2006). Transition from direct tunneling to field emission in metal–molecule–metal junctions. *Phys. Rev. Lett.* 97: 026801.
11 Reddy, P., Jang, S.Y., Segalman, R.A. et al. (2007). Thermoelectricity in molecular junctions. *Science* 315: 1568–1571.
12 Shamai, T. and Selzer, Y. (2011). Spectroscopy of molecular junctions. *Chem. Soc. Rev.* 40: 2293.
13 Mitsuishi, A. (2014). Progress in far-infrared spectroscopy: approximately 1890 to 1970. *J. Infrared Millimeter Terahertz Waves* 35: 243–281.
14 Jentoft, F.C. (2009). Ultraviolet–visible–near infrared spectroscopy in catalysis: Theory, experiment, analysis, and application under reaction conditions. *Adv. Catal.* 52: 129–211.
15 Surviliene, S., Cesuniene, A., Jasulaitiene, V. et al. (2015). Investigation of the surface composition of electrodeposited black chromium by X-ray photoelectron spectroscopy. *Appl. Surf. Sci.* 324: 837–841.
16 Yamamoto, S. and Matsuda, I. (2013). Time-resolved photoelectron spectroscopies using synchrotron radiation: past, present, and future. *J. Phys. Soc. Jpn.* 82: 021003.
17 Knuta, R., Lindblad, R., Gorgoi, M. et al. (2013). High energy photoelectron spectroscopy in basic and applied science: bulk and interface electronic structure. *J. Electron. Spectrosc.* 190: 278–288.

18 Galperin, M., Ratner, M.A., Nitzan, A. et al. (2008). Nuclear coupling and polarization in molecular transport junctions: beyond tunneling to function. *Science* 319: 1056–1060.

19 Song, H., Reed, M.A., and Lee, T. (2011). Single molecule electronic devices. *Adv. Mater.* 23: 1583–1608.

20 Hihath, J. and Tao, N.J. (2012). Electron–phonon interactions in atomic and molecular devices. *Prog. Surf. Sci.* 87: 189–208.

21 Okabayashi, N., Paulsson, M., and Komeda, T. (2013). Inelastic electron tunneling process for alkanethiol self-assembled monolayers. *Prog. Surf. Sci.* 88: 1–38.

22 Hapala, P., Temirov, R., Tautz, F.S. et al. (2014). Origin of high-resolution IETS–STM images of organic molecules with functionalized tips. *Phys. Rev. Lett.* 113: 226101.

23 Deng, M.S., Ye, G., Cai, S.H. et al. (2015). Probing flexible conformations in molecular junctions by inelastic electron tunneling spectroscopy. *AIP Adv.* 5: 017144.

24 Jaklevic, R.C. and Lambe, J. (1966). Molecular vibration spectra by electron tunneling. *Phys. Rev. Lett.* 17: 1139–1140.

25 Stipe, B.C., Rezaei, M.A., and Ho, W. (1998). Single-molecule vibrational spectroscopy and microscopy. *Science* 280: 1732–1735.

26 Ho, W. (2002). Single-molecule chemistry. *J. Chem. Phys.* 117: 11033.

27 Tsutsui, M., Taniguchi, M., and Kawai, T. (2010). Single-molecule identification via electric current noise. *Nat. Commun.* 138: 1–5.

28 Tsutsui, M. and Taniguchi, M. (2013). Vibrational spectroscopy of single-molecule junctions by direct current measurements. *J. Appl. Phys.* 113: 084301.

29 Petit, C. and Salace, G. (2003). Inelastic electron tunneling spectrometer to characterize metal-oxide-semiconductor devices with ultrathin oxides. *Rev. Sci. Instrum.* 74: 4462–4467.

30 Hipps, K.W. and Mazur, U. (1993). Inelastic electron-tunneling – an alternative molecular-spectroscopy. *J. Phys. Chem.* 97: 7803–7814.

31 Wang, W.Y., Lee, T., Kretzschmar, I., and Reed, M.A. (2004). Inelastic electron tunneling spectroscopy of an alkanedithiol self-assembled monolayer. *Nano Lett.* 4: 643–646.

32 Walmsley, D.G. and Tomlin, J.L. (1985). Compilation of inelastic electron tunnelling spectra of molecules chemisorbed on metal-oxides. *Prog. Surf. Sci.* 18: 247–447.

33 Hansma, P.K. (1983). Tunneling spectroscopy as a probe of adsorbate–surface interactions. *J. Electron Spectrosc.* 30: 163–174.

34 Kushmerick, J.G., Lazorcik, J., Patterson, C.H. et al. (2004). Vibronic contributions to charge transport across molecular junctions. *Nano Lett.* 4: 639–642.

35 Jafri, S.H.M., Lofas, H., Fransson, J. et al. (2013). Identification of vibrational signatures from short chains of interlinked molecule–nanoparticle junctions obtained by inelastic electron tunnelling spectroscopy. *Nanoscale* 5: 4673–4677.

36 Gregory, S. (1990). Inelastic tunneling spectroscopy and single-electron tunneling in an adjustable microscopic tunnel junction. *Phys. Rev. Lett.* 64: 689–692.

37 Kushmerick, J.G., Naciri, J., Yang, J.C. et al. (2003). Conductance scaling of molecular wires in parallel. *Nano Lett.* 3: 897–900.

38 Beebe, J.M., Moore, H.J., Lee, T.R. et al. (2007). Vibronic coupling in semi-fluorinated alkanethiol junctions: Implications for selection rules in inelastic electron tunneling spectroscopy. *Nano Lett.* 7: 1364–1368.

39 Yoon, H.P., Maitani, M.M., Cabarcos, O.M. et al. (2010). Crossed-nanowire molecular junctions: A new multispectroscopy platform for conduction-structure correlations. *Nano Lett.* 10: 2897–2902.

40 Milani, F., Grave, C., Ferri, V. et al. (2007). Ultrathin π-conjugated polymer films for simple fabrication of large-area molecular junctions. *ChemPhysChem* 8: 515–518.

41 Park, S., Wang, G., Cho, B. et al. (2012). Flexible molecular-scale electronic devices. *Nat. Nanotechnol.* 7: 438–442.

42 Li, T., Hauptmann, J.R., Wei, Z. et al. (2012). Solution-processed ultrathin chemically derived graphene films as soft top contacts for solid-state molecular electronic junctions. *Adv. Mater.* 24: 1333–1339.

43 Jeong, H., Kim, D., Wang, G. et al. (2014). Redox-induced asymmetric electrical characteristics of ferrocene–alkanethiolate molecular devices on rigid and flexible substrates. *Adv. Funct. Mater.* 24: 2472–2480.

44 Hihath, J., Arroyo, C.R., Rubio-Bollinger, G. et al. (2008). Study of electron–phonon interactions in a single molecule covalently connected to two electrodes. *Nano Lett.* 8: 1673–1678.

45 Martin, C.A., Smit, R.H., van Egmond, R. et al. (2011). A versatile low-temperature setup for the electrical characterization of single-molecule junctions. *Rev. Sci. Instrum.* 82: 053907.

46 Ueno, S., Tomoda, Y., Kume, W. et al. (2012). Field-emission-induced electromigration method for the integration of single-electron transistors. *Appl. Surf. Sci.* 258: 2153–2156.

47 Neuhausen, A.B., Hosseini, A., Sulpizio, J.A. et al. (2012). Molecular junctions of self-assembled monolayers with conducting polymer contacts. *ACS Nano* 6: 9920–9931.

48 Seo, S., Min, M., Lee, S.M. et al. (2013). Photo-switchable molecular monolayer anchored between highly transparent and flexible graphene electrodes. *Nat. Commun.* 4: 1920.

49 Li, T., Jevric, M., Hauptmann, J.R. et al. (2013). Ultrathin reduced graphene oxide films as transparent top-contacts for light switchable solid-state molecular junctions. *Adv. Mater.* 25: 4164–4170.

50 Ashwell, G.J., Wierzchowiec, P., Bartlett, C.J. et al. (2007). Molecular electronics: connection across nano-sized electrode gaps. *Chem. Commun.* 12: 1254–1256.

51 Preiner, M.J. and Melosh, N.A. (2008). Creating large area molecular electronic junctions using atomic layer deposition. *Appl. Phys. Lett.* 92: 213301.

52 Chen, W., Liu, X., Tan, Z. et al. (2006). Fabrication and characterization of novel cross point structures for molecular electronic integrated circuits. *J. Vac. Sci. Technol. B*24: 3217–3220.

53 Tyagi, P., Li, D., Holmes, S.M., and Hinds, B.J. (2007). Molecular electrodes at the exposed edge of metal/insulator/metal trilayer structures. *J. Am. Chem. Soc.* 129: 4929–4938.

54 Okabayashi, N., Paulsson, M., Ueba, H. et al. (2010). Site selective inelastic electron tunneling spectroscopy probed by isotope labeling. *Nano Lett.* 10: 2950–2955.

55 Tal, O., Krieger, M., Leerink, B. et al. (2008). Electron-vibration interaction in single-molecule junctions: from contact to tunneling regimes. *Phys. Rev. Lett.* 100: 196804.

56 Howell, S.W., Dirk, S.M., Childs, K. et al. (2005). Mass-fabricated one-dimensional silicon nanogaps for hybrid organic/nanoparticle arrays. *Nanotechnology* 16: 754–758.

57 Luber, S.M., Strobel, S., Tranitz, H.-P. et al. (2005). Nanometre spaced electrodes on a cleaved AlGaAs surface. *Nanotechnology* 16: 1182–1185.

58 Kim, Y., Pietsch, T., Erbe, A. et al. (2011). Benzenedithiol: a broad-range single-channel molecular conductor. *Nano Lett.* 11: 3734–3738.

59 Hihath, J., Bruot, C., and Tao, N.J. (2010). Electron–phonon interactions in single octanedithiol molecular junctions. *ACS Nano* 4: 3823–3830.

60 Song, H., Kim, Y., Ku, J. et al. (2009). Vibrational spectra of metal–molecule–metal junctions in electromigrated nanogap electrodes by inelastic electron tunneling. *Appl. Phys. Lett.* 94: 103110.

61 Tsutsui, M., Taniguchi, M., Shoji, K. et al. (2009). Identifying molecular signatures in metal–molecule–metal junctions. *Nanoscale* 1: 164–170.

62 Ren, H., Yang, J.L., and Luo, Y. (2010). Identifying configuration and orientation of adsorbed molecules by inelastic electron tunneling spectra. *J. Chem. Phys.* 133: 064702.

63 Leng, J.C., Lin, L.L., Song, X.N. et al. (2009). Orientation of decanethiol molecules in self-assembled monolayers determined by inelastic electron tunneling spectroscopy. *J. Phys. Chem. C* 113: 18353–18357.

64 Lin, L.L., Wang, C.K., and Luo, Y. (2011). Inelastic electron tunneling spectroscopy of gold-benzenedithiol-gold junctions: Accurate determination of molecular conformation. *ACS Nano* 5: 2257–2263.

65 Jiang, J., Kula, M., Lu, W. et al. (2005). First-principles simulations of inelastic electron tunneling spectroscopy of molecular electronic devices. *Nano Lett.* 5: 1551–1555.

66 Chiang, C.-L., Xu, C., Han, Z. et al. (2014). Real-space imaging of molecular structure and chemical bonding by single-molecule inelastic tunneling probe. *Science* 344: 885–888.

67 Seminario, J.M., Zacarias, A.G., and Tour, J.M. (2000). Theoretical study of a molecular resonant tunneling diode. *J. Am. Chem. Soc.* 122: 3015–3020.

68 Di Ventra, M., Kim, S.G., Pantelides, S.T. et al. (2001). Temperature effects on the transport properties of molecules. *Phys. Rev. Lett.* 86: 288–291.

69 Lang, N.D. and Avouris, P. (2000). Electrical conductance of parallel atomic wires. *Phys. Rev. B* 62: 7325–7329.

70 Ramachandran, G.K., Hopson, T.J., Rawlett, A.M. et al. (2003). A bond-fluctuation mechanism for stochastic switching in wired molecules. *Science* 300: 1413–1416.

71 He, J., Fu, Q., Lindsay, S. et al. (2006). Electrochemical origin of voltage-controlled molecular conductance switching. *J. Am. Chem. Soc.* 128: 14828–14835.

72 Paulsson, M., Frederiksen, T., and Brandbyge, M. (2006). Inelastic transport through molecules: Comparing first-principles calculations to experiments. *Nano Lett.* 6: 258–262.

73 Cai, L.T., Cabassi, M.A., Yoon, H. et al. (2005). Reversible bistable switching in nanoscale thiol-substituted oligoaniline molecular junctions. *Nano Lett.* 5: 2365–2372.

74 Cao, H., Jiang, J., Ma, J. et al. (2008). Identification of switching mechanism in molecular junctions by inelastic electron tunneling spectroscopy. *J. Phys. Chem. C* 112: 11018–11022.

75 Long, D.P., Lazorcik, J.L., Mantooth, B.A. et al. (2006). Effects of hydration on molecular junction transport. *Nat. Mater.* 5: 901–908.

76 Kim, Y., Garcia-Lekue, A., Sysoiev, D. et al. (2012). Charge transport in azobenzene-based single-molecule junctions. *Phys. Rev. Lett.* 109: 226801.

77 Hihath, J., Bruot, C., Nakamura, H. et al. (2011). Inelastic transport and low-bias rectification in a single-molecule diode. *ACS Nano* 5: 8331–8339.

78 Bruot, C., Hihath, J., and Tao, N. (2012). Mechanically controlled molecular orbital alignment in single molecule junctions. *Nat. Nanotechnol.* 7: 35–40.

79 Taniguchi, M., Tsutsui, M., Yokota, K. et al. (2010). Mechanically-controllable single molecule switch based on configuration specific electrical conductivity of metal-molecule-metal junctions. *Chem. Sci.* 1: 247–253.

80 Kim, Y., Hellmuth, T.J., Burkle, M. et al. (2011). Characteristics of amine-ended and thiol-ended alkane single-molecule junctions revealed by inelastic electron tunneling spectroscopy. *ACS Nano* 5: 4104–4111.

81 Kaneko, S., Motta, C., Brivio, G.P. et al. (2013). Mechanically controllable bi-stable states in a highly conductive single pyrazine molecular junction. *Nanotechnology* 24: 315201.

82 Kim, Y., Song, H., Strigl, F. et al. (2011). Conductance and vibrational states of single-molecule junctions controlled by mechanical stretching and material variation. *Phys. Rev. Lett.* 106: 196804.

83 Lykkebo, J., Gagliardi, A., Pecchia, A. et al. (2013). Strong overtones modes in inelastic electron tunneling spectroscopy with cross-conjugated molecules: a prediction from theory. *ACS Nano* 7: 9183–9194.

84 Lorente, N., Persson, M., Lauhon, L.J. et al. (2001). Symmetry selection rules for vibrationally inelastic tunneling. *Phys. Rev. Lett.* 86: 2593–2596.

85 Fock, J., Sorensen, J.K., Lortscher, E. et al. (2011). A statistical approach to inelastic electron tunneling spectroscopy on fullerene-terminated molecules. *Phys. Chem. Chem. Phys.* 13: 14325–14432.

86 Hou, J.G. and Zhao, A.D. (2006). Detecting and manipulating single molecules with STM. *Nano* 1: 15–33.

87 Jeong, H., Hwang, W.T., Kim, P. et al. (2015). Investigation of inelastic electron tunneling spectra of metal–molecule–metal junctions fabricated using direct metal transfer method. *Appl. Phys. Lett.* 106: 063110.

88 Luo, L., Benameur, A., Brignou, P. et al. (2011). Length and temperature dependent conduction of ruthenium-containing redox-active molecular wires. *J. Phys. Chem. C* 115: 19955–19961.

89 Wang, W.Y., Lee, T., and Reed, M.A. (2003). Mechanism of electron conduction in self-assembled alkanethiol monolayer devices. *Phys. Rev. B* 68: 035416.

90 Luo, L.A., Choi, S.H., and Frisbie, C.D. (2011). Probing hopping conduction in conjugated molecular wires connected to metal electrodes. *Chem. Mater.* 23: 631.

91 Yamada, R., Kumazawa, H., Tanaka, S. et al. (2009). Electrical resistance of long oligothiophene molecules. *Appl. Phys. Express* 2: 025002.

92 Hines, T., Diez-Perez, I., Hihath, J. et al. (2010). Transition from tunneling to hopping in single molecular junctions by measuring length and temperature dependence. *J. Am. Chem. Soc.* 132: 11658–11664.

93 Choi, S.H., Risko, C., Delgado, M.C.R. et al. (2010). Transition from tunneling to hopping transport in long, conjugated oligo-imine wires connected to metals. *J. Am. Chem. Soc.* 132: 4358–4368.

94 Luo, L. and Frisbie, C.D. (2010). Length-dependent conductance of conjugated molecular wires synthesized by stepwise "click" chemistry. *J. Am. Chem. Soc.* 132: 8854–8855.

95 Choi, S.H. and Frisbie, C.D. (2010). Enhanced hopping conductivity in low band gap donor–acceptor molecular wires up to 20 nm in length. *J. Am. Chem. Soc.* 132: 16191–16201.

96 Hsu, L.Y., Wu, N., and Rabitz, H. (2014). Gate control of the conduction mechanism transition from tunneling to thermally activated hopping. *J. Phys. Chem. Lett.* 5: 1831–1836.

97 Zhao, X.T., Huang, C.C., Gulcur, M. et al. (2015). Oligo(aryleneethynylene)s with terminal pyridyl groups: Synthesis and length dependence of the tunneling-to-hopping transition of single-molecule conductances. *Chem. Mater.* 25: 4340–4347.

98 Lu, Q., Yao, C., Wang, X.H. et al. (2012). Enhancing molecular conductance of oligo(*p*-phenylene ethynylene)s by incorporating ferrocene into their backbones. *J. Phys. Chem. C* 116: 17853–17861.

99 Lu, Q., Liu, K., Zhang, H.M. et al. (2009). From tunneling to hopping: A comprehensive investigation of charge transport mechanism in molecular junctions based on oligo(*p*-phenylene ethynylene)s. *ACS Nano* 3: 3861–3868.

100 Ferreira, Q., Braganca, A.M., Alcacer, L. et al. (2014). Conductance of well-defined porphyrin self-assembled molecular wires up to 14 nm in length. *J. Phys. Chem. C* 118: 7229–7234.

101 Poot, M., Osorio, E., O'Neill, K. et al. (2006). Temperature dependence of three-terminal molecular junctions with sulfur end-functionalized tercyclohexylidenes. *Nano Lett.* 6: 1031–1035.

102 Sedghi, G., Garcia-Suarez, V.M., Esdaile, L.J. et al. (2011). Long-range electron tunnelling in oligo-porphyrin molecular wires. *Nat. Nanotechnol.* 6: 517–523.

103 Nijhuis, C.A., Reus, W.F., Barber, J.R. et al. (2010). Charge transport and rectification in arrays of SAM-based tunneling junctions. *Nano Lett.* 10: 3611–3619.

104 Liang, X., Jung, Y.-S., Wu, S. et al. (2010). Formation of bandgap and subbands in graphene nanomeshes with sub-10 nm ribbon width fabricated via nanoimprint lithography. *Nano Lett.* 10: 2454–2460.

105 Yan, H.J., Bergren, A.J., McCreery, R. et al. (2013). Activationless charge transport across 4.5 to 22 nm in molecular electronic junctions. *Proc. Natl. Acad. Sci. U. S. A.* 110: 5326.

106 Kolivoska, V., Valasek, M., Gal, M. et al. (2013). Single-molecule conductance in a series of extended viologen molecules. *J. Phys. Chem. Lett.* 4: 589–595.

107 Sedghi, G., Esdaile, L.J., Anderson, H.L. et al. (2012). Comparison of the conductance of three types of porphyrin-based molecular wires: β-meso,β-fused tapes, meso-butadiyne-linked and twisted meso–meso linked oligomers. *Adv. Mater.* 24: 653–657.

108 Li, Z.H., Park, T.H., Rawson, J. et al. (2012). Quasi-ohmic single molecule charge transport through highly conjugated meso-to-meso ethyne-bridged porphyrin wires. *Nano Lett.* 12: 2722–2727.

109 Kim, B., Choi, S.H., Zhu, X.Y. et al. (2011). Molecular tunnel junctions based on π-conjugated oligoacene thiols and dithiols between Ag, Au, and Pt contacts: effect of surface linking group and metal work function. *J. Am. Chem. Soc.* 133: 19864–19877.

110 Galperin, M., Nitzan, A., and Ratner, M.A. (2006). Inelastic tunneling effects on noise properties of molecular junctions. *Phys. Rev. B* 74: 075326.

111 Secker, D., Wagner, S., Ballmann, S. et al. (2011). Resonant vibrations, peak broadening, and noise in single molecule contacts: the nature of the first conductance peak. *Phys. Rev. Lett.* 106: 136807.

112 Djukic, D. and van Ruitenbeek, J.M. (2006). Shot noise measurements on a single molecule. *Nano Lett.* 6: 789–793.

113 Wheeler, P.J., Russom, J.N., Evans, K. et al. (2010). Shot noise suppression at room temperature in atomic-scale Au junctions. *Nano Lett.* 10: 1287–1292.

114 Wu, Z.M., Wu, S.M., Oberholzer, S. et al. (2008). Scaling of $1/f$ noise in tunable break junctions. *Phys. Rev. B* 78: 235421.

115 Xiang, D., Lee, T., Kim, Y. et al. (2014). Origin of discrete current fluctuations in a single molecule junction. *Nanoscale* 6: 13396–13401.

116 Adak, O., Rosenthal, E., Meisner, J. et al. (2015). Flicker noise as a probe of electronic interaction at metal-single molecule interfaces. *Nano Lett.* 15: 4143–4149.

117 Kumar, M., Avriller, R., Yeyati, A.L. et al. (2012). Detection of vibration-mode scattering in electronic shot noise. *Phys. Rev. Lett.* 108: 144602.

118 Sydoruk, V.A., Xiang, D., Vitusevich, S.A. et al. (2012). Noise and transport characterization of single molecular break junctions with individual molecule. *J. Appl. Phys.* 112: 014908.

119 Ochs, R., Secker, D., Elbing, M. et al. (2006). Fast temporal fluctuations in single-molecule junctions. *Faraday Discuss.* 131: 281–289.

120 Blanter, Y.M. and Buttiker, M. (2000). Shot noise in mesoscopic conductors. *Phys. Rep.* 336: 1–166.

121 Rogers, C.T. and Buhrman, R.A. (1984). Composition of $1/f$ noise in metal–insulator–metal tunnel junctions. *Phys. Rev. Lett.* 53: 1272.

122 van den Brom, H.E. and van Ruitenbeek, J.M. (1999). Quantum suppression of shot noise in atom-size metallic contacts. *Phys. Rev. Lett.* 82: 1526.

123 Xiang, D., Sydoruk, V., Vitusevich, S. et al. (2015). Noise characterization of metal-single molecule contacts. *Appl. Phys. Lett.* 106: 063702.

124 Chen, R., Matt, M., Pauly, F. et al. (2014). Shot noise variation within ensembles of gold atomic break junctions at room temperature. *J. Phys.: Condens. Matter* 26: 474204.

125 Djukic, D., Thygesen, K.S., Untiedt, C. et al. (2005). Stretching dependence of the vibration modes of a single-molecule Pt–H_2–Pt bridge. *Phys. Rev. B*: 71, 161402(R).

126 Paulsson, M., Frederiksen, T., and Brandbyge, M. (2005). Modeling inelastic phonon scattering in atomic– and molecular–wire junctions. *Phys. Rev. B*: 72, 201101(R).

127 Ben-Zvi, R., Vardimon, R., Yelin, T. et al. (2013). Electron-vibration interaction in multichannel single-molecule junctions. *ACS Nano* 7: 11147.

128 Galperin, M., Ratner, M.A., and Nitzan, A. (2004). Inelastic electron tunneling spectroscopy in molecular junctions: Peaks and dips. *J. Chem. Phys.* 121: 11965.

129 Koch, J. and von Oppen, F. (2005). Franck–Condon blockade and giant fano factors in transport through single molecules. *Phys. Rev. Lett.* 94: 206804.

130 Schneider, N.L., Lu, J.T., Brandbyge, M. et al. (2012). Light emission probing quantum shot noise and charge fluctuations at a biased molecular junction. *Phys. Rev. Lett.* 109: 186601.

131 Haupt, F., Novotny, T., and Belzig, W. (2009). Phonon-assisted current noise in molecular junctions. *Phys. Rev. Lett.* 103: 136601.

132 Brunner, J., Gonzalez, M.T., Schonenberger, C. et al. (2014). Random telegraph signals in molecular junctions. *J. Phys.: Condens. Matter* 26: 474202.

133 Donhauser, Z.J., Mantooth, B.A., Kelly, K.F. et al. (2001). Conductance switching in single molecules through conformational changes. *Science* 292: 2303–2307.

134 Zandbergen, H.W., Pao, C.W., and Srolovitz, D.J. (2007). Dislocation injection, reconstruction, and atomic transport on {001} Au terraces. *Phys. Rev. Lett.* 2007 (98): 036103.

135 Ohshiro, T., Tsutsui, M., Yokota, K. et al. (2014). Detection of post-translational modifications in single peptides using electron tunnelling currents. *Nat. Nanotechnol.* 9: 835–840.

136 Chang, S.A., He, J., Lin, L.S. et al. (2009). Tunnel conductance of Watson–Crick nucleoside-base pairs from telegraph noise. *Nanotechnology* 20: 185102.

137 Bergren, A.J. and McCreery, R.L. (2011). Analytical chemistry in molecular electronics. *Annu. Rev. Anal. Chem.* 4: 95–173.

138 Elliott, A.B.S., Horvath, R., and Gordon, K.C. (2012). Vibrational spectroscopy as a probe of molecule-based devices. *Chem. Soc. Rev.* 41: 1929–1946.

139 Campion, A. and Kambhampati, P. (1998). Surface-enhanced Raman scattering. *Chem. Soc. Rev.* 27: 241–250.

140 Camp, C.H. and Cicerone, M.T. (2015). Chemically sensitive bioimaging with coherent Raman scattering. *Nat. Photonics* 9: 295–305.

141 Hung, K.K., Stege, U., and Hore, D.K. (2015). IR absorption, raman scattering, and IR–Vis sum-frequency generation spectroscopy as quantitative probes of surface structure. *Appl. Spectrosc. Rev.* 50: 351–376.

142 Bell, S.E.J. and Sirimuthu, N.M.S. (2006). Surface-enhanced Raman spectroscopy (SERS) for sub-micromolar detection of DNA/RNA mononucleotides. *J. Am. Chem. Soc.* 128: 15580–15581.

143 Bantz, K.C., Meyer, A.F., Wittenberg, N.J. et al. (2011). Recent progress in SERS biosensing. *Phys. Chem. Chem. Phys.* 13: 11551–11567.

144 Lee, H.M., Jin, S.M., Kim, H.M. et al. (2013). Single-molecule surface-enhanced Raman spectroscopy: A perspective on the current status. *Phys. Chem. Chem. Phys.* 15: 5276–5287.

145 Schlucker, S. (2014). Surface-enhanced Raman spectroscopy: concepts and chemical applications. *Angew. Chem. Int. Ed.* 53: 4756–4795.

146 Yang, L.B., Li, P., Liu, H.L. et al. (2015). A dynamic surface enhanced Raman spectroscopy method for ultra-sensitive detection: from the wet state to the dry state. *Chem. Soc. Rev.* 44: 2837–2848.

147 Xu, W.G., Mao, N.N., and Zhang, J. (2013). Graphene: A platform for surface-enhanced Raman spectroscopy. *Small* 9: 1206–1224.

148 Ward, D.R., Halas, N.J., Ciszek, J.W. et al. (2008). Simultaneous measurements of electronic conduction and Raman response in molecular junctions. *Nano Lett.* 8: 919–924.

149 Konishi, T., Kiguchi, M., Takase, M. et al. (2013). Single molecule dynamics at a mechanically controllable break junction in solution at room temperature. *J. Am. Chem. Soc.* 135: 1009–1014.

150 Jiang, N., Foley, E.T., Klingsporn, J.M. et al. (2012). Observation of multiple vibrational modes in ultrahigh vacuum tip-enhanced raman spectroscopy combined with molecular-resolution scanning tunneling microscopy. *Nano Lett.* 12: 5061–5067.

151 Cui, L., Liu, B., Vonlanthen, D. et al. (2011). In situ gap-mode raman spectroscopy on single-crystal Au(100) electrodes: tuning the torsion angle of 4,4′-biphenyldithiols by an electrochemical gate field. *J. Am. Chem. Soc.* 133: 7332–7335.

152 Ward, D.R., Corley, D.A., Tour, J.M. et al. (2011). Vibrational and electronic heating in nanoscale junctions. *Nat. Nanotechnol.* 6: 33–38.

153 Ozaki, Y., Morisawa, Y., Ikehata, A. et al. (2012). Far-ultraviolet spectroscopy in the solid and liquid states: a review. *Appl. Spectrosc.* 66: 1–25.

154 Li, Z., Berger, H., Okamoto, K. et al. (2013). Measurement of the internal orbital alignment of oligothiophene-TiO_2 nanoparticle hybrids. *J. Phys. Chem. C* 117: 13961–13970.

155 Kantchev, E.A.B., Norsten, T.B., Tan, M.L.Y. et al. (2012). Thiophene-containing Pechmann dyes and related compounds: synthesis and experimental and DFT characterisation. *Chem. Eur. J.* 18: 695–708.

156 Zhang, Y., Jiang, Y.B., Zhang, D.K. et al. (2011). On-line concentration measurement for anti-solvent crystallization of beta-artemether using UV–vis fiber spectroscopy. *J. Cryst. Growth* 314: 185–189.

157 Doherty, M.D. (2013). Kinetics and thermodynamics of small molecule binding to Pincer–PCP rhodium(I) complexes. *Inorg. Chem.* 52: 4160–4172.

158 Kobayashi, K. (2009). Hard X-ray photoemission spectroscopy. *Nucl. Instrum. Methods Phys. Res., Sect. A* 601: 32–47.

159 Cohen, H. (2010). Chemically resolved electrical measurements in organic self-assembled molecular layers. *J. Electron Spectrosc.* 176: 24–34.

160 Harada, Y., Koitaya, T., Mukai, K. et al. (2013). Spectroscopic characterization and transport properties of aromatic monolayers covalently attached to Si(111) surfaces. *J. Phys. Chem. C* 2013 (117): 7497–7505.

161 Ie, Y., Hirose, T., Nakamura, H. et al. (2011). Nature of electron transport by pyridine-based tripodal anchors: potential for robust and conductive single-molecule junctions with gold electrodes. *J. Am. Chem. Soc.* 133: 3014–3022.

162 Seitz, O., Dai, M., Aguirre-Tostado, F.S. et al. (2009). Copper-metal deposition on self assembled monolayer for making top contacts in molecular electronic devices. *J. Am. Chem. Soc.* 131: 18159–18167.

163 Zhu, Z.H., Daniel, T.A., Maitani, M. et al. (2006). Controlling gold atom penetration through alkanethiolate self-assembled monolayers on Au {111} by adjusting terminal group intermolecular interactions. *J. Am. Chem. Soc.* 128: 13710–13719.

164 Kimberg, V. and Miron, C. (2014). Molecular potentials and wave function mapping by high-resolution electron spectroscopy and ab initio calculations. *J. Electron Spectrosc.* 195: 301–306.

165 Turner, D.W. (1970). Molecular photoelectron spectroscopy. *Philos. Trans. R. Soc. London, Ser. A* 268: 7–31.

166 Svensson, S. (2005). Soft X-ray photoionization of atoms and molecules. *J. Phys. B* 38: S821.

167 Nguyen, N.L., Borghi, G., Ferretti, A. et al. (2015). First-principles photoemission spectroscopy and orbital tomography in molecules from Koopmans-compliant functionals. *Phys. Rev. Lett.* 114: 166405.

168 Kim, B., Beebe, J.M., Jun, Y. et al. (2006). Correlation between HOMO alignment and contact resistance in molecular junctions: aromatic thiols versus aromatic isocyanides. *J. Am. Chem. Soc.* 128: 4970–4971.

169 Yaffe, O., Qi, Y.B., Scheres, L. et al. (2012). Charge transport across metal/molecular (alkyl) monolayer-Si junctions is dominated by the LUMO level. *Phys. Rev. B* 85: 045433.

170 Hill, I.G., Rajagopal, A., Kahn, A. et al. (1998). Molecular level alignment at organic semiconductor-metal interfaces. *Appl. Phys. Lett.* 73: 662–664.

171 Ferre, A., Boguslavskiy, A.E., Dagan, M. et al. (2015). Multi-channel electronic and vibrational dynamics in polyatomic resonant high-order harmonic generation. *Nat. Commun.* 6: 5952.

172 Perry, D.L., Ma, Z.X., Olson, A. et al. (2015). Molecular characterization of gadolinium-doped zinc telluride films by X-ray photoelectron spectroscopy. *Spectroscopy* 30: 38.

173 Jia, C., Wang, J., Yao, C. et al. (2013). Conductance switching and mechanisms in single-molecule junctions. *Angew. Chem. Int. Ed.* 52: 8666–8670.

174 Beebe, J.M., Kim, B., Frisbie, C.D. et al. (2008). Measuring relative barrier heights in molecular electronic junctions with transition voltage spectroscopy. *ACS Nano* 2: 827–832.

175 Huisman, E.H., Guedon, C.M., van Wees, B.J. et al. (2009). Interpretation of transition voltage spectroscopy. *Nano Lett.* 9: 3909–3913.

176 Araidai, M. and Tsukada, M. (2010). Theoretical calculations of electron transport in molecular junctions: inflection behavior in Fowler–Nordheim plot and its origin. *Phys. Rev. B* 81: 235114.

177 Vilan, A., Cahen, D., and Kraisler, E. (2013). Rethinking transition voltage spectroscopy within a generic Taylor expansion view. *ACS Nano* 7: 695–706.

178 Bâldea, I. (2012). Ambipolar transition voltage spectroscopy: Analytical results and experimental agreement. *Phys. Rev. B* 85: 035442.

179 Chen, J., Markussen, T., and Thygesen, K.S. (2010). Quantifying transition voltage spectroscopy of molecular junctions: ab initio calculations. *Phys. Rev. B* 82: 121412.

180 Wang, G., Kim, Y., Na, S.-I. et al. (2011). Investigation of the transition voltage spectra of molecular junctions considering frontier molecular orbitals and the asymmetric coupling effect. *J. Phys. Chem. C* 115: 17979–17985.

181 Tan, A., Balachandran, J., Dunietz, B.D. et al. (2012). Length dependence of frontier orbital alignment in aromatic molecular junctions. *Appl. Phys. Lett.* 101: 243107.

182 Song, H., Kim, Y., Jeong, H. et al. (2010). Coherent tunneling transport in molecular junctions. *J. Chem. Phys. C* 114: 20431–20435.

183 Mirjani, F., Thijssen, J.M., and van der Molen, S.J. (2011). Advantages and limitations of transition voltage spectroscopy: A theoretical analysis. *Phys. Rev. B* 84: 115402.

184 Pakoulev, A.V. and Burtman, V. (2009). Temperature dependent barrier crossover regime in tunneling single molecular devices based on the matrix of isolated molecules. *J. Phys. Chem. C* 113: 21413–21421.

185 Wu, K., Bai, M., Sanvito, S. et al. (2014). Transition voltages of vacuum-spaced and molecular junctions with Ag and Pt electrodes. *J. Chem. Phys.* 141: 014707.

186 Brito Silva, C.A., da Silva, S.J.S., Leal, J.F.P. et al. (2011). Electronic transport in oligo-*para*-phenylene junctions attached to carbon nanotube electrodes: transition-voltage spectroscopy and chirality. *Phys. Rev. B* 83: 245444.

187 Bâldea, I. (2012). Effects of stochastic fluctuations at molecule–electrode contacts in transition voltage spectroscopy. *Chem. Phys.* 400: 65–71.

188 Guo, S., Hihath, J., Diez-Perez, I. et al. (2011). Measurement and statistical analysis of single-molecule current–voltage characteristics, transition voltage spectroscopy, and tunneling barrier height. *J. Am. Chem. Soc.* 133: 19189–19197.

189 Bennett, N., Xu, G., Esdaile, L.J. et al. (2010). Transition voltage spectroscopy of porphyrin molecular wires. *Small* 6: 2604–2611.

190 Lennartz, M.C., Atodiresei, N., Caciuc, V. et al. (2011). Identifying molecular orbital energies by distance-dependent transition voltage spectroscopy. *J. Phys. Chem. C* 115: 15025–15030.

191 Ricœur, G., Lenfant, S., Guérin, D. et al. (2012). Molecule/electrode interface energetics in molecular junction: A "transition voltage spectroscopy" study. *J. Phys. Chem. C* 116: 20722–20730.

192 Bâldea, I. (2012). Interpretation of stochastic events in single-molecule measurements of conductance and transition voltage spectroscopy. *J. Am. Chem. Soc.* 134: 7958–7962.

193 Xiang, A., Li, H., Chen, S. et al. (2015). Electronic transport in benzodifuran single-molecule transistors. *Nanoscale* 7: 7665–7673.

194 Lo, W.Y., Bi, W., Li, L. et al. (2015). Edge-on gating effect in molecular wires. *Nano Lett.* 15: 958–962.

195 Trouwborst, M.L., Martin, C.A., Smit, R.H.M. et al. (2011). Transition voltage spectroscopy and the nature of vacuum tunneling. *Nano Lett.* 11: 614–617.

196 Sotthewes, K., Hellenthal, C., Kumar, A. et al. (2014). Transition voltage spectroscopy of scanning tunneling microscopy vacuum junctions. *RSC Adv.* 4: 32438–32442.

197 Bâldea, I. (2012). Transition voltage spectroscopy in vacuum break junction: Possible role of surface states. *Europhys. Lett.* 98: 17010.

198 Wu, K., Bai, M., Sanvito, S. et al. (2013). Origin of the transition voltage in gold–vacuum–gold atomic junctions. *Nanotechnology* 24: 025203.

199 Xu, B. and Tao, N.J. (2003). Measurement of single-molecule resistance by repeated formation of molecular junctions. *Science* 301: 1221–1223.

200 Dell, E.J., Capozzi, B., and Xia, J.L. (2015). Molecular length dictates the nature of charge carriers in single-molecule junctions of oxidized oligothiophenes. *Nat. Chem.* 7: 209–214.

201 Capozzi, B., Xia, J.L., Adak, O. et al. (2015). Single-molecule diodes with high rectification ratios through environmental control. *Nat. Nanotechnol.* 10: 522–527.

202 Moreno-Garcia, P., La Rosa, A., Kolivoska, V. et al. (2015). Charge transport in C_{60}-based dumbbell-type molecules: mechanically induced switching between two distinct conductance states. *J. Am. Chem. Soc.* 137: 2318–2327.

203 Su, T.A., Li, H.X., Steigerwald, M.L. et al. (2015). Stereoelectronic switching in single-molecule junctions. *Nat. Chem.* 7: 215–220.

204 Li, Y., Kaneko, S., Fujii, S. et al. (2015). Symmetry of single hydrogen molecular junction with Au, Ag, and Cu electrodes. *J. Phys. Chem. C* 119: 19143–19148.

205 Makk, P., Tomaszewski, D., Martinek, J. et al. (2012). Correlation analysis of atomic and single-molecule junction conductance. *ACS Nano* 6: 3411–3423.

206 Nicolai, C. and Sachs, F. (2014). Fitting random data to state models with QuB software. *Biophys. Rev.* 8: 191–121.

207 Qin, F., Auerbach, A., and Sachs, F. (1996). Estimating single-channel kinetic parameters from idealized patch-clamp data containing missed events. *Biophys. J.* 70: 264–280.

208 Qin, F., Auerbach, A., and Sachs, F. (1997). Maximum likelihood estimation of aggregated Markov processes. *Proc. R. Soc. Lond. B* 264: 375–383.

209 Gu, C., Hu, C., Wei, Y. et al. (2018). Label-free dynamic detection of single-molecule nucleophilic-substitution reactions. *Nano Lett.* 18: 4156–4162.

210 Johnson-Buck, A., Su, X., Giraldez, M.D. et al. (2015). Kinetic fingerprinting to identify and count single nucleic acids. *Nat. Biotechnol.* 33: 730.

211 Guan, J., Jia, C., Li, Y. et al. (2018). Direct single-molecule dynamic detection of chemical reactions. *Sci. Adv.* 4: eaar2177.

212 Nayak, T.K., Bruhova, I., Chakraborty, S. et al. (2014). Functional differences between neurotransmitter binding sites of muscle acetylcholine receptors. *Proc. Natl. Acad. Sci. U. S. A.* 111: 17660–17665.

8

Theoretical Aspects for Electron Transport Through Molecular Junctions

When the scientific community began to realize the burgeoning experimental realities of molecular electronics, they felt the need to describe these results in rational theoretical systems. The electrical conduction in the macroscopic world establishes the current proportional to the applied voltage, which is described by an Ohm's law. The conductance is an importance quantity in the electronics of an ant size. In the mesoscopic view, different scale scattering regimes have different transport mechanisms. Basically, the electron transport properties of one sample can be described in the related size, which set the length scale of the sample as L. To evaluate L, two critical indexes can serve as our references, the phase-coherence length and elastic mean free path. Given the fundamental length scale, the phase-coherence length, denoted as $L\varphi$, represents the distance of the phase of electron wave function. The mesoscopic system is specifically described in the scale of $L < L\varphi$. Additionally, the elastic mean free path, which roughly measures the displacement between elastic collisions with static impurities, is denoted as l. When $l \ll L$, the system operating in a diffusive regime exhibits random movements in a step size l among the impurities. While $l > L$, the system works in a ballistic regime and momentum of electron could be assumed to be constant and limited within the sample boundaries. With the size decreases to the atomic scale, the quantum confinement effect has an impact on the electrical conduction, where Ohm's law is not applicable any more. A formidable challenge for the theory is to derive the conductance presented from the macroscopic scale to an atomic scale. In this chapter, we try to take a glance of the theoretical foundation of molecular electronics.

8.1 Theoretical Description of the Tunneling Process

The current flowing through a molecular junction consisting of two electrodes separated by a molecule/molecules is realized dominantly through tunneling [1, 2]. There are a number of approaches used to derive the characteristics of the tunneling current: the well-known Wentzel–Kramers–Brillouin (WKB) approximation, Fowler–Nordheim equation, Simmons equation, Borden formalism, and Landauer equation [3, 4]. The simplest and most fundamental 1D model is a free electron with energy E separated by a rectangular barrier of height (Φ)

Molecular-Scale Electronics: Concept, Fabrication and Applications,
First Edition. Xuefeng Guo, Dong Xiang, and Yu Li.

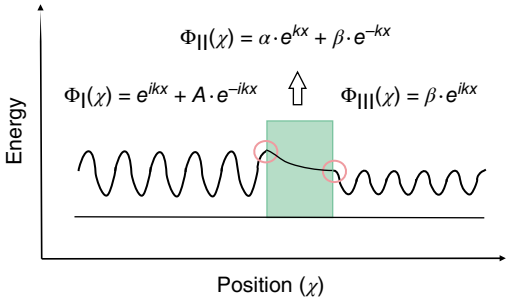

Figure 8.1 Schematic drawing of electron tunneling through a rectangular barrier. Source: Reproduced with permission from Xiang [5]. Copyright 2012, Elsevier.

and thickness (d). The time-independent Schrödinger in this scenario can be written as follows:

$$\left[-\frac{\hbar^2}{2m}\frac{\partial^2}{\partial x^2} + V(\mathbf{r})\right]\psi = E\psi \tag{8.1}$$

where m and E are the mass and the energy of the electron, respectively; and $V(\mathbf{r})$ describes the potential barrier. The exact solutions of Eq. (8.1) can be obtained corresponding to the wave functions outside and inside the barrier (Figure 8.1).

$$\psi_{\mathrm{I}} = e^{ikz} + A \cdot e^{-ikz} \tag{8.2}$$

$$\psi_{\mathrm{II}} = \alpha e^{i\kappa z} + \beta \cdot e^{-i\kappa z} \tag{8.3}$$

$$\psi_{\mathrm{III}} = B \cdot e^{ikz} \tag{8.4}$$

with

$$k = \frac{\sqrt{2mE}}{\hbar} \text{ and } \kappa = \frac{\sqrt{2m\phi - E}}{\hbar} \tag{8.5}$$

The relative probability of an incident electron transmitting the barrier, i.e. the transmission coefficient, is $T = |B|^2/|A|^2$. By matching the continuities of the wave functions and their first derivatives at the boundaries, the transmission coefficient can be expressed by the formula as follows:

$$T = \frac{1}{\left[\left(k^2+\kappa^2/2k\kappa\right)^2 \sinh(\kappa d)\right]} \tag{8.6}$$

For a high potential, where $\Phi \gg E$ or $\kappa d \gg 1$, T can be simplified as follows:

$$T \approx \frac{16k^2\kappa^2}{(k^2+\kappa^2)^2} \cdot e^{-2\kappa d} \tag{8.7}$$

The tunneling current is proportional to the transmission coefficient; thus, it will reduce its magnitude exponentially with an increase in the molecular length in a molecular junction. The potential barrier in the molecular junctions is approximated to be the highest occupied molecular orbital (HOMO) or the lowest unoccupied molecular orbital (LUMO) when either of them is close enough to the Fermi level of the metal electrodes. The barrier shape is not always a standard rectangle due to the applied voltage, which elevates the Fermi level of,

for instance, the left electrode while lowering down the right one. The Simmons model [1] assuming a trapezoidal barrier is an excellent approximation [6]. The tunneling current density in the $eV < \Phi$ regime can be described as follows:

$$J = \frac{e}{4\pi^2\hbar d^2}\left\{\left(\Phi - \frac{eV}{2}\right)\exp\left[-\frac{2(2m)^{\frac{1}{2}}}{\hbar}\alpha\left(\Phi - \frac{eV}{2}\right)^2 d\right] - \left(\Phi + \frac{eV}{2}\right)\exp\left[-\frac{2(2m)^{\frac{1}{2}}}{\hbar}\alpha\left(\Phi + \frac{eV}{2}\right)^2 d\right]\right\} \tag{8.8}$$

where Φ, d, and V are the barrier height, thickness, and applied voltage, respectively; and α is a parameter that accounts for either adjusting the effective mass of the tunneling electrons [7], providing a way of applying a rectangular tunneling to a non-rectangular case, or both [8]. The bare electron tunneling through a rectangular potential barrier corresponds to $\alpha = 1$. Equation (8.8) can be simplified in two limits based on the relative difference between the bias V and the barrier height Φ. In a low bias range, the simplified form can be expressed as follows:

$$J = \left(\frac{(2m\Phi)^{\frac{1}{2}}e^2\alpha}{\hbar d^2}\right)V\exp\left[-\frac{2(2m)^{\frac{1}{2}}}{\hbar}\alpha(\Phi)^{\frac{1}{2}}d\right] \tag{8.9}$$

In a high bias regime, the tunneling current density becomes

$$J = \left(\frac{e}{4\pi^2\hbar d^2}\right)\left(\Phi - \frac{eV}{2}\right)\exp\left[-\frac{2(2m)^{\frac{1}{2}}}{\hbar}\alpha\left(\Phi - \frac{eV}{2}\right)^{\frac{1}{2}}d\right] \tag{8.10}$$

Equations (8.9) and (8.10) illustrate that as the barrier thickness increases, often corresponding to the larger molecular length in the molecular junctions, the tunneling current shows an exponential decrease. This length-dependent regulation is widely used in the experimental analysis [9, 10] and commonly adopted in a further more simplified form expressed as follows [11]:

$$J = J_0 e^{-\beta d} \tag{8.11}$$

where $\beta = 2\sqrt{2m\varphi/\hbar^2}$ is defined as the tunneling decay coefficient and J_0 is the hypothetical zero-length current. The Simmons model for molecule junction is established on the assumptions that the molecular energy level (HUMO or LUMO) is constant throughout the entire tunneling distance and the uniform dielectric constant of the medium seldom affects the shape of the tunneling barrier. Additionally, the effects from an image potential are neglected in the tunneling process. However, in actual molecular junctions, due to the coupling between the molecules and the electrodes, the energy levels are shifted from the positions inherent to the isolated molecules, and the discrete energy levels are broadened to the bands, for which the density states, in a simplest way, are represented using the Lorentz function as follows:

$$D(E) = \frac{1}{2\pi}\frac{\Gamma}{(E - E_0)^2 + (\Gamma/2)^2} \tag{8.12}$$

where E_0 is the discrete energy level inherent to the single molecule and Γ is a parameter with an energy dimension describing the coupling strength of

the molecule to electrodes. The energy level distributions along the tunneling distance are not uniform, resulting from varied bond formations. The average energy level may be a compromised way to adopt the Simmons model; however, it is unsuitable when the non-uniform levels are close to the electrode Fermi levels [9]. Introducing a tunneling matrix, as inspired from the tunneling mechanisms in the scanning tunneling spectroscopy [12], would shed light on dealing with the tunneling process through molecular junctions with the energy levels far from uniform.

8.2 Electron Transport Mechanism

8.2.1 Coherent Electron Transport Through Molecular Junctions

The charge transport through a macroscopic conductor obeys Ohm's law, and the resistance is proportional to the length of the conductor. However, these laws are not valid for a conductor downscaling to the nanometer regime, in which the conductance is quantized. When the length is reduced to less than that of the mean free path of electrons, the transport mechanism changes from diffusive to ballistic. The quantum confinement arising from width narrowing results in not all transverse modes that come from the electron reservoir transmitting through the conductor. Electrons with an energy E (mass m) contributing to the conductance must satisfy $p_z^2 = 2mE - \left(p_x^2 + p_y^2\right) > 0$, where p_z is the momentum parallel to the length of the conductor, and both p_x and p_y are the transverse momentums, which are discretely constrained as p_x, $p_y = hn/2w$, with w representing the width of the conductor. The non-equality constrains the electrons to exceed the Fermi wavelength λ_F or the Fermi energy $E_F = h^2/2m\lambda_F^2$. The potential difference (V) between the two electrodes creates a transmission window $E_F \sim E_F + eV$. Each transverse mode in the transmission widow opens a conductance channel. In a ballistic transport scenario, this contributes a quantum unity conductance $G_0 = 2e^2/h$; thus, the total conductance of a nanowire can be given as follows:

$$G = N(2e^2/h) \tag{8.13}$$

where N is the total number of the conductance channels determined from the transmission window and the non-equality mentioned earlier. Increasing the applied voltage will allow more modes to be included, and because of the quantization of the wavelength, the current will rise stepwise [13]. The number of channels depends on the width of the conductor, thus narrowing the width will lead to a stepwise decrease in the conductance [14]. The transport in practical molecular junctions is generally non-idealistic, and it can take a more general form as follows:

$$G = 2e^2/h \sum T_i \tag{8.14}$$

where T_i is the transmission coefficient of the conductance channels associated with the molecular orbitals. By applying a gate that modulates the molecular orbitals, Topinka et al. clearly demonstrated a quantized conductance in the molecular junctions [15], as shown in Figure 8.2.

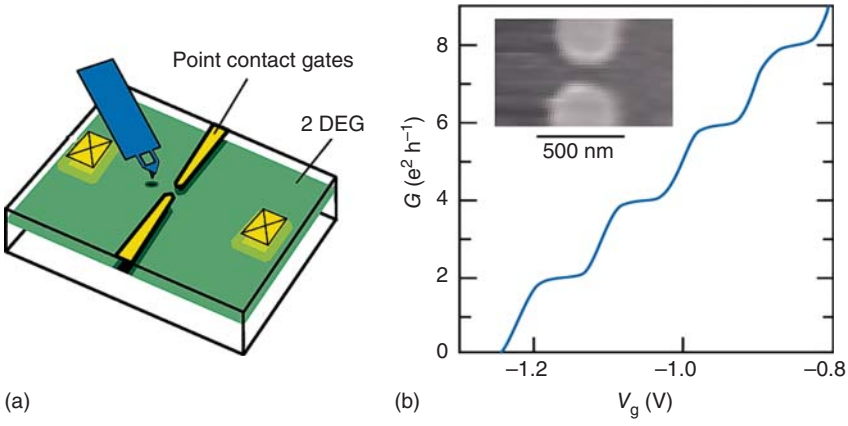

Figure 8.2 Quantized conductance effect. (a) Schematic diagram of the experimental setup. The quantum point contact (QPC) conductance was measured as a function of the atomic force microscopy (AFM) tip position. (b) Point contact conductance G versus gate voltage V_g with no tip present. The point contact conductance as a function of the gate voltage clearly depicts a quantized conductance effect. Source: Reprinted with permission from Topinka et al. [15]. Copyright 2000, AAAS.

A metal–molecule–metal junction is hypothesized as a phase coherence conductor connected to two electron reservoirs. Considering that the net current flow occurs only between the energy levels of μ_L and μ_R, the tunneling current can be expressed in a form of the Landauer formula as follows [3]:

$$I = \frac{2e}{h} \int T(E)[f_L(E) - f_R(E)]\mathrm{d}E \tag{8.15}$$

where

$$f_\beta = \frac{1}{1 + \exp[(E - \mu_\beta)/kT]} \quad (\beta = \mathrm{L}, \mathrm{R}) \tag{8.16}$$

is the Fermi distribution function for the left ($\beta = \mathrm{L}$) and right ($\beta = \mathrm{R}$) electrodes with an electrochemical potential μ_β and $T(E)$ is the transmission function.

The coupling of the molecule to the electrode affects both the transmission coefficient associated to each energy level and the molecular orbitals. Taking a simple model where a single spin-degenerated molecular orbital with an energy E_0 is regarded as the channel for the charge transport, the coupling of the leads characterized by Γ_β ($\beta \in \mathrm{L}, \mathrm{R}$) results in a level broadening, and the transmission coefficient changes into a Lorentz function as follows [16–18]:

$$T(E) = \frac{\Gamma_L \Gamma_R}{[E - E_0]^2 + [\Gamma_L - \Gamma_R]^2} \tag{8.17}$$

Addition energy (U_{add}) is the energy needed to release one electron from the HOMO minus the energy gained to add one electron onto the LUMO. $\Gamma_\beta \ll U_{add}$ corresponds to a weak coupling. In this scenario, electrons coming from the left electrode first hop to the molecule and then to the right electrode. Conversely, the strong coupling $\Gamma_\beta \gg U_{add}$ results in a significant broadening of the molecular levels. Therefore, the electrons in the left lead transport directly to the right,

thus eliminating the middle procedure of stopping at the molecular bridge. In the intermediate regime, the molecular orbitals are partially broadened, and the phenomena due to the electron–electron correlation effects, such as the Kondo effect and co-tunneling, are observed [19].

8.2.2 Electron–Phonon Interaction Effects on Transport Mechanism

The electron transport mechanism illustrated by the Landauer formula corresponds to the electrons traveling through a conductor in which ions are frozen in their equilibrium position. In practical molecular junctions, because of the thermal motion of the ions, the Landauer equation is treated as a limited case [20]. The traversal time is defined as the time it takes for an electron to finish one tunneling process, and it is proportional to the number of sites in the molecular linker [21]. For a molecular junction with a length of ~1 nm and an energy level of ~1 eV above the tunneling electrons, the value is approximately 0.2 fs [3]. For a short molecular linker at low temperatures, the traversal time is considerably smaller than that of the ionic motion periods, thus the coherent tunneling dominates [22]. The decoherence effects are important when the energy of the tunneling electron resonates with a molecular orbital, which causes a substantially long traversal time [23, 24]. This electron–phonon coupling enhances itself as the molecular length and the temperature increase [22, 25]. In an extremely strong coupling case, the localization effects of the electron wave functions change the transport mechanism from tunneling to thermally activated hopping, where the conductance increases as the temperature increases [26] and, in contrast, the conductance decreases when the temperature increases in the tunneling transmission.

The strong electron–phonon coupling means the breakdown of the coherent tunneling transmission depicted by the Landauer formulism, and the standard electron transfer theories are applicable, which describe the electrons hopping from an initial localization state (donor) to a final localization state (acceptor). When the electronic coupling between the donor and the acceptor is weak, the electron transfer rate k_{ET} can be expressed by using the Fermi Golden rule as follows [3, 27, 28]:

$$k_{ET} = \frac{4\pi^2}{h}|H_{DA}|^2 \left(\frac{1}{4\pi\lambda k_B T} \exp\left[-\frac{(\lambda + \Delta G^0)^2}{4\pi\lambda k_B T} \right] \right) \tag{8.18}$$

where h, k_B, and T is the Plank constant, Boltzmann constant, and temperature, respectively; $|H_{DA}|$ is the electronic coupling matrix of the donor to the acceptor; ΔG^0 is the free energy difference between the acceptor and the donor; and λ is the reorganization energy representing the energy difference between the donor and the acceptor if the system makes an instantaneous vertical transition from the donor state to the acceptor state.

For a strong electronic coupling between the donor and the acceptor, the charge transfer is essentially realized through a way of redistributing the electrons of the mixed states attached to the donor and the acceptor because of the

stochastic fluctuations. The electron transfer rate in this situation follows an Arrhenius relation given by

$$k_{\mathrm{ET}} \propto \exp\left(-\frac{E^*}{k_{\mathrm{B}}T}\right) \tag{8.19}$$

where E^* is the effective potential barrier between the donor and the acceptor, which is also known as the hopping activation energy [26, 29].

8.3 First-Principles Modeling

8.3.1 Introduction to Density Functional Theory

Using the first-principles modeling as a supplementary tool for the experimental studies in molecular electronics allows researchers to construct a quantitative picture of the mechanisms on the electron transport in the molecular junctions and form predictions to guide further experimental studies. The key task in the theoretical studies for molecule electronics is to calculate the electronic structures of the molecular linker under the electrode environments. By employing the transport mechanism, such as the Landauer formula, the Breit–Wigner formula and others, the characteristics of electron transport can be unraveled [30–33]. Depending on the coupling to the leads, the electronic structure of the molecules is generally different from that of the one in the isolated gas phase. One effective approach to tackle this problem is to extract an "extended molecule" with several electrode atoms attached to its two terminals [34, 35]. This is based on the assumption that the effects from the molecule–electrodes coupling are always localized to the small regimes on the contact surfaces where only small amounts of atoms are involved.

The electron behavior in the molecular linkers is essentially a multi-body problem. The density functional theory (DFT) reduces the complex electron–electron and electron–nuclei interactions to a single electron moving in an effective potential field that is the functional of the electron density. The Hamiltonian for an electron can be given by

$$\mathcal{H}[\rho(\mathbf{r})] = T[\rho(\mathbf{r})] + V_{\mathrm{eff}}[\rho(\mathbf{r})] \tag{8.20}$$

where T is the free-electron kinetic energy; and V_{eff} is the effective potential energy. In the Born–Oppenheimer approximation [36], when the electron–phone interaction is neglected, it can be expressed as follows:

$$V_{\mathrm{eff}} = \frac{e^2}{2}\int \frac{\rho(\mathbf{r}')}{|\mathbf{r}-\mathbf{r}'|}\mathrm{d}\mathbf{r}' + U_{\mathrm{e-nuc}}[\rho(\mathbf{r})] + \nu_{\mathrm{xc}}[\rho(\mathbf{r})] \tag{8.21}$$

where the first term in the right side of the equation is the Hartree mean potential representing the average potential caused by the electron–electron Coulomb repulsions; $U_{\mathrm{e-nuc}}$ describes the electron–nuclei electrostatic interactions; and ν_{xc} is the exchange-correlation energy, which is the only term of the three that

needs to be reasonably approximated. The local density approximation (LDA) assumes that the exchange-correlation energy for an infinitesimal $\rho(\mathbf{r})\mathrm{d}\mathbf{r}$ in a system is equal to that of a homogeneous electron gas of a density $\rho = \rho(\mathbf{r})$ [37]. The local spin density approximation develops the LDA by taking the electron spin as the parameters [38]. A further improvement in the exchange-correlation function assumes a gradient generalized gradient approximation (GGA) or a second-derivative dependency [39, 40]. The Hamiltonian of the electron–nuclei system is the spatial integral of the single electron Hamiltonian, which can be given as follows:

$$H = \int \mathcal{H}\rho(\mathbf{r})\mathrm{d}\mathbf{r} \tag{8.22}$$

The ground state of the system has the electron density function that minimizes the system energy. By applying the variational principle, we obtain

$$\frac{\delta H}{\delta \rho} = \mu \tag{8.23}$$

where μ is the Lagrange multiplier corresponding to the conservation of the total electron number of the system. In the self-consistent calculation method, the solution to Eq. (8.23) can be found by solving a set of one-particle Schrödinger equations as follows:

$$\left(-\frac{\hbar^2}{2m_\mathrm{e}}\nabla^2 + V_\mathrm{eff}\right)\psi_i = \epsilon_i\psi_i \tag{8.24}$$

and the electron density function can be expressed as follows:

$$\rho(r) = \sum \psi_i^* \psi_i \tag{8.25}$$

In the actual calculations, the plane wave basis is a simple and often effective way to represent the wave function [37, 41] for the ith electron; thus, we can obtain

$$\psi_i = \sum_n C_n^i \exp(i\mathbf{k_n} \cdot \mathbf{r}) \tag{8.26}$$

The work then becomes to vary the coefficients C_n^i rather than the wave function values at each spatial point to obtain the minimized system energy. In order to represent the wave functions for the system explicitly, the infinite wave basis should be collected. However, there generally are finite plane waves (labeled by $\mathbf{k_n}$) that have a predominant position on determining the characteristics of the system, thus only countable numbers of the wave bases are adopted in the actual calculations, and this work is called k-point sampling. Clearly, for a more massive k-point sampling, a more accurate result is obtained. In addition to the plane wave basis, several other wave bases, such as augmented plane waves, linearized muffin-tin orbitals, the Gaussian orbitals, and others, are widely used [35, 42, 43]. Once the electron density of the optimized system is derived from iteration, other properties, especially the electronic structures, can be calculated in terms of the corresponding specific approaches.

The model based on the self-consistent field approach mentioned earlier works fairly well in describing the electron behaviors in the molecular junctions, except

in a so-called Coulomb blockade regime, which is briefly elaborated here. For a system containing N electrons, the gross electron–electron interaction potential U can be given as follows:

$$U = U_0 C_N^2 \tag{8.27}$$

where U_0 describes the average potential between any two electrons. By adding one electron to the system, the system energy increment can be given as follows:

$$\Delta U = U_0 (C_{N+1}^2 - C_N^2) = N U_0 \tag{8.28}$$

where NU_0 is the charging energy for an N-electron system; and U_0 is regarded as the single electron charging energy. The effects of the electron–electron interactions will be predominant if the single electron charging energy exceeds the thermal energy $k_B T$ and the level broadening resulting from the coupling to the electrodes. Under this condition, the tunneling current at a low bias value is significantly suppressed, and this phenomenon is known as the Coulomb blockade. The single charging effect plays a dominant role in the Coulomb blockade regime, which is not well described by the self-consistent field approach, even at equilibrium. The self-consistent field models also do not work well when dealing with the systems associated with the non-equilibrium electron–electron interactions [44].

A further improvement in minimizing the gross energy of the system to determine the ground state considers the atomic coordinates as variables in the DFT energy functional. The optimized molecular geometric structures are those at the mechanical equilibrium states where the forces defined as the partial derivatives of the system energy with respect to the atomic coordinates reduce to zeros. The DFT approach was also developed for describing the excited electronic states of the molecular systems. For further information, interested readers can review the studies of Perdew and Levy [45] and Baruah and Pederson [46].

8.3.2 Current–Voltage Characteristics Calculations

The current–voltage characterization is a conventional approach used to investigate the properties of the electrical structures. The simplest structure is a metal wire, where we have Ohm's law or junctions in the mesoscopic regime. The theoretical model and its calculations provide a detailed understanding of the charge transport mechanisms, which are essentially important for the design of electronic devices with novel properties. Molecular junctions are often seen as a molecular linker connecting two infinite electron reservoirs. There is a coupling between the molecules and the leads where the fixed point boundary condition or the periodic boundary condition can no longer be used in the electronic structure calculation. Molecular junctions are open systems in which the molecules, or the extended molecules in metal contacts, have a continuous density of state rather than discrete energy levels owned by their isolated gas counterparts. The exchange of electrons occurs between the electrodes and the molecular linker; thus, the number of electrons in the spacer is generally not conservative. What makes the calculation more sophisticated is that the system formed by the molecular junctions is of non-equilibrium, and the effects,

such as chemisorptions, bonding types, molecular tilted angles, and molecular interactions in the self-assembled monolayer junctions, are expected to play a non-trivial role in the charge transport.

For a junction at the equilibrium state, where the chemical potential for both leads is the same, the electron density function in the linker regime can be written as follows:

$$n(\mathbf{r}) = \sum_i |\psi_i^2| f(\epsilon_\alpha - \mu) \tag{8.29}$$

where μ is the chemical potential, and ψ_i can be obtained by solving the Kohn–Sham equations as follows:

$$\left[-\frac{\hbar^2}{2m}\nabla^2 + V_{\text{eff}} + U\right]\psi_i = \epsilon_\alpha \psi_i \tag{8.30}$$

where V_{eff} is the DFT effective potential field, which, in its simplest case, can be approximated simply in the Hartree form as follows:

$$V_{\text{eff}} = \frac{e^2}{2}\int \frac{n(r')}{|r - r'|}\mathrm{d}r' \tag{8.31}$$

where U is the extra potential, which arises due to the electron transfer between the linker and the electrodes and needs to be calculated self-consistently. U satisfies the Poisson equation as follows:

$$\nabla^2 U = e^2(n_0 - n)/\varepsilon \tag{8.32}$$

where n_0 is the electron density of an isolated linker device without connecting to any electrodes.

By iterating between the Poisson equation and the equilibrium statistical mechanics, the charging potential profile and the electron density of the system can be solved self-consistently; furthermore, so long as the electron density of the system is known, all qualities of interest, such as energy and current, can be calculated. However, for a non-equilibrium system, the electron density function can no longer be expressed by Eq. (8.32) because there are different chemical potentials at the two contacts, and the correlated occupations between the different states cannot be neglected. In this case, the density function can be characterized by a density matrix ρ_{ij} and expressed as follows:

$$n(\mathbf{r}) = \Sigma_{ij}\rho_{ij}\psi_j^*\psi_i \tag{8.33}$$

Then, the non-equilibrium Green function (NEGF) is introduced to deal with problems in open systems. The system is generally partitioned into three parts, i.e. the device and the two contact parts, which correspond to the molecular linker and the electrodes in the molecular junctions, respectively. The molecular junction electrodes are often seen as semi-infinite entities; thus, the matrix representing the contact effects is regularly semi-infinite, which results in intractable calculations. The Green formulism replaces the effects arising out of contacts with a self-energy matrix that is the same size as the device's Hamiltonian, thus

making the problem tractable. The Hamiltonian of the system can be expressed using a blocked matrix as follows:

$$H = \begin{pmatrix} H_{\mathrm{L}} & H_{\mathrm{ML}}^{\dagger} & 0 \\ H_{\mathrm{ML}} & H_{\mathrm{M}} & H_{\mathrm{MR}} \\ 0 & H_{\mathrm{MR}}^{\dagger} & H_{\mathrm{R}} \end{pmatrix} \tag{8.34}$$

where subscript M, L, and R represent the molecule, left electrode, and right electrode, respectively; and subscript ML (MR) describes the coupling between the molecule and the left (right) electrode. Here, the coupling between the two electrodes is neglected. The Green function of the system can be written as follows:

$$\begin{aligned} G(\epsilon) &= \begin{pmatrix} G_{\mathrm{L}} & & \cdots \\ & G_{\mathrm{M}} & \\ \cdots & & G_{\mathrm{R}} \end{pmatrix} \\ &= \begin{pmatrix} (\epsilon + i\delta)S_{\mathrm{L}} - H_{\mathrm{L}} & \tau_{\mathrm{L}}^{\dagger} & 0 \\ \tau_{\mathrm{R}} & (\epsilon + i\delta)S_{\mathrm{M}} - H_{\mathrm{M}} & \tau_{\mathrm{R}} \\ 0 & \tau_{\mathrm{L}}^{\dagger} & (\epsilon + i\delta)S_{\mathrm{R}} - H_{\mathrm{R}} \end{pmatrix}^{-1} \end{aligned} \tag{8.35}$$

where $\delta \to 0^{+}$; S_{β} (β = L, M, R) is the overlap matrix; and τ_{β} (β = L, R) is the contact matrix. For the device part, S_{M} can be expressed in terms of the wave basis employed for solving the Kohn–Sham equation[47]

$$(S_{\mathrm{M}})_{ij} = \int \phi_i \phi_j \mathrm{d}\mathbf{r} \tag{8.36}$$

It is straightforward that the Green function for the device parts goes

$$G_{\mathrm{M}}(\epsilon) = \frac{1}{\epsilon S_{\mathrm{M}} - H_{\mathrm{M}} - \Sigma_{\mathrm{L}} - \Sigma_{\mathrm{R}}} \tag{8.37}$$

where Σ_{L} and Σ_{R} are the non-Hermitian self-energy matrixes:

$$\Sigma_{\beta} = \tau_{\beta} G_{\beta} \tau_{\beta}^{\dagger} \qquad (\beta = \mathrm{L}, \mathrm{R}) \tag{8.38}$$

The Hermitian part of the self-energy matrix describes the shift of the molecular energy levels and its anti-Hermitian part.

$$\Gamma_{\beta} = i(\Sigma_{\beta} - \Sigma_{\beta}^{\dagger}), \qquad (\beta = \mathrm{L}, \mathrm{R}) \tag{8.39}$$

represents the level broadening. If the molecular junction is at an equilibrium state where there is no applied bias, then the density matrix ρ_{ij} can be expressed as follows:

$$\rho_{ij} = \frac{1}{\pi} \int \mathrm{Im}[G_{ij}(\epsilon)] f(\epsilon - \mu) \mathrm{d}\epsilon \tag{8.40}$$

where μ is the equilibrium chemical potential of the system; and G_{ij} is the elementary of the retarded Green function for the device part, for which the self-energy is zero. This equation is essentially the same as Eq. (8.35). If a bias V is applied to the molecular junction, and $eV = \mu_{\mathrm{L}} - \mu_{\mathrm{R}}$, then the density matrix can be described using the NEGF as follows:

$$\rho = \frac{1}{\pi} \int G_{\mathrm{M}}(\epsilon) \mathrm{Im}[\Sigma_{\mathrm{L}}] G_{\mathrm{M}}^{\dagger} f_{\mathrm{L}} \mathrm{d}\epsilon + \frac{1}{\pi} \int G_{\mathrm{M}}(\epsilon) \mathrm{Im}[\Sigma_{\mathrm{R}}] G_{\mathrm{M}}^{\dagger} f_{\mathrm{R}} \mathrm{d}\epsilon \tag{8.41}$$

where $f_\beta(\beta = \mathrm{L}, \mathrm{R})$ is the Fermi function with an electron potential μ_β.

$$f_\beta = \left[1 + \exp\left(\epsilon - \frac{\mu_\beta}{k_\mathrm{B}T}\right)\right]^{-1} \tag{8.42}$$

Using the density matrix, the electron density can be derived as follows:

$$n(\mathbf{r}) = \sum_{ij} \rho_{ij}\phi_i\phi_j \tag{8.43}$$

It should be noted that there is an extra potential in the molecular junctions arising from the electron exchange between the electrodes and the molecular linker. By performing a transform for the right site of Eq. (8.43), $e^2(n_0 - n) \rightarrow e\mathrm{Tr}(\rho S_\mathrm{M})$, we can obtain the Poisson equation for the non-equilibrium system. In order to achieve a full description of the electronic behaviors in molecular junctions, we need to self-consistently calculate the Schrödinger equation and the Poisson equation simultaneously, which is similar to the work done for the equilibrium system. Once G_M and Γ_β ($\beta = \mathrm{L}, \mathrm{R}$) are available, the transmission for coherent transport can be calculated as follows [23, 35]:

$$T(\epsilon) = \mathrm{Tr}(\Gamma_\mathrm{L} G \Gamma_\mathrm{R} G^\dagger) \tag{8.44}$$

which is valid for being used in the Landauer formula to calculate the current flow, that is

$$I = \frac{2e}{h}\int \mathrm{Tr}(\Gamma_\mathrm{L} G \Gamma_\mathrm{R} G^\dagger)[f_\mathrm{L}(\epsilon) - f_\mathrm{R}(\epsilon)]\mathrm{d}\epsilon \tag{8.45}$$

We have presented an overview on how to calculate the charger transport characteristics of molecular junctions by using the NEGF formalism. The next task is to implement them into actual systems. The key work is to calculate the transmission coefficient, which relates to the number of propagating waves and corresponding conduction channels. To derive the transmission coefficient function, reasonable schemes should be constructed for calculating the self-energy matrix, which includes the calculations of the contact matrices τ_β ($\beta = \mathrm{L}, \mathrm{R}$) and the Green functions of the electrode. The "extended molecule" is artificially constructed to reduce the molecule–electrode interactions τ_β from semi-infinite dimensions to tractable finite dimensions. The electrodes are treated as semi-infinite entities, and the properties of interest are calculated using the standard DFT techniques for the 3D bulk systems [35, 47]. Once the contact matrix and the Green functions of the electrodes are available, the transmission spectrum can be obtained to calculate the current flow in the molecular junctions and perform a further analysis of the detailed mechanisms for the electron transport.

On the basis of the assumption that the electrodes induce an external potential localized in the scattering region, the NEGF in combination with the DFT works well on figuring out the details of how the electrodes affect the electron transport in molecular junctions. Xu et al. successfully demonstrated the relationship between the gate-modulated molecular levels and the current–voltage characteristics under varied gate voltages [33]. However, it should be noticed that the approximation of the electrodes with its 3D bulk form is not always adoptable.

In break junction experiments, the atomic structures exist on both contact surfaces. Similar cases can be found in the scanning tunneling microscopy (STM) experiments, where the atomic structures lie on the STM apex. For additional information, interested readers can review the studies listed in the references [13].

To date, the advances in the theoretical development are substantial but are beyond the primary goal of this book. As an outlook for this theoretical section, we want to point out that the gap between the theoretical calculations and the experimental data is decreasing for numerous relatively molecular systems. To further develop the electron transport theory, it is of critical importance to include a realistic treatment of molecules, electrodes, and atomic-scale details of the molecule–electrode interface [48]. Due to the lack of the atomic-scale detail in most experiments, the recent treatment of a range of different molecule–electrode contact geometries is an important step for a fair comparison between the theories and the experiments [49]. Furthermore, significant effort is still needed for the development of a computationally accurate theory of transport that involves a charge localization on the molecules (i.e. reduction and oxidation) [50]. A key important parameter in electron transport is the transmission coefficient, which is strongly affected by the quantum interference and yields the electrical conductance, current–voltage relations, and thermopower of single-molecule devices. The symbiotic relationship between the quantum interference and the electronic structure, which is sensitive to environmental factors and can be manipulated through conformational control, polarization, or redox processes, leads to new opportunities for controlling the electrical properties of single molecules [51]. The room-temperature quantum interference in single molecules was experimentally demonstrated recently, and it is opportune to develop new strategies for exploiting the quantum interference in both the technological and theoretical aspects. It should be noted that the goal of this theoretical tutorial is to gather a few basic concepts and mathematical tools, which emphasize the fundamentals of electron transport through molecules. We apologize to all colleagues whose work is not described in detail or cited here. Please consult the numerous excellent review articles [13, 51, 52], as well as the original research articles for a complete overview of the extensive literature on the theoretical progress.

References

1 Simmons, J.G. (1963). Generalized formula for the electric tunnel effect between similar electrodes separated by a thin insulating film. *J. Appl. Phys.* 34: 1793.

2 Zhu, X. (2004). Electronic structure and electron dynamics at molecule–metal interfaces: Implications for molecule-based electronics. *Surf. Sci. Rep.* 56: 1–83.

3 Nitzan, A. (2001). Electron transmission through molecules and molecular interfaces. *Annu. Rev. Phys. Chem.* 52: 681–750.

4 Metzger, R.M. (2015). Unimolecular electronics. *Chem. Rev.* 115: 5056–5115.

5 Xiang, D. (2012). *Fabrication and Utilization of Mechanically Controllable Break Junction for Bioelectronics*. Forschungszentrum Jülich.

6 Holmlin, R.E., Haag, R., Chabinyc, M.L. et al. (2001). Electron transport through thin organic films in metal–insulator–metal junctions based on self-assembled monolayers. *J. Am. Chem. Soc.* 123: 5075–5085.

7 Wang, W.Y., Lee, T., and Reed, M.A. (2003). Mechanism of electron conduction in self-assembled alkanethiol monolayer devices. *Phys. Rev. B* 68: 035416.

8 Joachim, C. and Magoga, M. (2002). The effective mass of an electron when tunneling through a molecular wire. *Chem. Phys.* 281: 347–352.

9 Nerngchamnong, N., Yuan, L., Qi, D.C. et al. (2013). The role of van der Waals forces in the performance of molecular diodes. *Nat. Nanotechnol.* 8: 113–118.

10 Tan, S.F., Wu, L., Yang, J.K.W. et al. (2014). Quantum plasmon resonances controlled by molecular tunnel junctions. *Science* 343: 1496–1499.

11 Joachim, C. and Ratner, M.A. (2005). Molecular electronics. *Proc. Natl. Acad. Sci. U. S. A.* 102: 8800–8800.

12 Tersoff, J. and Hamann, D.R. (1985). Theory of the scanning tunneling microscope. *Phys. Rev. B* 31: 805.

13 Zimbovskaya, N.A. and Pederson, M.R. (2011). Electron transport through molecular junctions. *Phys. Rep.* 509: 1–87.

14 He, J., Sankey, O., Lee, M. et al. (2006). Measuring single molecule conductance with break junctions. *Faraday Discuss.* 131: 145–154.

15 Topinka, M.A., LeRoy, B.J., Shaw, S.E.J. et al. (2000). Imaging coherent electron flow from a quantum point contact. *Science* 289: 2323–2326.

16 Hong, W.J., Valkenier, H., Meszaros, G. et al. (2011). An MCBJ case study: The influence of pi-conjugation on the single-molecule conductance at a solid/liquid interface. *Beilstein J. Nanotechnol.* 2: 699–713.

17 Kim, Y., Pietsch, T., Erbe, A. et al. (2011). Benzenedithiol: A broad-range single-channel molecular conductor. *Nano Lett.* 11: 3734–3738.

18 Kim, Y., Hellmuth, T.J., Sysoiev, D. et al. (2012). Charge transport characteristics of diarylethene photoswitching single-molecule junctions. *Nano Lett.* 12: 3736–3742.

19 Osorio, E.A., Bjornholm, T., Lehn, J.M. et al. (2008). Single-molecule transport in three-terminal devices. *J. Phys.: Condens. Matter* 20: 374121.

20 Wingreen, N.S., Jacobsen, K.W., and Wilkins, J.W. (1988). Resonant tunneling with electron–phonon interaction-an exactly solvable model. *Phys. Rev. Lett.* 61: 1396.

21 Buttiker, M. and Landauer, R. (1982). Traversal time for tunneling. *Phys. Rev. Lett.* 49: 1739.

22 Segal, D. and Nitzan, A. (2001). Steady-state quantum mechanics of thermally relaxing systems. *Chem. Phys.* 268: 315–335.

23 Landauer, R. and Martin, T. (1994). Barrier interaction time in tunneling. *Rev. Mod. Phys.* 66: 217.

24 Hauge, E.H. and Stovneng, J.A. (1989, 1989). Tunneling times: A critical review. *Rev. Mod. Phys.* 61: 917.

25 Choi, S.H., Kim, B., and Frisbie, C.D. (2008). Electrical resistance of long conjugated molecular wires. *Science* 320: 1482–1486.

26 Song, H., Reed, M.A., and Lee, T. (2011). Single molecule electronic devices. *Adv. Mater.* 23: 1583–1608.

27 Marcus, R.A. and Sutin, N. (1985). Electron transfers in chemistry chemistry and biology. *Biochim. Biophys. Acta* 811: 265–322.

28 Gosavi, S. and Marcus, R.A. (2000). Nonadiabatic electron-transfer at metal surfaces. *J. Phys. Chem. B* 104: 2067–2072.

29 Zhu, X.Y. (2004). Charge transport at metal-molecule interfaces: A spectroscopic view. *J. Phys. Chem. B* 108: 8778–8793.

30 Meir, Y. and Wingreen, N. (1992). Landauer formula for the current through an interacting electron region. *Phys. Rev. Lett.* 68: 2512.

31 Troisi, A. and Ratner, M.A. (2006). Molecular transport junctions: propensity rules for inelastic electron tunneling spectra. *Nano Lett.* 6: 1784–1788.

32 Papadopoulos, T.A., Grace, I.M., and Lambert, C.J. (2006). Control of electron transport through Fano resonances in molecular wires. *Phys. Rev. B* 74: 193306.

33 Xu, Y.Q., Fang, C.F., Cui, B. et al. (2011). Gated electronic currents modulation and designs of logic gates with single molecular field effect transistors. *Appl. Phys. Lett.* 99: 145.

34 Xue, Y.Q. and Ratner, M.A. (2003). Microscopic study of electrical transport through individual molecules with metallic contacts. I. Band lineup, voltage drop, and high-field transport. *Phys. Rev. B* 68: 115406.

35 Kim, Y.-H., Tahir-Kheli, J., Schultz, P. et al. (2006). First-principles approach to the charge-transport characteristics of monolayer molecular-electronics devices: application to hexanedithiolate devices. *Phys. Rev. B* 73: 235419.

36 Yonehara, T., Hanasaki, K., and Takatsuka, K. (2012). Fundamental approaches to nonadiabaticity: Toward a chemical theory beyond the Born–Oppenheimer paradigm. *Chem. Rev.* 112: 499–452.

37 Segall, M.D., Lindan, P.J.D., Probert, M.J. et al. (2002). First-principles simulation: Ideas, illustrations and the CASTEP code. *J. Phys.: Condens. Matter* 14: 2717.

38 Jones, R.O. (1989). The density functional formalism, its applications and prospects. *Rev. Mod. Phys.* 61: 689.

39 Becke, A.D. (1993). A new mixing of Hartree–Fock and local density-functional theories. *J. Chem. Phys.* 98: 1372.

40 Perdew, J.P., Burke, K., and Ernzerhof, M. (1996). Generalized gradient approximation made simple. *Phys. Rev. Lett.* 77: 3865.

41 Car, R. and Parrinello, M. (1985). Unified approach for molecular-dynamics and density-functional theory. *Phys. Rev. Lett.* 55: 2471.

42 Borshch, N.A., Pereslavtseva, N.S., and Kurganskii, S.I. (2011). Electronic structure and spectral characteristics of Zn-substituted clathrate silicides. *Semiconductors* 45: 713–723.

43 Khan, A.A., Srivastava, V., Rajagopalan, M. et al. (2012). Structural and electronic properties of Cd-rich lanthanide intermetallics. *J. Phys.: Conf. Ser.* 377: 012081.

44 Muralidharan, B., Ghosh, A.W., and Datta, S. (2006). Probing electronic excitations in molecular conduction. *Phys. Rev. B* 73: 155410.
45 Perdew, J.P. and Levy, M. (1985). Extrema of the density functional for the energy: Excited states from the ground-state theory. *Phys. Rev. B* 31: 6264.
46 Baruah, T. and Pederson, M.R. (2009). DFT calculations on charge-transfer states of a carotenoid-porphyrin-C_{60} molecular triad. *J. Chem. Theory Comput.* 5: 834–843.
47 Stokbro, K. (2008). First-principles modeling of electron transport. *J. Phys.: Condens. Matter* 20: 064216.
48 Li, Z.L., Zou, B., Wang, C.K. et al. (2006). Electronic transport properties of molecular bipyridine junctions: Effects of isomer and contact structures. *Phys. Rev. B* 73: 075326.
49 Tao, N.J. (2009). Electron transport in molecular junctions. In: *Nanoscience and Technology*, 185–193.
50 Lindsay, S.M. and Ratner, M.A. (2007). Molecular transport junctions: Clearing mists. *Adv. Mater.* 19: 23–51.
51 Lambert, C.J. (2015). Basic concepts of quantum interference and electron transport in single-molecule electronics. *Chem. Soc. Rev.* 44: 875–888.
52 Lin, L.L., Jiang, J., and Luo, Y. (2013). Elastic and inelastic electron transport in metal–molecule(s)–metal junctions. *Physica E* 47: 167–187.

9

Integrating Molecular Functionalities into Electrical Circuits

Undoubtedly, the substantial experimental and theoretical progress detailed in Chapters 1–8 lays the foundation for both the measurement capabilities and a fundamental understanding of the various physical phenomena of molecular junctions. Despite these considerable achievements, there are still no commercially available molecular electronic devices. To satisfy the requirements for actual applications, the development of practical molecular devices with specific functions is a prerequisite. In fact, recent experimental developments have demonstrated conductance switching/modulation and rectification as well as how quantum interference effects play a critical role in the electronic properties of molecular junctions. The focus of these experiments illustrates the engineering of functionalities that are beyond conventional electronic transport properties using a rational chemical design in single-molecule junctions. In this section, reviewing the ever-developing trends of integrating molecular functionalities into electrical circuits based on single molecules (Figure 9.1), which were neglected in most previous reviews/books, including (i) wiring toward nanocircuits; (ii) rectification toward diodes; (iii) negative differential conductance (NDC) toward oscillators; (iv) gating toward molecular transistors; (v) switching toward memory devices; (vi) molecular computing; (vii) transduction toward molecular sensors; (viii) high-frequency molecular devices; and (ix) molecular machines, are focused. For different functions that resulted from individual molecules, both molecular "cores" and molecular "tails" are equally important due to the fact that the proposed functions could be affected not only by molecular electrical characteristics but also by the electrode–molecule bonding. Therefore, in each part of this section, we will pay specific attention to the design of the molecular structures and its influence on the device functions.

9.1 Wiring Toward Nanocircuits

Electrical nanocircuits comprised of individual functional molecular electronic components are the ultimate goal of molecular electronics. Therefore, it is fundamentally necessary and critical to understand the role of molecular wires, which connect the electronic components to one another or to the macroscopic world, thus ensuring the efficient transport of the charge [1]. Meanwhile, molecular wires are the simplest of electrical devices and are particularly suited for the

Molecular-Scale Electronics: Concept, Fabrication and Applications,
First Edition. Xuefeng Guo, Dong Xiang, and Yu Li.

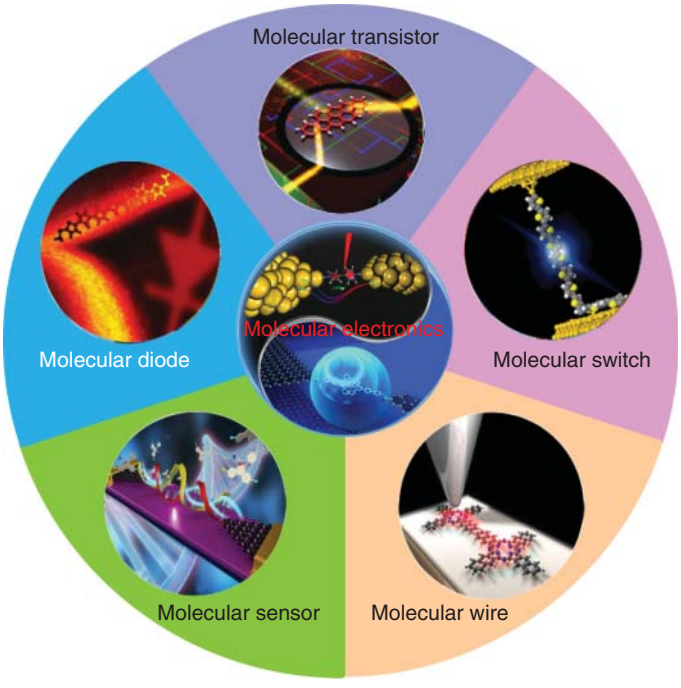

Figure 9.1 Schematic description of current trends in developing different types of functional molecular electronic devices.

development of certain fundamental understandings and techniques required for the realization of molecular-scale electronics [2]. Thus, several studies have been established centering on the design, synthesis, and conductance measurements of molecular wires. Generally, the molecular wires used in the nanocircuits can be structurally divided into two parts: anchoring groups that connect external electrodes and molecular backbones that function as charge transport pathways [3]. The superiority of the wire can be evaluated partly by its electrical conductivity, which can be determined from the conductance measurements. However, as generally accepted, both the structure of the molecules and the nature of the electrode–molecule contact interface can affect the conductance measurement; thus, the backbones and the anchoring groups of the molecular wires are designed based on the device architecture, and the electrode materials hold the same importance. It should be noted here that the term "molecular wires" has a relatively strict scope: discrete molecules rather than crystals, films, or chains of metal atoms formed through octahedral μ-bridging or flat-molecule stacking [4].

9.1.1 Backbones as Charge Transport Pathways

Several types of molecules with different backbones have been suggested as molecular wires: (i) hydrocarbon chains, including saturated and conjugated species; (ii) metal-containing compounds; (iii) porphyrin arrays; (iv) carbon

nanotubes (CNTs); and (v) biological molecules, such as DNAs. The most important requirement that these wire-shaped molecules share is electron or hole conductivity to provide a more efficient pathway other than space for charge transport from one reservoir to the other [2].

9.1.1.1 Hydrocarbon Chains

The continuous development of organic synthetic methodologies forms various types of molecular scaffolds with specific construction, configuration and conformation, as well as precise length to be accessible, thus providing a large wealth of probabilities to promote molecular electronics. Particularly, hydrocarbon molecules, including the saturated and conjugated species, have been prepared and explored systematically.

Saturated Chains Saturated hydrocarbon chains generally refer to the system of alkanes consisting of sp^3 C–C backbones and their terminated groups. Although these molecules are thought to possess poor conductivity due to the large gaps between their highest occupied molecular orbitals (HOMOs) and lowest unoccupied molecular orbitals (LUMOs), they calibrate the development of both experimental techniques and theoretical calculations [5]. As indicated by the theoretical prediction, alkane backbones have a limited degree of electron delocalization, resulting in poor conductance that decreases exponentially with the molecular length. In 2002, Wold et al. [6] measured the conductance of alkanes with different lengths and determined a quantitative result of $R = R_0 \exp(\beta L)$, where R_0 is a constant, L is the molecular length, and β is a decay constant with a value of 0.94 ± 0.06 Å^{-1}. In the light of this formula, Solomon et al. [7] systematically compiled, compared, and discussed the conductance of such saturated chains with different lengths established in different testbeds, further verifying the general relationship of the molecular length and the conductance. Recently, various protocols and efforts were presented to improve the conductance of saturated backbones by introducing active centers into the molecular chains. For example, Wierzbinski et al. prepared dithiolated oligoethers by inserting oxygen heteroatoms into chains of alkanedithiols [8]. Although the conductance of the oligoethers was lower than that of the alkanes with the same length, the idea showed a positive inspiration. Then, Sun et al. successfully enhanced the electrical conductivity of saturated wires by inserting ferrocene centers, which were postulated to reduce the tunneling barrier and the HOMO–LUMO gaps [9]. The conduction mechanism for these saturated molecules is considered to be electron tunneling, which can be supported by the exponential decay, characteristic current–voltage (I–V) curves and temperature independence [5]. It can be assumed that molecules with saturated hydrocarbon backbones have limited applications as molecular wires. However, the system of saturated alkanes also provides a significant contribution to the progress of the molecular components for their initial role in establishing the theoretical and experimental models.

Conjugated Chains Compared with saturated chains, conjugated hydrocarbon chains can ensure superior charge transport by providing π-conjugated systems

formed primarily by unsaturated bonds, such as double/triple carbon–carbon bonds or aromatic rings. Because of the excellent electrical conductivity and the ease of preparation, conjugated molecules have been and still are viewed as candidates for molecular wires with the most potential. By further developing the molecular electronics and synthetic methodologies, the research focus has evolved from obtaining insights into the structure–property relationship to controlling the conductance and installing multiple functions, such as switching and sensing (which are detailed elsewhere in this chapter), by elaborately changing the construction, configuration, and conformation of the molecular backbones. Generally, two primary types of molecular wires with conjugated hydrocarbon backbones attract the most attention: double/triple bond-dominated chains and aromatic ring-dominated chains, both of which can be achieved using mature organic and/or organometallic synthetic methods. The former includes limited types of variants, while the latter contains numerous types of derivatives due to several types of aromatic rings. In this section, only the commonly used molecules with the most general importance are covered.

Double/Triple Bond-Dominated Chains Molecules with double/triple bond-dominated backbones are commonly known as acetylene oligomers or oligoynes, which comprise an array of *sp*-hybridized carbon atoms with approximately cylindrical electron delocalization along a one-dimensional, rigid-rod, length-persistent backbone [10]. Several methods have been developed to prepare the π-conjugated backbones (Figure 9.2a) [11, 14]; furthermore, to enhance the conductivity, additional synthetic protocols are being introduced to encapsulate and insulate the backbones [12] (Figure 9.2b) as well as techniques to modify various anchoring groups to connect with the electrodes of the molecular testbed (Figure 9.2c) [13, 15, 16].

Based on these efforts, Wang et al. [10] reported the electrical conductance of oligoyne-based molecular wires at the single-molecule level by using scanning tunneling microscopy break junctions (STM-BJs), in which it was determined that the conductance was independent of the molecular length for the low decay constant, β, and dependent on the contact geometries between the pyridyl headgroups and the gold electrodes, as detailed in the following text. An extensive study was conducted by Moreno-Garcia et al. [17], who performed more experimental and theoretical efforts to obtain insights into the length and anchoring group dependence of the electrical conductance at the single-molecule level for a series of oligoyne molecular wires. These systematic studies demonstrated that the oligoynes or the acetylene oligomers are indeed an appealing type of linear molecular wires because their extensive conjugations have nearly cylindrical electron delocalization within a one-dimensional space [10]. This result may produce a higher efficiency of electron transport compared with that of molecular wires possessing aromatic ring-dominated chains (as discussed in the following text), because there is no rotation barrier between the adjacent conjugation units compared with the aromatic systems [18, 19]. The disadvantage of these wires, if any, is that it is contradictory to introduce other moieties with the linear configuration into the backbones, thus reducing the possibility to enrich the system.

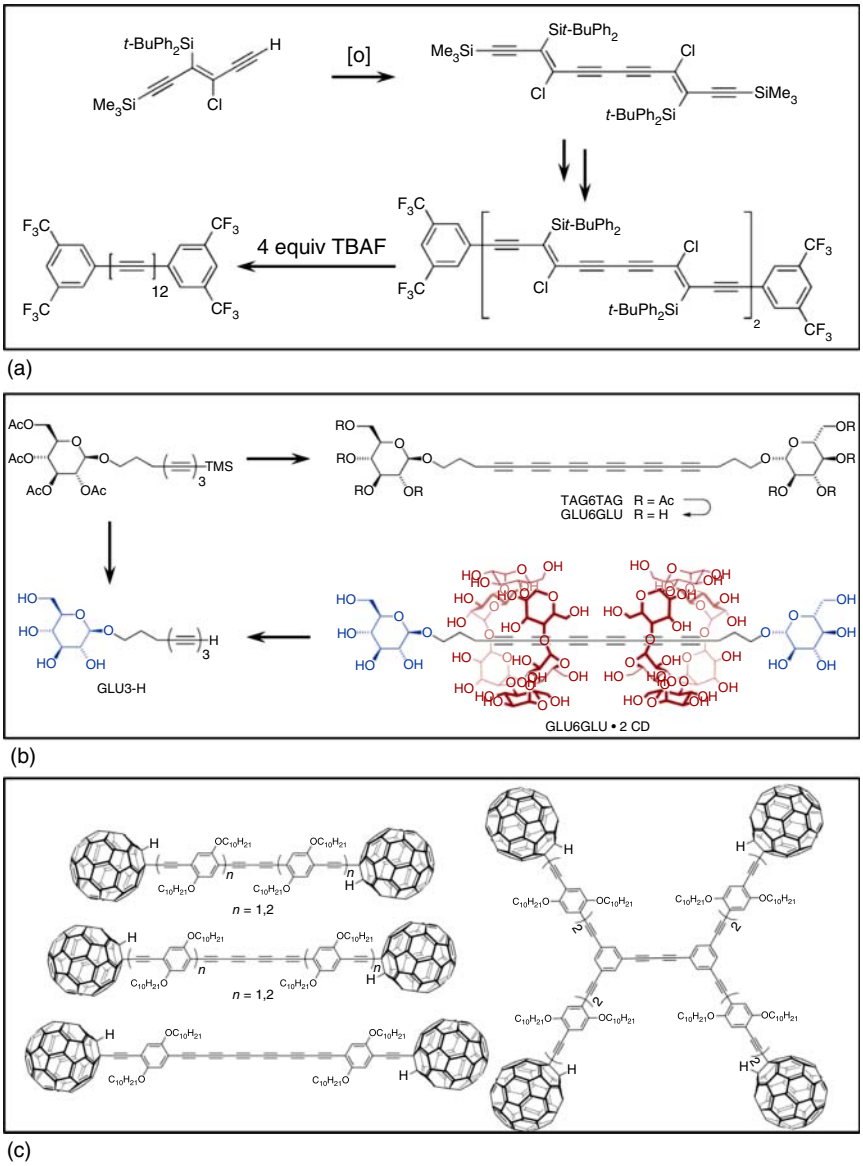

Figure 9.2 Examples for synthesis. (a) encapsulation (to ensure charge transport); (b) termination (to connect to electrodes); and (c) modification of oligoynes. Source: Reproduced with permission from Weller et al. [11], Schrettl et al. [12], and Zhou and Zhao [13]. Copyright 2008, 2015, 2010, American Chemical Society, Royal Society of Chemistry.

Aromatic Ring-Dominated Chains Another mature conjugated molecular backbone used in the nano-wiring are aromatic ring-dominated molecules, known as "oligoarylenes," which are broadly defined as a chain of aromatic rings linked by acetylene, ethylene, or other π-system units. The widely used aromatic rings include thiophene and benzene. Based on the types of inter-ring linkages, the

thiophene-dominated chains can be classified as oligothiophene (OT) and oligo(thiophene ethylene) while the benzene-dominated chains can be classified as oligophenylene (OP), oligo(phenylene ethylene) (OPE), and oligo(phenylene vinylene) (OPV).

Thiophene-Dominated Chains Previous studies have demonstrated that the effective conjugation length of the OTs is ∼20 thiophene units in the neutral state and ∼30 units in the oxidized state [2]. This fact, along with their thermal stability and superior electronic properties, inspired many interests in the synthesis, characterization, and optimization of the OTs because of their potential application in molecular electronics. A large number of synthetic methods have been developed for precisely controlling the molecular length [20, 21], which is fundamentally required by electronic circuits. In addition to length control, the structural and conformational determination of the α-connected thiophene oligomers at the single-molecule level are of significant importance for distinguishing two conformations induced by the rotational flexibility: s-*trans* and s-*cis*. The latter, with a torsional angle of approximately 145° between adjacent thiophenes and an approximately 0.5 kcal mol^{-1} energy barrier, is more stable compared with the former form with an angle of approximately 47° and a barrier of 2 kcal mol^{-1}. However, it proved to be challenging to characterize the conformation using conventional methods, such as NMR and X-ray scattering. To solve the problem, in 2008 Nishiyama et al. directly identified straight and all-s-trans chains using the STM imaging technique (Figure 9.3a) [22]. This research laid the foundation for constructing molecular junctions based on individual OTs, thus paving the way to systematically studying their electronic properties. For example, Lee et al. observed a universal temperature crossover behavior of the electrical conductance in a single OT wire in 2012 [23]. They proposed that the competition between the two transport mechanisms (superexchange and thermally induced hopping [TIH] processes, which are detailed in the succeeding text) depends not only on the wire length but also on the temperature (Figure 9.3b). To enhance the electronic transport property of the OTs, Endou and colleagues reported a strategy to completely encapsulate the OTs to prevent intermolecular electronic communication [24]. Using the STM technique, they determined the decay constant β of electronically neutral OT chains to have an estimated value of 1.9 nm^{-1}. Compared with OTs, oligo(thiophene ethynylene) (OTE) and oligo(thiophene vinylene) (OTV) can be viewed as their derivatives, where the thiophene units are connected by acetylene and vinylene instead of single C—C bonds. Both oligomers hold similar features to OTs: long effective conjugation and high stability in various oxidation states. Recently, additional methods have been developed to introduce heterostructures into the oligomer's backbones to realize specific functions beyond the electronic transport, which is discussed later.

Benzene-Dominated Chains Benzene-dominated oligomers, including OP, OPE, and OPV, all of which, similar to the thiophene-dominated ones, possess a large degree of electron delocalization to function as molecular wires. Furthermore, due to the structural symmetry, there are less conformational issues

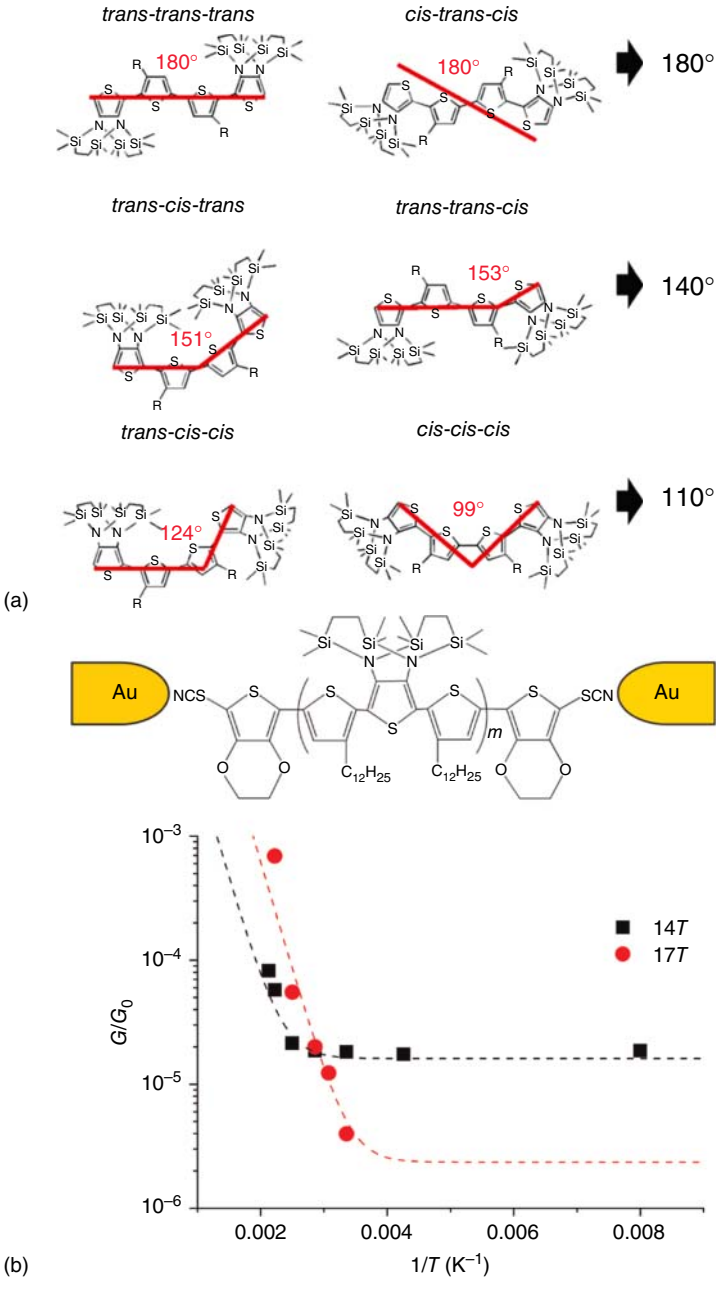

Figure 9.3 Conformation and conductance of OTs. (a) Six possible conformations of an *N*-silyl substituted QT, which were characterized by rotational variations in the thiophene rings at three thiophene–thiophene bonds. In these conformations, solid lines indicate bending angles of the quarter thiophene when coplanar conformations are assumed. These angles can reproduce the experimentally obtained angles (180°, 140°, and 110°) measured between two *N*-silyl groups. Source: Reproduced with permission from Nishiyama et al. [22]. Copyright 2008, American Chemical Society. (b) Device structure and scaling analyses of the experimental results for the 14T-di-thiocyanate (SCN) and 17T-di-SCN oligothiophene molecules. Source: Reproduced with permission from Lee et al. [23]. Copyright 2012, American Chemical Society.

to be considered in the synthesis or characterization process, thus leading to additional development in this field.

Based on mature synthetic methods [25, 26], OP molecules consisting of a chain of benzenes linked by C—C bonds can be synthesized and diversified by introducing special moieties. Because of their easy preparation, OPs were thoroughly investigated as molecular wires. As early as the year of 2002 [6], individual OP molecules with different lengths have been integrated into the nanogap in the conducting probe (CP)-AFM setup to explore the length–conductance relationship. In the following year, another study achieved the systematical conductance values of these molecules [7]. Benefitting from the convenience of side group substitution on the benzene ring, a relationship can be established between the conductance and the molecular conformation, which has been demonstrated by Venkataraman et al. in 2006 (Figure 9.4a) [27]. This study demonstrates that to reduce the twist angle between the two benzene rings to zero, two respective but adjacent α-sites were fixed, which was equal to introducing a fluorene unit. They determined that the conductance for the series decreases with an increasing twist angle, which is consistent with the cosine-squared relationship predicted for the transport through *p*-conjugated biphenyl systems (Figure 9.4b,c). Maximizing the ratio of the fluorene units in the OP chains formed the molecular basis of two studies performed in 2009 and 2011 (Figure 9.4d). The former used single oligofluorene molecules to explore the relationship between the conductance and the molecular length by changing the tip-substrate height in the STM setup (Figure 9.4e) [28] while the latter appended C_{60} terminal groups to the oligofluorene molecules, thus leading to the unambiguous formation of STM-based single-molecule junctions [29].

OPE is another benzene-dominated oligomer, whose backbones are formed by linking acetylene with benzene. These molecules have been systematically explored by Tour based on the iterative divergent/convergent methods developed at the beginning of this century [30]. Due to the ease of self-assembly, it is feasible to measure the conductance of these wire-shape molecules, which was performed by using an STM in 2003 [31] and a CP-AFM in 2004 [32]. Interestingly, Donhauser et al. determined the conductance switching behavior of single OPE molecules isolated in matrices of alkanethiolate monolayers, which may result from conformational changes in the molecules [33]. In another systematical study [34–36], the relationship between the molecular conformation and the conductance was established, where the authors carefully introduced specially designed moieties with different dihedral angles into the oligomer chains to vary the conformation of the molecules. Both the experimental and theoretical results suggested that the conductance of the OPE molecular junctions could be tuned by controlling their intramolecular conformation, which was consistent with a cosine-squared relationship, as reported by Venkataraman et al. [27] Remarkably, Kaliginedi et al. [35] determined that the introduction of a cross-conjugated anthraquinone (AQ) central unit resulted in lower conductance values. This observation may be attributed to a destructive quantum interference phenomenon. To enhance the one-dimensional conductivity of the OPE molecules, the oligomer's backbones could be isolated using a polyrotaxane protective sheath [37] or encapsulated by dendrimer shells [38, 39]. To install

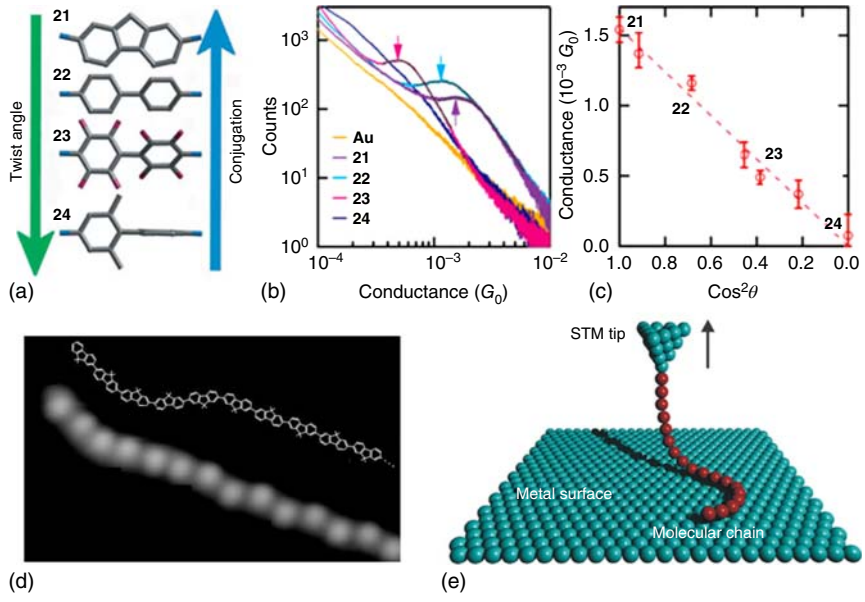

Figure 9.4 Structure–conductance relationship. (a) Structures of a subset of the biphenyl series studied, which are shown in order of increasing twist angle or decreasing conjugation. (b) Conductance histograms obtained from measurements using molecule 12 (purple), 14 (cyan), 16 (pink), and 18 (blue). Additionally, the control histogram obtained from the measurements is depicted without molecules between the contacts (yellow). The arrows denote the peak conductance values obtained from the Lorentzian fits (solid black curves). (c) Position of the peaks for all the molecules studied plotted against $\cos^2\theta$, where θ is the calculated twist angle for each molecule. Source: (c) Reproduced with permission from Venkataraman et al. [27]. Copyright 2006, Nature Publishing Group. (d) STM image of a single oligofluorene chain. (e) Conductance measurement of single oligofluorene molecules in the STM setup, which can explore the relationship between the molecular length and the conductance. Source: (e) Reproduced with permission from Lafferentz et al. [28]. Copyright 2009, Springer Nature.

new functionalities, other moieties can also be inserted into the backbones of the OPE molecules; for example, the rectification effect caused by the 9-[di(4-pyridyl)methylene]fluorene insertion [40] and switching caused by the tetrathiafulvalene insertion [41, 42].

Replacing ethylene with vinylene in the OPE backbones leads to OPV molecules [43, 44]. It is predicted that the conductance of the OPV and its derivatives is higher than that of the OPE. Because the degree of disrupting the conjugation of the backbone using a longer vinyl bond (C=C length c. 1.35 Å) in the OPV is less compared to using a shorter ethynyl linkage (C≡C length c. 1.22 Å) in the OPE, there is less bond alternation and a smaller HOMO–LUMO gap in the OPV than that in the OPE [10]. The exact conductance value was measured and estimated in two studies in 2003 [7, 31], whereas the charge transport mechanisms were discussed in detail in another two studies [45, 46]. It is evident that there are different configurations for the existence of the vinyl bond. In fact, Martin et al. elucidated the effects of E/Z isomerizations on the conductance

of such molecules at the single-molecule level using the STM technique [47]. They demonstrated that the isomerization led to significant changes in the electrical conductance of these molecules, with the *Z* isomer exhibiting a higher conductance than that of the *E* isomer. Using the method of controlled aryl imine addition chemistry, Choi et al. [48] prepared oligophenyleneimine (OPI) wires with different lengths (Figure 7.2) and studied the role of molecular length and bond architecture on the molecular conductivity. The theoretically predicted change in the direct current (DC) transport from tunneling to hopping was observed as a function of the systematically controlled wire length (Figure 7.2). The transition occurred near 4 nm. A systematic extension, in 2010, oligonaphthalenefluoreneimine (ONI) molecular wires were developed by assembling larger conjugated molecular building blocks based on naphthalene dialdehydes and fluorene diamines into the OPI backbones [49]. A consistent transition in the DC transport from tunneling to hopping was observed near 4 nm. These nanoscale transport measurements elucidated the role of the molecular length and the bond architecture on the molecular conductivity and led to opportunities for a greater understanding of the electrical transport in conjugated polymer films.

As indicated earlier, several types of conjugated hydrocarbon molecules in the context of molecular wires have been discussed. The accessibility of various types of molecular scaffolds makes it possible for wire-shaped molecules to be synthesized and modified with a large degree of precise controllability of construction, configuration, and conformation. Furthermore, due to the development of efficient strategies to introduce hetero-moieties, e.g. anchoring groups and functional centers, in specific positions of the chains, additional individual molecules could be connected into the nanogaps between the external electrodes to conduct current and/or function as, e.g. switches or rectifiers. The conjugated hydrocarbon molecules have been believed to have additional contributions to the improvements in the molecular wires.

9.1.1.2 Metal Containing Compounds

Recently, significant progress has been made in using tailored carbon-rich organometallic compounds as prototypes for molecular electrical wires because these molecules may have the potential to be more conductive than their all-carbon counterparts [50]. Furthermore, an optimal match in orbital energies can be achieved more readily to yield compounds with smaller HOMO–LUMO gaps by structurally engineering the metal unit together with carbon-rich bridges. This molecular engineering will endow a superior conductivity to the prototype wires [51]. In this section, we review the development and progress of organometallic compound-based molecular wires, which can be classified into three types: small molecules, coordination oligomers, and polymetallic systems (Figure 9.5) [52]. It should be noted that in literature surveys, a large number of studies focus on systems of unsaturated carbons capped with two metal moieties. These systems are not in the scope of this book, though they also contain metal, because they were initially developed for charge transfer rate studies instead of direct conductance measurements.

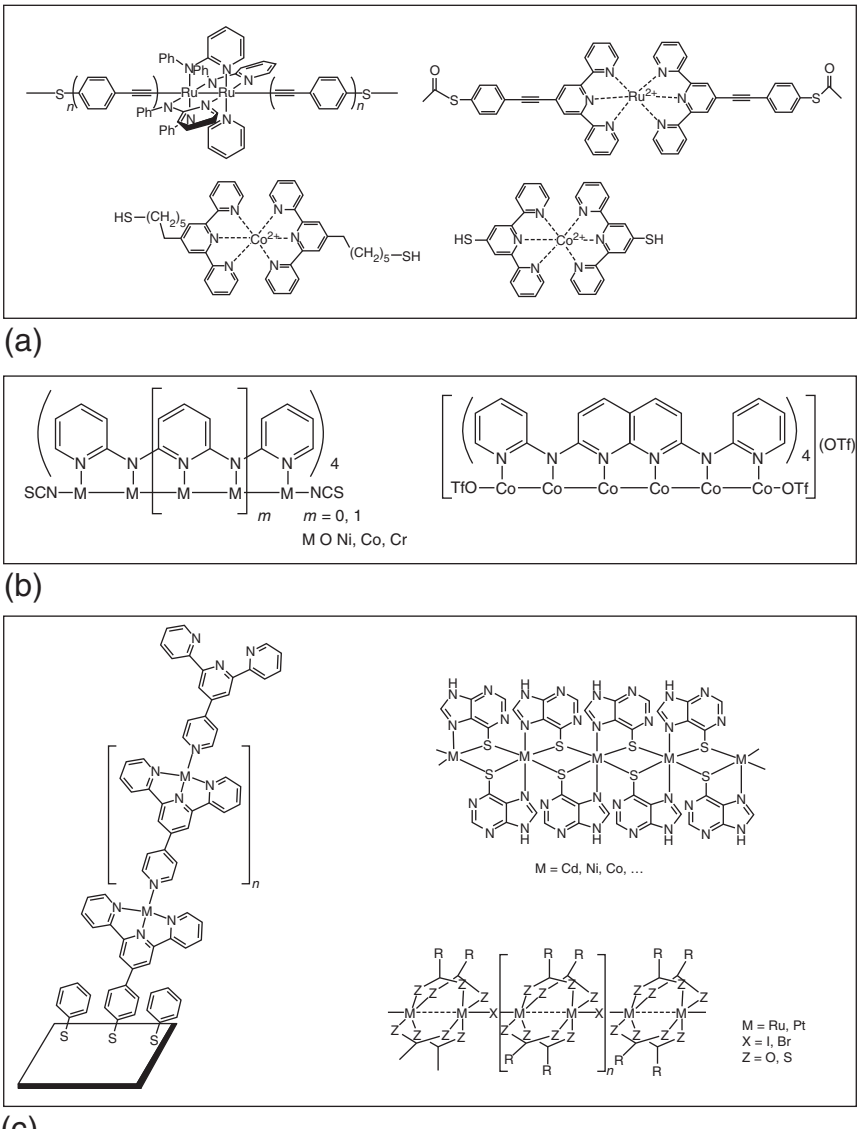

Figure 9.5 Representative organometallic compounds as prototypes of molecular electronic wires. (a) Single molecules, (b) oligomers or polymetallic systems, and (c) coordination polymers Source: Reproduced with permission from Mas-Ballesté et al. [52]. Copyright 2009, John Wiley and Sons.

Single Molecules or Oligomers Although the study performed by Mayor et al. [53] in 2002 appeared to decrease the conductivity of wire-shaped molecules, which was contrary to the trend of increasing the conductivity, it deserved to be highlighted for its pioneering exploration in the process of direct conductance measurements using the mechanically controllable break junction (MCBJ)

technique. In this study, the authors designed a molecular insulator based on *trans*-acetylene–platinum(II) complexes, for which the platinum–acetylene bond had hardly any π character and separated the molecular rod into two independent conjugated systems to increase its resistance. The key progress in the chemical synthesis provided access for the preparation of the σ-alkynyl compounds of $Ru_2(LL)_4(C_{2n}Y)_2$ (LL is an *N*,*N*′-bidentate bridging ligand and Y is an anchoring group), which were wire-shaped molecules containing double ruthenium centers used as building blocks in molecular electronics [51]. The development of the corresponding optical and electrochemical characterizations provided the possibility of clarifying the electronic structure and the redox characteristics of such molecules. All these studies led to their application as molecular wires as well as more sophisticated molecular switches that are described in the following text in detail.

Using the STM-BJs, the potential of the metal-alkynyl compounds as molecular wires was first discovered using $Ru_2(ap)_4$(σ-OPE) (ap: 2-anilinopyridinate) molecules as a representative [51]. The same results were also observed by Wen et al. [54], who established conductance measurements of different organometallic wires with two ruthenium(II) centers bridged by 1,3-butadiyne based on an electrochemically mechanically assisted controllable break junction approach. It was determined that the single-molecular conductance of these diruthenium(II) incorporated systems was significantly higher than that of the OPEs with comparable lengths. This result may be ascribed to a better energy match of the Fermi level of gold electrodes with a molecular HOMO. In 2008, another series of compounds belonging to the metal–alkynyl molecular set, *trans*-$Ru_2(ap)_4((C{\equiv}CC_6H_4)_2S{-})_n$ ($n = 1$ or 2) were integrated into the molecular junctions, and the hysteresis effects that occurred during voltage sweeping in different directions were discovered [55].

From 2007 to 2011, Rigaut and colleagues systematically developed and extended a series of redox-active conjugated organometallic wires, which consisted of covalently coupled ruthenium(II) bis(σ-arylacetylide) complexes [56–58]. The most important feature of this type of organometallic molecule is its precise length controllability during the synthetic process, leading to the production of Ru1–Ru3 compounds with a length ranging from 2.4 to 4.9 nm. The authors used this advantage to thoroughly investigate the length dependence of the molecular conductance under different temperatures, which facilitated the clarification of two general electron transport mechanisms: direct tunneling and thermally activated hopping.

One common characteristic of the previously discussed molecules is that they all contain ruthenium, which forms an important branch of the organometallic molecular wires. Additionally, Albrecht et al. and Chen et al. developed another class of Os(II)/(III)- and Co(II)/(III)-complexes (Figure 9.5a,b) [59, 60], which were robust and conductive for functioning as molecular wires. The former, Os-complexes $[Os(bpy)_2(p2p)_2]^{2+/3+}$ and $[Os(bpy)_2(p0p)Cl]^{1+/2+}$, were still new to being used in molecular electronics while the latter, Co-complexes, have been explored in several studies. For example, Guo et al. connected terpyridyl-containing molecules to both sides of either the single-walled carbon nanotube (SWCNT) or graphene electrodes using amide bonds and then added

Co^{2+} into the system to form Co-complexes [61, 62]. It should be noted that the covalent connection provided enough robustness to the interfacial linkage, leading to a good reliability for investigating the electrical conductance of the organometallic molecules as well as the corresponding coordination reaction at the single-molecule level. In two additional studies [63, 64], Park et al. and Tang et al. incorporated the Co-complexes into nanogapped metal electrodes to study how electrons were transported through the well-defined charge states of a single atom. It was determined that changing the length of the insulating linkages altered the coupling of the metal ion to the electrodes so that interesting single-electron phenomena, such as the Coulomb blockade and the Kondo effect, were observed.

Coordination Polymers The combination of Co ions and terpyridyl-related ligands inspires the idea that through the suitable selection of molecular building blocks, organometallic polymer architectures, which are defined as coordination polymers in Figure 9.5c, can be prepared. In fact, the coordination polymers are infinite aggregates of metal ions or fragments bridged by ligands. These aggregates can self-assemble by coordinate bonding into one, two, or three dimensions, thus producing a wide variety of supramolecular structures [65]. The study conducted by Guo and colleagues [66] involved the ideology of constructing prototypes of coordination polymers, in which the terpyridyl-related ligands were initially linked to both sides of graphene electrodes followed by the addition of cobalt ions and hexapyridyl sequentially (Figure 3.10). The apparent current flowing through the metallic molecules reflected both the conductivity of such molecular wires and the feasibility of molecular self-incorporation. Additionally, this strategy also allows the *in situ* construction of complex molecular wires through the implementation of programmable reactions, as discussed previously. In 2009, Tuccitto et al. prepared a coordination polymer as long as 40 nm by incorporating a large number of cobalt centers into rigid molecular backbones comprising terpyridyl-based ligands via a sequential stepwise coordination [67]. The remarkable mechanical robustness, length-independent conductance, and easy-to-assemble characteristics led to a new generation of molecular wires.

9.1.1.3 Porphyrin Arrays

Porphyrin, a square planar 18π aromatic macrocycle that possesses four pyrroles and four methine carbons, has been extensively studied in a wide range of research disciplines due to its tremendously advantageous properties, such as structural robustness, attractive optical properties, strong aromaticity, and rich metal coordination chemistry [2, 68–70]. Particularly, the HOMO and the LUMO of the conjugated porphyrin arrays are generally only separated by 2 eV. If this gap is slightly narrowed, the molecules would have useful electrical properties required for molecular wires [71]. Another important advantage in using porphyrin arrays as molecular wires is the large size of the monomeric unit, which is ~16 Å. Therefore, the linear tetramers have a span of ~56 Å. This size is large enough to bridge the nanogap in a molecular junction. In addition to these features, the porphyrin electronic system is susceptible to a

conjugative perturbation at the periphery and metal chelation, thus allowing a rational electronic modulation that can build systems displaying tunable optical and electronic properties. Consequently, the conjugated porphyrin arrays can be considered as promising candidates for molecular wires in future molecular electronics applications.

In the last two decades, a wide variety of conjugated porphyrin arrays have been synthesized and explored. Their synthetic chemistry can be found in detail in several previous reviews [72–75]. There are two methods used for linking large individual porphyrin rings together (Figure 9.6). The first method is to fuse porphyrins with multiple direct bonds, i.e. each porphyrin structure is directly linked to the next. Generally, the fused porphyrins were synthesized through the oxidation of metallo-porphyrins with tris(4-bromophenyl)aluminum hexachloroantimonate, where the two porphyrin units are doubly or triply linked through the ring carbon atoms. This forces a coplanar geometry that should be favorable for the electronic π conjugation, thus displaying remarkable photophysical properties, such as extremely red-shifted absorption profiles that reach the IR region, large two-photon-absorption cross-section values and drastically reduced charge-transport attenuation factors. Compared with the doubly fused diporphyrins, the triply-linked diporphyrin structures indicated greater conjugation, which is likely due to more planar geometries, thus leading to a better π-overlap (Figure 9.6). Furthermore, stronger electronic interactions and smaller optical HOMO–LUMO gaps (1.14–1.33 eV) were demonstrated. In addition to the doubly/triply fused porphyrins, new conjugated arrays of porphyrinoids have been developed, including directly linked corrole oligomers, hybrid tapes of porphyrin and rectangular hexaphyrins, and subporphyrin dimers. The second method is to bridge the porphyrins with a π-linker, such as ethyne and

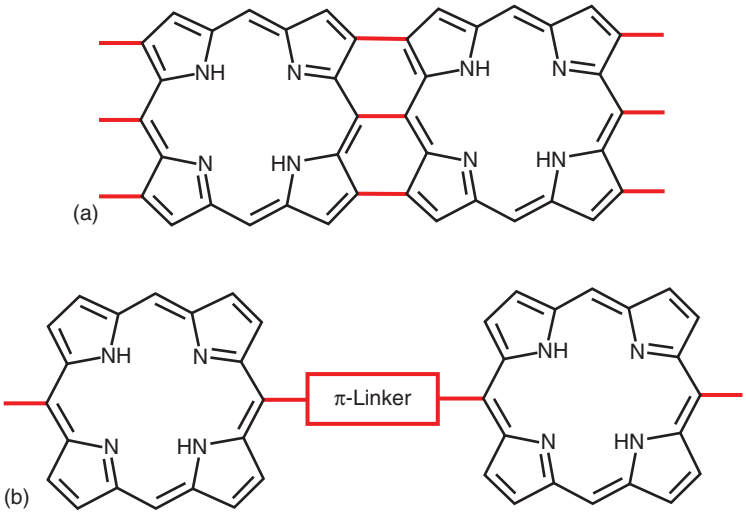

Figure 9.6 Two representative types of conjugated porphyrin wires. (a) Triply fused porphyrin oligomer and (b) π-bridged porphyrin oligomer. Source: Reproduced with permission from Tanaka and Osuka [72]. Copyright 2015, Royal Society of Chemistry.

ethene, which has been conducted in a controlled manner using classical organic reactions or transition metal catalyzed reactions. The electronic interaction depends highly on the nature of the linker, bridging position, and geometric relationship of the functionalized porphyrins. For example, it was determined that porphyrin oligomers could behave similar to photonic molecular wires, which absorbed light at one end of an array of porphyrins and then emitted a different photon at the other end. These results strongly highlight the necessity for the further exploration of the conjugated porphyrinoids.

Most of the reported studies are based on large areas of the self-assembled monolayers (SAMs) for porphyrinoids, where minimal molecular or nanoscale level measurements have been performed. Recently, single-molecule conductance measurements of porphyrin-based molecular wires were demonstrated using an STM-BJ technique [76–78]. In this system, the molecular conductance, σ_M, generally decreased exponentially with the molecular length, as quantified by the attenuation factor, β, which is a useful measure of the ability to mediate long-range charge transportation. It was determined that the β value of butadiyne-bridged porphyrin wires with terminal thioacetate anchors was 0.04, which is significantly lower than those of typical organic molecules (0.1–0.6). Compared with the butadiyne-bridged arrays ($\beta = 0.04$) and the meso–meso linked arrays ($\beta = 0.11$), the fused porphyrin arrays indicated an exceptionally weak attenuation nature ($\beta = 0.02$). Similar to the butadiyne-bridged arrays, the ethyne-bridged porphyrin wires bearing terminal thiophenol anchor groups indicated β values of 0.03. Although current practical and technological limitations confine the fabrication of molecular junctions formed from these conjugated porphyrin arrays, the remarkable features of the conjugated porphyrin arrays, as detailed earlier, receive considerable attention and can lead to significant scientific breakthroughs in the near future.

9.1.1.4 Carbon Nanotubes

In Section 9.3, we demonstrated the potential of CNTs to be used as point contacts for forming molecular electronic devices. In fact, CNTs themselves are macromolecular systems with unique physical and chemical properties. A CNT can be defined as being formed by rolling a piece of graphene to create a seamless cylinder. Depending on their chirality and diameter, they can be metallic or semiconducting [79–81]. Another key feature of the CNTs is that all chemical bonds are satisfied and strong, leading to extremely high mechanical, thermal, and chemical stability. Furthermore, the small diameter and the long length of SWCNTs lead to large aspect ratios and suggest the possibility of ballistic devices with drastically reduced carrier scattering, thus making them nearly ideal one-dimensional molecular wire systems.

There are four primary approaches to produce CNTs: (i) arc discharge; (ii) chemical vapor deposition (CVD) over metal catalysts; (iii) laser ablation; and (iv) electrolysis using graphite electrodes immersed in molten ionic salts [82]. The ample availability, unique electrical properties, and mechanical rigidity associated with the CNTs lead to the construction of a device that indicates one possible method in which integrated molecular electronics can operate [83, 84]. In 2000, Rueckes et al. developed a concept for molecular electronics using CNTs

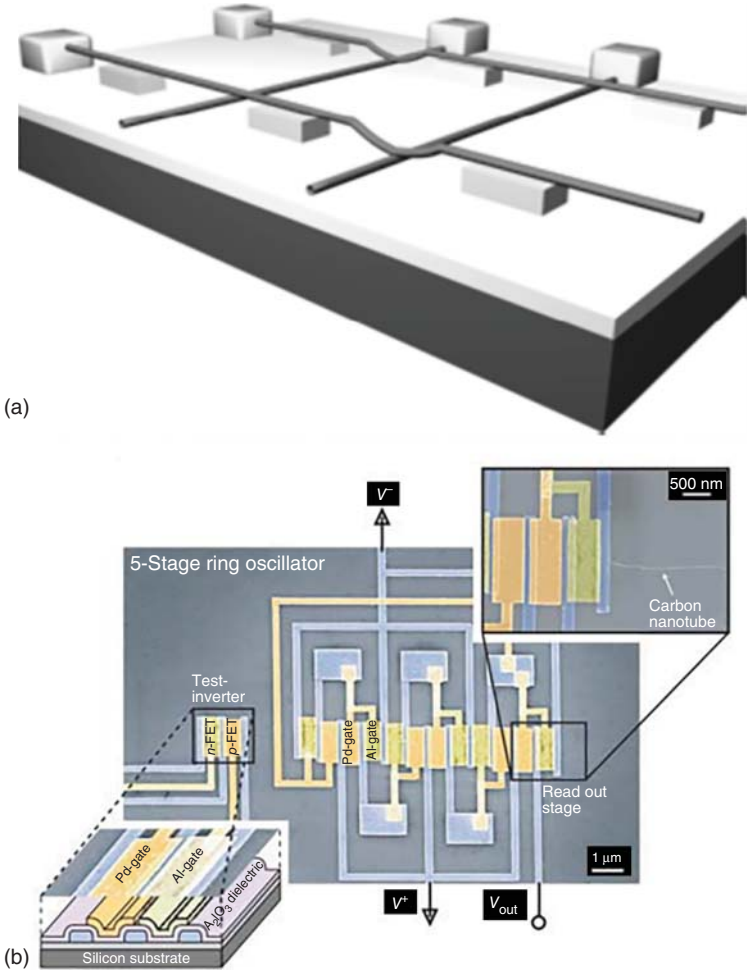

Figure 9.7 Carbon nanotube device architectures. (a) 3D view of a suspended crossbar array of carbon nanotubes, which indicates four junctions with two elements in the ON (contact) state and two elements in the OFF (separated) state. Source: (a) Reproduced with permission from Rueckes et al. [85]. Copyright 2000, AAAS. (b) SEM image of an SWCNT ring oscillator consisting of five CMOS inverter stages. A test inverter was added to determine the parameter set for the actual measurement. Source: (b) Reproduced with permission from Chen et al. [86]. Copyright 2006, AAAS.

as both molecular device elements and molecular wires for information reading and writing (Figure 9.7a) [85]. Each point on the array where two nanotubes cross represents a device element that can be switched between two positions. The OFF state is used when the two SWCNTs are separated by the gap created by the supports, and the resistance between the two separated wires is high. The transient charging of the nanotubes produces an attractive force, which causes them to move so that they are touching, leading to a higher conductivity between the wires and an ON state. The advantage of this approach is that

the device elements are naturally addressable by the CNT molecular wires in large arrays. These reversible, bistable device elements can be used to construct non-volatile random-access memory and logic function tables at an integration level approaching 10^{12} elements per square centimeter and an element operation frequency in excess of 100 GH. This concept is important because it identified a method where a few of the requirements concerning the integration of wires into addressable devices could be achieved.

For practical applications, an important next step would be the construction of integrated circuits along a single SWCNT. This has been demonstrated by the study performed by Chen et al. [86], where a complementary metal oxide semiconductor (CMOS)-type 5-stage ring oscillator was built entirely on one 18 mm-long SWCNT (Figure 9.7b). The polarities of the filed-effect transistors (FETs) were controlled using metals with different work functions as the gates, and Pd was selected as the metal gate for the p-FET, while Al was selected for the n-FET. The key feature of this design is that the distinct difference in the work functions of these two metals effectively shifts the SWCNT FET characteristics to form a p/n-FET pair. By arranging five pairs (10 FETs) side by side on one SWCNT, a ring oscillator circuit with a frequency reaching 52 MHz could be achieved. Another breakthrough study performed by Shulaker et al. demonstrated the first computer built entirely using CNT array-based transistors [87]. The CNT computer was able to run an operating system that was capable of multitasking. To demonstrate the generality of the CNT computer, they implemented 20 different instructions from the commercial microprocessor without interlocked pipeline stages (MIPSs) instruction set. This is a significant development because it confirms that carbon nanotube field-effect transistors (CNT-FETs)-based circuits are a feasible and plausible emerging technology. However, the significant challenges are clearly the current inability to selectively and cleanly synthesize particular nanotubes with a specific diameter and chirality as well as the lack of sites for further functionalization. This result makes constructing electronics from nanotubes difficult because there is no control over the electrical properties. Fortunately, recent remarkable developments have been achieved to realize the controllable growth of chirality-specific individual SWCNTs using solid alloy catalysts [88], temperature control and cloning [89], or high-density SWCNT arrays using Trojan catalysts [90], thus promising a bright future for CNT-based nano-/molecular electronics.

9.1.1.5 Biological Wires

Although synthetic methodologies are steadily being used for realizing various types of artificial molecular scaffolds, which accommodate the specific requirements that are necessary for molecular electronics, considerable attention is being given to nature, i.e. producing numerous unbelievable structures through time accumulation and survival of the fittest to determine the best candidates for the most convenient accessibility and low-cost applications. In this section, we discuss the feasibility and superiority of using biological molecules, such as DNA and carotene, as molecular wires.

DNA is the carrier of genetic information and is of crucial importance in the continuation of life and of great interest as a functional nanosized material due to its unique features, which possesses the ability of self-assembling base pairs,

i.e. adenine with thymine and guanine with cytosine, using hydrogen bonds with extreme complementarity and veracity. Importantly, the hydrogen-bonded base pairs parallel stacks with the face-to-face mode, which implies that the DNA should be electrically conductive over significant distances. In fact, the use of DNA as molecular wires has been explored for decades, and the answer to the question whether single DNA can conduct an electrical current remains uncertain [91]. However, it should be noted that the controversy may stem from the differences in the measured samples (e.g. base sequences, structure of DNA) or the measurement environments and methods. By developing advanced testing methods and systems along with an improved controllability for subtle and uniform testing conditions to study the DNA conductivity, it is imperative to evaluate the conductance of such one-dimensional biopolymers.

On the basis of previous studies, the intrinsic conductivity of DNAs can be affected by their length, base-pair related sequence and conformation types, including Z, A, and B forms. In addition to these factors, single DNA conductance measurements are also influenced by the contact nature, temperature, and testing medium. Several early studies on the length dependence of the DNA conductivity consistently concluded that electrical transport was feasible in short DNA molecules and blocked in long single molecules [92–94]. The sequence-dependent conductance is also a hot point in the field. Generally, DNA can be classified as homogeneous sequence and complex sequence. The former refers to DNAs with poly(G)–poly(C) or poly(A)–poly(T) base pairs, among which G–C based sequences have been demonstrated to be more conductive [95, 96]. The latter can be defined as arbitrary base pair based DNAs, where considerable attention has been given to the phenomenon of single-nucleotide polymorphisms (SNPs). Tao and colleagues [97] and Guo et al. [98] promoted the fundamental understanding of the relationship between the conductance and the SNP, both of which observed that well-matched DNAs were more conductive than those with mismatched base pairs. In addition to length and sequence, DNA configurations or DNA structure types also have important effects on its conductance, which have been comprehensively discussed by Kawai and colleague [91]. In addition to the common types (Z, A, and B forms), G-quadruplex structures formed by single-strand DNAs with certain guanine-rich bases were also investigated, thus providing higher conductance.

As mentioned previously, the DNA conductance acquired by different methods varies in the insulator, semiconductor, or conductor regimes primarily due to the differences in the samples. However, testing conditions may result in discrepancies in various measurement systems, such as temperature and medium, which may be an important aspect in inducing the inconsistency. For example, van Zalinge et al. systematically explored the effects of temperature on the conductance of different homogeneous-sequence DNAs, in which the $I–V$ curve did not indicate (within experimental error) any dependence of the DNA conductance on the temperature. This result is contrary to the observation of long homogeneous-base sequence DNAs in a vacuum [99]. The authors analyzed that such differences indicated that the medium had a significant influence on the temperature dependence of the DNA conductance. In fact, the importance of the medium, such as the concentration of the counter cation and the relative

humidity, could affect the structure types of the DNA as well as the conductance measurement.

The possibility of transporting charge carriers along short single DNA molecules has been verified by further evidence from direct electrical transport measurements [100], but the conductivity is relatively poor. The transport through long single DNA molecules (>40 nm) is evidently blocked. Therefore, suitable strategies are needed to enhance the conductivity of the DNA if they are going to be used as molecular wires in electrical circuits or as a model system for studying electrical transport in a single one-dimensional molecular wire. Generally, there are two primary approaches for improving the DNA conductivity. The first is to use more exotic structures, such as DNA quadruple helices, instead of double-stranded structures, which may offer an improved stiffness and electronic overlap to potentially enhance the conductivity of these molecules. This proposal has been demonstrated by Erbe and colleagues [101] and Guo and colleagues [102]. The second approach is to dope DNAs through the addition of intercalators or metal ions. To verify this technique, in 2012, Guo and colleagues [103] provided direct evidence that it was possible to enhance the electrical conductance of DNA using a rational arrangement of multiple metal ions inside the core of the DNA base-pair stack. These results demonstrated that DNA molecules bridging nanodevices could serve as an effective mediator for charge transport, thus introducing a new scientific research field that interfaces molecular nanodevices with biological systems.

Carotene is a prototypical natural molecular conductor with a large delocalized π-electron system produced from electronic states that are delocalized over a chain of approximately twenty carbon atoms connected by alternative single/double bonds. The efficiency of this natural molecule in photoinduced electron transfer (PET) as donors as well as the importance of its role in photosynthesis as electron shuttles reflect its considerable potential to be used as molecular wires [104]. In fact, there have been several direct conductance measurements demonstrating the high conductivity of carotene and its derivatives. As early as 1999, Leatherman et al. embedded carotenoid molecules in insulating *n*-alkanethiol SAMs and measured the single-molecule electrical properties using the CP-AFM. It was determined that the conductance of these natural molecules was over a million times higher than that of an alkane chain of similar length [105]. As an improvement for forming through-bond electrical contacts, Lindsay and colleagues tethered an Au nanoparticle to each molecule via the protruding thiol group and observed a more recognizable single-molecule conductance of carotene in the matrix of the docosanethiol monolayer, which again stressed the possibility of using carotene as nanowires [106]. However, one of the most important issues in the carotene conductance measurements at the single-molecule level is to distinguish whether the current is through one or more molecule. To solve this problem, Tao and colleague introduced a new method for single-molecule measurements based on repeated STM-BJs, which was easier to use for various molecule lengths and yielded better data in comparison with the CP-AFM approach [107]. Based on this method, Lindsay and colleagues tested a series of homologous carotenoid molecules with different lengths and obtained a corresponding electronic decay

constant, $\beta = 0.22 \pm 0.04$ Å^{-1}, in close agreement with the value obtained from the first-principles simulations ($\beta = 0.22 \pm 0.01$ Å^{-1}) [108]. By incorporating different polar aromatic substituents, Koo and colleagues demonstrated the capability of modulating the conductance of various carotenoid wires [109, 110].

Recently, Lindsay and colleagues determined that the conductance of carotenoid molecules could be enhanced by oxidization through direct measurements at the single-molecule level under the potential control of a membrane-mimicking environment [111]. In view of the requirements for molecular wires, the stability in the electrical conduction is necessary to operate the molecular device. However, the antioxidant activities of the carotenoid molecules in quenching singlet oxygen and scavenging reactive radical species lead to apparent instability. Inspired by the natural prevention of free radical-mediated carotenoid degradation or the repair of semi-oxidized carotenoid molecules via vitamin E, Koo and colleagues [110] devised novel carotenoid wires to provide a labile conjugated polyene chain with stability as well as a range of conductance by attaching aromatic phenyl groups containing the para-substituent X (OMe, Me, H, and Br) of diverse electronic natures to the polyene chain at C-13 and C-13′. The origin of this stability can be expected from the repulsive steric interactions between the phenyl substituents with attacking nucleophiles and/or the reversible trapping of incoming radicals (e.g. reactive oxygen species) that would cause fragmentations of the conjugate polyene chain.

9.1.2 Conductance of Single Molecules

To function as conductive wires, a material should have the ability to transport electrical current with minimal resistance. However, unlike bulk materials, the conductance of single molecules is a complicated issue because it is highly related not only to the intrinsic molecular structures but also to the details of connecting and communicating with the external world [112]. Generally, conductance can be defined as $G = I/V$, and it is an important property describing the efficiency of electron transport in bulk materials. Similarly, in addition to this definition, the conductance of single molecules is proportional to the transmission probability of electrons from one electrode (L) to another (R) and can be described as follows (also see Eq. (9.1)) [113]:

$$G = \frac{2e^2}{h} T \tag{9.1}$$

where e is the electron charge; h is Planck's constant; and T is the total transmission probability over all possible transmission channels. It should be noted that T is related to the coupling strengths (Γ^{L} and Γ^{R}) of the molecule to the two electrodes as well as the transmission probability through the molecule as follows:

$$T = \Gamma^{\mathrm{L}} \Gamma^{\mathrm{R}} |G_{1N}| \tag{9.2}$$

where G_{1N} is the Green function [114, 115]. Therefore, the single-molecule conductance can be defined as follows:

$$G = \frac{2e^2}{h} \Gamma^{L} \Gamma^{R} |G_{1N}| \tag{9.3}$$

Clearly, the measured conductance has relationships with both the molecule and the coupling strengths between the electrodes and the molecules.

Equation (9.3) indicates the mathematical relationship between the interfacial coupling strength and the conductance. This formula can also be written as follows:

$$G = \frac{2e^2}{h} T_{\mathrm{R}} T_{\mathrm{L}} T_{\mathrm{mol}} \tag{9.4}$$

where T_{R}, T_{L}, and T_{mol} are the transmission coefficients of the left interface, right interface, and molecule, respectively. This definition form expresses that single-molecule conductance can also be affected by the alignment of the molecular energy levels, especially the HOMO and the LUMO, relative to the Fermi levels of the electrodes for the tunneling transport mode [112, 116], in which the Fermi levels of the electrodes lie in the gap between the HOMO and the LUMO of the molecules. Following the molecular conductance discussion earlier, we systematically clarify the critical aspects that have considerable effects on the single-molecule conductance and the conductance measurements.

9.1.2.1 Interfacial Coupling

The occurrence of both the charge injection and the collection across the molecule–electrode interfaces underlines the significance of the interfacial properties. A clear recognition of the interfacial coupling strength can lead to obtaining insights into distinct transport mechanisms, thus facilitating the improvement in the molecular conductance. Generally, the interfacial properties depend considerably on the coupling between the molecules and the electrodes, which has a relationship with both the intramolecular coupling of the molecules and the coupling between the terminal of the molecules and the electrodes [113]. For the former, the saturated carbon providing weak coupling and the direct π-conjugated bond offering strong coupling can affect the intramolecular coupling, whereas for the latter, both the interaction types and contact geometries at the molecule–electrode interface are significant [116].

Interaction Types The types of interfacial linkages between the molecules and the electrodes are primarily determined by the materials and the corresponding physical or chemical interactions. Generally, non-covalent interfacial linkages, such as donor–acceptor (D–A) coordination [117], van der Waals binding [106, 108, 118], and aromatic stacking [119], are thought of as weak coupling, while covalent interactions, due to the formation of robust chemical bonds, are viewed as strong coupling. Venkataraman and colleagues systematically studied the interaction of amines and gold as a non-covalent interfacial linkage [117, 120]. Initially, they determined that molecules with amines as anchoring groups could couple with gold electrodes through the interaction of electron lone pairs from the amine nitrogen to coordinately unsaturated surface Au atoms [117]. This bonding mode possesses sufficient angular flexibility for easy junction formation and a well-defined electronic coupling of the N lone pair to the Au, thus facilitating conductance measurements of single-molecule junctions in a statistical manner. Furthermore, using single-molecule mechanics

measurements, it was discovered that anchoring groups of pyridine can bind to nanostructured Au electrodes through a van der Waals interaction beyond the chemically specific Au—N D–A bond [120]. Although the reproducibility of the interfacial linkage in these studies is sufficient to obtain statistical information on conductance, the contact resistance is higher than that of the covalent bonding, such as the Au–S interaction, which is contradictory to the efficient electrical conductance. In fact, metal-based non-covalent interaction is rarely used for constructing a reliable molecule–electrode interface due to its weakness. However, aromatic stacking, which is another type of non-covalent interaction, is widely used to create molecular junctions, especially in systems currently containing carbon electrodes [119, 121, 122]. The detailed discussions can be found in Section 9.3. In terms of conductance, the aromatic stacking is considered to be a weak coupling, which results in a large contact resistance, thus discounting the efficiency of the charge transport. Furthermore, it is difficult to use these interaction types to provide robust linkages against external perturbations, which is of crucial importance to the ultimate goal of developing molecular electronics.

Conversely, covalent bonding is superior in creating the interfacial linkages in molecular devices, which can provide robustness and reliability. For the charge transport, there is a vast majority of criteria when selecting electrodes and anchoring groups; however, the concern of whether the interfacial linkage is covalent or not is often considered first. The detailed discussions have been provided in Sections 9.2–9.4. It should be noted that the metal-containing covalent bonds could potentially be affected by both the σ and π characters due to the distinct orbital characteristics of the electrode atoms. For example, because Pd and Pt are group 10 elements with significant d-orbital characteristics, π contributions are expected at the contact, especially for –*N*-chloro-succinimide (NCS) headgroups with a strong π character, which may generate an additional channel for electron transport [116, 123].

Although there were a few reports clarifying the insensitivity of the molecular junctions on the interfacial contacts [124, 125], additional studies consistently prove that different interfacial interactions result in different coupling strengths. Figure 9.8 displays the conductance of several single-alkane chains of different lengths and linker groups by plotting log(*G*) versus *L* (molecular length) [126]. A similar slope for each molecular set with distinct anchoring groups could be viewed as a representation that the alignment between the molecular energy levels and the Fermi energy of the electrodes does not change significantly in the case of the alkanes, and that the difference in conductance for different molecular sets is due to the contact resistance resulting from the linker groups. The implication of these results is that the best possible interface for the molecular electronic system should have strong covalent bonding, thus underlining the importance of selecting electrodes and anchoring groups as well as developing interfacial chemistry and characterization methods (such as the inelastic electron tunneling spectroscopic [IETS] [127], as detailed in Section 9.7), especially at the single-molecule level. If the molecules are charged, other potential interactions, such as the rearrangement of electron density, partial charge transfer, and attraction through image forces, could be further involved in the interface

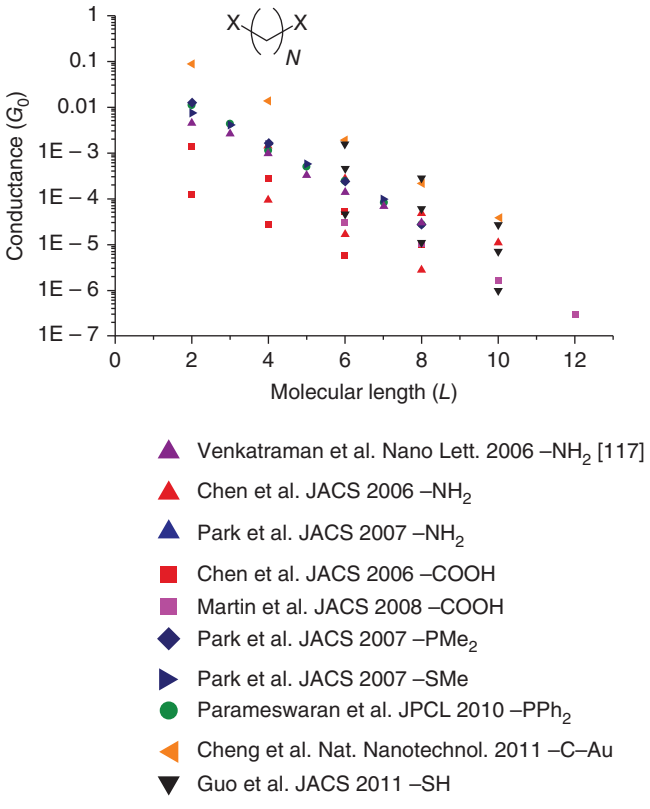

Figure 9.8 Conductance values for alkane chains of several different lengths with different end groups, as indicated in the legend. Although the conductance for each different linker group is different, the β value does not appear to change significantly with the contact resistance. Source: Reprinted with permission from Joshua and Nongjian [126]. Copyright 2014, IOP Publishing Ltd.

formation [113]. Therefore, due to the complexity of the interface formation, it is crucial to determine the exact way in which the interface is formed.

Contact Geometries In certain cases, the same molecular junction can display different conductance values due to the different headgroup–substrate binding geometries, which generally play a significant role in the molecular conductance. Different structures of electrodes at the binding points could result in various contact geometries with different coupling strengths, which are evident in the systems using break junction techniques, such as STM and atomic force microscopy (AFM) [123, 128]. The molecular junctions are formed by pulling the gold atoms out of the electrodes, resulting in the possibility of top and hollow geometries at the two ends of the molecular junctions (Figure 9.9). For the Au–S contacts created using these techniques, when one headgroup is connected to the threefold hollow sites of the substrate and the other is connected to the top sites (denoted top–hollow), a high conductance can be obtained; molecular termini sitting on the two top sites (top–top) result in a low conductance.

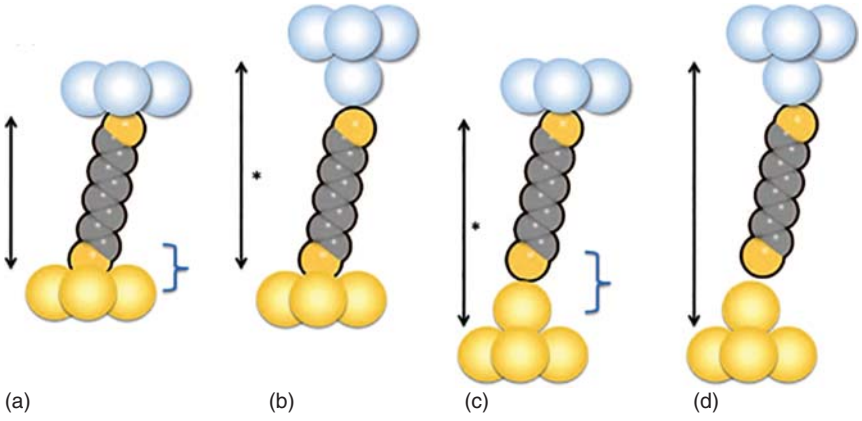

Figure 9.9 Different contact configurations. The distance between the electrodes affects the binding force, and the number of involved electrons for the charge transport can determine the conductance of the metal–molecule–metal system. The double arrows indicate the transport lengths for (a) hollow–hollow (HC), (b/c) hollow–top/top–hollow (MC), and (d) top–top (LC). * refers to hollow-top/top-hollow lengths. Source: Reprinted with permission from Kim and Bechhoefer [128]. Copyright 2013, American Institute of Physics.

Although its existence is relatively rare, the hollow–hollow configuration is the ideal contact geometry.

In addition to the geometry of the contact points, the electrode orientations have a clear effect on the interfacial coupling because different electrode orientations have different band structures. Sen and Kaun obtained the results of high/low conductance values for Au–alkanedithiol–Au single-molecule junctions with two distinct electrode orientations [129]. Based on the theoretical calculations, they attributed the observed binary conductance of the junctions to the distinct electrode orientations and determined that the interfacial coupling is stronger for Au electrodes with the (100) direction than that with the (111) direction. In fact, the contact structures in the single-molecule junctions play a significant role in affecting the conductance, as discovered by Venkataraman and colleagues experimentally and theoretically [130]. A modified conducting AFM was used to simultaneously probe the conductance of a single-molecule junction and the force required to rupture the junction, which accommodated the possibilities of obtaining various molecule–electrode contact structures (Figure 9.10). The experimental data verified that the broadly distributed conductance values resulted from substantial variations in the Au–S linking structure, which was also supported by the density functional theory (DFT) calculation. The fact that the interfacial contact strength could be characterized by the value of the bond rapture force and that the corresponding conductance could be confirmed simultaneously in this study led to obtaining insights into the relationship between the interfacial coupling and the conductance [131]. However, the factors affecting the contact details and the molecular conductance are considerably more complicated than those previously described. Generally, the contact geometry has been accepted as a determining value in the absolute conductance of a molecule, for which any perturbance may change the interfacial

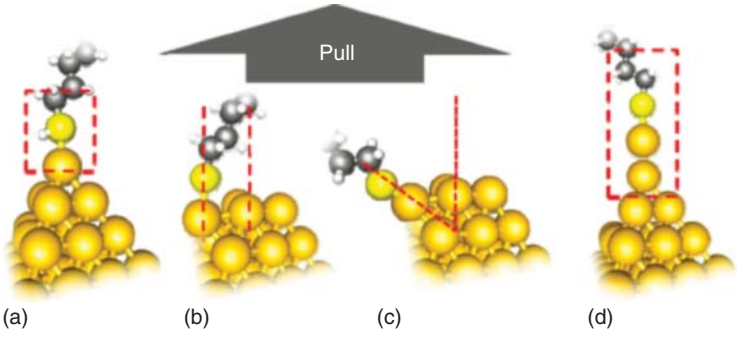

Figure 9.10 Possible Au–S contact structures in AFM-based single-molecule junctions. Scenarios: (a) H atom remains on S; (b) Au atom is not at the apex of the electrode; (c) junction is formed at an angle; and (d) Au atom coordination is different. Source: Reprinted with permission from Frei et al. [130]. Copyright 2012, American Chemical Society.

coupling as well as the contact resistance without a significant change in the orbital alignment [126]. The lack of corresponding methods of characterization and recognition signifies that the ability to understand and control the charge transport precisely is far from realized.

Coupling Strength and Transport Mechanism The coupling strength between the electrons in the molecules and those in the electrodes, which can be physically depicted as an energy barrier between the molecules and the electrodes, is one of the most important properties of the molecule–electrode interface. Based on the results of comparing the strength of the interfacial coupling (Γ) with the addition energy (U), three different coupling regimes are classified: weak coupling ($\Gamma \ll U$), strong coupling ($\Gamma \gg U$), and intermediate coupling, where the addition energy is the difference between the energy needed to take one electron from the HOMO of the system ($U^{N-1} - U^N$) and the energy obtained by injecting one electron to the LUMO of the system ($U^{N+1} - U^N$). Intrinsically, different coupling regimes indicate different degrees of mixing of the wave functions of the molecules and the electronic states of electrodes, thus leading to different transporting mechanisms and electrical conductances [116].

In the weak coupling regime, no charge transfer or an integer charge transfer occurs between the molecules and the electrodes so that the electron transport in this case may be accomplished through a two-step process in which the electrons first hop from one electrode to the molecule, which has matching energy levels at a proper position, and then hop to the other electrode (Figure 9.11a). At low temperatures (LTs), the absence of matching energy levels will lead to the electron transport being blocked unless the bias voltages are high enough to bring the Fermi energy of the electrodes to the molecular energy levels or the external tuning, such as the gate voltage, gives rise to such an energy-level alignment. This phenomenon is also known as the Coulomb blockade, which forms classic Coulomb diamonds in differential conductance maps [63]. In the intermediate coupling regime, due to the partial broadening of the molecular energy levels, the transferred electrons can be affected by the electrons on

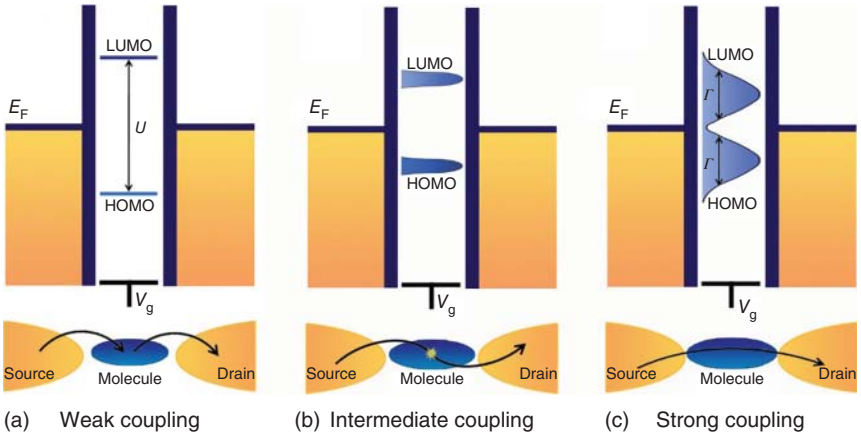

Figure 9.11 Schematic representation of the energy levels and the charger transport processes of the molecular junctions with different coupling strengths between the molecules and the electrodes. (a) In the weak coupling regime, the HOMO and the LUMO of the molecules are well defined, and the electron transport occurs in a two-step process. (b) In the intermediate coupling regime, the HOMO and the LUMO become broader and closer to the Fermi energy of electrodes (E_F), and the electron transport occurs through the molecules interacting with the electrons on the molecules. (c) In the strong coupling regime, a large broadening of the molecular energy levels occurs, and electrons move from the source to the drain through a one-step process. Source: Reprinted with permission from Jia and Guo [116]. Copyright 2013, Royal Society of Chemistry.

the molecules (Figure 9.11b). In the presence of an unpaired electron on the molecules, its spin state can be reversed by electrons passing through the molecules, thus leading to a spin screening that could result in new transport channels. A zero-bias Kondo resonance below a certain temperature is the result of the spin screening. Additionally, a co-tunneling process can occur in this regime, in which one electron tunnels into the LUMO of the molecule with another electron simultaneously tunneling out of the HOMO, thus leaving the molecule in the excited state. In the strong coupling regime, the energy levels of the molecules are considerably broadened for the significant overlapping of the molecule–electrode electronic states as well as the feasibility of the partial charger transfer between the molecules and the electrodes (Figure 9.11c). Therefore, the electrons could efficiently transport from one electrode to another through a one-step coherent process without stopping on the molecules. Based on these general transport mechanisms, it can be predicted that strong interfacial coupling with low contact resistance would facilitate acquiring a high conductance. Therefore, the proper selection of the electrodes and anchoring groups, precise control of the interfacial interactions and contact geometries, and extensive understanding of the corresponding transport mechanisms are necessary for improving the molecular conductance.

9.1.2.2 Energy Level Alignment

Another important factor that significantly affects the molecular conductance is the alignment of the molecular energy levels, especially the HOMO and the

LUMO, relative to the Fermi levels of the electrodes [112]. Generally, when the energy level of the frontier molecular orbitals is sufficiently close to the Fermi level of the electrodes, resonant transport occurs, and the conductance depends only on the contact resistance due to the different coupling strengths, as detailed earlier. Conversely, for the tunneling transport, where the Fermi level of the electrodes lies in the gap between the HOMO and the LUMO of the molecules, the energy level alignment between the Fermi level of the electrodes and the molecular energy level responsible for the charge transport can play a dominant role.

The energy level alignment is primarily determined by the intrinsic properties of the molecule and the electrodes and the molecule–electrode interactions, which are often difficult to determine in both theory and experiment. It is evident that different molecules hold distinct HOMO and LUMO energies, which can be tailored using molecular engineering. For example, Jia et al. intended to modify the diarylethene (DAE) backbones by substituting hydrogenated cyclopentene with rationally designed fluorinated side groups to tune the energy level alignments at the molecule–electrode interface, leading to a decrease in both the HOMO and the LUMO and a reduction in the HOMO–LUMO gap by 0.5 eV at the open state and 0.1 eV at the closed state [132]. For the electrodes, as described elsewhere in this report, various types of materials with identified but distinct work functions can be selected to adjust the interfacial energy level alignment as well as the coupling strength. For example, when Ag, Au, Pd, and Pt are used as the electrodes [133], which have work functions of 4.26, 5.10, 5.12, and 5.65 eV, respectively, the Fermi energy of the electrodes reduces with an increase in the work function. Correspondingly, the energy offsets between the Fermi energy of the electrodes and the HOMO of the molecules decrease for the hole tunneling systems, in which the HOMO dominates the conduction of the molecular junctions, but increase for the LUMO-mediated tunneling systems. Additionally, the different anchoring groups used to create interfacial linkages can adjust the energy levels of the frontier molecular orbitals for the charge transport, which can be exemplified by the Au—N D–A bonds. Specifically, electron-donating amine [134] groups can bring the HOMO of the molecules closer to the Fermi level, thus favoring the hole transport by lifting the frontier orbital energies, while electron-withdrawing pyridine [135] and nitrile (—C≡RN) [136] groups can reduce the energy barrier between the LUMO of the molecules and the Fermi level of the electrodes to promote electron transport by decreasing the frontier orbital energies.

Although there are numerous difficulties in characterizing the alignment between the Fermi level of the electrodes and the molecular energy level related to the charge transport at the single-molecule level, the transition voltage spectroscopy (TVS)-related techniques possess a strong hold on this field. As elaborated in Section 9.7, the TVS exploits the nonlinear current–voltage characteristics of the molecular junctions to investigate the energy offset between the Fermi energy of the electrodes and the closest molecular energy levels. Based on this technique, Guo et al. systematically studied the transport features of single-alkanedithiol junctions to determine whether different binding geometries could cause the differences in the energy barrier of the molecules [137]. Recently, Bruot et al. performed a study on single-molecule junctions

based on benzenedithiol (BDT), in which the anionic state is predicted to possess an HOMO level energy similar to the Fermi energy of the gold electrodes, using the TVS to directly explore the possibility of the conductance increase and the energy offset decrease while weakening the interfacial linkage by straining [138]. For graphene-based single-molecule systems, the TVS was also used by Jia et al. to explain the observation of the photogated transport mechanism transition from direct tunneling to field emission due to the photoinduced conformation transformation [132].

In addition to the interfacial coupling and energy level alignment, the local environment of a molecule can influence its conductance, which has been demonstrated by studies established for obtaining the relationship between the conductance and the external stimuli, such as the solvent, pH, ion, and dopant. In fact, this relationship underlies the operational principle for developing various molecular sensors, as discussed later.

9.1.2.3 Photon-Assisted Conductance Enhancement

To date, there are several recognized mechanisms for photoconductance – a change in the electronic conductance of the molecular junction under illumination [139, 140]. The first mechanism is a photo induced structural change, in which the molecular structure was changed upon light illumination [141–143]. The second one is a result from an inherent asymmetry in the junction, which the open an additional conduction channels under illumination, following resonant optical transitions [144, 145]. The third mechanism is the opening of photo induced conduction sidebands in the single-electron transmission function, so-called adiabatic photo-assisted tunneling or Tien–Gordon mechanism [140, 146]. The fourth one is from the exciton binding in molecular junctions [139]. We will explain it in more detail in the following paragraphs.

Let us address the first mechanism, so-called photoinduced structural change. There are large number of molecules, such as azobenzene (AB) and DAE, whose structure can be changed, and the energy structure will be changed upon the light illumination [147]. Thus, the conductance of molecular junction show switches behavior when it is illuminated by light with different frequency. One of the most challenging issues in fabricating stable and reproducible molecular switches is the lack of control of the properties of the molecule–electrode interface. In the previous report, only one-way optoelectronic switching (from the insulating open form to the conducting closed form, and vice versa) was observed for single DAEs sandwiched between electrodes [132, 148]. This one-way response was attributed to quenching of the excited state in the presence of the gold electrode or the quenching effect resulted from the strong molecule–electrode couplings produced by the covalent amide/sulfur linkages.

To overcome this issue, Jia et al. successfully incorporated three methylene (CH_2) groups into each side of the molecular backbone so as to decrease the effective molecule–electrode coupling, which wondrously led to a reversible photo-switched conductivity, as shown in Figure 9.12 [141]. They have demonstrated a fully reversible, single-molecule electrical switch with amazing levels of accuracy (ON/OFF ratio of ~100), stability (over a year), and reproducibility (more than 100 cycles for photoswitching). The success of building fully

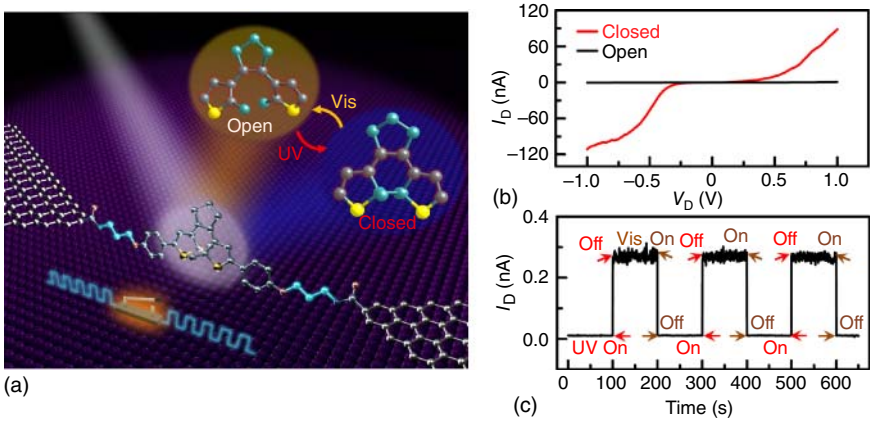

Figure 9.12 Photoinduced structural change. (a) Schematic of a graphene–diarylethene–graphene junction, which highlights the molecular structure. (b) Measurement of the *I–V* curves through a diarylethene molecule that reversibly switches between the closed and open forms, upon exposure to ultraviolet (UV) and visible (Vis) radiation, respectively. (c) Measurement of the current as a function of time when expose to UV and Vis radiation periodically. Source: Reproduced with permission from Jia et al. [141]. Copyright 2016, AAAS.

reversible single-molecule photoelectric switch with large ON/OFF ratio is a crucial step toward the practicable development of photoelectronic devices that uses molecular electronic properties.

Small structural changes in a molecular junction can lead to significant variation in the single-molecule electronic properties, which offers a tremendous opportunity to examine a reaction on the single-molecule level by monitoring the conductance changes. Huang et al. explore the potential of the single-molecule break junction technique in the detection of photo-thermal reaction processes of a photochromic dihydroazulene/vinylheptafulvene system [143]. Employing MCBJ technique, they perform the conductance measurement upon the light illumination and heating. They clearly observed the conductance changes during the molecular photo-thermal reaction process. Statistical analysis of the break junction data provides an approach for probing the reaction kinetics and reversibility, including the occurrence of isomerization during the reaction. Their study opens a window to using nanostructured environments, e.g. molecular junctions, to tailor product ratios in chemical reactions.

The third mechanism is the so-called photon-assisted tunneling mechanism [140, 149]. Surface plasmon polaritons can be excited by photons if the momentum matching condition is satisfied. Vadai et al. design a new platform to investigate the photon assisted tunneling mechanism in which the surface plasmons can be excited [140]. As shown by Figure 9.13a, the break junction consists of two 40 nm thick gold electrodes evaporated glass slides with an initial gap ~500 nm between two slides. The gap can be mechanically controlled with high accuracy by bending or relax the top slide. Because the squeezable break junction (SBJ) is based on two Au-covered glass slides, measurements of single-atom contacts are made possible due to sufficient roughness of the Au surfaces. Also, this roughness

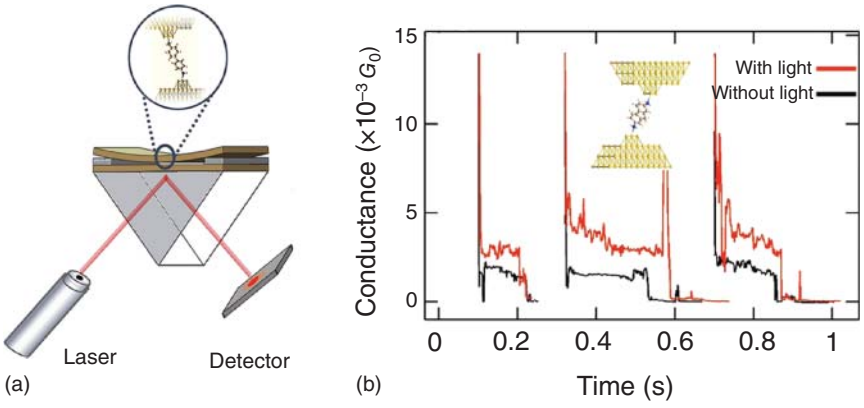

Figure 9.13 A squeezable molecule break junction setup for single-molecule conductance measurements. (a) Schematics of the experimental approach. Free photons and surface plasmons are coupled and confined within the gap employing a prism upon laser illumination. (b) Representative conductance traces recorded during the separation process without (black) and with (red) laser illumination. Source: Reproduced with permission from Vadai et al. [140]. Copyright 2013, American Chemical Society.

is essential for plasmon creation within the gap. Creation of plasmons within the gap is achieved by attaching a glass prism to the bottom slide. Plasmon resonance conditions are found by varying the θ of the incident laser (the angle of p-polarized incident light with respect to the surface normal) by monitoring the intensity of the reflected light. When the maximum plasmon coupling is evidenced, a sharp drop in the reflectivity will be observed. The typical conductance traces is presented in Figure 9.13b. It can be found that the conductance of single molecule upon light illumination is higher than the one in dark.

The authors rule out the possibility that the enhanced conductance is due to photon absorption by the molecules within the junctions based on the fact that the HOMO–LUMO energy gap of the measured molecule (>3 eV) is larger than the energy of the created plasmons (1.59 eV). They point out that plasmonic oscillating field on the conductance of the junctions can be analyzed using the Tien–Gordon model, that is, by considering a time-dependent modulation of the electronic energies [145]. In the Tien–Gordon model, the plasmon field is treated as a potential, V_ω, across the nanoscale gap, which oscillates at the plasmon frequency ω. An electron tunneling through the junction with initial energy E can either absorb or emit n photons with energy $\hbar\omega$ and hence finish the tunneling process at energy $E \pm \hbar\omega$. As a result, the transmission probability of an electron across a junction that strongly depends on the electron energy can be changed, and thus overall DC conductance of a junction can be changed. In other words, V_ω acts like a gate that shifts transmission probability of an electron across a junction.

Finally, let us discuss the fourth kind of mechanism, so-called photoconductance from exciton binding in molecular junctions. Zhou et al. reported a theoretical analysis and experimental verification of this mechanism for photoconductance, in which the change in conductance upon illumination was

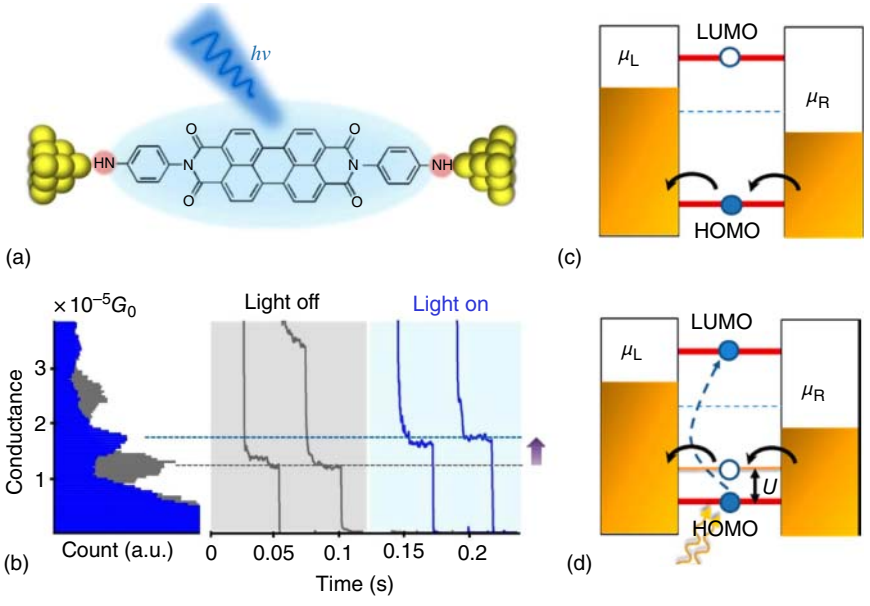

Figure 9.14 Mechanism for the enhanced conductance upon light illumination. (a) Schematic illustration of the measurement strategy, a NH_2–PTCDI–NH_2 molecule bridged two electrodes employing STM setup and illuminated with laser light. (b) Conductance histograms in the dark (gray) and under illumination (blue) generated from more than 1000 curves. The left figure presents several typical conductance traces used to generate the histograms. (c) The current is dominated by hole-transport through the HOMO in dark. (d) Under illumination, the electron is excited to LUMO and thus the LUMO becomes partially filled. Consequently, a hole entering the HOMO is attracted to it, resulting in an effective shift of the HOMO level toward the Fermi level and an increasing in conductance. Source: Reproduced with permission from Zhou et al. [139]. Copyright 2018, American Chemical Society.

attributed to the Coulomb interaction between the electrons and holes in the molecular bridge [139]. They use NH_2–PTCDI–NH_2 molecule, which is perfectly symmetric and without any structural changes upon light illuminations. The experiments were performed on STM-BJs with perylene tetracarboxylic diimide (PTCDI) molecules attached to gold electrode via Au–amine bonds, as shown by Figure 9.14a. They used a monochromator to apply photon emissions with fixed wavelength ~495 nm (corresponding to energy of 2.5 eV, in resonance with PTCDI's HOMO–LUMO gap). The photon illuminates the molecular junction in toluene solution through an ultrathin (~600 μm in diameter) fiber optical cable. The conductance traces recorded in the electrode separation process was shown in Figure 9.14b. It can be found that the plateau of gray curves (measured in dark) is low than the one of blue curves (measured under illumination). The conductance histogram generated from more than 1000 conductance traces is shown in Figure 9.14c, demonstrating a clear photocurrent effect, i.e. the conductances peak in the dark are centered around $G_{dark} \approx 1.25 \times 10^{-5}\ G_0$, while the conductances under illumination are centered around $G_{light} \approx 1.75 \times 10^{-5}\ G_0$, which is higher than the one in dark.

Since the molecule is perfect symmetric and without any structural changes upon light illuminations, they put forward a new mechanism to explain the observation. Consider the simplest model for transport through a molecular junction, namely, the HOMO and LUMO coupled to gold electrodes, as shown in Figure 9.14c, d. They assume that the electrodes' Fermi level is closer to the HOMO than the LUMO, in which case the conductance is dominated by tunneling of holes through the HOMO. In the dark, the conductance exponentially depends on the energy gap between the HOMO and the electrodes' Fermi level. Under illumination (the frequency of light is close to resonance with the HOMO–LUMO gap), electrons have the high possibility to be excited from the HOMO to the LUMO. A hole that tunnels from the electrode to the HOMO now feels the charge in the LUMO and is attracted to it due to the Coulomb interaction. As a result, the HOMO energy is pushed toward the Fermi level, which reduces the tunneling barrier, resulting in an increase in conductance.

9.1.2.4 Molecular Conductance Measurements

The research on molecular conductance and its measurements was initiated from bulk electrode approaches, in which mono- or multilayer molecular films prepared either by self-assembly or Langmuir–Blodgett (LB) methods were sandwiched between two bulk and flat electrodes [112]. Due to the introduction of several novel micro-/nano-systems created using the crude-tip AFM [150, 151], crossbar techniques [152–154] or nanopore fabrication [155], the area of the molecular films decreased, and the conductance measurement was closer to the molecular level. Clearly, it is difficult to accurately determine the number of molecules successfully connecting both electrodes, thus making the averaging calculation impossible. In fact, even if the averaging process is possible, the calculated value cannot exactly represent single-molecule conductance because there is no way to ensure each connection possesses identical types and geometries, both of which have a significant effect on the single-molecule conductance. Furthermore, the conformational changes in the molecules could be suppressed by the interaction with neighboring molecules in a closely packed film, which may affect their electron-transport properties [44].

To determine the conductance of a molecule, it must be first brought into contact with at least two external electrodes. The contact must be robust, reproducible, and able to provide sufficient electronic coupling between the molecule and the electrodes, which is one of the most significant aspects needed to reduce the discrepancies between the groups measuring the same molecules. In fact, the development of various methods to control, tailor, and characterize the interfacial interactions as well as the contact details leads to realizing this goal. Additionally, the electronic signature indicating the current not only through molecules but also through one molecule between a pair of electrodes should be identified, which was challenging before the introduction of techniques using nanoscale moveable electrodes that could be mechanically controlled with sub-ångström precision. Furthermore, the capability of efficiently measuring thousands of individual junctions accommodates the feasibility for establishing statistical investigations, which can provide the most likely conductance of a single-molecule junction by analyzing the resulting current versus distance traces

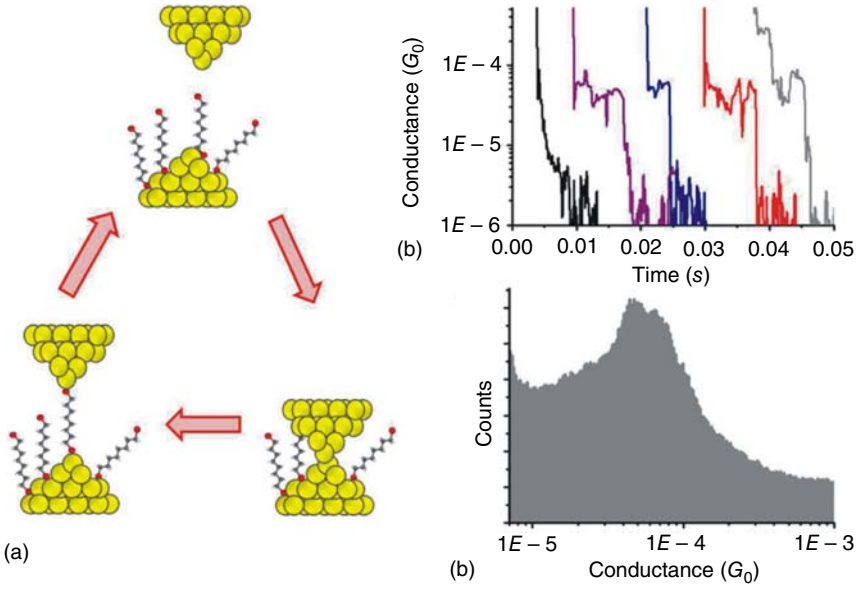

Figure 9.15 Break junction-based measurements for obtaining single-molecule conductance values. (a) Schematic depiction of break junction system used for measuring conductance. The distance between the two electrodes is cycled repeatedly while a bias is applied between them and the measured current. (b) Several sample conductance versus time traces used to construct a conductance histogram. (c) Conductance histogram with a peak at the most probable conductance value for a single-molecule junction. Source: Reprinted with permission from Joshua and Nongjian [126]. Copyright 2014, IOP Publishing Ltd.

(Figure 9.15). In Sections 9.2–9.4, we comprehensively reviewed state-of-art methodologies to obtain the measurements of single-molecule conductance. Among these approaches, the AFM and STM-BJ techniques are primarily known for the advantages listed earlier.

In this section, we systematically reviewed various types of molecular candidates to be potentially used as conductive wires. The combination of enriched molecular scaffolds with ever-improving molecular engineering offers the possibility of creating novel molecular wires with superior conductance. Additionally, the interfacial issues between the molecules and the electrodes, including interaction types, contact geometries, and energy level alignments, have a significant impact on the conductance of molecular junctions. Therefore, beyond the development of synthesizing wire-type molecules, the exploration of efficient methods to accurately tailor the interfacial properties is of the same significance. In fact, controllability on the electrode–molecule interface is not just needed in the molecular wires but also necessary for realizing other functionalities in molecular electronics. Due to the maturity of the molecular conductance measurements, in the following Section 9.2, we summarize the primary contributions and new concepts of integrating molecular functionalities into electrical circuits toward practical applications using the holistic consideration of device fabrication and measurements, including the testbed architectures, molecule number and defect density, and nature of the molecule–electrode interface.

9.2 Rectification Toward Diodes

The diode or rectifier, which facilitates the current flow in one (forward) bias direction and suppresses under the opposite (reverse) direction, is an important two-terminal electronic component. Conventionally, rectifiers can be integrated as p–n junctions by two types of materials with different electronic states using crystal doping, one of the most mature semiconductor techniques in the silicon industry [156]. Briefly, a crystal of group IV, such as Ge or Si, can be doped with dilute concentrations of interstitial or substitutional electron-rich elements (group V, such as N, P, and As) to achieve an "n-doped" material whereas a "p-doped" crystal can be formed by doping with group III elements (such as Al, Ga, and In). Benefitting from the development of the semiconductor industry, diodes, similar to any other digital and computational electronic components, evolve extremely but experience the same problems in the size miniaturization and performance enhancement processes. The idea of using single molecules to fabricate a new generation of rectifiers was proposed theoretically by Aviram and Ratner [157] and received significant attention since the 1970s. In this initial prototype, an organic molecule containing an electron-donating moiety (donor) and an electron-withdrawing moiety (acceptor) bridged by the σ linkage that serves as an insulating barrier for electrically separating the two segments was proposed. After bridging a pair of electrodes to construct a D–σ–A junction, it would be ideal to energetically use a simple acceptor-to-donor electron transfer for the current rectification. Similar to the conventional rectifying systems, "D" corresponds to "n" and "A" corresponds to "p," as indicated in Figure 9.16 [158]. Single-molecule diodes are of crucial importance because, for example, they enable the electrical addressing of an individual molecular node in an ultimately scaled crossbar-type architecture, where the node consists of an ensemble or of a single functional molecule with both current-rectifying and switching/storing moieties [159].

The past 40 years have witnessed a tremendous improvement in molecular electronics in both experimental and theoretical aspects, which includes progress in

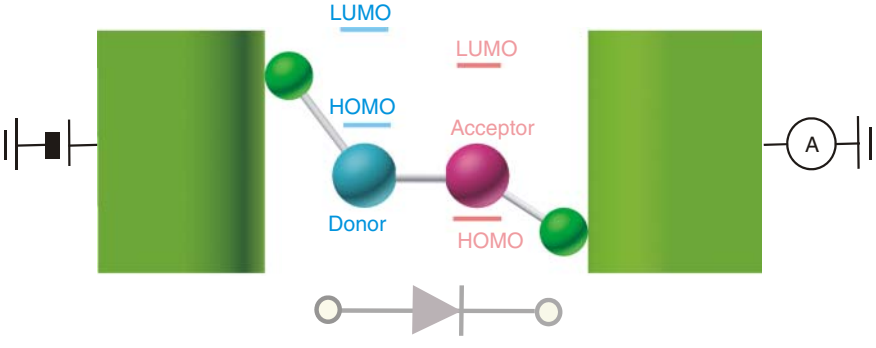

Figure 9.16 Schematic description of rectifiers based on single molecules and corresponding simplified potential profile for rectifying mechanisms. Source: Reprinted with permission from Tsutsui and Taniguchi [158]. Copyright 2012, MDPI Switzerland.

the development of molecular rectifiers. In fact, in addition to the Aviram–Ratner (AR) model, several other models have been proposed [159] that not only enrich the explanation for molecular rectification but also incite several ideas for the design and preparation of novel molecular diodes. In this section, we review the studies on different types of diodes using a single molecule as a core component starting with three fundamental mechanisms responsible for molecular rectification behaviors. It should be noted that the major realization of the current single-molecule rectification still depends on monolayer-based techniques that are beyond the scope of this review. However, to present a thorough development of the molecular rectifiers, we provide a succinct but systematic introduction to these contributions. For additional detail, interested readers are recommended to reference other studies [156, 160–162].

9.2.1 General Mechanisms for Molecular Rectification

As mentioned earlier, the D region (electron-rich) of the molecular rectifiers resembles the n-doped region of the inorganic counterparts, and the A region (electron-poor) resembles the p region. However, the underlying mechanisms related to rectification for the two types of diodes are reversed. For example, in the case of the D–σ–A molecular rectifiers, the preferred direction of electron flow under a forward bias is from the metal electrode to A to D to the other metal electrode, whereas in a p–n junction rectifier, the preferred direction is from n to p. Furthermore, due to the complexity arising from the significant influence of the electrode–molecule interface on the charge transport, the explanation used for understanding the conventional p–n junction diodes is insufficient for the molecular diodes. Based on the theological development as well as the experimental discovery, three mechanisms, i.e. the AR model, Kornilovitch–Bratkovsky–Williams [163] (KBW) model, and Datta–Paulsson [164] (DP) model, were proposed to explain the rectification behaviors based on single molecules [159], which are described schematically in Figure 9.17.

9.2.1.1 Aviram–Ratner Model

In the millstone-like study contributed by Aviram and Ratner, the molecule with an electron-poor moiety of tetracyanoquinodimethane (TCNQ) and an electron-rich moiety of tetrathiofulvalene (TTF) linked by a covalent triple-methylene bond was assumed to be attached to a pair of electrodes (Figure 9.18a), thus creating a molecular diode in which the molecule functionalizes as a core component for electrical current rectification. Afterwards, the specific molecule was generalized as a D–σ–A model consisting of a donor region, insulator region, and acceptor region. In fact, the corresponding mechanism underlying this proposal was the earliest approach that acquired wide agreement. In the AR model, the two electrodes are connected through three tunneling barriers, linking one electrode to the acceptor unit, the acceptor unit to the donor unit, and the donor unit to the other electrode. At a zero applied voltage bias, the HOMO of the donor is slightly below the electrode's Fermi energy and the LUMO of the acceptor is slightly above, whereas upon application of a voltage bias across the junction, the LUMO (or the HOMO)

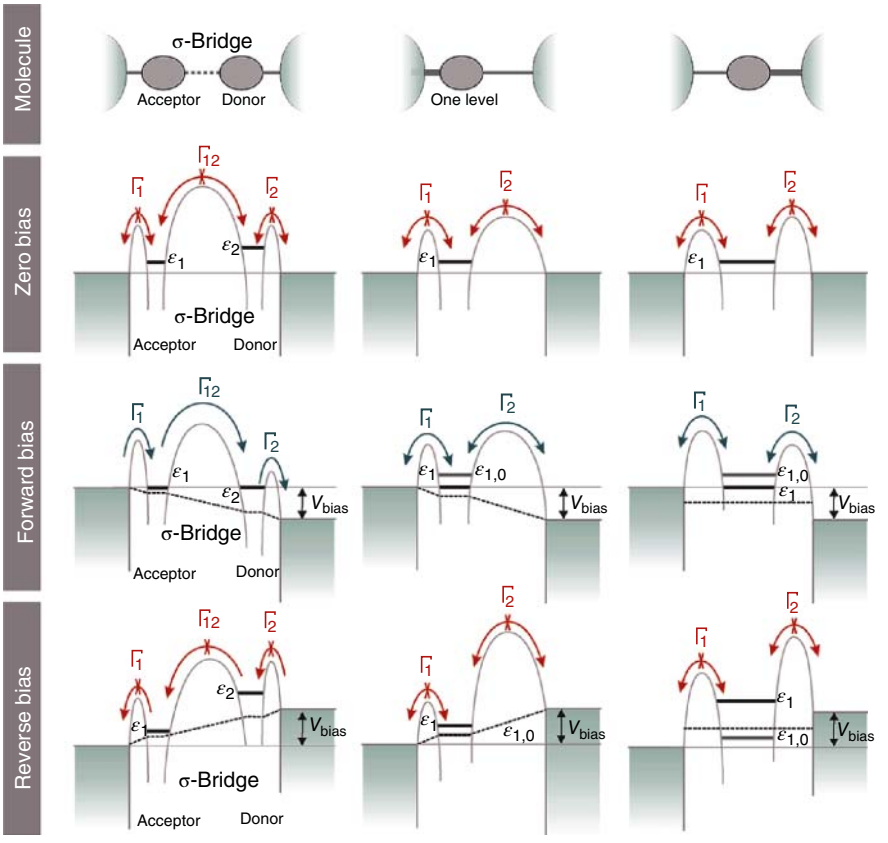

Figure 9.17 Comparison of three models for molecular diodes (Γ_i represents the rates of tunneling steps). (a) Aviram–Ratner proposal with molecule levels shifting through the applied electric field. The subtle energy-level alignment for the donor and acceptor moieties, in combination with the large electrical spacer separating the two moieties, eventually leads to a difference in the current onset. (b) Simplified model, as proposed by Kornilovitch, Bratkovsky, and Williams (KBW), with one level. The level is shifted with respect to the applied electric field. (c) Considering the charging of the energy levels (proposed by Datta and Paulsson) can lead to diode behavior, even without level shifting by an electric field. Source: Reprinted with permission from Lortscher et al. [159]. Copyright 2012, American Chemical Society.

can be aligned to the Fermi energy of the leads or separated depending on the bias direction. Thus, the rectification behavior that was expected to occur due to the different thresholds at the positive and negative bias voltages and shifts of the energy levels of the molecular orbitals according to their energetic positions in the gap was dominated by the electric field between the electrodes, which is depicted schematically in Figure 9.17a. The two separate energy levels, ε_1 and ε_2 (with respect to the Fermi energy of the electrodes, E_F), which belong to the donor and acceptor, respectively, respond differently to the electric field between the electrodes upon application of a bias voltage, thus leading to the energy-level alignment or misalignment responsible for the asymmetric charge transport.

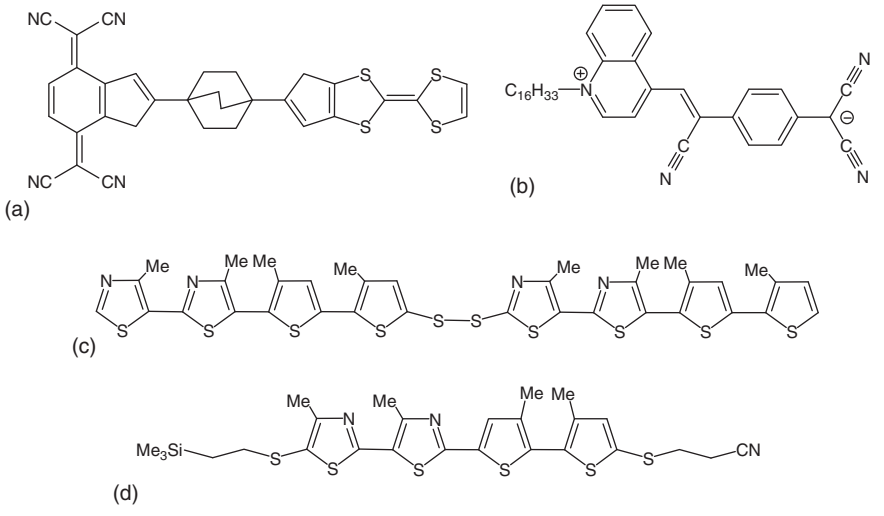

Figure 9.18 Molecular structures proposed for current rectification. (a) Initial model D–σ–A proposed by Aviram and Ratner. (b) D–π–A molecules used for rectification based on the Langmuir–Blodgett monolayer. (c) Conjugated diblock oligomers used for rectification through the formation of the SAMs. (d) p–n Junction types of molecules used for rectification through the directed formation of SAMs with a specific orientation. Source: Reprinted with permission from Metzger [160]. Copyright 2003, American Chemical Society.

In summary, the rectification of an AR diode could be viewed as a different onset of resonant tunneling for the two bias directions [159].

9.2.1.2 Kornilovitch–Bratkovsky–Williams Model

Later, Kornilovitch et al. generalized the AR mechanism to a simpler system (referred to as the KBW model) with only one molecular orbital, in which asymmetric tunneling barriers led to the current rectification (Figure 9.17b) [163]. Specifically, in this approach, the position of the orbital is not located symmetrically between the electrodes but is closer to one of them due to the terminated tails with different lengths. Because most of the applied voltage drops on the longer insulating barrier, the conditions required for resonant tunneling through the level are achieved at different voltages for the two opposite polarities. In fact, the molecular orbital can be aligned or separated with the Fermi energy of the electrodes depending on the bias direction, which will result in the rectification behavior. In a similar study, Mahmoud and Lugli noted that the rectification of a molecular device could be controlled by inserting a resistive molecular path near the metallic electrodes, thus enforcing the potential drop profile along the molecule through calculations [165]. More importantly, the KBW model led to enhancing the development of molecular diodes with ease because molecules with different-length tails providing tunneling barriers were more accessible than complex structures needed in the AR model. Furthermore, by changing the lengths of these insulating tails, the rectification ratio can be systematically changed.

9.2.1.3 Datta–Paulsson Model

For spatially symmetric molecules, the current rectification could be also achieved through unequal coupling with the electrodes at the two ends, which was reported by Datta and colleagues based on experimental and theoretical studies [164]. In the charge transport measurements of these molecules (Figure 9.17c), the $I-V$ curves were initially symmetric but picked up a weak and reversible asymmetry as the contacts were manipulated. Specifically, for resonant conduction, this asymmetry is indicated by conductance peaks of different heights occurring at symmetrically disposed voltage values. Clearly, the conduction in these molecules at opposite voltages occurs essentially through the same molecular levels with similar wave functions, which is different from the two previous models mentioned earlier. The authors verified that the origin of the observed contact-induced asymmetry was non-trivial and involved self-consistent shifts in the energy levels due to the charging effects that typically exist in single-molecular devices with tunneling barriers to the electrodes. The asymmetric charging energies will lead to different tunneling rates between the orbital and the two electrodes, which imply that the average population of the orbital with electrons depends on the bias direction in the resonant tunneling condition, thus realizing the rectification. Although this mechanism cannot be easily separated from the asymmetric coupling to the electric field described previously, it can be considered as a distinct mechanism of the rectification. In principle, molecules can be designed that allow for better coupling to either of the electrodes while maintaining the position of the resonant orbital in the center.

It should be noted that for experimental verification, it is difficult to distinguish between the three previously discussed mechanisms for several reasons. (i) A pure AR diode is difficult to chemically synthesize, and a complete decoupling of the donor and acceptor orbitals is not always guaranteed [166]. (ii) Experimental transport measurements suffer from uncontrolled coupling between the electrodes and the terminated groups of molecules for various interfacial interactions and random contact geometries previously detailed [167]. Recently, Zhang et al. [168] conducted a study to identify whether molecular rectification is caused by asymmetric electrode couplings or a molecular bias drop. The result is that the bias drop is responsible for rectification, whereas the asymmetric couplings do not directly lead to rectification indicates a discrepancy with other results, which demonstrates the complexity of differentiating specific mechanisms. In fact, in most of the studies experimentally pursuing molecular diode prototypes, the phenomenon of rectification is always a combined effect of different mechanisms. Molecular rectifiers based on pure operating principles are relatively rare [161].

9.2.2 Rectification Stemming from Molecules

9.2.2.1 D–σ–A and D–π–A System

Encouraged by the visionary AR proposal, several groups pursued building diodes with single molecules. Due to the limitations of current organic synthesis methodologies and the capability of tuning inter-/intramolecular energy-level alignment with controllability, a standard diode using single molecules with

D–σ–A architecture has not been reported. However, in certain efforts based on multi-/monolayer LB films or block copolymers [169], the D–σ–A model was demonstrated to be successful and thoroughly confirmed [170–175]. Furthermore, considerable attention has been given to molecules with D–π–A structures because of their synthetic feasibility to rectify the electrical current at the molecule-film level [173, 176, 177]. For the rectifying process using this type of molecule, there are a few ambiguous issues related to the rectification mechanism. For example, it should be considered whether the ground state is exactly $D^{+1.0}$–π–$A^{-1.0}$ and the excited-state $D^{0.0}$–π–$A^{0.0}$ or whether their corresponding intermediate ionicities are $D^{+\rho}$–π–$A^{-\rho}$ ($\rho \geq 0.8$ for the ground state and $\rho \leq 0.2$ for the excited state) [178]. However, the D–π–A model, which is the derivative of the D–σ–A model, promotes the development of the molecular rectifiers and increases the access for realizing actual single-molecule diodes.

Several exceptional studies based on the SAM system have been reported to realize single-molecule rectifiers. In 1997, Metzger et al. demonstrated a unimolecular rectification behavior with a rectification ratio (defined as the ratio of the highest conductance at the forward bias and that at the reverse bias) of up to ~13 using an LB monolayer of zwitterionic hexadecylquinolinium tricyanoquinodimethanide ($C_{16}H_{33}Q$–3CNQ) molecules sandwiched between two Au electrodes (Figure 9.18b) [160, 161]. By probing the SAMs with the STM techniques [179, 180], Ng et al. and Jiang et al. achieved molecular rectifiers based on diblock molecules at the single-molecule level with a rectification of ~7 (Figure 9.18c). It is evident that the orientation of molecules in the junction will have a significant impact on the direction of rectifying regardless of being in the SAM system or in the single-molecule system, which has been well described elsewhere [181]. Therefore, the controllability of the molecular orientation is of tremendous significance, which has been fundamentally acquired through a rational utilization of chemical reactions. The molecules terminated with a thiol at each end, both of which are protected with different groups, could be localized in a direct manner by removing the protection groups sequentially, which has been used successfully in both the SAM [180, 182] and single-molecule [183] systems (Figure 9.18d).

9.2.2.2 D–A Diblock Molecular System

The lack of synthetic methods and controllability for the energy-level alignment in the D–σ–A structures and the inferior performance of the rectifiers based on D–π–A molecules drive the focus back to the semiconductor counterparts for a breakthrough in single-molecule diodes. In this context, p–n junction molecules (known as diblock molecules) containing donor and acceptor moieties, which connect to each other through direct C—C covalent bonds rather than a σ- or π-bridge, were prepared by taking advantage of the mature polysynthetic method. Specifically, in 2002, Ng and Yu [169] first synthesized a regioregular, head-to-tail coupled diblock co-oligomer comprising an electron-rich oligo(3-alkylthiophene) as the donor block and an electron-poor oligo(4-alkylthiazole) as the acceptor block and demonstrated its rectification effect using the STM technique. The synthetic approach was generally used for coupling heterocycles and thus promised sizeable access for the introduction

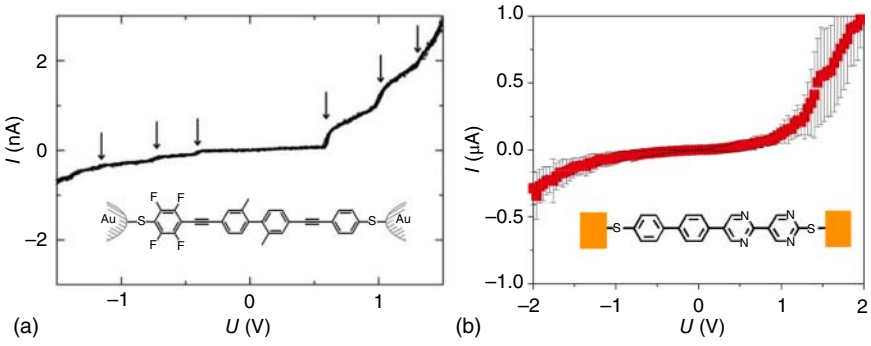

Figure 9.19 *I–V* characteristics of rectifiers based on single-diblock molecules. (a) Rectification of phenyl–ethynyl–phenyl molecules immobilized between two Au electrodes in an MCBJ setup. The arrows point to step-like features of the *I–V* curves. Source: (a) Reprinted with permission from Elbing et al. [184]. Copyright 2005, American National Academy of Sciences. (b) Rectification of the dipyrimidinyldiphenyl molecules integrated in an STM setup at $T = 30$ K. Source: (b) Reprinted with permission from Díez-Pérez et al. [183]. Copyright 2009, Springer Nature.

of other p–n junction diblock molecules, which has been recognized as the primary impetus for the progress in this field.

For example, in 2005, Elbing et al. [184] designed and synthesized a series of D–A diblock molecules and integrated them into electrical nanocircuits using the MCBJ technique to study their rectification behaviors (Figure 9.19a). These molecules consisted of two phenyl–ethynyl–phenyl π-systems, which were fused by a biphenylic C—C bond. To achieve electronic asymmetry, the parent unit of one segment was functionalized with four electron-deficient fluorine atoms, while that of the other was kept pristine at hydrogen-substituted. Furthermore, the steric repulsion of two methyl groups in an ortho position to the biphenylic C–C link induces a torsion angle between the segments, reducing the overlap of their π-orbitals and hence their electronic coupling. Combined with rigorous and systematic control experiments, the single-molecule rectification was confirmed with a current ratio of $1 : 4.5 \pm 1.5$ V, which is explained qualitatively in the following text. The structurally asymmetric molecule could be viewed as two quantum dots coupled in series, termed F-dot (fluorized) and H-dot (not fluorized), for which the electronic orbitals were localized to avoid overlapping. When sweeping the bias voltage, the electronic levels of both dots are shifted with respect to one another, and at certain voltages, the two levels will cross. When an unoccupied level passes an occupied one, an additional transport channel opens for inelastic transmission from the H-dot into the F-dot. For each additional transport channel, the current grows by a certain amount, implying a stepwise increase in the $I–V$ curves (or peaks in the differential conductance ($\mathrm{d}I/\mathrm{d}V$)).

In 2009, Tao and colleagues [183] used STM-BJs to probe a structurally similar but parent-unit-distinct molecule with specific bound orientation using selective deprotection strategy for its diode-like property. These non-symmetric diblock dipyrimidinyldiphenyl molecules exhibited a pronounced rectification behavior (rectifying ratio of 5) compared with its homologous symmetric block, with

current flowing from the dipyrimidinyl to the diphenyl moieties (Figure 9.19b). In a further study, the same group utilized the same system as well as the same molecules along with an IETS analysis to explore the mechanism responsible for the rectification behavior at cryogenic temperatures [185]. The results of the rectification onset beginning near the zero bias and clear asymmetric currents at biases below 200 mV demonstrated that the transport mechanism was dominated by tunneling. More importantly, this study demonstrated that the bias-dependent asymmetry in the electronic coupling was important for both the elastic and inelastic processes in the diblock diode molecule. This result was deduced from the fact that the IETS, with similar phonon energies and intensities, were anti-symmetric in the forward and reverse bias directions, despite the asymmetry in the $I–V$ and $G–V$ characteristics at low biases. For further exploration of the mechanism for rectification based on the diblock dipyrimidinyldiphenyl molecule, Lörtscher et al. [159] used the MCBJ technique to study its charge transport in the low-bias regime and as a function of bias at different temperatures, where the $I–V$ characteristics could be semi-empirically explained by the combination of the KBW and DP models, which indicates that the rectification originates from an asymmetric Coulomb blockade (charging effect) in combination with an electric-field-induced level shift.

It should be noted that the electronic decoupling between the donor unit and the acceptor unit is necessary for the rectification in these types of D–A diblock molecules, which could be achieved by controlling the torsion of one segment of the molecule relative to another. In fact, in one recent study established by Cui et al. [186], further insight was obtained into the correlation between the rectification effect (the ratio) and the degree of molecular twist based on the DFT combined with the non-equilibrium Green's function (NEGF) method (Figure 9.20a). The authors claimed that the rectification could be enhanced by the geometrical torsion-induced reduction in the conjugation length of the organic molecules. Furthermore, this significance of reducing the overlap between the orbitals of part D and part A was stressed experimentally by Luo et al. [188], who developed a series of long D–A diblock molecular wires with lengths ranging from 3 to 10 nm and studied their charge transport using the CP-AFM technique in the hopping regime. It was determined that when an insulating cyclohexane bridge was inserted between the 4,4′(5′)-diformyltetrathiafulvalene electron donors (D) and the *N*,*N*′-di(4-anilino)-1,2,4,5-benzenebis(dicarboximide) electron acceptors (A), an electrical rectification was achieved with ratios as high as 30 ± 1.0 V, whereas the absence of an insulating bridge led to current flow without rectification due to a large degree of conjugation in the D and A regions. When considering the initial D–σ–A model, both the intramolecular twist and the insulating barrier insertion have the function of reducing the electronic coupling between the donor part and the acceptor part, which is essential for the design of molecular diodes.

In addition to considering various methods to decouple the electronic overlap between the two distinct parts of the D–A molecules, the proportion effect on the rectification in diblock co-oligomer diodes also played an important role, which was recently proven by Hu et al. using theoretical calculations

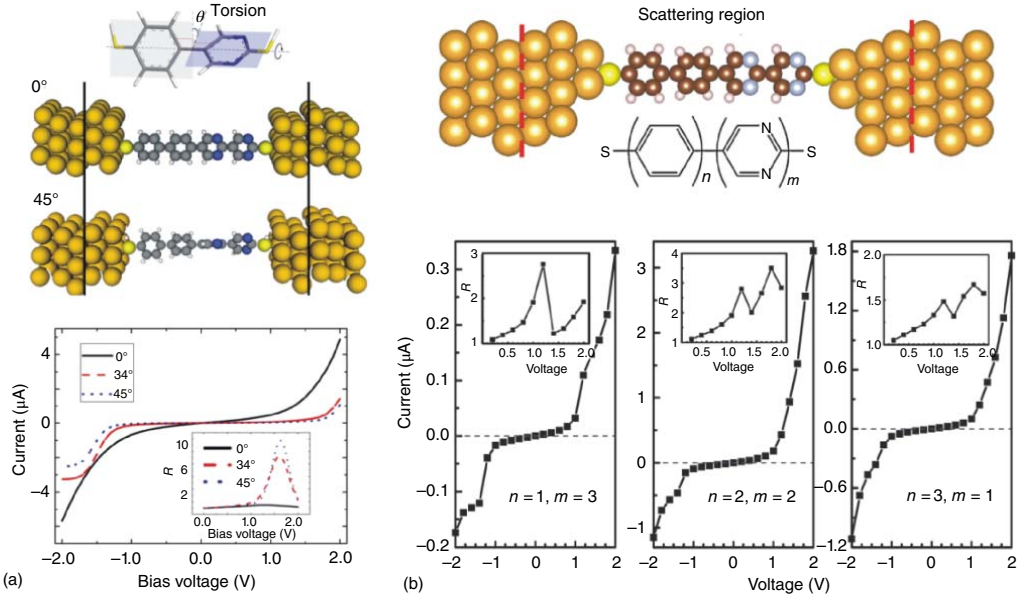

Figure 9.20 Torsion/proportion dependence of the rectification effect. (a) The influence of torsion between the donor part (phenyl segment) and the acceptor part (pyrimidinyl part) on the rectification. The corresponding rectification ratios are depicted in the inset. Source: (a) Reprinted with permission from Cui et al. [186]. Copyright 2014, AIP Publishing. (b) The influence of proportion of the donor part (phenyl segment) and the acceptor part (pyrimidinyl part) on the rectification. Source: (b) Reprinted with permission from Hu et al. [187]. Copyright 2014, Elsevier.

(Figure 9.20b) [187]. For rectifiers based on pyrimidinyl–phenyl diblock co-oligomers, it was determined that the 1 : 1 proportion of the two moieties favored a large rectification ratio for a short co-oligomer diode. However, for a long co-oligomer diode, the optimal proportion for the largest rectification ratio was not 1 : 1; however, an interesting proportion-dependent variation of the rectifying direction was observed. Furthermore, the perturbation from the external environment could impose an interference on the rectification behavior, as noted by Zhang et al. in the study where the protonation effects on the electron transport were investigated using a conjugated dipyrimidinyl–diphenyl diblock oligomer diode [189]. Their calculation indicated that the protonation in the outer pyrimidinyl was favorable for enhancing the rectification ratio, whereas the protonation in the inner pyrimidinyl played a dominative role in inverting the rectifying direction, which is the first time the experimental findings of the diblock molecular diodes have been clearly explained in the case of protonation in 2005 [182].

9.2.3 Rectification Stemming from Different Interfacial Coupling

The presence of the donor and the acceptor groups introduces non-symmetry into the molecular junctions. Generally, one may expect rectification to occur from non-symmetric molecular junctions that do not necessarily contain a pair of donor and acceptor groups or symmetric systems but have an unequal physical process in the forward and reverse bias. In fact, different couplings between the electrodes and the molecules on the two ends could lead to rectification, which has been predicted by the DP model. This prediction becomes common in nearly all of the single-molecule systems based on the published data. Although this rectification is not sufficient to achieve a larger diode effect if the bias voltage drop at the molecule–electrode interfaces cannot be controlled with subtlety, it still leads to new ideas for the design and implementation of molecular diodes. In Section 9.1.2, we discussed the factors that influence the interfacial coupling, which coincidentally frames the outline of this section. In fact, a pair of different electrodes with distinct work functions, molecules with asymmetric terminated moieties, or both, which could lead to unequal interfacial coupling, were used to construct molecular diodes, among which several studies, were based on monolayers or films instead of single-molecule junctions.

9.2.3.1 Different Electrodes

In the early 1990s, Ashwell et al. [170, 190–192] developed suitable techniques for sandwiching LB multilayers or monolayers between two electrodes of different work functions to study molecular rectification. Generally, metals with different work functions provide different charge injection barriers, which may result in molecular rectification. For example, for HOMO-dominated molecules, i.e. molecules whose HOMO is closer to the Fermi level than that of the LUMO, metals with a high work function provide a lower charge (hole) injection barrier compared with metals with a low work function. Although molecules of interest in these asymmetric systems contain both donor and acceptor parts, the presence of a high-work function noble metal (Ag or Pt) on one side and

a low-work function metal (Mg) on the other side lays the foundation for the molecular diodes. In these studies, metal electrodes, especially noble ones, such as Au, Pt, or Ag, possess an approximately constant density of electronic states within a narrow energy window relevant to the charge transport, which results in molecular junctions with relatively smooth and featureless transmission probabilities near the Fermi energy, thus limiting their applications including rectification. Fortunately, based on the developments in material science as well as nanofabrication technology, various types of electrodes are being introduced into molecular electronics. Vuillaume and colleagues demonstrated a molecular rectifying junction constructed from a sequential self-assembly on silicon using Al on the other side of the electrode, which widened the selection of electrodes for molecular rectification [193]. Recently, Kim et al. introduced a hybrid device structure with a molecule trapped across a gold/graphite gap in the STM-BJ system (Figure 3.11) [194]. Based on this system, the charge transport characteristics of oligophenylamines were investigated, where the authors discovered a relatively high rectification ratio despite the inherent symmetry in the molecules, which could be due to the asymmetry in the voltage drop across the junction caused by the different interfacial coupling.

9.2.3.2 Anchoring Groups

As discussed previously, molecules with different anchoring groups or different tail lengths can result in asymmetric interfacial coupling, thus suggesting the considerable potential for achieving molecular rectification. Moreover, single-molecule systems with movable electrodes, such as STM, CP-AFM, and MCBJ, make it possible to tune the molecule–electrode distance with an atomic resolution, therefore modulating the interfacial coupling strength. In this context, in 2004, Kushmerick et al. [195] experimentally demonstrated the ability to achieve and tune the current rectification in metal–molecule–metal junctions through the control of the interaction strength of one metal–molecule contact by changing the anchoring groups. In 2014, this effect was further confirmed both experimentally and theoretically by Wang et al. [196]. A molecule terminated by the thiol group and the amine group was attached at two ends between the Au surface and an STM tip. Similarly, Batra et al. [197] designed a molecular rectifier based on a symmetric, conjugated molecular backbone with a single methylsulfide group linking one end to a gold electrode and the other end to a covalent gold–carbon bond (Figure 9.21). The non-equilibrium transport calculations indicated that a hybrid gold-molecule "gateway" state was pinned close to the Fermi level of one electrode due to the formation of the gold–carbon bond, which could shift drastically with an applied bias, thus resulting in rectification at surprisingly low voltages. This study constituted the experimental demonstration of a predictably and efficiently tunable system of single-molecule rectifiers through a rational design of the anchoring groups. Recently, a theoretical study noted that the rectifying behavior of the dipyrimidinyl–diphenyl co-oligomer diode could even be reversed or largely enhanced by adjusting the asymmetric anchoring groups [189]. These studies set the foundation for a new generation of molecular rectifiers with high rectifying ratios and high tunability through interface engineering [198].

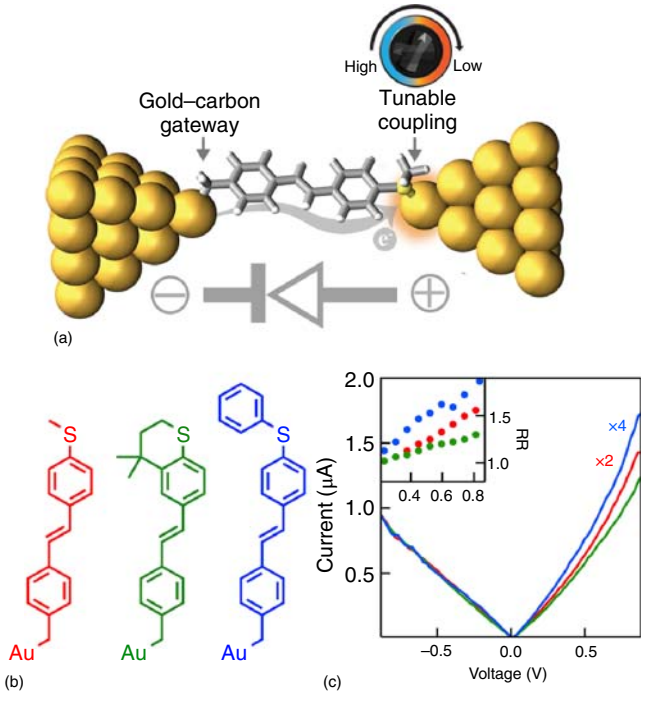

Figure 9.21 Molecular rectifiers with different anchoring groups. (a) Schematic for molecular circuits with a carbon–gold bond and a methylsulfide–gold bond. (b) Chemical structures for the three molecular rectifiers used. (c) Corresponding *I–V* curves for the three molecules. Inset: Rectification ratio as a function of the bias. Source: Reprinted with permission from Batra et al. [197]. Copyright 2013, American Chemical Society.

9.2.3.3 Contact Geometry

As previously discussed in this report, the contact geometry in the electrode–molecule interface has a significant influence on the charge transport properties of the molecular junctions. Clearly, this effect is also embodied in the molecular rectification. In the task of building a diblock co-oligomer rectifier by adjusting the anchoring groups [189], the authors determined that the asymmetric contact geometries playing a positive or negative role in improving the rectifying behavior is closely related to each molecular diode. In fact, one recent theoretical study precisely and systematically calculated the effects of different interfacial contact geometries, especially the absorption sites of an S atom in the headgroups of molecules on the surface of Au electrodes, on the rectifying behaviors of the molecular diodes [167]. These studies provide direct evidence highlighting the significance of the contact-geometry asymmetry to the rectification behavior, which serves as an aid to interpret future single-molecule electronic behavior.

9.2.3.4 Interfacial Distance

Additionally, the coupling strength could be tuned by the length of the insulating terminated tails used to connect to the electrodes. As noted by Kornilovitch, Bratkovsky, and Williams in their KBW model [163], different tails on each

side indicate different tunneling barriers, consequently leading to molecular rectification. For example, a single electroactive unit positioned asymmetrically with respect to the electrodes, and the corresponding HOMO and LUMO being distributed asymmetrically with respect to the Fermi level, could rectify electrical current. It should be noted that the construction of this model was an interesting accident, where the long insulating tail of $C_{16}H_{33}$ added to the molecule core not only leads to asymmetry but also helps form suitable LB films [199]. Afterwards, additional studies, combined with other considerations for designing molecular diodes, were conducted based on this general mechanism. Recently, Liu et al. [200] studied the rectification of current through a single molecule with an intrinsic spatial asymmetry. In this study, a rectifier with a large voltage range, high current, and low threshold was predicted by taking advantage of the relatively localized and high-energy *d* states of the cobaltocene moiety in the molecule. Combined with the calculations based on a self-consistent NEGF, the plausibility of forming excellent molecular diodes using metallocenes was demonstrated, resulting in a productive class of molecules.

In addition to terminated tails with unequal lengths, the spatially asymmetric molecule–electrode distance could also result in different interfacial coupling. In 2002, Taylor et al. [201] calculated the change in the current–voltage characteristics by securing one of the molecule–electrode interfaces while increasing the distance of the other, thus weakening the molecule-tip coupling. They stated that the operation range and rectification in the strongly chemisorbed molecules was limited by the width of the transmission resonances and their proximity to the Fermi level, both of which were strongly related to the interfacial coupling strength. Recently, using the theoretical calculation, the effects of the interfacial stretch or contraction on the rectification in diblock co-oligomer molecular diodes were investigated by Zhang et al. [202], who determined that different mechanical treatments could inverse the rectification direction. Additionally, two competitive mechanisms, deduced from the asymmetric molecular level shift and the asymmetric evolution of orbital wave functions under biases, were proposed to be responsible for the rectification inversion due to their different sensitivities to the electrode–molecule distance. Furthermore, these results clarified that the rectification performance in the molecular diodes could be manipulated using the mechanically controllable method.

9.2.4 Other Molecular Rectifiers

The improvements in the theory of electrical conduction through molecules allowed for a relatively good understanding of the rectification molecular rectifiers observed in the aforementioned cases. The principle of molecular rectifiers can be summarized briefly as being that the electronic resonance between the Fermi level, and the molecular energy level related to the charge transport occurs at different voltages in the forward and reverse bias directions, and that the barriers inhibiting the electron conduction are asymmetric at the two electrode–molecule interfaces. As further insight is obtained into the essence of rectification based on experimental and theoretical progress,

additional molecular rectifiers depending on novel operation principles are being proposed, as reviewed briefly in this section.

Although the development of the molecular diodes based on rigid-structure molecules flourishes, investigations focusing on molecules with flexible nuclear degrees of freedom, i.e. conformational changes, used to achieve current rectification increase. Ratner and colleague [203, 204] studied unimolecular rectification based on voltage-controlled intramolecular stereochemical modification (Figure 9.22a). Briefly, it was predicted that different conformations induced by an external electrical field could dominate the charge transport and result in rectification because of the inherently unequal capability to conduct electrons, which, to the best of our knowledge, has not been demonstrated experimentally. To achieve a transition between configurations driven by the external field, a strong dipole, potentially provided by one or more C—F or C—CN bonds, is necessary, and the simplest model is the system with a single flexible degree of freedom, in which the asymmetry of the junction can be preserved through a chemical bond between the molecule and at least one electrode.

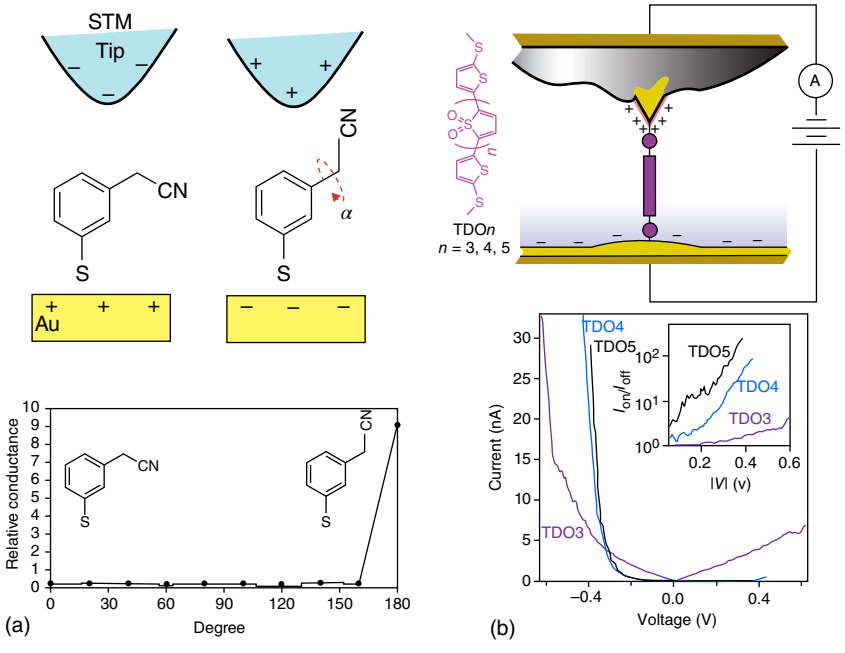

Figure 9.22 Other types of molecular rectifiers. (a) Top: schematic representation of current rectification based on molecular conformational change; bottom: corresponding conductance as a function of a dihedral angle. Source: (a) Reprinted with permission from Troisi and Ratner [203, 204]. Copyright 2002, American Chemical Society. (b) Top: TDO molecular structure used and schematic of molecular junctions created using asymmetric area electrodes through environmental control; bottom: average *I*–*V* curves for TDOs (with $n = 3$–5). Inset: Rectification ratio (I_{on}/I_{off}) versus magnitude of applied voltages, which depict ratios of ~200 at 0.37 V for TDO5. Source: (b) Reprinted with permission from Capozzi et al. [205]. Copyright 2015, Springer Nature.

A gate-controlled single-molecule diode was proposed theoretically by Zhang in 2004, where a clear modulation by the gate was obtained. Furthermore, when the positive voltage was high enough, the rectification could be reversed [206]. This prediction is valuable for designing and building future molecular logic devices and integrated circuits. Recently, Capozzi et al. provided another remarkable study on single-molecule diodes, where an approach was demonstrated to induce current rectification through environmental control [205, 207]. The symmetry of a symmetric single-molecule junction with two electrodes of the same metal was broken by exposing considerably different electrode areas to an ionic solution (Figure 9.22b). This technique allowed them to control the junction's electrostatic environment in an asymmetric manner by simply changing the bias polarity. Using this approach, they achieved rectification ratios in excess of 200 at voltages as low as 370 mV based on a symmetric oligomer of thiophene-1,1-dioxide (TDO). This result is reproducible because they observed a similar rectification using other molecules/solvent systems. This method of environmental control provides a general route for tuning nonlinear nanoscale device phenomena that is beyond single-molecule junctions.

In summary, because they are the origin of molecular electronics, molecular rectifiers have received academic and commercial attention for more than 40 years. Benefitting from both the theoretical and experimental efforts engaged in this field, this digital component critical for logic devices has evolved from an initial D–σ–A model to a derived D–π–A model to a simplified D–A model, in which the precise energy level alignment as well as the subtle electronic coupling between the donor region and the acceptor region in the molecule are significant for the rectification behavior. By enhancing the feasibility and the ease of construction of the single-molecule system, current–voltage curves with diode-like characteristics are common, even for molecules without donor or acceptor units, which could be ascribed to asymmetric interfacial coupling, as discussed earlier. Driven by this phenomenon, various methodologies have been injected into the design of single-molecule rectifiers. Furthermore, due to a thorough understanding of the charge transport through single molecules, additional models are being proposed for current rectification with novel operating principles. Clearly, a long process remains to realize commercially feasible rectifiers related to single molecules; however, a positive scenario can be imagined for the continuous attention and effort.

9.3 Negative Differential Conductance Toward Oscillators

9.3.1 Mechanisms for Negative Differential Conductance

NDC is a common phenomenon in electronic semiconductor devices, which featured by decreasing the current with the increase of voltage. It also can be discovered in molecular devices, including SAMs and single molecules [208, 209]. There are many reasons for the negative differential resistance (NDR) effect, such as, the interaction between two localized narrow energy states or the chemical

changes involved in the molecular reaction process [210, 211], the characteristics of the electrode or contact interface [208, 212], the potential barrier related to the bias voltage [209], or the changes in the internal characteristics of the molecules (such as the molecular spin or the blocking of the phonons [213], and the switching of the molecular conformation [214]). In general, the NDR effect is very weak, and a larger NDR effect can be observed in the molecular layer [215]. The peak-to-valley ratio in this molecular layer junction can be more than 2, which is mainly caused by chemical reaction or redox reaction within the molecular layer [210, 211], or defects at the interface of the electrode [216].

Reed's group developed a large ON–OFF ratios and NDR in OPE molecular junction containing a nitroamine redox center with MCBJ technique at the single molecule level [210]. They measured the current–voltage of the junction and observed the NDR effect, which showed a high ON–OFF peak-to-valley ratio excess 1000 : 1. They proposed that a possible mechanism for the NDR effect was a two-step reduction process, which modifies charge transport through molecule, which can be illustrated by Figure 9.23. Chen et al. introduced a new method to generate NDR with nonatomic sharp or even flat STM tip [217]. With this method, NDR always appears in a well-defined bias in which the spatial localization orbital components in the wide band of the tip match the symmetry of the molecular orbital. They proposed a new mechanism to explain NDR effect, which is derived from the local orbital symmetry matching between electrodes

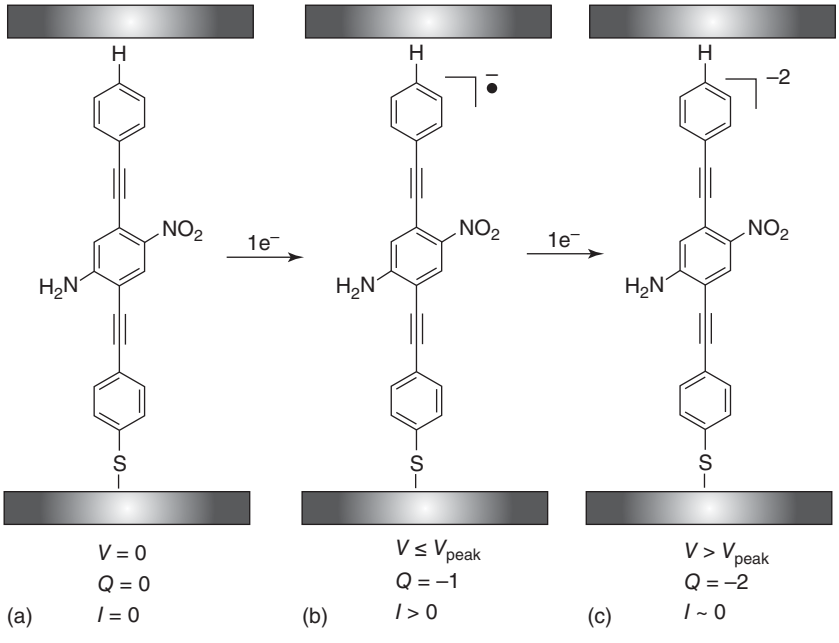

Figure 9.23 Potential mechanical for the NDR effect. As voltage is applied, the molecules in the SAM (a) undergo a one-electron reduction to form the radical anion (b) that provides a conductive state. Further increase of the voltage causes another one-electron reduction to form the dianion insulating state (c). *Q* is the charge. Source: Reproduced with permission from Chen et al. [210]. Copyright 1999, AAAS.

and molecules in single-molecule electronic devices. NDR appears not only in single molecules but also in molecular films. He and Lindsay studied the reactions between ferrocene based charged species and ambient oxygen at high bias, and studied the underlying mechanism of NDR [211]. They speculated that the NDR effect was caused by the chemical changes in the ferrocene based materials, and it's irreversible. Xiao et al. also considered that the NDR effect was originating from the irreversible reduction process, i.e. the current decreases with the increase of bias voltage, which is because the irreversible chemical reaction removes the molecules from the current carrying path [218].

Besides the common metal–molecule–metal system, silicon–molecular system also produces the NDR effect by making use of the intrinsic surface states of the silicon surface and the molecular orbital of cobalt(II) phthalocyanine (CoPc) molecules, which has been demonstrated by Wang et al. [219] By combining the experimental results with the first principle calculation, they concluded that the NDR effect in the silicon molecular system originated from the resonance between the intrinsic surface state band S1 of the R3Ag/Si surface and the local unoccupied Co^{2+} d_{Z^2} orbital of the adsorbed CoPc molecules.

9.3.2 Measurement of NDC

The NDC is usually presented in a certain range of bias voltages of a particular system, and there is an experimentally challenge to control the area of NDC in the current–voltage (I–V) curve. van der Zant's group measured the current–voltage characteristics of a single thiolated arylethynylene molecule with a 2,6-bis(((4-acetylthio)phenyl) ethynyl)-9,10-dihydroantracene (AH) in break junctions with MCBJ and observed obviously large NDC [220]. Figure 9.24a showed a typical I–V curve at low bias, a sharply first decrease and then increase appeared around ±60 mV, which is a pronounced NDC feature. When the higher bias was applied, a similar I–V characteristic also appeared in Figure 9.24b. In investigating the electrode spacing's influence on NDC effect, they measured the I–V curves at different various electrode distance by mechanically control with MCBJ device, the different NDC was displayed in Figure 9.24c,d. It is clear that the NDC characteristics were most obvious when the electrode separation was short (d_0), and the NDC characteristics were still visible when the electrode spacing increased; see Figure 9.24c,d. With the increase of electrode spacing, the peak-to-valley ratio increased from 3 to 7.1, while the peak position shifted slightly outward. Besides, they spent approximately nine hours to measure the relationship between NDC feature and electrode separation, and confirmed that the NDC effect was very stable.

Except controlling the NDC characteristics with mechanically control the electrode separation, the magnetic field also can control the NDC feature. He's group has successfully switched ON and OFF the NDC, and adjusted the regions of the NDC in the I–V curves, which are all achieved with the controlling of magnetic field in graphene *npn* junction resonators [221]. They added a large vertical magnetic field and observed quite sharp and obvious Landau level (LL) peaks

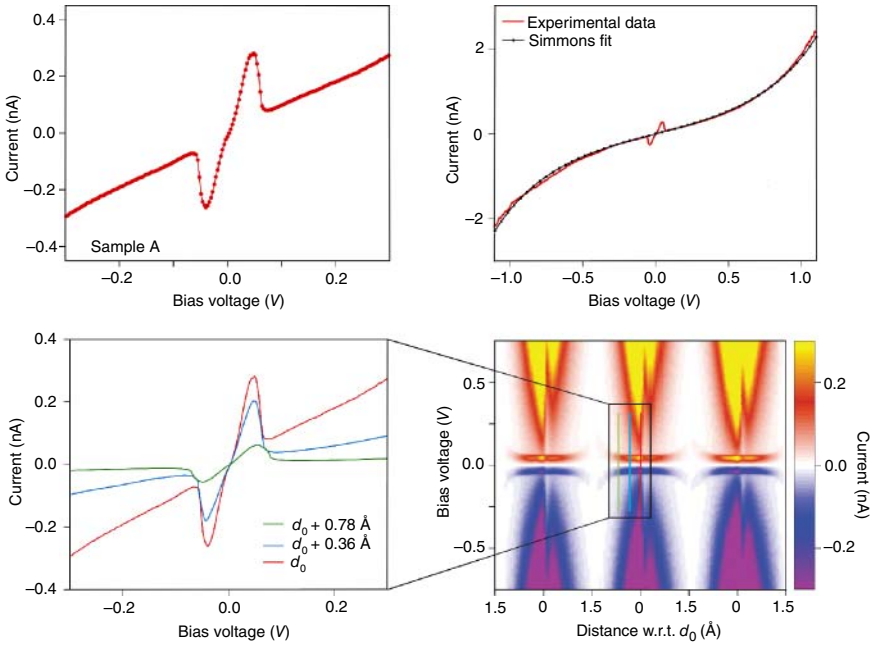

Figure 9.24 NDC effect: mechanical tunability and stability. (a, b) Typical *I–V* characteristic for low bias (a) and the full bias range (b). The black line is a fit to the Simmons model, with an electrode spacing of 11.0 Å. (c) Low-bias *I–V* characteristics for increasing electrode separation. (d) Map of *I–V* characteristics recorded from left to right while repeatedly increasing and reducing the electrode spacing. The spacing is relative to d_0, the electrode separation at which the NDC feature is most pronounced. Source: Reproduced with permission from Perrin et al. [220]. Copyright 2014, Nature Publishing Group.

under the electron confinement of graphene *npn* junction resonators. The tip of STM induces the local potential in graphene below the needle tip, which leads to the relative displacement of LLs. In the scanning tunneling spectroscopy (STS) spectrum, the tunneling between the misaligned LLs leads to the strong NDC. Figure 9.25a shows the evolution of the series of NDC as a function of magnetic field, and it can be seen from the recorded spectrum that the spectra at different locations can be reproduced, and the magnetic field can control the NDC. Figure 9.25b shows the ratio h/d of different LLs in different magnetic fields for revealing the relationship between LLs and NDC. Here h is the height of the LLs and d is the full width at half maximum of the LLs in the STS spectra. The NDC only appeared when the LLs have large ratio h/d values above the dash line in Figure 9.25b, which means Sharp and obvious LLs in the spectrum. Thus, the NDC can only appear in the P doped region of graphene *npn* junction. The magnetic field can control the quantization of Landau and the energy level of LLs in graphene, so the NDC can be opened and closed by controlling the magnetic field. To achieve more significant NDC effect, more and more experiments and measurements needed to be designed and performed.

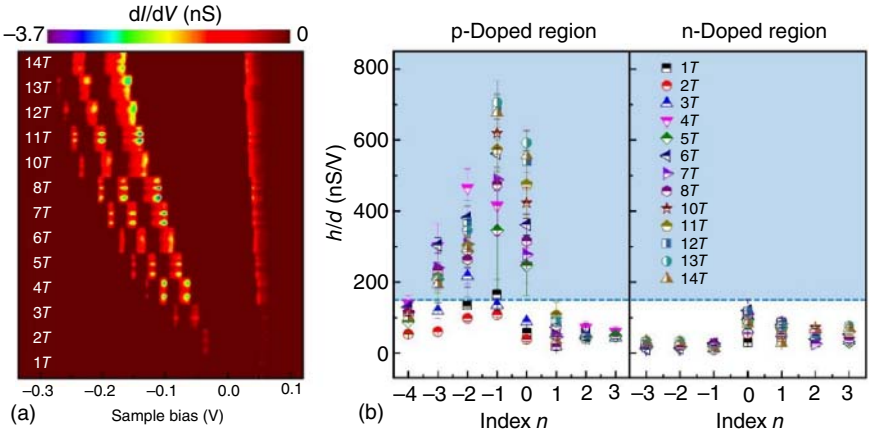

Figure 9.25 The observed NDC in the p-doped region as a function of magnetic field. (a) Experimental result of the NDC recorded in the p-doped region as a function of magnetic field. Each panel of a fixed magnetic field contains ten typical spectra measured at different positions in the p-doped region. The horizontal axis for all panels is the sample bias voltage and the intensity of the NDC is shown in a color scale. Here only show the tunneling conductance below zero of the STS spectra to emphasize the NDC. (b) Summarization of the ratios *h*/*d* for different LLs measured at different magnetic fields in the p-doped region and the n-doped region. For those LLs with value of the ratio *h*/*d* above the dashed lines, we can observe the NDC accompanying them. This indicates that the sharp and pronounced LLs play a vital role in the emergence of the NDC. Source: Reproduced with permission from Li et al. [221]. Copyright 2018, American Physical Society.

9.3.3 Application of NDC

The NDC has been extensively applied in double barrier quantum well (QW) hetero structures [222], super lattices (SLs) [223], and quantum cascade lasers [224]. Besides, the diode [225], FETs [226], and photodetectors [227] have also utilized the NDC effect. A symmetric molecule consisting of two conjugated arms connected by a non-conjugated part displayed an obvious NDC effect, and the asymmetry introduced into the symmetric molecule changed the properties of molecule, which made them being a molecule diode [228]. NDC is a common behavior and designates a specific device, which is the tunnel diode. van der Zant's group [229] proposed a design of single-molecule diodes based on intramolecular coherent resonant transport and proved that it can produce large rectification ratios. The NDC was reported in the charge diagram of the normal metal–metal oxide single-electron transistor prepared on quartz substrate by George et al. [230] Combining the experiment and theory, they discovered that the charging pattern associated with trap charging remains the same after warming the sample to room temperature though position in V_g coordinates changes. Thus, they thought that the NDC with distinct features can be used as markers to characterize background charge in single-electron transistors. The multiple NDC characteristics in long wavelength interband cascade infrared photodetectors (ICIPS) above 300 K have been investigated by Lei et al. [227] Except the above applications, Hitachi et al. [231] proposed a new scheme of detecting electron spin

resonance (ESR), which was based on the NDC in a quantum dot. NDC will have more and more applications with its unique characteristics in molecular electronics in the future.

9.4 Gating Toward Molecular Transistors

Transistors, which are typically three-terminal electrical devices that constitute the heart of the electrical circuits, control the current flow between two electrodes (source and drain electrodes) by modifying the voltage applied at a third electrode (gate electrode). Because the microelectronics industry is enthusiastically developing highly integrated circuits that require devices with smaller dimensions, a logical limit to device miniaturization is transistors, whose channels are defined by a single molecule (Figure 9.26). Therefore, the construction and understanding of such a device has been a long-standing goal of nanoelectronics. Thus, as detailed in Sections 9.2–9.4, discrete approaches have been developed for creating nanometer-spaced electrodes. Among these approaches, carbon electrode–molecule junctions and electromigration break junctions are particularly attractive because of their intrinsic three-terminal device architectures [232]. One important feature of the former is the improved device stability due to the use of covalent chemistry for forming molecular junctions, which is of considerable importance to build molecular devices with desired functions toward practical applications. This topic has been briefly discussed in Section 9.3 and will be provided in more detail in Section 9.7. In this section, we focus on the primary progress of single-molecule transistors with back-gating, side-gating, and chemical-gating configurations.

9.4.1 Back Gating for Novel Physical Phenomenon Investigation

One of the most generalized gate configurations, the back gate is commonly found in solid-state device architectures, in which the entire nanocircuit is supported by heavily doped Si, Al, or polymer substrates and insulated from the gate electrodes in the bottom by an insulating layer to ensure that only

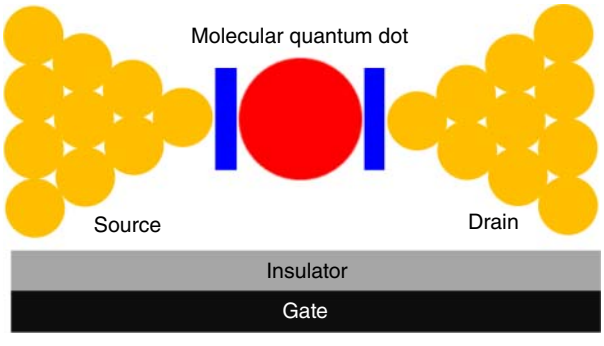

Figure 9.26 Schematic representation of single-molecule transistors with back gating architecture.

molecules in the nanogaps between the source and the drain electrodes would be electrostatically modulated. The insulating layer above could be produced by oxidizing the substrate to achieve the corresponding oxide insulator, such as SiO_2, Al_2O_3, etc., or a ten-of-nanometer vacuum gap [5], for which the thickness and dielectric constant are the two most critical parameters for determining the scale that the gate modulation could reach without incurring gate-drain leakage or gate breakdown. Therefore, selecting the gate and insulator materials is important for the total level shift, and an insulator with a high breakdown voltage, reduced thickness, and easy fabrication is required to obtain high-performance single-molecule devices.

The electromigration technique is one of the most important techniques used to fabricate source–drain electrodes with a functional back-gating configuration. In fact, solid-state single-molecule transistors with back gating were reported by two separate groups as early as 10 years ago [63, 233]. To achieve the strong effects of the gate voltage on the molecules, both groups used electromigration-induced break junctions to fabricate their device on silicon wafers with extremely thin dielectrics (30 nm silicon oxide or 3 nm aluminum oxide) (Figure 9.27a). This approach is difficult because with the gate dielectric scaling down, parasitic currents generally caused by various mechanisms (e.g. quantum tunneling,

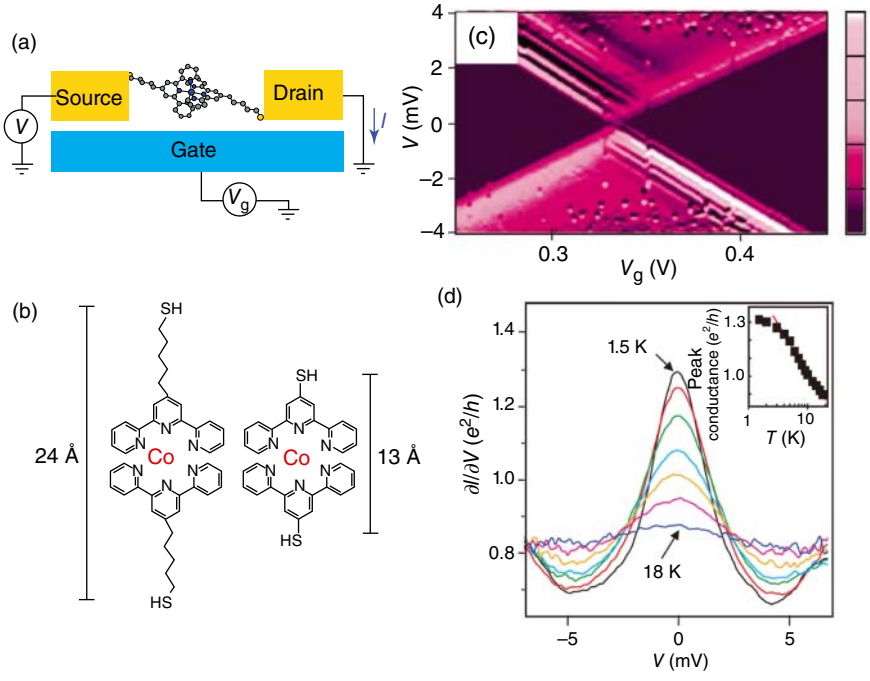

Figure 9.27 Solid-state single-molecule transistors. (a) Schematic diagram of the single-molecule transistors. (b) Molecular structures of the Co complexes. (c) Coulomb blockade observed in devices formed from longer molecules. (d) Kondo peaks as a function of the voltage. The inset depicts the conductance as a function of the temperature at $V = 0$. Source: Reprinted with permission from Park et al. [63]. Copyright 2002, Springer Nature.

electron hopping) can lead to a current between the gate and the drain, thus overshadowing the molecular signature. Therefore, the primary challenge in device fabrication is to design a junction geometry, in combination with the proper material selection, which can reduce the gate leakage as much as possible and maximize the electric field reaching the molecule. The need for such precise control may partly explain why so few of the devices prepared by the authors functioned properly as transistors. In their studies, they observed novel physical phenomena based on two mechanisms: Coulomb blockade, in which the flow of electrons is controlled by the sequential charging of a molecule; and the Kondo effect, in which conducting electrons interact with a local spin (intrinsic angular momentum) in a molecular junction. Interestingly, changing the length of the insulating tether alters the coupling of the molecules to the electrodes, enabling the fabrication of devices that exhibit either of the single-electron phenomena mentioned previously. For example, Park et al. [63] examined two related molecules containing a Co ion bonded to polypyridyl ligands and attached to insulating tethers of different lengths (Figure 9.27b). It was determined that devices formed using the longer molecules indicated a blocking of the current due to the presence of the Co ion island (Coulomb blockade) (Figure 9.27c), whereas devices created using the shorter molecules indicated the Kondo effect (Figure 9.27d). This Kondo effect is indicative of the formation of a bound state between a local spin on an island and the conduction electrons in the electrodes that enhance the conductance at low biases. In another example of single-electron-transistor measurements [234], Kubatkin et al. observed that the molecular electronic levels were strongly perturbed compared with those of the molecules in the solution, leading to a significant reduction in the gap between the HOMO and the LUMO. This surprising observation could be caused by image charges generated in the source and drain electrodes, thus resulting in a strong localization of the charges on the molecule.

In addition to the two single-electron phenomena discussed previously, Ghosh et al. [235] predicted a third phenomenon based purely on the electrostatic modulation of the molecular-orbital energy of a single molecule. Remarkably, this result was realized by Song et al. [236], where unprecedented insight was provided into the underlying physics of the charge transport in their molecular transistors created using the electromigration technique. In this study, they performed an IETS measurement on a gate voltage with two prototype molecules, a 1,8-octanedithiol (ODT) with an alkyl backbone and a 1,4-BDT with a delocalized aromatic ring, to examine the interactions between the tunneling electrons and the vibrational modes of the molecules. Because each dithiol had its own vibrational "fingerprint," this technique provided definitive proof that the measured currents actually passed through the molecules in single-molecule transistors (Figure 9.28a). More importantly, it was determined that the spectra of the ODT junction remained essentially unchanged at different values of the gate voltages, which is because the HOMO level for the ODT is energetically considerably farther away from the Fermi level (E_F). However, the IET spectra of the BDT junction were drastically modified by the gate voltages, thus exhibiting an enhanced spectral intensity. This observation was attributed to the dominant transport orbital (the HOMO) being strongly coupled to the

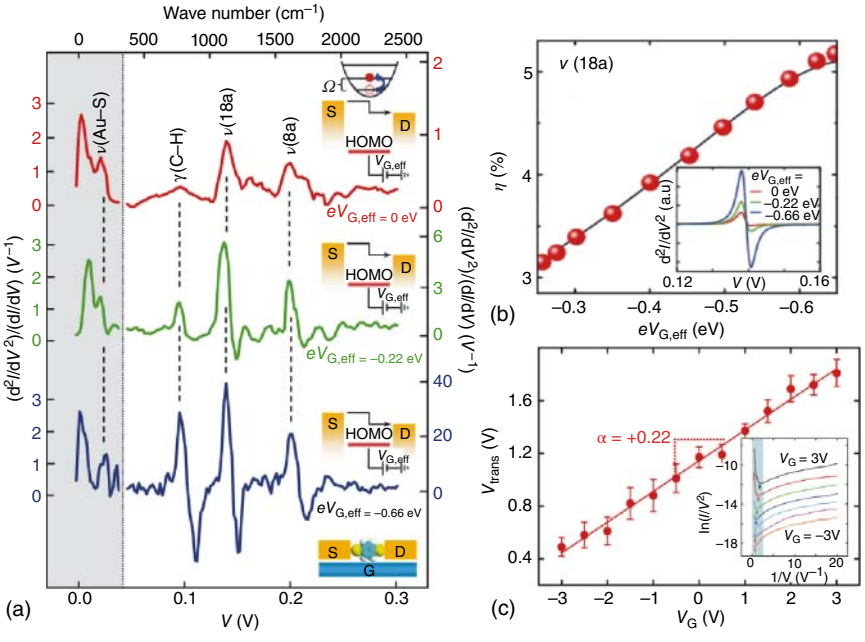

Figure 9.28 Gate modulation of molecular orbitals in single-molecule transistors. (a) IETS measured at 4.2 K for different values of the effective molecular orbital gating energy ($eV_{G,eff}$), with the vibration modes assigned. The left-hand *y*-axis corresponds to the gray shaded region of the spectra, and the various right-hand *y*-axes (with different scales) correspond to the related (color-coded) spectra in the non-shaded region. (b) The relative change, η, in the normalized conductance for the ν(18a) mode as a function of $eV_{G,eff}$. The circles depict the experimental data, and the solid curve represents the theoretical fit. The inset is the gate-variable IETS for the ν(18a) mode. (c) Plot of V_{trans} versus V_G. The inset is the corresponding TVS spectra. Source: Reprinted with permission from Song et al. [236]. Copyright 2009, Springer Nature.

internal vibrational modes of the BDT, resulting in a resonantly enhanced IETS (Figure 9.28b). Additionally, the TVS technique was used to reveal the energy offset (V_{trans}) between the gating orbital of the molecular junction (the orbital that modulates electron tunneling) and the Fermi levels of the source and drain electrodes. By measuring V_{trans} using the TVS at different applied gate voltages, a linear relationship was determined to exist between the gate voltage and the molecular-orbital energy in their devices, as expected for single-molecule transistors (Figure 9.28c). These findings demonstrated the direct gate modulation of the molecular orbitals, thus enhancing the prospects for true molecularly engineered electronic devices.

Furthermore, the three-terminal electrostatic back gate can be achieved via an MCBJ. Champagne et al. first reported a device in which a gold wire was lithographically patterned on top of a silicon/silicon-oxide substrate [237]. The silicon was heavily doped, thus acting as a back-gate electrode. After etching the oxide layer, a suspended gold wire was obtained above the substrate using a vacuum as an insulator. Their gated MCBJs provided the capability to simultaneously

adjust the spacing between the electrodes and the molecule energy levels. It was determined that the mechanical motion could change a molecule's capacitance, conductance, and gate voltage value for the Coulomb blockade degeneracy. It is anticipated that this new experimental tool will enable systematic studies of how changes in molecular conformation affect the electrical conduction and how transport varies between the weak coupling Coulomb blockade and the strong coupling Kondo regimes. A few years later, using the same device, further experiments were reported in which the spin states in the Spin-1 molecules could be mechanically controlled in the absence of a magnetic field by stretching the individual cobalt complexes [238]. This control enabled quantitative studies of the underscreened Kondo effect and could serve as model systems for performing precise tests on correlated-electron theories.

A similar back-gate approach was introduced by Martin et al. [239] In contrast to Champagne et al., the greatest difference is that the flexibility of the substrate was used instead of that of the rigid silicon substrate; thus, the junctions could be easily broken by mechanical means. However, upon application of a gate voltage, the freshly broken electrodes were pulled toward the substrate due to the electric field. To prevent the drift of the source–drain electrodes under electrostatic gating, Martin et al. created an improved design in which the gate and the source–drain electrode were suspended (i.e. the source–drain electrode, insulation layer, and gate electrode were sandwiched and suspended above the substrate together) [240]. To test the gate action of this device, the C_{60} molecules were studied, and it was determined that the total shift in the molecular levels for the devices was approximately 40 meV. Recently, the same group further investigated the image-charge effects in single-molecule junctions using this MCBJ with a back gate [241]. It was determined that a substantial increase in the transport gap and level shifts as high as several hundreds of millielectronvolt appeared when the electrode separation increased by a few ångströms. An analysis of this large and tunable gap renormalization based on atomic charges revealed the dominant role of image-charge effects in the single-molecule junctions.

Carbon-based electrodes (i.e. graphene sheets and CNTs) are interesting candidates to replace noble metals because they provide a higher structural stability, even under ambient conditions, and reduce the size mismatch between the electrodes and the molecule. Another advantage of carbon-based electrodes is that they allow the molecular junctions to be brought closer to the gate compared with bulky gold, and they typically do not have electrostatic shielding properties, thus enhancing the gating efficiency. There are several significant reports in which different strategies were used to link the molecules to the carbon electrodes, and the gating of the current was observed [232]. Here, we only focus on the novel physical phenomenon investigation using back gating with carbon electrodes. For example, Marquardt et al. first reported an example of a single molecular junction at room temperature displaying electroluminescence [119]. The selected molecules have fluorescent cores extended with organic spacers, which not only increase the molecule length but also allow for easy electrostatical trapping of the molecules in the gap using dielectrophoresis. These results suggested a new characterization and functional possibilities as well as demonstrated a significant potential of CNTs for use in molecular electronics.

One disadvantage to back gating with CNT electrodes is that, for example, an SWCNT with a p-type semiconductor behavior may completely mask the gate response of the molecule. This problem could be solved using the multiple walled carbon nanotube (MWCNT) or thicker few-layer graphene flakes. The versatility of graphene may allow the production of electrodes with intrinsic functional devices. For example, it was predicted that graphene electrodes terminated in zigzag edges may act as Fano-like resonances and spin filters, which allow the injection of spin-polarized currents into the bridged molecules [242]. However, the fabrication of the reliable, nanometer-sized, and adjustable gaps between the source and the drain electrodes in the graphene sheets remains a considerable challenge. Particularly, improving the control of the edge chemistry is crucial.

9.4.2 Side Gating for Electron Transport Control

The creation of a single-molecule FET has been considered a critical step in molecular electronics. A nanoscale gap junction formed by "electromigration" is a highly efficient method for creating a highly integrated single-molecule FET. However, this method is limited in practice by its extremely low device yield [236]. Conversely, the MCBJ technique is advantageous because it can easily form single-molecule junctions several times mechanically, and it does not suffer from low yield [243]. In the MCBJ, the primary challenge is the method that is used to form reliable three-terminal FET junctions from single molecules. The three-terminal MCBJ with back gating geometry may suffer from the gating electrode breaking because it bears a large strain to separate the source–drain electrodes by bending the substrate. Xiang et al. demonstrated a completely different single-molecule FET junction with the MCBJ using a nanometer scale non-contact side gate to the molecular junctions (Figure 9.29) [244]. In this geometry, the gate electrode and source–drain electrodes were located in the same plane (thus the deformation of the gate electrode was extremely reduced during bending of the substrate), and the electrical field was enhanced in the thickness of the gate electrodes, especially on the gate side compared to that of a typical back-gate configuration [245]. Using this side-gating MCBJ, the ability to form a stable single-molecule junction via the MCBJ technique and shift the energy levels of the molecule by side gating was successfully demonstrated.

Generally, to directly visualize the electromigration process and discriminate trapped molecules/metal clusters from dusts inside the gap or visualize a source–drain breaking process, a transmission electron microscopy (TEM) requires the use of electron transparent substrates, which are non-compatible with the most common three-terminal devices with a back-gate electrode. The side-gate geometry is relatively compatible with the TEM inspection and can overcome this problem [245]. In addition to this advantage, the gate potential could be screened by the source–drain electrodes, which indicates that only those molecules facing the gate electrodes can be easily influenced by the gate electrodes. Nevertheless, the in-plane three-terminal molecular junction presents a new platform for fabricating highly stable single-molecule transistor junctions.

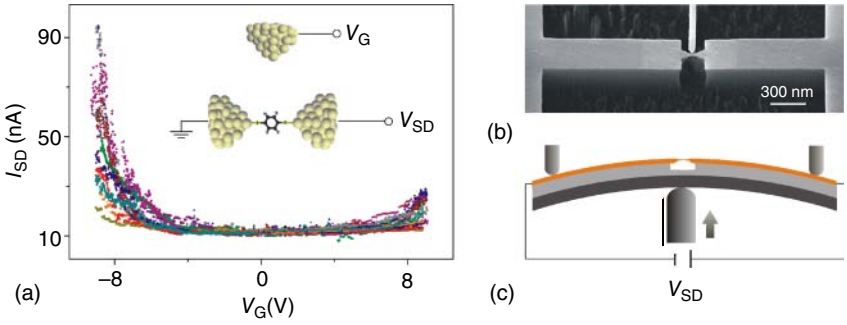

Figure 9.29 Molecular transistors with side gating. An external electric field generated by a side-gate electrode was applied to single-molecule junctions formed by the MCBJ. (a) Source drain current (I_{SD}) versus gate voltage (V_G) curves for the Au–BDT–Au molecule. The current was modulated by the gate voltage in twelve different molecular junctions. The inset illustrates a three-terminal junction with the BDT bridged between the source and drain electrodes. (b) Top view of a scanning electron microscopy (SEM) image of a micro-fabricated MCBJ chip consisting of a freestanding metal bridge with a gate electrode. (c) Schematic of the MCBJ setup. The distance between the electrodes for opening and closing the operation modes can be tuned by bending or relaxing the substrate, respectively. Source: Reprinted with permission from Xiang et al. [244]. Copyright 2013, American Chemical Society.

9.4.3 Electrochemical Gating for Efficient Gate Coupling

Electrochemical gating is a promising method for efficient gate coupling that provides a unique opportunity to manipulate the energy alignment and the molecular redox processes for a single-molecule junction [246]. Because the gate voltage falls across the double layers at the electrode-electrolyte interfaces, which are only a few ions thick, a field of approximately 1 V $Å^{-1}$ can be reached. Hence, a large gate field and a high gating efficient can be achieved using an electrochemical gate [247]. One advantage of an electrified solid/liquid interface is that the two potential differences can be controlled simultaneously: (i) the bias voltage between the source and the drain electrodes; and (ii) the potential drop between the working electrodes and the reference electrode. Generally, the electrochemical gating effect is realized via tuning the Fermi level of the junction electrodes, thus changing the redox state of the molecular functional unit. The EC-STM-BJ is the most widely used technique in electrochemical gating studies thus far, and numerous significant results, such as current enhancement mechanisms, electrolyte gating models, and molecule structure changes via electrochemical gating, have been reported [247–251]. It should be noted that to reduce the electrochemical leakage currents, it is necessary to insulate the STM tip by a non-conductive material, except for the very end of the tip. The tip insulation is a simple procedure and can be performed in any laboratory in the EC-STM-BJ configuration. However, the insulation process is challenging for fixed nanospaced electrodes in the MCBJ configuration [252, 253].

It should be noted that the control of the charge transport in a single-molecule junction using electrolytic gating based on one non-redox active molecular system is also possible [254–256]. For example, Capozzi et al. reported modulation of the conductance of electrochemically inactive molecules in single-molecule

junctions using an electrolytic gate [256]. This experimental study combined with the DFT calculations indicated that electrochemical gating can directly modulate the alignment of the conducting orbital relative to the metal Fermi energy, thus changing the junction transport properties. More recently, Baghernejad et al. demonstrated that the single-molecule conductance could be controlled via both the Fermi level tuning and redox switching [255]. In the small potential region (redox-inactive), the effect of the gating is to shift the Fermi level relative to the molecular energy level, thus leading to a modest change in the conductance. A further shift in the electrode potential led to large and reversible jumps in the conductance due to the change in the molecular redox state and the molecular conjugation switching. The study indicated that the electrochemical gating of single-molecule junctions could be modeled using computational models via conversion of the potential to the energy scale.

In summary, different approaches, including carbon electrode–molecule junctions, electromigration-induced molecular junctions, and three-terminal MCBJ-based break junctions, have been successfully developed to realize single-molecule transistors and demonstrated a direct gate modulation of molecular orbitals through the multi-spectroscopy approaches [232]. These studies set the benchmark for the validation of future studies in the charge transport for molecular systems. However, additional work must be performed before molecular electronic devices can effectively compete with their larger silicon-based equivalents. One of the most urgent issues is to develop an efficient fabrication method that allows high yields of densely packed single-molecule devices. It is expected that the electron transport through the molecule may be controlled by a universal gate electrode, including electrical gates, electrochemical gates, magnetic gates, optical gates, terahertz wave gates, and mechanical gates. Additional new designs and device architectures are needed to transition from laboratory research to practical applications.

9.5 Switching Toward Memory Devices

The important next step in molecular electronics toward actual applications is the construction of a reliable molecular switch, i.e. a particularly attractive molecular electronic device. It is improbable to build a circuit without a switch. The reason for this is that transistors, a core component of current computer circuits, are ultimately operating as switches, where the conductance is efficiently and controllably turned ON and OFF by a gate electrode. Therefore, single-molecule switches could be the prototypical devices used as a complement silicon in the logic and memory elements because of its clear advantage for ultra-high-density integration.

In principle, a molecular switch can alter the conductance, which occurs from changes in its physical properties (such as the electronic structure of the molecule and correspondingly its density of states) upon exposure to external stimuli (e.g. light, heat, ion, magnetic, or electric field). This requires the molecules to have several (at least two) stable isomers and transition between

the isomers. From an engineering point of view, the challenge is to build single-molecule switches whose conductance changes are detectable, ideally from zero (OFF state) to infinity (ON state). Early studies on molecular switches were performed based on SAMs [257–261], particularly using the STM or AFM setups, which have been surveyed in a recent review [262]. In the following paragraphs, we focus on summarizing the design, construction, and electrical properties of recent single-molecule switches, including conformation-induced switches, electrochemically-triggered switches, and spintronics-based switches.

9.5.1 Switch Stem from Conformation Change

Most molecular switches are based on drastic conformational changes in the molecule. Conformational changes in bi-states even multistates of molecules are ideal properties for the switching. It will not produce unnecessary reactants or redundant products. The current strategies of the conformational changes of the switches focus on different conformational isomers and molecular reorientations.

9.5.1.1 Electrical Field Induced Switch

At the beginning of this century, scientists predicted the conformational change induced by electric field [263, 264]. Just one year later, Donhauser et al. observed stochastic conformational changes for OPE derivatives with the patterned SAMs technology by STM [33]. The authors used a dodecanethiolate monolayer matrix as a host to contain, support, and isolate derivatized OPE molecules. This consideration has been discussed widely for the mechanism of the conformation switching [265–268].

Subsequently, Qiu et al. investigated conformation switching of the Zn(II) Etioporphyrin I (ZnEtioI) molecules adsorbed on NiAl(110) at 13 K by STM technique [269]. Two types of STM image have been obtained (Figure 9.30a). When the tip is positioned over the center of a molecule in type I conformation, the I–V characteristics showed sudden jump at the 1.35 and −1.38 V, which corresponded to the conformation change (Figure 9.30b). In order to determine the mechanism of the conformational variations, the authors studied the dependence of conformational change on bias voltage as a function of the tip-sample separation, shown in Figure 9.30c. The linear dependence of the type II to type I transition at negative bias voltage was the evidence for a mechanism involving the electric field acting on the dipole and overcoming the energy barrier for conformational change. They explained that the conformation change depends on the presence and orientation of an intrinsic dipole moment, as well as the polarizability of the molecule.

Alemani et al. demonstrated an electric field induced reversible *trans–cis* isomerization of 3,3′,5,5′-tetra-*tert*-butylazobenzene (TBA) by STM [270]. The isomerization experiments were displayed by fixing the position of the STM tip at a given height above a molecular island with the feedback loop off and applying a pulse voltage V_m to the center of the island. These results, together with the large distance over which switched molecules were observed, suggested the trans–cis isomerization change driven by the electric field in the STM junction.

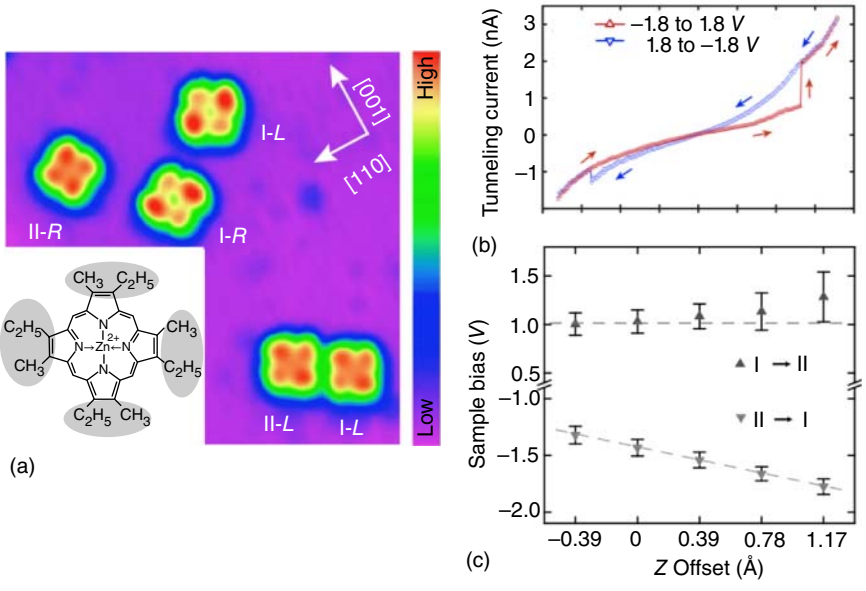

Figure 9.30 Conformation switching. (a) STM image of ZnEtiol molecules adsorbed on the NiAl[110] surface at 13 K. The color palette represents a variation in apparent height of 3.3 Å. (b) *I–V* characteristics of a ZnEtiol molecule. (c) Variations of threshold voltages for a ZnEtiol molecule to undergo the reversible conformational transitions from type I to type II to type I as a function of the change in tip-substrate separation. Source: Reprinted with permission from Qiu et al. [269]. Copyright 2004, American Physical Society.

9.5.1.2 Tunneling Electron (Charge) Triggered Switch

The current-induced switches have been reported in STM technique [271–273]. In 2001, Moresco et al. reported the intramolecular conformations of Cu-tetra-3,5 di-*tert*-butyl-phenyl porphyrin (Cu-TBPP) molecules deposited on Cu(211), which is investigated by LT-STM [273]. They actualized the reversible switch via σ bond rotation of the single leg of the Cu-TBPP driven by the electron tunneling.

The aforementioned system has several equivalent conformational isomers, which is not suitable for the switches design. AB was chosen to study the conformational change with STM [274]. AB has two isomers, which are determined by dihedral angles between two phenyl rings and the CN=NC plane. *trans*-Azobenzene (*t*AB) can be transformed to *cis*-azobenzene (*c*AB) by rotating or inverting a phenyl ring through tunneling electrons with a specific bias in the STM geometry (Figure 9.31a). When applied bias voltage, the *t*AB changed to *c*AB, as shown in the STM image (Figure 9.31b, inset). Their theoretical calculation suggested that the isomerization took place either by electron impact resonant excitation or by vibrational excitation.

Another type of the reorientation switch has been reported [275]. Liljeroth et al. presented a single-molecule switch based on hydrogen tautomerization. Depending on the position of the two inner hydrogens in the central cavity of the molecule, the LUMO of a free-base naphthalocyanine (Figure 9.32a)

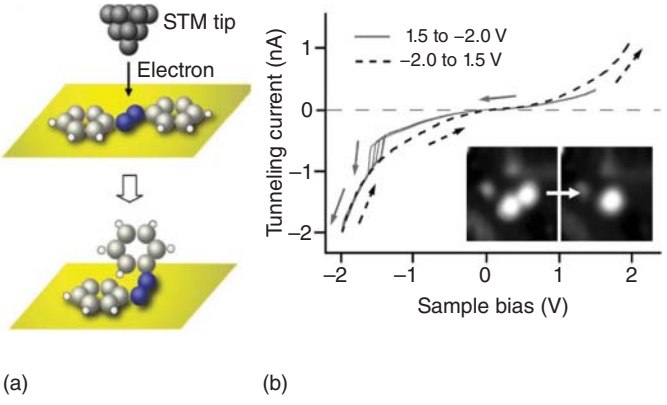

Figure 9.31 Azobenzene-based switches. (a) A concept of electron-induced isomerization of an AB molecule adsorbed onto a metallic surface with a scanning tunneling microscopy. (b) A current–voltage (*I*–*V*) curve obtained at the center of *t*AB (left inset) and a newly produced molecule (right inset) by sweeping the voltage twice. Source: Reprinted with permission from Choi et al. [274]. Copyright 2006, American Physical Society.

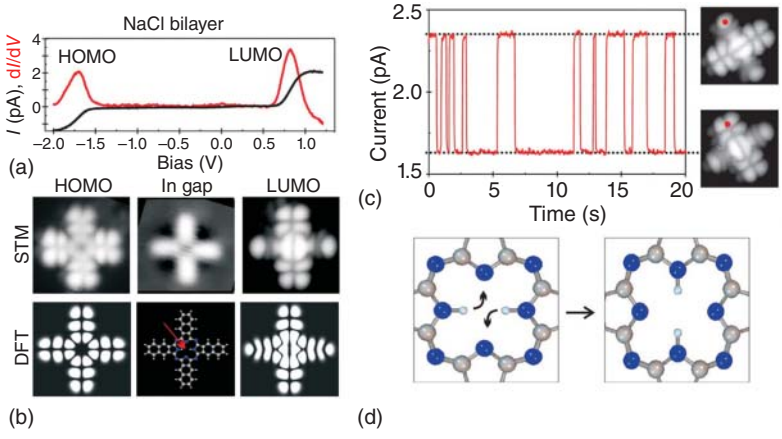

Figure 9.32 Spectroscopic and orbital images of naphthalocyanine. (a) Spectroscopy of naphthalocyanine on a NaCl bilayer on Cu(111) where the peaks correspond to tunneling into the LUMO (positive bias) and out of the HOMO (negative bias). (b) STM images at 1 pA, −1.6 V (left) and 1 pA, 0.65 V (right), as well as at low bias (1 pA, 0.05 V) compared with the calculated HOMO and LUMO of the free molecule. (c) Left: current-trace obtained at a bias of 1.7 V when the tip was positioned at one end of the molecule (red dot in STM images). Right: orbital images showing the orientation of the LUMO corresponding to the high- or low-current state (2 pA, 0.7 V). (d) Schematic of the hydrogen tautomerization reaction responsible for the switching. Source: Reprinted with permission from Liljeroth et al. [275]. Copyright 2007, AAAS.

has two orientations. The molecules were adsorbed on NaCl bilayer ultrathin insulating films on Cu single crystals and studied by LT STM operated at 5 K. Their DFT calculation predicted two isomers for the LUMO orbitals, which is consistent with the STM image (Figure 9.32b–d). The arms with hydrogens showed a single-lobe structure at the end, while opposed to the nodal plane

along the other two arms. They demonstrated hydrogen tautomerization of naphthalocyanine resulted from positioning the tip above the molecule and applied substantially increasing bias above the LUMO resonance. The authors ruled out the electric field mechanism by observing the conformational change of adjacent molecules.

In 2006, Riel and colleagues [276] reported an Au/bipyridyl-dinitro oligophenylene-ethynylene dithiol (BPDN-DT) molecule/Au single molecular memory performed by MCBJ as a new mechanism switch. The BPDN-NT contacted strongly with the gold electrodes by –SH group and switched automatically due to electron tunneling. This system could work at 100 K, do the write, read, and erase with voltage pulse pattern applied, corresponding to different switching states as shown in Figure 9.33. The ratio of the current of "OFF" state and "ON" state was observed 7–70 times and can keep working for 30 seconds.

Using MCBJ-based two-terminal junctions, Schirm et al. [277] demonstrated that a metallic atomic-scale contact could be operated as a reliable switch driven

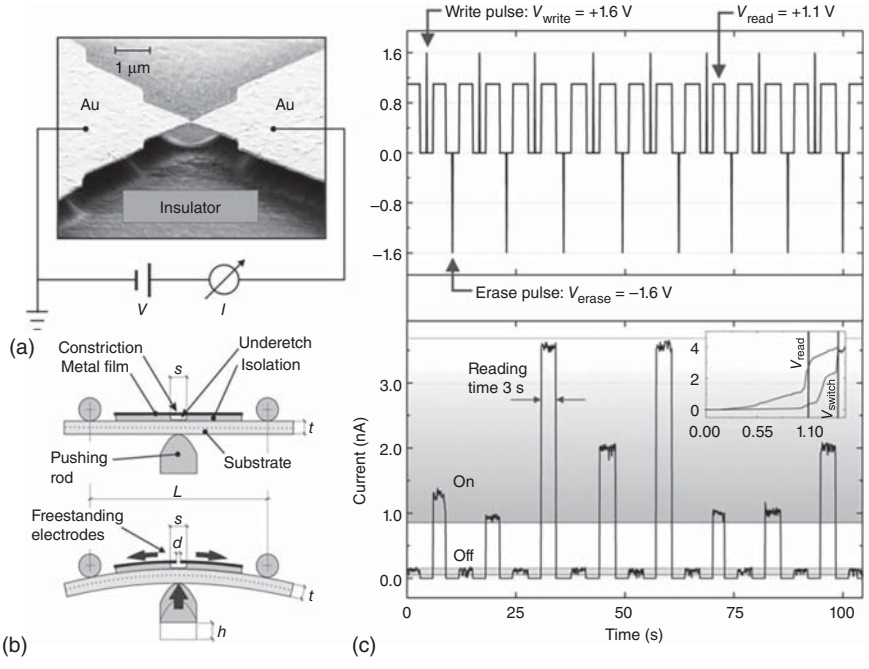

Figure 9.33 The principle of MCBJ. (a) Scanning electron microscope image of a micro-fabricated MCBJ sample consisting of a freestanding metal bridge with a central lateral constriction on top of a flexible isolating substrate. The electric circuit is schematically drawn. (b) The MCBJ sample is mounted onto a three-point bending mechanism. (c) Memory operation of the BPDN-DT system: (top) Write, read, and erase voltage pulse pattern applied. (Bottom) Resulting switching between "OFF" and "ON" state: I_{off} varies between 0.05 and 0.13 nA, I_{on} between 0.9 and 3.6 nA. Reading times of three seconds display excellent signal stability. The inset shows the corresponding *I*–*V* curve, indicating switching at 1.4 V and reading at 1.1 V (black lines). Source: Reprinted with permission from Lörtscher et al. [276]. Copyright 2006, John Wiley and Sons.

by the controlled current. They also provided evidence proving that the switching process was caused by the reversible rearrangement of single atoms in the MCBJs. Basically, the field-induced and current-induced switches cannot be controlled by external signals due to their stochastic nature. In several cases, the two mechanisms often work simultaneously in the same system [269].

9.5.1.3 Mechanical Force Induced Switch

The engineering of the electrode–molecule–electrode junction is a critical issue in fabricating molecular devices via the mechanical controllable technique. The interface engineering was considered firstly, which determined the strength of the interface coupling. Based on this conception, many explorations on mechanical controllable molecular level have been demonstrated [278–280].

Venkataraman's group demonstrated a reversible binary switching in a single-molecule junction by mechanical control of the metal–molecule contact geometry [281]. From the conductance behavior of the 4,4′-bipyridine–gold junctions, they observed a bistable state (Figure 9.34a,b), which centered around 1.6×10^{-4} G_0 (low G) and 6×10^{-4} G_0 (high G). They assigned the switching behavior to the properties of the pyridine-gold linkage. Besides, their theoretical calculation gave reasonable interpretation for the binary state occurrence. As the elongation of the junction, the π*-orbital of LUMO is orthogonal to the nitrogen lone pair, while the N-gold bond aligned to the backbone, resulting in low electronic coupling and low conductance (Figure 9.34c, left). On the

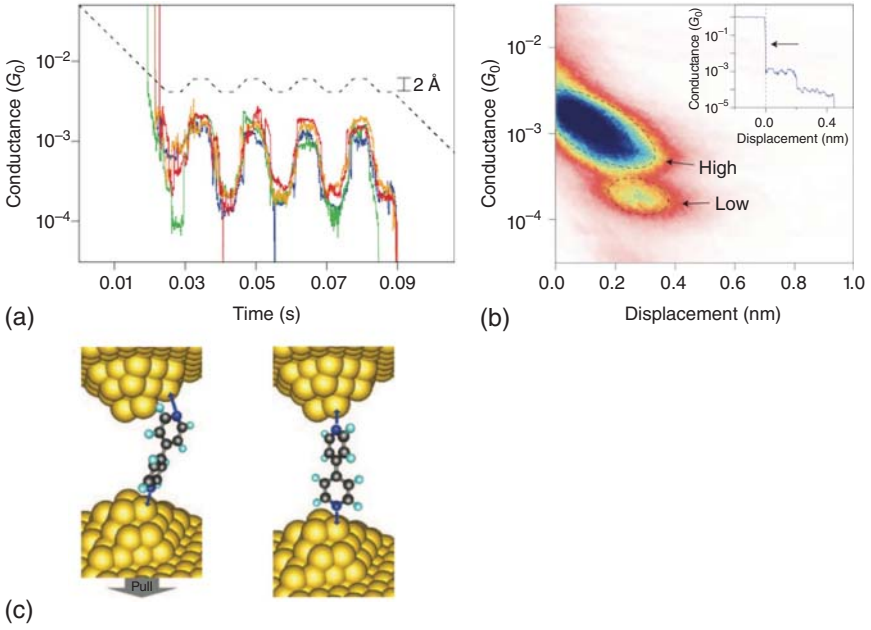

Figure 9.34 Contact geometric effect. (a) Sample bipyridine switching conductance traces (colored solid lines). (b) Two-dimensional histogram constructed from all traces with a clear G_0 break. (c) Schematics illustrating the high G (left) and low G (right). Source: Reprinted with permission from Quek et al. [281]. Copyright 2009, Springer Nature.

other hand, the constraints imposed by the compressed junctions will drive strong tilting of the N-gold bond, which leads to the stronger coupling and higher conductance (Figure 9.34c, right). With precise control of the tip-sample distance, which tuned the strength of the coupling of the N–Au interface actually, the author fabricated a binary conductance switching (Figure 9.34a). Kaneko et al. reported the nitrogen involving mechanical controllable switch [282]. They investigated Pt–pyrazine–Pt molecular junction with the MCBJ technique. They repeated a mechanical elongation/compression processes to perform the switching behavior of their system. Interestingly, their experimental and DFT calculation suggested that bistable states of the present junction derived from the pyrazine anchoring to the Pt electrodes by its N atom and by its two C atoms alternatively. Another conventional interface of Au—S bond has been estimated [283, 284]. In Au–1,6-hexanedithiol (HDT)–Au junction with nano-MCBJ technique, the break junction measurements revealed two distinct conductance states of $G_{\mathrm{H}} \sim 1.3\,\mathrm{m}G_0$ and $G_{\mathrm{L}} \sim 0.4\,\mathrm{m}G_0$ [283]. Their analysis of single-molecule structures has offered evidence that the mechanically controllable bistate conductance switching occurs via repeated deformations of the Au–S linkage between top and hollow motifs. Kiguchi et al. reported a single-molecular resistive switch of a partially covered quaterthiophene (QT) molecular junction by means of STM-BJ technique [284]. Their mechanical elongation/compression process leads to that the terminal S in the thiophene ring was bound to the tip Au atom and the anchoring point shifted one by one in the QT moiety.

Beyond the interface design, subsequently, molecular engineering has also been reported. In specific, another possibility for controlling electronics at the single-molecule level by directing molecular conformation is stereoelectronic effects because they determine how the properties and reactivates of the molecules depend on the relative spatial orientations of their electron orbitals. This idea was first demonstrated by Su et al. [285], who developed a single-molecule switch that operated through the stereoelectronic effect. By using permethyloligosilanes with methylthiomethyl electrode linkers, it was determined that the strong σ conjugation in the oligosilane backbone coupled the stereoelectronic properties of the sulfur–methylene σ bonds at the contact interface. As predicted by theory, this strong coupling led to three distinct dihedral conformations that had extremely different electronic characteristics (Figure 9.35a). Remarkably, by simply lengthening or compressing the molecular junction, the transition between the three species could be controlled, thus realizing conductance switching between the two states (Figure 9.35b). This study leads to a unique technique incorporating reaction chemistry into the design of a new generation of functional molecular electronic devices. In addition, other strategies with AFM have also been considered [286].

9.5.1.4 Chemical Stimuli Triggered Switch (Redox and pH)

The oxidation–reduction reaction as another important reaction here for the bistate molecular devices has also drawn so much attention. Generally, electrochemical studies of single-molecule conductance have focused on primarily organic redox moieties [247, 248, 287–289] and organometallic

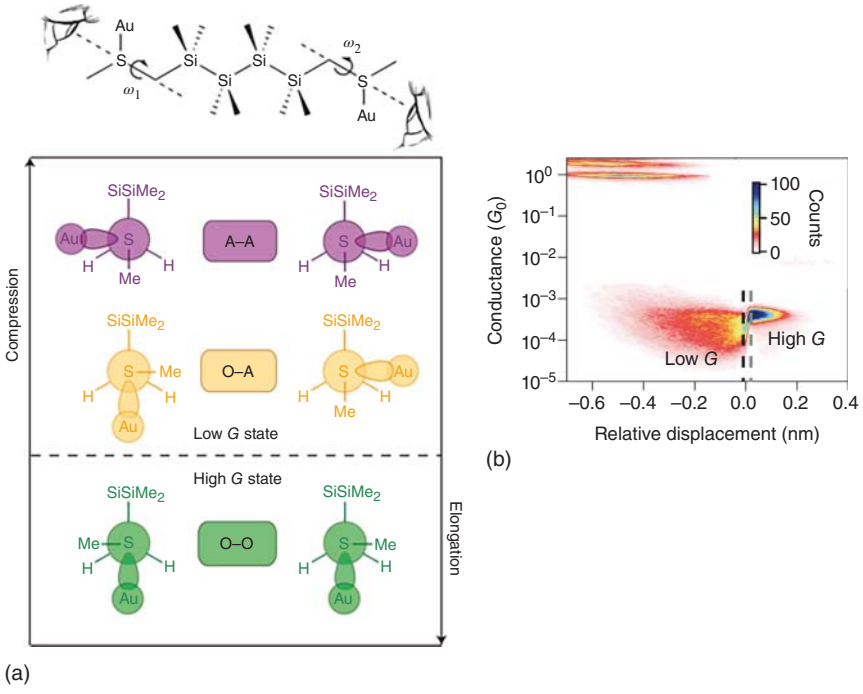

Figure 9.35 Directing molecular conformation by stereoelectronic effects. (a) Three dihedral configurations: A–A (purple), O–A (yellow) and O–O (green) from the perspective of the sulfur–methylene σ bond in the Au–Si_4–Au system. (b) 2D conductance–displacement histogram for Si_4 compiled from traces that demonstrate switching. Source: Reprinted with permission from Su et al. [285]. Copyright 2015, Springer Nature.

compounds [290–294]. Gittins et al. used an organic molecules containing redox center, which can be changed reversibly by the oxidation–reduction reaction. With $bipy^{2+}$ oxidation state, no current goes through the circuit, which means "OFF". With the proper bias voltage, the radical $Bipy^{\cdot+}$ let the current increase [295]. Recently, new type of switches have been developed with stabilization of unstable states, such as radicals and antiaromatic ions [296, 297].

Another essential kind of binary-state molecules, catenane and rotaxane, has been reported as molecular switch and memory. Heath's group proposed a [2]catenane-based solid state electronically reconfigurable switch [154]. They fabricated a bistable [2]catenene and sandwiched between an n-type polycrystalline Si electrodes and a Ti/Al top electrode (Figure 9.36). The device exhibits hysteretic I–V characteristics can be open at +2 V closed at −2 V and could be recycled many times. The different position of the rings represents 0 or 1 state. They succeeded in fabricating 16-bite, 64-bite memory circuit in the further work and even implemented a molecular electronic memory patterned at 10^{11} bit cm^{-2} [298].

Proton triggered switch is one type of important chemical stimuli switches. Guo et al. developed carbon-based electrodes, which connected with the target molecules by covalent amide linkage [61]. Their robust and tolerate linkage

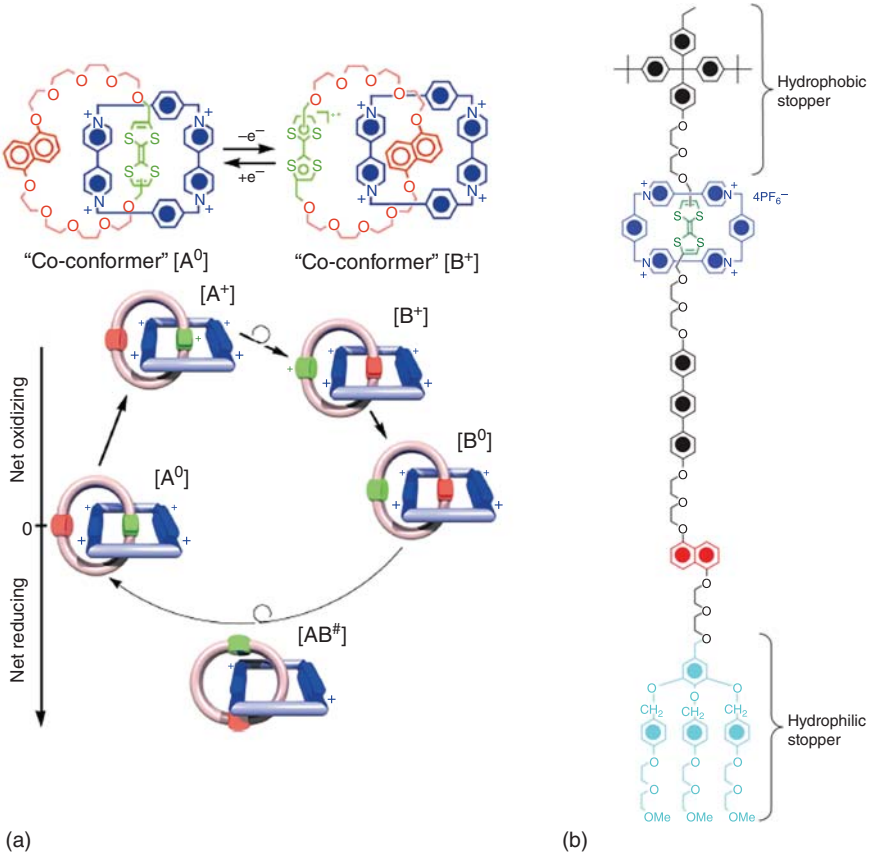

Figure 9.36 Catenane-based switches. (a) The principle of molecular switch made by catenane molecules, rotaxane molecules, and cross wire technique. Source: (a) Reprinted with permission from Collier et al. [154]. Copyright 2006, AAAS. (b) Structural formula of the bistable [2]rotaxane used in the crossbar memory. Source: (b) Reprinted with permission from Guo et al. [61]. Copyright 2007, Springer Nature.

has been estimated under various pH (Figure 9.37a,b). The current change as the function of the pH varies is shown in Figure 9.37b. Oligoanilines displayed low/high alternative current, which they demonstrated stem from the inherent protonation and deprotonations process. Li et al. built a proton-triggered switch with a novel edge-on gate with STM-BJ technique [299]. The "ON" and "OFF" of the pyridinoparacyclophane (PPC) switch reversibly by deprotonation and protonation of the pyridine ring (Figure 9.37c). Furthermore, they studied the para-position of pyridine, which was functionalized with $-NO_2$, –Cl, –H, $-OCH_3$, and $-N(CH_3)_2$ (Figure 9.37d). They set a series of control experiments. The conductance value of these protonated molecules remained consistent indicating the independence of the substituents on the pyridine ring. The switching mechanism was explained as the variable in charge tunneling channels form HOMO in neutral molecules to LUMO in protonated ones.

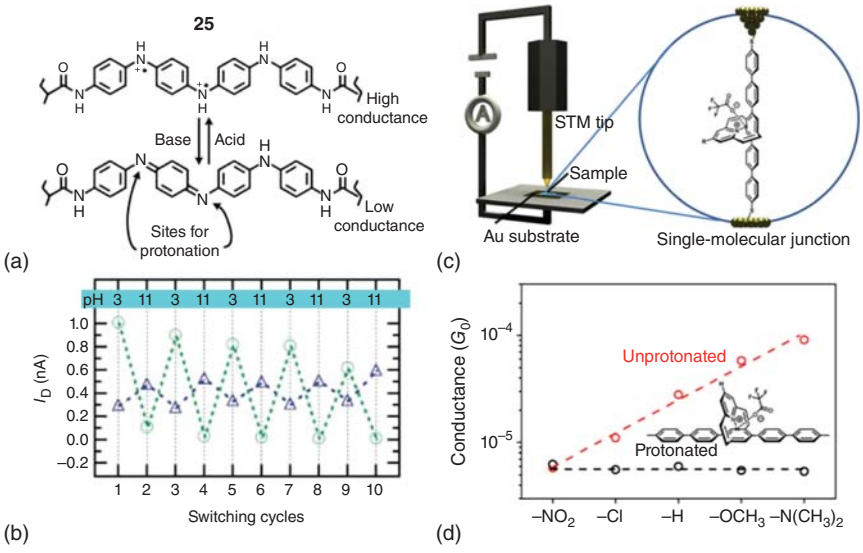

Figure 9.37 Proton-triggered switches. (a) Protonation and deprotonation to give high- and low-conductance forms of oligoaniline **25**. (b) Green circles show the ON-state resistance for molecule **25** when alternately immersed in solutions of low and high pH. Source: (b) Reprinted with permission from Guo et al. [61]. Copyright 2006, AAAS. (c) An illustration of the metal–molecule–metal junction in the STM-BJ technique. (d) The most probable conductance values of the protonated and unprotonated molecular wires. The dotted lines are only used as an eye guide. Source: (d) Reprinted with permission from Green et al. [298]. Copyright 2016, Springer Nature.

9.5.1.5 Light-Triggered Switch

To achieve electrical bistability, a promising approach recently developed relies on the use of molecular photochromics because they undergo reversible photoisomerization between two isomers upon irradiation with light of different wavelengths [300, 301]. These conformational changes result in remarkable differences in their electronic structures and their distinct photophysical properties, which has been well observed in solution, thus forming the basis for new types of optoelectronic devices and molecular switches [302]. However, in practice, a significant challenge is to maintain the photophysical properties existing in solution when sandwiched between two solid-state electrodes at the single-molecule level. This is because the operational parameters, switching voltages, and bistability are sensitive to the environment. The strong coupling with the electrodes and/or electrostatic interaction with the substrate could be detrimental for realizing the single-molecule switches. For example, Lara-Avila et al. [303–305] demonstrated an environmental effect on the electronic structure of a bianthrone molecule that was connected to silver electrodes on aluminum oxide substrates. In addition to the observation of persistent switching of the electric conductance at low temperatures, it was determined that the measured activation energy of the photoisomerization process was in the order of 35–90 meV, which is 1 order of magnitude lower than that measured for free bianthrone ($\Delta E_{act} = \sim 0.9$ eV). The reason for this is that when positioned

in intimate contact with silver and on an aluminum oxide dielectric with high permittivity, one bianthrone isomer acquires a negative charge that shifted the molecular geometry (due to image forces in the substrate), which in turn decreases the transition barrier.

Another series of examples that highlight the importance of the electrode–molecule contact interface are single-molecule photoswitches based on photochromic DAEs [132, 148, 306, 307]. In 2003, Dulić et al. [148] first fabricated dithiolated photochromic molecular switches using an MCBJ technique (Figure 9.38a). They observed the molecules switching from the conducting to the insulating state when illuminated with visible light ($\lambda = 546\,\text{nm}$) but failed to observe the reverse process, even when illuminated with ultraviolet (UV) light ($\lambda = 313\,\text{nm}$) (Figure 9.38b). They attributed this to quenching of the molecule's excited state in the open form due to the presence of the gold surface plasmon through the Au—S bonds. To decouple the strong interaction between the DAE molecules and the electrodes, innovative molecular design and device architectures are required to preserve the molecular functions. In an attempt to solve this problem, Guo and colleagues [306] built different types of single-molecule switches using the SWCNTs as point contacts, where they used covalent amide linkages to form a robust contact interface (Figure 9.38c). It was observed that these SWCNT-DAE single-molecule junctions could switch from the low conductance state (open form) to the high conductance state (closed form), but not back again (Figure 9.38d). Interestingly, this phenomenon is contrary to the situation occurring in the devices made from gold electrode break junctions with dithiolated molecules, as discussed earlier. In the case of SWCNT-DAE single-molecule junctions, it is most likely due to the energy dissipation of the excited state of the closed form by the electrodes. This result is consistent with the fact that the length of the π-conjugation on the termini of the DAE switches decreases the quantum yield for opening [308]. The nanotube is the ultimate extension of this conjugation. These results imply that the electrode–molecule contact interface is one of the most challenging issues in realizing functional molecular electronic devices.

In another attempt, Guo and colleagues [132] developed a series of single-molecule photoswitches based on a new device platform of graphene-molecule single-molecule junctions (Figure 9.39a). In this study, to tailor the energy level alignments at the molecule–electrode interface, the DAE backbones were modified with rationally designed side and anchoring groups. As indicated in Figure 9.39b, the second molecule was achieved by substituting the hydrogenated cyclopentene of the first molecule with the fluorinated unit, while the third was based on the second by further introducing a methylene group (CH_2) between the terminal amine group and the functional center on each side. Demonstrated by the theoretical calculations, molecular engineering can be an efficient tool for tuning the molecule–electrode coupling strength. A reproducible optoelectronic switching from the OFF state to the on state (Figure 9.39c) was achieved. Unfortunately, continuous reversible switching was not realized, which indicated that the presence of the strong coupling between the molecules and the electrodes remained, hence consistent with the case of the SWCNT-based molecular junctions. In addition to the observation of one-way photoswitching,

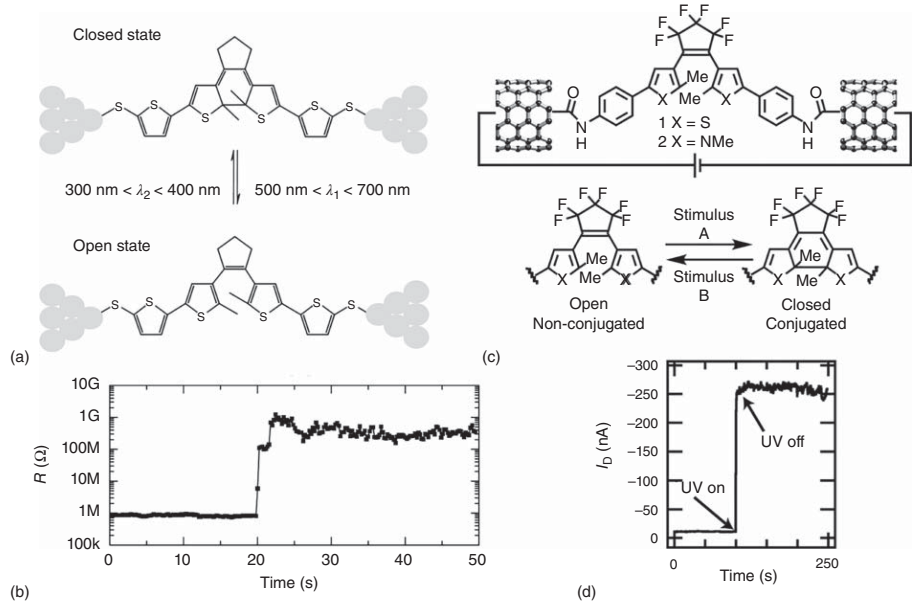

Figure 9.38 One-way photoswitching in single-molecule junctions. (a) Photochromic molecular switch between two Au contacts in the closed state (top) and the open state (bottom). (b) Resistance versus time, which depicts the switching of the junctions from the conducting to the insulating state. Source: (b) Reprinted with permission from Dulic et al. [148]. Copyright 2003, American Physical Society. (c) Molecular bridges between the ends of an individual SWCNT electrode. (d) Drain current as a function of time, which depicts the switching of the junctions from the low to the high state. Source: (d) Reprinted with permission from Whalley et al. [306]. Copyright 2007, American Chemical Society.

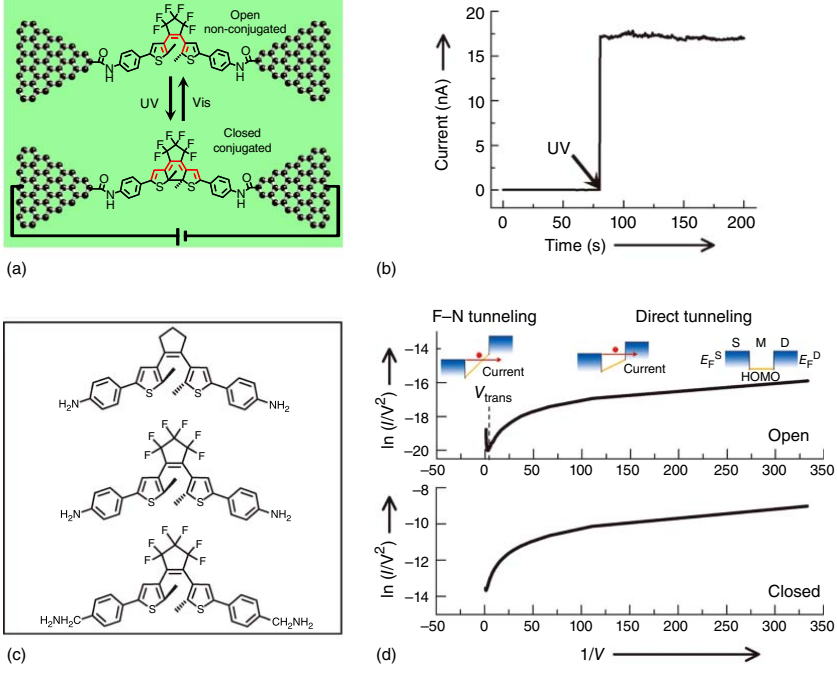

Figure 9.39 Switching properties of graphene–diarylethene single-molecule junctions. (a) Switching of graphene–diarylethene junctions. (b) Molecular structures. (c) Current-versus-time curve of a graphene–diarylethene junction. (d) F–N plots of the *I*–*V* characteristics for the same junction. The insets indicate the conventional barrier model. Source: Reprinted with permission from Jia et al. [132]. Copyright 2013, Wiley and Sons.

detailed spectroscopic analyses based on both barrier and resonant tunneling models were performed, which supported the experimental observation of the photogated tunneling transition in the molecular junctions from direct to Fowler–Nordheim (F–N) tunneling (Figure 9.39d). This approach of molecular engineering was also reported by Kim et al. [307], where four sulfur-free DAE molecules were developed to reduce the possibility of unintended binding. Furthermore, the charge transport of the open and closed isomers of the photoswitching molecules in the mechanically controllable break junctions (MCBJs)-based single-molecule junctions were studied at low temperatures (Figure 9.40a). The single-molecule conductance was examined by breaking and forming the atomic contacts repeatedly, which revealed that both the conduction properties and the conductance switching ratios were significantly influenced by the end groups as well as the side chains of the molecules (Figure 9.40b). By analyzing the $I–V$ curves within the framework of the single-level transport model, an unexpected behavior of the current-dominating molecular orbital was found upon isomerization. These investigations provide new insight into designing novel types of functional molecule-based devices toward practical applications. The realization of *in situ* continuous reversible switching of the single-molecule photoswitches between two measurable conductance levels remains a formidable challenge, thus leaving an interesting opportunity for future studies to address. More details in the effort toward reversible single-molecule switches have been discussed in Section 9.1.2.3.

Recently, Roldan et al. developed an *in situ* photo-thermally triggered conductance switching [309]. The two isomers of dimethyldihydropyrene molecules have a switch ON/OFF ratio $\sim 10^4$. Beyond the poor fatigue resistance, the reported molecules performed good electronic properties and mechanical stability.

9.5.2 Electrochemically Gated Switch

As discussed in Section 9.4, three-terminal molecular junctions have the capability of tuning wave functions and, particularly, the redox energy states of the molecular bridges due to the consequent control over the junction conductance. However, placing three electrodes in intimate proximity of a molecule is extremely challenging. This result has been demonstrated in solid-state planar device architectures, where a metal gate electrode is separated from the source–drain contacts by a thin dielectric film. One disadvantage of these approaches is the lack of precisely controlling the degree of molecule-gate electrode coupling, which is crucial to modulate the molecular energy levels of the molecule necessary for sufficient electrical coupling with both leads. Additionally, another possible challenge is to avoid the evaporation of metal grains in the electrode gap during metal evaporation in the junction fabrication, which is detrimental to the electrical characterization of the molecular junctions. To solve these issues, an alternative approach to realizing strong gating effects is an electrochemical gate. The measurement of the electrochemical gating of a single molecule is performed in an electrolyte, as schematically illustrated in

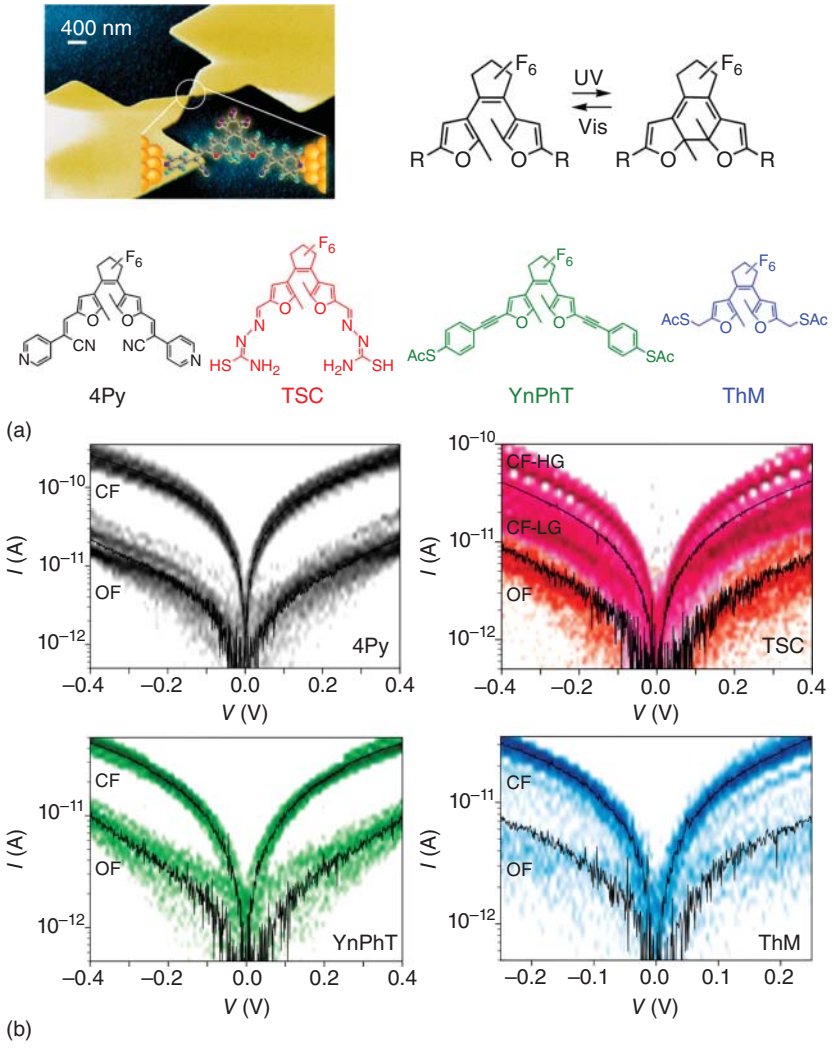

Figure 9.40 Switching properties of sulfur-free diarylethene molecules. (a) SEM image of an MCBJ device and the structure of four photochromic molecules: 4Py (black), TSC (red), YnPhT (green), and ThM (blue). (b) Density plots of approximately 20 *I*–*V* curves of the open form (OF) and the closed form (CF). Source: Reprinted with permission from Kim et al. [307]. Copyright 2012, American Chemical Society.

Figure 9.41. In this setup, the bridge energies are controlled through the electrochemical potential for molecular devices immersed in an electrolyte solution relative to a reference electrode. This is typically achieved in a four-electrode electrochemical setup with counter and reference electrodes serving alongside the source and drain electrodes (both of which are the working electrodes of the electrochemical cell). In strong electrolytes, a remarkable feature of the electrochemical setup is that the Debye screening length can be extremely short, i.e. approximately a few ångströms. Although the counter and reference electrodes

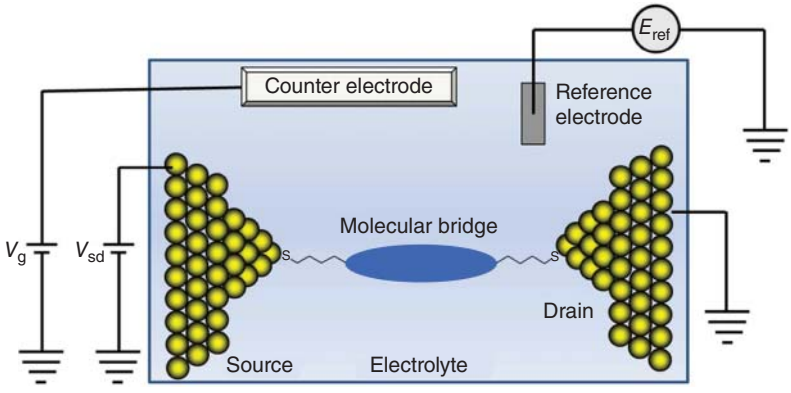

Figure 9.41 Schematic illustration of the electrochemical gating in a single molecule in an electrolyte. Source: Reprinted with permission from Kay et al. [310]. Copyright 2012, American Chemical Society.

are physically far from the molecular bridge, any charge on the molecular bridge can be detected by the charge in the solution at a distance significantly shorter than what can be generally achieved in the solid-state planar device architectures (see Section 9.4). For example, if a 0.5 V potential difference exists across an electrochemical double layer with a thickness of 0.5 nm, a mean electric field strength of 10^9 V m^{-1} can be achieved across this double layer region. Therefore, this strong and reproducible gate field is sufficient to significantly modulate the current across single molecules. It should be noted that to minimize the electrochemical leakage currents and the capacitive current components, the source–drain electrodes should be insulated by a non-conductive material, except at the very end of the electrode. However, in the case of nanogapped electrodes in the break junction configuration, the insulation process is relatively challenging.

To obtain the switching property using electrochemical gating, redox-active molecules represent a particularly attractive class of switches because they can be reduced or oxidized upon an applied electrochemical gate field. In this context, the primary challenge is to achieve a high ratio between the ON and OFF states of the nanojunction conductance. For example, Kay et al. [310] assembled a redox active pyrrolo-tetrathiafulvalene (pTTF) derivative (Figure 9.42) to gold contacts at both ends using $-(CH_2)_6S-$ groups. By using an *in situ* STM-BJ configuration (Figure 9.42), they observed a multiple OFF–ON–OFF–ON–OFF conductance switching behavior with a conductance ratio of ~4 when the electrode potentials matched the redox peak positions (Figure 9.42). These redox peaks can be ascribed to two reversible redox processes of the pTTF moiety: the formation of a radical cation and a dication. This molecular conductance versus electrochemical potential relation could be modeled well as a sequential two-step charge transfer process with full or partial vibrational relaxation (Kuznetsov–Ulstrup (KU) model) [311]. Using this view, the reorganization energies of ~1.2 eV were estimated for both the first and the second redox transitions for the pTTF bridge in the 1-butyl-3-methylimidazolium trifluoromethanesulfonate ionic liquid

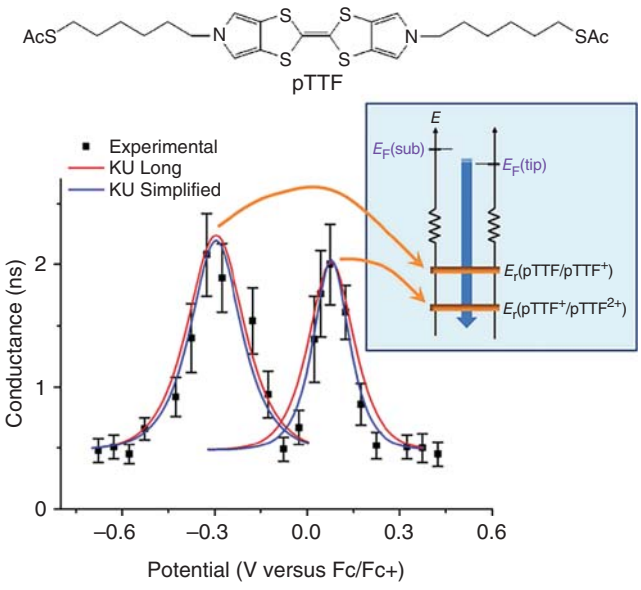

Figure 9.42 Conductance–sample potential relationship of pTTF. The red lines depict the long KU model, and the blue lines depict the simplified KU model. For both redox transitions, the KU model versions fit the experimental data well. The inset depicts a schematic energy level representation of the KU model for the two redox transitions. When the electrode potential is scanned positive, the pTTF/pTTF$^+$ redox transition is first brought into "resonance," and then at more positive potentials, the second redox transition (pTTF^{2+}/pTTF$^+$) comes into resonance. Source: Reprinted with permission from Kay et al. [310]. Copyright 2012, American Chemical Society.

environment. This value is significantly larger compared with that obtained for the same molecular bridge in aqueous environments (~0.4 eV). These differences should be attributed to the large, outer-sphere reorganization energy for the charge transfer across the molecular junction in the ionic liquid environment. To improve the electrochemical switching behavior of the molecular junctions, Li et al. chose redox-active benzodifuran-based molecules with optimal anchoring groups ($-CS_2^-$ anchoring group) instead of thiolate, thus resulting in a significant increase in both the junction conductance and the switching efficiency (ON/OFF ratio: ~8) [312].

Another example of a single-molecule switch was developed by Darwish et al. [313], where a redox couple of anthraquinone/hydroanthraquinone (AQ/H_2AQ) was selected as the functional element (Figure 9.43a). A key feature of this design is the cementing of the AQ group into a rigid, structurally well-defined norbornylogous unit bearing two pairs of thiol groups at each end, thereby conferring additional stability to the SAMs. Using *in situ* STM-BJs, they were able to electrochemically and reversibly switch the molecules between the high-conducting H_2AQ system and the low-conducting AQ system with a conductance ON/OFF ratio of 1 order of magnitude (Figure 9.43b,c). This high magnitude is attributed to destructive quantum interference effects operating in the AQ form, which is consistent with both the theoretical prediction and the

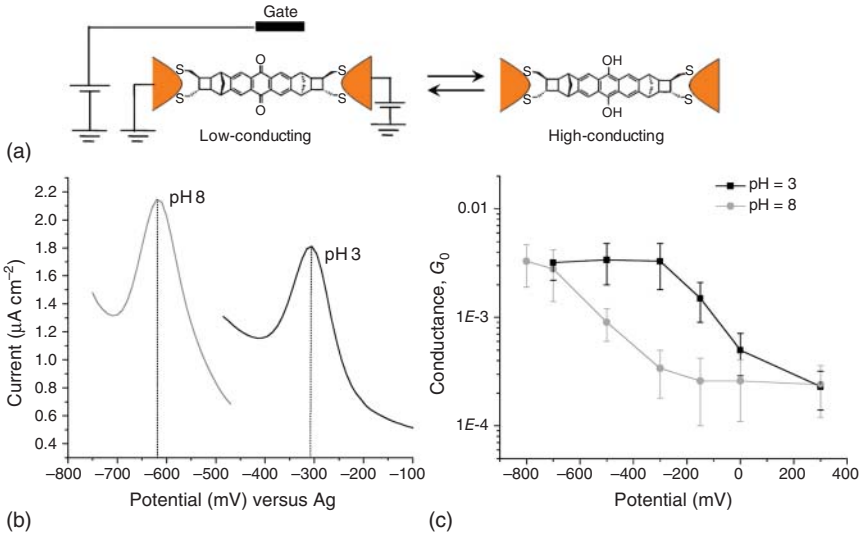

Figure 9.43 Electrochemical gating of an anthraquinone/hydroanthraquinone redox couple. (a) Redox reaction of an AQ moiety to an H_2AQ moiety. (b) Alternating current voltammograms at pH 3 (black line) and pH 8 (gray line). (c) Evolution of the conductance of the AQ molecule with a gate potential at pH 3 (black line) and pH 8 (gray line). Source: Reprinted with permission from Darwish et al. [313]. Copyright 2012, Wiley and Sons.

bulk conductance results across the SAMs. Additionally, the possibility of modulating the potential range of the conductance enhancement was demonstrated by different pH values. Recently, a similar result was also reported by Baghernejad et al. [255], where a conductance ratio of over >1 order of magnitude was achieved based on organic molecules containing an AQ center. In comparison with the study discussed earlier, one important distinction observed in this study was that in the redox-inactive potential region, the effect of the gating is to shift the Fermi level relative to the molecular resonances, thus leading to a modest change in the conductance.

It should be noted that in addition to redox active molecules, non-redox active molecular systems, such as 1,2-bis(4,4-dimethylthiochroman-6-yl)ethylene and 4,4-bipyridine, also indicated a tunable charge transport, as demonstrated experimentally and theoretically by Capozzi et al. [256] and Baghernejad et al. [254] The working principle is that the electrochemical gate potential could suitably tune the energy level alignment between the LUMO or the HOMO in the molecular orbitals with the Fermi level of the electrode, thus resulting in the modulation of the charge transport in the single-molecule junctions.

9.5.3 Spintronics-Based Switch

Recent years have witnessed the emergence and rapid growth of a new field, known as "molecular spintronics," which combines the ideas and the advantages of spintronics and molecular electronics [314]. The key is to use one or a few molecules, which respond to a magnetic field, to create molecular devices.

Because of their apparent advantages, such as fine tunability of their rich properties (for example, spin-orbit and hyperfine interaction), high degree of purity and ease of synthesis, these molecular materials appear as an incredibly versatile and unique playground for exploring new spintronics concepts and/or implementing existing ones. Among these molecules, single-molecule magnet (SMM) compounds appear to be particularly attractive because their magnetization relaxation time is extremely long at low temperatures, reaching years below 2 K. In conjunction with the advantages of the molecular scale using the properties of bulk magnetic materials, these systems are promising for high-density information storage as well as quantum computing due to their long coherence times [315]. Furthermore, their molecular nature may lead to several appealing quantum effects of the static and dynamic magnetic properties [316, 317]. The rich physics behind the magnetic behaviors present interesting effects, such as an NDC and a complete current suppression, which are useful for molecular electronics. More importantly, specific functions (for example, switching ability with light and electric field) can be directly integrated into the molecule. In this section, we are going to briefly review the primary developments in exploring the switching behaviors in single-molecule spintronics. For additional fundamental information on the different aspects of molecular spintronics, interested readers are recommended to refer to several comprehensive reviews [314, 318–326].

Currently, there are two techniques to attach a magnetic molecule between two electrodes. One possibility is to use an STM tip as the first electrode and the conducting substrate as the second electrode. Because this method has been detailed in Refs. [321, 327] and is irrelevant to the topic in this section, we omit this approach. Although STM is a powerful tool for understanding the basic mechanism of the magnetic interaction between a molecule and a substrate, such as Kondo effects [328] and single-atom magnetic anisotropies [329], it is not a device fabrication platform. Another possibility is based on the three-(or two-) terminal break junctions, which have an additional gate electrode in addition to the source and drain electrodes. This three-terminal transport device, known as a molecular spin-transistor, is a single-electron transistor with non-magnetic electrodes and a single magnetic molecule as the island. The current passes through the magnetic molecule through the source and drain electrodes, and the electronic transport properties are tuned by using a gate voltage V_G (Figure 9.26). It is worth to point out that Schwarz et al. recently demonstrated the oxidation and reduction of Mo compounds can solely be triggered by the electric field applied to a two-terminal molecular junction presenting voltage-induced conductance switching [330].

Reliable molecular spin transistors is a fundamental issue to be solved due to the fact that, despite numerous classes of magnetic molecules that can be chemically synthesized, most of them are extremely fragile away from the solution and often sensitive to a metallic surface. In a few cases, certain molecules will lose their magnetic moment entirely due to coupling with electrodes. This disadvantage leads to a substantial difficulty in constructing robust magnetic single-molecule devices. By assuming that these three-terminal devices incorporating magnetic molecules, which preserve their SMM properties, can be

achieved, the next important question is: how should these devices operate? Particularly, how do these devices function as a switch or sensor to read, write, and process information upon exposure to an external stimulus? In the case of the SMMs, two key ingredients useful in making the devices function are the ability of the electrodes to produce a spin-polarized current and the possibility of altering the mutual orientation of the electrodes' magnetization vectors. The first property depends on the ability of manipulating the exchange interaction in a controllable way, thus converting spin information to molecular orbital information. The second property relies on the magneto-crystalline anisotropy, i.e. spin–orbit coupling.

In fact, recent experimental and theoretical developments demonstrated the possibilities for switching the magnetic molecules as well as the effects that the switch produces on the electron transport [321, 327] using two classes of magnetic molecules: spin-crossover compounds and molecules presenting valence tautomerism [331]. These two broad classes of molecules are particularly appealing for a number of reasons. Firstly, they have an extremely long-living magnetization relaxation time, which signifies that such molecules have an intrinsic non-volatile nature. Secondly, because the crossover generally depicts an internal charge rearrangement and an atomic relaxation, the two different molecular states display distinct electronic structures. The different electronic structures are expected to indicate different $I-V$ curves for different spin states, i.e. the spin state is likely to be electrically readable. Finally, the crossover transition is sensitive to the local electrostatic environment such that an electric field may be used to induce the transition, which indicates that a potential device may be electrically switchable.

For example, in 2009 Rocha et al. [332] theoretically predicted a type of organic spin valves, which was obtained by sandwiching an organic molecule between magnetic contacts. Using a combination of state-of-the-art non-equilibrium transport methods and the DFT, they demonstrated that these spin valves could display a large bias-dependent magnetoresistance and that it could be engineered by an appropriate selection of molecules and anchoring groups. Four years later [318], the same group proposed another general route, i.e. the possibility of switching the sign of the exchange coupling between two magnetic centers using an electric potential. This general effect, which they named the electrostatic spin crossover, occurs in insulating molecules with superexchange magnetic interaction and inversion symmetry breaking. To prove its efficiency, a family of di-cobaltocene-based molecules was selected to demonstrate that these molecules had critical fields for switching of approximately $1\,\mathrm{V\,nm^{-1}}$, as calculated from the first principles. More importantly, the critical fields could be engineered by incorporating appropriate substituents into the basic di-cobaltocene unit. Consistently, this possibility of controlling the molecular spin state by an electric field is also proved by Diefenbach and Kim [333] They used $Ba_2(C_6H_6)$ to obtain the distinct difference in response to the molecular electronic states upon perturbation with an external electric field. These results may inspire future experimental studies toward the synthesis and

spectroscopic characterization of molecular magnetic switches to prove this switching concept.

In fact, these theoretical predictions inspired a series of remarkable experimental studies. For example, in 2009, Prins et al. [334] demonstrated that nanoparticles consisting of spin crossover molecules presented a temperature hysteresis in their conductivity, which was attributed to the spin crossover transition. Intriguingly, although this activity used nanoparticles or crystals, not single molecules, this experiment demonstrated that the crossover could be induced by a static electric field, thus paving the way for electrically controlled spin devices at the molecular level. In fact, these functional single-molecule spin devices were realized recently by Osorio et al. [335] and Wagner et al. [336] In the former study, they used electromigration to create a three-terminal device incorporating a single Mn^{2+} ion coordinated by two terpyridine ligands and demonstrated an electrically controlled high-spin ($S = 5/2$) to low-spin ($S = 1/2$) transition by adjusting the gate voltage. Using LT inelastic co-tunneling spectroscopy, they also uncovered a strongly gate-dependent singlet-triplet splitting on the low-spin side, which was consistent with an exact diagonalization of the Mn-complex. In the latter study, they used the MCBJ technique to measure the electron transport through a single-molecule junction containing two coupled spin centers that were confined to two Co^{2+} ions (Figure 9.44a). They claimed that this method could detect a coupled spin pair in a single magnetic molecule and that a bias voltage could be used to switch between two states of the molecule. This claim was proven experimentally and theoretically. In theory, spin–orbit configuration interaction methods were used to calculate the combined spin system, which indicated that the ground state was determined to be a pseudo-singlet, whereas the first excitation behaved as a pseudo-triplet. In the experiments, these states could be assigned to the absence and the occurrence of a Kondo-like zero-bias anomaly in the LT conductance data (Figure 9.44b). This result is remarkable because one can repeatedly switch the molecules between the pseudo-singlet state and the pseudo-triplet state by simply applying a finite bias.

Last, another idea to be noted is to build molecular multidot devices, where a controlled number of molecules or multiple centers inside the same molecule are attached to two electrodes. This approach may lead to more interesting phenomena. For example, NDC effects were discovered in a double-metallocene molecule as a multidot system with molecular-level crossings [337]. In another study, Ouyang and Awschalom executed the chemical self-assembly approach to form multidot devices [338] containing a programmed sequence of CdSe quantum dots (QDs) connected by *p*-BDT molecular bridges. Using a femtosecond time-resolved Faraday rotation spectroscopy, the authors probed the spin transfer process through the π-conjugated molecular bridge, which proved that the process was coherent and that the bridging molecule functioned as a quantum-information bus. The primary advantage of these multidot devices is that the intrinsic properties of the SMMs can be preserved because the coupling between the SMMs and the quantum conductor is weak, potentially enabling a non-destructive readout of the spin states.

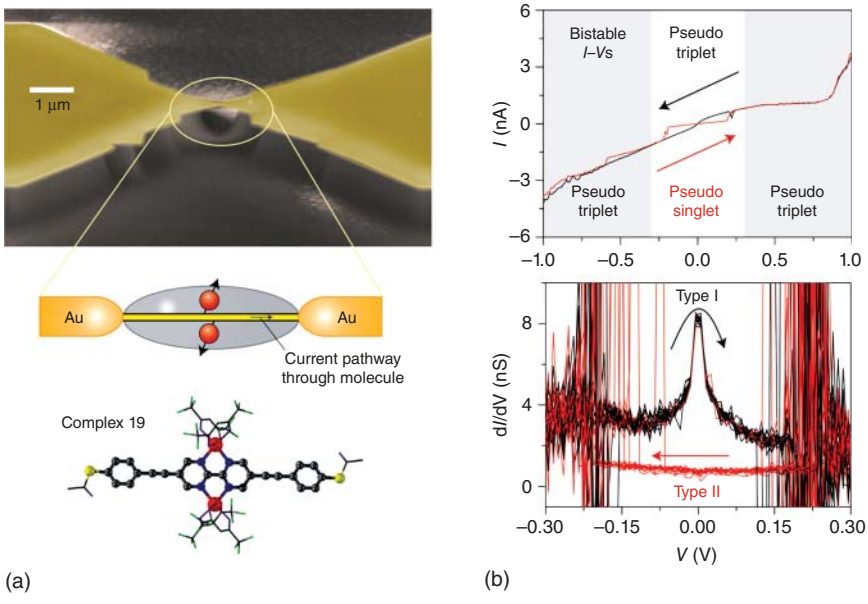

Figure 9.44 Switchable single-molecule spin devices created using the MCBJ technique. (a) Schematic of the experiment and molecular structure of complex 19. A molecule with a pair of spin centers is contacted in a single-molecule junction. The magnetic ion pair is attached orthogonally to the current pathway. (b) Bistable *I–V* characteristics due to the hysteresis of the coupled spin pair. Type I is a Kondo-like zero-bias anomaly; this is identified as the electrical fingerprint of the pseudo-triplet state. Type II is not a Kondo-like anomaly; this is assigned as the pseudo singlet. Source: Reprinted with permission from Wagner et al. [336]. Copyright 2013, Springer Nature.

9.5.4 Other Memory Devices

In some molecular cases, the energy barrier between binary states is relatively low. Thus, it is possible to drive a molecular switch by thermal excitation. Weigelt et al. reported a model thermally induced conformational molecular switch [339]. The 1,4-bis[(5-*tert*-butyl-3-formyl-4-hydroxyphenyl)ethynyl]benzene has been found that a spontaneous flipping of *t*-butyl groups occasionally occurred from one side of the molecular backbone to the other, from the time-lapse sequence of STM images. Their mechanism discussion demonstrated that the reported conformational changes of the 1,4-bis[(5-*tert*-butyl-3-formyl-4-hydroxyphenyl)ethynyl]benzene underwent a thermally induced process. However, the thermal induced switching was not very directional due to the relative low energy barrier.

Besides, there is only one memory device driven by pressure, in our knowledge so far. The pressure controlled bistable [2]rotaxane $R6101^{4+}$ was reported by Jeppesen and colleagues (Figure 9.45) [340]. It is too early to comment on the potential scope of pressure-driven memory device; however, this example presents the pressure sensitivity a promising new avenue of research.

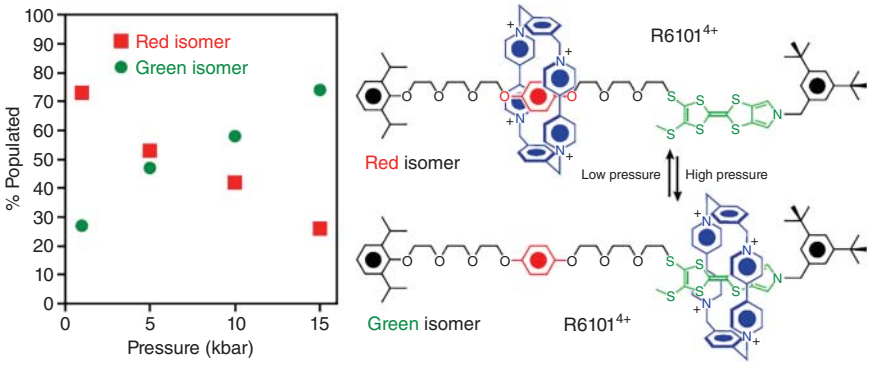

Figure 9.45 The ratio of red (ground-state co-conformation [GSCC]) and green (metastablestate co-conformation [MSCC]) co-conformers of R6101^{4+} is sensitive to pressure. Source: Reprinted with permission from Sørensen et al. [340]. Copyright 2013, The Royal Society of Chemistry.

9.6 Molecular Computing

For the sake of artificial "brains", we human beings keep challenging the limitation of the integrated circuits from silicon to carbon. By analogy to conventional microprocessors using elementary logic gates to construct electronic circuits capable of performing Boolean logic [341], the design of addressable molecular logic gates is a kernel task in this molecular computation. This emerging field is mainly building individual molecules that can perform functions identical or analogous to the key components of today's microcircuits, such as the transistors, diodes, and conductors. Yet, scientists proposed revolutionary advances within the past year. The recent advances were in molecular scale electronics. This short chapter illustrates the progress of the molecular logic systems.

9.6.1 DNA-Based Computing

Molecular computation contains a series of distinct bottom-up approaches toward molecular scale electronics, chemical and biological computers [295, 342–348]. DNA has been considered as a reliable media to construct molecular computer. DNA computing is pretty promising based on two fundamental features, the Watson–Crick complementarity and the parallelism of DNA strands. Watson–Crick complementarity is provided for free by the nature. DNA molecular consists of polymer chains, which composed of nucleotides. There are adenine (A), guanine (G), cytosine (C), and thymine (T), four bases correspond to four nucleotides. Different nucleotides differ only by the bases. The nucleotides in the same single strand via a phosphodiester bond. After that two single stranded nucleotides interact with each other to form hydrogen bonds. These bonds work according to the following restriction on the base pairing: A and T and C and G are capable to pair together – no other pairings are possible. This rule is known as Watson–Crick complementarity. The four

distinct nucleotides and these sequences are the answer of the diversity of lives encoded by Nature. The massive density of information stored in DNA strands and ease of constructing many copies of them is akin to cryptanalysis of a ciphertext, offering all possible solutions to figure out the intractable problems simultaneously. However, the ability to encode and solve computational problems by the Watson–Crick complementarity, called "hybridization logic," is not the only possibility of the DNA computation. Furthermore, with more complex structure of DNA polymer, the DNA computations can be loosely classified as "generative" and "subtractive." The generative ones usually operate with molecular biological hybridization, ligation, and amplification to build correct sequence solutions. On the other hand, the subtractive DNA computation operates conventionally via molecular biological hybridization, cleavage with endonucleases or RNase H, and amplification to remove incorrect sequence solutions from large solutions sets. Ghadiri and colleagues reported DNA photonic AND, NAND, and INHIBIT logic operations by using the recognition properties of DNA [349]. So far, most computational biological investigations concentrated on classic mathematical problems [347, 350].

In 1994, Adleman solved a non-deterministic polynomial-time complete (non-deterministic polynomial-time [NP] complete) problems, instances of Hamiltonian path problem (HPP) [351]. In Adleman's proposal, a set of "cities" and directed paths between the "cities" has been given. This HPP problem is trying to visit every city exactly once from a given city as the start and finish at another given city. The key to this answer is to find the appropriate solutions from all possibilities. For limited number of "cities" and limited solutions, the nowadays computation technique is able to solve it easily. However, with increasing the number of "cities" and solutions, the time for finding the solutions increases exponentially. Adleman proposed that the DNA computation can be scaled-up 10^{20} operations. Furthermore, a single molecule of adenosine triphosphate hydrolysis provides the Gibbs free energy for one ligation operation [351]. Herein, 1 J is sufficient for approximately more than 10^{19} operations. DNA computation is much more efficient than the computation ever. In Adleman's research, seven "cities" has been considered (Figure 9.46). To figure this HPP problem, the following algorithm is needed:

Step 1. To generate random paths through the "cities";
Step 2. Reserve the paths that start with V_{in} and end with V_{out};
Step 3. Keep only the paths through all vertices;
Step 4. Remove the paths which tour all vertices more than one time.

If any path remains, output is "Yes," otherwise is "No."

In terms of dealing the HPP with DNA computation, Adleman rational associated vertex *i* with a random 20-mer sequence of DNA denoted as O_i and each edge with other 20-mers. Based on the Watson–Crick complementarity, an oligonucleotide $O_{i\to j}$ was formed by each edge 3′ 10-mer of the vertex followed by the 5′ 10-mer of the edge. The mixing DNA has been denatured and annealed to form DNA molecule encoding random paths. The scale of ligation reaction is capable to form 10^{13} copies of the associated oligonucleotide, which is far exceeded for the necessary number. Next, the paths begin at V_{in}, end at V_{out} were amplified by the

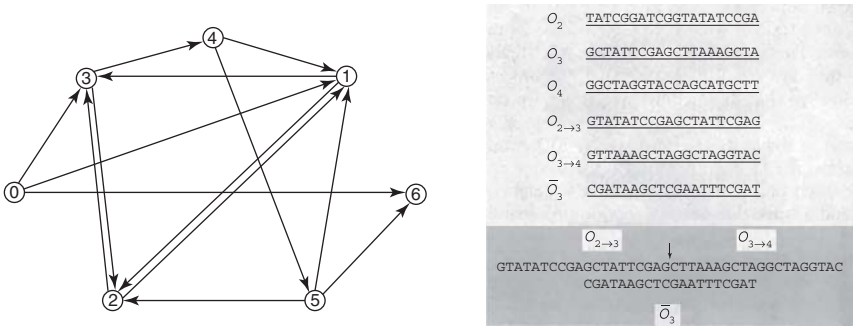

Figure 9.46 DNA computation. (a) Adleman's directed graph. When $V_{in} = 0$ and $V_{out} = 6$, a unique Hamiltonian path exists: $0 \to 1$, $1 \to 2$, $2 \to 3$, $3 \to 4$, $4 \to 5$, $5 \to 6$. (b) Encoding a graph in DNA. Source: Reprinted with permission from Adleman [351]. Copyright 1994, AAAS.

polymerase chain reaction (PCR). The untargeted paths will be removed from the 140-base pair (bp) band by agarose gel. Finally, the products were affinity-purified with a biotin–avidin magnetic beads system. These processes were repeated until figure out the Hamiltonian path evaluated by "graduated PCR." The whole experiments last seven days. This is the first biological experimental breakthrough of DNA computation.

After Adleman's work, the famous NP problem, such as the maximal clique problem [352], satisfiability problem (SAT problem) [352–355], has been investigated. Landweber expended the conception of the DNA computation with RNA solution for the Knight problem [356]. With decades of development, scientists concluded sticker model, splicing model, equality checking model for the molecular biology DNA computing operations. The Turing-like computational completeness of these models have been approved [357–360].

Although proponents believe the DNA an appropriate computational medium due to the lure of bypassing mathematical constraints for problems ranging from the basic two binary integers to the development of a working Turing machine [361, 362]. Currently, there are still challenges for DNA computing: (i) neither DNA nor RNA is recycling; (ii) accuracy is limited; and (iii) the operation takes too much time. Besides, they also suggested that the ultimate success of DNA computing relied heavily on the development of proper fabrication techniques [363].

9.6.2 Molecular Logic Gates

DNA computation gives us the fundamental conception of the artificial solution of the molecular computation. Almost at the same period in 1993, de Silva et al. reported the first molecular logic gate with more specific design with the molecule chemical structure [364]. Unlike the nature helix structure of DNA, the rational designed chemical molecular logic is much more purposeful, which can be decided by a small but extremely versatile toolbox of excited state processes.In a conventional computational idea operating based on silicon circuitry, the information has been coded following a binary system. Briefly, the binary

system allows the assignment of "true" and "false" to "1" and "0," respectively. When it goes to a molecular logic gate, the switches like what we discussed in Section 9.5 with binary states are promising, which also can be modulated chemically or physically to alter. The simplest logic gates have just one input and one output. As a matter of fact, the molecular logic gates are composed of a set of switches, which follow the Boolean logic (Figure 9.47). Therefore, here three kernel points should be noted in the design phase of the molecular logic gates: (i) the input and output for a better performance of the logic gates; (ii) the functional part, with reasonable switches; and (iii) the integration of separated switches for a given logic gates.

Although the input and output way have been reported by countless means after decades of great efforts, the optical outputs are still classical and crucial ones. Thereinto, PET [364, 366], internal charge transfer (ICT) [343, 367, 368], fluorescence resonance energy transfer (FRET) [369–371], proton transfer (PT) [372], and photochromic (PC) processes were utilized most commonly. de Silva and his first molecular logic gate works based on the PET mechanism, shown in Figure 9.48 [364, 373]. Their molecule structure was shown in Figure 9.48a, which comprises three functional moieties separated by spacers. They integrated the anthracenyl group as the fluorophore and crown ethers and amines as two separated receptors. The aromatic anthracenyl ring normally fluoresce blue under the UV light exposure; however, when the electron transfers to the anthracenyl group from either the N or O atoms of the receptors, the fluorescence quenched due to the PET process. As shown in Figure 9.48b, the amines and crown ether can interact with protons and sodium cations respectively. When the receptors are occupied, the PET process has been blocked. However, the amine group and crown ether parts contribute the same for the PET process. Thus, blocking only one receptor cannot stop the PET, the fluorescence quenching occurs. That is, both H^+ and Na^+ ions present, the electrons tied up binding ions, the PET is prevented, consequently, a strong fluorescence observed (Figure 9.48c). The overall result displays an AND logic operation. Based on this example, the general structure of PET pathway can be concluded as fluorophore–spacer–receptor. As a precondition, the free receptors should be redox-active. Classical molecular PET systems are linking the fluorophores to crown ethers, amines, or polyammonium, which can act as receptors for metal ions, hydrogen ions, and anions, respectively. In the following work, de Silva and colleagues reported a three-input AND gate based on the PET mechanism (Figure 9.48d) [366].

In 2000, de Silva and McClenaghan developed another molecular arithmetic through an intramolecular charge transfer (ICT) process [343]. In this case, they integrated the hydrogen receptor and calcium receptor shown in Figure 9.49a, and sandwiched a photoactive chromophore for separating the two chemical active receptors. The key of this system is the electron density of the chromophore. The presence of the electron-pulling and electron-pushing group at the both ends causes a shift of the electron density when excited. That results in a red or blue-shifting of the absorption band. The cases in Figure 9.49a is designed so that the quinolone nitrogen is the H^+ receptor and the aniline nitrogen is a part of the Ca^{2+} binding amino acid receptor. The H^+ addition results in a bathochromic shift while the Ca^{2+} introduction causes a

Input (A)	Output			
0	0	1	1	0
1	1	0	1	0
Name	YES	NOT	PASS 1	PASS 0
Symbol	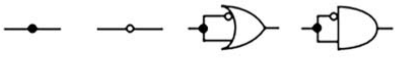			
Algebraic expression	A	$\overline{A}$	1	0

Input		Output						Output		Output	
(A)	(B)							(Carry)	(Sum)	(Borrow)	(Diff.)
0	0	0	0	0	0	1	1	0	0	0	0
0	1	0	1	1	1	0	0	0	1	1	1
1	0	0	1	0	1	0	0	0	1	0	1
1	1	1	1	0	0	1	0	1	0	0	0
Name		AND	OR	INH	XOR	XNOR	NOR	Half-adder		Half-subtractor	
Symbol		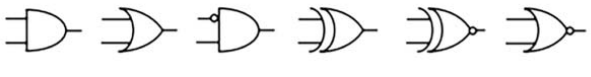						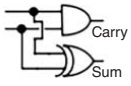		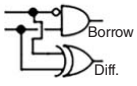	
Algebraic expression		$A \cdot B$	$A + B$	$\overline{A} \cdot B$	$A \cdot \overline{B} + \overline{A} \cdot B$	$\overline{A \cdot \overline{B} + \overline{A} \cdot B}$	$\overline{A + B}$				

Figure 9.47 Boolean binary logic operations: truth tables, symbols, and algebraic expressions. Source: Reprinted with permission from de Silva and Uchiyama [365]. Copyright 2007, Springer Nature.

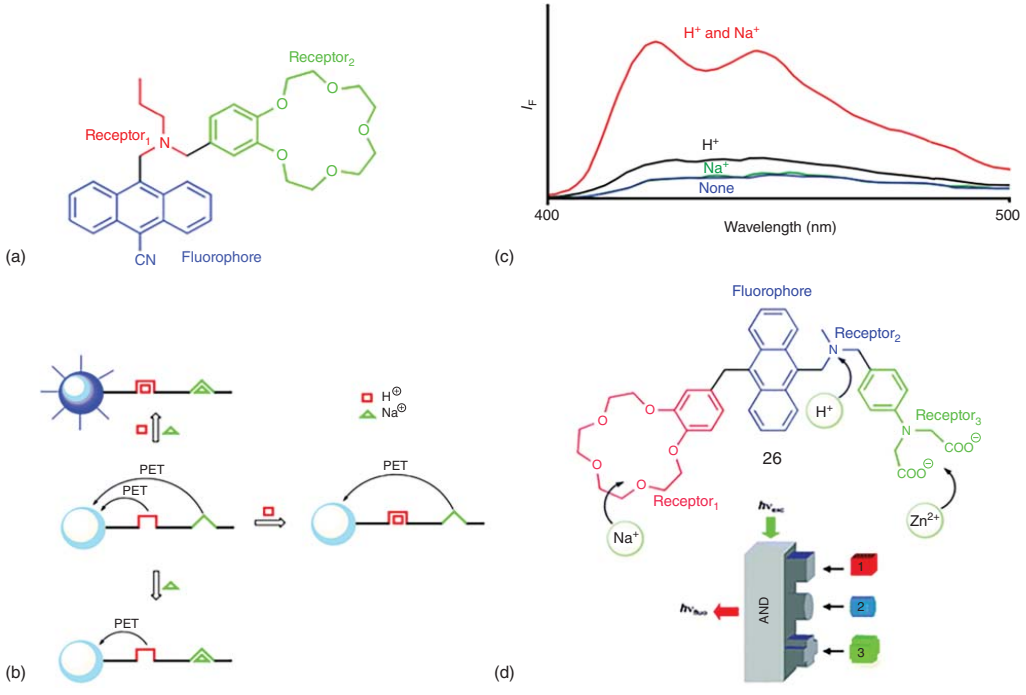

Figure 9.48 A molecular logic gate based on photoinduced electron transfer. (a, b) First molecular logic gate, mimicking an AND operation, and its photomechanistic working principle. Two chemical receptors (green) comprising an amine (receptor 1), which serves to bind H^+, and a benzocrown ether (receptor 2), which targets Na^+, are connected by hydrocarbon spacers (red) to each other and to a cyanoanthracene dye (blue) – a fluorophore that absorbs and emits light. The "fluorophore–spacer 1–receptor 1–spacer 2–receptor 2" system has two possible paths of transferring an electron to the excited fluorophore: only one from each unoccupied receptor could result in quenching of the fluorescence. (c) Fluorescence emission spectroscopy of molecule shown in (a). (d) Three-input molecular logic AND gate. Source: Reprinted with permission from de Silva et al. [364] and Andréasson and Pischel [373]. Copyright 2010, The Royal Society of Chemistry.

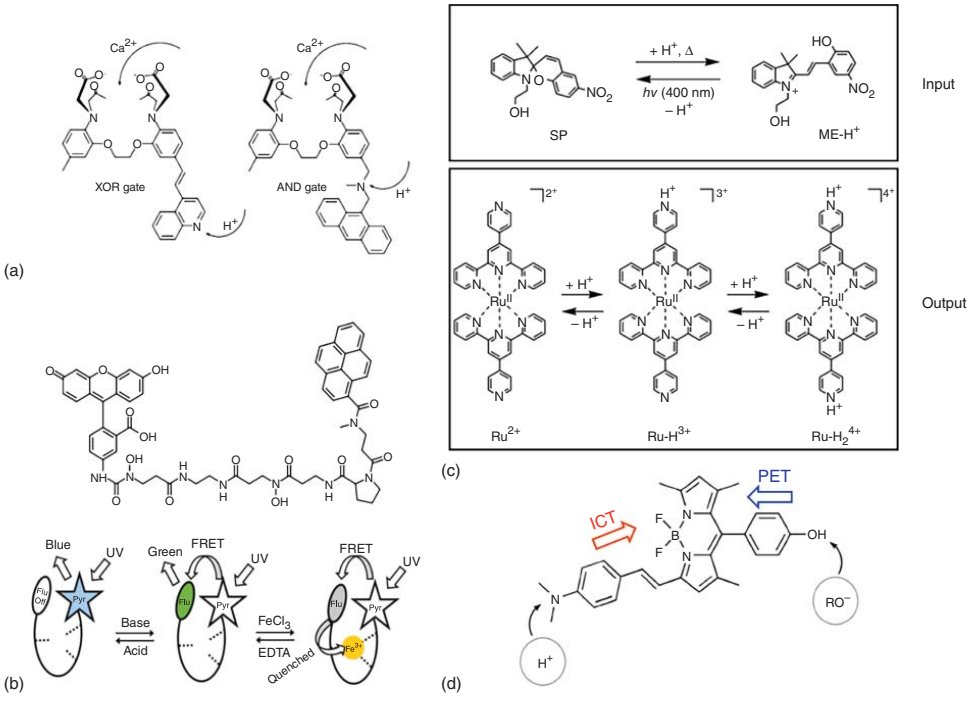

Figure 9.49 Illustration of chemical logic gates. (a) Molecular structures of the XOR and AND gate. Source: (a) Reproduced with permission from de Silva and McClenaghan [343]. Copyright 2000, American Chemical Society. (b) Molecular structure that can operate as a half-adder and half-subtractor depending on the choice of inputs and outputs and three different fluorescence states of the molecular logic gate. Source: (b) Reproduced with permission from Margulies et al. [371]. Copyright 2004, American Chemical Society. (c) Communication between molecular switches through proton transfer, involving a spiropyran photochrome and a Ru(II) polypyridyl complex with pH-dependent luminescence output. Source: (c) Reproduced with permission from Margulies et al. [371]. Copyright 2009, Wiley & Sons (d) A XOR molecular logic gates. Source: (d) Reproduced with permission from Coskun et al. [374]. Copyright 2005, American Chemical Society.

hypochromic shift by an ICT process. When both the protonation and Ca^{2+} are present, the contribution to the electron density of the excited chromophore offsets, yielding the absorption unchanged. This modulation operated as an XOR behavior. Similarly, the molecule in Figure 9.49a is an AND logic. The FRET process is another most investigated mechanism for the molecular logic gates. In 2004, Shanzer and colleagues reported a molecular half-adder gate and a half-subtractor with the same structure but different chemical inputs and distinguished fluorescence outputs [371]. The molecular structure displayed in Figure 9.49b, whose fluorescence output is modulated by the FRET process. When the fluorescent pyrene irradiated under acidic conditions leading to a blue emission at 390 nm, the FRET is OFF. On the other hand, when at a higher pH, the FRET takes place so that green emission is observed at 525 nm. Interestingly, when Fe(III) is present, the FRET weakens. However, the iron quenching is dependent on pH. Totally, a half-subtractor logic operation can be detected with the Fe-complex blue and green emission modulated by acid and base inputs. Also, the same structure can work as a half-adder by changing the acid input into an ethylenediaminetetraacetic acid (EDTA). Raymo and colleagues explored a spiropyran–merocynine system, which can release or capture proton involved in the PC process [372]. The photochrome process operates depending on the protonation of the Ru(II) complex (Figure 9.49c). The luminescence output varies in presence of changeable acid–base conditions. Besides, the multi-mechanisms can be utilized in the same molecular logic gates (Figure 9.49d) [374]. Of note, the systems described earlier constitute elegant examples for chemical communication between molecular switches.

With ingenious integration of molecular switches, the scientific community created a series of molecular logic gates, which is mimic of silicon-based computing applications [366, 375–379]. The molecular computing is the first step of realizing the functions and integration of the molecular logic toward real applications in the future.

9.7 Transduction Toward Molecular Sensors

A sensor can be generally defined as a transductor that is able to reflect the specific presence of an invisible event or substance by using certain types of signals with clear resolution. Based on this definition, electrical sensors imply that the detection of targets can be read through the electrical current. In fact, various types of electrical sensors have been created by taking advantage of the relationship between the conductance of the sensing centers and their interaction with external targets over the years, which provides a convenience and improvement for several fields, including disease diagnosis, food security, and environment monitoring. Compared with conventional sensors that are based on optical, chemical, or physical methods, such as fluorescence/Raman spectroscopies, PCR and enzyme-linked immunosorbent assays (ELISAs), electrical sensors are complementary but still offer unique advantages, such as simplicity, low cost, portability, ultrahigh sensitivity, excellent selectivity, and label-free real-time electrical detection, in a non-destructive manner [380–387].

Driven by the digitalization and informalization of contemporary society, electrical sensors are leading toward structural minimization, functional intelligentialization and highly detecting resolution, which constitutes an important branch of molecular electronics, i.e. molecular sensors. Instead of the average properties of large numbers of molecules being detected by conventional electrical sensors based on nanomaterials, such as CNTs, nanowires, nanopores, nanoclusters, or graphene, the molecular sensors discussed here have the capability of probing the complex behaviors of targets at the molecular level and consequently providing new opportunities to uncover the wealth of molecular information that is typically hidden in conventional ensemble experiments. It should be noted that probing the interaction of individual molecules could address the "unanswerable" questions in the physical, chemical, and biological sciences, which is meaningful for understanding the fundamental scientific essence and developing accurate molecular diagnosis in the biological regime [388]. Promoted by the significance of molecular detection as well as the continuous and diligent efforts, various electrical sensors have been developed for capturing the minimum events, thus displaying a great potential to excavate the "elementary information." In fact, the burgeoning development of standard wafer-scale semiconductor processing techniques, especially the construction of molecular devices, provides the feasibility of molecular sensing, which is driving the field to move from fundamental problems toward practical biosensors. In this section, we review the primary advances of single-molecule sensors in three regimes: chemical reaction, biological interaction, and thermoelectricity, focusing on studies that use single molecules as the core component. Here, the operation principles of electrical sensing and the primary strategies for enhancing their performance are discussed, in addition to key challenges and opportunities in current stages and further development.

9.7.1 Sensing Based on Chemical Reactions

Generally, chemical reactions are responsible for most of the changes in nature. The establishment of understanding and controllability for these chemical reactions, which are embodied in mature methods based on kinetic and thermodynamic investigations, is of crucial importance in both basic science and industry communities. Particularly, incorporating the paradigms of reaction chemistry into the design of molecular electronic components can provide a tremendous impetus to advance the field of molecular electronics. In fact, the development of deeper insight into chemical reactions, especially for the interaction between two reactants at the single-molecule level essential in chemical reactions, leads to creating various sensors with high selectivity and extreme sensitivity and clarifies previously indecipherable intrinsic reaction mechanisms. As detailed in Section 9.5, chemical principles such as photocyclization, tautomerization, and redox reaction have inspired the genesis of several new types of molecular electronic switches. In this section, we highlight the chemical principles and strategies used to develop functional single-molecule chemical sensors.

The manipulation of molecular reactions remains a formidable challenge. To address this problem, we first chose a photoreactive DAE as a functional central component. DAE is a typical photochromic molecule that can exist in the form of two (open- and closed-configuration) isomers interconverted via irradiation with UV–Vis light. However, in previous works, only one-way photoswitching have been achieved in the nanocarbon electrode-based electrical detection platform because of the strong coupling between molecules and electrodes at the contact interface induced by covalent amide bonds [148, 306]. This coupling gives rise to energy transfer between the molecular excited state and the π-electron system of carbon electrodes, which facilitates the quenching of the former and highlights the importance of the molecule–electrode contact interface, the most challenging issue that hampers the measurement of intrinsic molecular properties. To overcome this problem, Guo and colleagues introduced three methylene (CH_2) groups on each side of the molecular backbone to weaken the molecule–electrode coupling without affecting molecular conductivity (Figure 9.50a) [141] and covalently sandwiched a single DAE between graphene point contacts to form a reversible molecular photoswitch. The reversible photoswitching of DAE driven by UV–Vis light irradiation was confirmed by real-time electrical detection (Figure 9.50b). DAE open and closed states corresponded to different current levels with good stability (over a year) and an unprecedented level of accuracy (ON/OFF ratio ≈ 100) and reproducibility, as demonstrated by the analysis of 46 different devices. Remarkably, this is the first example of a fully reversible, bimodal, single-molecule electrical switch achieved by exquisite control over matter through intellectual pursuit.

In another interesting experiment, a reversible, reproducible AB-based single-molecule photoswitch by making use of light- and electrical field-driven *cis–trans* isomerization has been focused. Specifically, an AB molecular bridge was covalently incorporated between nanogapped graphene electrodes through amide linkage formation (Figure 9.50c) [389]. To avoid the quenching of the molecular excited state, the AB moiety was introduced as the side chain of the molecular bridge, while backbone CH_2 groups were replaced by benzene rings to enhance charge transport. Both experimental and theoretical investigations demonstrated that the switching behavior could be easily detected under different source–drain biases (Figure 9.50d) or at low-bias voltages under alternate UV–Vis light irradiation (Figure 9.50e) through efficient side-group chemical gating. This concept of *in situ* chemical gating offers a fresh perspective for creating future multifunctional single-molecule optoelectronic devices in a practical way. In addition, these results clearly demonstrate the possibility of visualizing the dynamic details of chemical reaction processes through sophisticated molecular design and engineering.

In order to explore the capability of molecular devices to detect the dynamic details of chemical reaction processes, a standard nucleophilic substitution (S_N1) reaction, one of the most fundamental reactions in organic chemistry, has been investigated as a proof of concept. In general, as rate-determining intermediates, carbocations have very short lifetimes and are therefore difficult to detect and manipulate. Guo and colleagues used the high temporal

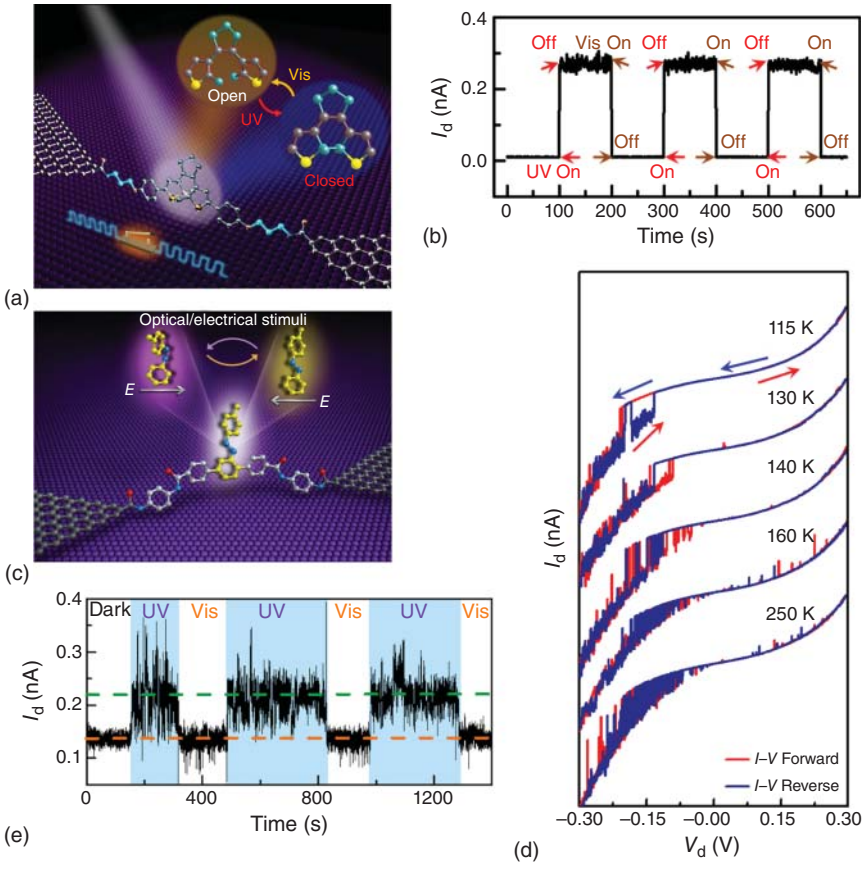

Figure 9.50 Photochromism. (a) Schematics of a single-DAE graphene-molecule-graphene single molecular junction (GMG–SMJ) device fabricated to achieve reversible photocyclization. (b) *I–t* curve of the device in (a) recorded under alternate irradiation with UV and visible light. Source: (b) Reproduced with permission from Jia et al. [141]. Copyright 2016, AAAS. (c) Schematics of a single-azobenzene GMG–SMJ device fabricated to achieve reversible photoisomerization. (d) *I–V* curves of the device in (c) recorded at different temperatures and source–drain biases. (e) *I–t* curve of the device in (c) recorded under alternate irradiation with UV and visible light at $V_{bias} = 10$ mV. Source: (e) Reproduced with permission from Meng et al. [389]. Copyright 2019, Springer Nature Limited.

resolution of electrical detection (micro- or nanoseconds) to investigate an S_N1 reaction by label-free, real-time single-molecule electrical measurements [390]. A 9-phenyl-9-fluorenol functional center integrated into graphene electrodes through amide bonds (Figure 9.51a) underwent reversible transitions between the acetate (Ac) and carbocation forms during controlled acidity experiments (different acetic acid (HAc)/trifluoroacetic acid (TFA) ratios were used), which gave rise to repeated fluctuations between low- and high-current states in *I–t* plots (Figure 9.51b). The high-current state was ascribed to the carbocation form because of its higher extent of conjugation due to the transition of the central carbon atom from sp^3 to sp^2 hybridization, in agreement with the results of

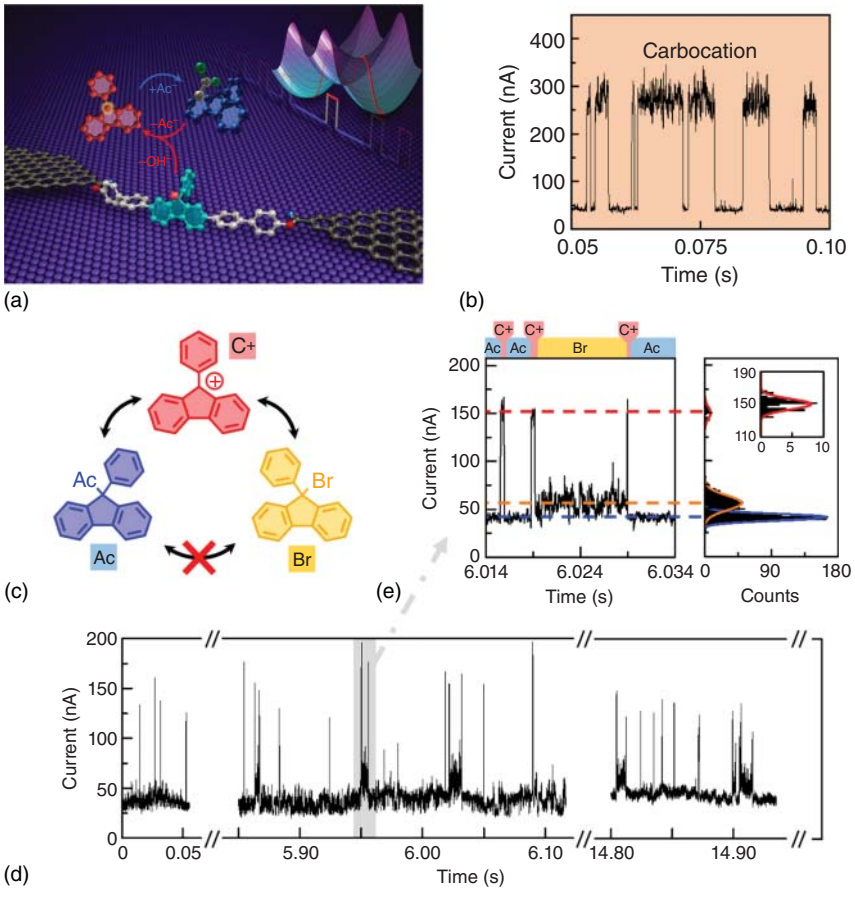

Figure 9.51 S_N1 reaction dynamics. (a) Schematics of a single 9-phenyl-9-fluorenol-based device used to detect the S_N1 reaction. (b) *I–t* curve indicating carbocation formation in the presence of TFA/HAc (3 : 1, v/v). (c) Schematics of competitive carbocation reactions with Ac^- and Br^-. (d, e) Representative *I–t* trajectories and corresponding enlarged views (TFA/HAc (3 : 1, v/v); 10 μM Br^-). Ac, Br, and C^+ represent the acetate form, the bromide form, and the carbocation form, respectively. V_{bias} = 300 mV. Source: Reproduced with permission from Gu et al. [390]. Copyright 2018, American Chemical Society.

theoretical calculations. Upon the subsequent introduction of Br^-, a third state with medium conductance was observed and ascribed to the formation of the bromide form (Figure 9.51c,e). Interestingly, all transitions from Ac to Br forms involved the formation of a high-conductance state, i.e. the competitive S_N1 reaction between acetate and bromide occurred via an inevitable carbocation intermediate (Figure 9.51c). After careful idealization of acidity-dependent *I–t* curves, the dynamic parameters of transitions between carbocation and nucleophilic substitutes were obtained, which were consistent with those obtained in ensemble experiments. Thus, these results established the reliability of the molecular electronics platform and demonstrated its suitability for the analysis of more complex reaction systems.

In comparison with the nucleophilic substitution reaction, the nucleophilic addition reaction has a more complex mechanism, which has been probed next. Previous works proved that the nucleophilic addition of NH_2OH to 9-fluorenone generally takes thousands of hours, and the final elimination product is obtained with great difficulty, which allows one to investigate the reaction mechanism without confusing the addition intermediate with the final product. Analogously, 9-fluorenone was incorporated between the graphene pointed electrodes using amide linkages [391], and the carbonyl group of 9-fluorenone was reacted with NH_2OH through nucleophilic addition (Figure 9.52a). By monitoring the current change as a function of time, we observed distinct binary conductance states (Figure 9.52b,c). According to theoretical calculations, the high-current state was ascribed to 9-fluorenone, while the low-current state was attributed to the addition intermediate. The decrease of current upon nucleophilic addition was

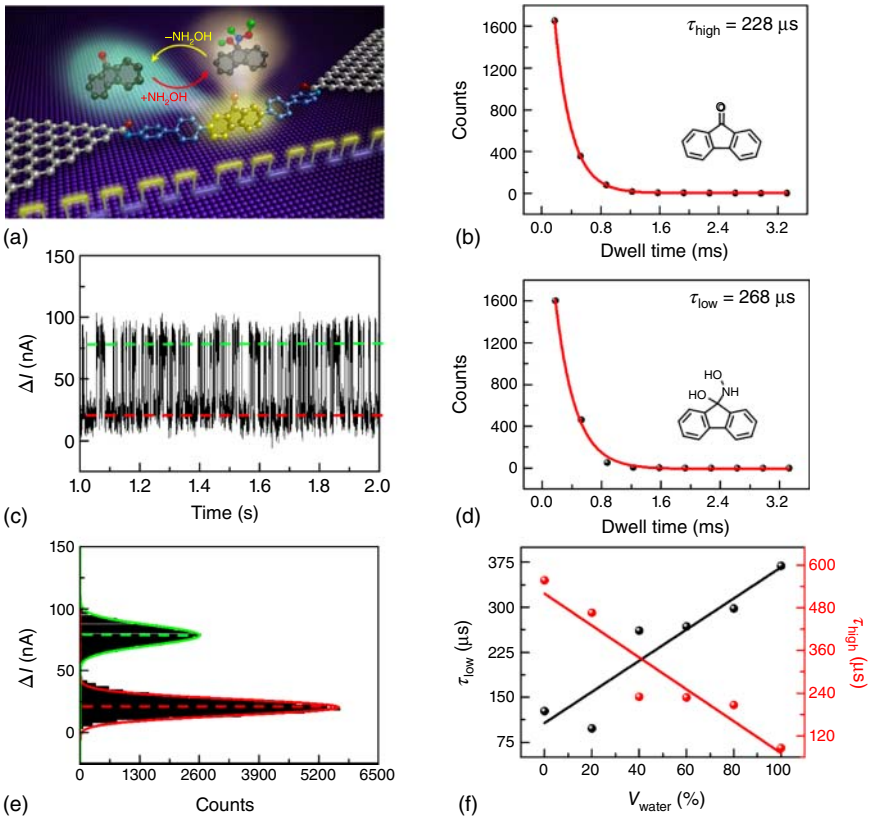

Figure 9.52 Nucleophilic addition reaction dynamics. (a) Schematics of a single 9-fluorenone molecule-based device used to detect the nucleophilic addition reaction. (b, c) *I–V* curve and corresponding histogram of current values showing a distinct bimodal current distribution. $V_{bias} = 300$ mV. (d, e) Plots of time intervals used to determine the lifetimes of each state (intermediate: τ_{low}, substrate: τ_{high}) (60% water in EtOH at 298 K). (f) Lifetimes of the low- (intermediate: black) and high-current states (substrate: red) as functions of water content. Source: Reproduced with permission from Guan et al. [391]. Copyright 2018, AAAS.

rationalized by the concomitant transition of the central carbon atom from sp^2 to sp^3 hybridization (opposite to the carbocation case) and demonstrated the successful capture of a new addition intermediate, as predicted. Furthermore, the solvent polarity-dependent experiments to systematically analyze the dwell times of the substrate (τ_{high}) and the intermediate (τ_{low}) (Figure 9.52d,e), revealing that the intermediate stability increased with solvent polarity, as the intermediate was more polar than the substrate. Correspondingly, with increasing the solvent polarity, the equilibrium position shifted to the side of the intermediate (Figure 9.52f), in agreement with the results of ensemble experiments. Thus, this study presents a powerful and elegant combination of molecular electronics, quantum chemistry, and single-molecule physics, providing a textbook-like clarity.

The essence of a chemical reaction is the vibrational rupture and generation of chemical bonds between atoms. Therefore, the different vibration states of a molecule should inevitably impact the dynamics of a chemical reaction. Vibration or rotation of functional groups could cause changes in molecular conjugation and thus the electronic structure. The scientific community are curious about whether these tiny changes lead to different conductivities [27, 285]. By exploiting the good stability of the graphene-molecule-graphene single molecular junction (GMG-SMJ) electrical detection platform, we have previously established a reversible bimodal single-molecule photoswitch based on individual DAEs. Notably, reproducible stochastic switching of the closed junction between two conductive modes was observed in a DAE system during systematical measurements at low temperatures, as demonstrated by I–V (Figure 9.53a) and I–t (Figure 9.53b) curves. This surprising finding was attributed to a DAE conformational change such as rotation around the σ bond between thiophene and benzene rings in the closed DAE form. Inspired by this hypothesis, the stereoelectronic effects in a specifically designed hexaphenyl aromatic chain has been investigated, where the central biphenyl was introduced in a fluorene form to fix the dihedral angle. In a similar approach, an amine-terminated hexaphenyl aromatic chain was sandwiched between carboxylic acid-terminated graphene electrodes to disclose single-molecule charge transport properties (Figure 9.53c) [392]. In temperature-dependent experiments, we did observe a similar stochastic switching of conductance in the temperature range of 120–140 K (Figure 9.53d). According to theoretical calculations, this stochastic switching originated from rotation around the σ bond between biphenyl rings to alternately form strongly and weakly conjugated states, which proved the correctness of the above hypothesis. Thus, the switching of conductance originated from a typical stereoelectronic effect that is ubiquitous in organic chemistry, which offered a fresh perspective for revealing structures–property relationships and constructing future functional molecular electronic devices on the sophisticated platform of GMG–SMJs.

9.7.2 Sensing Based on Biological Interactions

A key goal of modern bioscience is to monitor biomolecular interactions with high sensitivity and high selectivity in real time, with the ultimate aim of detecting

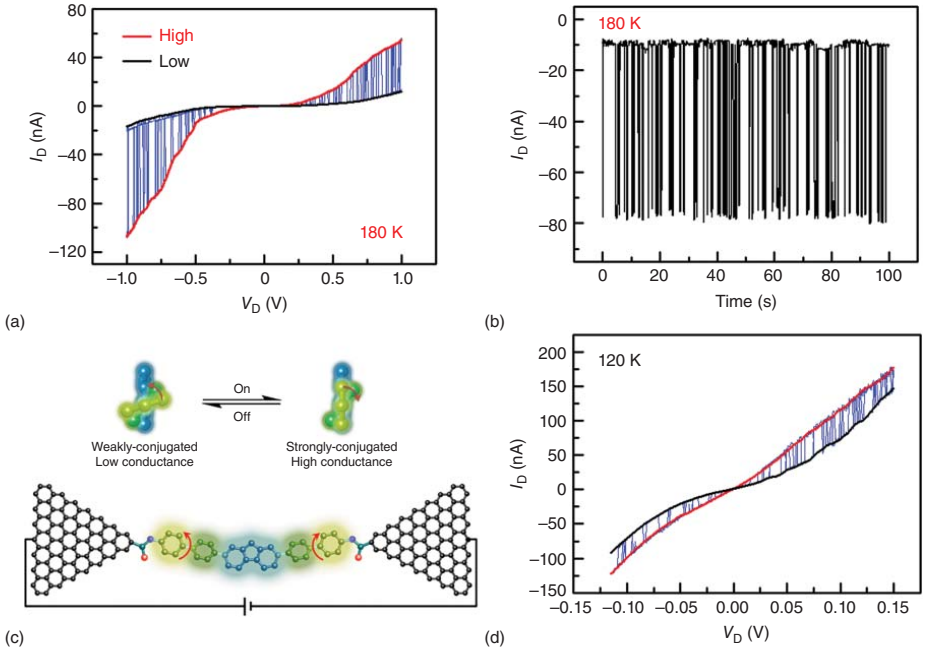

Figure 9.53 Stereoelectronic effect. (a) Stochastic switching between two conductive states of individual closed DAEs at 180 K. (b) Corresponding real-time recording of stochastic conductance switching at 180 K. $V_{bias} = -800$ mV. Source: (b) Reproduced with permission from Jia et al. [141]. Copyright 2016, AAAS. (c) Schematics of a single-molecule hexaphenyl aromatic device. (d) *I–V* curves of the device in (c) recorded at 120 K and showing similar stochastic switching. Source: (c) Reproduced with permission from Xin et al. [392]. Copyright 2017, American Chemical Society.

single-molecule events in natural samples. Directly probing the *in situ* activities of biological species at the single-molecule level can provide access to uncovering the incredible wealth of molecular information that is typically hidden in conventional ensemble experiments and addressing the previously "unanswerable" questions. Therefore, establishing a practical platform for achieving this goal is clearly of great importance to fundamental biology, diagnosis, and drug discovery. In this section, we review the recent progress of a system of single-molecule electrical biosensors, with a particular focus on those based on nanocarbon-based electrode-molecule single-molecule junction and silicon nanowire-based platforms [382, 384, 385, 393–395].

9.7.2.1 Nanocarbon-Based Molecular Electronics

Among the different molecular junction platforms, as detailed in Sections 9.2–9.4, single-molecule devices formed from the carbon electrode-molecule molecular junction platform are particularly appealing because they are synthesized through covalent amide bonds, thus significantly improving the device stability. Therefore, these devices are sufficiently robust to endure a wide range of chemistries and conditions, even in aqueous environments. Another unique feature of these devices is that they consist of one or two (at most) molecules as conductive elements. Because the current flow traverses a single molecule, the devices are sensitive to the local configuration and environment around the bridging molecule. In combination with their high stability, they have a great potential for further applications in building ultrasensitive functional optoelectronic devices and new classes of chemo/biosensors with single-molecule sensitivity.

Several approaches involve in fabrication of molecular electronics, one of which a non-covalent bioconjugation strategy has been reported by Philip Collin's group in 2012, rather than introducing a point defect, tailoring its chemistry, and then conjugating the damaged site to the molecules of interest [384]. They developed a non-covalent immobilization method based on pyrene linkers, which provided dilute anchor points for subsequent derivatization of the nanotube surface (Figure 9.54a). The pyrene attached to SWCNT through π–π stacking. In their particular implementation, the target protein was covalently conjugated to the pyrene-maleimide anchor site via a thiol from a single cysteine. Figure 9.54a displays a single lysozyme interrogated by a carbon nanocircuit. The AFM image experimentally confirmed the adhesion of the lysozyme on the SWCNT (Figure 9.54b). By monitoring the *I*–*t* plots of an SWCNT–FET, they demonstrated that the dynamics of a single T4 lysosome hydrolyzed the glycosidic bond. Specifically, 100 glycosidic bonds are hydrolyzed processively at a 15-Hz rate, before lysozyme returns to its nonproductive, 330-Hz hinge motion. Further statistical analysis suggested the single-step hinge closure from enzyme opening, actually calls for two steps. With the pyrene linker and π–π stacking strategy for attaching the biomolecules of interest onto SWCNT–FETs, the authors investigated the dynamics of homopolymeric process of the single DNA polymerase I (Klenow fragment) and single-molecule catalysis by cAMP-dependent protein kinase A [397, 398].

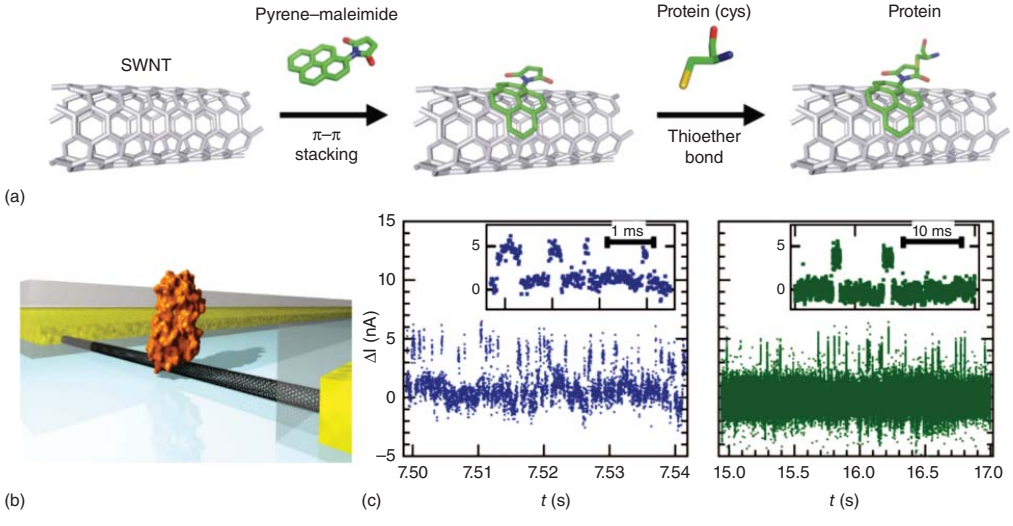

Figure 9.54 SWCNT-FET-based single-molecule technique. (a) Strategy used for adhering biomolecules to the SWCNT by using a pyrene–maleimide linker, providing reactive sites for protein attachment. Source: Reproduced with permission from Choi et al. [396]. Copyright 2009, American Physical Society. (b) Schematic diagram of the single lysozyme being interrogated by a carbon nanocircuit. The partial poly(methyl methacrylate) coating is depicted in gray. (c) The faster (blue) and slower (green) current oscillates. The insets show individual switching events for each case. Source: Reproduced with permission from Choi et al. [384]. Copyright 2012, AAAS.

Another strategy of nanocarbon molecular devices toward biosensing, Guo et al. [399] developed a proof-of-principle strategy for realizing single-molecule biodetection based on carbon electrode-molecule single-molecule junctions by combining programmed chemical reactivity and directed biological self-assembly (Figure 9.55a). In this study, they used a molecular wire with a ketone sidearm (diaminofluorenone) to bridge SWCNT point contacts. Then, they demonstrated the capability of electrically sensing the oxime formation on the molecular bridge using a biochemical probe molecule and further monitoring the non-covalent binding between the probe and the protein (Figure 9.55b,c). Furthermore, the use of a biological assembly was demonstrated to localize individual nanoparticles at the molecular bridge, thus providing a method to sense the biological process at the single-event level.

Following this approach, one further primary effort is to integrate DNAs into electrical circuits [98, 102, 400] because DNA molecules bridging nanodevices could serve as powerful reporters to transduce biochemical events into electrical signals at the single-molecule level. Thus, a general method was described to incorporate DNA strands between the SWCNT electrodes and measure their electrical properties. The statistical results demonstrated that the well-matched duplex DNA in the gap between the electrodes exhibited a resistance of approximately 1 MΩ, which is comparable with the bulk c-axis resistance of highly oriented pyrolytic graphite (HOPG) with similar dimensions, and a single GT or CA mismatch in a DNA 15-mer increased the resistance of the duplex ~300-fold relative to that of a well-matched one. More importantly, when certain DNA sequences, which are substrates for *Alu I*, i.e. a blunt end restriction enzyme, were oriented within this gap, this enzyme sliced the DNA and eliminated the conductive path. This result is valuable because it supports the supposition that the DNA retains its native conformation and the corresponding biological activity when sandwiched between the SWCNT point contacts, thus setting the foundation for developing future DNA-based molecular biosensors. This conclusion was further strengthened by the study performed by Wang et al. [401], where they reported a molecular-scale electrical device that could sense an individual reaction between a DNA duplex and a methyltransferase enzyme. The methyltransferase M.SssI can specifically and reversibly bind the sequence 5′-CG-3′ and, in the presence of the cofactor *S*-adenosyl methionine, catalyze the complete rotation of the cytosine base out of the π-stacked core of the DNA duplex (referred to as base flipping) followed by methylation, thus leading to an interruption of the charge transport.

Inspired by the aforementioned studies, Guo and colleagues created an integrated system that could achieve rapid real-time measurements with single-molecule sensitivity [102]. In this study, individual metallo-DNA aptamers, which could selectively and reversibly interact with a target protein thrombin, were used to react with SWCNT point contacts to form stable molecular devices (Figure 9.56a). After treatment with thrombin, these single-molecule devices depicted a consistent conductance increase (Figure 9.56b). This change results from enhanced DNA charge transfer because of the rigidification of the DNA conformation due to the DNA–thrombin interactions. To achieve a real-time measurement, an integrated SWCNT transistor array was designed and fabricated (Figure 9.56c). Combining this pattern with microfluidics led

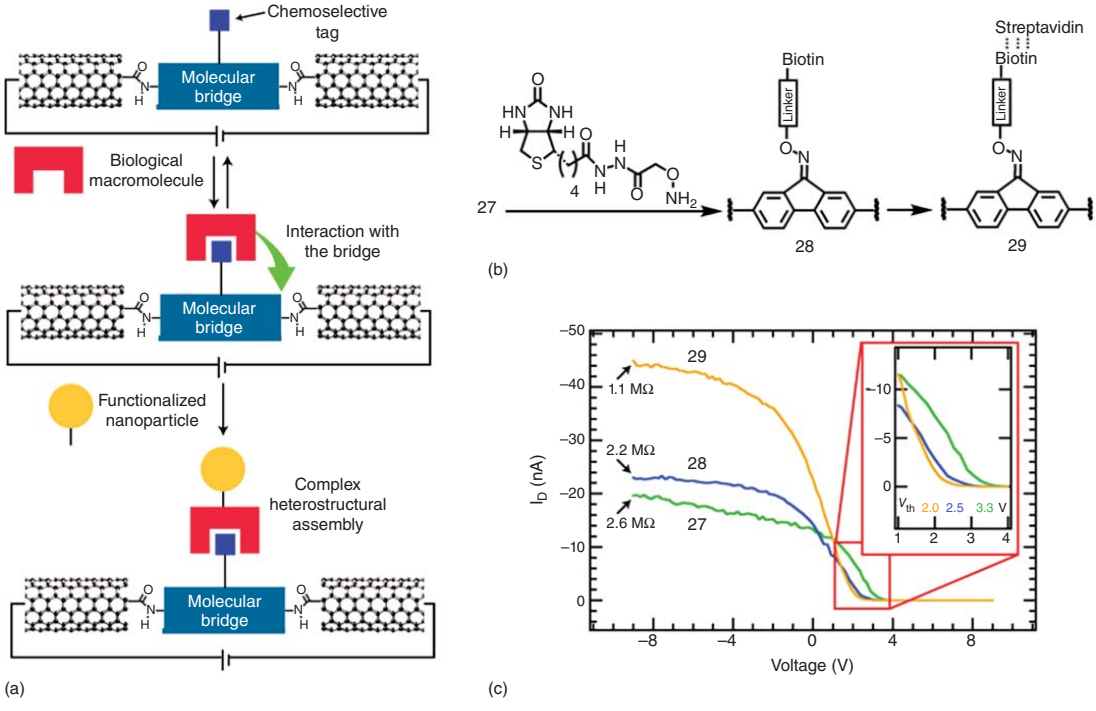

Figure 9.55 Proof-of-principle strategy for single-molecule biodetection. (a) Schematic depicting the use of single-molecule electronic devices as scaffolding for the assembly of biological macromolecules and complex, multimeric assemblies. (b) Reaction sequence, where a fluorenone (**27**) is condensed with a biotin derivative that bears an alkoxyamine to form an oxime (**28**) on the molecular bridge. The derivatized bridge is then able to bind streptavidin to form non-covalent complex (**29**). (c) Current–voltage characteristics, which depict the gate voltage versus the drain current at a constant source–drain voltage for each step in the reaction sequence. Source: Reprinted with permission from Guo et al. [399]. Copyright 2007, American Chemical Society.

to detecting protein and monitoring stochastic DNA–protein interactions in real time (Figure 9.56d). Reversible and consistent conductance changes at different thrombin concentrations without a concentration dependence (from 2.6 fM to 2.6 pM and 2.6 nM) were observed, therefore demonstrating the reproducibility and single-molecule sensitivity. These results distinguished this method as a unique platform to achieve real-time, label-free, reversible detection of DNA–protein interactions and enzymatic activity with high selectivity and actual single-molecule sensitivity. Compared with more conventional optical techniques, this nanocircuit-based architecture is complementary with clear advantages, such as no bleaching issues and no fluorescent labeling, which are of crucial importance for future single-molecule biodetection.

Analogously, the amide linkage strategy is reliable and proven by another study, where the capability of controlling the conductivity of individual DNAs was demonstrated by using coordination chemistry [103]. Briefly, the carbon nanoelectrodes were bridged by single ODN-H1 (Figure 9.56) by using amide linkages to form single DNA molecular devices. Similarly, it was determined that the electrical properties of these devices can be efficiently switched ON and OFF by sequentially alternating treatments with the EDTA and the Cu^{2+} ions. This is because sequential treatments with the EDTA and Cu^{2+} formed metal-free or metallo DNA structures, respectively, which have different electronic structures and different conductance. The sensing property of these devices is reproducible because a similar phenomenon was observed using different metal ions, such as Ni^{2+} and Fe^{3+}. Among these metal ions, Fe^{3+} had the best reversibility. The proven switching reproducibility and reversibility of the single-molecule devices bridged by metallo-DNAs form the basis for new types of molecular switches and chemical sensors.

Subsequently, a further step toward molecular chemical sensors by constructing a platform that integrated a Cu^{2+}-dependent DNAzyme into graphene–molecule junctions, which was capable of directly detecting paramagnetic Cu^{2+} with femtomolar sensitivity and high selectivity, has been reported (Figure 9.57a) [402]. DNAzymes belong to a type of DNA-based biocatalysts with the ability to perform chemical and biological reactions in the presence of specific metal ions. In this study, Guo and colleagues designed a Cu^{2+} electrical sensor consisting of a DNA substrate strand with amines on both ends for connecting to the graphene–molecule junctions as well as an enzyme strand that could hybridize to the substrate strand through two base-pairing regions (Figure 9.57a). The sensing principle is that Cu^{2+} could recognize and then bind with the specific site in the DNAzyme sequence, followed by the cleavage reaction that thus destroyed the conducting pathway (Figure 9.57b). The contribution of this study could be summarized from three aspects: (i) ultralow sensitivity with the femtomolar level due to the single-molecule sensing component (Figure 9.57c); (ii) high selectivity resulting from the specific biological catalysts, as demonstrated by a series of control experiments using different metals (Figure 9.57d); and (iii) potential universality for other metal-ion sensors because various types of DNAzymes specific for different ions are available.

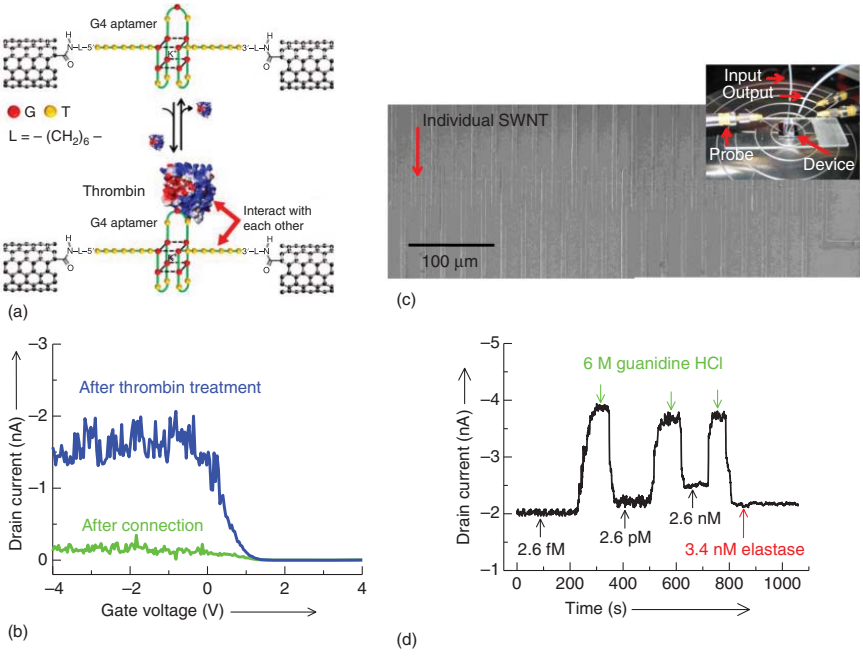

Figure 9.56 Real-time, label-free, reversible detection of DNA–protein interactions. (a) Schematic representation of the sensing mechanism, which indicates how single-molecule devices can detect proteins at the single-molecule level. (b) Device characteristics of a device rejoined by individual DNAs after DNA connection (green) and further treatment with thrombin (blue). (c) SEM images, which depicts a highly integrated identical SWCNT device array. The inset depicts an optical image of a single-molecule device during real-time measurements. (d) Current-versus-time data recorded for an aptamer-rejoined device upon alternate additions of the thrombin tris-HCl buffer solution at different concentrations (from 2.6 fm to 2.6 pm and 2.6 nm), a 6 m guanidine HCl solution, and an elastase (3.4 nm) tris-HCl buffer solution. Source: Reprinted with permission from Liu et al. [102]. Copyright 2004, Wiley-VCH.

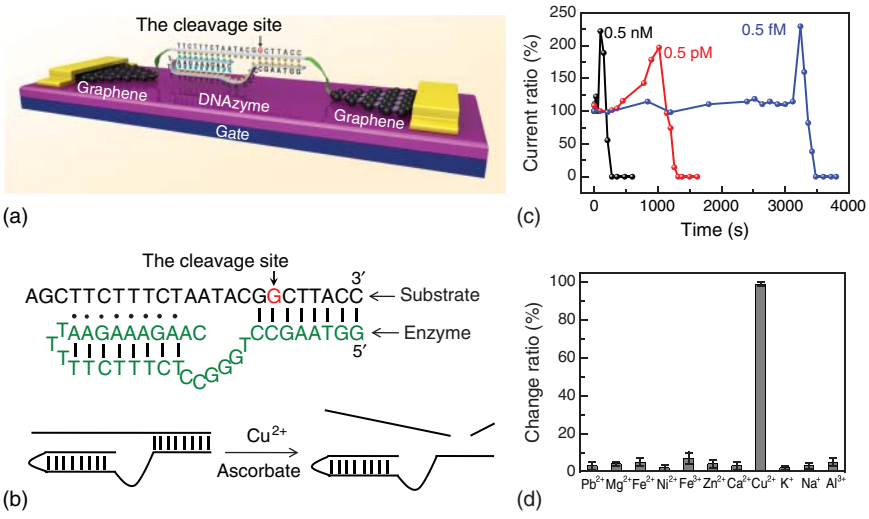

Figure 9.57 DNAzyme-based Cu^{2+} sensors. (a) Schematic representation of graphene–DNAzyme junctions. (b) The structure of the Cu^{2+}-sensitive DNAzyme and corresponding catalytic activity. The DNA substrate has been functionalized by amines on both ends for molecular connection. (c) Concentration-dependent dynamics of the Cu^{2+} catalytic reactions, which depict the femtomolar sensitivity. (d) Statistical comparisons of conductance changes under the same conditions in the presence of different ions (0.5 nM of Pb^{2+}, Mg^{2+}, Fe^{2+}, Ni^{2+}, Fe^{3+}, Zn^{2+}, Ca^{2+}, and Cu^{2+}; and 5 mM of K^{+}; 135 mM of Na^{+}; 60 nM of Al^{3+}). Source: Reprinted with permission from Gao et al. [402]. Copyright 2015, Royal Society of Chemistry.

This universality has been strengthened by another study [403], where a similar approach was described for directly revealing the stepwise effect of individual intercalations on DNA conductance based on DNA-functionalized molecular junctions by using ethidium bromide and SYBR Green I as representatives. Generally, the ability to detect chemical and biological species at ultralow concentrations is important in several areas, ranging from the diagnosis of life-threatening diseases to the detection of biological agents in warfare or terrorist attacks. These results demonstrate that these device-like architectures are promising for actual sensors with extreme sensitivity and high selectivity, thus leading to commercial applications.

9.7.2.2 Silicon-Based Devices

As the Si/SiO_2 interface is the basis for the prosperity of today's mainstream microelectronics, it is natural that one-dimensional silicon nanowires (1D SiNWs) have attracted much attention as basic nanobuilding blocks [404, 405]. SiNWs exhibit the unique advantages of high biocompatibility, size comparability, capability of integration with the existing silicon industry, and flexible surface tailorability, while their easy availability through bottom-up approaches and superior electrical properties with precise controllability make SiNWs well suited for the fabrication of high-gain FETs whose conductance is highly dependent on the local charge density [406, 407]. The above merits allow SiNW–FETs to be intimately interfaced with biological circuits at different scales ranging

from individual molecules to animal organs. In this section, we demonstrate the capability of SiNW–FETs to sense individual biomolecules or probe the dynamic processes of biological systems.

Lieber's group first reported a direct, real-time electrical detection of single virus particles with high-selective SiNWs-FETs [408]. The antibody receptors were modified on the surface of SiNWs. When the single virus specifically bonded to the receptors, the conductance of the nanowire biosensor changed. This is a landmark of the SiNW-based biosensor. Subsequently, rapid, selective, and sensitive detection of viruses is an effective tool for the diagnosis of viral infections. Previous studies reported highly selective SiNW–FETs as a promising platform for ultrasensitive virus detection [408]. For a practical attempt, we modified the surface of SiNW sensors with antibodies to detect influenza viruses H3N2 and H1N1 that were collected from clinical exhaled breathe condensates (EBCs) of patients with and without flu symptoms (Figure 9.58a) [409]. As a result, the SiNW biosensors could selectively detect influenza A viruses within minutes at levels as low as ∼285 viruses/μl in 100-fold diluted flu EBC samples (Figure 9.58b) and thus distinguish them from non-flu EBC samples (∼29 viruses/μl). This method considerably extends the scope of SiNW sensing to the diagnosis of flu in clinical settings and is 2 orders of magnitude faster than the gold standard method of room temperature real-time quantitative polymerase chain reaction (RT-qPCR).

In another work, single-protein detection was realized by surface functionalization before SiNW transfer to build an SiNW-FET-based biosensor capable of directly detecting protein adsorption/desorption at the single-event level, where the biomolecules of interest act as a local gate after assembly and electrostatically modulate the carrier intensity inside the nanowires [410, 411]. Specifically, Ni-NTA end groups (Ni^{2+} chelated *N*α,*N*α-bis(carboxymethyl)-L-lysine hydrate) serving as selective binding sites for His-tag F_1-adenosine triphosphate (ATP)ase (F_1) immobilization were used, and the stepwise adsorption of individual F_1 molecules was monitored by real-time electrical detection (Figure 9.58c) and AFM (Figure 9.58d). This approach was used to fabricate single F_1 molecule-grafted SiNW-FETs that displayed steady conductance in buffer solution [411]. Interestingly, the introduction of ATP resulted in a reproducible two-level current fluctuation, which originated from the bi-conformational transition of the γ shaft of F_1 corresponding to ATP hydrolysis and Pi release (Figure 9.58e,f), respectively. Importantly, the rate of label-free F_1 hydrolysis obtained in this work was 1 order of magnitude higher ($1.69 \times 10^8\ M^{-1}\ s^{-1}$ at 20 °C) than that in the case of fluorescent tag-labeled F_1, which manifested the capability of SiNW-based electrical nanocircuits to nondestructively probe the intrinsic dynamics of biological activities.

A particularly interesting feature of CVD-grown SiNWs is their 1D Si/SiO_2 core-shell structure [412], which allows one to open functional nanogaps for subsequent biocompatible assembly. Taking advantages of this feature, Guo and colleagues developed a reliable method of point functionalization with precise high-resolution electron-beam lithography, which is able to open a ∼10-nm window in the spin-cast polymethylmethacrylate layer (Figure 9.59a,b). This process produced an H-terminated Si surface perpendicular to SiNWs for

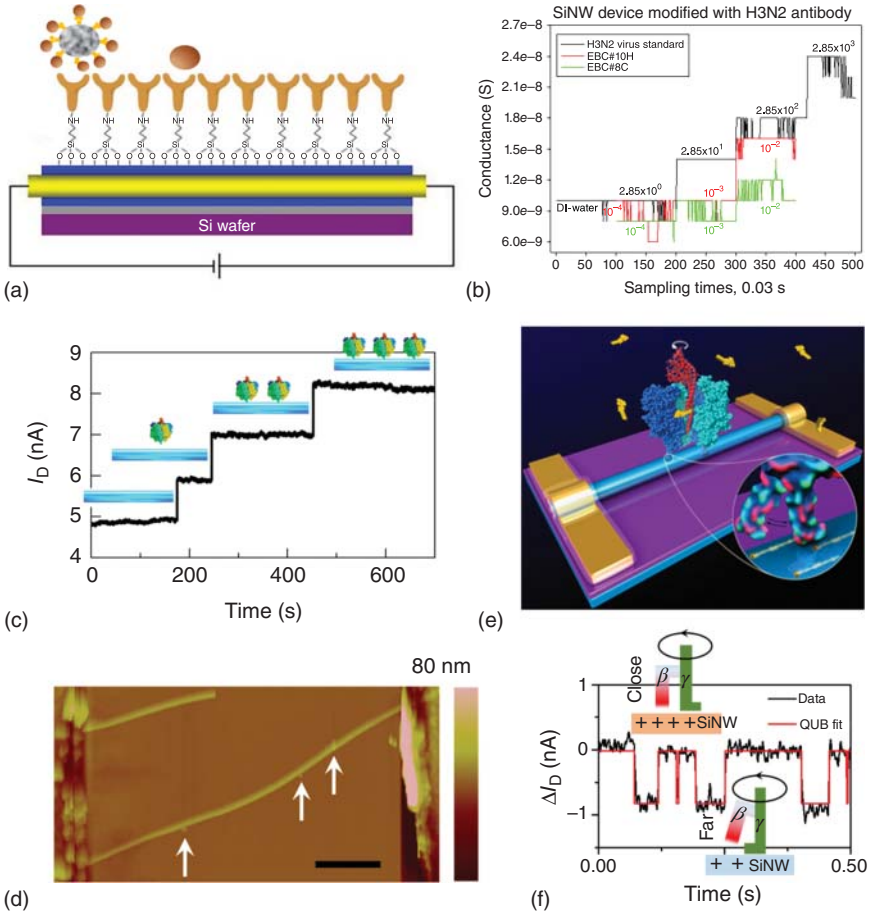

Figure 9.58 SiNW–FET-based biosensors. (a) Antibody-modified SiNW–FET-based sensors for influenza virus detection. (b) Detection of H3N2 viruses at different concentrations in 100-fold-diluted EBC samples. (c, d) Real-time recordings of absorption/desorption of F_1-ATPases and corresponding AFM images. Source: (c) Reproduced with permission from Shen et al. [409]. Copyright 2012, American Chemical Society. (e, f) Schematics of a single F_1 molecule-modified SiNW–FET nanocircuit and statistical analysis of F_1 hydrolysis. Inset in (f) shows different β conformations corresponding to high- and low-conductance states. Source: (d–f) Reproduced with permission from Li et al. [410, 411]. Copyright 2017, American Chemical Society.

programmed point decoration assembly and subsequent detection of single proteins in combination with microfluidics [413]. Remarkably, at very low protein concentrations (7.8–78 and 780 pg ml^{-1}), *in situ* electrical measurements showed no concentration dependence, thus demonstrating single-molecule sensitivity (Figure 9.59c).

DNA hybridization/polymorphism is a fundamental process in biology, with the DNA hairpin loop being a classical folding/unfolding system for DNA hybridization studies. With the development of optical detection techniques, the

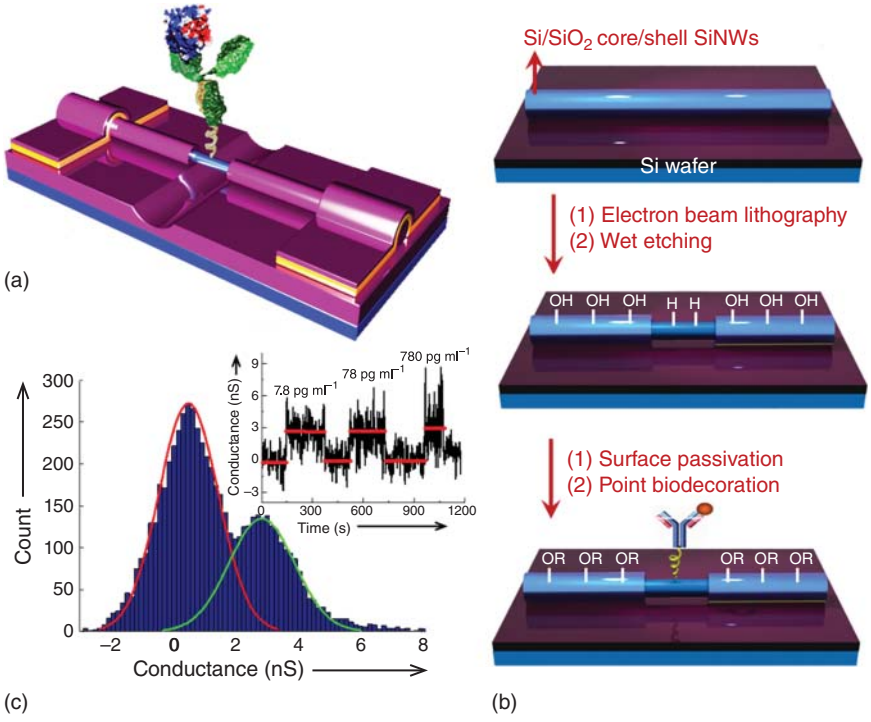

Figure 9.59 Point decorated SiNW-based sensors. (a) Device structure of single-molecule biosensors formed by point decoration of SiNWs. (b) Three-step process used to fabricate SiNW–FET-based single-molecule electrical biosensors. (c) Conductance histograms recorded in deionized water (red line) and antigen solution (green line). Inset shows the results of corresponding *in situ* electrical measurements. V_{bias} = 50 mV. Source: Reproduced with permission from Wang et al. [413]. Copyright 2014, John Wiley & Sons, Inc.

generally adopted mechanism of DNA hybridization has gradually changed from the initially proposed two-state model to the multistate model [414]. However, accurate information on each stage of hybridization is still lacking. To bridge this gap, Guo et al. [415] tethered individual hairpin DNAs on SiNWs through active ester terminals on the platform of SiNW–FET-based single-molecule biosensors described earlier (Figure 9.60a,b) [416] and observed multiple-step current changes during DNA hybridization dynamic measurements, which were performed at precisely controlled temperatures of 20–65 °C (temperature increase step = 5 °C) (Figure 9.60c). This observation agreed with the number of base pairs in the stem of hairpin DNAs, thus clearly demonstrating the single-base resolution of the DNA folding/unfolding processes within a time scale of a few milliseconds (Figure 9.60d). As a further step toward real-life applications, Guo and colleagues utilized a molecular hairpin DNA probe to establish a low-cost, high-throughput, simple, and accurate SNP genotyping technique [417]. Collectively, the aforementioned investigations prove that SiNW-FET single-molecule electrical circuits offer a powerful platform for researchers to study fast single-molecule biophysics in an interdisciplinary realm

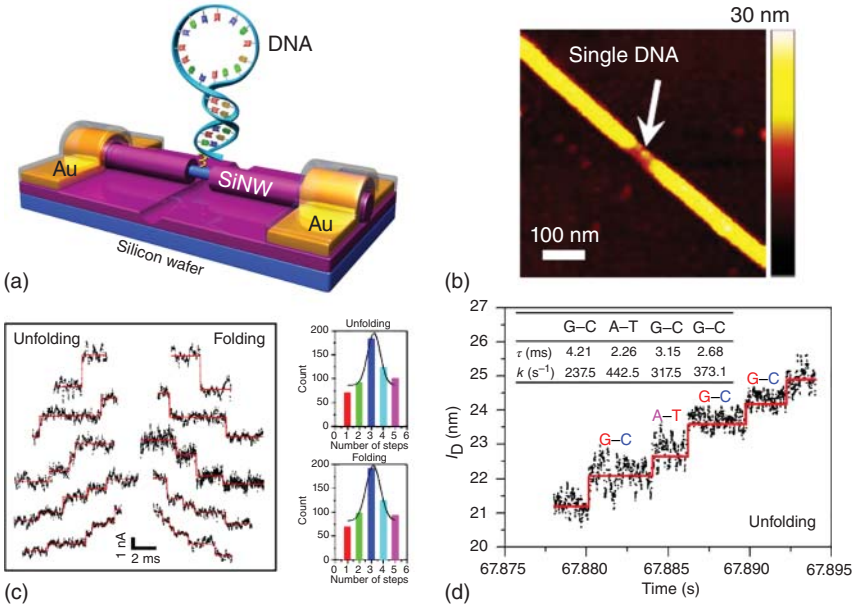

Figure 9.60 DNA hybridization/polymorphism. (a, b) Schematic diagram of a single-hairpin DNA-decorated SiNW biosensor and corresponding AFM image. (c) Stepwise folding/unfolding processes fitted by a step-finding algorithm (red), showing zero- to five-step changes, and corresponding histograms of step numbers in unfolding and folding data counted from thousands of current oscillating events. (d) Representative five-step unfolding data. Inset shows the kinetic parameters of each plateau (lifetime τ and rate constant k). Source: Reproduced with permission from He et al. [415]. Copyright 2016, John Wiley & Sons, Inc.

and can be used in numerous applications such as genic polymorphism, protein folding, enzymatic activity, and reaction mechanism elucidation.

9.7.3 Sensing Based on Thermoelectrical Conversion

In addition to the strong motivation for the development of molecular electrical biosensors, there is increasing interest in understanding the thermoelectric transport in single-molecule junctions [158, 418]. If one side of a material is heated to a higher temperature (T_1) and the other side is kept at a low temperature (T_2), then free charges tend to accumulate at the cold end, resulting in a potential difference ΔV between the sides. This thermoelectricity enables the heat energy to be directly converted to electricity and vice versa, without using any mechanical components. Thus far, experimental studies on thermoelectricity for nanojunctions are limited. However, a few key results have already emerged. For example, Reddy et al. performed the first measurement of thermopower in molecular junctions, and the Seebeck coefficients ($\Delta V/\Delta T$) for several types of molecular junctions were determined [419]. Then, a framework was established for understanding heat dissipation for a range of mesoscopic systems, which demonstrated that the heat dissipation was asymmetric if the junctions had

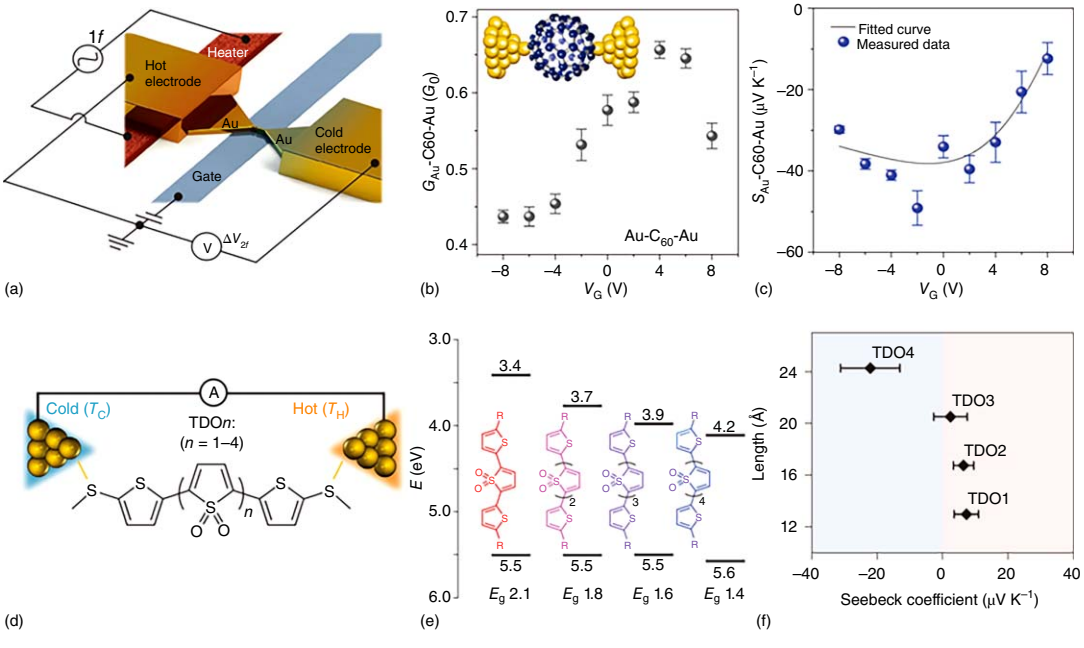

Figure 9.61 Tuning the thermoelectric properties of molecular junctions. (a) Schematic of the electromigrated break junctions with integrated heater (left). (b) Electrical conductance as a function of the gate voltage (V_G) for the C_{60} junction (see inset). (c) Seebeck coefficient of the molecular junction as a function of V_G. Source: (c) Reprinted with permission from Kim et al. [427]. Copyright 2014, Nature Publishing Group. (d) Schematic representation of the STM junction. (e) Cyclic voltammetry (CV)-derived HOMO and LUMO levels (eV) and the HOMO–LUMO gap (E_g) for the TDO*n* family (R = SMe). (f) Plot of Seebeck coefficients as a function of the molecular length for the TDO*n* family. A shift from positive to negative Seebeck values with increasing length is observed, which indicates a change in the charge carriers from holes to electrons. Source: (f) Reprinted with permission from Dell et al. [428]. Copyright 2015, Springer Nature.

strong energy-dependent transmission characteristics [420]. Widawsky et al. [421] developed the STM-based break junction technique and simultaneously determined the conductance and thermopower of single-molecule junctions, revealing the dependence of the Seebeck coefficients on the conducting molecule orbitals. This dependence was also proven by the results obtained by the Tao's group [422], who determined that the thermopower correlated with the transition voltage, which was indicative of the molecular energy level alignment between the molecular energy levels and the electrodes' Fermi energy level.

These pioneering experimental studies combined with the recent systematic computational predictions [423–425] established the feasibility of achieving efficient thermoelectric energy conversion in molecular junctions. The key to obtain deeper insights and optimize the thermoelectric properties of molecular junctions is to tune their charge transmission characteristics at the Fermi level (E_F) of the electrodes. Thus, Evangeli et al. [426] utilized the imaging capability of the STM technique to simultaneously measure the thermopower and the conductance, thus demonstrating a potential approach of enhancing the thermoelectric performance by manipulating the intermolecular interactions. Kim et al. [427] used an electromigration approach to build three-terminal molecular junctions with large temperature gradients, which allowed for the simultaneous measurements of the Seebeck coefficient and the electrical conductance of the individual molecules (Figure 9.61a) to be obtained. Using this platform, the prototypical Au–biphenyl-4,4′-dithiol–Au and Au–fullerene–Au junctions were studied, indicating that both the Seebeck coefficient and the molecular conductance could be increased by electrostatic control (Figure 9.61b,c). Additionally, it was determined that the thermoelectric properties could be significantly enhanced when the dominant transport orbital was located close to the E_F of the electrodes (Figure 9.61b,c). Recently, Dell et al. [428] reported another interesting study, where the STM technique was used to demonstrate that the charge carriers in single-molecule junctions could be tuned by molecular engineering (Figure 9.61d,e). By performing thermopower measurements, it was proven that the dominant charge carriers changed from holes to electrons within a family of molecules that contained electron-deficient TDO building blocks when the number of TDO units was increased (Figure 9.61f). This result provided a new method to tune the length-dependent p- and n-type transport in organic materials. Collectively, these rapid, impressive demonstrations suggest that molecular thermoelectricity is an area of research where new breakthroughs can occur in the future.

9.8 High-Frequency Molecular Devices

Molecular electronics proposed that molecules sandwiched between electrodes would accomplish electronic functions and have been extensively studied for their DC properties. In order to enable molecular devices to replace traditional semiconductor devices in the future, the research of both high frequency (radio frequency (RF)) and alternating current (AC) performance is indispensable.

However, so far, functional molecular devices have only been demonstrated at low frequency, a serious limitation from a device perspective. To reach high-frequency molecular components, several issues have to be addressed. Firstly, one main issue in high frequency devices is that the conductance has remained extremely low (quantum of conductance $G_0 = 77.5\,\mu S$), seriously impacting the cut-off frequency of the device which could be approximated, in a simple dipole configuration, by $G/(2\pi C)$, with G (the device dynamic conductance) and C (capacitance). A second issue, barely addressed in molecular electronics, is the capacitive circuitry for frequency bandwidth optimization. Whereas the low dielectric constant (~2–3) [429] of organic monolayers should be an advantage, fringe capacitances may be dominant when reducing the devices dimension to single or few molecules. In addition, molecular electronics requires statistical studies for convincing demonstrations, which add more difficulty for the measurement of high-frequency signals. This section summarizes the solutions for implementing high-frequency molecular devices.

Before summarizing the high frequency or AC molecular devices, transistors that constitute the heart of electronic circuits and have been the building blocks of the digital revolution would be first introduced. A transistor is an electronic component that which has at least three terminals. By applying a voltage or current to one pair of the terminals, one can regulate the current through another pair of terminals. The output power can be higher than the input power and therefore a transistor can act as an amplifier. Another transistor application is that of an electrical switch, in which the voltage on one of the terminals regulates the current between two other terminals. In the field of molecular electronics, transistors with carbon-based electrodes are interesting candidates as they provide a higher structural stability. Different strategies are proposed to link molecules to carbon electrodes. The first approach is a covalent bonding through a chemical reaction, which can lead to robust junctions at room temperature. An example is the amide bond achieved by peptide chemistry [430–432]. This strong link could avoid the stochastic switching of thiols to neighboring gold atoms observed in conventional gold electrodes, making the amide bond more stable. The most critical task is how to apply high frequency to the transistors.

To address this issue, Nijhuis et al. reported a molecular half-wave rectifier, but the selected frequency of operation was 50 Hz [433]. They described the performance of junctions based on SAM as the functional elements of a half-wave rectifier (a simple circuit that converts, or rectifies, an AC signal to a DC signal). These junctions comprised SAMs of 11-(ferrocenyl)-1-undecanethiol ($SC_{11}Fc$) or 11-(biferrocenyl)-1-undecanethiol ($SC_{11}Fc_2$), supported on template-stripped Ag bottom electrodes, and contacted by the top electrode of eutectic indium–gallium as shown in Figure 9.62a. Figure 9.62b shows the measured input voltage, V_{in} (black line), and the corresponding measured output voltage, V_{out} (red line). V_{in} is a 50-Hz sinusoidal signal with a peak voltage of 2.1 V. They found that the V_{out} signal is not detectably phase-shifted relative to V_{in}, but the values of V_{out} are significantly less than the values of V_{in}.

More specifically in molecular electronics, an RF break-junction setup, which is compatible with the single-molecule device, has been reported by Guo et al. for an atomic contact device, but without the presence of molecules [434].

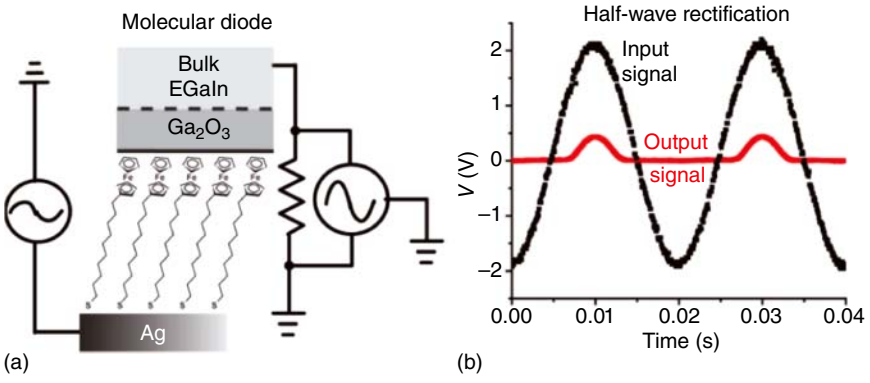

Figure 9.62 Experiments of half-wave rectification with molecular junctions. (a) Schematic representation of the Ag^{TS}–$SC_{11}Fc$//Ga_2O_3/EGaIn, consisting of an Ag^{TS} bottom electrode and a cone-shaped Ga_2O_3/EGaIn top electrode. (b) Sinusoidal input signals (V_{in} = 2.1 V, black) with the corresponding output signal (V_{out}, red). Source: Reproduced with permission from Nijhuis et al. [433]. Copyright 2011, American Chemical Society.

This approach leads to a time resolution 3–4 orders of magnitude faster than the measurements carried out to date, making it possible to observe fast transient conductance-switching events associated with the breakdown, re-formation, and atomic scale structural rearrangements of the contact.

In order to realize the development of high-frequency molecular devices, the related simulation work has also been carried out. Kienle and Leonard presented an approach for time-dependent quantum transport based on a self-consistent NEGF formalism and applied it to determine the high-frequency (terahertz) properties of CNTFETs [435]. They showed that the dynamic conductance exhibits both smooth oscillations and divergent features in the terahertz regime, indicating the coexistence of single-particle and collective excitations (plasmons). The system is divided into a device region, which is connected to two semi-infinite leads consisting of NTs embedded in source and drain metals as shown in Figure 9.63a. The dynamic source–drain conductance g (ω) is dependent on the potential at the gate terminal V_g, which consists of AC and DC signals. From Figure 9.63b, we can find that the conductance is affected by the gate voltage. The band diagram in the ON and OFF states is shown in Figure 9.63c, from which we can see that the bandwidth is regulated by DC gate voltage. In addition, they showed that the real and imaginary parts of the AC conductance in the OFF state displayed smooth oscillations as a function of frequency, which is a signature of the single-particle excitation spectrum. In contrast, in the ON state, they observed that the conductance exhibits a pronounced divergent response at 24 THz with an underlying oscillatory behavior for high frequencies. The presence of these oscillatory modes suggests that plasmons are responsible for the divergent behavior. There results suggest that low-dimensional systems with nanometer-sized channels show promising potential for novel detectors and emitters of terahertz radiation.

In addition, Wu et al. reported a theoretical analysis, which shows that a critical control of the conductance of short molecules can be achieved by a finite

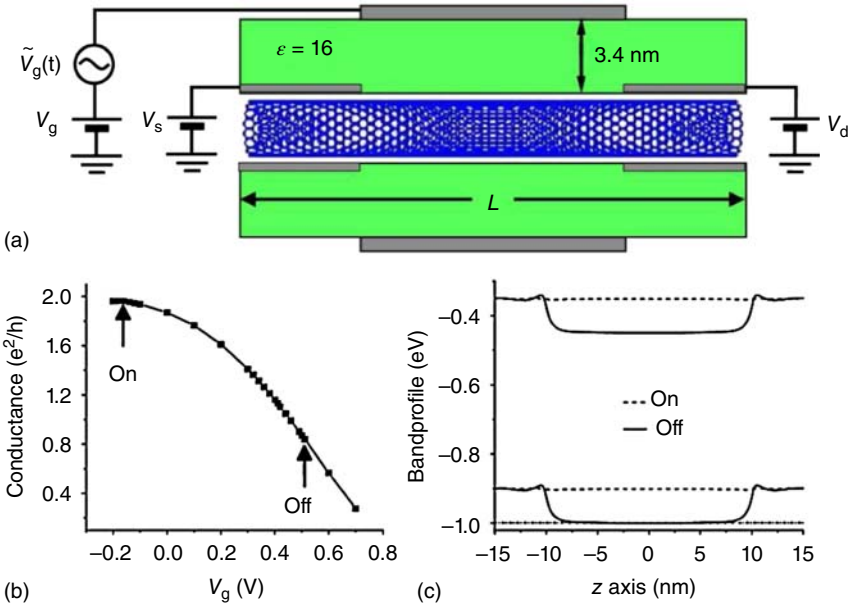

Figure 9.63 Dynamic source–drain conductance dependent on the potential at the gate. (a) Cross section of the cylindrical NTFET geometry. (b) DC transfer characteristics for $L = 30$ nm. (c) Band diagram in the ON and OFF states, as marked by arrows in panel (b); the dashed-dotted line at −1 eV is Fermi level. Source: Reproduced with permission from Kienle and Leonard [435]. Copyright 2009, The American Physical Society.

frequency AC bias [436], demonstrating that there exists a giant enhancement of dynamic conductance, by many orders of magnitudes, as a function of the AC frequency. However, such a theoretical prediction needs a confirmation from experimental results. Recently, Trasobares et al. demonstrated molecular diodes operating up to 17.8 GHz, which is the highest frequency functional device reported so far at room temperature [437]. They measured DC and RF properties simultaneously on a large array of molecular junctions composed of gold nanocrystal electrodes, ferrocenyl undecanethiol molecules ($FcC_{11}SH$) and the tip of an interferometric scanning microwave microscope (iSMM) [438]. The measurement of the molecular diode is presented in Figure 9.64a. It is found that the present nanometer-scale molecular diodes offered a current density increase by several orders of magnitude compared with that of micrometer-scale molecular diodes, allowing the RF operation. The measured S11 parameters showed a diode rectification ratio of 12 dB, which is linked to the rectification behavior of the DC conductance as shown in Figure 9.64b. There is a tradeoff between the conductance, function (rectification), and capacitances. The present configuration was optimized to demonstrate a 17 GHz molecular rectifier with a 520 GHz cut-off frequency: the ~150 molecules sandwiched between a gold nanocrystal and a Pt tip electrode enables to get a ~0.36 mS dynamic conductance while keeping a small capacitance in the 100 aF range. In addition, a comparison with the silicon RF-Schottky diode architecture suggests that the

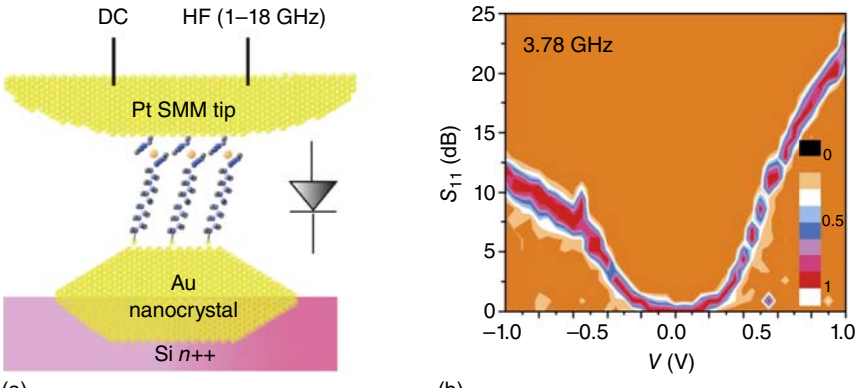

Figure 9.64 Molecular diodes. (a) Schematic representation of the molecular junction composed of a gold nanocrystal, ferrocenylundecanethiol (Fc C11) molecules enabling rectification properties, and a Pt tip. (b) 2D |S11| histogram (normalized to one) versus tip bias generated from 100 molecular rectifier junctions. The voltage step was 0.05 V and the contour plot generated automatically (OriginLab). The applied load was 18 nN. Source: Reproduced with permission from Trasobares et al. [437]. Copyright 2006, Springer Nature.

RF-molecular diodes are extremely attractive for scaling and high-frequency operation. High-frequency molecular devices are indispensable elements for the future development of molecular electronics. It brings new hopes and perspectives for chemistry-based electronics. All the work summarized above evidence the interesting perspectives of the molecular electronics approach for high-frequency operation.

9.9 Molecular Machines

The original intention of the molecular device design is to break through the limitation of the silicon-based miniaturization. However, the mimic of the basic units and functions of silicon-based devices are far from making sense. The rational design of molecular electronics is called for exploring the intrinsic molecular functionality [439–443]. Indeed, contemporary research in molecular electronics is already moving toward this direction. With decades of efforts, diverse molecular machines have been developed, such as the molecular motors, molecular elevators, molecular scissors, and so forth.

9.9.1 Molecular Motors

A motor must be the most important part of a machine, which can convert chemical energy into mechanical force and movement. The molecular motor is defined as a machine, which is capable of using an energy input to produce useful work. Natural molecular-level machines and motors are extremely complicated systems. The operational mechanisms of the motion of molecular machines at the molecular level have to deal with the phenomena different

from those that govern the macroscopic world, such as gravity, inertia motions, viscous forces, etc. Additionally, only simple prototype of molecular components can be constructed artificially by the bottom-up process. Herein, completely copying the natural machine systems by artificial bottom-up means is hopeless. Fortunately, the rational utilization of the chemical toolbox for the construction of the molecular motors, namely, a variety of chemical reactions, is much larger than the one used in nature [444].

In 1999, Kelly's group and Feringa's group published their marvelously designed, chemically powered rotary molecular motor separately [445, 446]. Differently, Kelly motor was unable to rotate while the Feringa motor worked, which awarded with the Nobel Prize. Kelly and his coworker designed a system that is fueled by phosgene and accomplishes a unidirectional, 120° clockwise rotation. Unfortunately, their motor did not accomplish a repeated rotation [447–449]. To be able to construct a molecular motor, three basic requirements need to be fulfilled in the following order: (i) consumption of energy; (ii) unidirectional rotation; and (iii) repetitive rotary. After fulfilling all three points, Feringa and his coworker made the dream of light-driven photoinduced unidirectional full 360° rotary motion of C=C double bond isomerization to come true [450]. They developed the first and second generation light-driven unidirectional molecular motors [446, 451]. The molecules comprise a chiral overcrowded alkene conformation, in which two halves are connected by a central olefinic bond (Figure 9.65, molecule **30**). Two halves were regarded as a rotor unit and a stator part respectively. The connecting olefin operates as the axle of the rotational system. In contrast to the molecular switch, the Feringa motor possesses both an intrinsic helical chiral structure and stereogenic centers in allylic positions with respect to the axis of rotation. Basically, a full unidirectional rotary cycle has four steps, the full 360° unidirectional rotary cycle of 1*R*,1*R*-(*P*,*P*)-*trans*-**30** as shown in Figure 9.65a. The formation of all the isomers during the cycle can be determined by ^{1}H-NMR, UV–Vis spectroscopy, and circular dichroism (CD) spectroscopy (Figure 9.65b). Their results suggested that upon continuous irradiation and in the condition of appropriate temperature, the rotor part performed unidirectional rotary motion relative to the stator part [452, 453]. Subsequently, they investigated the Feringa motor assembled with gold nanoparticles for further integration into the molecular circuits [450].

What should be noticed is that motors discussed here mainly refer to the rotary ones. In fact, linear-like movements inspired another essential motor. In nature, enzymes like myosin and kinesin and their derivatives are linear motors that move [454]. Here, we would like to concentrate on the artificial molecular electronics; thus, the natural molecular electronics are not described too much in this book.

9.9.2 Molecular Elevators

Since the very first example reported in 1994 [455], a variety of controllable molecular machines, which are capable to shuttle along the axis component relying on chemical, electrochemical, and photochemical stimulation, have been described elsewhere [456–459]. Based on the continuous efforts, Balzani's group

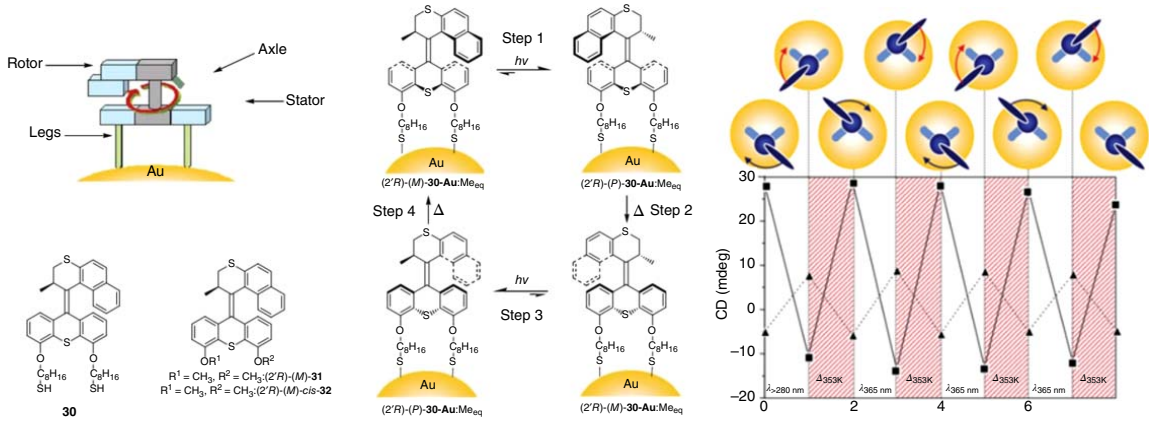

Figure 9.65 Molecular motors anchored to a surface. (a) Design of a surface-bound rotary motor. (b) Structure of motor **30** for surface studies and **31**, **32** for solution studies; **30**-Au denotes motor molecule **30** assembled onto Au. (c) The four-state unidirectional rotation of functionalized nanoparticle **30**-Au is shown. (d) Schematic representation of the unidirectional rotation of **30** (as viewed along the rotation axis) and two full four-stage 360° rotary cycles followed by CD spectroscopy. Source: Reproduced with permission from van Delden et al. [450]. Copyright 2005, Springer Nature.

designed and synthesized a molecular elevator [460]. Firstly, a chemically driven bistable switching **33**-H^{3+} compound has been evaluated with good performance (Figure 9.66a,b) [462, 463]. Specifically, the compound is made of a dumbbell component, an ammonium and an electron acceptor 4,4′-bipyridinium unit. These structures are able to establish hydrogen bonding or CT interaction between a crown ether and electron donor ring component dibenzo-24-crown-8 (DB24C8). An anthracene moiety is regarded as a stopper. Additionally, its absorption, luminescence, and redox properties are helpful to monitor the state of the system. The N^+—H· · ·O hydrogen bonding interactions between the ammonium center and macrocyclic ring are much stronger than the CT interactions of the ring with the bipyridinium moiety. As a result, the rotaxane performs as only one of the two translational isomers (State [**33**H]$^{3+}$). With the presence of the base, the deprotonation of the ammonium center of **33**-H^{3+} weakens the hydrogen bonding interactions, leading to the quantitative displacement caused by the DB24C8 ring moving to the bipyridinium moiety in Brownian motion (State $[1]^{3+}$). Oppositely, with an acid introduction, the ring goes back to the ammonium center. The deprotonation and reprotonation processes have been investigated by ^{1}H NMR spectroscopy together with electrochemical and photophysical measurements [462]. Stoddart's group has investigated the kinetics of the ring shuttles in solution and the properties of LB films containing **33**-H^{3+} [464, 465]. The fully chemically reverse mechanical movement induced by the acid-base reaction offered the rotaxane complexes a binary stability.

Subsequently, inspired by the acid-base switchable rotaxane **33**-H^{3+} described earlier, Balzani et al. incorporated it into a triply threaded two-component supramolecular bundle to form a two-component molecular device **34**-H^{9+} (Figure 9.59c) [461]. The three legs of **34**-H^{9+} work similarly as the deprotonation and reprotonation processes under the base–acid condition. However, the aforementioned interlocking by a tritopic host played a role of a platform able to stop at the two different levels, which behaves like a nanoscale elevator [460]. The three legs, which consisted of a tripod component containing one ammonium center and one 4,4′-bipyridinium unit, hamper the platform from slipping off. Two states can be performed with the **34**-H^{9+}. State 0 in Figure 9.66c, with the three rings surrounding the ammonium centers, which stem from the strong N^+—H· · ·O hydrogen bond and weak π–π stacking forces between the aromatic cores of the platform, is "upper" level initial. Upon introduction of the phosphazene base, deprotonation led to the occurring of ammonium center. Consequently, the platform moved down to the "lower" level, in which the three DB24C8 rings surrounded the bipyridinium moieties (State 1). Analogously, acid introduction made the platform to move back to the upper level. The elevator behavior has been monitored quantitatively by ^{1}H NMR spectroscopy together with electrochemical and photophysical measurements [466]. They also suggested that their systems are promising in the drug delivery. With analogous consideration, a Japanese team fabricated a double-leg donor acceptor based on a stable CT complex containing a divalent host and a guest through the "click chemistry" approach [467]. The molecular elevators are more reminiscent of a legged animal than they are of passengers on freight elevators, which hold considerable promise for use in molecular devices.

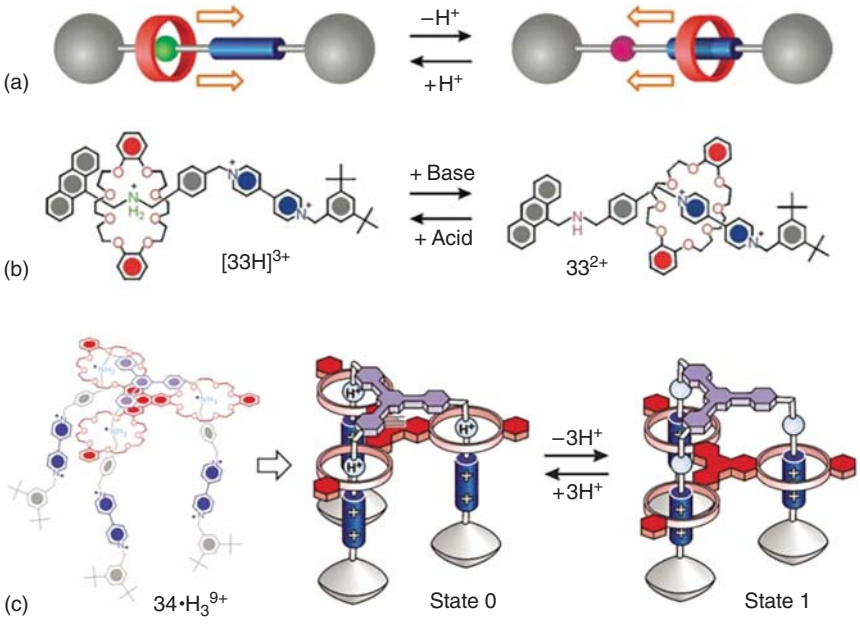

Figure 9.66 Molecular elevator. (a) Schematic representation of a controllable, bistable [2]rotaxane, containing in its dumbbell-shaped component two different recognition sites or "stations," to one of which the ring component is attracted much more than the other. The two different states of the molecule can be switched by an external stimulus, such as a change in pH. (b) In the [2]rotaxane $[1H]^{3+}$, the dumbbell-shaped component contains a $–NH_2^+–$ center and a BIPY2+ unit as stations for the DB24C8 component. In acid, the preferred station for the DB24C8 ring to encircle is the $–NH_2^+–$ center because of the formation of strong hydrogen bonds. After adding the base, however, the $–NH_2^+–$ center is deprotonated and the DB24C8 moves to the $BIPY^{2+}$ unit, where the donor–acceptor interactions become stabilized. (c) Chemical formula and operation scheme in CH_3CN solution (state 0 and state 1) of the molecular elevator 2-$H_3$9$^+$. According to molecular models, the elevator is approximately 2.5 nm high and 3.5 nm wide. Source: Reproduced with permission from Balzani et al. [459, 461]; Badjić et al. [460]. Copyright 2006, The Royal Society of Chemistry.

9.9.3 Molecular Scissors

Since the first proposal of molecular electronics, scientists never stop to explore the possibilities of making molecular devices with desired functionalities. In 2006, a fascinating work relevant to a 3-nm molecular scissors has been published in *Nature*. As soon as the reported work brought out, it was focused by the whole scientific society. In fact, the molecular scissor has been designed creatively by a Japanese group based on the development of a series of photoresponsive molecules, which were inspired by molecular biological systems.

In terms of photoresponsive molecules, AB is considered as one of the most representative models. The good performance in photoresponsive elongation/contraction motion of AB offers the opportunity to convert solar energy to mechanical energy. Aida's group designed molecule **35**, in which the AB isomerization contributed to the pivotal motion of ferrocene to achieve a

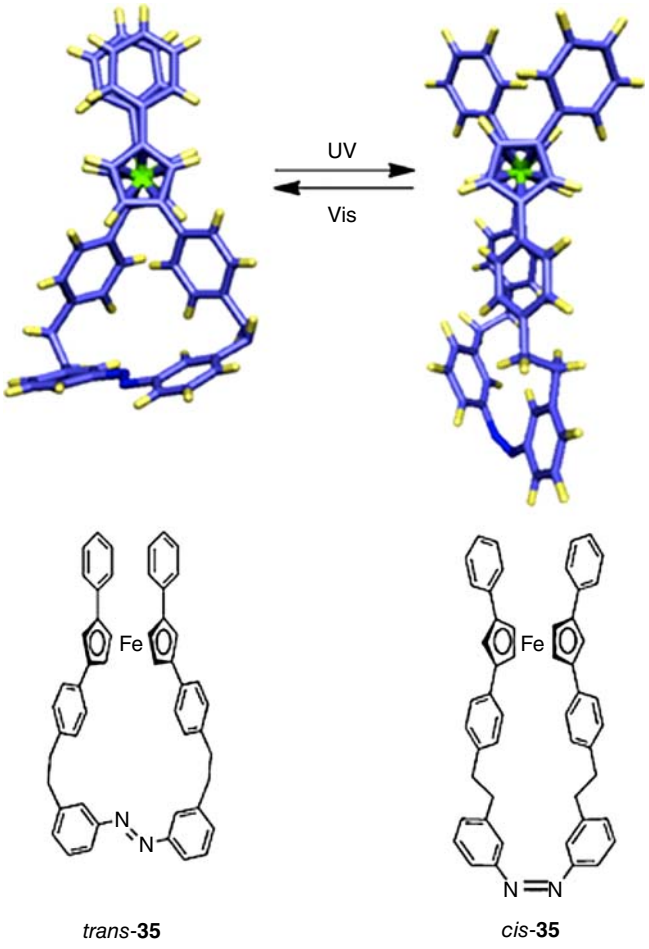

Figure 9.67 A crystal structure of *trans*-**35** (left) and a molecular structure of *cis*-**35** (right), optimized with DFT calculation (B3LYP/3–21G*). Source: Reproduced with permission from Muraoka et al. [468]. Copyright 2003, American Chemical Society.

scissoring behavior [468]. As shown in Figure 9.67, molecule **35** consists of 1,1′-3,3′-tetrasubstituted ferrocene, whose 1- and 1′-positions are strapped by AB via ethylene units. The X-ray crystallographic analysis demonstrated that the two phenylene groups connected to the cyclopentadienyl (Cp) rings are separated with an angle of 62.78° due to the elongated geometry of the AB unit. As a result, the Cp-attached phenyl groups are in close proximity to each other in a twisting angle of only 8.75°. The two Cp rings are almost parallel with a distance of 3.334 Å [469]. As in the initial design and theoretical calculation, the covalently interlocked structure of molecule **35** changes in response to the geometric transformation of the AB unit, which resulted in the distance between the two Cp-attached phenylene groups. Consequently, the phenyl group goes through an opening/closing motion by an angular motion of

the ferrocene unit. The CD spectroscopy and ^{1}H nuclear magnetic resonance (^{1}H NMR) spectroscopy gave evidence of the interlocked motion of **35** upon irradiation of UV (350 nm) and Vis (>400 nm). Additionally, they suggested that the moderate flexible ethylene unit is essential for the interlocking movable units as the linker parts. Besides, for higher ratio of the trans/cis molar ratio of the photostationary state, they modulated the light control of molecular scissors with a plus redox control [470].

The success of the covalently interlocked structure in modulating the scissor's behavior encouraged them to develop an operative non-covalent molecular pliers **37** (Figure 9.68a) [471]. Molecular plier **37** is composed of a zinc porphyrin unit attached on each Cp ring of the ferrocene unit of **37**. The zinc porphyrin binds to a bidentate rotary guest 13 via coordination of the zinc ion with nitrogenous bases, forming a host–guest complex **37•36**. The photochromic isomerization of the AB moiety has been confirmed by the CD spectroscopy. Interestingly, they found that the trapped **36** is fixed in a non-planer chiral geometry, and concurrently changes with photoisomerization of the host (Figure 9.68b). Between 250 and 350 nm, the CD signal intensity decreased upon UV irradiation, while the visible irradiation gave rise to the increment of the signal. These results indicated that the dihedral angle between the isoquinoline rings of the guest **36** was modulated by the geometric change zinc porphyrin of *trans*-**37** and *cis*-**37** [472, 473].

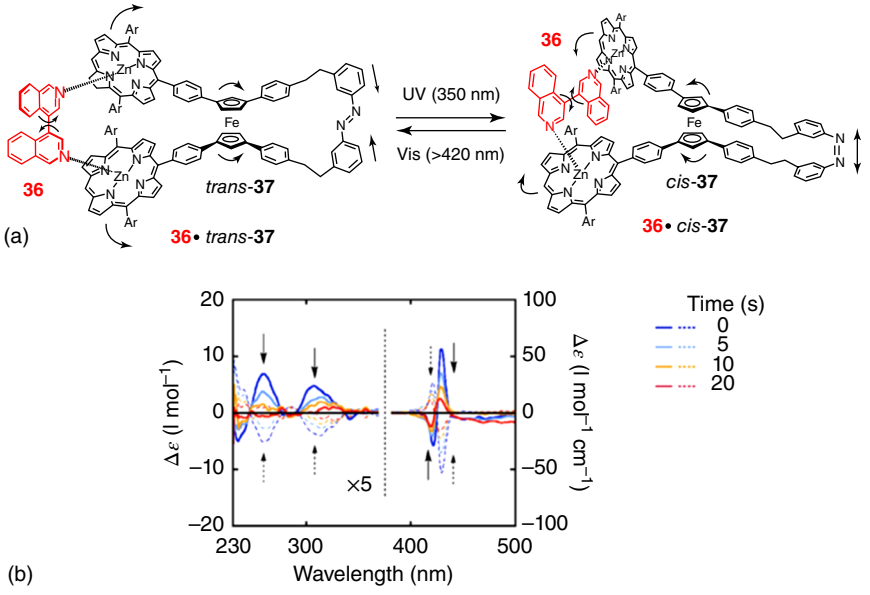

Figure 9.68 Molecular scissor. (a) Schematic representation of photoisomerization of a 1 : 1 complex of molecular pliers **37** with rotary guest **36** (**36•37**). Ar represents 4-decyloxyphenyl group. Arrows indicate the directions of interlocked motions. (b) Differential spectra by subtraction of the CD spectra of *trans*-**37•36** from those of *trans*-**37•**3,3′-bipyridine ([*trans*-**37**] = 7.2×10^{-6} M, [**36**]/[*trans*-**37**] = [3,3′-bipyridine]/[*trans*-**37**] = 1.0) in CH_2Cl_2 at 20 °C upon UV irradiation (350 nm) for 5, 10, and 20 seconds (solid curves, (1*R*,1′ *R*)-*trans*-**37**; broken curves, (1*S*,1′*S*)-*trans*-**37**). Source: Reproduced with permission from Muraoka et al. [471]. Copyright 2006, Springer Nature.

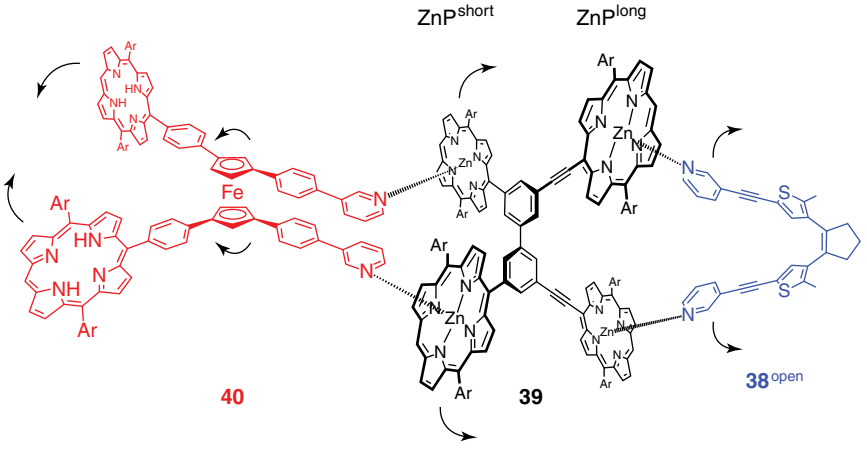

Figure 9.69 Schematic representation of an expected ternary complex **38**^{open}•**39**•**40**. Ar represents 3,5-dioctyloxyphenyl group. Arrows indicate the directions of interlocked motions. Source: Reproduced with permission from Kai et al. [475]. Copyright 2008, American Chemical Society.

Considering the timescale of the isomerization performed in CD spectroscopy (Figure 9.68b) together with the dynamic NMR study [474], they attributed second-level photoinduced conformation of 2–13 bound to the host. Namely, the host physically twists guest through non-covalent bond in response to irradiation. A change in molecular shape of cis–trans photoisomerization of an AB unit is transmitted via a pivot point (a ferrocene unit) and a pedal-like motion of large flat zinc porphyrin units to induce a clockwise or anticlockwise rotary motion in a bound rotor guest. Together with the covalent and non-covalent strategies of the modulation of scissors like motion, furthermore, they studied a ternary complex **38**•**39**•**40**, which is mechanically interconnected with each other, and allows for long-distance transmission of motions. (Figure 9.69) [475]. Molecular scissors can be considered as prototypes of "molecular reactors" and can be extended to larger polymeric systems, allowing remote manipulation of molecular events.

9.9.4 Other Multicomponent Mechanical Machines

The construction of molecular machines, whose mechanical motion of different parts operates in concert, calls for the design of integrated multicomponent systems. In fact, the molecular elevator and molecular scissors mentioned earlier are related examples. Here, we would like to introduce other molecular machines consisting of multicomponents.

A family of nanovehicles, whose directions are carefully tuned, were developed to transport on surfaces, with an ultimate goal to transport cargo from one place to another like the macroscopic car does [476]. The key structure of the nanocar is a molecular motor that provides the driving force and an oligo(phenylene ethynylene) chassis together with an axle system to serve as the wheels. The first generation of nanocars was developed with carbon-based C_{60} wheels driven by electricity [477, 478]. However, the nanocar has been given up due to the fact

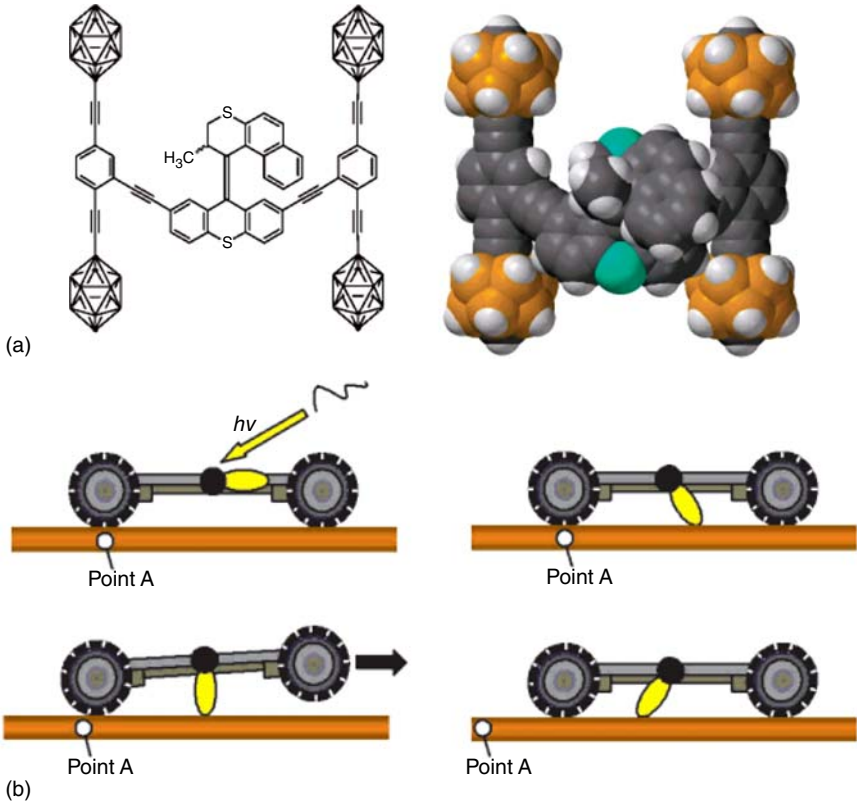

Figure 9.70 Motorized nanocars. (a) The *p*-carborane wheels have BH at every intersection except at the top and bottom vertexes, which represent C and CH positions, iso and para, respectively, relative to the alkynes. (b) Affording motor rotation and sweeping across the surface to propel the nanocar forward. Source: Reproduced with permission from Morin et al. [481]. Copyright 2006, American Chemical Society.

that the C_{60} wheel impedes the photoisomerization process of molecular motors [479, 480]. Instead of C_{60}, Tour's group chose the *p*-carborane wheels [481] with a light-driven motor shown in Figure 9.63a. In their approach, carborane "wheels" were attached covalently to a molecular rotor "engine." After design and synthesis of the nanocars, Tour and colleagues tracked the individual nanocar by a single-molecule fluorescence microscopy (SMFM) technique to support their previous work and demonstrated the feasibility of a variety of nanocars (Figure 9.70) [482].

Recently, a remarkable artificial molecular machine has been reported, which achieved the sequence-specific peptide synthesis [483]. The authors tried to mimic the ribosome behavior in assembling amino acids from tRNA building blocks into a peptide chain with an order defined by the sequence of the mRNA strand. Their rotaxane machine system contained a macrocycle carrying a reactive arm (molecule **39**) and a thread functionalized with a predetermined sequence of building blocks, which determined the sequence of the peptide

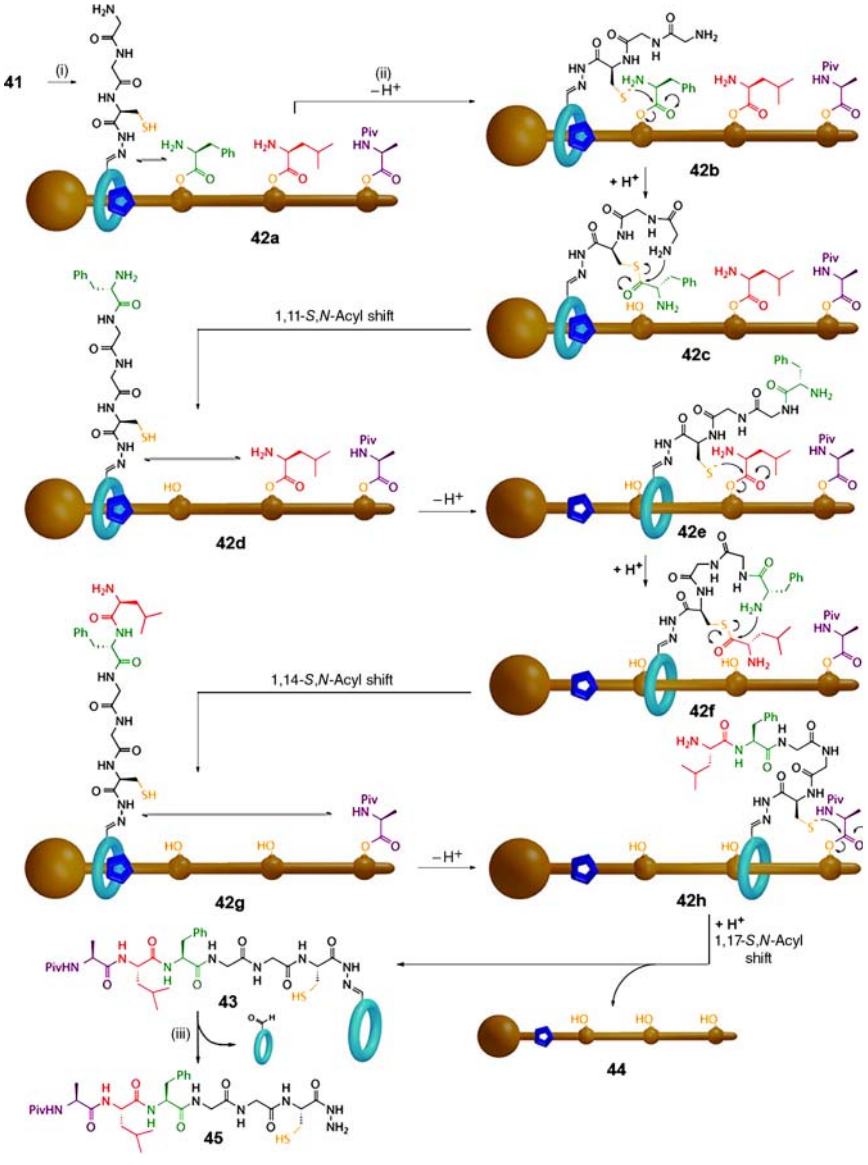

Figure 9.71 A sequentially operating rotaxane catalyst. (a) Structure of the small artificial rotaxane based molecular machine used in the sequential peptide synthesis. (b) Proposed mechanism for the peptide synthesis. See text for details. Source: Reproduced with permission from Lewandowski et al. [483]. Copyright 2013, AAAS.

of interest (Figure 9.71). The catalytic part located on the macrocycle was a tethered thiol group. The catalytic part located on the macrocycle was a tethered thiol group. The terminal blocking group of the thread prevented the macrocycle from sliding off before the peptide synthesis process completes. This molecular machine contained three amino acid building blocks attached to

the thread via weak phenolic ester linkages. The synthesis process started with the acid-catalyzed deprotecion of Boc and trityl groups. The whole synthesis process spent 36 hours to complete. This is the first case of performing a reaction in a sequential processive fashion relied on a rotaxane-based artificial molecular machine. Following this demonstration, scientists keep trying on developing a variety of functional molecular machines. Multicomponent machines including molecular pistons [484], etc. have been constructed. Inspired by the concept of multivalency in living systems initially, the molecular machines brought out the possibility to manipulate the world at the molecular level.

References

1 Carroll, R.L. and Gorman, C.B. (2002). The genesis of molecular electronics. *Angew. Chem. Int. Ed.* 41: 4378–4400.
2 Robertson, N. and McGowan, C.A. (2003). A comparison of potential molecular wires as components for molecular electronics. *Chem. Soc. Rev.* 32: 96–103.
3 McCreery, R.L. (2004). Molecular electronic junctions. *Chem. Mater.* 16: 4477–4496.
4 Cotton, F.A., Daniels, L.M., Murillo, C.A. et al. (1999). Getting the right answer to a key question concerning molecular wires. *Chem. Commun.* 24: 2461–2462.
5 Tao, N.J. (2009). Electron transport in molecular junctions. *Nanoscience and Technology*: 185–193.
6 Wold, D.J., Haag, R., Rampi, M.A., and Frisbie, C.D. (2002). Distance dependence of electron tunneling through self-assembled monolayers measured by conducting probe atomic force microscopy: unsaturated versus saturated molecular junctions. *J. Phys. Chem. B* 106: 2813–2816.
7 Salomon, A., Cahen, D., Lindsay, S. et al. (2003). Comparison of electronic transport measurements on organic molecules. *Adv. Mater.* 15: 1881–1890.
8 Wierzbinski, E., Yin, X., Werling, K. et al. (2013). The effect of oxygen heteroatoms on the single molecule conductance of saturated chains. *J. Phys. Chem. B* 117: 4431–4441.
9 Sun, Y.-Y., Peng, Z.-L., Hou, R. et al. (2014). Enhancing electron transport in molecular wires by insertion of a ferrocene center. *Phys. Chem. Chem. Phys.* 16: 2260–2267.
10 Wang, C., Batsanov, A.S., Bryce, M.R. et al. (2009). Oligoyne single molecule wires. *J. Am. Chem. Soc.* 131: 15647–15654.
11 Weller, M.D., Kariuki, B.M., and Cox, L.R. (2008). β-Halovinylsilanes in oligoyne synthesis: A fluoride-catalysed unmasking of alkynes from beta-fluorovinylsilanes. *Tetrahedron Lett.* 49: 4596–4600.
12 Schrettl, S., Contal, E., Hoheisel, T.N. et al. (2015). Facile synthesis of oligoyne amphiphiles and their rotaxanes. *Chem. Sci.* 6: 564–574.
13 Zhou, N.Z. and Zhao, Y.M. (2010). Conjugated oligoyne-bridged 60 fullerene molecular dumbbells: Syntheses and thermal and morphological properties. *J. Org. Chem.* 75: 1498–1516.

14 Weller, M.D., Kariuki, B.M., and Cox, L.R. (2009). Synthesis of hybrid masked triyne-phenylene axial rods containing (E)-beta-chlorovinylsilanes in the pi-conjugated framework. *J. Org. Chem.* 74: 7898–7907.

15 Champness, N.R., Khlobystov, A.N., Majuga, A.G. et al. (1999). An improved preparation of 4-ethynylpyridine and its application to the synthesis of linear bipyridyl ligands. *Tetrahedron Lett.* 40: 5413–5416.

16 Lee, C.K.Y., Groneman, J.L., Turner, P. et al. (2006). Synthesis and X-ray crystallographic analysis of chiral pyridyl substituted carbocyclic molecular clefts. *Tetrahedron* 62: 4870–4878.

17 Moreno-Garcia, P., Gulcur, M., Manrique, D.Z. et al. (2013). Single-molecule conductance of functionalized oligoynes: length dependence and junction evolution. *J. Am. Chem. Soc.* 135 (33): 12228.

18 Taylor, J., Brandbyge, M., and Stokbro, K. (2003). Conductance switching in a molecular device: The role of side groups and intermolecular interactions. *Phys. Rev. B* 68: 121101.

19 James, P.V., Sudeep, P.K., Suresh, C.H., and Thomas, K.G. (2006). Photophysical and theoretical investigations of oligo(p-phenyleneethynylene)s: effect of alkoxy substitution and alkyne-aryl bond rotations. *J. Phys. Chem. A* 110: 4329–4337.

20 Fraysse, S., Coudret, C., and Launay, J.P. (2003). Molecular wires built from binuclear cyclometalated complexes. *J. Am. Chem. Soc.* 125: 5880–5888.

21 Tour, J.M. (2007). Transition to organic materials science. Passive, active, and hybrid nanotechnologies. *J. Org. Chem.* 72: 7477–7496.

22 Nishiyama, F., Ogawa, K., Tanaka, S., and Yokoyama, T. (2008). Direct conformational analysis of a 10 nm long oligothiophene wire. *J. Phys. Chem. B* 112: 5272–5275.

23 Lee, S.K., Yamada, R., Tanaka, S. et al. (2012). Universal temperature crossover behavior of electrical conductance in a single oligothiophene molecular wire. *ACS Nano* 6: 5078–5088.

24 Ie, Y., Endou, M., Lee, S.K. et al. (2011). Completely encapsulated oligothiophenes: Synthesis, properties, and single-molecule conductance. *Angew. Chem. Int. Ed.* 50: 11980–11984.

25 Flatt, A.K., Dirk, S.M., Henderson, J.C. et al. (2003). Synthesis and testing of new end-functionalized oligomers for molecular electronics. *Tetrahedron* 59: 8555–8570.

26 Lipton-Duffin, J.A., Ivasenko, O., Perepichka, D.F., and Rosei, F. (2009). Synthesis of polyphenylene molecular wires by surface-confined polymerization. *Small* 5: 592–597.

27 Venkataraman, L., Klare, J.E., Nuckolls, C. et al. (2006). Dependence of single-molecule junction conductance on molecular conformation. *Nature* 442: 904–907.

28 Lafferentz, L., Ample, F., Yu, H. et al. (2009). Conductance of a single conjugated polymer as a continuous function of its length. *Science* 323: 1193–1197.

29 Leary, E., Teresa Gonzalez, M., van der Pol, C. et al. (2011). Unambiguous one-molecule conductance measurements under ambient conditions. *Nano Lett.* 11 (6): 2236.

30 Tour, J.M. (2000). Molecular electronics. Synthesis and testing of components. *Acc. Chem. Res.* 33: 791–804.

31 Blum, A.S., Yang, J.C., Shashidhar, R., and Ratna, B. (2003). Comparing the conductivity of molecular wires with the scanning tunneling microscope. *Appl. Phys. Lett.* 82: 3322–3324.

32 Walzer, K., Marx, E., Greenham, N.C. et al. (2004). Scanning tunneling microscopy of self-assembled phenylene ethynylene oligomers on Au(111) substrates. *J. Am. Chem. Soc.* 126: 1229–1234.

33 Donhauser, Z.J., Mantooth, B.A., Kelly, K.F. et al. (2001). Conductance switching in single molecules through conformational changes. *Science* 292: 2303–2307.

34 Wang, L.-J., Yong, A., Zhou, K.-G. et al. (2013). Conformation-controlled electron transport in single-molecule junctions containing oligo(phenylene ethynylene) derivatives. *Chem. Asian J.* 8: 1901–1909.

35 Kaliginedi, V., Moreno-Garcia, P., Valkenier, H. et al. (2012). Correlations between molecular structure and single-junction conductance: A case study with oligo(phenylene-ethynylene)-type wires. *J. Am. Chem. Soc.* 134: 5262–5275.

36 González, M.T., Zhao, X., Manrique, D.Z. et al. (2014). Structural versus electrical functionalization of oligo(phenylene ethynylene) diamine molecular junctions. *J. Phys. Chem. C* 118: 21655–21662.

37 Terao, J., Tanaka, Y., Tsuda, S. et al. (2009). Insulated molecular wire with highly conductive pi-conjugated polymer core. *J. Am. Chem. Soc.* 131: 18046–18047.

38 Wang, H., Tan, L., Wang, L.-J. et al. (2008). Shell dominated molecular packing in dendrimer encapsulated 'core-shell' molecular wires. *Chem. Phys. Lett.* 461: 271–275.

39 Wang, L.-J., Zhou, K.-G., Tan, L. et al. (2011). A core-shell strategy for constructing a single-molecule junction. *Chem. Eur. J.* 17 (30): 8414.

40 Cui, X.D., Primak, A., Zarate, X. et al. (2001). Reproducible measurement of single-molecule conductivity. *Science* 294: 571–574.

41 Giacalone, F., Herranz, M.A., Grueter, L. et al. (2007). Tetrathiafulvalene-based molecular nanowires. *Chem. Commun.* 46: 4854–4856.

42 Parker, C.R., Leary, E., Frisenda, R. et al. (2014). A comprehensive study of extended tetrathiafulvalene cruciform molecules for molecular electronics: synthesis and electrical transport measurements. *J. Am. Chem. Soc.* 136: 16497–16507.

43 Seferos, D.S., Szuchmacher Blum, A., Kushmerick, J.G., and Bazan, G.C. (2006). Single-molecule charge-transport measurements that reveal technique-dependent perturbations. *J. Am. Chem. Soc.* 128: 11260–11267.

44 Selzer, Y., Cai, L., Cabassi, M.A. et al. (2005). Effect of local environment on molecular conduction: isolated molecule versus self-assembled monolayer. *Nano Lett.* 5: 61–65.

45 Davis, W.B., Svec, W.A., Ratner, M.A., and Wasielewski, M.R. (1998). Molecular-wire behaviour in p-phenylenevinylene oligomers. *Nature* 396: 60–63.

46 Prins, P., Grozema, F.C., and Siebbeles, L.D.A. (2006). Efficient charge transport along phenylene-vinylene molecular wires. *J. Phys. Chem. B* 110: 14659–14666.

47 Martin, S., Haiss, W., Higgins, S.J., and Nichols, R.J. (2010). The impact of E-Z photo-isomerization on single molecular conductance. *Nano Lett.* 10: 2019–2023.

48 Choi, S.H., Kim, B., and Frisbie, C.D. (2008). Electrical resistance of long conjugated molecular wires. *Science* 320: 1482–1486.

49 Luo, L. and Frisbie, C.D. (2010). Length-dependent conductance of conjugated molecular wires synthesized by stepwise "click" chemistry. *J. Am. Chem. Soc.* 132: 8854–8855.

50 Schull, T.L., Kushmerick, J.G., Patterson, C.H. et al. (2003). Ligand effects on charge transport in platinum(II) acetylides. *J. Am. Chem. Soc.* 125: 3202–3203.

51 Ren, T. (2005). Diruthenium sigma-alkynyl compounds: a new class of conjugated organometallics. *Organometallics* 24: 4854–4870.

52 Mas-Ballesté, R., Castillo, O., Sanz Miguel, P.J. et al. (2009). Towards molecular wires based on metal-organic frameworks. *Eur. J. Inorg. Chem.* 2009: 2885–2896.

53 Mayor, M., von Hänisch, C., Weber, H.B. et al. (2002). Atrans-platinum(II) complex as a single-molecule insulator. *Angew. Chem. Int. Ed.* 41: 1183–1186.

54 Wen, H.M., Yang, Y., Zhou, X.S. et al. (2013). Electrical conductance study on 1,3-butadiyne-linked dinuclear ruthenium(II) complexes within single molecule break junctions. *Chem. Sci.* 4: 2471–2477.

55 Mahapatro, A.K., Ying, J.W., Ren, T., and Janes, D.B. (2008). Electronic transport through ruthenium-based redox-active molecules in metal-molecule-metal nanogap junctions. *Nano Lett.* 8: 2131–2136.

56 Kim, B., Beebe, J.M., Olivier, C. et al. (2007). Temperature and length dependence of charge transport in redox-active molecular wires incorporating ruthenium(II) bis(sigma-arylacetylide) complexes. *J. Phys. Chem. C* 111: 7521–7526.

57 Luo, L., Benameur, A., Brignou, P. et al. (2011). Length and temperature dependent conduction of ruthenium-containing redox-active molecular wires. *J. Phys. Chem. C* 115: 19955–19961.

58 Benameur, A., Brignou, P., Di Piazza, E. et al. (2011). Redox-active ruthenium(II) sigma-arylacetylide wires for molecular electronics incorporating insulating chains. *New J. Chem.* 35: 2105–2113.

59 Albrecht, T., Moth-Poulsen, K., Christensen, J.B. et al. (2006). In situ scanning tunnelling spectroscopy of inorganic transition metal complexes. *Faraday Discuss.* 131: 265–279.

60 Chen, I.W.P., Fu, M.-D., Tseng, W.-H. et al. (2006). Conductance and stochastic switching of ligand-supported linear chains of metal atoms. *Angew. Chem. Int. Ed.* 45: 5814–5818.

61 Guo, X., Small, J.P., Klare, J.E. et al. (2006). Covalently bridging gaps in single-walled carbon nanotubes with conducting molecules. *Science* 311: 356–359.

62 Cao, Y., Dong, S.H., Liu, S. et al. (2012). Building high-throughput molecular junctions using indented graphene point contacts. *Angew. Chem. Int. Ed.* 51: 12228–12232.

63 Park, J., Pasupathy, A.N., Goldsmith, J.I. et al. (2002). Coulomb blockade and the Kondo effect in single-atom transistors. *Nature* 417: 722–725.

64 Tang, J.Y., Wang, Y.L., Klare, J.E. et al. (2007). Encoding molecular-wire formation within nanoscale sockets. *Angew. Chem. Int. Ed.* 46: 3892–3895.

65 Constable, E.C. (2008). Expanded ligands-an assembly principle for supramolecular chemistry. *Coord. Chem. Rev.* 252: 842–855.

66 Jia, C.C., Li, H., Jiang, J.L. et al. (2013). Interface-engineered bistable [2]rotaxane-graphene hybrids with logic capabilities. *Adv. Mater.* 25: 6752–6759.

67 Tuccitto, N., Ferri, V., Cavazzini, M. et al. (2009). Highly conductive similar to 40-nm-long molecular wires assembled by stepwise incorporation of metal centres. *Nat. Mater.* 8: 41–46.

68 Anderson, H.L. (1999). Building molecular wires from the colours of life: conjugated porphyrin oligomers. *Chem. Commun.*: 2323–2330.

69 Tsuda, A. and Osuka, A. (2001). Fully conjugated porphyrin tapes with electronic absorption bands that reach into infrared. *Science* 293: 79–82.

70 de la Torre, G., Bottari, G., Sekita, M. et al. (2013). A voyage into the synthesis and photophysics of homo- and heterobinuclear ensembles of phthalocyanines and porphyrins. *Chem. Soc. Rev.* 42: 8049–8105.

71 Katsunori, T. and Masaru, T. (2003). Theoretical predictions of electronic transport properties of differently conjugated porphyrin molecular wires. *Jpn. J. Appl. Phys* 42: 3606–3610.

72 Tanaka, T. and Osuka, A. (2015). Conjugated porphyrin arrays: synthesis, properties and applications for functional materials. *Chem. Soc. Rev.* 44: 943–969.

73 Anderson, S., Anderson, H.L., and Sanders, J.K.M. (1993). Expanding roles for templates in synthesis. *Acc. Chem. Res.* 26: 469–475.

74 Nakamura, Y., Aratani, N., and Osuka, A. (2007). Cyclic porphyrin arrays as artificial photosynthetic antenna: Synthesis and excitation energy transfer. *Chem. Soc. Rev.* 36: 831–845.

75 Jurow, M., Schuckman, A.E., Batteas, J.D., and Drain, C.M. (2010). Porphyrins as molecular electronic components of functional devices. *Coord. Chem. Rev.* 254: 2297–2310.

76 Sedghi, G., Sawada, K., Esdaile, L.J. et al. (2008). Single molecule conductance of porphyrin wires with ultralow attenuation. *J. Am. Chem. Soc.* 130: 8582–8583.

77 Sedghi, G., Garcia-Suarez, V.M., Esdaile, L.J. et al. (2011). Long-range electron tunnelling in oligo-porphyrin molecular wires. *Nat. Nanotechnol.* 6 (8): 517.

78 Sedghi, G., Garcia-Suarez, V.M., Esdaile, L.J. et al. (2012). Comparison of the conductance of three types of porphyrin-based molecular wires: β,meso,β-fused tapes, meso-butadiyne-linked and twisted meso-meso linked oligomers. *Adv. Mater.* 24: 653–657.

79 Avouris, P. (2002). Molecular electronics with carbon nanotubes. *Acc. Chem. Res.* 35: 1026–1034.

80 Dai, H. (2002). Molecular electronics with carbon nanotubes. *Acc. Chem. Res.* 35 (12): 1035.

81 Li, Z.H., Park, T.H., Rawson, J. et al. (2012). Quasi-ohmic single molecule charge transport through highly conjugated meso-to-meso ethyne-bridged porphyrin wires. *Nano Lett.* 12: 2722–2727.

82 Wong, H.-S.P. and Akinwande, D. (2011). *Carbon Nanotube and Graphene Device Physics*. Cambridge University Press.

83 Derycke, V., Martel, R., Appenzeller, J., and Avouris, P. (2001). Carbon nanotube inter- and intramolecular logic gates. *Nano Lett.* 1: 453–456.

84 Javey, A., Wang, Q., Ural, A. et al. (2002). Carbon nanotube transistor arrays for multistage complementary logic and ring oscillators. *Nano Lett.* 2: 929–932.

85 Rueckes, T., Kim, K., Joselevich, E. et al. (2000). Carbon nanotube-based nonvolatile random access memory for molecular computing. *Science* 289: 94–97.

86 Chen, Z.H., Appenzeller, J., Lin, Y.-M. et al. (2006). An integrated logic circuit assembled on a single carbon nanotube. *Science* 311: 1735.

87 Shulaker, M.M., Hills, G., Patil, N. et al. (2013). Carbon nanotube computer. *Nature* 501: 526–530.

88 Yang, F., Wang, X., Zhang, D.Q. et al. (2014). Chirality-specific growth of single-walled carbon nanotubes on solid alloy catalysts. *Nature* 510: 522–524.

89 Chen, Y.B. and Zhang, J. (2014). Chemical vapor deposition growth of single-walled carbon nanotubes with controlled structures for nanodevice applications. *Acc. Chem. Res.* 47: 2273–2281.

90 Hu, Y., Kang, L.X., Zhao, Q.C. et al. (2015). Growth of high-density horizontally aligned SWCNT arrays using Trojan catalysts. *Nat. Commun.* 6: 6099.

91 Taniguchi, M. and Kawai, T. (2006). DNA electronics. *Physica E* 33: 1–12.

92 Porath, D., Cuniberti, G., and Di Felice, R. (2004). Long-range charge transfer in DNA. *Top. Curr. Chem.* 237: 183–227.

93 Storm, A.J., van Noort, J., de Vries, S., and Dekker, C. (2001). Insulating behavior for DNA molecules between nanoelectrodes at the 100 nm length scale. *Appl. Phys. Lett.* 79: 3881–3883.

94 Slinker, J.D., Muren, N.B., Renfrew, S.E., and Barton, J.K. (2011). DNA charge transport over 34 nm. *Nat. Chem.* 3: 228–233.

95 Giese, B., Amaudrut, J., Kohler, A.-K. et al. (2001). Direct observation of hole transfer through DNA by hopping between adenine bases and by tunnelling. *Nature* 412: 318–320.

96 Artes, J.M., Lopez-Martinez, M., Giraudet, A. et al. (2012). Current–voltage characteristics and transition voltage spectroscopy of individual redox proteins. *J. Am. Chem. Soc.* 134: 20218–20221.

97 Hihath, J., Xu, B.Q., Zhang, P.M., and Tao, N. (2005). Study of single-nucleotide polymorphisms by means of electrical conductance measurements. *Proc. Natl. Acad. Sci. U. S. A.* 102: 16979–16983.

98 Guo, X.F., Gorodetsky, A.A., Hone, J. et al. (2008). Conductivity of a single DNA duplex bridging a carbon nanotube gap. *Nat. Nanotechnol.* 3: 163–167.

99 van Zalinge, H., Schiffrin, D.J., Bates, A.D. et al. (2006). Variable-temperature measurements of the single-molecule conductance of double-stranded DNA. *Angew. Chem. Int. Ed.* 45: 5499–5502.

100 Genereux, J.C. and Barton, J.K. (2010). Mechanisms for DNA charge transport. *Chem. Rev.* 110 (3): 1642.

101 Liu, S.P., Weisbrod, S.H., Tang, Z. et al. (2010). Direct measurement of electrical transport through G-quadruplex DNA with mechanically controllable break junction electrodes. *Angew. Chem. Int. Ed.* 49: 3313–3316.

102 Liu, S., Zhang, X.Y., Luo, W.X. et al. (2011). Single-molecule detection of proteins using aptamer-functionalized molecular electronic devices. *Angew. Chem. Int. Ed.* 50: 2496–2502.

103 Liu, S., Clever, G.H., Takezawa, Y. et al. (2011). Direct conductance measurement of individual metallo-DNA duplexes within single-molecule break junctions. *Angew. Chem. Int. Ed.* 123: 9048–9052.

104 Moore, T.A., Gust, D., Mathis, P. et al. (1984). Photodriven charge separation in a carotenoporphyrin-quinone triad. *Nature* 307: 630–632.

105 Leatherman, G., Durantini, E.N., Gust, D. et al. (1999). Carotene as a molecular wire: Conducting atomic force microscopy. *J. Phys. Chem. B* 103: 4006–4010.

106 Ramachandran, G.K., Tomfohr, J.K., Li, J. et al. (2003). Electron transport properties of a carotene molecule in a metal-(single molecule)-metal junction. *J. Phys. Chem. B* 107: 6162–6169.

107 Xu, B.Q. and Tao, N.J.J. (2003). Measurement of single-molecule resistance by repeated formation of molecular junctions. *Science* 301: 1221–1223.

108 He, J., Chen, F., Li, J. et al. (2005). Electronic decay constant of carotenoid polyenes from single-molecule measurements. *J. Am. Chem. Soc.* 127: 1384–1385.

109 Zhao, Y.A., Lindsay, S., Jeon, S. et al. (2013). Combined effect of polar substituents on the electronic flows in the carotenoid molecular wires. *Chem. Eur. J.* 19: 10832–10835.

110 Maeng, J., Kim, S.B., Lee, N.J. et al. (2010). Conductance control in stabilized carotenoid wires. *Chem. Eur. J.* 16: 7395–7399.

111 Visoly-Fisher, I., Daie, K., Terazono, Y. et al. (2006). Conductance of a biomolecular wire. *Proc. Natl. Acad. Sci. U. S. A.* 103: 8686–8690.

112 Chen, F., Hihath, J., Huang, Z.F. et al. (2007). Measurement of single-molecule conductance. *Annu. Rev. Phys. Chem.* 58: 535–564.

113 Karthaeuser, S. (2011). Control of molecule-based transport for future molecular devices. *J. Phys.: Condens. Matter* 23: 013001.

114 Nitzan, A. (2001). A relationship between electron-transfer rates and molecular conduction. *J. Phys. Chem. A* 105: 2677–2679.

115 Nitzan, A. (2001). Electron transmission through molecules and molecular interfaces. *Annu. Rev. Phys. Chem.* 52: 681.

116 Jia, C. and Guo, X. (2013). Molecule-electrode interfaces in molecular electronic devices. *Chem. Soc. Rev.* 42: 5642–5660.

117 Venkataraman, L., Klare, J.E., Tam, I.W. et al. (2006). Single-molecule circuits with well-defined molecular conductance. *Nano Lett.* 6: 458–462.

118 Rawlett, A.M., Hopson, T.J., Nagahara, L.A. et al. (2002). Electrical measurements of a dithiolated electronic molecule via conducting atomic force microscopy. *Appl. Phys. Lett.* 81: 3043–3045.

119 Marquardt, C.W., Grunder, S., Baszczyk, A. et al. (2010). Electroluminescence from a single nanotube-molecule-nanotube junction. *Nat. Nanotechnol.* 5: 863–867.

120 Aradhya, S.V., Frei, M., Hybertsen, M.S., and Venkataraman, L. (2012). Van der Waals interactions at metal/organic interfaces at the single-molecule level. *Nat. Mater.* 11: 872–876.

121 Wei, D.C., Liu, Y.Q., Cao, L.C. et al. (2008). Real time and in situ control of the gap size of nanoelectrodes for molecular devices. *Nano Lett.* 8: 1625–1630.

122 Prins, F., Barreiro, A., Ruitenberg, J.W. et al. (2011). Room-temperature gating of molecular junctions using few-layer graphene nanogap electrodes. *Nano Lett.* 11: 4607–4611.

123 Ko, C.-H., Huang, M.-J., Fu, M.-D., and Chen, C.-H. (2010). Superior contact for single-molecule conductance: Electronic coupling of thiolate and isothiocyanate on Pt, Pd, and Au. *J. Am. Chem. Soc.* 132: 756–764.

124 Thuo, M.M., Reus, W.F., Simeone, F.C. et al. (2012). Replacing -CH_2CH_2- with -CONH- does not significantly change rates of charge transport through Ag^{TS}-SAM//Ga_2O_3/EGaIn junctions. *J. Am. Chem. Soc.* 134: 10876–10884.

125 Yoon, H.J., Shapiro, N.D., Park, K.M. et al. (2012). The rate of charge tunneling through self-assembled monolayers is insensitive to many functional group substitutions. *Angew. Chem. Int. Ed.* 51: 4658–4661.

126 Joshua, H. and Nongjian, T. (2014). The role of molecule-electrode contact in single-molecule electronics. *Semicond. Sci. Technol.* 29: 054007.

127 Kim, Y., Hellmuth, T.J., Burkle, M. et al. (2011). Characteristics of amine-ended and thiol-ended alkane single-molecule junctions revealed by inelastic electron tunneling spectroscopy. *ACS Nano* 5: 4104–4111.

128 Kim, C.M. and Bechhoefer, J. (2013). Conductive probe AFM study of Pt-thiol and Au-thiol contacts in metal-molecule-metal systems. *J. Chem. Phys.* 138: 014707.

129 Sen, A. and Kaun, C.-C. (2010). Effect of electrode orientations on charge transport in alkanedithiol single-molecule junctions. *ACS Nano* 4: 6404–6408.

130 Frei, M., Aradhya, S.V., Hybertsen, M.S., and Venkataraman, L. (2012). Linker dependent bond rupture force measurements in single-molecule junctions. *J. Am. Chem. Soc.* 134: 4003–4006.

131 Jiang, C.L., Lin, Y., Zhang, Z. et al. (2015). WASAR imaging based on message passing with structured sparse constraint: approach and experiment. In: *2015 3rd International Workshop on Compressed Sensing Theory and Its Application to Radar, Sonar, and Remote Sensing (CoSeRa)*, 219–213.

132 Jia, C.C., Wang, J.Y., Yao, C.J. et al. (2013). Conductance switching and mechanisms in single-molecule junctions. *Angew. Chem. Int. Ed.* 52: 8666–8670.

133 Beebe, J.M., Kim, B., Frisbie, C.D., and Kushmerick, J.G. (2008). Measuring relative barrier heights in molecular electronic junctions with transition voltage spectroscopy. *ACS Nano* 2: 827–832.

134 Davis, W.B., Wasielewski, M.R., Ratner, M.A. et al. (1997). Electron transfer rates in bridged molecular systems: a phenomenological approach to relaxation. *J. Phys. Chem. A* 101: 6158–6164.

135 González, M.T., Wu, S., Huber, R. et al. (2006). Electrical conductance of molecular junctions by a robust statistical analysis. *Nano Lett.* 6: 2238–2242.

136 Jang, S.-Y., Reddy, P., Majumdar, A., and Segalman, R.A. (2006). Interpretation of stochastic events in single molecule conductance measurements. *Nano Lett.* 6: 2362–2367.

137 Guo, S.Y., Hihath, J., Diez-Perez, I., and Tao, N. (2011). Measurement and statistical analysis of single-molecule current–voltage characteristics, transition voltage spectroscopy, and tunneling barrier height. *J. Am. Chem. Soc.* 133: 19189–19197.

138 Bruot, C., Hihath, J., and Tao, N.J. (2012). Mechanically controlled molecular orbital alignment in single molecule junctions. *Nat. Nanotechnol.* 7: 35–40.

139 Zhou, J.F., Wang, K., Xu, B.Q. et al. (2018). Photoconductance from exciton binding in molecular junctions. *J. Am. Chem. Soc.* 140: 70–73.

140 Vadai, M., Nachman, N., Ben-Zion, M. et al. (2013). Plasmon-induced conductance enhancement in single-molecule junctions. *J. Phys. Chem. Lett.* 4: 2811–2816.

141 Jia, C.C., Migliore, A., Xin, N. et al. (2016). Covalently bonded single-molecule junctions with stable and reversible photoswitched conductivity. *Science* 352: 1443–1445.

142 Tebikachew, B.E., Li, H.P.B., Pirrotta, A. et al. (2017). Effect of ring strain on the charge transport of a robust norbornadiene-quadricyclane-based molecular photoswitch. *J. Phys. Chem. C* 121: 7094–7100.

143 Huang, C.C., Jevric, M., Borges, A. et al. (2017). Single-molecule detection of dihydroazulene photo-thermal reaction using break junction technique. *Nat. Commun.* 8: 15436.

144 Galperin, M. and Nitzan, A. (2006). Optical properties of current carrying molecular wires. *J. Chem. Phys.* 124: 234709.

145 Galperin, M. and Nitzan, A. (2012). Molecular optoelectronics: the interaction of molecular conduction junctions with light. *Phys. Chem. Chem. Phys.* 14: 9421–9438.

146 Arielly, R., Ofarim, A., Noy, G. et al. (2011). Accurate determination of plasmonic fields in molecular junctions by current rectification at optical frequencies. *Nano Lett.* 11: 2968–2972.

147 Xiang, D., Wang, X.L., Jia, C.C. et al. (2016). Molecular-scale electronics: from concept to function. *Chem. Rev.* 116: 4318–4440.

148 Dulic, D., van der Molen, S.J., Kudernac, T. et al. (2003). One-way optoelectronic switching of photochromic molecules on gold. *Phys. Rev. Lett.* 91: 207402.

149 Noy, G., Ophir, A., and Selzer, Y. (2010). Response of molecular junctions to surface plasmon polaritons. *Angew. Chem. Int. Ed.* 49: 5734–5736.

150 Fan, F.-R.F., Yang, J., Cai, L. et al. (2002). Charge transport through self-assembled monolayers of compounds of interest in molecular electronics. *J. Am. Chem. Soc.* 124: 5550–5560.

151 Wold, D.J. and Frisbie, C.D. (2000). Formation of metal-molecule-metal tunnel junctions: Microcontacts to alkanethiol monolayers with a conducting AFM tip. *J. Am. Chem. Soc.* 122: 2970–2971.

152 Kushmerick, J.G., Holt, D.B., Pollack, S.K. et al. (2002). Effect of bond-length alternation in molecular wires. *J. Am. Chem. Soc.* 124: 10654–10655.

153 Stewart, D.R., Ohlberg, D.A.A., Beck, P.A. et al. (2004). Molecule-independent electrical switching in Pt/organic monolayer/Ti devices. *Nano Lett.* 4: 133–136.

154 Collier, C.P., Mattersteig, G., Wong, E.W. et al. (2000). A [2]catenane-based solid state electronically reconfigurable switch. *Science* 289: 1172–1175.

155 Mbindyo, J.K.N., Mallouk, T.E., Mattzela, J.B. et al. (2002). Template synthesis of metal nanowires containing monolayer molecular junctions. *J. Am. Chem. Soc.* 124: 4020–4026.

156 Metzger, R.M. (1999). Electrical rectification by a molecule: the advent of unimolecular electronic devices. *Acc. Chem. Res.* 32: 950–957.

157 Aviram, A. and Ratner, M.A. (1974). Molecular rectifiers. *Chem. Phys. Lett.* 29: 277–283.

158 Tsutsui, M. and Taniguchi, M. (2012). Single molecule electronics and devices. *Sensors* 12: 7259–7298.

159 Lortscher, E., Gotsmann, B., Lee, Y. et al. (2012). Transport properties of a single-molecule diode. *ACS Nano* 6: 4931–4939.

160 Metzger, R.M. (2003). Unimolecular electrical rectifiers. *Chem. Rev.* 103: 3803–3834.

161 Metzger, R.M. (2008). Unimolecular electronics. *J. Mater. Chem.* 18: 4364–4396.

162 Metzger, R.M. (2015). Unimolecular electronics. *Chem. Rev.* 115: 5056–5115.

163 Kornilovitch, P.E., Bratkovsky, A.M., and Williams, R.S. (2002). Current rectification by molecules with asymmetric tunneling barriers. *Phys. Rev. B* 66: 165436.

164 Zahid, F., Ghosh, A.W., Paulsson, M. et al. (2004). Charging-induced asymmetry in molecular conductors. *Phys. Rev. B* 70: 245317.

165 Mahmoud, A. and Lugli, P. (2012). Designing the rectification behavior of molecular diodes. *J. Appl. Phys.* 112: 113720.

166 Mujica, V., Ratner, M.A., and Nitzan, A. (2002). Molecular rectification: why is it so rare? *Chem. Phys.* 281: 147–150.

167 Ma, J., Yang, C.L., Wang, L.Z. et al. (2014). Controllable low-bias negative differential resistance, switching, and rectifying behaviors of dipyrimidinyl–diphenyl induced by contact mode. *Physica B* 434: 32–37.

168 Zhang, G., Ratner, M.A., and Reuter, M.G. (2015). Is molecular rectification caused by asymmetric electrode couplings or by a molecular bias drop? *J. Phys. Chem. C* 119: 6254–6260.

169 Ng, M.-K. and Yu, L. (2002). Synthesis of amphiphilic conjugated diblock oligomers as molecular diodes. *Angew. Chem. Int. Ed.* 41: 3598–3601.

170 Ashwell, G.J., Sambles, J.R., Martin, A.S. et al. (1990). Rectifying characteristics of Mg/($C_{16}H_{33}$-Q3CNQ LB film)/Pt structures. *J. Chem. Soc., Chem. Commun.* 19: 1374–1376.

171 Metzger, R.M., Chen, B., Höpfner, U. et al. (1997). Unimolecular electrical rectification in hexadecylquinolinium tricyanoquinodimethanide. *J. Am. Chem. Soc.* 119: 10455–10466.

172 Metzger, R.M., Baldwin, J.W., Shumate, W.J. et al. (2003). Electrical rectification in a Langmuir–Blodgett monolayer of dimethyanilinoazafullerene sandwiched between gold electrodes. *J. Phys. Chem. B* 107: 1021–1027.

173 Honciuc, A., Jaiswal, A., Gong, A. et al. (2005). Current rectification in a Langmuir–Schaefer monolayer of fullerene-bis-[4-diphenylamino-4″-(N-ethyl-N-2‴-ethyl)amino-1,4-diphenyl-1,3-butadiene] malonate between Au electrodes. *J. Phys. Chem. B* 109: 857–871.

174 Shumate, W.J., Mattern, D.L., Jaiswal, A. et al. (2006). Spectroscopy and rectification of three donor–sigma–acceptor compounds, consisting of a one-electron donor (pyrene or ferrocene), a one-electron acceptor (perylenebisimide), and a C_{19} swallowtail. *J. Phys. Chem. B* 110: 11146–11159.

175 Honciuc, A., Metzger, R.M., Gong, A., and Spangler, C.W. (2007). Elastic and inelastic electron tunneling spectroscopy of a new rectifying monolayer. *J. Am. Chem. Soc.* 129: 8310–8319.

176 Metzger, R.M., Xu, T., and Peterson, I.R. (2001). Electrical rectification by a monolayer of hexadecylquinolinium tricyanoquinodimethanide measured between macroscopic gold electrodes. *J. Phys. Chem. B* 105: 7280–7290.

177 Jaiswal, A., Rajagopal, D., Lakshmikantham, M.V. et al. (2007). Unimolecular rectification of monolayers of $CH_3C(O)S–C_{14}H_{28}Q^+–3CNQ^-$ and $CH_3C(O)S–C_{16}H_{32}Q^+$-$3CNQ^-$ organized by self-assembly, Langmuir–Blodgett, and Langmuir–Schaefer techniques. *Phys. Chem. Chem. Phys.* 9: 4007–4017.

178 Honciuc, A., Otsuka, A., Wang, Y.-H. et al. (2006). Polarization of charge-transfer bands and rectification in hexadecylquinolinium 7,7,8-tricyanoquinodimethanide and its tetrafluoro analog. *J. Phys. Chem. B* 110: 15085–15093.

179 Ng, M.-K., Lee, D.-C., and Yu, L. (2002). Molecular diodes based on conjugated diblock co-oligomers. *J. Am. Chem. Soc.* 124 (40): 11862.

180 Jiang, P., Morales, G.M., You, W., and Yu, L. (2004). Synthesis of diode molecules and their sequential assembly to control electron transport. *Angew. Chem. Int. Ed.* 43: 4471–4475.

181 Elke, S. and Carlos, C.J. (2017). *Molecular Electronics. An Introduction to Theory and Experiment*. World Scientific.

182 Morales, G.M., Jiang, P., Yuan, S. et al. (2005). Inversion of the rectifying effect in diblock molecular diodes by protonation. *J. Am. Chem. Soc.* 127: 10456–10457.

183 Díez-Pérez, I., Hihath, J., Lee, Y. et al. (2009). Rectification and stability of a single molecular diode with controlled orientation. *Nat. Chem.* 1: 635–641.

184 Elbing, M., Ochs, R., Koentopp, M. et al. (2005). A single-molecule diode. *Proc. Natl. Acad. Sci. U. S. A.* 102: 8815–8820.

185 Hihath, J., Bruot, C., Nakamura, H. et al. (2011). Inelastic transport and low-bias rectification in a single-molecule diode. *ACS Nano* 5: 8331–8339.

186 Cui, B., Zhao, W.K., Wang, H. et al. (2014). Effect of geometrical torsion on the rectification properties of diblock conjugated molecular diodes. *J. Appl. Phys.* 116: 073701.

187 Hu, G.C., Zhang, G.P., Li, Y. et al. (2014). Proportion effect in diblock co-oligomer molecular diodes. *Chem. Phys. Lett.* 614: 207–213.

188 Luo, L., Balhorn, L., Vlaisavljevich, B. et al. (2014). Hopping transport and rectifying behavior in long donor–acceptor molecular wires. *J. Phys. Chem. C* 118: 26485–26497.

189 Zhang, G.P., Hu, G.C., Song, Y. et al. (2012). Modulation of rectification in diblock co-oligomer diodes by adjusting anchoring groups for both symmetric and asymmetric electrodes. *J. Phys. Chem. C* 116: 22009–22014.

190 Geddes, N.J., Sambles, J.R., Jarvis, D.J. et al. (1990). Fabrication and investigation of asymmetric current–voltage characteristics of a metal/Langmuir–Blodgett monolayer metal structure. *Appl. Phys. Lett.* 56: 1916.

191 Geddes, N.J., Sambles, J.R., Jarvis, D.J. et al. (1992). The electrical-properties of metal-sandwiched Langmuir–Blodgett multilayers and monolayers of a redox-active organic molecular-compound. *J. Appl. Phys.* 71: 756.

192 Martin, A.S., Sambles, J.R., and Ashwell, G.J. (1993). Molecular rectifier. *Phys. Rev. Lett.* 70: 218.

193 Lenfant, S., Krzeminski, C., Delerue, C. et al. (2003). Molecular rectifying diodes from self-assembly on silicon. *Nano Lett.* 3 (6): 741–746.

194 Kim, T., Liu, Z.-F., Lee, C. et al. (2014). Charge transport and rectification in molecular junctions formed with carbon-based electrodes. *Proc. Natl. Acad. Sci. U. S. A.* 111: 10928–10932.

195 Kushmerick, J.G., Whitaker, C.M., Pollack, S.K. et al. (2004). Tuning current rectification across molecular junctions. *Nanotechnology* 15: S489.

196 Wang, K., Zhou, J.F., Hamill, J.M., and Xu, B. (2014). Measurement and understanding of single-molecule break junction rectification caused by asymmetric contacts. *J. Chem. Phys.* 141: 054712.

197 Batra, A., Darancet, P., Chen, Q.S. et al. (2013). Tuning rectification in single-molecular diodes. *Nano Lett.* 13: 6233–6237.

198 Yu, H.B., Luo, Y., Beverly, K. et al. (2003). The molecule–electrode interface in single-molecule transistors. *Angew. Chem. Int. Ed.* 42: 5706–5711.

199 Krzeminski, C., Delerue, C., Allan, G. et al. (2001). Theory of electrical rectification in a molecular monolayer. *Phys. Rev. B* 64: 085405.

200 Liu, R., Ke, S.H., Yang, W.T., and Baranger, H.U. (2006). Organometallic molecular rectification. *J. Chem. Phys.* 124: 024718.

201 Taylor, J., Brandbyge, M., and Stokbro, K. (2002). Theory of rectification in tour wires: The role of electrode coupling. *Phys. Rev. Lett.* 89: 138301.

202 Zhang, G.-P., Hu, G.-C., Song, Y. et al. (2013). Stretch or contraction induced inversion of rectification in diblock molecular junctions. *J. Chem. Phys.* 139: 094702.

203 Capozzi, B., Xia, J., Adak, O., et al. (2015). Single-molecule diodes with high rectification ratios through environmental control. *Nat. nanotechnol.* 10: 522.

204 Troisi, A. and Ratner, M.A. (2004). Conformational molecular rectifiers. *Nano Lett.* 4: 591–595.

205 Capozzi, B., Xia, J., Adak, O. et al. (2015). Single-molecule diodes with high rectification ratios through environmental control. *Nat. Nanotechnol.* 10: 522–527.

206 Zhang, Q. (2014). A gate controlled conjugated single molecule diode: Its rectification could be reversed. *Physica B* 450: 90–93.

207 Adak, O., Korytar, R., Joe, A.Y. et al. (2015). Impact of electrode density of states on transport through pyridine-linked single molecule junctions. *Nano Lett.* 15: 3716–3722.

208 Guisinger, N.P., Greene, M.E., Basu, R. et al. (2004). Room temperature negative differential resistance through individual organic molecules on silicon surfaces. *Nano Lett.* 4: 55–59.

209 Tu, X.W., Mikaelian, G., and Ho, W. (2008). Controlling single-molecule negative differential resistance in a double-barrier tunnel junction. *Phys. Rev. Lett.* 100: 126807.

210 Chen, J., Reed, M.A., Rawlett, A.M., and Tour, J.M. (1999). Large on-off ratios and negative differential resistance in a molecular electronic device. *Science* 286: 1550–1552.

211 He, J. and Lindsay, S.M. (2005). On the mechanism of negative differential resistance in ferrocenylundecanethiol self-assembled monolayers. *J. Am. Chem. Soc.* 127: 11932–11933.

212 Xue, Y.Q., Datta, S., Hong, S.H. et al. (1999). Negative differential resistance in the scanning tunneling spectroscopy of organic molecules. *Phys. Rev. B* 59: 7852–7855.

213 Heersche, H.B., de Groot, Z., Folk, J.A. et al. (2006). Electron transport through single Mn_{12} molecular magnets. *Phys. Rev. Lett.* 96: 206801.

214 Gaudioso, J., Lauhon, L.J., and Ho, W. (2000). Vibrationally mediated negative differential resistance in a single molecule. *Phys. Rev. Lett.* 85: 1918.

215 Kratochvilova, I., Kocirik, M., Zambova, A. et al. (2002). Room temperature negative differential resistance in molecular nanowires. *J. Mater. Chem.* 12: 2927–2930.

216 Chen, J.S., Xu, L.L., Lin, J. et al. (2006). Negative differential resistance effect in organic devices based on an anthracene derivative. *Appl. Phys. Lett.* 89: 083514.

217 Chen, L., Hu, Z.P., Zhao, A.D. et al. (2007). Mechanism for negative differential resistance in molecular electronic devices: local orbital symmetry matching. *Phys. Rev. Lett.* 99: 146803.

218 Xiao, X., Nagahara, L.A., Rawlett, A.M., and Tao, N. (2005). Electrochemical gate-controlled conductance of single oligo(phenylene ethynylene)s. *J. Am. Chem. Soc.* 127: 9235–9240.

219 Wang, W.H., Ji, Y.F., Zhang, H. et al. (2012). Negative differential resistance in a hybrid silicon-molecular system: resonance between the intrinsic surface-states and the molecular orbital. *ACS Nano* 6: 7066–7076.

220 Perrin, M.L., Frisenda, R., Koole, M. et al. (2014). Large negative differential conductance in single-molecule break junctions. *Nat. Nanotechnol.* 9: 830–834.

221 Li, S.Y., Liu, H., Qiao, J.B. et al. (2018). Magnetic-field-controlled negative differential onductance in graphene *npn* junction resonators. *Phys. Rev. B* 97: 115442.

222 Capasso, F., Sen, S., Cho, A.Y., and Sivco, D.L. (1988). Multiple negative transconductance and differential conductance in a bipolar transistor by sequential quenching of resonant tunneling. *Appl. Phys. Lett.* 53: 1056.

223 Choi, K., Levine, B., Malik, R. et al. (1987). Periodic negative conductance by sequential resonant tunneling through an expanding high-field superlattice domain. *Phys. Rev. B* 35: 4172(R).

224 Kumar, S. and Hu, Q. (2009). Coherence of resonant-tunneling transport in terahertz quantum-cascade lasers. *Phys. Rev. B* 80: 245316.

225 Cui, B., Xu, Y.Q., Ji, G.M. et al. (2014). A single-molecule diode with significant rectification and negative differential resistance behavior. *Org. Electron.* 15: 484–490.

226 Oh, S.K., Cho, M.U., Dallas, J. et al. (2017). High-power flexible AlGaN/GaN heterostructure field-effect transistors with suppression of negative differential conductance. *Appl. Phys. Lett.* 111: 133502.

227 Lei, L., Li, L., Huang, W. et al. (2017). Resonant tunneling and multiple negative differential conductance features in long wavelength interband cascade infrared photodetectors. *Appl. Phys. Lett.* 111: 113504.

228 Galan, E., Perrin, M.L., Lutz, M. et al. (2016). Synthesis of 1,2-biphenylethane based single-molecule diodes. *Org. Biomol. Chem.* 14: 2439–2443.

229 Perrin, M.L., Galan, E., Eelkema, R. et al. (2015). Single-molecule resonant tunneling diode. *J. Phys. Chem. C* 119: 5697–5702.

230 George, H.C., Pierre, M., Jehl, X. et al. (2010). Application of negative differential conductance in Al/AlO_x single-electron transistors for background charge characterization. *Appl. Phys. Lett.* 96: 042114.

231 Hitachi, K., Inoue, A., Oiwa, A. et al. (2009). Negative differential conductance in a quantum dot and possible application to ESR detection. *J. Phys.: Conf. Ser.* 150 (2): 022026.

232 Perrin, M.L., Burzuri, E., and van der Zant, H.S.J. (2015). Single-molecule transistors. *Chem. Soc. Rev.* 44: 902–919.

233 Liang, W.J., Shores, M.P., Bockrath, M. et al. (2002). Kondo resonance in a single-molecule transistor. *Nature* 417: 725–729.

234 Kubatkin, S., Danilov, A., Hjort, M. et al. (2003). Single-electron transistor of a single organic molecule with access to several redox states. *Nature* 425: 698–701.

235 Ghosh, A.W., Rakshit, T., and Datta, S. (2004). Gating of a molecular transistor: Electrostatic and conformational. *Nano Lett.* 4: 565–568.

236 Song, H., Kim, Y., Jang, Y.H. et al. (2009). Observation of molecular orbital gating. *Nature* 462: 1039–1043.

237 Champagne, A.R., Pasupathy, A.N., and Ralph, D.C. (2005). Mechanically adjustable and electrically gated single-molecule transistors. *Nano Lett.* 5: 305–308.

238 Parks, J.J., Champagne, A.R., Costi, T.A. et al. (2010). Mechanical control of spin states in spin-1 molecules and the underscreened Kondo effect. *Science* 328: 1370–1373.

239 Martin, C.A., Smit, R.H.M., van der Zant, H.S.J., and van Ruitenbeek, J.M. (2009). A nanoelectromechanical single-atom switch. *Nano Lett.* 9: 2940–2945.

240 Martin, C.A., van Ruitenbeek, J.M., and van der Zant, H.S.J. (2010). Sandwich-type gated mechanical break junctions. *Nanotechnology* 21: 265201.

241 Perrin, M.L., Verzijl, C.J.O., Martin, C.A. et al. (2013). Large tunable image-charge effects in single-molecule junctions. *Nat. Nanotechnol.* 8: 282–287.

242 Carrascal, D., Garcia-Suarez, V.M., and Ferrer, J. (2012). Impact of edge shape on the functionalities of graphene-based single-molecule electronics devices. *Phys. Rev. B* 85: 195434.

243 Xiang, D., Jeong, H., Lee, T., and Mayer, D. (2013). Mechanically controllable break junctions for molecular electronics. *Adv. Mater.* 25: 4845–4867.

244 Xiang, D., Jeong, H., Kim, D. et al. (2013). Three-terminal single-molecule junctions formed by mechanically controllable break junctions with side gating. *Nano Lett.* 13: 2809–2813.

245 Mangin, A., Anthore, A., Della Rocca, M.L. et al. (2009). Transport through metallic nanogaps in an in-plane three-terminal geometry. *J. Appl. Phys.* 105: 014313.

246 Huang, C.C., Rudnev, A.V., Hong, W.J., and Wandlowski, T. (2015). Break junction under electrochemical gating: testbed for single-molecule electronics. *Chem. Soc. Rev.* 44: 889–901.

247 Xu, B.Q., Xiao, X.Y., Yang, X.M. et al. (2005). Large gate modulation in the current of a room temperature single molecule transistor. *J. Am. Chem. Soc.* 127: 2386–2387.

248 Chen, F., He, J., Nuckolls, C. et al. (2005). A molecular switch based on potential-induced changes of oxidation state. *Nano Lett.* 5: 503–506.

249 Pobelov, I.V., Li, Z.H., and Wandlowski, T. (2008). Electrolyte gating in redox-active tunneling junctions–an electrochemical STM approach. *J. Am. Chem. Soc.* 130: 16045–16054.

250 Cui, L., Liu, B., Vonlanthen, D. et al. (2011). In situ gap-mode Raman spectroscopy on single-crystal Au(100) electrodes: Tuning the torsion angle of 4,4′-biphenyldithiols by an electrochemical gate field. *J. Am. Chem. Soc.* 133: 7332–7335.

251 Guo, S.Y., Artes, J.M., and Diez-Perez, I. (2013). Electrochemically-gated single-molecule electrical devices. *Electrochim. Acta* 110: 741–753.

252 Yi, Z.W., Trellenkamp, S., Offenhausser, A., and Mayer, D. (2010). Molecular junctions based on intermolecular electrostatic coupling. *Chem. Commun.* 46: 8014–8016.

253 Yang, Y., Liu, J.Y., Chen, Z.B. et al. (2011). Conductance histogram evolution of an EC–MCBJ fabricated Au atomic point contact. *Nanotechnology* 22: 275313.

254 Baghernejad, M., Manrique, D.Z., Li, C. et al. (2014). Highly-effective gating of single-molecule junctions: An electrochemical approach. *Chem. Commun.* 50: 15975–15978.

255 Baghernejad, M., Zhao, X.T., Ornso, K.B. et al. (2014). Electrochemical control of single-molecule conductance by Fermi level tuning and conjugation switching. *J. Am. Chem. Soc.* 136: 17922–17925.

256 Capozzi, B., Chen, Q.S., Darancet, P. et al. (2014). Tunable charge transport in single-molecule junctions via electrolytic gating. *Nano Lett.* 14: 1400–1404.

257 Katsonis, N., Kudernac, T., Walko, M. et al. (2006). Reversible conductance switching of single diarylethenes on a gold surface. *Adv. Mater.* 18: 1397–1400.

258 Kronemeijer, A.J., Akkerman, H.B., Kudernac, T. et al. (2008). Reversible conductance switching in molecular devices. *Adv. Mater.* 20: 1467–1473.

259 van der Molen, S.J., Liao, J., Kudernac, T. et al. (2009). Light-controlled conductance switching of ordered metal–molecule–metal devices. *Nano Lett.* 9: 76–80.

260 Meng, F., Hervault, Y.-M., Norel, L. et al. (2012). Photo-modulable molecular transport junctions based on organometallic molecular wires. *Chem. Sci.* 3: 3113–3118.

261 Li, T., Jevric, M., Hauptmann, J.R. et al. (2013). Ultrathin reduced graphene oxide films as transparent top-contacts for light switchable solid-state molecular junctions. *Adv. Mater.* 25: 4164–4170.

262 Zhang, J.L., Zhong, J.Q., Lin, J.D. et al. (2015). Towards single molecule switches. *Chem. Soc. Rev.* 44: 2998–3022.

263 Füchsel, G., Klamroth, T., Dokić, J., and Saalfrank, P. (2006). On the electronic structure of neutral and ionic azobenzenes and their possible role as surface mounted molecular switches. *J. Phys. Chem. B* 110: 16337–16345.

264 Saalfrank, P. (2000). Manipulation of adsorbates with electric fields. *J. Chem. Phys.* 113: 3780.

265 Lewis, P.A., Inman, C.E., Yao, Y. et al. (2004). Mediating stochastic switching of single molecules using chemical functionality. *J. Am. Chem. Soc.* 126: 12214–12215.

266 Lewis, P.A., Inman, C.E., Maya, F. et al. (2005). Molecular engineering of the polarity and interactions of molecular electronic switches. *J. Am. Chem. Soc.* 127: 17421–17426.

267 Moore, A.M., Mantooth, B.A., Donhauser, Z.J. et al. (2007). Real-time measurements of conductance switching and motion of single oligo(phenylene ethynylene) molecules. *J. Am. Chem. Soc.* 129: 10352–10353.

268 Ramachandran, G.K., Hopson, T.J., Rawlett, A.M. et al. (2003). A bond-fluctuation mechanism for stochastic switching in wired molecules. *Science* 300: 1413–1416.

269 Qiu, X.H., Nazin, G.V., and Ho, W. (2004). Mechanisms of reversible conformational transitions in a single molecule. *Phys. Rev. Lett.* 93: 196806.

270 Alemani, M., Peters, M.V., Hecht, S. et al. (2006). Electric field-induced isomerization of azobenzene by STM. *J. Am. Chem. Soc.* 128: 14446–14447.

271 Leonhard, G. (2008). Functionalized molecules studied by STM: motion, switching and reactivity. *J. Phys.: Condens. Matter* 20: 053001.

272 Hla, S.-W. and Rieder, K.-H. (2003). STM control of chemical reactions: single-molecule synthesis. *Annu. Rev. Phys. Chem.* 54: 307–330.

273 Komeda, T. (2005). Chemical identification and manipulation of molecules by vibrational excitation via inelastic tunneling process with scanning tunneling microscopy. *Prog. Surf. Sci.* 78: 41–85.

274 Choi, B.-Y., Kahng, S.-J., Kim, S. et al. (2006). Conformational molecular switch of the azobenzene molecule: A scanning tunneling microscopy study. *Phys. Rev. Lett.* 96: 156106.

275 Liljeroth, P., Repp, J., and Meyer, G. (2007). Current-induced hydrogen tautomerization and conductance switching of naphthalocyanine molecules. *Science* 317: 1203–1206.

276 Lörtscher, E., Ciszek, J.W., Tour, J. et al. (2006). Reversible and controllable switching of a single-molecule junction. *Small* 2: 973.

277 Schirm, C., Matt, M., Pauly, F. et al. (2013). A current-driven single-atom memory. *Nat. Nanotechnol.* 8: 645–648.

278 Kim, Y.-H., Kim, H.S., Lee, J. et al. (2017). Stretching-induced conductance variations as fingerprints of contact configurations in single-molecule junctions. *J. Am. Chem. Soc.* 139: 8286–8294.

279 Shen, S., Narayanaswamy, A., and Chen, G. (2009). Surface phonon polaritons mediated energy transfer between nanoscale gaps. *Nano Lett.* 9: 2909–2913.

280 Xu, B., Xiao, X., and Tao, N.J. (2003). Measurements of single-molecule electromechanical properties. *J. Am. Chem. Soc.* 125: 16164–16165.

281 Quek, S.Y., Kamenetska, M., Steigerwald, M.L. et al. (2009). Mechanically controlled binary conductance switching of a single-molecule junction. *Nat. Nanotechnol.* 4: 230–234.

282 Kaneko, S., Motta, C., Brivio, G.P., and Kiguchi, M. (2013). Mechanically controllable bi-stable states in a highly conductive single pyrazine molecular junction. *Nanotechnology* 24: 315201.

283 Taniguchi, M., Tsutsui, M., Yokota, K., and Kawai, T. (2010). Mechanically-controllable single molecule switch based on configuration specific electrical conductivity of metal–molecule–metal junctions. *Chem. Sci.* 1: 247–253.

284 Kiguchi, M., Ohto, T., Fujii, S. et al. (2014). Single molecular resistive switch obtained via sliding multiple anchoring points and varying effective wire length. *J. Am. Chem. Soc.* 136: 7327–7332.

285 Su, T.A., Li, H., Steigerwald, M.L. et al. (2015). Stereoelectronic switching in single-molecule junctions. *Nat. Chem.* 7 (3): 215–220.

286 Liu, L., Jayanthi, C., Tang, M. et al. (2000). Controllable reversibility of an sp^2 to sp^3 transition of a single wall nanotube under the manipulation of an AFM tip: a nanoscale electromechanical switch? *Phys. Rev. Lett.* 84: 4950.

287 Haiss, W., van Zalinge, H., Higgins, S.J. et al. (2003). Redox state dependence of single molecule conductivity. *J. Am. Chem. Soc.* 125: 15294–15295.

288 Tsoi, S., Griva, I., Trammell, S.A. et al. (2008). Electrochemically controlled conductance switching in a single molecule: quinone-modified oligo(phenylene vinylene). *ACS Nano* 2: 1289–1295.

289 Li, C., Mishchenko, A., Li, Z. et al. (2008). Electrochemical gate-controlled electron transport of redox-active single perylene bisimide molecular junctions. *J. Phys.: Condens. Matter* 20: 374122.

290 Albrecht, T., Guckian, A., Kuznetsov, A.M. et al. (2006). Mechanism of electrochemical charge transport in individual transition metal complexes. *J. Am. Chem. Soc.* 128: 17132–17138.

291 Zhou, X.-S., Liu, L., Fortgang, P. et al. (2011). Do molecular conductances correlate with electrochemical rate constants? Experimental insights. *J. Am. Chem. Soc.* 133: 7509–7516.

292 Xiao, X., Brune, D., He, J. et al. (2006). Redox-gated electron transport in electrically wired ferrocene molecules. *Chem. Phys.* 326: 138–143.

293 Ricci, A.M., Calvo, E.J., Martin, S., and Nichols, R.J. (2010). Electrochemical scanning tunneling spectroscopy of redox-active molecules bound by Au—C Bonds. *J. Am. Chem. Soc.* 132: 2494–2495.

294 Ting, T.-C., Hsu, L.-Y., Huang, M.-J. et al. (2015). Energy-level alignment for single-molecule conductance of extended metal-atom chains. *Angew. Chem.* 127: 15960–15964.

295 Gittins, D.I., Bethell, D., Schiffrin, D.J., and Nichols, R.J. (2000). A nanometre-scale electronic switch consisting of a metal cluster and redox-addressable groups. *Nature* 408: 67–69.

296 Liu, J., Zhao, X., Al-Galiby, Q. et al. (2017). Radical-enhanced charge transport in single-molecule phenothiazine electrical junctions. *Angew. Chem. Int. Ed.* 56: 13061–13065.

297 Yin, X., Zang, Y., Zhu, L. et al. (2017). A reversible single-molecule switch based on activated antiaromaticity. *Sci. Adv.* 3: eaao2615.

298 Green, J.E., Wook Choi, J., Boukai, A. et al. (2007). A 160-kilobit molecular electronic memory patterned at 10^{11} bits per square centimetre. *Nature* 445: 414–417.

299 Li, L., Lo, W.-Y., Cai, Z. et al. (2016). Proton-triggered switch based on a molecular transistor with edge-on gate. *Chem. Sci.* 7: 3137–3141.

300 Irie, M. (2000). Diarylethenes for memories and switches. *Chem. Rev.* 100: 1685–1716.

301 Feringa, B.L. (2001). In control of motion: from molecular switches to molecular motors. *Acc. Chem. Res.* 34: 504–513.

302 Glebov, E.M., Pozdnyakov, I.P., Plyusnin, V.F., and Khmelinskiic, I. (2015). Primary reactions in the photochemistry of hexahalide complexes of platinum group metals: a minireview. *J. Photochem. Photobiol., C: Photochem. Rev.* 24: 1–15.

303 Lara-Avila, S., Danilov, A., Geskin, V. et al. (2010). Bianthrone in a single-molecule junction: Conductance switching with a bistable molecule facilitated by image charge effects. *J. Phys. Chem. C* 114: 20686.

304 Lara-Avila, S., Danilov, A.V., Kubatkin, S.E. et al. (2011). Light-triggered conductance switching in single-molecule dihydroazulene/vinylheptafulvene junctions. *J. Phys. Chem. C* 115: 18372–18377.

305 Lara-Avila, S., Danilov, A.V., Kubatkin, S.E. et al. (2012). Dihydroazulene photoswitch operating in sequential tunneling regime: synthesis and single-molecule junction studies. *Adv. Funct. Mater.* 22: 4249–4258.

306 Whalley, A.C., Steigerwald, M.L., Guo, X., and Nuckolls, C. (2007). Reversible switching in molecular electronic devices. *J. Am. Chem. Soc.* 129: 12590–12591.

307 Kim, Y., Hellmuth, T.J., Sysoiev, D. et al. (2012). Charge transport characteristics of diarylethene photoswitching single-molecule junctions. *Nano Lett.* 12: 3736–3742.

308 Irie, M., Eriguchi, T., Takada, T., and Uchida, K. (1997). Photochromism of diarylethenes having thiophene oligomers as the aryl groups. *Tetrahedron* 53: 12263–12271.

309 Roldan, D., Kaliginedi, V., Cobo, S. et al. (2013). Charge transport in photoswitchable dimethyldihydropyrene-type single-molecule junctions. *J. Am. Chem. Soc.* 135: 5974–5977.

310 Kay, N.J., Higgins, S.J., Jeppesen, J.O. et al. (2012). Single-molecule electrochemical gating in ionic liquids. *J. Am. Chem. Soc.* 134: 16817–16826.

311 Zhang, J., Kuznetsov, A.M., Medvedev, I.G. et al. (2008). Single-molecule electron transfer in electrochemical environments. *Chem. Rev.* 108: 2737–2791.

312 Li, Z.H., Li, H., Chen, S.J. et al. (2014). Regulating a benzodifuran single molecule redox switch via electrochemical gating and optimization of molecule/electrode coupling. *J. Am. Chem. Soc.* 136: 8867–8870.

313 Darwish, N., Diez-Perez, I., Da Silva, P. et al. (2012). Observation of electrochemically controlled quantum interference in a single anthraquinone-based norbornylogous bridge molecule. *Angew. Chem. Int. Ed.* 51: 3203–3206.

314 Sanvito, S. and Rocha, A.R. (2006). Molecular-spintronics: the art of driving spin through molecules. *J. Comput. Theor. Nanos.* 3: 624–642.

315 Leuenberger, M.N. and Loss, D. (2001). Quantum computing in molecular magnets. *Nature* 410: 789–793.

316 Thomas, L., Lionti, F., Ballou, R. et al. (1996). Macroscopic quantum tunnelling of magnetization in a single crystal of nanomagnets. *Nature* 383: 145–147.

317 Wernsdorfer, W. and Sessoli, R. (1999). Quantum phase interference and parity effects in magnetic molecular clusters. *Science* 284: 133–135.

318 Baadji, N., Piacenza, M., Tugsuz, T. et al. (2009). Electrostatic spin crossover effect in polar magnetic molecules. *Nat. Mater.* 8: 813–817.

319 Sanvito, S. (2007). Injecting and controlling spins in organic materials. *J. Mater. Chem.* 17: 4455–4459.

320 Bogani, L. and Wernsdorfer, W. (2008). Molecular spintronics using single-molecule magnets. *Nat. Mater.* 7: 179–201.

321 Sanvito, S. (2011). Molecular spintronics. *Chem. Soc. Rev.* 40: 3336–3355.

322 Affronte, M. (2009). Molecular nanomagnets for information technologies. *J. Mater. Chem.* 19: 1731–1737.

323 Camarero, J. and Coronado, E. (2009). Molecular vs. inorganic spintronics: The role of molecular materials and single molecules. *J. Mater. Chem.* 19: 1678–1684.

324 Lehmann, J., Gaita-Arino, A., Coronado, E., and Loss, D. (2009). Quantum computing with molecular spin systems. *J. Mater. Chem.* 19: 1672–1684.

325 Gehring, P., Thijssen, J.M., and van der Zant, H.S.J. (2019). Single-molecule quantum-transport phenomena in break junctions. *Nat. Rev. Phys.* 1: 381–396.

326 Stamp, P.C.E. and Gaita-Arino, A. (2009). Spin-based quantum computers made by chemistry: hows and whys. *J. Mater. Chem.* 19: 1718–1730.
327 Wiesendanger, R. (2009). Spin mapping at the nanoscale and atomic scale. *Rev. Mod. Phys.* 81: 1495.
328 Wahl, P., Simon, P., Diekhöner, L. et al. (2007). Exchange interaction between single magnetic adatoms. *Phys. Rev. Lett.* 98: 056601.
329 Hirjibehedin, C.F., Lin, C.-Y., Otte, A.F. et al. (2007). Large magnetic anisotropy of a single atomic spin embedded in a surface molecular network. *Science* 317: 1199–1203.
330 Schwarz, F., Kastlunger, G., Lissel, F. et al. (2015). Field-induced conductance switching by charge-state alternation in organometallic single-molecule junctions. *Nat. Nanotechnol.* 11: 170–176.
331 Gütlich, P. and Goodwin, H.A. (2004). *Spin Crossover in Transition Metal Compounds*. Springer Science & Business Media.
332 Rocha, A.R., Garcia-suarez, V.M., and Bailey, S.W. (2005). Towards molecular spintronics. *Nat. Mater.* 4: 335–339.
333 Diefenbach, M. and Kim, K.S. (2007). Towards molecular magnetic switching with an electric bias. *Angew. Chem. Int. Ed.* 119: 7640–7643.
334 Prins, F., Monrabal-Capilla, M., Osorio, E.A. et al. (2011). Room-temperature electrical addressing of a bistable spin-crossover molecular system. *Adv. Mater.* 23: 1545–1549.
335 Osorio, E.A., Moth-Poulsen, K., van der Zant, H.S.J. et al. (2010). Electrical manipulation of spin states in a single electrostatically gated transition-metal complex. *Nano Lett.* 10: 105–110.
336 Wagner, S., Kisslinger, F., Ballmann, S. et al. (2013). Switching of a coupled spin pair in a single-molecule junction. *Nat. Nanotechnol.* 8: 575–579.
337 Liu, R., Ke, S.-H., Baranger, H.U., and Yang, W. (2006). Negative differential resistance and hysteresis through an organometallic molecule from molecular-level crossing. *J. Am. Chem. Soc.* 128: 6274–6275.
338 Ouyang, M. and Awschalom, D.D. (2003). Coherent spin transfer between molecularly bridged quantum dots. *Science* 301: 1074–1078.
339 Weigelt, S., Busse, C., Petersen, L. et al. (2006). Chiral switching by spontaneous conformational change in adsorbed organic molecules. *Nat. Mater.* 5: 112–117.
340 Sørensen, A., Andersen, S.S., Flood, A.H., and Jeppesen, J.O. (2013). Pressure effects in the synthesis of isomeric rotaxanes. *Chem. Commun.* 49: 5936–5938.
341 Millman, J. and Grabel, A. (1987). *Microelectronics*. McGraw-Hill, Inc.
342 Stojanovic, M.N., Mitchell, T.E., and Stefanovic, D. (2002). Deoxyribozyme-based logic gates. *J. Am. Chem. Soc.* 124: 3555–3561.
343 de Silva, A.P. and McClenaghan, N.D. (2000). Proof-of-principle of molecular-scale arithmetic. *J. Am. Chem. Soc.* 122: 3965–3966.
344 Huang, Y., Duan, X., Cui, Y. et al. (2001). Logic gates and computation from assembled nanowire building blocks. *Science* 294: 1313–1317.
345 Huang, Y., Duan, X., Wei, Q., and Lieber, C.M. (2001). Directed assembly of one-dimensional nanostructures into functional networks. *Science* 291: 630–633.

346 Benenson, Y., Paz-Elizur, T., Adar, R. et al. (2001). Programmable and autonomous computing machine made of biomolecules. *Nature* 414: 430–434.

347 Liu, Q., Wang, L., Frutos, A.G. et al. (2000). DNA computing on surfaces. *Nature* 403: 175–179.

348 Lipton, R. (1995). DNA solution of hard computational problems. *Science* 268: 542–545.

349 Saghatelian, A., Völcker, N.H., Guckian, K.M. et al. (2003). DNA-based photonic logic gates: AND, NAND, and INHIBIT. *J. Am. Chem. Soc.* 125: 346–347.

350 Chen, J. and Wood, D.H. (2000). Computation with biomolecules. *Proc. Natl. Acad. Sci. U. S. A.* 97: 1328–1330.

351 Adleman, L. (1994). Molecular computation of solutions to combinatorial problems. *Science* 266: 1021–1024.

352 Ouyang, Q., Kaplan, P.D., Liu, S., and Libchaber, A. (1997). DNA solution of the maximal clique problem. *Science* 278: 446–449.

353 Frutos, A.G., Liu, Q., Thiel, A.J. et al. (1997). Demonstration of a word design strategy for DNA computing on surfaces. *Nucleic Acids Res.* 25: 4748–4757.

354 Liu, Q., Frutos, A.G., Wang, L. et al. (1999). Progress toward demonstration of a surface based DNA computation: A one word approach to solve a model satisfiability problem. *Biosystems* 52: 25–33.

355 Smith, L.M., Corn, R.M., Condon, A.E. et al. (1998). A surface-based approach to DNA computation. *J. Comput. Biol.* 5: 255–267.

356 Faulhammer, D., Cukras, A.R., Lipton, R.J., and Landweber, L.F. (2000). Molecular computation: RNA solutions to chess problems. *Proc. Natl. Acad. Sci. U. S. A.* 97: 1385–1389.

357 Burgoyne, S.R.E.W.R., Chelyapov, N.V., Goodman, M.F. et al. (1999). A sticker based model for DNA computation. *DNA Based Comput. Two* 44: 1.

358 Xiao, X. and Hu, H. (2004). Development of formal models for DNA computing. *Comput. Appl.* 24: 123–126.

359 Păun, G. (2000). DNA computing based on splicing: Universality results. *Theor. Comput. Sci.* 231: 275–296.

360 Kari, L., Păun, G., Rozenberg, G. et al. (1998). DNA computing, sticker systems, and universality. *Acta Inf.* 35: 401–420.

361 Guarnieri, F., Fliss, M., and Bancroft, C. (1996). Making DNA Add. *Science* 273: 220–223.

362 Bennett, C.H. (1982). The thermodynamics of computation—a review. *Int. J. Theor. Phys.* 21: 905–940.

363 Paun, G., Rozenberg, G., and Salomaa, A. (2005). *DNA Computing: New Computing Paradigms*. Springer Science & Business Media.

364 de Silva, P.A., Gunaratne, N.H.Q., and McCoy, C.P. (1993). A molecular photoionic AND gate based on fluorescent signalling. *Nature* 364: 42–44.

365 de Silva, A.P. and Uchiyama, S. (2007). Molecular logic and computing. *Nat. Nanotechnol.* 2: 399–410.

366 Magri, D.C., Brown, G.J., McClean, G.D., and de Silva, A.P. (2006). Communicating chemical congregation: A molecular AND logic gate with three

chemical inputs as a "lab-on-a-molecule" prototype. *J. Am. Chem. Soc.* 128: 4950–4951.

367 de Silva, A.P., Gunaratne, H.Q.N., Gunnlaugsson, T. et al. (1997). Signaling recognition events with fluorescent sensors and switches. *Chem. Rev.* 97: 1515–1566.

368 de Silva, A.P. and McClenaghan, N.D. (2002). Simultaneously multiply-configurable or superposed molecular logic systems composed of ICT (Internal Charge Transfer) chromophores and fluorophores integrated with one- or two-ion receptors. *Chem. Eur. J.* 8: 4935–4945.

369 Wagner, R.W., Lindsey, J.S., Seth, J. et al. (1996). Molecular optoelectronic gates. *J. Am. Chem. Soc.* 118: 3996–3997.

370 Fukaminato, T., Sasaki, T., Kawai, T. et al. (2004). Digital photoswitching of fluorescence based on the photochromism of diarylethene derivatives at a single-molecule level. *J. Am. Chem. Soc.* 126: 14843–14849.

371 Margulies, D., Melman, G., Felder, C.E. et al. (2004). Chemical input multiplicity facilitates arithmetical processing. *J. Am. Chem. Soc.* 126: 15400–15401.

372 Silvi, S., Constable, E.C., Housecroft, C.E. et al. (2009). All-optical integrated logic operations based on chemical communication between molecular switches. *Chem. Eur. J.* 15: 178–185.

373 Andréasson, J. and Pischel, U. (2010). Smart molecules at work—mimicking advanced logic operations. *Chem. Soc. Rev.* 39: 174–188.

374 Coskun, A., Deniz, E., and Akkaya, E.U. (2005). Effective PET and ICT switching of boradiazaindacene emission: A unimolecular, emission-mode, molecular half-subtractor with reconfigurable logic gates. *Org. Lett.* 7: 5187–5189.

375 Soboleva, T., Esquer, H.J., Benninghoff, A.D., and Berreau, L.M. (2017). Sense and release: a thiol-responsive flavonol-based photonically driven carbon monoxide-releasing molecule that operates via a multiple-input AND logic gate. *J. Am. Chem. Soc.* 139: 9435–9438.

376 Pischel, U. (2007). Chemical approaches to molecular logic elements for addition and subtraction. *Angew. Chem. Int. Ed.* 46: 4026–4040.

377 Andréasson, J. and Pischel, U. (2015). Molecules with a sense of logic: A progress report. *Chem. Soc. Rev.* 44: 1053–1069.

378 Reddy G, U., Axthelm, J., Hoffmann, J. et al. (2017). Co-registered molecular logic gate with a CO-releasing molecule triggered by light and peroxide. *J. Am. Chem. Soc.* 139: 4991–4994.

379 Kink, F., Collado, M.P., Wiedbrauk, S. et al. (2017). Bistable photoswitching of hemithioindigo with green and red light: Entry point to advanced molecular digital information processing. *Chem. Eur. J.* 23: 6237–6243.

380 Liu, S. and Guo, X. (2012). Carbon nanomaterials field-effect-transistor-based biosensors. *NPG Asia Mater.* 4: e23.

381 Li, Y., Yang, C., and Guo, X. (2020). Single-molecule electrical detection: A promising route toward the fundamental limits of chemistry and life science. *Acc. Chem. Res.* 53: 159169.

382 Kauffman, D.R. and Star, A. (2008). Electronically monitoring biological interactions with carbon nanotube field-effect transistors. *Chem. Soc. Rev.* 37: 1197–1206.

383 Sorgenfrei, S., Chiu, C.Y., Gonzalez, R.L. et al. (2011). Label-free single-molecule detection of DNA-hybridization kinetics with a carbon nanotube field-effect transistor. *Nat. Nanotechnol.* 6: 125–132.

384 Choi, Y., Moody, I.S., Sims, P.C. et al. (2012). Single-molecule lysozyme dynamics monitored by an electronic circuit. *Science* 335: 319–324.

385 Liu, H., He, J., Tang, J. et al. (2010). Translocation of single-stranded DNA through single-walled carbon nanotubes. *Science* 327: 64–67.

386 Zhao, Y.A., Ashcroft, B., Zhang, P.M. et al. (2014). Single-molecule spectroscopy of amino acids and peptides by recognition tunnelling. *Nat. Nanotechnol.* 9: 466–473.

387 Huang, S., He, J., Chang, S.A. et al. (2010). Identifying single bases in a DNA oligomer with electron tunnelling. *Nat. Nanotechnol.* 5: 868–873.

388 Chen, X., Guo, Z., Yang, G.-M. et al. (2010). Electrical nanogap devices for biosensing. *Mater. Today* 13: 28–41.

389 Meng, L., Xin, N., Hu, C. et al. (2019). Side-group chemical gating via reversible optical and electric control in a single molecule transistor. *Nat. Commun.* 10: 1450.

390 Gu, C., Hu, C., Wei, Y. et al. (2018). Label-free dynamic detection of single-molecule nucleophilic-substitution reactions. *Nano Lett.* 18: 4156–4162.

391 Guan, J.X., Jia, C.C., Li, Y.W. et al. (2018). Direct single-molecule dynamic detection of chemical reactions. *Sci. Adv.* 4: eaar2177.

392 Xin, N., Wang, J., Jia, C. et al. (2017). Stereoelectronic effect-induced conductance switching in aromatic chain single-molecule junctions. *Nano Lett.* 17: 856–861.

393 Choi, Y., Moody, I.S., Sims, P.C. et al. (2012). Single-molecule dynamics of lysozyme processing distinguishes linear and cross-linked peptidoglycan substrates. *J. Am. Chem. Soc.* 134: 2032–2035.

394 Lee, H.J., Park, J., Yoon, O.J. et al. (2011). Amine-modified single-walled carbon nanotubes protect neurons from injury in a rat stroke model. *Nat. Nanotechnol.* 6: 121–125.

395 Sorgenfrei, S., Chiu, C.-Y., Johnston, M. et al. (2011). Debye screening in single-molecule carbon nanotube field-effect sensors. *Nano Lett.* 11: 3739–3743.

396 Choi, Y., Olsen, T.J., Sims, P.C. et al. (2013). Dissecting single-molecule signal transduction in carbon nanotube circuits with protein engineering. *Nano Lett.* 13: 625–631.

397 Olsen, T.J., Choi, Y., Sims, P.C. et al. (2013). Electronic measurements of single-molecule processing by DNA polymerase I (Klenow fragment). *J. Am. Chem. Soc.* 135: 7855–7860.

398 Sims, P.C., Moody, I.S., Choi, Y. et al. (2013). Electronic measurements of single-molecule catalysis by cAMP-dependent protein kinase A. *J. Am. Chem. Soc.* 135: 7861–7868.

399 Guo, X., Whalley, A., Klare, J.E. et al. (2007). Single-molecule devices as scaffolding for multicomponent nanostructure assembly. *Nano Lett.* 7: 1119–1122.

400 Roy, S., Vedala, H., Roy, A.D. et al. (2008). Direct electrical measurements on single-molecule genomic DNA using single-walled carbon nanotubes. *Nano Lett.* 8: 26–30.

401 Wang, H., Muren, N.B., Ordinario, D. et al. (2012). Transducing methyltransferase activity into electrical signals in a carbon nanotube-DNA device. *Chem. Sci.* 3: 62–65.

402 Gao, L., Li, L.-L., Wang, X. et al. (2015). Graphene-DNAzyme junctions: a platform for direct metal ion detection with ultrahigh sensitivity. *Chem. Sci.* 6: 2469–2473.

403 Wang, X., Gao, L., Liang, B. et al. (2015). Revealing the direct effect of individual intercalations on DNA conductance toward single-molecule electrical biodetection. *J. Mater. Chem. B* 3: 5150–5154.

404 Dai, X., Hong, G., Gao, T., and Lieber, C.M. (2018). Mesh nanoelectronics: seamless integration of electronics with tissues. *Acc. Chem. Res.* 51: 309–318.

405 Liu, S., Shen, Q., Cao, Y. et al. (2010). Chemical functionalization of single-walled carbon nanotube field-effect transistors as switches and sensors. *Coord. Chem. Rev.* 254: 1101–1116.

406 Tian, B., Zheng, X., Kempa, T.J. et al. (2007). Coaxial silicon nanowires as solar cells and nanoelectronic power sources. *Nature* 449: 885–889.

407 Stern, E., Klemic, J.F., Routenberg, D.A. et al. (2007). Label-free immunodetection with CMOS-compatible semiconducting nanowires. *Nature* 445: 519–522.

408 Patolsky, F., Zheng, G., Hayden, O. et al. (2004). Electrical detection of single viruses. *Proc. Natl. Acad. Sci. U. S. A.* 101: 14017–14022.

409 Shen, F., Wang, J., Xu, Z. et al. (2012). Rapid flu diagnosis using silicon nanowire sensor. *Nano Lett.* 12: 3722–3730.

410 Li, J., He, G., Ueno, H. et al. (2016). Direct real-time detection of single proteins using silicon nanowire-based electrical circuits. *Nanoscale* 8: 16172–16176.

411 Li, J., He, G., Hiroshi, U. et al. (2017). Direct measurement of single-molecule adenosine triphosphatase hydrolysis dynamics. *ACS Nano* 11: 12789–12795.

412 Cui, Y., Zhong, Z., Wang, D. et al. (2003). High performance silicon nanowire field effect transistors. *Nano Lett.* 3: 149–152.

413 Wang, J., Shen, F., Wang, Z. et al. (2014). Point decoration of silicon nanowires: An approach toward single-molecule electrical detection. *Angew. Chem.* 126: 5138–5143.

414 Yin, Y. and Zhao, X.S. (2011). Kinetics and dynamics of DNA hybridization. *Acc. Chem. Res.* 44: 1172–1181.

415 He, G., Li, J., Ci, H. et al. (2016). Direct measurement of single-molecule DNA hybridization dynamics with single-base resolution. *Angew. Chem. Int. Ed.* 55: 9036–9040.

416 Frisenda, R., Janssen, V.A.E.C., Grozema, F.C. et al. (2016). Mechanically controlled quantum interference in individual π-stacked dimers. *Nat. Chem.* 8: 1099–1104.

417 He, G., Li, J., Qi, C., and Guo, X. (2017). Single nucleotide polymorphism genotyping in single-molecule electronic circuits. *Adv. Sci.* 4: 1700158.

418 Dubi, Y. and Di Ventra, M. (2011). *Colloquium*: heat flow and thermoelectricity in atomic and molecular junctions. *Rev. Mod. Phys.* 83: 131–155.

419 Reddy, P., Jang, S.Y., Segalman, R.A., and Majumdar, A. (2007). Thermoelectricity in molecular junctions. *Science* 315: 1568–1571.

420 Lee, W., Kim, K., Jeong, W. et al. (2013). Heat dissipation in atomic-scale junctions. *Nature* 498: 209–212.

421 Widawsky, J.R., Darancet, P., Neaton, J.B., and Venkataraman, L. (2012). Simultaneous determination of conductance and thermopower of single molecule junctions. *Nano Lett.* 12: 354–358.

422 Guo, S., Zhou, G., and Tao, N. (2013). Single molecule conductance, thermopower, and transition voltage. *Nano Lett.* 13: 4326–4332.

423 Finch, C.M., García-Suárez, V.M., and Lambert, C.J. (2009). Giant thermopower and figure of merit in single-molecule devices. *Phys. Rev. B* 79: 033405.

424 Karlström, O., Linke, H., Karlström, G., and Wacker, A. (2011). Increasing thermoelectric performance using coherent transport. *Phys. Rev. B* 84: 113415.

425 Bergfield, J.P., Solis, M.A., and Stafford, C.A. (2010). Giant thermoelectric effect from transmission supernodes. *ACS Nano* 4: 5314–5320.

426 Evangeli, C., Gillemot, K., Leary, E. et al. (2013). Engineering the thermopower of C_{60} molecular junctions. *Nano Lett.* 13: 2141–2145.

427 Kim, Y., Jeong, W., Kim, K. et al. (2014). Electrostatic control of thermoelectricity in molecular junctions. *Nat. Nanotechnol.* 9: 881–885.

428 Dell, E.J., Capozzi, B., Xia, J. et al. (2015). Molecular length dictates the nature of charge carriers in single-molecule junctions of oxidized oligothiophenes. *Nat. Chem.* 7: 209–214.

429 Moth-Poulsen, K. and Bjornholm, T. (2009). Molecular electronics with single molecules in solid-state devices. *Nat. Nanotechnol.* 4: 551–556.

430 Qi, P., Javey, A., Rolandi, M. et al. (2004). Miniature organic transistors with carbon nanotubes as quasi-one-dimensional electrodes. *J. Am. Chem. Soc.* 126: 11774–11775.

431 Cao, Y., Wei, Z., Liu, S. et al. (2010). High-performance Langmuir–Blodgett monolayer transistors with high responsivity. *Angew. Chem. Int. Ed.* 49: 6319–6323.

432 Cao, Y., Liu, S., Shen, Q. et al. (2010). High-performance photoresponsive organic nanotransistors with single-layer graphenes as two-dimensional electrodes. *Adv. Funct. Mater.* 19: 2743–2748.

433 Nijhuis, C.A., Reus, W.F., Siegel, A.C., and Whitesides, G.M. (2011). A molecular half-wave rectifier. *J. Am. Chem. Soc.* 133: 15397–15411.

434 Guo, S., Hihath, J., and Tao, N. (2011). Breakdown of atomic-sized metallic contacts measured on nanosecond scale. *Nano Lett.* 11: 927–933.

435 Kienle, D. and Leonard, F. (2009). Terahertz response of carbon nanotube transistors. *Phys. Rev. Lett.* 103: 026601.

436 Wu, J., Wang, B., Wang, J., and Guo, H. (2005). Giant enhancement of dynamic conductance in molecular devices. *Phys. Rev. B* 72: 195324.

437 Trasobares, J., Vuillaume, D., Theron, D., and Clément, N. (2016). 17 GHz molecular rectifier. *Nat. Commun.* 7: 12850.

438 Ballmann, S. and Weber, H.B. (2012). An electrostatic gate for mechanically controlled single-molecule junctions. *New J. Phys.* 14: 123028.

439 Aradhya, S.V. and Venkataraman, L. (2013). Single-molecule junctions beyond electronic transport. *Nat. Nanotechnol.* 8: 399–410.

440 Ratner, M. (2013). A brief history of molecular electronics. *Nat. Nanotechnol.* 8: 378–381.

441 Lörtscher, E. (2013). Wiring molecules into circuits. *Nat. Nanotechnol.* 8: 381–384.

442 Scheer, E. (2013). Visions for a molecular future. *Nat. Nanotechnol.* 8: 386.

443 Gao, H.-J. and Gao, L. (2010). Scanning tunneling microscopy of functional nanostructures on solid surfaces: manipulation, self-assembly, and applications. *Prog. Surf. Sci.* 85: 28–91.

444 Balzani, V., Credi, A., and Venturi, M. (2008). *Molecular Devices and Machines: Concepts and Perspectives for the Nanoworld*. Wiley.

445 Kelly, T.R., De Silva, H., and Silva, R.A. (1999). Unidirectional rotary motion in a molecular system. *Nature* 401: 150–155.

446 Koumura, N., Zijlstra, R.W.J., van Delden, R.A. et al. (1999). Light-driven monodirectional molecular rotor. *Nature* 401: 152–155.

447 Kelly, T.R., Silva, R.A., De Silva, H. et al. (2000). A rationally designed prototype of a molecular motor. *J. Am. Chem. Soc.* 122: 6935–6949.

448 Kelly, T.R. (2001). Progress toward a rationally designed molecular motor. *Acc. Chem. Res.* 34: 514–522.

449 Kelly, T.R., Cai, X., Damkaci, F. et al. (2007). Progress toward a rationally designed, chemically powered rotary molecular motor. *J. Am. Chem. Soc.* 129: 376–386.

450 van Delden, R.A., ter Wiel, M.K.J., Pollard, M.M. et al. (2005). Unidirectional molecular motor on a gold surface. *Nature* 437: 1337–1340.

451 Vicario, J., Walko, M., Meetsma, A., and Feringa, B.L. (2006). Fine tuning of the rotary motion by structural modification in light-driven unidirectional molecular motors. *J. Am. Chem. Soc.* 128: 5127–5135.

452 Koumura, N., Geertsema, E.M., Meetsma, A., and Feringa, B.L. (2000). Light-driven molecular rotor: Unidirectional rotation controlled by a single stereogenic center. *J. Am. Chem. Soc.* 122: 12005–12006.

453 Koumura, N., Geertsema, E.M., van Gelder, M.B. et al. (2002). Second generation light-driven molecular motors. Unidirectional rotation controlled by a single stereogenic center with near-perfect photoequilibria and acceleration of the speed of rotation by structural modification. *J. Am. Chem. Soc.* 124: 5037–5051.

454 Bakewell, D.J. and Nicolau, D.V. (2007). Protein linear molecular motor-powered nanodevices. *Aust. J. Chem.* 60: 314–332.

455 Bissell, R.A., Córdova, E., Kaifer, A.E., and Stoddart, J.F. (1994). A chemically and electrochemically switchable molecular shuttle. *Nature* 369: 133–137.

456 Zhu, K., O'keefe, C.A., Vukotic, V.N. et al. (2015). A molecular shuttle that operates inside a metal–organic framework. *Nat. Chem.* 7: 514–519.

457 Niewoehner, J., Bohrmann, B., Collin, L. et al. (2014). Increased brain penetration and potency of a therapeutic antibody using a monovalent molecular shuttle. *Neuron* 81: 49–60.

458 Brouwer, A.M., Frochot, C., Gatti, F.G. et al. (2001). Photoinduction of fast, reversible translational motion in a hydrogen-bonded molecular shuttle. *Science* 291: 2124–2128.

459 Balzani, V., Credi, A., and Venturi, M. (2007). Molecular devices and machines. *Nano Today* 2: 18–25.

460 Badjić, J.D., Balzani, V., Credi, A. et al. (2004). A molecular elevator. *Science* 303: 1845–1849.

461 Balzani, V., Clemente-León, M., Credi, A. et al. (2003). Controlling multivalent interactions in triply-threaded two-component superbundles. *Chem. Eur. J.* 9: 5348–5360.

462 Ashton, P.R., Ballardini, R., Balzani, V. et al. (1998). Acid-base controllable molecular shuttles. *J. Am. Chem. Soc.* 120: 11932–11942.

463 Martínez-Díaz, M.-V., Spencer, N., and Stoddart, J.F. (1997). The self-assembly of a switchable [2]rotaxane. *Angew. Chem. Int. Ed.* 36: 1904–1907.

464 Garaudée, S., Silvi, S., Venturi, M. et al. (2005). Shuttling dynamics in an acid-base-switchable [2]rotaxane. *ChemPhysChem* 6: 2145–2152.

465 Clemente-León, M., Credi, A., Martínez-Díaz, M.-V. et al. (2006). Towards organization of molecular machines at interfaces: Langmuir films and Langmuir–Blodgett multilayers of an acid–base switchable rotaxane. *Adv. Mater.* 18: 1291–1296.

466 Badjic, J.D., Ronconi, C.M., Stoddart, J.F. et al. (2006). Operating molecular elevators. *J. Am. Chem. Soc.* 128: 1489–1499.

467 Zhang, Z.-J., Han, M., Zhang, H.-Y., and Liu, Y. (2013). A double-leg donor–acceptor molecular elevator: new insight into controlling the distance of two platforms. *Org. Lett.* 15: 1698–1701.

468 Muraoka, T., Kinbara, K., Kobayashi, Y., and Aida, T. (2003). Light-driven open–close motion of chiral molecular scissors. *J. Am. Chem. Soc.* 125: 5612–5613.

469 Muraoka, T., Kinbara, K., and Aida, T. (2006). A self-locking molecule operative with a photoresponsive key. *J. Am. Chem. Soc.* 128: 11600–11605.

470 Muraoka, T., Kinbara, K., and Aida, T. (2007). Reversible operation of chiral molecular scissors by redox and UV light. *Chem. Commun.* 14: 1441–1443.

471 Muraoka, T., Kinbara, K., and Aida, T. (2006). Mechanical twisting of a guest by a photoresponsive host. *Nature* 440: 512–515.

472 Hanazaki, I. and Akimoto, H. (1972). Optical rotatory power of 2, 2′-dihydroxy-1, 1′-binaphthyl and related compounds. *J. Am. Chem. Soc.* 94: 4102–4106.

473 Harada, N., Chen, S.-M.L., and Nakanishi, K. (1975). Quantitative definition of exciton chirality and the distant effect in the exciton chirality method. *J. Am. Chem. Soc.* 97: 5345–5352.

474 Stephenson, D.S. and Binsch, G. (1978). Improved algorithm for the computation of exchange-broadened NMR bandshapes. *J. Magn. Reson.* 30: 625–626.

475 Kai, H., Nara, S., Kinbara, K., and Aida, T. (2008). Toward long-distance mechanical communication: studies on a ternary complex interconnected by a bridging rotary module. *J. Am. Chem. Soc.* 130: 6725–6727.

476 Shirai, Y., Morin, J.-F., Sasaki, T. et al. (2006). Recent progress on nanovehicles. *Chem. Soc. Rev.* 35: 1043–1055.

477 Shirai, Y., Osgood, A.J., Zhao, Y. et al. (2006). Surface-rolling molecules. *J. Am. Chem. Soc.* 128: 4854–4864.

478 Shirai, Y., Osgood, A.J., Zhao, Y. et al. (2005). Directional control in thermally driven single-molecule nanocars. *Nano Lett.* 5: 2330–2334.

479 Shirai, Y., Sasaki, T., Guerrero, J.M. et al. (2008). Synthesis and photoisomerization of fullerene– and oligo(phenylene ethynylene)–azobenzene derivatives. *ACS Nano* 2: 97–106.

480 Sasaki, T. and Tour, J.M. (2008). Synthesis of a new photoactive nanovehicle: a nanoworm. *Org. Lett.* 10: 897–900.

481 Morin, J.-F., Shirai, Y., and Tour, J.M. (2006). En route to a motorized nanocar. *Org. Lett.* 8 (8): 1713.

482 Chu, P.-L.E., Wang, L.-Y., Khatua, S. et al. (2013). Synthesis and single-molecule imaging of highly mobile adamantane-wheeled nanocars. *ACS Nano* 7: 35–41.

483 Lewandowski, B., De Bo, G., Ward, J.W. et al. (2013). Sequence-specific peptide synthesis by an artificial small-molecule machine. *Science* 339: 189–193.

484 Ashton, P.R., Balzani, V., Kocian, O. et al. (1998). A light-fueled "piston cylinder" molecular-level machine. *J. Am. Chem. Soc.* 120: 11190–11191.

10

Summary and Perspectives

With the rapid development of molecular-scale electronics, using molecular devices as the future of next-generation electrical circuit units with lower power consumption, higher speed, and higher level of integration, has received significant attention [1–5]. To conveniently and efficiently fabricate molecule-based devices, electrode fabrication is a key step. In this book, we presented the developments of different techniques for molecular junction fabrications using both metal and non-metal materials as contacts. We summarized the characterization methods as well as the theoretical approaches for molecular electronics. Moreover, we highlighted the significant advancements in molecule-based functional devices toward practical applications. The history, challenges, and future of molecular electronics were also discussed.

Each type of material and technique has advantages and disadvantages. For example, metallic materials are the most widely used materials for the molecular junction fabrication due to their several advantages, such as few defects, low cost, and high conductance. However, from a device's standpoint, several serious concerns for metal nanoelectrodes exist. (i) Incompatibility: several types of metals (e.g. commonly used gold) may form deep level traps in silicon, making it difficult to integrate gold tunnel junctions with complementary metal–oxide–semiconductor (CMOS) electronics [6]. (ii) Unexpected mobility: the atom at the metal electrode surface may rearrange or move due to the electric field and local heating, especially under ambient conditions, which strongly influence the stability of single-molecule devices [7]. (iii) Contact nature: molecular electronics is often limited by the poorly defined nature of the contact between the molecules and the metal surface [8]. Even for the most well-studied system, such as thiolated molecules on Au contacts, there are no methods to control the types of metal–molecule bonds [9]. Carbon-based electrodes can overcome these problems, e.g. incompatibility and unexpected mobility. Using single walled carbon nanotubes (SWCNTs) as point contacts, well-defined covalent bonds between the electrode and the molecule with a limited number of molecular bonding sites can be created [8]. However, single-molecule studies based on SWCNTs also face considerable challenges before they can realize their full commercial application [10]. Due to a lack of precise diameter and chirality control for the SWCNTs, the device-to-device properties varied. Developing a reliable fabrication technique for mass-producing identical SWCNT arrays and

Molecular-Scale Electronics: Concept, Fabrication and Applications,
First Edition. Xuefeng Guo, Dong Xiang, and Yu Li.

integrating individual SWCNTs into functional single-molecule devices with high yields are one of the future challenges [11]. Graphene does not have the inherent variability of the SWCNTs and may therefore circumvent these problems. Graphene is currently considered a potential candidate for the post-CMOS era because its defect-free monolayer can be grown at the wafer scale, and the significant gate screening issues can be reduced compared with that of metal electrodes, thus putting molecular electronics into a more favorable position due to the junction's dimensions being reduced to two dimensions. Nanometer-scale gaps in graphene have been obtained using different strategies, such as atomic force microscopy nanolithography [12], anisotropic etching via thermally activated nanoparticles [13], electron-beam sculpting [14], "dash-line" lithography [15, 16], mechanical stress [17], or electroburning [18, 19]. Functional single-molecule devices based on graphene, such as optical switches with low-ohmic contacts [20–22], transistors with low field screening [23, 24], and ultrasensitive biosensors [25], have been reported. Carbon-based materials, such as SWCNTs and graphene, may be better suited as electrode materials for molecular electronics. The realization of atomic-level precision in the cutting procedure, precise control of the molecular conformation on the substrate within the graphene gaps, and contact configuration are challenges for future studies to overcome.

Each electrode fabrication technique has its own unique advantages but is far from perfect [26]. For example, there are three general techniques for forming top contacts for large-area electrical measurements on the self-assembled monolayers (SAMs). (i) Direct deposition of metals using an electron-beam or thermal evaporation ensures atomic-level contact; however, the device yield is low due to the damage of the evaporated hot metals and the formation of metal filaments that short the junctions. (ii) The installation of a buffer-conducting polymer between the SAM and a metallic top contact exhibits a high device yield and efficiently avoids electrical shorts. However, the electrical properties of these molecular junctions may be influenced by the thermal treatment and the morphology of the interlayer conducting films. And the interface between the conducting polymer and molecular layer isn't well understood. (iii) The use of liquid metals allows the formation of the conformal contacts at low cost under room temperature conditions. However, liquid metal is difficult to form small contacts at the individual molecular level. For single molecule junctions, single molecules can be addressed using the electromigration method on the nanoconstrictions. However, the electrode separation is fixed, which indicates that the gap size cannot be further changed after electromigration, thus leading to a low yield of molecular junctions. The mechanically controllable junction technique with a precise adjustable gap size indicated a high yield of the junction. However, it is not facile to fabricate highly integrated molecular commercial devices because of the constraint of the out-of-plane push rod components and the difficulty of introducing a third electrode for gating.

Each characterization technique has drawbacks [27]. For example, scanning tunneling microscopy (STM) continues to play an important role in understanding the electron transport in single molecules due to its capability for both microscopy and tunneling spectroscopy. However, STM requires well-defined

surfaces, such as single crystals, and it is not available for several devices or samples. The surface spectroscopy techniques (e.g. photoemission spectroscopy) are powerful in determining the electronic properties of the molecule–electrode interfaces and the relative energy alignments [28]. X-ray spectroscopy has been demonstrated to provide angstrom-resolution structural information in silicon–molecule–mercury junctions [29]. However, most of the spectroscopic techniques are difficult to apply to molecules sandwiched between two electrodes due to the screen of electrodes. Inelastic electron tunneling spectroscopy (IETS) can be easily used in sandwiched molecular junctions at the single-molecule level to provide information on molecular identity and conformation. However, it requires cryogenic temperatures to distinguish the vibration modes. Optical techniques, such as infrared and Raman spectroscopies, can be used to probe the chemical properties of molecules at room temperature, but it is still a considerable challenge at the single-molecule level [30]. Additionally, although several useful analytical techniques (e.g. transition voltage spectroscopy and thermoelectricity) have been developed for characterizing molecular junctions, those methods are indirect techniques to reveal the characterization of molecules. Developing new efficient techniques for directly extracting additional details from the molecular junctions is highly expected.

10.1 Primary Challenges

10.1.1 *In Situ* Measurement

We had witnessed the *in situ* molecular synthesis of molecular wires to bridge on-wire lithography (OWL)-fabricated nanogaps using the "click chemistry" method as demonstrated by Chen et al. [31]. With this *in situ* approach, the molecule length can be increased to bridge two electrodes. In comparison with the *in situ* molecular synthesis, the *in situ* measurement is also essentially important but faces the bigger challenges. For example, as a pioneer experiment, the IETS measurements were performed as molecules changed their conformations (cis–trans transition) when exposed to ultraviolet or visible light irradiation [32]. The IETS of cis and trans forms showed distinct vibrational fingerprints that can be used for identifying the isomers. However, due to the engineer technique limitation, this important experiment can only be performed *ex situ*, that is, the IETS measurement cannot be performed simultaneously with cis–trans transition. In order to fully understand the switch mechanism for cis–trans transition, the *in situ* IETS measurement is desired in the future. Also, due to the technique imitation, transmission electron microscopy (TEM) images for nanogaps were captured *ex situ* after the electromigration process occurred. It will be wonderful if one can continuously take the TEM images with high frequency (behavior like video recorder) and simultaneously measure the conductance, then the full mechanism for the quantized conductance change and the electron migration process will be cleared. Another challenge lies in obtaining a microscopic understanding of charge transport that involves reduction or oxidation of molecules in which the *in situ* measurements is especially important.

10.1.2 Device Fabrication Yield

Over the past several decades, a variety of innovative approaches have been developed to experimentally conduct charge-transport studies at the few-molecule level, and functional devices based on individual molecules have been demonstrated. However, most of the studies were performed with only a limited number of molecular devices. The device yield was notoriously poor primarily because of the top electrode's penetration through the molecular layer in a vertically structured metal–molecule–metal device structure or an inaccurate electrodes gap separation across the molecules in a horizontally structured metal–molecule–metal device structure. As mentioned previously, a few methods have been developed to improve the device yield significantly using a polymer interlayer, graphene film, or special metal layer (see Section 2.2.8). However, these high-yield device structures possess both advantages and disadvantages, and there is still a great need to seek a better technique to fabricate molecular devices at a high yield with good reliability and stability.

10.1.3 Device-to-Device Variation and Instability

Once the number of active molecules in the junction was reduced to a single molecule, the devices became extremely sensitive to the microscopic detail of their atomistic configuration and local environment, resulting in an increase in the variability of the "devices." To our knowledge, only a few experiments have demonstrated the ability to control the crucial atoms in the devices [33]. Even for assembled molecular devices, there is little control over the atomic-level structure of the metal–molecule interface, thus leading to an increase in the "uniqueness" of each sample [3]. Although individual labs have achieved acceptable yield and reproducibility, an agreed-upon standard junction that can serve as the starting point for correlating the junction structure with the electronic properties is still absent [2]. It is a tremendous challenge to generate such a standard junction facilitating the changes in the contacts, molecular components, geometry, and integration.

It is essentially important to create molecular devices with high stability. However, compared with the traditional semiconductor industry, there are additional factors resulting in the stability of molecular devices. Firstly, to align the Fermi energy with the molecular orbital to enable resonant transport in certain cases, it was necessary to apply several volts over a few nanometer junctions. This high electric field gradient may lead to non-equilibrium dynamic changes in the molecular structure [34] and the diffusion of metal atoms at the electrode surface [7]. Both the atomic movements and the molecular structural changes, including the bond fluctuation, will result in a notable junction-to-junction variability and a limited stability. Secondly, molecular devices are generally sensitive to the local environment, e.g. temperature, humidity, illumination, and electromagnetic field. The changes in each element may result in instability. Thirdly, laboratories typically use the SAM or L–B structures as the most common strategy to build the junctions. However, these structures involve several labile surface bonds so that they can evolve into a minimum-energy conformation. This process will also

lead to instability and the stochastic behavior of the electronic properties [2]. Finally, the most critical issue hindering the development of the stable devices is the nature of the molecule–electrode interface. Because both the charge injection and collection occur across the molecule–electrode interfaces, it is evident that the interfacial properties, such as the contact chemistry and the coupling strength between the molecules and the electrodes, play an important role in the electrical characteristics and stability of the molecular devices. Reliable approaches are greatly needed to develop robust molecular devices through a proper selection of electrode materials, anchoring groups, intramolecular connections, and external environments to precisely control the interfacial properties of the molecule–electrode interfaces.

10.1.4 Integration Capability

The ultimate goal for molecular electronics is to fabricate commercial devices and apply them to the daily life. Hence, it is inevitable for molecular electronic components to be integrated into modern microelectronics so that information can be easily read. Unfortunately, efficient integration strategies for bridging hard electronics with the vast store of the soft-molecular world are still lacking [4, 35]. Thus far, most of the measurements were conducted in ideal media at the laboratory level. The actual devices are far more complex and can definitely introduce a range of interfering and ruining effects. The development of fabricating parallel integrated junction arrays with specific functionalities in selective areas remains challenging [11]. For an efficient integration, the molecular components and processing should be compatible with existing fabrication techniques and conventional semiconductor structures, such as CMOS. In addition to integration, there are further challenges that need to be addressed. (i) The SAM and L–B structures are extremely fragile for practical devices in packaging [2]. To package single molecule devices, a clean environment and a gentle contact force are necessary to avoid contamination and damage. Taking this rigorous requirement into consideration, using an atomic layer deposition technology to bury the single molecule with dielectrics is one option for realization a practical device in the future [36]. (ii) Although a single molecule is relatively small, the electrodes for the outside connection and the readout are relatively large, which strongly limits the device integration simultaneously on possibly hundreds of chips per wafer. (iii) Today's silicon based chips used for information processing are operated at gigahertz frequencies, and the typical times of charge transport processes in molecules are in the femtosecond (fs) range [37]. Although the charge transport process in molecules is quite fast, it is challenging to operate molecular devices at gigahertz frequencies considering the high resistance and correspondingly the small currents of single molecule junctions. Therefore, the incompatibleness between silicon-based chips and molecular-based devices can be foreseen. (iv) In order to make a reproducible device, the integration process should be reversible, i.e. the devices should be able to be disassembled. Predictably, the next generation of electrical devices will be a network of interfaces where the molecules function as key elements to control the interface. Therefore, the challenge for integration remains significant.

10.1.5 Energy Consumption

For molecular devices to be widely used in the market, their energy consumption needs to be considered. It is expected that molecular devices can operate under low biases with minimum energy consumption. However, the contact resistance of the molecule–metal contacts (such as the Au–1,4-benzenedithiol–Au system) is in the range of 1–100 MΩ [38], which indicates that the molecules behave more like insulators rather than conductors, thus leading to a heavy energy consumption. Fortunately, there are at least three strategies that can be used to achieve an efficient molecule–metal coupling. (i) A highly efficient coupling can be achieved via simple direct C–Au σ bonding, in which the junction conductance is 100 times larger than that of most other terminations [39, 40]. This is a promising discovery for the efficient coupling of molecules to metals because it allows molecular devices to operate under significantly lower voltages. (ii) Graphene can be used instead of metals to achieve highly efficient coupling. Graphene is a remarkable material with extraordinary electronic properties, e.g. high mobility, high conductance, and stable covalent bonding with molecules. Additionally, the geometry of the graphene electrodes can be designed as a triangle to reduce the resistance of the electrodes themselves [23, 41]. (iii) Seeking new molecules with a high conductance and a low transport decay constant β. For typical cases, the resistance across the molecular junctions obeys an approximately exponential decay of the measured conductance with an increasing molecular length. When the metal Fermi energies are resonant with the relevant bridging states, electrons (or holes) can be injected directly into the bridging molecule, resulting in a weak distance dependence of the conductance corresponding to a small value of β. A case in point, Li et al. reported a quasi-ohmic single-molecule charge transport using highly conjugated molecule wires with the lowest β value ($\beta = 0.034\ \text{Å}^{-1}$) [42].

10.1.6 Addressability

Despite the considerable developments in nanofabrication, significant challenges remain, such as how to manufacture electrodes with a nanogap in large numbers and how to precisely and unambiguously graft the desired molecules into the gap electrodes [1]. More importantly, when thousands of junctions are integrated into one wafer, each junction should be addressable, thus making them more competitive. However, to our knowledge, there are only a few methods thus far possess the ability to address single-molecule junctions, as depicted in Table 2.1. One remaining challenge is to develop efficient methods to fabricate multiple single-molecule devices in a parallel way [43]. A way to achieve this goal would be to improve the resolution and decrease the feature sizes offered by the advanced nanofabrication techniques [44, 45]. Another possible approach might be the development of a molecular network using chemical synthesis and design to materialize large-scale single-molecule electronics.

10.1.7 General Strategies to Meet Challenges

Here, we try to offer several constructive suggestions to address the challenges in different aspects. Regarding the challenges for devices fabrication, one should try as best as possible to consider all the parameters as a holistic one. Due to a lack of precise control in the fabrication process, contact geometry, molecular conformation, exact number of molecules, and measurement condition, molecular electronics depicts heterogeneity and is still in its infancy despite significant developments achieved over the past decade. To fabricate reliable molecular devices, the electrode materials, molecular materials, contact interfaces, device fabrications, and experimental environments should be considered a whole because they are so closely interrelated and cannot be optimized independently. Consequently, developing a reliable and scalable fabrication methodology for mass producing identical molecular tunneling junction arrays in high yields by the holistic consideration of all of the parameters is a current research focus.

To promote a continuous development of molecular electronics, the combination of the newly development nanofabrication techniques, macro-techniques, various characterization techniques, and different techniques for data analysis will enable us to achieve new success. (i) Integrating different fabricated techniques. For example, a new technique was recently reported for molecular junction fabrication, known as the direct metal transfer method, which used the advantages of both the nanowell method and the nanotransfer printing method [46]. (ii) Combining the newly developed fabrication techniques with the classical characterization techniques. For example, if a gated mechanically controllable break junction (MCBJ) can be performed simultaneously using the TEM as a novel characterization technique, the gating mechanism can be clarified, and the new phenomenon may be observed. (iii) Application of the well-studied technique to novel materials. For instance, several groups reported on fabricating single-molecule junction using graphene electrodes by the lithographic and electrical breakdown methods [23, 47]. In principle, if one applies the MCBJ technique to precisely stretch graphene ribbons, graphene nanogaps with a tunable gape size can be obtained in high yield. (iv) Combining nanofabrication technique with a traditional controllable macro-technique. For example, the merger of the traditional terahertz technique and MCBJ technique, a new technique, may be developed to control the nanogap size via terahertz modulation based on bimaterial microcantilever [48].

To achieve a continuously rapid development of molecular electronics, the market motivation and its real application should be definitely taken into consideration. To obtain a strong support from enterprises in the market, we face two challenges: (i) a significantly enhanced function or cost advantage must be demonstrated before the traditional CMOS industry will consider a new technology and invest in it; and (ii) the traditional electronics industry will be reluctant to suffer radical changes in the highly sophisticated and extensive fabrication infrastructure to incorporate molecular components [2]. For the

former challenge, we had witnessed more and more novel functions in molecular devices, which are unavailable for traditional electronics. The small size of the molecules meets the needs in miniaturizing electronic devices, which is the principal driving force behind the semiconductor industry and has led to significant improvements in the computational power and energy efficiencies [49]. In view of the actual functional applications in the market, two-terminal devices, such as wires, rectifiers, and switches, and logic single-molecule devices, can be regarded as the most feasible routes toward practical molecular devices. At the same time, three-terminal molecular devices not only offer an experimental platform to study electronics but also pave the road to realize fast market applications beyond the laboratory research. Hence, it is highly desirable to make a first breakthrough in market applications using a molecular transistor, e.g. digital circuits based on molecular transistors. For the latter challenge, we should demonstrate the priority of the compatibility with the traditional industry when a molecular device is fabricated. Despite the rapid development of molecular electronics in past decades, it is still a long way to win the battle in the pure market.

10.2 Open Questions

Several open questions remain, which contend and contradict each other, even in the basic field of electron transport. For example, regarding the observation of the discrete conductance change during the separation of the two nanoscale electrodes, one opinion is that the rearrangement of metal atoms results in the discrete conductance, and G_0 corresponds to the single gold atom conductance [50]. However, another opinion claimed that the underneath quantum mechanism is responsible for the discrete conductance change, and G_0 corresponds to a small size of point contacts (few atomic diameter width comparable with the conduction electrons' Fermi wavelength) rather than a single gold atom [51]. Each of the opinions has solid evidence to support its claims, resulting in a remaining question. The relationship between the molecular structure and inner-molecule quantum interference has not yet achieved a standard answer also. Vazquez et al. demonstrated that the conductance of a double-backbone molecular junction can be more than twice that of a single-backbone junction, providing clear evidence for constructive interference [52]. At the same time, Guedon et al. demonstrated that the electron can transport through two different pathways via unaligned localized molecular orbitals, thus yielding a destructive partial wave interference and poor conductance of the molecules [53]. Thus far, there are only individual cases instead of systematical investigations and a general model to relate the molecular structure with the type of the interference. The similar awkward situation also exists for intermolecular interactions. A few groups reported that parallel molecular wires are not strongly coupled along their molecular backbone and thus can be thought as individual conductance channels [54]. However, certain groups pointed out that the intermolecular tunneling is quite important

in the electron transport process and may lead to a considerable enhancement of the tunneling current [55]. To clarify this argument, it is important to realize junctions that provide a transition from single molecule experiments to 2D multi-molecule junctions, which would allow the influence of the intermolecular electron transport of the adjacent molecules and a dephasing of the coherent electron transport to be studied [56].

We noted that several functional devices well-fabricated in the traditional semiconductor industry have no counterpart in molecular electronics, such as commercial resonant tunneling diodes, which are easily realized in the traditional semiconductor domain. Due to the coupling of the molecule–metal and the temperature effects, the discrete energy level of the molecules is broad, resulting in an inexact energy alignment during the voltage sweeping process. Hence, it is difficult to realize molecular resonant tunneling diodes (MRTDs), especially at room temperature. There may be two strategies to address this untouched field. (i) Using Si–molecule–Si junctions to realize the MRTD since the silicon, unlike metal electrodes, has a forbidden energy gap between the conduction band and the valence band. When the molecular orbital level falls into the forbidden band of silicon during bias sweeping, a sharp decrease occurs in the tunneling current, thus facilitating the achievement of the MRTD. (ii) Employing graphene as electrodes to realize the MRTD because the special Dirac-cone energy structure and a non-zero bandgap of graphene can be easily obtained via hybrid graphene or applying a gating voltage [57].

In this book, the topic mainly involves molecular-scale electronics, with a particular focus on single-molecule electronics. Numerous topics, which are related to molecular electronics, are not addressed in this book due to our limited knowledge. For example, bulk organic molecules are interesting materials because of their structures and their electronic, electrical, magnetic, optical, biological, and chemical properties. Functional conjugated organic molecules with structural features have been assembled into the nanostructures, and several organic molecules have been applied in the market [58]. Large-area devices containing thin films of molecular materials represent the ultimate scaling of flexible devices based on organic materials. Several significant results of flexible molecular-scale electronic devices for insulating molecules, rectifying molecules, and photoswitching molecules have been reported using polyimide as the flexible substrate [59–61]. The potential of molecule-based nanotechnology for energy related applications is enormous. For example, two-terminal molecular junctions have potential applications in terahertz rectification for energy harvesting, which has real-world frequency limitations for traditional devices [62]. Nanomaterials can address several unmet needs in energy applications: they can be used to improve energy densities, promote energy efficiencies, increase energy transfer rates, and increase stabilities. Within the field of nanotechnology, new material development will play an important role toward a sustainable energy future but also meet tremendous challenges. However, these interesting topics are mostly beyond the scope of this book.

10.3 Outlook

The ultimate limit for electronic device minimization is controlling the building blocks with atomic accuracy. Only molecules can provide such precise control over sub-nanometer distances as well as the possibility to reproducibly fabricate identical building blocks. Therefore, molecular electronics may be the only option to overcome the bottleneck of semiconductor-based technologies. Although it appears that molecular-based electronics will not replace most of the silicon-based electronics, there are convincing reasons to believe that molecular electronic devices can complement silicon-based devices by providing small dimensions of the molecules and new functionalities beyond the scope of conventional solid-state devices [63].

The first decade of experimental and theoretical research on molecular electronics exhibited both rapid growth and significant scientific achievement. Molecular electronics has become one of the fastest growing fields and has brought scientists and engineers from different disciplines together. However, in certain cases, the strong enthusiasm for rapid exploration of a new area works against the requirement for a careful and systematic science, which is essential in the microelectronics industry. Until now, we have not yet reached a consensus on a robust and reproducible junction fabrication, and it is a long way to reach very high yield fabrication, highly integrated, and wide market application [2].

From the market's point of view, carbon-based architectures with multiple junctions may provide a more robust platform for laboratory research and help validate molecular electronic concepts for room-temperature operation, potentially providing a wider application in the future. According to the sophistication level of the technologies, we may first achieve the market breakthrough in molecule-based chemo/biosensors, as previously demonstrated, and then move to realize molecule-based digital circuits for future information processing. For a wide application of general molecular electronics, it is expected that more chemical tools and building blocks provided by a huge molecular structural and functional variety are needed. It is desirable that using designed molecules, which can be either (i) linked together, where each molecule performs a different function, such as rectification/switching so that logical operations can be performed in a "single" molecule junction, or (ii) conformational changes triggered by external stimuli (magnetic, optical, and chemical), leads to a tremendous change in the junction current. These conformational changes can be used to unlock a security junction, which requires a "chemical key."

As single-molecule researches continue to grow, another aspect becoming increasingly important is the theoretical calculation. Side-by-side use of the molecular calculation theory and simulations is equally important for a better understanding of the molecular system, and therefore verify and even guide molecular experiments [11]. We expect that molecular-scale electronics will foster truly excellent collaboration in bringing chemistry, physics, materials, engineers, and biology together, in return promoting the rapid development of this field. We have enough reason to believe that molecular-scale electronics has a bright future for bridging hard electronics to the soft molecular world.

References

1 Li, Z.Y., Li, B., Yang, J.L. et al. (2010). Single-molecule chemistry of metal phthalocyanine on noble metal surfaces. *Acc. Chem. Res.* 43: 954–962.
2 McCreery, R.L. and Bergren, A.J. (2009). Progress with molecular electronic junctions: Meeting experimental challenges in design and fabrication. *Adv. Mater.* 21: 4303–4322.
3 Moth-Poulsen, K. and Bjornholm, T. (2009). Molecular electronics with single molecules in solid-state devices. *Nat. Nanotechnol.* 4: 551–556.
4 Shen, Q., Guo, X.F., Steigerwald, M.L. et al. (2010). Integrating reaction chemistry into molecular electronic devices. *Chem. Asian J.* 5: 1040–1057.
5 Aradhya, S.V. and Venkataraman, L. (2013). Single-molecule junctions beyond electronic transport. *Nat. Nanotechnol.* 8: 399–410.
6 Chang, S., Sen, S.M., Zhang, P.M. et al. (2012). Palladium electrodes for molecular tunnel junctions. *Nanotechnology* 23: 425202.
7 Xiang, D., Lee, T., Kim, Y. et al. (2014). Origin of discrete current fluctuations in a single molecule junction. *Nanoscale* 6: 13396–13401.
8 Song, L., Guo, X.F. et al. (2013). Functional single-walled carbon nanotube-based molecular devices. *Acta Chim. Sinica* 71: 478–484.
9 Ramachandran, G.K., Hopson, T.J., Rawlett, A.M. et al. (2003). A bond-fluctuation mechanism for stochastic switching in wired molecules. *Science* 300: 1413–1416.
10 Jia, C.C., Ma, B.J., Xin, N. et al. (2015). Carbon electrode–molecule junctions: a reliable platform for molecular electronics. *Acc. Chem. Res.* 48: 2565–2575.
11 Guo, X.F. (2013). Single-molecule electrical biosensors based on single-walled carbon nanotubes. *Adv. Mater.* 25: 3397–3408.
12 He, Y., Dong, H., Li, T. et al. (2010). Graphene and graphene oxide nanogap electrodes fabricated by atomic force microscopy nanolithography. *Appl. Phys. Lett.* 97: 133301.
13 Campos, L.C., Manfrinato, V.R., Sanchez-Yamagishi, J.D. et al. (2009). Anisotropic etching and nanoribbon formation in single-layer graphene. *Nano Lett.* 9: 2600–2604.
14 Borrnert, F., Fu, L., Gorantla, S. et al. (2012). Programmable sub-nanometer sculpting of graphene with electron beams. *ACS Nano* 6: 10327–10334.
15 Zandvliet, H.J. and van Houselt, A. (2009). Scanning tunneling spectroscopy. *Annu. Rev. Anal. Chem.* 2: 37–55.
16 Sedghi, G., Esdaile, L.J., Anderson, H.L. et al. (2012). Comparison of the conductance of three types of porphyrin-based molecular wires: β,meso, β-fused tapes, meso-butadiyne-linked and twisted meso-meso linked oligomers. *Adv. Mater.* 24: 653–657.
17 Wang, H.M., Zheng, Z., Wang, Y.Y. et al. (2010). Fabrication of graphene nanogap with crystallographically matching edges and its electron emission properties. *Appl. Phys. Lett.* 96: 023106.
18 Kim, B., Choi, S.H., Zhu, X.Y. et al. (2011). Molecular tunnel junctions based on π-conjugated oligoacene thiols and dithiols between Ag, Au, and Pt contacts: effect of surface linking group and metal work function. *J. Am. Chem. Soc.* 133: 19864–19877.

19 Galperin, M., Nitzan, A., and Ratner, M.A. (2006). Inelastic tunneling effects on noise properties of molecular junctions. *Phys. Rev. B* 74: 075326.

20 Jia, C.C., Wang, J.Y., Yao, C.J. et al. (2013). Conductance switching and mechanisms in single-molecule junctions. *Angew. Chem. Int. Ed.* 52: 8666–8670.

21 Whalley, A.C., Steigerwald, M.L., Guo, X.F. et al. (2007). Reversible switching in molecular electronic devices. *J. Am. Chem. Soc.* 129: 12590–12591.

22 Jia, C.C., Li, H., Jiang, J.L. et al. (2013). Interface-engineered bistable [2]rotaxane-graphene hybrids with logic capabilities. *Adv. Mater.* 25: 6752–6759.

23 Cao, Y., Dong, S.H., Liu, S. et al. (2013). Toward functional molecular devices based on graphene–molecule junctions. *Angew. Chem. Int. Ed.* 125: 3998–4002.

24 Cao, Y., Wei, Z.M., Liu, S. et al. (2010). High-performance Langmuir–Blodgett monolayer transistors with high responsivity. *Angew. Chem. Int. Ed.* 49: 6319–6323.

25 Wang, X.L., Gao, L., Liang, B. et al. (2015). Revealing the direct effect of individual intercalations on DNA conductance toward single-molecule electrical biodetection. *J. Mater. Chem. B* 3: 5150–5154.

26 Chiechi, R.C., Weiss, E.A., Dickey, M.D. et al. (2008). Eutectic gallium–indium (EGaIn): A moldable liquid metal for electrical characterization of self-assembled monolayers. *Angew. Chem. Int. Ed.* 47: 142–144.

27 Tao, N.J. (2006). Electron transport in molecular junctions. *Nat. Nanotechnol.* 1: 173–181.

28 Kim, B., Beebe, J.M., Jun, Y. et al. (2006). Correlation between HOMO alignment and contact resistance in molecular junctions: aromatic thiols versus aromatic isocyanides. *J. Am. Chem. Soc.* 128: 4970–4971.

29 Lefenfeldt, M., Baumert, J., Sloutskin, E. et al. (2006). Direct structural observation of a molecular junction by high-energy x-ray reflectometry. *Proc. Natl. Acad. Sci. U. S. A.* 103: 2541–2545.

30 McCreery, R.L. (2006). Analytical challenges in molecular electronics. *Anal. Chem.* 78: 3490–3497.

31 Chen, X.D., Braunschweig, A.B., Wiester, M.J. et al. (2009). Spectroscopic tracking of molecular transport junctions generated by using click chemistry. *Angew. Chem. Int. Ed.* 48: 5178–5181.

32 Kim, Y., Garcia-Lekue, A., Sysoiev, D. et al. (2012). Charge transport in azobenzene-based single-molecule junctions. *Phys. Rev. Lett.* 109: 226801.

33 Schirm, C., Matt, M., Pauly, F. et al. (2013). A current-driven single-atom memory. *Nat. Nanotechnol.* 8: 645–648.

34 Xiang, D., Sydoruk, V., Vitusevich, S. et al. (2015). Noise characterization of metal-single molecule contacts. *Appl. Phys. Lett.* 106: 063702.

35 Yu, X., Lovrincic, R., Kraynis, O. et al. (2014). Fabrication of reproducible, integration-compatible hybrid molecular/Si electronics. *Small* 10: 5151–5160.

36 Javey, A., Kim, H., Brink, M. et al. (2002). High-kappa dielectrics for advanced carbon-nanotube transistors and logic gates. *Nat. Mater.* 1: 241–246.

37 Nitzan, A. (2001). Electron transmission through molecules and molecular interfaces. *Annu. Rev. Phys. Chem.* 52: 681–750.

38 Kim, Y., Pietsch, T., Erbe, A. et al. (2011). Benzenedithiol: A broad-range single-channel molecular conductor. *Nano Lett.* 11: 3734–3738.

39 Cheng, Z.L., Skouta, R., Vazquez, H. et al. (2011). *In situ* formation of highly conducting covalent Au–C contacts for single-molecule junctions. *Nat. Nanotechnol.* 6: 353–357.

40 Scholz, F., Kaletova, E., Stensrud, E.S. et al. (2013). Formation of *n*-alkyl mono layers by organomercury deposition on gold. *J. Phys. Chem. Lett.* 4: 2624–2629.

41 Cao, Y., Dong, S.H., Liu, S. et al. (2012). Building high-throughput molecular junctions using indented graphene point contacts. *Angew. Chem. Int. Ed.* 51: 12228–12389.

42 Li, Z.H., Park, T.H., Rawson, J. et al. (2012). Quasi-ohmic single molecule charge transport through highly conjugated meso-to-meso ethyne-bridged porphyrin wires. *Nano Lett.* 12: 2722–2727.

43 Nitzan, A. and Ratner, M.A. (2003). Electron transport in molecular wire junctions. *Science* 300: 1384–1389.

44 Song, H., Kim, Y., Jang, Y.H. et al. (2009). Observation of molecular orbital gating. *Nature* 462: 1039–1043.

45 Jia, C.C. and Guo, X.F. (2013). Molecule–electrode interfaces in molecular electronic devices. *Chem. Soc. Rev.* 42: 5642–5660.

46 Jeong, H., Kim, D., Kim, P. et al. (2015). A new approach for high-yield metal–molecule–metal junctions by direct metal transfer method. *Nanotechnology* 26: 025601.

47 Nef, C., Posa, L., Makk, P. et al. (2014). High-yield fabrication of nm-size gaps in monolayer CVD graphene. *Nanoscale* 6: 7249–7254.

48 Gong, C., Zhao, Y.J., Dong, L.Q. et al. (2013). The tolerable target temperature for bimaterial microcantilever array infrared imaging. *Opt. Laser Technol.* 45: 545–550.

49 Shulaker, M.M., Hills, G., Patil, N. et al. (2013). Carbon nanotube computer. *Nature* 501: 526–530.

50 Yanson, A.I., Bollinger, G.R., van den Brom, H.E. et al. (1998). Formation and manipulation of a metallic wire of single gold atoms. *Nature* 395: 783–785.

51 Ohnishi, H., Kondo, Y., and Takayanagi, K. (1998). Quantized conductance through individual rows of suspended gold atoms. *Nature* 395: 780–783.

52 Vazquez, H., Skouta, R., Schneebeli, S. et al. (2012). Probing the conductance superposition law in single-molecule circuits with parallel paths. *Nat. Nanotechnol.* 7: 663–667.

53 Guedon, C.M., Valkenier, H., Markussen, T. et al. (2012). Observation of quantum interference in molecular charge transport. *Nat. Nanotechnol.* 7: 304–309.

54 Kushmerick, J.G., Naciri, J., Yang, J.C. et al. (2003). Conductance scaling of molecular wires in parallel. *Nano Lett.* 3: 897–900.

55 Song, H., Lee, H., and Lee, T. (2007). Intermolecular chain-to-chain tunneling in metal-alkanethiol-metal junctions. *J. Am. Chem. Soc.* 129: 3806–3807.

56 Dubi, Y. (2014). Transport through self-assembled monolayer molecular junctions: Role of in-plane dephasing. *J. Phys. Chem. C* 118: 21119–21127.

57 Xu, H., Chen, Y.B., Xu, W.G. et al. (2011). Modulating the charge-transfer enhancement in GERS using an electrical field under vacuum and an n/p-doping atmosphere. *Small* 7: 2945–2952.
58 Liu, H.B., Xu, J.L., Li, Y. et al. (2010). Aggregate nanostructures of organic molecular materials. *Acc. Chem. Res.* 43: 1496–1508.
59 Park, S., Wang, G., Cho, B. et al. (2012). Flexible molecular-scale electronic devices. *Nat. Nanotechnol.* 7: 438–442.
60 Jeong, H., Kim, D., Wang, G. et al. (2014). Redox-induced asymmetric electrical characteristics of ferrocene-alkanethiolate molecular devices on rigid and flexible substrates. *Adv. Funct. Mater.* 24: 2472–2480.
61 Kim, D., Jeong, H., Lee, H. et al. (2014). Flexible molecular-scale electronic devices composed of diarylethene photoswitching molecules. *Adv. Mater.* 26: 3968–3973.
62 Celestin, M., Krishnan, S., Bhansali, S. et al. (2014). A review of self-assembled monolayers as potential terahertz frequency tunnel diodes. *Nano Res.* 7: 589–625.
63 Son, J.Y. and Song, H. (2013). Molecular scale electronic devices using single molecules and molecular monolayers. *Curr. Appl. Phys.* 13: 1157–1171.

Index

Molecular-Scale Electronics: Concept, Fabrication and Applications,
First Edition. Xuefeng Guo, Dong Xiang, and Yu Li.

d

n